DECLASSIFIED [redacted]

COPY 586

N-35667

NATIONAL ADVISORY COMMITTEE
FOR AERONAUTICS

NACA CONFERENCE ON AIRCRAFT LOADS, FLUTTER, AND STRUCTURES

A COMPILATION OF THE PAPERS PRESENTED

Langley Aeronautical Laboratory
Langley Field, Virginia

March 2-4, 1955

DECLASSIFIED- AUTHORITY
US: 1286 DROBKA TO LEBOW
MEMO DATED
6/8/66

GPO PRICE $ ____________

CFSTI PRICE(S) $ ____________

Hard copy (HC) 4.36

Microfiche (MF) 3.00

ff 653 July 65

NACA

Declassified by authority of NASA
Classification Change Notices No. 67
Dated **6/29/66

[redacted]

FACILITY FORM 602

N66 33351 (ACCESSION NUMBER)

(THRU)

586 (PAGES)

1 (CODE)

TMX 57821 (NASA CR OR TMX OR AD NUMBER)

32 (CATEGORY)

[redacted]

U

DECLASSIFIED

[redacted]

NACA CONFERENCE ON
AIRCRAFT LOADS, FLUTTER, AND STRUCTURES

A Compilation of the Papers Presented

Langley Aeronautical Laboratory
Langley Field, Va.

March 2-4, 1955

[redacted]

[redacted]

TABLE OF CONTENTS

INTRODUCTION

LIST OF CONFEREES

TECHNICAL PAPERS PRESENTED

LOADS AND LOAD DISTRIBUTION

Session Chairman: Philip Donely

Critical Loading Conditions

Recent Stability and Aerodynamic Problems and Their Implications as to Load Estimation . . . by Charles H. Zimmerman

Flight Experience of Inertia Coupling in Rolling Maneuvers . . . by Joseph Weil, Ordway B. Gates, Jr., Richard D. Banner, and Albert E. Kuhl

A Study of Means for Rationalizing Airplane Design Loads . . . by John P. Mayer and Harold A. Hamer

Loads on Lifting Surfaces and Bodies

Load Distributions on Wings and Wing-Body Combinations at High Angles of Attack and Supersonic Speeds . . . by Elliott D. Katzen and William C. Pitts

Loads on Thin Wings at Transonic Speeds . . . by Don D. Davis, Jr., and Gerald Hieser

Effect of Body Indentation on Body Loads and the Division of Loads at Transonic Speeds . . . by Thomas C. Kelly

Some Results From Load and Deflection Measurements on the Boeing B-47 Airplane . . . by Paul W. Harper and Alton P. Mayo

Comparison of Calculated and Experimental Span-Load Distribution on Wings up to M = 1.0 . . . by John L. Crigler

Loads on External Stores at Transonic and Supersonic Speeds . . . by Lawrence D. Guy

[redacted]

[redacted]

Effects of Wing-Fuselage Flow Fields on Missile Loads at Subsonic Speeds . . . by William J. Alford, Jr.

Some Effects of Configuration Variables on Store Loads at Supersonic Speeds . . . by Norman F. Smith and Harry W. Carlson

An Investigation of Jet Effects on Adjacent Surfaces . . . by Walter E. Bressette and Maxime A. Faget

Loads on Stabilizing and Control Surfaces

An Investigation of Loads on Ailerons at Transonic Speeds . . . by Jack F. Runckel and W. H. Gray

Simplified Procedures for Estimating Flap-Control Loads at Supersonic Speeds . . . by K. R. Czarnecki and Douglas R. Lord

Loads on Wings Due to Spoilers at Subsonic and Transonic Speeds . . . by Alexander D. Hammond

Loads Associated With Spoilers at Supersonic Speeds . . . by Douglas R. Lord and K. R. Czarnecki

Some Interference Effects That Influence Vertical-Tail Loads at Supersonic Speeds . . . by S. Sherman Edwards

A Discussion of Recent Wind-Tunnel Studies Relating to the Problem of Estimating Vertical- and Horizontal-Tail Loads . . . by Richard E. Kuhn, Joseph M. Hallissy, Jr., and Ralph W. Stone, Jr.

Gust Loads

A Reevaluation of Gust-Load Statistics for Applications in Spectral Calculations . . . by Harry Press

A Discussion of Gust Loads as Influenced by the Stability of the Airplane . . . by Clarence L. Gillis

Ground and Water Loads

Reduction of Hydrodynamic Impact Loads for Waterborne Aircraft . . . by Emanuel Schnitzer

Landing Conditions for Large Airplanes in Routine Operations . . . by Norman S. Silsby and Eziaslav N. Harrin

Vertical and Drag Ground-Reaction Forces Developed in Landing Impacts of a Large Airplane . . . by Richard H. Sawyer

[redacted]

[redacted]

On Spectral Analysis of Runway Roughness and Loads Developed During Taxiing . . . by John C. Houbolt, James H. Walls, and Robert F. Smiley

FLUTTER AND BUFFETING

Session Chairman: I. E. Garrick

Buffeting and Acoustic Excitation

A Study of the Correlation Between Flight and Wind-Tunnel Buffeting Loads . . . by Wilber B. Huston, A. Gerald Rainey, and Thomas F. Baker

A Study of the Response of Panels to Random Acoustic Excitation . . . by Robert W. Hess, Leslie W. Lassiter, and Harvey H. Hubbard

Oscillating Air Forces

Recent Results of the Calculation of Aerodynamic Loading and Flutter of Several Wings at Subsonic and Sonic Speeds . . . by Harry L. Runyan and Donald S. Woolston

Some Recent Experimental Data on Three-Dimensional Oscillating Air Forces . . . by Sumner A. Leadbetter and Sherman A. Clevenson

Exploratory Investigation of the Moments on Oscillating Control Surfaces at Transonic Speeds . . . by Dennis J. Martin, Robert F. Thompson, and C. William Martz

A Study of the Fluctuating Loads on Oscillating Airfoils in Supercritical Flow . . . by John A. Wyss

Wing Flutter

Flutter Characteristics of Swept Wings at Transonic Speeds . . . by Laurence K. Loftin, Jr.

Experimental Flutter Results for Cantilever-Wing Models at Mach Numbers up to 3.0 . . . by W. J. Tuovila and John Locke McCarty

An Investigation of the Effects of System Nonlinearities in the Problem of Aircraft Flutter . . . by Donald S. Woolston, Harry L. Runyan, and Thomas A. Byrdsong

Some Effects of Fluid in Pylon-Mounted Tanks on Flutter . . . by James R. Reese

[redacted]

[redacted]

Panel Flutter

Experimental and Theoretical Studies of Panel Flutter . . . by Maurice A. Sylvester, Herbert C. Nelson, and Herbert J. Cunningham

STRUCTURES

Session Chairman: John E. Duberg

Introductory Remarks on the Structural Effects of Aerodynamic Heating . . . by John E. Duberg

Aerodynamic Heating

A Discussion of Methods for Reducing Aerodynamic Heating in Supersonic Flight . . . by A. J. Eggers, Jr.

Aerodynamic Heating of Rocket-Powered Research Vehicles at Hypersonic Speeds . . . by Robert O. Piland

Structures at Elevated Temperatures

Tensile Properties of Some Sheet Materials Under Rapid-Heating Conditions . . . by George J. Heimerl and John E. Inge

Preliminary Investigation of the Compressive Strength and Creep Lifetime of 2024-T3 (Formerly 24S-T3) Aluminum-Alloy Plates at Elevated Temperatures . . . by Eldon E. Mathauser and William D. Deveikis

Some Effects of Rapid Heating on Box Beams . . . by Richard A. Pride and L. Ross Levin

Behavior of a Cantilever Plate Under Rapid-Heating Conditions . . . by Louis F. Vosteen and Kenneth E. Fuller

Some Design Implications of the Effects of Aerodynamic Heating . . . by Richard R. Heldenfels

Stresses and Deflection

Summary of Recent Theoretical and Experimental Work on Box-Beam Vibrations . . . by John M. Hedgepeth

Comparison Between Theoretical and Experimental Stresses in Circular Semimonocoque Cylinders With Rectangular Cutouts . . . by Harvey G. McComb, Jr., and Emmet F. Low, Jr.

[redacted]

DECLASSIFIED

[redacted]

Deflection Analysis of Low-Aspect-Ratio Wings . . . by J. Lyell Sanders, Jr., and Manuel Stein

Experimental Analysis of Multicell Wings by Means of Plastic Models . . . by George W. Zender

Strength

Effect of Riveted-Joint Geometry on Strength of Stiffened Plates in Compression . . . by James P. Peterson and Joseph W. Semonian

Minimum-Weight Structures for Wings of Given Strength and Stiffness . . . by B. Walter Rosen and Roger A. Anderson

Fatigue Failures

Some Observation on Loss of Static Strength Due to Fatigue Cracks . . . by Walter Illg and Herbert F. Hardrath

Preliminary Investigation of the Failure of Pressurized Stiffened Cylinders . . . by Norris F. Dow and Roger W. Peters

[redacted]

INTRODUCTION

This document contains reproductions of technical papers on some of the most recent research results on aircraft loads, flutter, and structures from the NACA Laboratories. These papers were presented by members of the staff of the NACA Laboratories at the NACA Conference held at the Langley Aeronautical Laboratory March 2-4, 1955. The primary purpose of this conference was to convey to contractors of the military services and others concerned with the design of aircraft these recent research results and to provide those attending an opportunity to discuss the results.

The papers in this document are in the same form in which they were presented at the conference in order to facilitate their prompt distribution. The original presentation and this record are considered as complementary to, rather than as substitutes for, the Committee's more complete and formal reports. Accordingly, if information from this document is utilized it is requested that this document not be listed as a reference.

A list of the conferees is included.

[redacted]

LIST OF CONFEREES

The following were registered at the NACA Conference on Aircraft Loads, Flutter, and Structures, Langley Aeronautical Laboratory, Langley Field, Va., March 2-4, 1955:

ABBOTT, Ira H.	NACA Headquarters
ABBOTT, Col. Nathan M.	Tactical Air Command
ALFORD, William J., Jr.	NACA - Langley Laboratory
AMES, Milton B.	NACA Headquarters
ANDERSON, Arnold Windsor	David Taylor Model Basin
ANDERSON, Roger A.	NACA - Langley Laboratory
ANDREWS, Chris W.	Douglas Aircraft Company
ASHLEY, Prof. Holt	Subcommittee on Vibration and Flutter
AULT, G. Mervin	NACA - Lewis Laboratory
BAILEY, Frederick J.	NACA - Langley Laboratory
BAIRD, Eugene F.	Submittee on Vibration and Flutter
BAIRD, Richard B.	Wright Air Development Center
BAKER, Paul	Republic Aviation Corporation
BAKER, Thomas F.	NACA High-Speed Flight Station
BAMBER, Millard John	David Taylor Model Basin
BANK, Herman	Jet Propulsion Laboratory, C.I.T.
BANNER, Richard D.	NACA High-Speed Flight Station
BARLOW, Cecil B.	Boeing Airplane Company
BARNES, John C.	North American Aviation
BARTON, Dr. Millard V.	Air Research and Development Command
BAUM, Clete P.	Bureau of Aeronautics
BECHT, John J.	Lockheed Aircraft Corporation
BECK, Edgar B.	NACA Headquarters
BECKER, John V.	NACA - Langley Laboratory
BEELER, De E.	NACA High-Speed Flight Station
BEZBATCHENKO, John W.	Goodyear Aircraft Corporation
BIESEMEIER, Clark F.	Civil Aeronautics Administration
BLEICH, Prof. Hans H.	Columbia University
BOCCIUS, Walter G. C.	Wright Air Development Center
BOGERT, George D.	Civil Aeronautics Administration
BOUTON, Innes	Northrop Aircraft
BOWMAN, John C.	Ryan Aeronautical Company
BOWMAN, Richard	Republic Aviation Corporation
BOZAJIAN, John M.	Hughes Aircraft Company
BREMER, Paul H.	Lockheed Aircraft Corporation
BRESSETTE, Walter E.	NACA - Langley Laboratory
BREUER, Delmar W.	USAF Institute of Technology
BROOKS, Philip D.	Northrop Aircraft
BROWN, Harvey H.	NACA Headquarters

[redacted]

BRULLE, Capt. Robert V.	USAF Institute of Technology
BRYAN, Guy L.	Johns Hopkins University
BUCKLEY, Edmond C.	NACA - Langley Laboratory
BURRIDGE, James L.	Glenn L. Martin Company
BUTERBAUGH, Floyd F.	Naval Air Development Center
BYRDSONG, Thomas A.	NACA - Langley Laboratory
CALHOUN, John Thompson	Beech Aircraft Corporation
CAMERON, Capt. Burton G.	Wright Air Development Center
CARL, Robert A.	Bureau of Aeronautics
CARLSON, Harry W.	NACA - Langley Laboratory
CARPENTER, James E.	Cornell Aeronautical Laboratory
CARTA, Franklin O.	United Aircraft Corporation
CARTER, Maj. David L.	Air Research and Development Command
CELNIKER, Leo	Lockheed Aircraft Corporation
CHAMBERLIN, Robert B.	General Electric Company
CHAPEK, Henry Lee	Cessna Aircraft Company
CHARAK, Mason T.	NACA Headquarters
CLAY, 2d Lt. James T.	Wright Air Development Center
CLEVENSON, Sherman A.	NACA - Langley Laboratory
COLLINS, Ivey K.	Strategic Air Command
COOK, Frederick G.	British Joint Services Mission
COX, Lt. Comdr. D. W.	U. S. Naval Air Test Center
CREEL, Ralph L.	Subcommittee on Aircraft Structures
CRIGLER, John L.	NACA - Langley Laboratory
CROWLEY, John W.	NACA Headquarters
CUNNINGHAM, Herbert J.	NACA - Langley Laboratory
CZARNECKI, K. R.	NACA - Langley Laboratory
DAVIS, Don D., Jr.	NACA - Langley Laboratory
DECKER, James	Glenn L. Martin Company
DeMERITTE, Frederick J.	Naval Ordnance Laboratory
DIEHL, Capt. W. S., USN (Ret.)	Committee on Aerodynamics
DIX, Edgar H., Jr.	Subcommittee on Aircraft Structural Materials
DOIG, Leroy L., Jr.	U. S. Naval Ordnance Test Station, Inyokern
DONELY, Philip	NACA - Langley Laboratory
DONLAN, Charles J.	NACA - Langley Laboratory
DONNELLAN, William G.	Lockheed Aircraft Corporation
DOTY, Ralph J., Jr.	Boeing Airplane Company
DOUGHERTY, James E., Jr.	Subcommittee on Aircraft Structural Materials
DOW, Norris F.	NACA - Langley Laboratory
DRALEY, Eugene C.	NACA - Langley Laboratory
DRINKWATER, William D.	U. S. Naval Ordnance Test Station, Inyokern

DRYDEN, Dr. Hugh L.	NACA Headquarters
DUBERG, John E.	NACA - Langley Laboratory
DUKE, William M.	Subcommittee on Aircraft Loads
DUNN, Maurice B.	Boeing Airplane Company
EDWARDS, S. Sherman	NACA - Ames Laboratory
EGBERT, Douglas T.	Northrop Aircraft
EGGERS, A. J., Jr.	NACA - Ames Laboratory
EPSTEIN, Albert	Republic Aviation Corporation
FAGET, Maxime A.	NACA - Langley Laboratory
FEDENIA, John N.	Naval Ordnance Laboratory
FEDZIUK, Henry A.	NACA - Langley Laboratory
FETTIS, Henry E.	Wright Air Development Center
FORBRAGD, Maj. M. H.	Wright Air Development Center
FRANCESCHI, Renzo	Raytheon Manufacturing Company
FRANKLAND, Dr. J. M.	Subcommittee on Vibration and Flutter
FRENCH, Maj. Philip M.	Ballistic Research Laboratory
FRIEDMAN, Richard	Naval Air Material Center
FUHRMAN, Robert A.	Ryan Aeronautical Company
FULLER, Kenneth E.	NACA - Langley Laboratory
FUNG, Dr. Yuan-Cheng	Ramo-Wooldridge Corporation
GARRICK, I. E.	NACA - Langley Laboratory
GATEWOOD, Dr. Buford E.	USAF Institute of Technology
GEARY, Richard H.	Military Air Transport Service
GILLIS, Clarence L.	NACA - Langley Laboratory
GILRUTH, Robert R.	NACA - Langley Laboratory
GILSON, Robert D.	Fairchild Engine and Airplane Corp.
GILSTAD, Douglas A.	Subcommittee on Aircraft Loads
GOLDIN, Robert	Bell Aircraft Corporation
GOPPERT, Maj. J. G.	AF Development Field Representative, NACA, Langley Field, Va.
GORANSON, R. Fabian	NACA Headquarters
GORDON, Samuel A.	Battelle Memorial Institute
GOTT, Richard	Bureau of Ordnance
GOUGH, Melvin N.	NACA - Langley Laboratory
GRAY, Edward Z.	Boeing Airplane Company
GRAY, W. H.	NACA - Langley Laboratory
GREEN, G. Garner	Subcommittee on Aircraft Structures
GUY, Lawrence D.	NACA - Langley Laboratory
HALL, Bertrand M.	Douglas Aircraft Company
HALL, Lt. Col. James N.	Aeronautical Division, Director of Research and Development, USAF
HALLISSY, Joseph M., Jr.	NACA - Langley Laboratory
HAMMOND, Alexander D.	NACA - Langley Laboratory
HAMSHER, John W.	North American Aviation

[redacted]

HANJIAN, Capt. Jerry	Strategic Air Command
HARDESTY, Prentice R.	Glenn L. Martin Company
HARDRATH, Herbert F.	NACA - Langley Laboratory
HARPER, Paul W.	NACA - Langley Laboratory
HARPOOTHIAN, Edward	Douglas Aircraft Company
HARRIN, Eziaslav N.	NACA - Langley Laboratory
HARRINGTON, Joseph H.	Subcommittee on Aircraft Loads
HARRIS, Thomas A.	NACA - Langley Laboratory
HARRIS, William Henry	Civil Aeronautics Administration
HEDGEPETH, John M.	NACA - Langley Laboratory
HEIMERL, George J.	NACA - Langley Laboratory
HELDENFELS, Richard R.	NACA - Langley Laboratory
HELLEBRAND, Emil A. H.	Subcommittee on Vibration and Flutter
HESS, Robert W.	NACA - Langley Laboratory
HIESER, Gerald	NACA - Langley Laboratory
HOEKSTRA, Harold D.	Committee on Aerodynamics
HOGE, H. J.	Subcommittee on Aircraft Loads
HOLLENBERG, Harold O.	Bureau of Aeronautics
HOLTBY, Kenneth F.	Boeing Airplane Company
HOUBOLT, John C.	NACA - Langley Laboratory
HOWARD, Charles M.	Arnold Engineering Development Center
HUBBARD, Harvey H.	NACA - Langley Laboratory
HUGLI, Wilfred C., Jr.	Subcommittee on Seaplanes
HUNTER, Hugh F.	Subcommittee on Vibration and Flutter
HUNTLEY, Harold W.	North American Aviation
HUSTON, Wilber B.	NACA - Langley Laboratory
ILLG, Walter	NACA - Langley Laboratory
INGE, John E.	NACA - Langley Laboratory
IRWIN, Horace G.	Douglas Aircraft Company
IVEY, Henry Reese	Tactical Air Command
JABLECKI, Lt. Col. Leon S.	Subcommittee on Aircraft Structures
JACKSON, Charles E.	Boeing Airplane Company
JAKOSKY, Milton	Subcommittee on Aircraft Structures
JEPPESEN, Gordon L.	Goodyear Aircraft Corporation
JEWELL, Lt. Laurence D.	Air Force Special Weapons Center
JEWETT, Frederic D.	Glenn L. Martin Company
JOHNSON, Carl G.	Wright Air Development Center
JOHNSON, H. Clay	Subcommittee on Vibration and Flutter
JOHNSON, J. A.	Subcommittee on Aircraft Loads
JOHNSON, J. B.	Subcommittee on Aircraft Structural Materials
JOHNSON, John E.	Consolidated Vultee Aircraft Corp.
JOHNSON, Roger P.	The RAND Corporation
JOHNSTON, J. Ford	Lockheed Aircraft Corporation
JONES, Arthur L.	FluiDyne Engineering Corporation
JONES, Lt. Col. Rodney A.	Air Research and Development Command
JORDAN, Gareth H.	NACA High-Speed Flight Station

KAMM, Raymond	Douglas Aircraft Company
KAPLAN, Dr. Abner	Ramo-Wooldridge Corporation
KAPLAN, Carl	NACA - Langley Laboratory
KARTVELI, Dr. A.	Committee on Aerodynamics
KATZ, Henry	Wright Air Development Center
KATZEN, Elliott D.	NACA - Ames Laboratory
KEIRSEY, Robert L.	Douglas Aircraft Company
KELLY, Edward J.	Grumman Aircraft Engineering Corp.
KELLY, Thomas C.	NACA - Langley Laboratory
KERFOOT, H. Potter, Jr.	North American Aviation
KLINE, Leo V.	Redstone Arsenal
KLOPP, Comdr. James W.	Bureau of Aeronautics
KOEGLER, Richard K.	Cornell Aeronautical Laboratory
KRAMER, Edward H.	Fairchild Engine and Airplane Corp.
KUGEL, Howard E.	Wright Air Development Center
KUHL, Albert E.	NACA High-Speed Flight Station
KUHN, Paul	NACA - Langley Laboratory
KUHN, Richard E.	NACA - Langley Laboratory
KULLAS, Albert J.	Glenn L. Martin Company
LAIDLAW, William R.	North American Aviation
LASSITER, Leslie W.	NACA - Langley Laboratory
LAUVER, Dean C.	Bureau of Aeronautics
LEADBETTER, Sumner A.	NACA - Langley Laboratory
LEE, James M.	Bureau of Aeronautics
LEVIN, L. Ross	NACA - Langley Laboratory
LEVY, Samuel	National Bureau of Standards
LIEBOWITZ, Dr. Harold	Office of Naval Research
LOCKE, F. W. S., Jr.	Subcommittee on Seaplanes
LOFTIN, Laurence K., Jr.	NACA - Langley Laboratory
LOMBARD, Dr. Albert E., Jr.	Committee on Aerodynamics
LORD, Douglas R.	NACA - Langley Laboratory
LOW, Emmet F., Jr.	NACA - Langley Laboratory
LOWRIE, Walter	Glenn L. Martin Company
LUIDENS, Roger W.	NACA - Lewis Laboratory
LUNDQUIST, Eugene E.	NACA - Langley Laboratory
LUNNEY, Edward J.	Wright Air Development Center
MacDIARMID, Capt. Donald B., USCG	Subcommittee on Seaplanes
MADSEN, Alfred P.	Consolidated Vultee Aircraft Corp.
MAGGIN, Bernard	NACA Headquarters
MAHAFFEY, Phil T.	Consolidated Vultee Aircraft Corp.
MANGURIAN, George N.	Subcommittee on Aircraft Structures
MARKS, Clifford D.	McDonnell Aircraft Corporation
MARSHALL, H. M.	Douglas Aircraft Company
MARTIN, Dennis J.	NACA - Langley Laboratory
MARTIN, James	Republic Aviation Corporation
MARTIN, James E.	Chance Vought Aircraft
MARTZ, C. William	NACA - Langley Laboratory

[redacted]

[redacted]

MATHAUSER, Eldon E.	NACA - Langley Laboratory
MATULAITIS, Joseph	Subcommittee on Seaplanes
MAY, Ralph W.	NACA Headquarters
MAYER, John P.	NACA - Langley Laboratory
MAYO, Alton P.	NACA - Langley Laboratory
McBREARTY, Jerome F.	Committee on Operating Problems
McCARTY, John Locke	NACA - Langley Laboratory
McCOMB, Harvey G., Jr.	NACA - Langley Laboratory
McINTYRE, Hugh H.	United Aircraft Corporation
MEIRS, John	Grumman Aircraft Engineering Corp.
MEYER, John H.	Subcommittee on Aircraft Structures
MICKS, William R.	The RAND Corporation
MIROWITZ, Leo I.	McDonnell Aircraft Corporation
MITCHELL, Bruce	Ryan Aeronautical Company
MOLELLA, Roslo J.	Naval Air Material Center
MORDFIN, Leonard	National Bureau of Standards
MOREHOUSE, Maj. Gilbert G.	Arnold Engineering Development Center
MORROW, John D.	Redstone Arsenal
MORTON, Earl E.	Fairchild Engine and Airplane Corp.
MOZLEY, Paul P.	Subcommittee on Aircraft Structural Materials
MULHOLLAND, Frank J.	Subcommittee on Stability and Control
MULTHOPP, Hans	The Glenn L. Martin Company
NEILSON, James A.	Fairchild Engine and Airplane Corp.
NELSON, Herbert C.	NACA - Langley Laboratory
NEULS, George S.	Douglas Aircraft Company
NEWBY, Clinton T.	Bureau of Aeronautics
OSBORN, Earl P.	Grumman Aircraft Engineering Corp.
OSBORNE, Henry Harrison, Jr.	David Taylor Model Basin
OWEN, John M.	Northrop Aircraft
PAHL, John F.	Civil Aeronautics Board
PALMER, Carl B.	NACA Headquarters
PAPPAS, Costas	Republic Aviation Corporation
PARKINSON, John B.	NACA - Langley Laboratory
PEARSON, E. O.	NACA Headquarters
PEDERSEN, Arthur H.	McDonnell Aircraft Corporation
PENNONI, Richard J.	Office of Inspector General, Norton AFB
PETERS, Roger W.	NACA - Langley Laboratory
PETERSON, Ivar C.	Aircraft Industries Association of America
PETERSON, James P.	NACA - Langley Laboratory
PHILLIPS, Franklyn W.	NACA Headquarters
PIERPONT, Wm. G.	Beech Aircraft Corporation
PILAND, Robert O.	NACA - Langley Laboratory

[redacted]

DEC[redacted]FIED

PLEWES, Kenneth C.	Wright Air Development Center
PONSFORD, Henry T.	The RAND Corporation
PRESS, Harry	NACA - Langley Laboratory
PREWITT, Carl H.	Beech Aircraft Corporation
PRIDE, Richard A.	NACA - Langley Laboratory
PUSIN, Herman	Glenn L. Martin Company
RABER, William H.	Naval Air Development Center
RAFEL, Norman	U. S. Naval Ordnance Experimental Unit, Bureau of Standards
RAFFERTY, Christopher A.	Bendix Aviation Corporation
RAINEY, A. Gerald	NACA - Langley Laboratory
RAITHEL, Dr. Wilhelm	Subcommittee on Aircraft Structures
RAMEY, Madison L.	McDonnell Aircraft Corporation
RATHERT, George A.	NACA - Ames Laboratory
RAY, George D.	Subcommittee on Aircraft Loads
REESE, James R.	NACA - Langley Laboratory
REGIER, Arthur A.	NACA - Langley Laboratory
REID, Dr. H. J. E.	NACA - Langley Laboratory
REYNOLDS, Lawrence B.	Wright Air Development Center
RHODE, Richard V.	NACA Headquarters
RICE, James E.	Goodyear Aircraft Corporation
RICHARD, George J.	Lockheed Aircraft Corporation
RITTER, Robert A.	Naval Air Material Center
ROBERTS, Paul V.	Raytheon Manufacturing Company
ROBINSON, Arnold	Naval Air Material Center
ROCHÉ, Jean A.	AF Development Field Office, NACA, Langley Field, Va.
ROGERS, John T.	NACA High-Speed Flight Station
ROLFE, Rial E.	McDonnell Aircraft Corporation
ROSCHÉ, Melvin G.	NACA Headquarters
ROSEN, B. Walter	NACA - Langley Laboratory
ROSENBAUM, Robert	Subcommittee on Vibration and Flutter
ROUKIS, John G.	Grumman Aircraft Engineering Corp.
RUNCKEL, Jack F.	NACA - Langley Laboratory
RUNYAN, Harry L.	NACA - Langley Laboratory
RYKEN, John M.	Bell Aircraft Corporation
SADOFF, Melvin	NACA - Ames Laboratory
SANDERS, J. Lyell, Jr.	NACA - Langley Laboratory
SANDOZ, Paul L.	Boeing Airplane Company
SAWYER, Richard H.	NACA - Langley Laboratory
SCHAPIRO, Dr. Leo	Committee on Aircraft Construction
SCHENDEL, James W.	Cessna Aircraft Company
SCHNITT, Arthur	Bell Aircraft Corporation
SCHNITZER, Emanuel	NACA - Langley Laboratory
SCHUERCH, Hans U.	Aerophysics Development Corporation
SCHUETTE, Evan H.	Dow Chemical Company

[redacted]

[redacted]

SEABERG, Maj. John D.	Wright Air Development Center
SEARS, Richard I.	Raytheon Manufacturing Company
SECKLER, Sam	Bureau of Aeronautics
SEMONIAN, Joseph W.	NACA - Langley Laboratory
SHAPTER, Nelson M.	Civil Aeronautics Administration
SHAW, Spencer L.	Douglas Aircraft Company
SHORTAL, Joseph A.	NACA - Langley Laboratory
SILSBY, Norman S.	NACA - Langley Laboratory
SKOOG, James A.	Boeing Airplane Company
SMETANA, Lt. Frederick O.	Air Force Flight Test Center
SMILEY, Robert F.	NACA - Langley Laboratory
SMITH, Frank	Royal Aircraft Establishment
SMITH, Norman F.	NACA - Langley Laboratory
SORENSON, Arne S.	Boeing Airplane Company
SOULE, Harold V.	Sylvania Electric Products
SOULÉ, Hartley A.	NACA - Langley Laboratory
SPRINGER, Burdell L.	Subcommittee on Aircraft Loads
STAUFFER, Warren A.	Lockheed Aircraft Corporation
STEIGER, Capt. Arthur R.	Air Force Special Weapons Center
STEIN, Manuel	NACA - Langley Laboratory
STEPHENSON, William B.	Sandia Corporation
STEVENS, John E.	Chance Vought Aircraft
STEWART, Dr. Homer J.	Jet Propulsion Laboratory, C.I.T.
STONE, Melvin	Douglas Aircraft Company
STONE, Ralph W., Jr.	NACA - Langley Laboratory
STRAUSS, Louis	Lockheed Aircraft Corporation
SWANSON, Lt. Col. Arthur R.	Aeronautical Div., Director of Research and Development. USAF
SWIFT, Herbert A.	Consolidated Vultee Aircraft Corp.
SYLVESTER, Maurice A.	NACA - Langley Laboratory
TARGOFF, Walter P.	Cornell Aeronautical Laboratory
TAVERNETTI, Lt. Comdr. Thomas F.	Bureau of Aeronautics
TETENS, Robert C.	Temco Aircraft Corporation
THOMPSON, Floyd L.	NACA - Langley Laboratory
THOMPSON, Robert F.	NACA - Langley Laboratory
TILGNER, Charles	Committee on Aerodynamics
TILLINGHAST, N. W.	U. S. Naval Air Test Center
TRAPP, W. J.	Wright Air Development Center
TROHA, Charles C.	Bureau of Aeronautics
TULIN, Marshall P.	Subcommittee on Seaplanes
TUOVILA, W. J.	NACA - Langley Laboratory
UNDERWOOD, William J.	NACA Liaison Office, Wright-Patterson AFB
UPTON, George T.	Chance Vought Aircraft
UTTER, Emmet	Beech Aircraft Corporation

[redacted]

VALENTINE, Gordon A.	Stanley Aviation Corporation
VETERITO, A. Michael	Fairchild Engine and Airplane Corp.
VINSON, Lt. Jack R.	Wright Air Developmenter Center
VOGELEY, Arthur W.	NACA - Langley Laboratory
VOLLMECKE, Albert A.	Committee on Aircraft Construction
VOSTEEN, Louis F.	NACA - Langley Laboratory
WAGNER, John	Republic Aviation Corporation
WALKER, Kelsey	Lockheed Aircraft Corporation
WALLS, James H.	NACA - Langley Laboratory
WEHLE, Louis B.	Grumman Aircraft Engineering Corp.
WEIHMAN, Clifford	Glenn L. Martin Company
WEIL, Joseph	NACA High-Speed Flight Station
WEINBERGER, Robert A.	Bureau of Aeronautics
WEISMAN, Yale	Consolidated Vultee Aircraft Corp.
WESTVIG, Roger T.	North American Aviation
WIGNOT, Jackson E.	Lockheed Aircraft Corporation
WILKINS, Lieut. Paul E.	Air Technical Intelligence Center
WILSON, Herbert A., Jr.	NACA - Langley Laboratory
WILSON, Homer B., Jr.	Redstone Arsenal
WILSON, James	Jet Propulsion Laboratory, C.I.T.
WILSON, Leo E.	Southwest Research Institute
WILSON, Robert E.	Naval Ordnance Laboratory
WOLCOTT, Verne V.	Consolidated Vultee Aircraft Corp.
WOODALL, Capt. Robert E., Jr.	Wright Air Development Center
WOOLSTON, Donald S.	NACA - Langley Laboratory
WYSS, John A.	NACA - Ames Laboratory
YAGIELA, Stanley	Civil Aeronautics Administration
YATES, William B.	Subcommittee on Aircraft Loads
YORK, Anthony J.	Lockheed Aircraft Corporation
ZENDER, George W.	NACA - Langley Laboratory
ZIMMERMAN, Arthur V.	NACA - Lewis Laboratory
ZIMMERMAN, Charles H.	NACA - Langley Laboratory
ZISFEIN, Melvin B.	Bell Aircraft Corporation

[redacted]

DECLASSIFIED

LOADS AND LOAD DISTRIBUTION

DECL[redacted]SIFIED

RECENT STABILITY AND AERODYNAMIC PROBLEMS AND THEIR IMPLICATIONS AS TO LOAD ESTIMATION

By Charles H. Zimmerman

Langley Aeronautical Laboratory

SUMMARY

Certain trends in the design of modern fighter aircraft tend to produce stability deficiencies which may result in large inadvertent structural loads. The deficiencies becoming increasingly important are: (a) loss of directional stability at high angles of attack, (b) loss of directional stability at high Mach numbers, and, probably most important, (c) a tendency to perform whirling divergences in angle of attack and/or sideslip from rolling maneuvers.

It is emphasized that the aerodynamic loads which will be imposed on a modern fighter airplane cannot be predicted without a careful and complete study of both its quasi-static and its dynamic stability characteristics, including time-history analyses of rolling maneuvers using five degrees of freedom. Deficiencies (a) and (b) are aerodynamic and can be remedied by configuration changes based on wind-tunnel investigations. Deficiency (c) is a dynamic phenomenon which requires a great deal more study and may impose limitations on rolling velocities or necessitate the use of automatic stabilization during rolling maneuvers.

INTRODUCTION

Recent flight experiences with research and service airplanes have emphasized the absolute necessity for careful and complete consideration of the stability characteristics when estimating loads. For example, as shown in figure 1, a research airplane went from what was intended to be a normal aileron roll into what the pilot referred to as a "hairy" maneuver in which it reached large angles of attack and sideslip and developed normal accelerations of +7g and -6.7g and a transverse acceleration of 2g, all in the space of about 2 seconds. As would be expected, a large number of items on the airplane were stressed to large percentages of their ultimate loads.

Some of the stability deficiencies which result in advertent high loads have been present for some time. The problem of pitch-up has been discussed previously and the causes of pitch-up and methods for its

[redacted]

[redacted]

alleviation are well known (refs. 1 to 7). These include use of a low horizontal tail, wing fences, drooped leading-edge extensions, and leading-edge slats.

The fact that poorly damped airplanes suffer relatively large loadings in turbulent air has been discussed in various published papers (refs. 8 to 10). At present, there are three other types of stability deficiencies which are assuming increasing importance from a loads viewpoint. These deficiencies are as follows:

(1) Loss of directional stability at high angles of attack

(2) Loss of directional stability at high Mach numbers

(3) Tendency to perform whirling divergences from maneuvers involving high rolling velocities.

These will discussed in order.

SYMBOLS

b	wing span, ft
C_L	lift coefficient
C_{n_β}	partial derivative of yawing-moment coefficient with respect to sideslip, per radian
$\left(C_{n_\beta}\right)_{REQ'D}$	partial derivative of yawing-moment coefficient required to avoid resonance in yaw, per radian
$\left(C_{n_\beta}\right)_{RES}$	partial derivative of yawing-moment coefficient corresponding to resonance in yaw, per radian
I_X	moment of inertia about X-axis, slug-ft^2
I_Y	moment of inertia about Y-axis, slug-ft^2
I_Z	moment of inertia about Z-axis, slug-ft^2
k_Z	radius of gyration about Z-axis, ft
M	Mach number

[redacted]

[redacted]

N_β	partial derivative of yawing moment with respect to sideslip, ft-lb/radian
p_{RES}	rolling velocity for resonance in yaw, radians/sec
S	wing area, sq ft
V	flight velocity, fps
W	weight, lb
α	angle of attack, deg
β	angle of sideslip, deg
ρ	density of air, slugs/cu ft

DISCUSSION

Modern fighter configurations tend to have large, long fuselages and low-aspect-ratio wings. They require large angles of attack to develop large lift coefficients. Figure 2 illustrates a stability deficiency which is likely to occur with such a configuration. With the original tail, the static directional stability fell to zero well before maximum lift because of the induced flow field of the fuselage-wing arrangement at high angles of attack. An airplane having such a loss in directional stability will tend to diverge in sideslip with a resulting high tail load if the divergence should take place at large values of dynamic pressure. This has been demonstrated by the X-5 airplane and was discussed in reference 11. For the configuration of figure 2 a larger vertical tail greatly increased the static stability and correspondingly lessened the likelihood of divergences in sideslip.

The second stability deficiency arising from aerodynamics which is currently an increasing problem is shown in figure 3. This figure is a plot of some data on the X-1A from the Langley 9-inch supersonic tunnel which illustrates a typical tendency for airplanes to lose static directional stability with increasing Mach number at supersonic speeds. Violent maneuvers have been experienced with the X-1A airplane in this Mach number range. This loss in stability is due to loss in tail effectiveness with Mach number. Notice, however, that the tail is still capable of developing high loads in sideslip even though its effectiveness has been reduced enough to destroy the directional stability of the airplane. A supersonic airplane recently suffered a structural failure because of directional divergence at a Mach number of 1.5 for which a similar loss in C_{n_β} with Mach number was probably primarily responsible.

[redacted]

[redacted]

The third major stability deficiency which is going to be of great concern to the structural designer is a dynamic problem and was predicted by Phillips in reference 12. This type of instability is encountered in rolling maneuvers. Essentially, it tends to occur when the rate of roll approaches the natural circular frequency in pitch or yaw on an aircraft having its weight concentrated in the fuselage. The resonance between rolling and pitching, or yawing, causes what is perhaps best described as a whirling motion in which the fuselage attempts to set itself at right angles to the flight path. Large angles of sideslip and/or angles of attack are generated. It was this type of maneuver which gave rise to the extreme loadings on the research airplane mentioned earlier.

In order to understand why modern high-performance airplanes are prone to such motions, compare a modern fighter with a 1935 fighter (fig. 4). The modern fighter has the same span but is nearly twice as long. It has about three times the wing loading. It flies at twice the altitude. The radius of gyration in yaw is two-thirds larger. Its weight is concentrated in the fuselage. It will be shown that these factors combine in a way which indicates that the modern airplane will tend to be much more prone to become uncontrollable in rolling motions than the 1935 airplane.

The analysis in reference 12 indicated that the value of rolling velocity at which resonance with the natural frequency in yaw occurred could be given by

$$p_{RES} = \sqrt{\frac{N_{\beta}/I_Z}{\dfrac{I_Y - I_X}{I_Z}}} \qquad (1)$$

Nondimensionalizing and rearranging this expression gives the directional stability required to avoid resonance in yaw as

$$\left(C_{n_{\beta}}\right)_{REQ'D} > \left(\frac{pb}{2V}\right)^2 \frac{\dfrac{I_Y - I_X}{I_Z}}{4.03b\left(\dfrac{\rho}{W/S}\,\dfrac{b^2}{{k_Z}^2}\right)} \qquad (2)$$

[redacted]

A similar expression can be developed for resonance in pitch but will not be presented since the points of interest are illustrated by the yawing equation. Notice that the value of C_{n_β} required depends on the square of the rolling velocity, a wing-loading inertia parameter, and a gyroscopic inertia coupling parameter.

In figure 5 is presented the variation of the gyroscopic inertia coupling parameter for fighter and research airplanes studied in the Langley 15-foot and 20-foot free-spinning tunnels over the 20-year period from 1935 to 1955. This parameter stayed substantially constant at a value of approximately 0.3 from 1935 to 1945 but has risen to a mean value of 0.7 at the present time. This increase tends to increase the directional stability required to avoid resonance.

Figure 6 gives the variation of the mass inertia parameter over that same period. This parameter has been normalized at the value in 1935. Notice that its value in 1955 has fallen to about one-sixteenth its value in 1935. This decrease corresponds to a large increase in the required directional stability.

Now it can be seen how the value of C_{n_β} corresponding to resonance in yaw $\left(C_{n_\beta}\right)_{RES}$ at $pb/2V = 0.09$ has varied over the 20-year period (fig. 7). This value from 1935 to 1945 was about 0.00015, considerably less than the typical value of 0.0005 to 0.001 used in World War II airplanes. Beginning with the advent of jet engines, the value of $\left(C_{n_\beta}\right)_{RES}$ has risen rapidly since 1945 until the value of $\left(C_{n_\beta}\right)_{RES}$ in the typical fighter airplane of 1955 is of the order of 0.006, 40 times the value in the World War II airplane and considerably larger than the typical range of values of $\left(C_{n_\beta}\right)_{RES}$, 0.001 to 0.002, provided for these airplanes.

The analysis of the trend of directional stability required presented in figure 7 was based on the assumption that the reduced rolling velocity $pb/2V$ remained constant at a value of 0.09. This is not true, however, for transonic and supersonic speeds. Figure 8 indicates the variation of $pb/2V$ with Mach number. In general, the ability of lateral controls to produce $pb/2V$ falls off with increases in Mach number at transonic and supersonic speeds somewhat as indicated by the "typical" curve. This is an alleviating effect upon the trend toward increasing troubles with divergent whirls. Equation (2) indicates that $\left(C_{n_\beta}\right)_{RES}$ decreases as $(pb/2V)^2$. It may be necessary for the designer to take steps to insure that the specified rolling velocities cannot be exceeded in order to avoid unnecessary troubles with whirling divergences.

[redacted]

REAC studies have indicated that, although the analysis of reference 12 gives an excellent picture of the nature of this phenomenon and is an excellent indicator that a dangerous condition exists, it does not take sufficient factors into account to permit it to be used as criterion of the amount of sideslip to be expected in a rolling maneuver. In the light of present knowledge, it appears that the sideslip response to rolling excitation is of the nature of a frequency-response curve in which both the amplification factor and the forcing function are dependent on such things as the timing, rate, and magnitude of control applications, the angle between the airplane principal axis and the zero-lift line, the initial angle of attack, and the aerodynamic characteristics of the configuration. The main point that has emerged is that, in order to predict the angle of sideslip or angle of attack which will be generated in rapid rolling motions of modern fighters, it is necessary to make a careful and thorough study of possible maneuvers by means of a simulator or analog computer, using five degrees of freedom including the nonlinear inertia terms and the engine gyroscopic couples. The aerodynamic characteristics of the configuration must be carefully represented and factors such as the pitching moment due to ailerons when sideslipping, for example, must in general be included. Cross-coupling effects may be very important. For example, a large increase in damping of the pitching motion, such as might be achieved by artificial means, was indicated to be very effective in reducing the sideslip angle.

CONCLUDING REMARKS

It should be emphasized that the aerodynamic loads which will be imposed on a modern fighter airplane cannot be predicted without a careful and complete study of both its quasi-static and its dynamic stability characteristics. The well-known problems of pitch-up and poor damping of oscillations in turbulent air have been present for some time. Three more must be added - divergence in sideslip at high angles of attack, divergence in sideslip at high Mach numbers, and, probably most difficult of all, a tendency for modern fighters to enter a whirling divergence from rolling maneuvers. The first two of these are aerodynamic deficiencies which can be remedied by configuration changes based on wind-tunnel investigations. The third is a dynamic condition which requires a great deal more study and may impose limitations on rolling velocities or necessitate the use of automatic stabilization during rolling maneuvers.

[redacted]

[redacted]

REFERENCES

1. Shortal, Joseph A., and Maggin, Bernard: Effect of Sweepback and Aspect Ratio on Longitudinal Stability Characteristics of Wings at Low Speeds. NACA TN 1093, 1946.

2. Queijo, M. J., and Wolhart, Walter D.: Wind-Tunnel Investigation of the Effects of Horizontal-Tail Position on the Low-Speed Longitudinal Stability Characteristics of an Airplane Model With a 35° Sweptback Wing Equipped With Chordwise Fences. NACA RM L51H17, 1951.

3. Furlong, G. Chester, and McHugh, James G.: A Summary and Analysis of the Low-Speed Longitudinal Characteristics of Swept Wings at High Reynolds Number. NACA RM L52D16, 1952.

4. Toll, Thomas A.: Longitudinal Characteristics of Wings. NACA RM L53I21b, 1953.

5. Weil, Joseph, and Gray, W. H.: Recent Design Studies Directed Toward Elimination of Pitch-Up. NACA RM L53I23c, 1953.

6. Few, Albert G., Jr., and King, Thomas J., Jr.: Some Effects of Tail Height and Wing Plan Form on the Static Longitudinal Stability Characteristics of a Small-Scale Model at High Subsonic Speeds. NACA RM L54G12, 1954.

7. Stephenson, Jack D., Bandettini, Angelo, and Selan, Ralph: Longitudinal Stability Characteristics at Mach Numbers Up to 0.92 of a Wing-Body-Tail Combination Having a Wing With 45° of Sweepback and a Tail in Various Vertical Positions. NACA RM A54K09, 1955.

8. Press, Harry, and Mazelsky, Bernard: A Study of the Application of Power-Spectral Methods of Generalized Harmonic Analysis to Gust Loads on Airplanes. NACA Rep. 1172, 1954. (Supersedes NACA TN 2853.)

9. Vitale, A. James, Press, H., and Shufflebarger, C. C.: An Investigation of the Use of Rocket-Powered Models for Gust-Load Studies With an Application to a Tailless Swept-Wing Model at Transonic Speeds. NACA TN 3161, 1954.

10. Vitale, A. James: Characteristics of Loads in Rough Air at Transonic Speeds of Rocket-Powered Models of a Canard and a Conventional-Tail Configuration. NACA RM L54L17, 1955.

[redacted]

[redacted]

11. Drake, Hubert M., Robinson, Glenn H., and Kuhl, Albert E.: Loads Experienced in Flights of Two Swept-Wing Research Airplanes in the Angle-of-Attack Range of Reduced Stability. NACA RM L53D16, 1953.

12. Phillips, William H.: Effect of Steady Rolling on Longitudinal and Directional Stability. NACA TN 1627, 1948.

[redacted]

DECLASSIFIED [redacted]

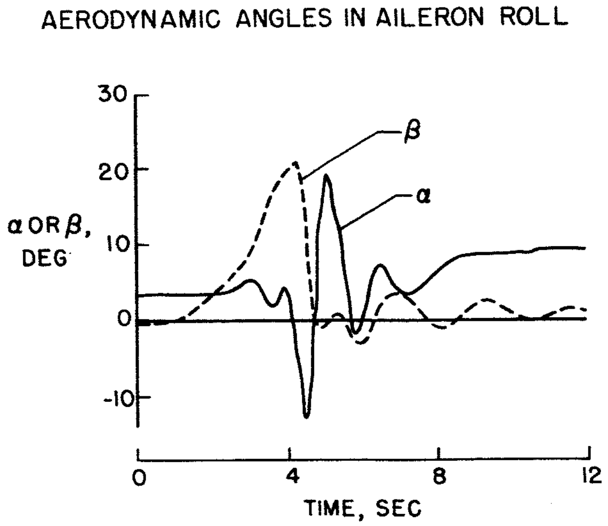

Figure 1

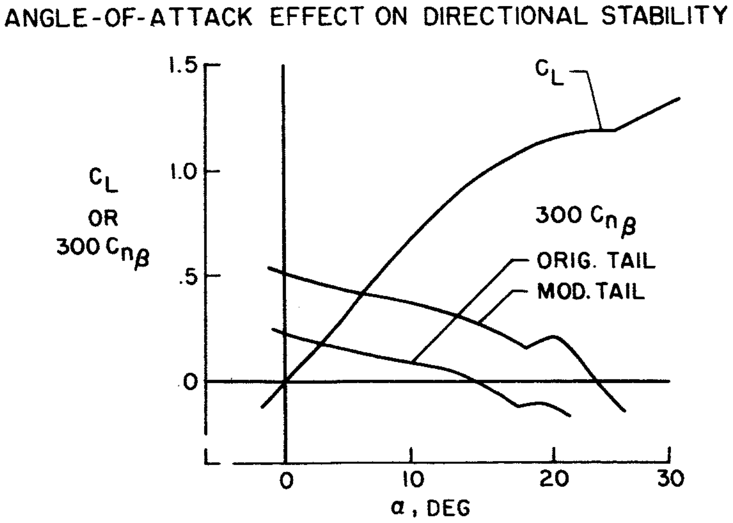

Figure 2

[redacted]

[redacted]

EFFECT OF MACH NUMBER ON DIRECTIONAL STABILITY

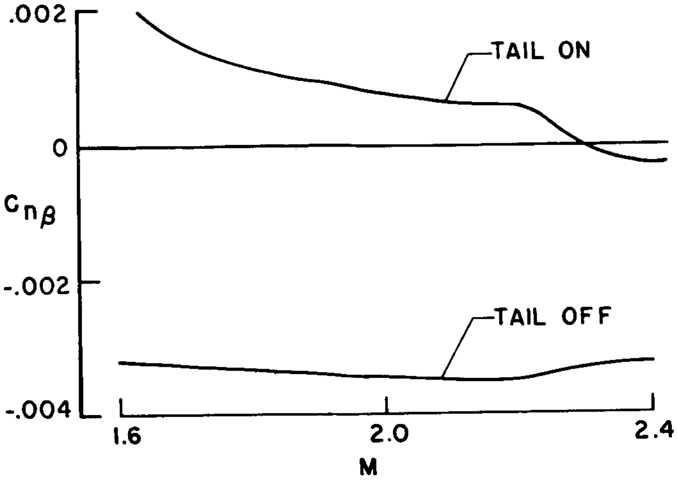

Figure 3

FIGHTER COMPARISON

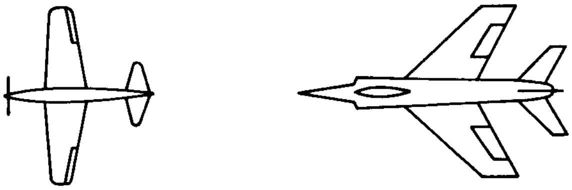

35	b, FT	35
20	$\frac{W}{S}$, LB/SQ FT	60
20,000	ALT., FT	40,000
6	k_Z, FT	10
0.3	$\frac{I_Y - I_X}{I_Z}$	0.72

Figure 4

[redacted]

5U

[redacted]

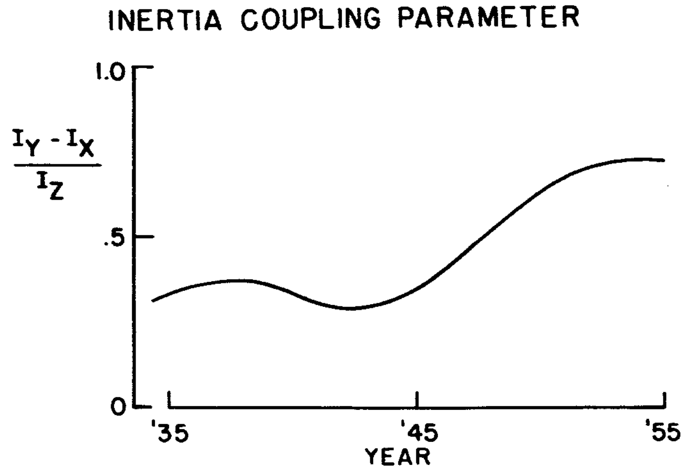

Figure 5

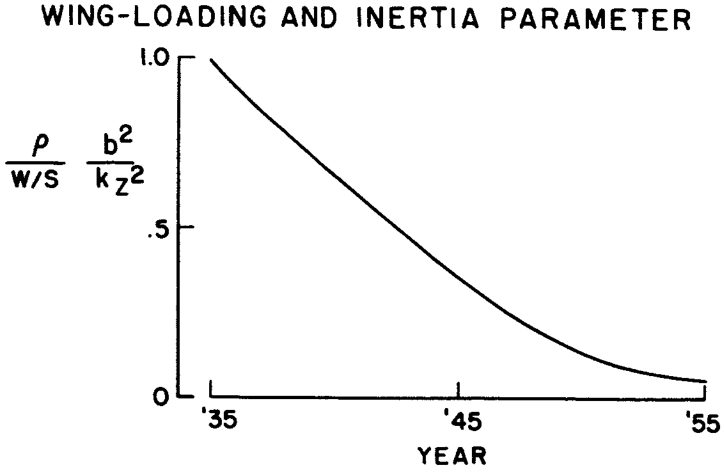

Figure 6

[redacted]

[redacted]

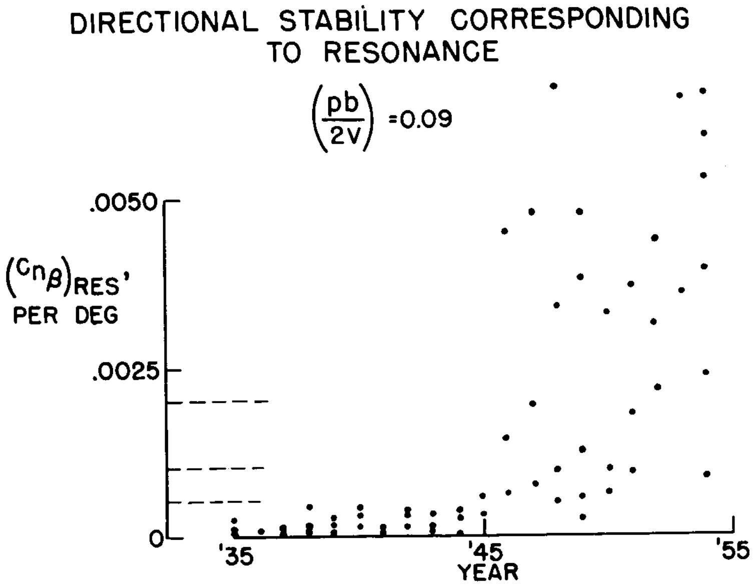

Figure 7

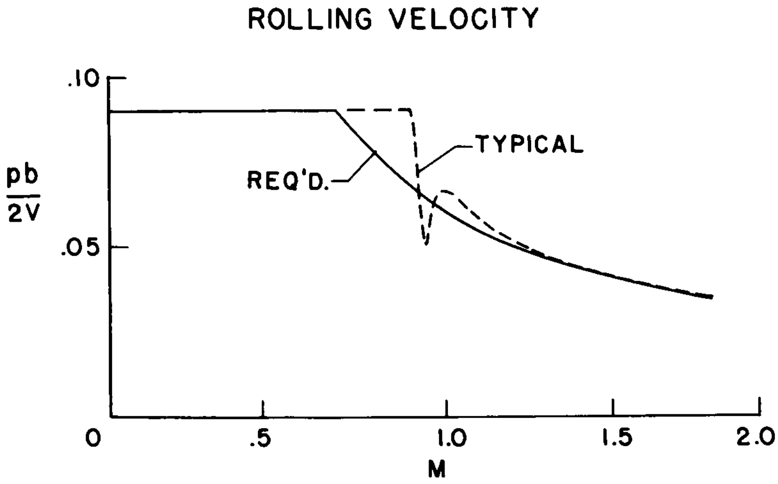

Figure 8

[redacted]

DECL[redacted]SIFIED

FLIGHT EXPERIENCE OF INERTIA COUPLING IN ROLLING MANEUVERS

By Joseph Weil, Ordway B. Gates, Jr., Richard D. Banner,
and Albert E. Kuhl

NACA High-Speed Flight Station

and

Langley Aeronautical Laboratory

SUMMARY

Violent coupled lateral-longitudinal motions have been encountered in flight on two airplanes during abrupt aileron rolls at relatively high speed. During these motions, various structural design loads and load factors were either exceeded or approached. It was demonstrated on one airplane that the motions can be approximated reasonably well by using a five-degree-of-freedom analysis.

From flight tests of the swept-wing airplane at relatively high altitude, it was found that the severity of the divergent tendency increased with roll velocity and was sensitive to roll direction and stabilizer input. Calculated results indicated that considerably more critical conditions from the loads standpoint can be expected at lower altitudes when the roll is initiated from a pull-up condition.

Perhaps one of the fundamental reasons for the occurrence of the large motions on both airplanes was the presence of insufficient directional stability. Doubling the directional stability level of the swept-wing airplane resulted in substantially improved flight characteristics; but calculations indicated that, if the tail size is increased beyond a certain point, considerably higher tail loads and larger peak normal accelerations can be obtained than with a tail affording a somewhat lower level of stability.

At present, analytical investigations are under way to enable a better understanding of the overall problem of coupled lateral-longitudinal motions in rolling maneuvers. It is not yet known whether a practical design approach exists that would produce desirable characteristics for a large range of flight conditions without the sacrifice of performance or the resort to artificial stabilization. It is also true that coupling can have a large effect on the predicted loads, even for configurations that have satisfactory handling qualities; therefore, the coupling of the lateral and longitudinal degrees of freedom should be considered for load evaluations of rolling maneuv[redacted]gh-speed airplanes.

[redacted]

[redacted]

INTRODUCTION

There is a deterioration in the static directional stability of many contemporary designs at the higher angles of attack and sideslip, and also with increase in supersonic Mach number, that can and have produced violent motions in flight.

Recently at the NACA High-Speed Flight Station, some rather violent coupled lateral-longitudinal motions have been experienced during abrupt aileron rolls on several airplanes in which a level of directional stability was present that would probably have been deemed acceptable for previous airplanes. Because this flight experience should be of considerable general interest to the loads engineer, inasmuch as it obviously affects the determination of design loads, it is believed timely to review briefly the problem and indicate some of the factors affecting its severity.

SYMBOLS

A	aspect ratio
a_n	normal acceleration
a_t	transverse acceleration
C_{n_β}	directional stability parameter
H_p	pressure altitude
I_X,I_Y,I_Z	moments of inertia about X-, Y-, and Z-axes, respectively
i_t	stabilizer deflection
L_V	shear load on vertical tail, radians/sec
M	Mach number
p_{max}	maximum roll velocity
t	time, sec
α	angle of attack, deg
β	angle of sideslip, deg
δ_{a_t}	total aileron deflection
δ_r	rudder deflection

[redacted]

[redacted]

$\Lambda_{c/4}$ angle of sweep measured at 0.25 chord, deg

$\Lambda_{\frac{3}{4}c}$ angle of sweep measured from 0.75 chord, deg

$\Delta\phi$ incremental bank angle

DISCUSSION

The basic outlines of the two airplanes discussed in this paper are shown in figure 1. One airplane had 45° sweepback; the other was essentially unswept. It can be seen from the moment-of-inertia ratios that these airplanes were rather heavily loaded along the fuselage, and such inertia characteristics can appreciably lower the roll rate at which large coupled motions might be encountered as indicated in reference 1.

The results of a time history of an abrupt two-thirds aileron roll to the left made on the swept-wing airplane from level flight at a Mach number of 0.70 and altitude of 32,000 feet are presented in figures 2 and 3. Soon after the aileron-control input, there is a steady decrease in angle of attack and development of negative (adverse) sideslip. (See fig. 2.) Between 3 and 4 seconds, the rates of divergence in angles of attack and sideslip increased markedly and the maneuver became uncontrollable. Recovery was made when the controls were brought close to their initial settings. During the motion, a left sideslip angle of 26° was recorded and angles of attack much larger than -16° were attained followed by 12° at recovery.

In order to determine the mechanism of this type of coupled lateral-longitudinal motion (including the effects of changes in the various derivatives), a five-degree-of-freedom analysis was made using an analogue computer. It is seen that the basic character of the motion is predicted fairly well. In order to illustrate the powerful effect of the coupling between the longitudinal and lateral modes of the motion, the sideslip estimated by the usual three-degree-of-freedom lateral equations and the angle of attack estimated by a two-degree-of-freedom analysis are also included. Although the initial sideslip motion is seen to be the same for the two methods, the three-degree-of-freedom method reaches a peak of only about $\beta = -5^{\circ}$. The angle-of-attack comparison is even more revealing in that the stabilizer input of the pilot would have resulted in a large positive angle-of-attack change from a purely longitudinal analysis as opposed to the negative divergence shown by flight and the more refined analysis. The complexity of the problem can be further illustrated by the fact that calculations indicated that the indirect effect of the stabilizer input actually aggravated the sideslip and angle-of-attack divergence appreciably.

[redacted]

A normal acceleration of -4.4g was recorded and about 50 percent of the design vertical-tail load attained. (See fig. 3.) The low dynamic pressure at which the maneuver was made saved the airplane from possible structural damage.

The question naturally arises whether such violent behavior could be expected at higher dynamic pressure where, from the loads standpoint, more critical conditions might be reached. An analogue computer has been used to study this question. Figure 4 summarizes the results of many of these calculations presenting the maximum estimated vertical-tail shear load as a function of the maximum rolling velocity attained in 360° left rolls. The dashed line represents data for a condition similar to that shown in figures 2 and 3 - an altitude of 32,000 feet and an initial 1 g condition. The solid lines show results for rolls made at 10,000 feet from initial conditions of 1 g and 2.5g. It was found from the calculations that 1 g rolls made at the lower altitude so greatly reduced the sideslip angles that, even if the 2.5 fold increase in dynamic pressure is considered, the tail loads for the most rapid rolls never approach the loads attainable at the higher altitude at somewhat lower rolling velocities. When the rolls were made at 10,000 feet from an initial 2.5g pull-up condition, however (the initial angle of attack being maintained at the higher altitude level), much larger tail loads were estimated at high roll velocities than for the higher altitude condition.

In order to study the effect of increasing the directional stability on the rolling characteristics, flight tests were made with two enlarged vertical tails. Figure 5 shows a sketch of the small and enlarged tails. Also shown is the variation of C_{n_β} with Mach number measured in flight. The largest tail (tail C) roughly doubled the directional stability of the small tail through most of the Mach number range.

The effect of increasing tail size on the characteristics in abrupt-left rudder-fixed aileron rolls at an average Mach number of 0.70 and altitude of about 31,000 feet are shown in figure 6. Presented are the maximum change in sideslip angle and the maximum change in angle of attack at the first peak plotted against the maximum roll rate attained in a maneuver. The first roll made for this flight condition (using tail A) resulted in the violent maneuver previously discussed and is approximately located in figure 6 by the circle. The remainder of the data obtained with tail A was restricted to small aileron deflections and bank angles of the order of 45° to 60°. The data for the larger tails represent 360° rolls. If a calculated curve for 360° rolls with tail A is used (as a guide in lieu of flight data), it is seen from the sideslip data that increasing the tail size delayed somewhat the roll velocity at which $\Delta\beta$ increases much more rapidly with further increase in roll rate. Also, for the largest tail there appears to be a substantial

[redacted]

[redacted]

decrease in the divergent tendency at high roll rates. The five-degree-of-freedom calculations show good agreement for the tail A data at small bank angles and illustrate the large effect of the duration of the maneuver on the characteristics at higher roll velocities.

From the lower portion of figure 6, it can be seen that the initial negative change in angle of attack was relatively small for the larger tails, never approaching the divergent tendencies of the original maneuver. It should be mentioned, however, that the positive change in angle of attack in recovery was often somewhat larger than the first peak with tail C.

The results of figure 6 indicate that doubling the level of the directional stability greatly improved the overall characteristics, and one might wonder how further large increases in the size of the vertical tail would affect the results. Figure 7 presents the results of time histories calculated for directional stability levels of $0.001 C_{n_\beta}$, $0.002 C_{n_\beta}$, and $0.004 C_{n_\beta}$ per degree for a roll velocity of about -3.0 radians/sec. The sideslip data show the large reduction in β when C_{n_β} is increased from 0.001 to 0.002. When C_{n_β} is again doubled, however, the sideslip angle developed is only slightly reduced and the maximum tail load would be much larger because of the increased tail area required.

It should also be noted that, although the initial angle-of-attack change is practically nil for the largest tail, the peak positive angle on recovery is almost as large as that with the smallest tail. (See fig. 7.)

The results of figure 7 indicate the possibility of an optimum tail size from the loads standpoint for a given flight condition and further illustrate the complexity of the overall problem.

The effect of Mach number and roll direction on the maximum sideslip angle developed in flight in abrupt 360° rolls is presented in figure 8 for the largest tail (tail C). In order to clarify the comparison, $\Delta\beta$ is plotted for left rolls shown by solid lines and $-\Delta\beta$ for right rolls shown by dashed lines. It is seen that "adverse" sideslip is present in the subsonic maneuvers and "favorable" sideslip at $M = 1.25$. A very interesting point is the much greater sideslip attained in the left rolls than in corresponding right rolls at the higher roll velocities. This roll-direction effect is directly attributable to engine gyroscopic effects and is in general agreement with calculated results. At $M = 1.25$, the right rolls developed slightly greater maximum sideslip angles than left rolls. Although there was no adverse pilot comment on the supersonic rolls, the sideslip angle attained of almost 8° exceeded the temporary limit by 1°.

[redacted]

[redacted]

The time history of an abrupt aileron roll made at a Mach number of 1.05 on the unswept airplane at an altitude of 30,000 feet is shown in figures 9 and 10. The level of directional stability for this maneuver was about $C_{n_\beta} = 0.0038$ per degree. In this maneuver, favorable sideslip builds up rapidly with rolling velocity; however, no large change in α occurs until a sideslip angle of almost 20° is reached ($t = 4$ seconds) at which time the angle of attack abruptly decreases to -13°. (See fig. 9.) The pilot applied considerable up-stabilizer control to stop the pitch-down tendency and this possibly contributed somewhat to the 19° angle of attack reached when the airplane pitched up. When the rolling motion stopped, the airplane quickly recovered.

The violence of this maneuver can best be appreciated from the fact that the load factor reached -6.7g at $t = 4.5$ seconds and then reached 7.0g less than 1/2 second later. (See fig. 10.) A lateral acceleration of -2g, pitching accelerations as high as 8 radians/sec^2, and a vertical-tail shear load approximately 56 percent of design were also measured.

As in the case of the violent maneuver experienced with the swept-wing airplane, one of the fundamental causes of this maneuver on the unswept airplane is believed to be a deficiency in directional stability in conjunction with mass distributed primarily along the fuselage. The statement concerning the lack of directional stability might seem contradictory inasmuch as the value of C_{n_β} for this airplane was about three to four times the value for the swept-wing airplane with the small tail. However, the value of the derivative C_{n_β} can be misleading because of relatively small wing size. When the two airplanes are compared by using the more rational lateral period, for example, the unswept airplane has a directional stiffness approximating the original swept-wing airplane.

CONCLUDING REMARKS

In conclusion, it has been shown that violent coupled lateral-longitudinal motions have been encountered in flight on two airplanes during abrupt aileron rolls at relatively high speed. During these motions, various structural design loads and load factors were either exceeded or approached. It was demonstrated on one airplane that the motions can be approximated reasonably well by using a five-degree-of-freedom analysis.

From flight tests of the swept-wing airplane at relatively high altitude, it was found that the severity of the divergent tendency increased with roll velocity and was sensitive to roll direction and

[redacted]

[redacted]

stabilizer input. Calculated results indicated that considerably more critical conditions from the loads standpoint can be expected at lower altitudes when the roll is initiated from a pull-up condition.

Perhaps one of the fundamental reasons for the occurrence of the large motions on both airplanes was the presence of insufficient directional stability. Doubling the directional stability level of the swept-wing airplane resulted in substantially improved flight characteristics; but calculations indicated that, if the tail size is increased beyond a certain point, considerably higher tail loads and larger peak normal accelerations can be obtained than with a tail affording a somewhat lower level of stability.

At present, analytical investigations are under way to enable a better understanding of the overall problem of coupled lateral-longitudinal motions in rolling maneuvers. It is not yet known whether a practical design approach exists that would produce desirable characteristics for a large range of flight conditions without the sacrifice of performance or the resort to artificial stabilization. It is also true that coupling can have a large effect on the predicted loads, even for configurations that have satisfactory handling qualities; therefore, the coupling of the lateral and longitudinal degrees of freedom should be considered for load evaluations of rolling maneuvers on most high-speed airplanes.

REFERENCES

1. Zimmerman, Charles H.: Recent Stability and Aerodynamic Problems and Their Implications as to Load Estimation. (Prospective NACA paper.)

[redacted]

[redacted]

[redacted]

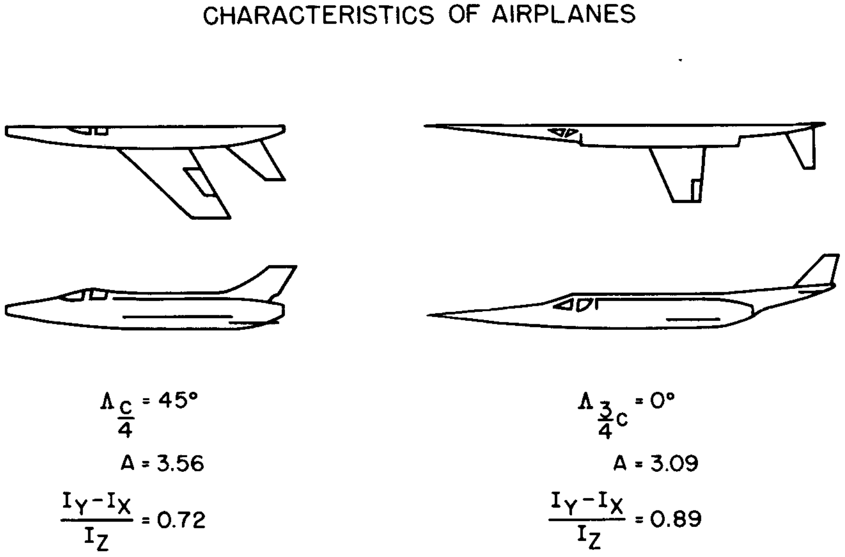
CHARACTERISTICS OF AIRPLANES
$\Lambda_{\frac{c}{4}} = 45°$
$A = 3.56$
$\frac{I_Y - I_X}{I_Z} = 0.72$
$\Lambda_{\frac{3}{4}c} = 0°$
$A = 3.09$
$\frac{I_Y - I_X}{I_Z} = 0.89$

Figure 1

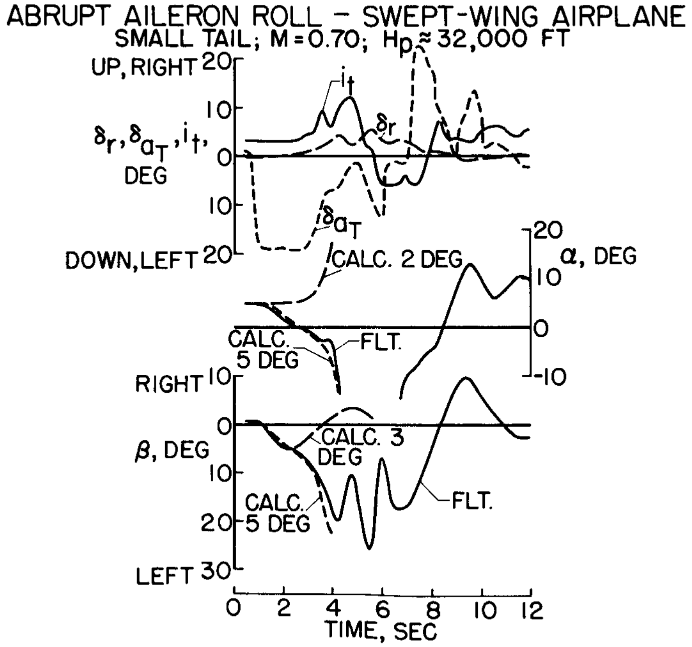

Figure 2

[redacted]

[redacted]

DECLASSIFIED [redacted]

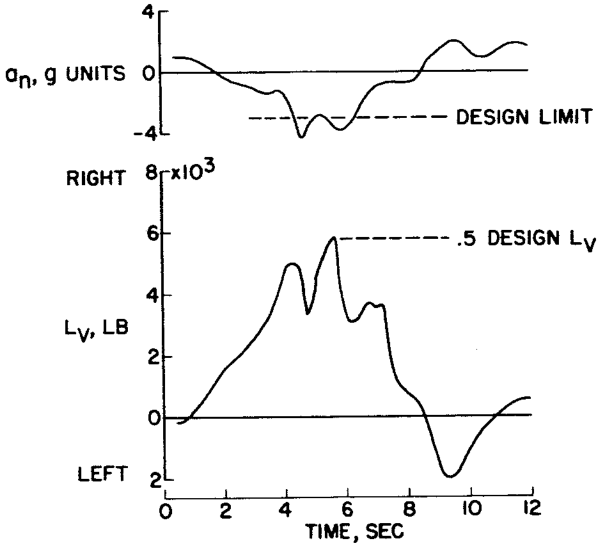

Figure 3

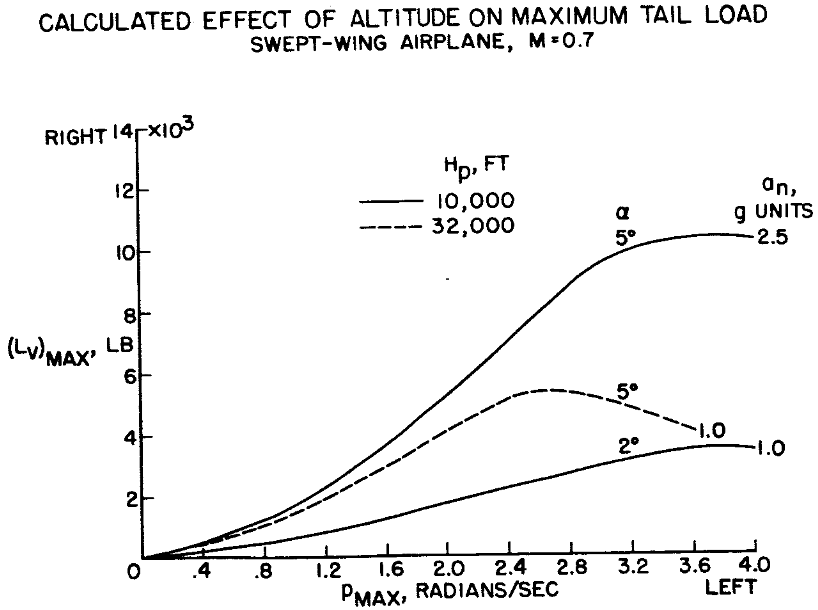

Figure 4

[redacted]

[redacted]

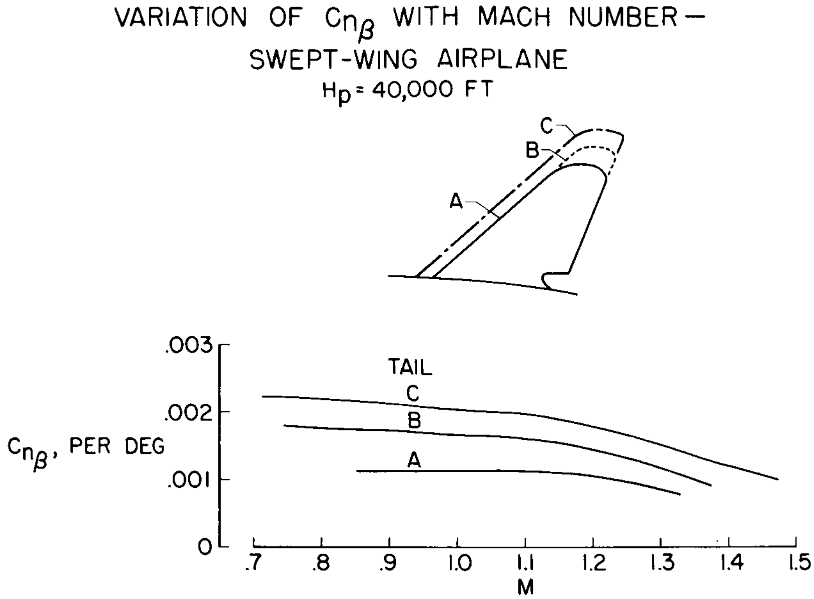

Figure 5

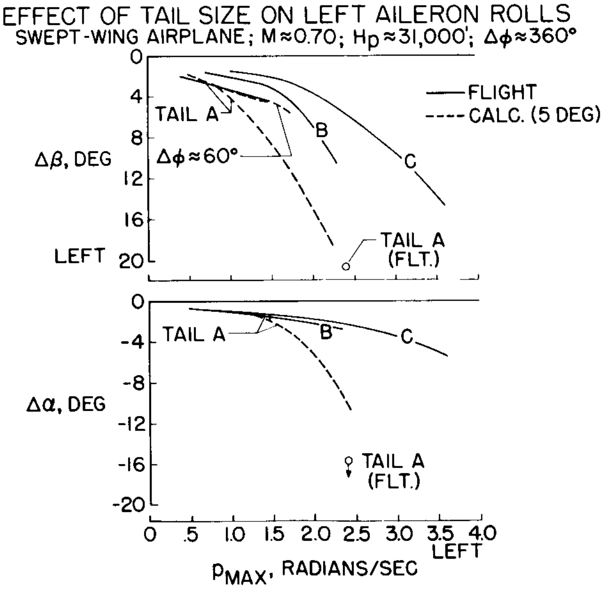

Figure 6

[redacted]

[redacted]

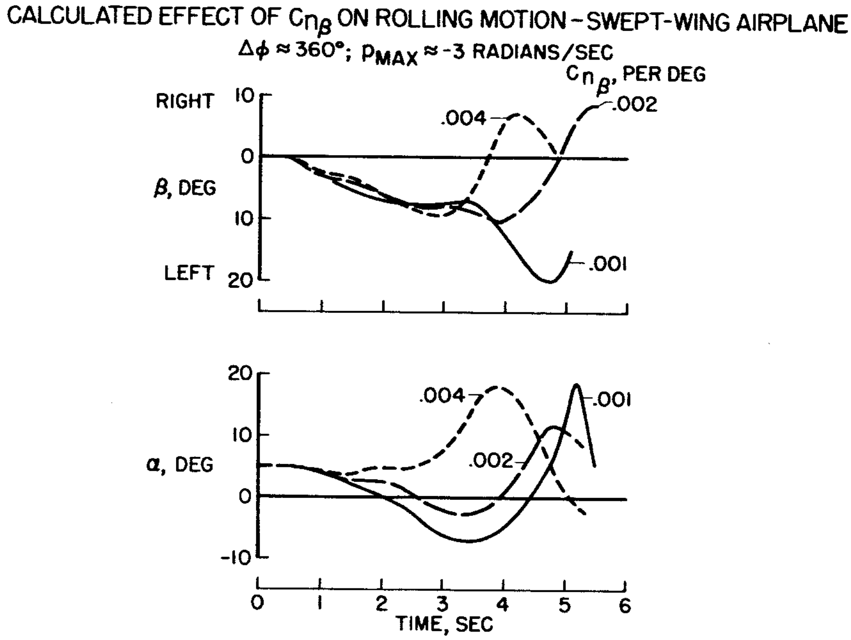

Figure 7

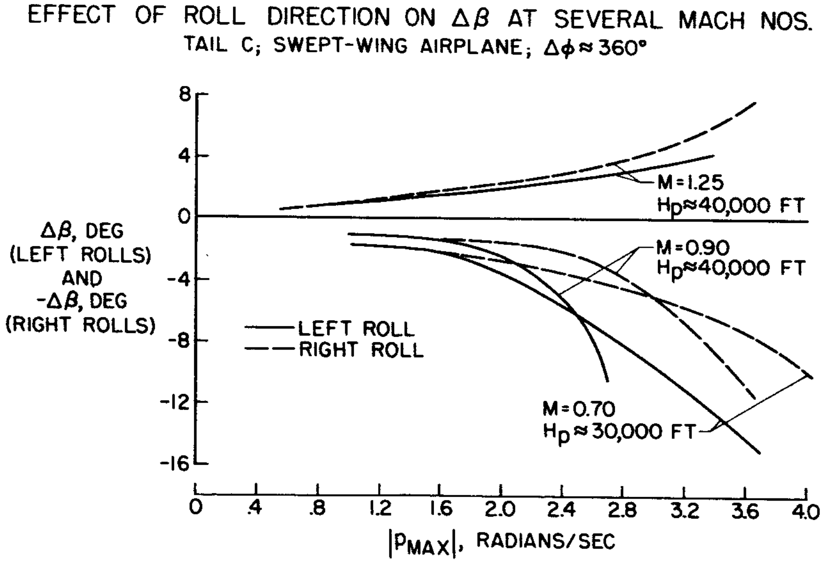

Figure 8

[redacted]

[redacted]

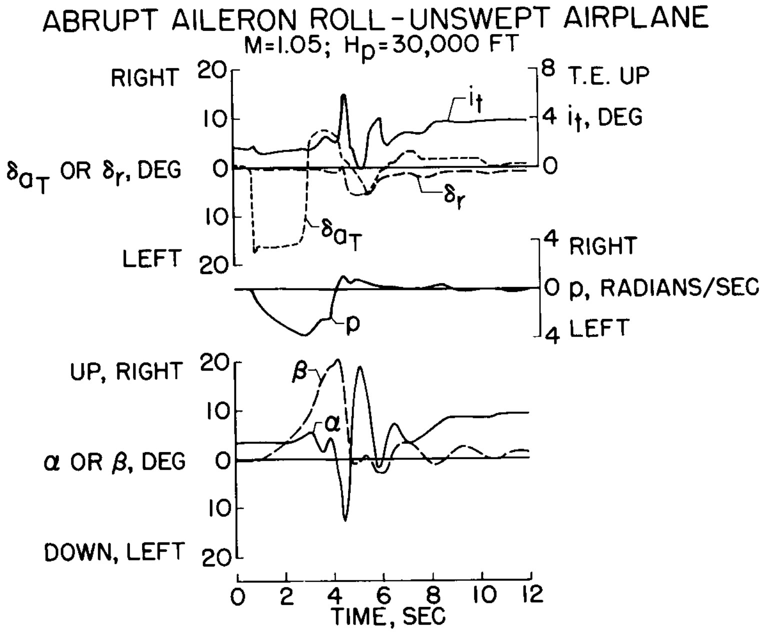

Figure 9

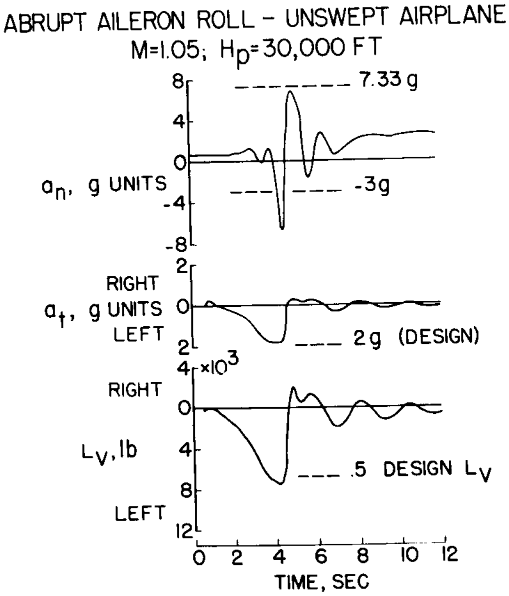

Figure 10

[redacted]

DECLASSIFIED [redacted]

A STUDY OF MEANS FOR RATIONALIZING AIRPLANE DESIGN LOADS

By John P. Mayer and Harold A. Hamer

Langley Aeronautical Laboratory

The NACA has been making a study of means for rationalizing the design loads of airplanes based on mission requirements. The study, which utilizes statistical methods, is in its initial stages but it is believed that some of the preliminary ideas may be of some interest at this time.

This study has been based on the premise that an airplane should be designed for the mission or missions for which it is to be used. Conceivably, in the future it may be desirable to design for more specific missions which will be governed by the range of the detection apparatus, the armament, and the type of directing devices. It may then be found necessary to do something a little different from in the past.

Of course, all statistical measurements which are used must, of necessity, be based on operational airplanes which by some standards are obsolete when they become operational. The airplanes for which statistical data are now available are all subsonic or low-supersonic airplanes which are reasonably stable airplanes. The results for airplanes such as referred to in the previous papers by Charles H. Zimmerman and by Joseph Weil, Ordway B. Gates, Jr., Richard D. Banner, and Albert E. Kuhl could be considerably different if they were flown operationally with such stability deficiencies. In the following discussion, therefore, it will be assumed that the stability deficiencies will have been corrected or the airplanes restricted such that they will be able to perform their design mission without encountering any uncontrollable motions.

Table I lists some of the missions and operations for which a fighter-type airplane might be used. In the group above the double line are the missions for which the airplane might be designed, and in the group below the double line are other operations for which the airplane will be used but which may be of secondary importance to the missions. Several missions or uses are indicated in the first two columns, and of course there are other missions that could be added to the list. In the third column are listed percentages of the total flight time which might be spent in each activity. For each of these uses of the airplane, there would be an associated probability function such as shown in the fourth column. In this column, probability functions for the airplane uses are indicated as average flight time required to exceed a given load factor. The probability curves for the part of the table above the double line are dictated by the mission requirements, whereas the probability curves for the lower part of the table or nonmission operations appear to depend

[redacted]

mostly on the pilot's ability to observe a placard load-factor restriction. These component curves are then combined according to the percentage of flight time spent in missions or in other operations to obtain a resultant probability curve.

It appears that the probability curves for the individual missions may be calculated in some cases. The first work of this type was done by Brönn of the SAAB of Sweden. In figure 1 a simple mission is indicated for which probability curves have been calculated. In this case, it is assumed that a Mach number 2 piloted interceptor is to intercept a Mach number 1 bomber which is approaching the target at an altitude of 60,000 feet. The bomber is detected by ground radar stations. Probability curves are then calculated or estimated for the various phases of the mission such as the take-off, climb, cruise, turn on to target, attack, breakaway, and landing. The possibilities of a miss on the first attack and subsequent attacks are also included in the calculations although not indicated in this figure. The turn on to the target is assumed to be directed from the ground control stations. The probability function for this turn is related to the ability and probability of the ground radar installation to direct the interceptor to the optimum position for attack.

The method of calculating the probability functions for a simplified version of the attack phase of the mission is indicated in figure 2. The interceptor is located at the position indicated at the beginning of the attack phase. The lines denoting various loads represent possible locations of the bomber at the beginning of the attack. For example, if the bomber were located anywhere along the line labeled 2g at the beginning of the attack, the interceptor would have to make at least a 2g turn for a successful interception; if the bomber were located anywhere along the line labeled 4g, the interceptor would have to make at least a 4g turn, and so forth. The dashed-line circle represents the interceptor's initial airborne radar range, which in this case was assumed to be 20 miles. The concentric solid-line circles are lines of constant probability which are a function of the ability of the ground control to position the interceptor in the optimum location for a successful attack. For example, the bomber will be located within the area enclosed by the circle labeled 10% in 10 percent of the cases, the bomber will be located within the area enclosed by the circle labeled 50% in 50 percent of the cases, and so forth. The probability of the interceptor exceeding a given load factor is then determined by the volume of the probability distribution falling outside of a given load-factor line. Of course, this is a simplified version of the attack phase of the mission, but it is presented in order to illustrate the use of the mission concept to determine the loads which might be imposed. It is not intended to be an actual interception problem.

[redacted]

The probability curve obtained in this manner is shown in figure 3. The probability curve for the attack phase is shown as the average flight time required to exceed a given load factor. The probability curves for the other phases of the mission are also calculated or estimated. A few of these are shown, such as the take-off, turn on to target, and the gust expectancy. These individual probability curves are then combined to form the total mission probability curve which is shown as the heavy line.

For the other uses of the airplane such as shown in the lower part of table I, it has been indicated from experience with present-day airplanes that the load experience other than the specialized mission may be approximated by one probability function which is proportional to the airplane service limit load factor. This is shown in figure 4.

In figure 4, the ratio of the time to exceed a given load factor to the time to exceed 1 g in maneuvers is shown plotted against the ratio of incremental load factor to incremental service limit load factor. The data shown represent about 20,000 hours of total flight time in training and combat. It may be seen that, although there is considerable scatter, the data may be represented by one line and the curve shown appears to fit the data for airplanes with limit load factors as low as 2.8 and as high as 7.5 at load factors up to the service limit load factor.

It is indicated that this tentative standard curve may be represented by an equation of the type shown in figure 4. It can be shown from statistical theory that such an equation represents the distribution of the larger peak load factors if it could be assumed that the maneuvering load factors were of a random nature and symmetrical about 1 g. It may be noted that the load-distribution curve is determined only by the term N_0/T and the term σ; N_0/T represents the average number of large load-factor peaks per hour and σ represents the root-mean-square value of the load-factor ratio. For present operational U. S. Air Force fighters in training and in combat, the value of N_0/T varies between 10 and 25 peaks per hour and the value of σ is roughly 0.3. Of course, individual maneuvers are not of a random nature; however, when many maneuvers are considered together it appears that they may approach the concept of a random process.

If, now, it is assumed that the mission probability curve may be calculated and that the probability curve for other airplane operations can be given as shown in figure 4, the two types of probability curves may be combined to form the resultant curve. If it is assumed, for example, that the airplane will spend 20 percent of its flight time in the specialized high-altitude interception mission described previously and 80 percent of its flight time in other operational uses, the limit load factor could be selected in the manner indicated in figure 5.

[redacted]

[redacted]

On the left side of figure 5 is shown the probability curve for the specialized high-altitude interception mission in terms of flight time required to exceed a given load factor. On the right side of figure 5, the standard maneuver curve for the other operational uses is shown as a function of limit load factor. The curve shown is given for an assumed value of the average number of load-factor peaks per hour which may be estimated on the basis of past experience.

By assigning various values of the limit load factor to the upper curve, a series of probability curves are obtained as shown at the bottom on the right side of figure 5. At this point the limit load factor to select is not known; however, it is known that the airplane with the longest life at the least expense in weight is wanted. Therefore, if the mission curve is combined with each of the curves representing different limit load factors on the basis of 20 percent of the flight time spent performing the mission and 80 percent spent in nonmission operations, a series of resultant probability curves, one for each limit load selected, would be obtained. The flight time required to exceed limit load factor for each of the resultant curves would vary for the different cases.

In figure 6 the standard (or nonmission) curve based on limit load factor has been combined with the mission curve in the manner indicated above. Each bar represents an airplane having a given limit load factor and capable of performing the high-altitude interception mission previously mentioned. The height of each bar represents the flight time required to exceed the particular limit load factor for each case. For example, the height of the bar labeled 2g represents the time to exceed 2g and the height of the bar labeled 8g represents the time to exceed 8g, both of which are designed for the high-altitude mission previously discussed.

From figure 6 the limit load factor for the most suitable high-altitude interceptor may be selected. The airplane to select for the mission, therefore, would be the one which has the longest time to reach limit load factor but at the lowest practical limit load factor. In this hypothetical case, it would appear that an airplane with a limit load factor of 4g would be sufficient since it can be seen that little is gained in the time to reach limit load factor by selecting a higher strength airplane. It might be added that if the percentage of flight time spent in the mission was as low as 1 percent or even 0.1 percent, approximately the same limit load factor would be selected for this case.

At this time it should be pointed out that these results do not indicate that every high-altitude interceptor should be a 4g airplane. The results shown here are a result of the particular conditions assumed for the simplified mission. The results obtained in other cases could be different from those shown here, depending on the radar ranges, speed ratios, and altitudes chosen.

[redacted]

[redacted]

If, on the other hand, the airplane were to be designed for both high- and low-altitude missions, the results could be considerably different. For example, the right side of figure 6 indicates the results for a case where 20 percent of the airplane flight time was spent in performing the high-altitude interception, 1 percent in a different low-altitude interception such as dive-bombing, and 79 percent in other operations. In this case, the high-altitude-mission probability curve, the low-altitude probability curve, and the standard curve are combined as before. It may be seen for this particular case that the low-altitude mission dictated the design limit load factor even though the airplane was assumed to be used in this mission only 1 percent of the time, and it is indicated that an 8g airplane would be selected as the airplane which would have a long time to reach limit load factor at the lowest practical limit load factor. Low-altitude missions would not always affect the results in this manner, however, for it is possible that the probability functions for some low-altitude missions might not involve the probability of high load factors, as was the case in this illustration.

Therefore, after selecting the limit load factor on this basis, the time-to-exceed curves for the mission are combined with the standard time-to-exceed curve for the airplane selected (in this case it would be a 4g airplane) to form the resultant curve, shown in figure 7. Here the probability curve for the high-altitude mission is shown with the standard curve for a 4g airplane. These curves are then combined according to the percentages of flight time spent in each activity to form the resultant curve which is shown on the right side of figure 7. The peak at the lower load factors is caused by gusts.

Although the possibilities of calculating probability curves for specific missions and the combination of these specific probability curves with more general curves to predict the overall load experience have been mentioned only in regard to positive symmetrical wing loads, there exists the possibility of extending the reasoning to other loads such as negative wing loads and horizontal- and vertical-tail loads, although more factors will enter into the problem and tend to complicate the situation.

It is realized that in all the preceding discussion many questions still exist and will have to be dealt with by either analytical studies or the analysis of statistical data. For example, there are questions as to the validity and accuracy of the calculations of probability functions for a given mission. Such calculations could probably be made for many missions; however, for some missions, the probability function may require correlation with previous experience. One of the major questions concerns the determination of the percentage of flight time spent in performing each mission. This could be of importance if a large percentage of the flight time is spent in many specific missions such as indicated in table I.

[redacted]

Also there are questions concerning the use of a universal standard curve based on limit load factors for all the other airplane uses. It is believed that, on the basis of present knowledge, such a curve may be adequate up to the limit load factor. This curve, of course, will have to be revised gradually as the airplane characteristics change in future years. One of the important questions concerning this curve is the determination of the average number of load-factor peaks per hour. This number varies for different airplane types and uses and must be estimated from statistical data on past airplanes.

From the results of this study, the concept of stipulating the design loads on the basis of mission requirements appears to be feasible; however, statistical data will be needed in establishing the effect of missions on the load experience and the amount of time spent in each activity.

The work on this approach to the problem of design loads at the NACA is, as mentioned before, in a beginning stage, and the results that have been shown here have been presented to indicate a few of the possibilities of using statistical methods for correlation with design load requirements.

DEC[redacted]SIFIED

TABLE I

UTILIZATION OF AIRPLANE	FLIGHT MISSION	% OF TOTAL TIME	COMPONENT TIME-TO-EXCEED CURVES	% OF TOTAL TIME	
COMBAT AND COMBAT TRAINING	HIGH-ALTITUDE INTERCEPTION	10	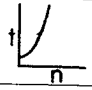	20	20
	MED.-ALTITUDE INTERCEPTION	1	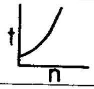	0	0
	LOW-ALTITUDE INTERCEPTION	5	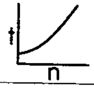	0	1
	STRAFING	1/4		0	0
	DIVE BOMBING	1/4		0	0
	AIR PATROL, ETC.	12		0	0
	OTHER MISSIONS	1/2		0	0
PILOT FAMILIARIZATION AND SQUADRON OPERATIONAL TRAINING	CROSS COUNTRY (NAVIG., FERRY, ETC.)	60	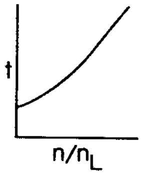	80	79
	ACROBATICS	2			
	TAKE-OFF AND LANDING PRACTICE	5			
EQUIP. DEVELOP. DURING SQUAD. OPER.	TRIALS OF RADAR EQUIPMENT, ETC.	4			

HIGH-ALTITUDE INTERCEPTION MISSION

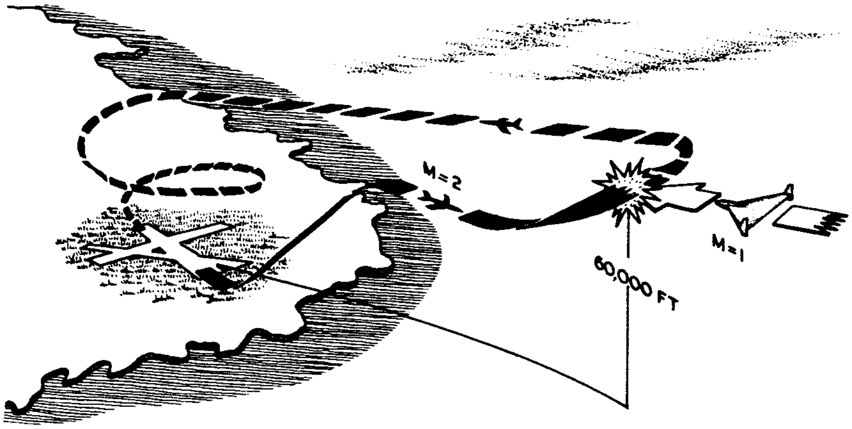

Figure 1

[redacted]

[redacted]

HIGH-ALTITUDE MISSION, ATTACK PHASE

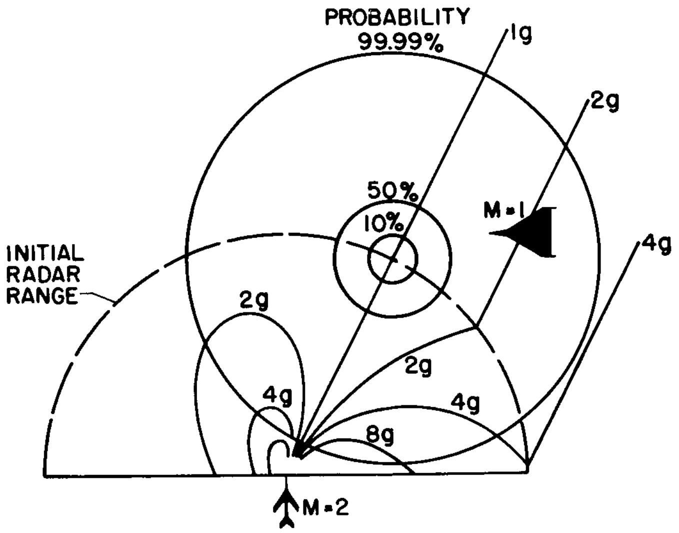

Figure 2

BREAKDOWN OF MISSION LOADS

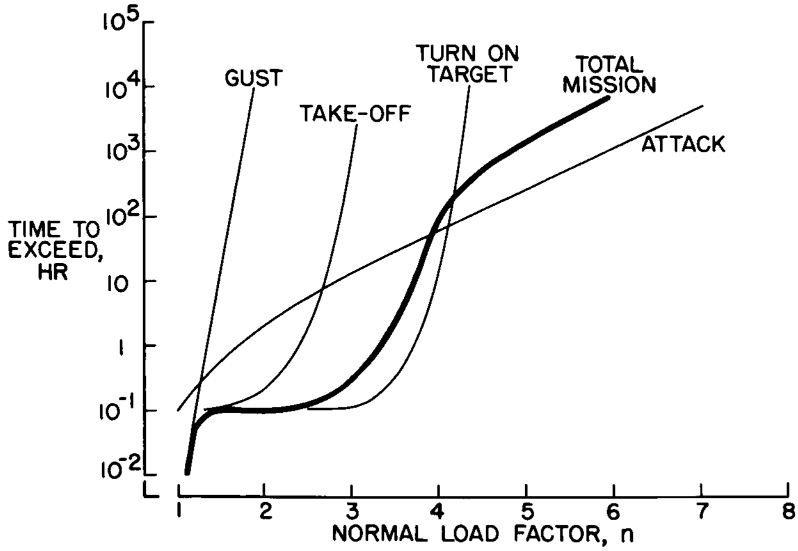

Figure 3

[redacted]

DEC[redacted]SIFIED

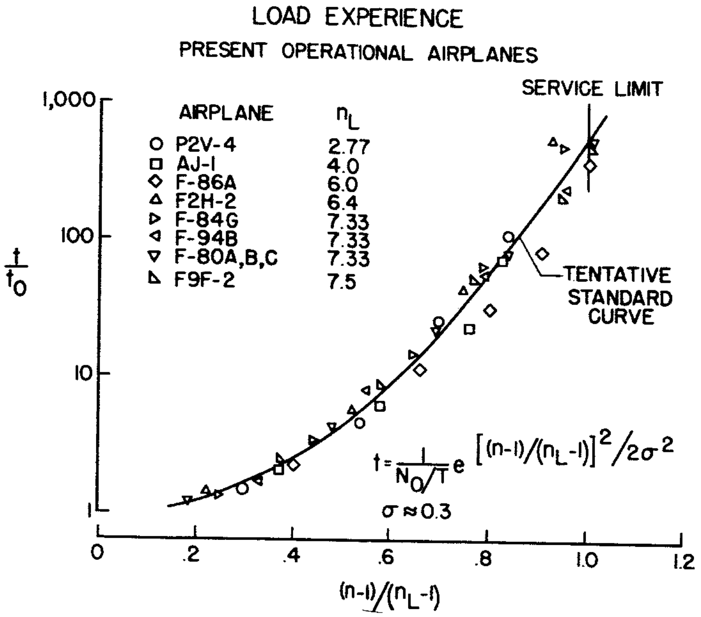

Figure 4

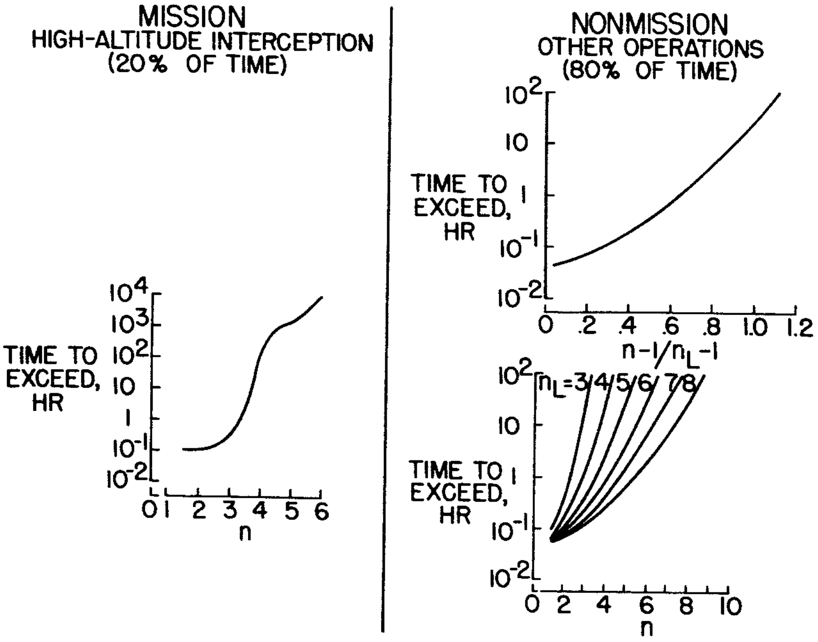

Figure 5

[redacted]

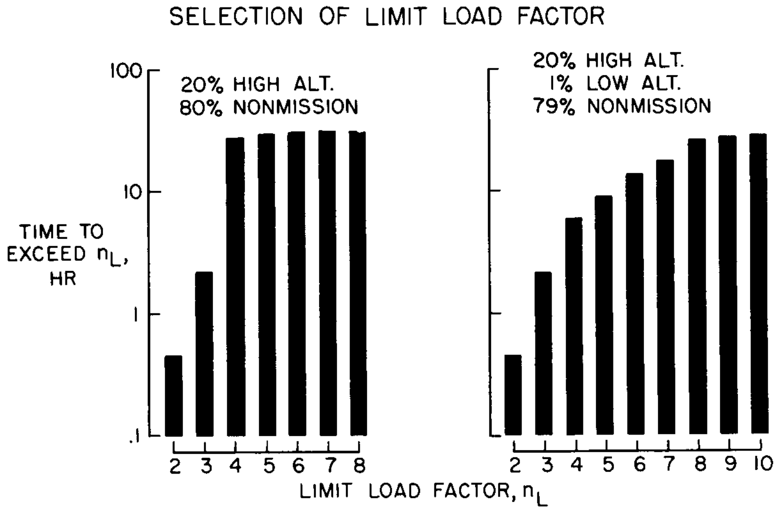

Figure 6

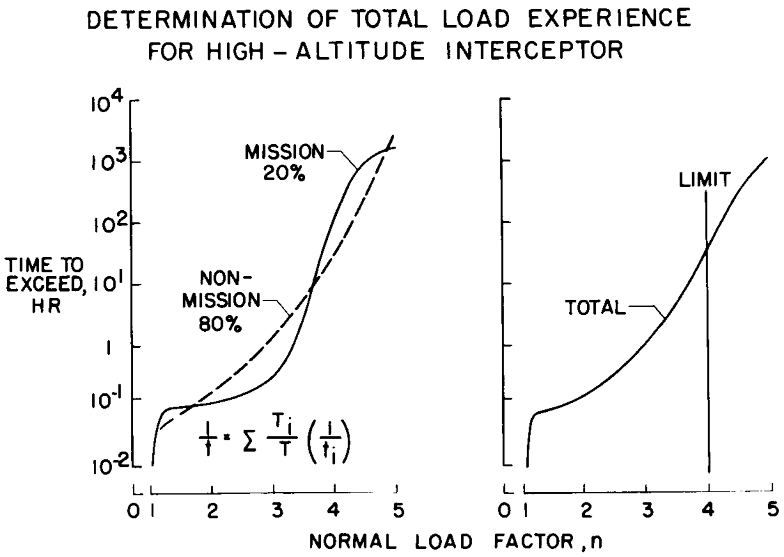

Figure 7

DE[redacted]SSIFIED

LOAD DISTRIBUTIONS ON WINGS AND WING-BODY COMBINATIONS AT HIGH ANGLES OF ATTACK AND SUPERSONIC SPEEDS

By Elliott D. Katzen and William C. Pitts

Ames Aeronautical Laboratory

INTRODUCTION

Maximum loads on present-day airplanes have generally been reached at high speed and high dynamic pressures at relatively low altitudes and low angles of attack. For aircraft which are required to maneuver rapidly at extreme altitudes, maximum loads are reached at high angles of attack. For the Mach numbers considered in present designs, loads information is necessary for both flight conditions. To provide the required information, extensive research programs have been undertaken (ref. 1, 2, and 3). In figure 1, the scope of the investigations is outlined. Data were obtained through the Mach number range from 1.45 to 3.36, which covers the current range in design for airplanes and missiles. The angle-of-attack range of the tests was 0° to 45°. The wing sweepback angles varied from 0° to 85°. In addition to wings alone, wing-body combinations were also studied.

The data obtained illustrate many nonlinear effects which make accurate prediction of loads difficult. These nonlinear effects on loads are usually, but not always, alleviating. They occur at low, as well as at high, angles of attack. The purpose of the present paper is to summarize these nonlinear effects and to indicate where departures from linearity and linear-theory predictions become important.

RESULTS AND DISCUSSION

Wings

Departures from the predictions of linear theory, for a thin wing, depend on sweep angle, Mach number, and angle of attack. For moderate sweep, moderate supersonic Mach numbers, and low angles of attack, linear theory is expected to give adequate answers. An example of such a case will be presented; then, typical nonlinear effects of variations in these test parameters will be illustrated.

An example of a case in which linear theory is applicable is shown in figure 2. The delta wing has an aspect ratio of 4, corresponding to

[redacted]

[redacted]

a sweepback angle of 45°. The wing section is 5-percent thick and has a trailing edge of 50-percent bluntness. The Mach number is 1.45 and the Reynolds number, based on the wing mean aerodynamic chord, is 2.1×10^6. At 3° angle of attack it is seen that agreement between theory and experiment is good. It is best at the inboard stations, toward the leading edge, and deteriorates somewhat toward the trailing edge and at the outboard stations. Curiously, even at 20° angle of attack where linear theory is not expected to be applicable, the agreement is still good at the inboard stations. At the 75-percent-semispan station the effects of separation and shock waves on the wing are large and are not accounted for theoretically. The predicted tip loads are higher than the experimental values so that wing bending moments, predicted on the basis of linear theory, would be conservative.

As the wing aspect ratio is reduced, or the leading-edge sweep increased, viscosity and separation affect a larger part of the wing. These results are exemplified (fig. 3) by a delta wing having a very low aspect ratio. The wing semiapex angle is 5°, corresponding to an aspect ratio of about 1/3. The wing section is a 1-percent-thick wedge with a trailing edge of 100-percent bluntness. The Mach number is 1.9 and the Reynolds number, based on the mean aerodynamic chord, is about 1×10^7. In figure 3, upper- and lower-surface lifting pressures are presented for the local semispan at the 78-percent-root-chord station. In addition to the experimental data at 3° and 6° angle of attack, linear theory is shown, and also a vortex theory (ref. 4) developed by Brown and Michael. The vortex-theory curve pertains to 3° angle of attack. The theory was developed by using a vortex model as shown, except that, for simplicity in the calculations, the spiral sheet was replaced by a concentrated vortex and a flat feeding sheet of vorticity. On the upper surface, at 3° angle of attack, the experimental data exhibit a region of increased suction, compared to linear theory, at about 75 percent of the semispan. The increased suction causes the total wing load, as predicted by linear theory, to be too low, or unconservative. At 6° angle of attack the suction peak moves inboard. The vortex theory also shows a suction peak at 3° but the magnitude and position are not properly estimated. The theory does predict inboard movement of the suction peak with increased angle of attack. Thus, qualitatively but not quantitatively, the estimated effects are in agreement with the experimental results for this wing which has a very low aspect ratio. For quantitative prediction, it appears that the simple vortex model must be modified.

As the Mach number and aspect ratio are increased the important nonlinear effects are no longer caused by viscosity and separation. Instead, there are nonlinearities from compression and expansion. An example of these effects is shown in figure 4. The Mach number is increased to 3.36 and the aspect ratio to 4. The wing is the same as that for which data were presented in figure 2 for a Mach number of 1.45. The section is 5-percent thick and has a trailing edge of 50-percent bluntness. The

[redacted]

Reynolds number is 2.1 × 10^6. The lifting-pressure coefficients are plotted along the chord for the various spanwise stations. The linear theory indicates uniform loading for that part of the wing forward of the Mach wave from the apex, with decreased loading behind the Mach wave. Comparison of the experimental data and linear theory shows large systematic differences, even at 3° angle of attack. The predicted loading is too low at the leading edge and too high at the trailing edge, so that the wing torsional loads would not be estimated properly.

For that part of the wing forward of the influence of the apex, a nonlinear solution can be obtained by extension of the shock-expansion method to three dimensions. This has been done by Vincenti and Fisher at the Ames Aeronautical Laboratory (ref. 5). In figure 5, theoretical curves obtained by this method for the wing at 0° and 3° angle of attack are shown. Linear theory, and the experimental data for that part of the wing forward of the influence of the apex, are also shown. The surface-pressure coefficients (due to wing thickness) at 0° and the lifting pressures at 3° are presented as functions of percentage distance along the local chord. The experimental data from the various spanwise stations have, at given chordwise positions, approximately the same value of surface-pressure and lifting-pressure coefficients. This means that the flow is essentially conical with respect to the tip; that is, the pressures are constant along rays from this point. This is to be expected, as the wing is a cone with respect to the tip; the geometry can be described by directions from this point since there is no characteristic length in the problem. For the pressures due to wing thickness at 0° angle of attack the differences between the linear theory and the three-dimensional shock-expansion theory are not large and there is good agreement with experiment. For the lifting pressures at 3° angle of attack, however, it is seen that the variation of lifting pressure along the chord is estimated more accurately by the three-dimensional shock-expansion theory. This theory is applicable to shock detachment, which occurs at about 15° angle of attack for this wing and Mach number. The differences between pressures given by three-dimensional shock-expansion theory and those predicted by the more familiar two-dimensional theory, for streamwise sections, are small for the present case. For example, at 10° angle of attack, the largest differences (10 percent to 15 percent) occur on the lower surface. On the upper surface the differences between the two theories are negligible at this Mach number of 3.36. For lower Mach numbers or more highly swept wings, the differences are larger. The differences are decreased as the Mach number normal to the leading edge is increased.

The nonlinearity in load distribution between the upper and lower surfaces of the wing at a Mach number of 3.36 and at high angles of attack is illustrated in figure 6. The wing is at 20° angle of attack where the bow wave is detached from the leading edge of the wing. At this angle of attack, the upper-surface pressure coefficients are

[redacted]

[redacted]

approaching a vacuum. The variation in lower-surface pressures along the chord resembles that given by two-dimensional shock-expansion theory, for streamwise sections, or Newtonian theory; but, as would be expected, the magnitudes are not given properly. As the angle of attack is increased beyond 20°, the upper-surface pressures approach a vacuum more closely. At 45° angle of attack, a 90-percent vacuum was reached.

Wing-Body Combinations

For the wing-body combinations, there are additional nonlinear effects resulting from interference. These nonlinearities are evaluated by comparison of high-angle experimental data with low-angle data or with existing slender-body or linear theories (ref. 6). For example, the result of body interference on wing-load distribution at angles of attack is shown in figure 7. The wing is the same aspect-ratio-4 wing studied previously. The ratio of body radius to wing semispan is 0.2 and the Mach number is 3.36. The nondimensional span loading, as a function of the percentage distance along the wing semispan, is given for 6° and 20° angle of attack. The normal-force coefficients, from the integrated span loadings, are shown for the angle-of-attack range. At 6° angle of attack, the loading for the wing in the presence of the body is increased by the body upwash over that for the wing alone. It would be unconservative to estimate the loads on the wing of the combination by using wing-alone data and ignoring the interference. The integrated increase in loading on the wing, as shown by the normal-force coefficient, is given accurately at 6° by the theory. At 20° angle of attack, however, the loading of the wing in the presence of the body is only slightly increased over that of the wing alone. This is also the case for the normal-force coefficient above about 10° angle of attack. The estimated wing bending moments would be conservative if the slender-body interference factor were used at high angles of attack.

The results of the interference of the body on wing-load distribution at angles of incidence - that is, incidence relative to the body - are illustrated in figure 8. Nondimensional span loading with the wing at 6° and 20° incidence and the body at 0° angle of attack is shown and the normal-force coefficients for the incidence angles from 0° to 40° are also presented. The span loadings for the wing alone are not greatly different from those of the wing in the presence of the body. The interference (the difference between the span loading for the wing alone and that for the wing of the combination) is less at 6° incidence than at 6° angle of attack. This is especially so for the span loading on the outboard part of the wing. Near the root, at 6° and 20° incidence angles, the loading on the wing of the combination is reduced from that of the wing alone because the body is not a perfect reflection plane, due to its curvature. The normal force on the wing of the combination is

[redacted]

predicted with good accuracy throughout the incidence range from 0° to 40° by applying a small interference factor from slender-body theory (ref. 6) to the experimental wing-alone results.

The effect of the presence of the wing on body loading at angles of attack is shown in figure 9. The local body loading along the body length at 6° and 20° angle of attack and the normal-force coefficients as a function of angle of attack are presented. At both angles of attack the loading on the afterbody of the body alone is given with fair accuracy by the viscous-crossflow method (see, for example, ref. 7). At 6° angle of attack the loading carried over from the wing is increased in the region near the wing and decreases toward the base of the body. At 20° angle of attack the presence of the wing is felt forward of the wing through the boundary layer on the body. In this forward region the loading starts to increase slightly. Near the wing the loading is increased rapidly. Behind the wing, the interference loading over the afterbody does not decrease toward the body base. This is a different result than at 6° angle of attack, or at high angles of attack at lower supersonic Mach numbers (see, for example, ref. 8). The integrated increase in normal force on the body, due to the wing, is predicted with good accuracy at high angles of attack even though the bending moments on the rear of the body, predicted by extrapolating from low-angle pressure data, would be unconservative.

The interference load distribution on the body with the wing at angles of incidence is illustrated in figure 10. The body is at 0° angle of attack so that the loading on the body alone is zero. The local loading along the body length for the body in the presence of the wing at 6° and 20° incidence angles and the normal-force coefficients of the body as a function of incidence angles from 0° to 40° are presented. At 6° incidence the loading on the body increases in the region of the wing and decreases toward the base in much the same manner as the loading at an angle of attack. At 20° incidence, however, the positive pressures from the lower surface of the wing are felt on the top of the body near the raised, or unported, wing leading edge. The result is a downward, or negative, loading on the body. Further downstream, the body loading becomes positive, decreasing toward the base of the body. The bending moments on the body at high angles of wing incidence could not be predicted by extrapolating low-angle data.

The effect on the agreement between theory and experiment of the negative loading is also shown for normal-force coefficients. At low incidence angles, the predicted normal force is in good agreement with experiment. Above about 10° the predicted total loads for the body are far above experiment. For wings of rectangular plan form having larger chords relative to the body than the present wing, the negative and positive body loadings were equal at large incidence angles so that the resultant was a couple: zero normal force and large local bending moments.

[redacted]

CONCLUDING REMARKS

Comparisons of the predicted and experimental loadings on wings and wing-body combinations have been presented, from which the following summarizing remarks can be made:

1. On very highly swept delta wings at moderate supersonic Mach numbers, viscosity and separation must be considered, even at low angles of attack, for accurate prediction of load distribution. For wings with less sweepback, but at higher Mach numbers, nonlinear effects of compression and expansion must be considered at all angles of attack.

2. For the wing-body combinations, there were additional nonlinear effects resulting from interference. At large angles of attack the effective body upwash was reduced so that the wing performed essentially as a wing alone. At large angles of wing incidence, unporting of the wing created a body loading which was highly nonlinear.

[redacted]

REFERENCES

1. Kaattari, George E.: Pressure Distributions on Triangular and Rectangular Wings to High Angles of Attack - Mach Numbers 1.45 and 1.97. NACA RM A54D19, 1954.

2. Kaattari, George E.: Pressure Distributions on Triangular and Rectangular Wings to High Angles of Attack - Mach Numbers 2.46 and 3.36. NACA RM A54J12, 1955.

3. Michael, William H., Jr.: Flow Studies on Flat-Plate Delta Wings at Supersonic Speed. (Prospective NACA paper.)

4. Brown, C. E., and Michael, W. H., Jr.: Effect of Leading-Edge Separation on the Lift of a Delta Wing. Jour. Aero. Sci., vol. 21, no. 10, Oct. 1954, pp. 690-694, 706.

5. Vincenti, Walter G., and Fisher, Newman H., Jr.: Calculation of the Supersonic Pressure Distribution on a Single-Curved Tapered Wing in Regions Uninfluenced by the Root or Tip. (Prospective NACA paper.)

6. Nielsen, Jack N., Kaattari, George E., and Drake, William C.: Comparison Between Prediction and Experiment for All-Movable Wing and Body Combinations at Supersonic Speeds - Lift, Pitching Moment, and Hinge Moment. NACA RM A52D29, 1952.

7. Allen, H. Julian, and Perkins, Edward W.: A Study of Effects of Viscosity on Flow Over Slender Inclined Bodies of Revolution. NACA Rep. 1048, 1951. (Supersedes NACA TN 2044).

8. Bright, Loren G.: A Flight Investigation at Transonic Speeds of a Model Having a Triangular Wing of Aspect Ratio 4. NACA RM A54L27, 1955.

[redacted]

[redacted]

[redacted]

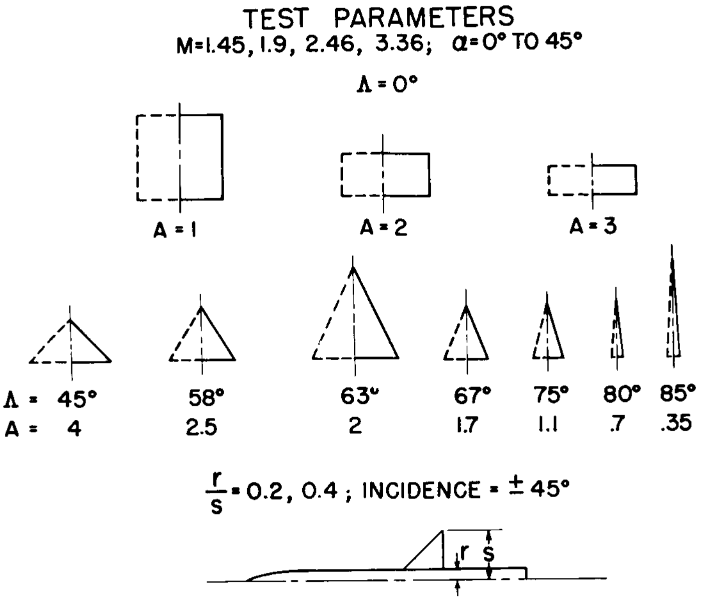
TEST PARAMETERS
M=1.45, 1.9, 2.46, 3.36; α=0° TO 45°
Λ = 0°
A = 1
A = 2
A = 3
Λ = 45° 58° 63° 67° 75° 80° 85°
A = 4 2.5 2 1.7 1.1 .7 .35
r/s = 0.2, 0.4 ; INCIDENCE = ± 45°
r
s

Figure 1

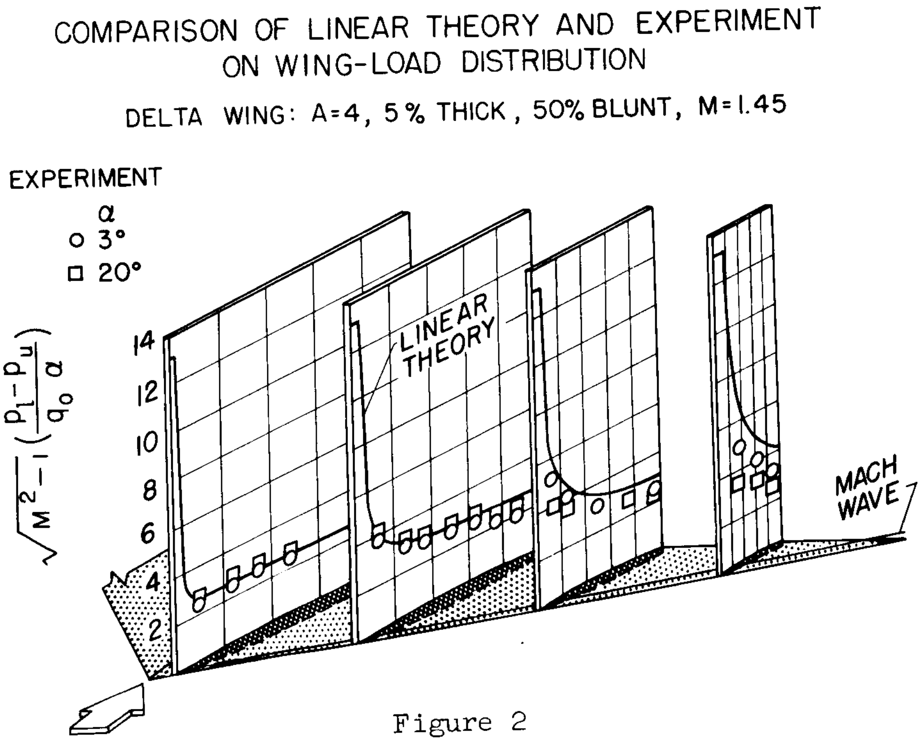

Figure 2

[redacted]

[redacted]

COMPARISON OF THEORY AND EXPERIMENT FOR PRESSURES

DELTA WING: A=0.35, 1% THICK, 100% BLUNT, M=1.9

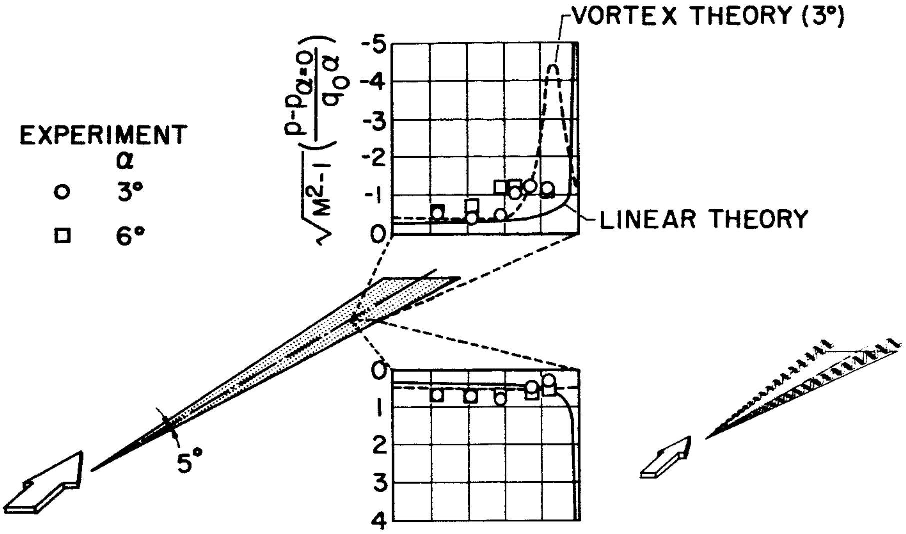

Figure 3

COMPARISON OF LINEAR THEORY AND EXPERIMENT ON WING-LOAD DISTRIBUTION

DELTA WING: A=4, α=3°, 5% THICK, 50% BLUNT, M=3.36

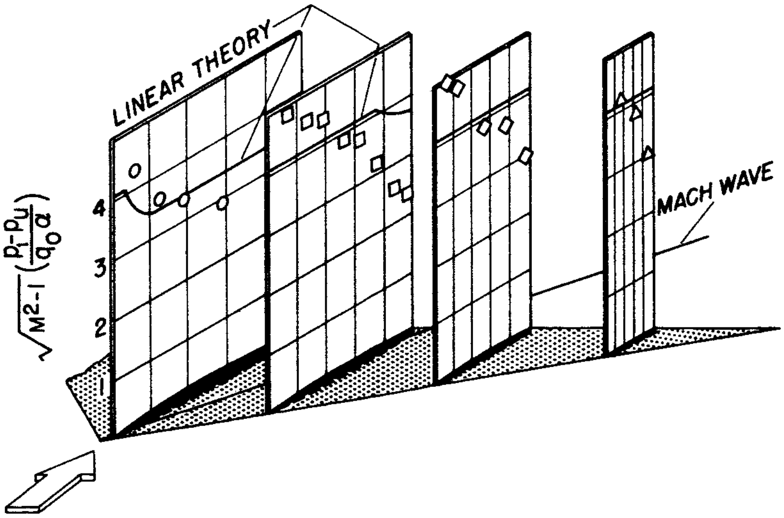

Figure 4

[redacted]

[redacted]

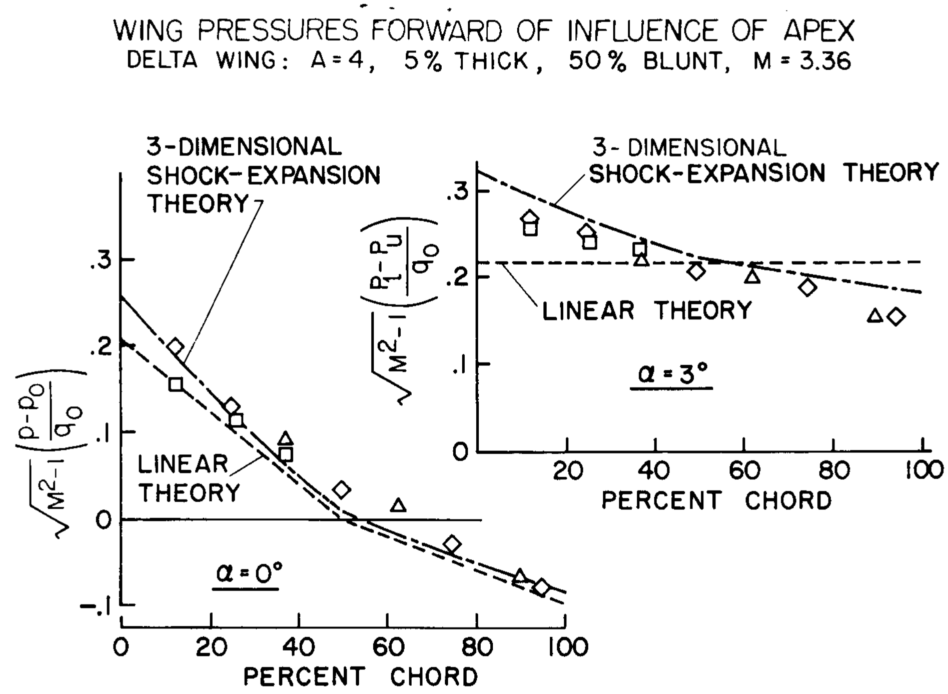

Figure 5

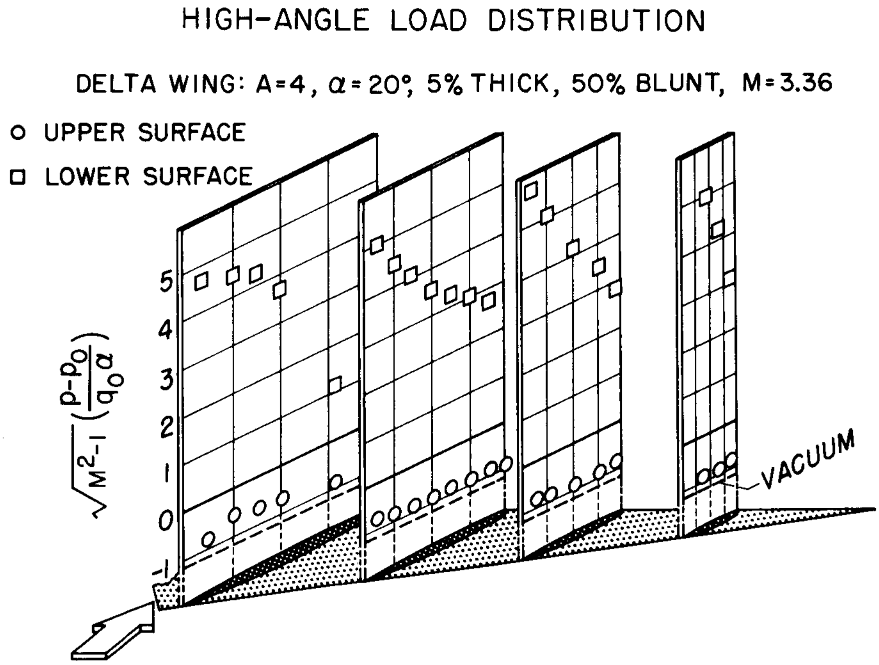

Figure 6

[redacted]

DE[redacted]SIFIED

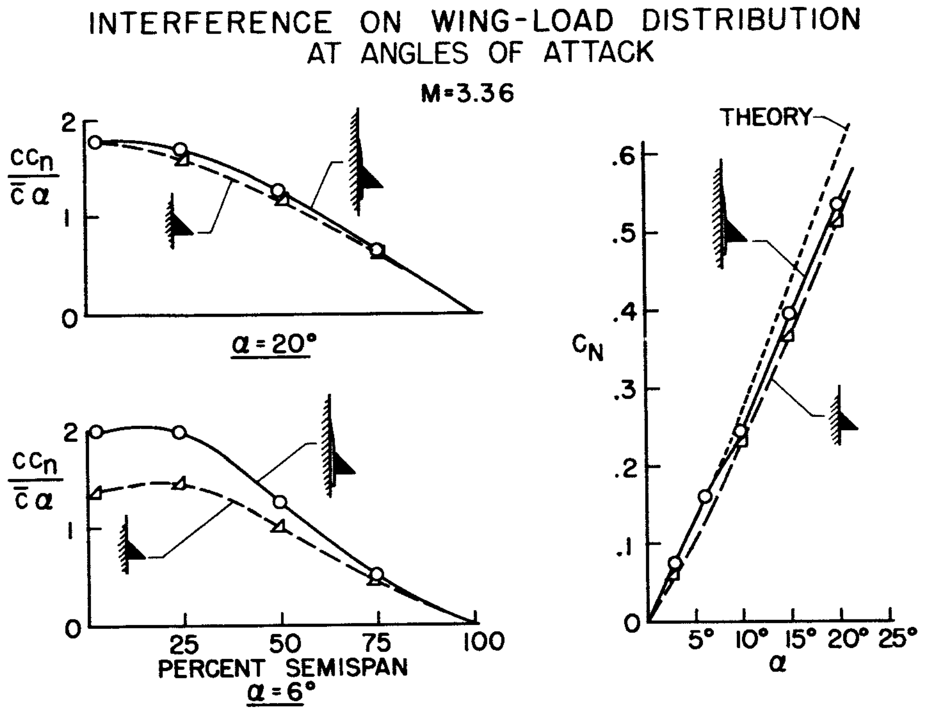
INTERFERENCE ON WING-LOAD DISTRIBUTION AT ANGLES OF ATTACK

M=3.36

Figure 7

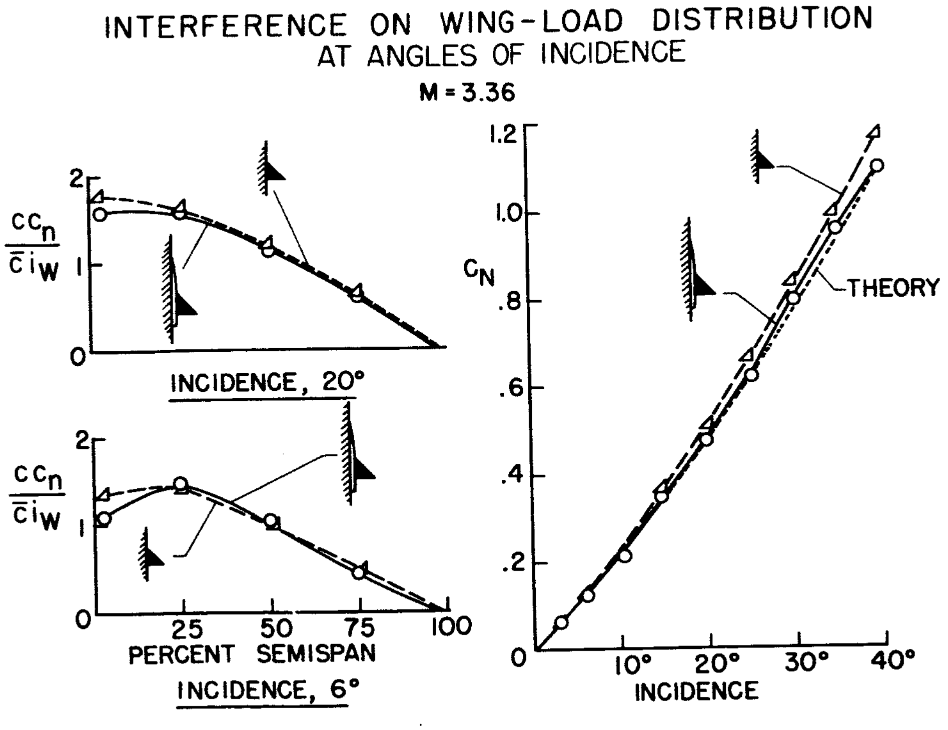
INTERFERENCE ON WING-LOAD DISTRIBUTION AT ANGLES OF INCIDENCE

M = 3.36

Figure 8

[redacted]

[redacted]

INTERFERENCE ON BODY-LOAD DISTRIBUTION AT ANGLES OF ATTACK

M=3.36

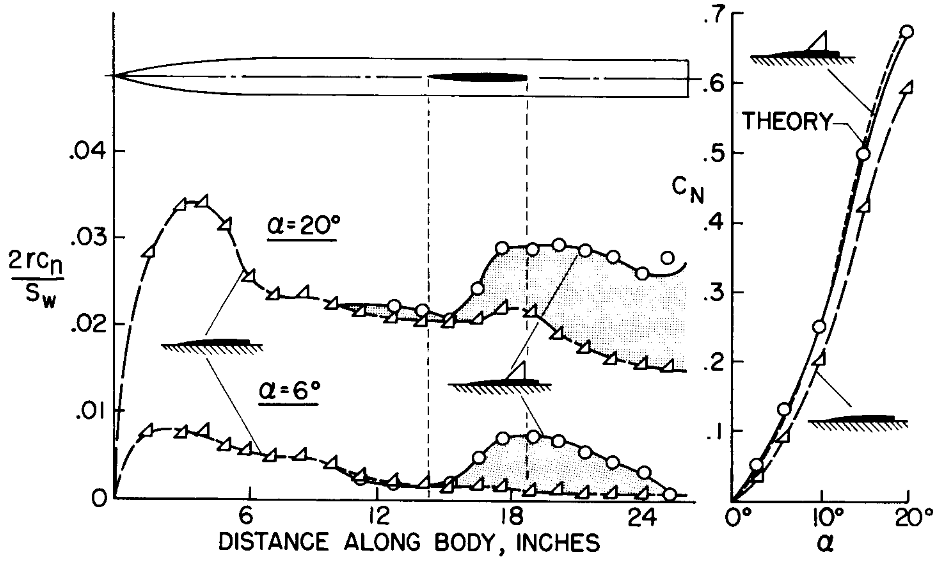

Figure 9

INTERFERENCE ON BODY-LOAD DISTRIBUTION AT INCIDENCE

M=3.36

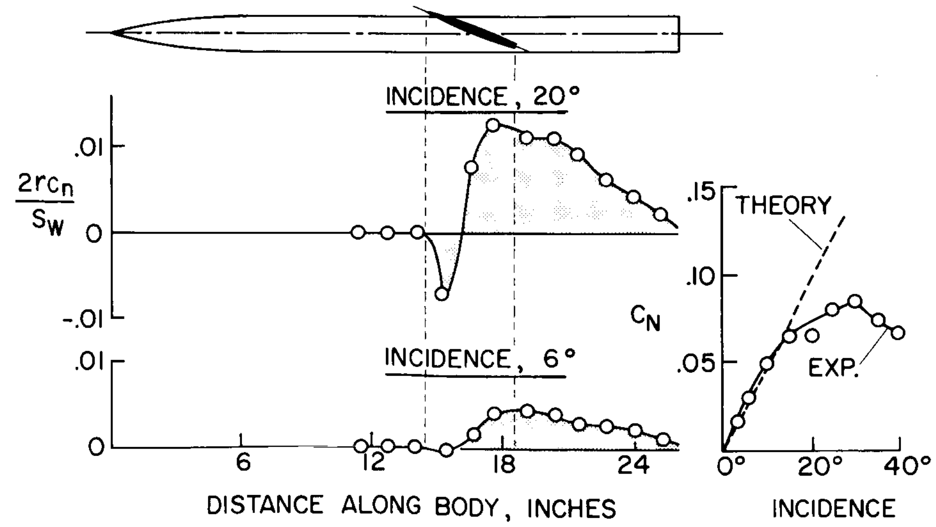

Figure 10

[redacted]

DEC[redacted]SIFIED

LOADS ON THIN WINGS AT TRANSONIC SPEEDS

By Don D. Davis, Jr., and Gerald Hieser

Langley Aeronautical Laboratory

SUMMARY

Experimental loads data at transonic speeds are reviewed in an attempt to sort out the effects of several configuration variables on the overall wing loads, and to establish the relative importance of these variables.

All plan forms show a large rearward shift of the center of pressure in the transonic speed range, but the Mach number at which this shift begins is found to be a function of such factors as taper ratio, thickness ratio, sweep angle, and the shape of the body. The center of pressure also tends to shift outboard in the transonic speed range, but this shift is found to be much larger for swept wings of medium taper than for highly tapered swept wings or for unswept or delta wings.

Wing loads measured in flight on the D-558-II airplane, which has a wing thickness ratio of about 0.09, are similar to those measured on a 6-percent-thick wing of similar sweep and aspect ratio, except that the transition from subsonic to supersonic loading characteristics begins at a lower Mach number for the thicker wing. This similarity indicates the possibility of applying these flight-test results in the structural design of thinner wings.

INTRODUCTION

Studies of aerodynamic loading at transonic speeds (for example, ref. 1) have revealed that a change in wing thickness ratio from a large value such as 0.09 to a smaller value such as 0.06 often results in large changes in wing loading characteristics. Several research programs have been conducted at the NACA for the purpose of determining the effects of configuration changes on the aerodynamic loading of thin wings (6 percent thick and less) at transonic speeds. The purpose of this paper is to summarize this information in a manner that will aid in the evaluation of the relative importance of the variables that affect wing loads. For the most part, the location of the center of loading on the wing will be used as an indicator of the overall wing loads.

[redacted]

[redacted]

SYMBOLS

A	aspect ratio
b	span
c	chord
$\bar{c}$	mean aerodynamic chord
c_{av}	average chord
i	incidence angle
M	Mach number
P	pressure coefficient
t/c	thickness ratio
x/c	distance along wing chord, measured from leading edge, fraction of chord
x_{cp}	chordwise location of center of pressure
y	lateral distance
y_{cp}	spanwise location of center of pressure measured from wing-body juncture
C_{B_e}	exposed-wing bending-moment coefficient
C_{m_e}	exposed-wing pitching-moment coefficient
C_{N_e}	exposed-wing normal-force coefficient
α	angle of attack
δ_N	nose droop angle
Λ	sweepback angle (subscripts .25, .30, and .50 specify reference chord line)
λ	taper ratio

[redacted]

[redacted]

Subscripts:

e	exposed wing
LE	leading edge

Test designations (used in fig. 1):

F	flight (including pressure measurements)
P	wind-tunnel pressure
WB	wind-tunnel wing balance

DISCUSSION

Some of the wing-body combinations and airplanes for which wing loads data are available are represented in figure 1 (refs. 2 to 11). The symbol P in the figure signifies wind-tunnel pressure tests, and the symbol F refers to flight tests during which pressures were also measured. For the remainder of the configurations, data have been obtained from wing balances as signified by the symbol WB. The available pressure data have made it possible to study in some detail the changes in wing loading that occur in the region of transition from subsonic to supersonic speeds. However, very little detailed pressure information is included in this paper.

In figure 2, chordwise and spanwise center-of-pressure locations obtained from the data of reference 7 are plotted as a function of Mach number at a normal-force coefficient of 0.5 for two wings differing only in thickness ratio. Note that the data in this and all ensuing figures are reduced on the basis of exposed-wing geometry as indicated by the subscript e. The unusually rearward position of the wings on the research body shown in figure 2 probably has no major effect on the wing loads.

The large rearward movement of the center of pressure between Mach numbers of about 0.8 and 0.95 is due to the rearward travel of the wing shock (fig. 2). This shock reaches the trailing edge at a Mach number of about 0.95 at which speed the flow over the upper surface of the wing is almost entirely supersonic, and further increases in Mach number up to 1.2 result in only small additional movement of the center of pressure. For these thin straight wings, the lateral position of the center of pressure is affected little by the variation of Mach number. Reducing the thickness ratio from 0.06 to 0.04 results in only a small shift of the center of pressure - rearward and outboard - and thus in only a small

[redacted]

change in the loads. This trend exists throughout the normal-force range below the stall. Unpublished data from a different wing, for which chordwise pressure distributions were obtained at two spanwise stations, show that reducing the thickness ratio from 0.04 to 0.02 has an even smaller effect on the chordwise center of pressure than shown here.

Plots of the center of pressure for three wings with about 35° of sweep - a wind-tunnel model (ref. 7) and the F86-A (ref. 12) and D-558-II (ref. 8) airplanes - are shown in figure 3. Note that the center of pressure for the F-86A airplane shows a rather severe forward and inboard movement in the transonic speed range which results from a loss of lift at the tip of the wing. This characteristic has been described in the past as being typical of thick wings, because it was found that, when the thickness ratio was reduced sufficiently, the forward and inboard movement of center of pressure was eliminated. The data for the D-558-II research airplane show that the center of pressure moves rearward and outboard as the speed is increased in the transonic range, a characteristic which has been described as typical of thin swept wings. In this particular case, however, the wide difference in the behavior of center of pressure between the F-86A and D-558-II airplanes cannot be explained on the basis of wing thickness because the thickness ratios average about 0.09 for both airplanes. The differences in sweep and taper ratio are also small, but there is a significant change in aspect ratio from 3.6 for the D-558-II to 4.8 for the F-86A. Increasing the aspect ratio thus is seen to have an effect similar to that of increasing the thickness ratio, in that eventually a point is reached where further increases result in a loss in lift at the wing tips at transonic speeds with a resultant inboard and forward movement of the center of pressure. The solid lines in figure 3 indicate the center of pressure of the 6-percent-thick wind-tunnel model. The only significant difference between these curves and those for the D-558-II airplane is a delay in the Mach number at which the rearward and outboard movement of the center of pressure begins. This delay is due to the decreased thickness ratio of the wind-tunnel model which reduces the induced velocities over the wing. It is apparent from the comparison in figure 3 that the flight data from the D-558-II airplane can be used with some confidence in estimating the loads on much thinner wings of about the same plan form, whereas the F-86A data are likely to give misleading results if applied to thin wings.

In connection with the data of figure 2, it was noted that the center-of-pressure movement at supersonic speeds was relatively small for unswept wings. A similar trend is shown in figure 3 for swept wings. The flight data not only verify this trend but also show that it extends to the limit of the test data at a Mach number of 1.5. The spanwise center of pressure for the 6-percent-thick wing has been calculated at $M = 1.2$, 1.26, and 1.5 by linearized theory. The results are plotted as the diamond points and show good agreement between the theory and experiment. With decreasing supersonic Mach number, the linearized theory predicts a sizeable inboard shift of the center of loading beginning at the point where the Mach lines become parallel to the wing trailing edge - the so-called subsonic trailing-edge case. Experimentally, this shift is found to occur at subsonic rather than low supersonic speeds. If the calculations are started at the lowest Mach number for which the supersonic trailing-edge theory is applicable, and the resulting curves are simply extrapolated back to $M = 1$, the spanwise center of load for swept wings will be predicted with better accuracy than by using the theory for subsonic trailing edges.

The advantages of thin wings for high-speed flight have been clearly established from a performance standpoint. However, the choice of plan form depends to some extent on the intended mission of the airplane and therefore unswept, swept, and delta wings are all under consideration. The chordwise and spanwise center of pressure is shown in figure 4 as a function of Mach number for one of the unswept wings shown previously and also for a swept (ref. 7) and a delta wing (unpublished data) at a value of C_{N_e} of 0.5. The wings utilized here are representative of the three types of plan form, but are not necessarily optimum from a performance standpoint. Only the unswept and swept wings have the same aspect ratio, taper ratio, and thickness ratio. Although the thickness ratio of the delta wing is considerably lower than that of the other two wings, the differences shown here are primarily due to the change in plan form. Comparing the chordwise center-of-pressure location for the unswept and swept wings reveals that sweep has resulted in an increase in the Mach number at which the rearward shift of the center of pressure begins; but, at a Mach number of 1.2, the center of pressure of the two wings is in nearly the same chordwise location. The lateral center of pressure for the swept wing shows an outboard movement of about 7 percent of the exposed semispan, as Mach number is increased from subsonic to supersonic speeds. For the delta wing, the chordwise center of pressure is considerably farther rearward than for the other wings. However, because of the change in plan form the mean aerodynamic chord for the delta wing is farther inboard and considerably longer than for the other two wings, although the wing areas are the same. As a result, the rearward center-of-pressure movement with increasing Mach number for the delta wing is larger, relative to that for the other two wings, than might appear from the data of figure 4. The spanwise center of pressure for the delta wing is located farther inboard than that for the other two wings and, like the unswept wing, it shows a much smaller movement through the transition from subsonic to supersonic flow than does the spanwise center of pressure of the swept wing.

The variation of the chordwise and spanwise center-of-pressure locations with wing normal-force coefficient for the same three wings of figure 4 is shown in figure 5. At a Mach number of 0.8, the chordwise center of pressure for the unswept wing shows a large rearward movement in the upper range of C_{N_e}, and is accompanied by an outboard movement. For the swept and delta wings, the inboard and forward movement of center of pressure that begins at normal-force coefficients of 0.5 to 0.8 is associated with tip stalling. This characteristic is undesirable from a longitudinal-stability standpoint and modifications incorporated to improve the stability generally delay the beginning of this center-of-pressure shift to higher normal-force coefficients. At a Mach number of 1.2, for the unswept and delta wings, the chordwise position of the center of pressure shows very little movement with increasing C_{N_e} within the range of the data. The center of pressure of the swept wing again shows a forward movement at high values of C_{N_e}. The spanwise center of pressure for the unswept wing is nearly constant at $M = 1.2$, whereas the swept and delta wings experience an inboard movement of the center of pressure that is similar to that shown at $M = 0.8$, although it is less severe. At a Mach number of 1.2, the spanwise center of pressure of the swept wing is outboard of that for the unswept wing throughout most of the range of C_{N_e}. As a result the root bending moments for the swept wing will be higher, in general, than those for the unswept wing. For example, in a maneuver at $C_{N_e} = 0.4$ and $M = 1.2$, the root bending moment for the swept wing would be about 17 percent higher than for the unswept wing.

Structural considerations lead to a desire for rather highly tapered wings. Center-of-pressure locations for two swept wings identical except for taper ratio were obtained from reference 6 and are presented in figure 6. In comparing wings of different taper ratio, it is important to recognize that the mean aerodynamic chord of the more highly tapered wing is located farther inboard and is also longer. There is one chord on the wing, however, that is unaffected by a change in taper ratio; namely, the average chord of the complete wing. Consequently, the average chord has been selected as a basis for this comparison, and on this basis the change in taper ratio from 0.6 to 0.3 is found to have very little effect on the center-of-pressure location at subsonic and supersonic speeds. The transition in the transonic speed range, however, begins at a lower Mach number for the more highly tapered wing.

Some unpublished data on an even more highly tapered wing ($\lambda = 0.15$) showed an outboard movement in the spanwise center of loading of less than 2 percent of the exposed semispan at transonic speeds as compared to about 7 percent for the wings shown in figure 6. The bending-moment characteristics of a very highly tapered wing thus seem to approach those of a delta wing, and the moment increase at transonic speeds is smaller than for the wings shown in figure 6. This is, of course, a favorable effect as for as the wing loads are concerned. The wing with a taper ratio of 0.15 has the same sweep and aspect ratio as the wings shown in figure 6, but it was specifically designed for efficient flight at transonic speeds and has camber and thinner airfoil sections. The division of load between the wing and the body and the spanwise distribution of load for this wing are shown in subsequent papers by Thomas C. Kelly and John L. Crigler.

At the present time, contoured bodies are being considered in the design of transonic and supersonic airplanes. In figure 7 is shown the effect of body indentation on the center-of-pressure location for a wing of aspect ratio 2.67 (unpublished data). The change in body shape is seen to result in a somewhat rearward and inboard movement of the center of pressure throughout the speed range. Tests of other wings have shown that the effect of body contouring on wing loads is less for wings of higher aspect ratio (ref. 6). This is to be expected because the effect of the body shape on the wing pressures is confined largely to the region of the wing near the body (ref. 13).

Another factor that has received increased attention recently is the use of leading-edge camber on the wings of high-speed airplanes. In order to discuss the effects of such camber on the aerodynamic loads, it is necessary to inspect chordwise pressure distributions. Pressures at the 28-percent-semispan station are shown in figure 8 for an unswept wing with the leading edge undrooped (ref. 10) and drooped 6° and 10° along the 17-percent-chord line, at angles of attack of about 5° and 13°. Pressures for the drooped cases were obtained from unpublished data. The results shown in this figure are typical of those at other spanwise stations. As the leading edge is drooped to progressively higher angles at an angle of attack of about 5°, the suction above the leading edge is reduced at Mach numbers of both 0.8 and 1.0. Thus, the loads on the mechanism that are required to droop the leading edge are highest at the breakaway point, and they can be estimated from pressure distributions on the undrooped wing.

At a Mach number of 0.8 and an angle of attack of about 5°, increasing the droop results in a rearward movement of the wing shock, but behind this shock the droop has little effect on the wing loads (fig. 8). As the angle of attack is increased, the loads on the undrooped nose increase until the flow separates, at which point the loads are considerably reduced. At an angle of attack of about 13° and a Mach number of 0.8, the flow is completely separated at the leading edge for the 0° and 6° droop cases, but there is still a negative pressure peak at 10° of droop. At about the same angle of attack and a Mach number of 1.0, there is still a small reduction in the leading-edge load as the droop is increased. Note that the trailing-edge loads are not affected by droop at either Mach number.

Unpublished results from chordwise loadings for a 45° swept wing with a drooped leading edge show trends similar to the unswept-wing data of figure 8.

An indication of the effect of leading-edge droop on the total wing loads is given in figure 9 which shows the pitching-moment and root-bending-moment coefficients for a swept wing with and without droop, and the root-bending-moment coefficient for the unswept wing with and without droop. The moments, rather than the center of pressure, are plotted in this figure because it is felt that they may give a somewhat clearer picture of the effect of droop. The bending moment at a constant C_{N_e} is essentially unaffected by the camber for both the swept and unswept wings, within the range of the data. Application of camber to the swept wing causes a negative increment in the pitching-moment coefficient that is nearly constant up to a normal-force coefficient of 0.4.

Camber effects are of particular interest in the case of delta wings. Although no data can be presented at this time, tests are being made on a delta wing with conical leading-edge camber.

The effect of a change in wing incidence from 0° to 4° on the pitching-moment and root-bending-moment coefficients for a swept wing is presented in figure 10 at a Mach number of 1.0 (unpublished data). The effect of this incidence change on the loads is only a small proportion of the maximum loads. Incidence causes an essentially constant increment in the pitching and bending moments through a large part of the normal-force range. Thus, the principle of superposition of a basic loading due to incidence and an additional loading due to angle of attack is apparently valid at sonic speed as well as at subsonic speed.

CONCLUDING REMARKS

This discussion of experimental loads data at transonic speeds has been an attempt to sort out the effects of several configuration variables on the overall wing loads, and to establish the relative importance of these variables.

All plan forms show a large rearward shift of the center of pressure in the transonic speed range, but the Mach number at which this shift begins is found to be a function of such factors as taper ratio, thickness ratio, sweep angle, and the shape of the body. The center of pressure also tends to shift outboard in the transonic speed range, but this shift is found to be much larger for swept wings of medium taper than for highly tapered swept wings or for unswept or delta wings.

[redacted]

Wing loads measured in flight on the D-558-II airplane, which has a wing thickness ratio of about 0.09, are similar to those measured on a 6-percent-thick wing of similar sweep and aspect ratio, except that the transition from subsonic to supersonic loading characteristics begins at a lower Mach number for the thicker wing. This similarity indicates the possibility of applying these flight-test results in the structural design of thinner wings.

REFERENCES

1. Williams, Claude V., and Kuhn, Richard E.: A Study of Aerodynamic Loads on Sweptback Wings at Transonic Speeds. NACA RM L53E08b, 1953.

2. Williams, Claude V.: An Investigation of the Effects of a Geometric Twist on the Aerodynamic Loading Characteristics of a 45° Sweptback Wing-Body Configuration at Transonic Speeds. NACA RM L54H18, 1954.

3. Robinson, Harold L.: The Effects of Wing Incidence on the Aerodynamic Loading Characteristics of a Sweptback Wing-Body Combination at Transonic Speeds. NACA RM L54G23b, 1954.

4. Runckel, Jack F., and Steinberg, Seymour: Effects of Leading-Edge Slats on the Aerodynamic Characteristics of a 45° Sweptback Wing-Fuselage Configuration at Mach Numbers of 0.4 to 1.03. NACA RM L53F23, 1953.

5. West, F. E., Jr., and Henderson, James H.: Relationship of Flow Over a 45° Sweptback Wing With and Without Leading-Edge Chord-Extensions to Longitudinal Stability Characteristics at Mach Numbers From 0.60 to 1.03. NACA RM L53H18b, 1953.

6. Delano, James B., and Mugler, John P., Jr.: Transonic Wind-Tunnel Investigation of the Effects of Taper Ratio and Body Indentation on the Aerodynamic Loading Characteristics of a 45° Sweptback Wing in the Presence of a Body. NACA RM L54L28, 1955.

7. Platt, Robert J., Jr., and Brooks, Joseph D.: Transonic Wind-Tunnel Investigation of the Effects of Sweepback and Thickness Ratio on the Wing Loads of a Wing-Body Combination of Aspect Ratio 4 and Taper Ratio 0.6. NACA RM L54L31b, 1955.

8. Robinson, Glenn H., Cothren, George E., Jr., and Pembo, Chris: Wing-Loads Measurements at Supersonic Speeds of the Douglas D-558-II Research Airplane. NACA RM H54L27, 1955.

[redacted]

9. Kuhl, Albert E., and Johnson, Clinton T.: Flight Measurements of Wing Loads on the Convair XF-92A Delta-Wing Airplane. (Prospective NACA paper.)

10. Hieser, Gerald, Henderson, James H., and Swihart, John M.: Transonic Aerodynamic and Loads Characteristics of a 4-Percent-Thick Unswept-Wing—Fuselage Combination. NACA RM L54B24, 1954.

11. Jordan, Gareth H., and Hutchins, C. Kenneth, Jr.: Preliminary Flight-Determined Pressure Distributions Over the Wing of the Douglas X-3 Research Airplane at Subsonic and Transonic Mach Numbers. NACA RM H55A10, 1955.

12. Rolls, L. Stewart, and Matteson, Frederick H.: Wing Load Distribution on a Swept-Wing Airplane in Flight at Mach Numbers up to 1.11, and Comparison With Theory. NACA RM A52A31, 1952.

13. Byrd, Paul F.: Theoretical Pressure Distributions for Some Slender Wing-Body Combinations at Zero Lift. NACA RM A54J07, 1955.

WING-LOADS TESTS AT TRANSONIC SPEEDS
P, PRESSURES; WB, WING BALANCE; F, FLIGHT TESTS

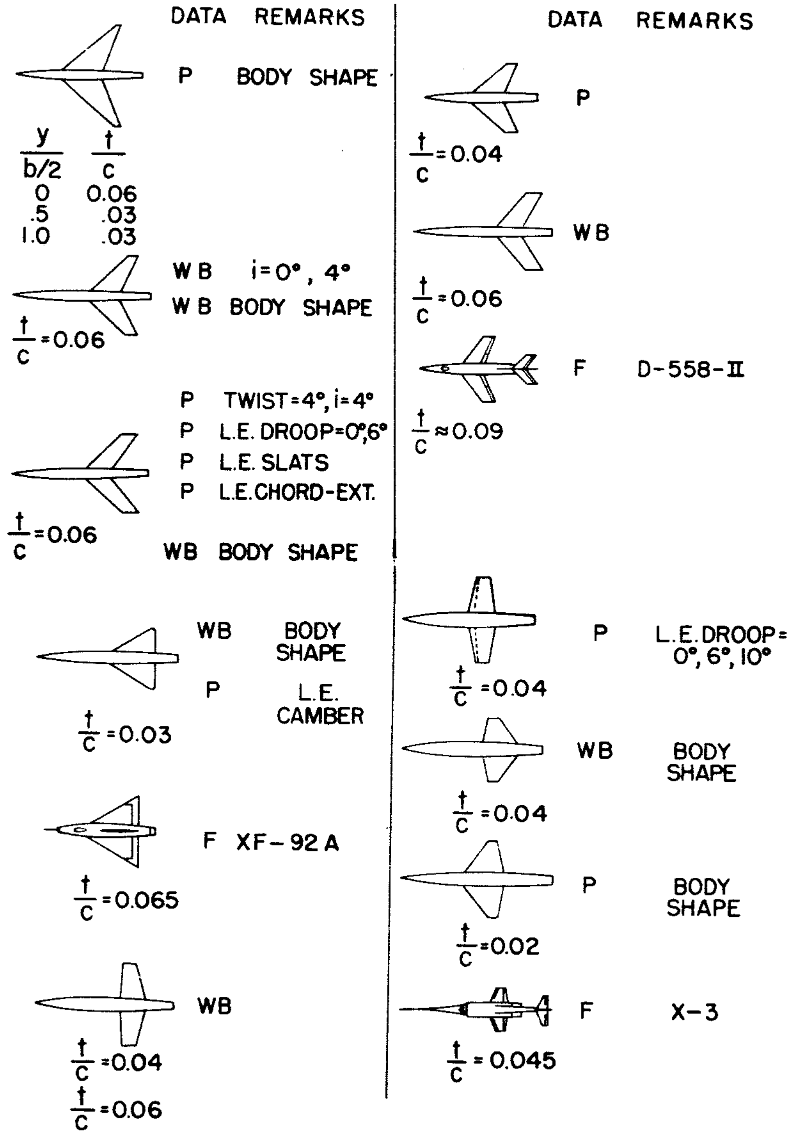

Figure 1

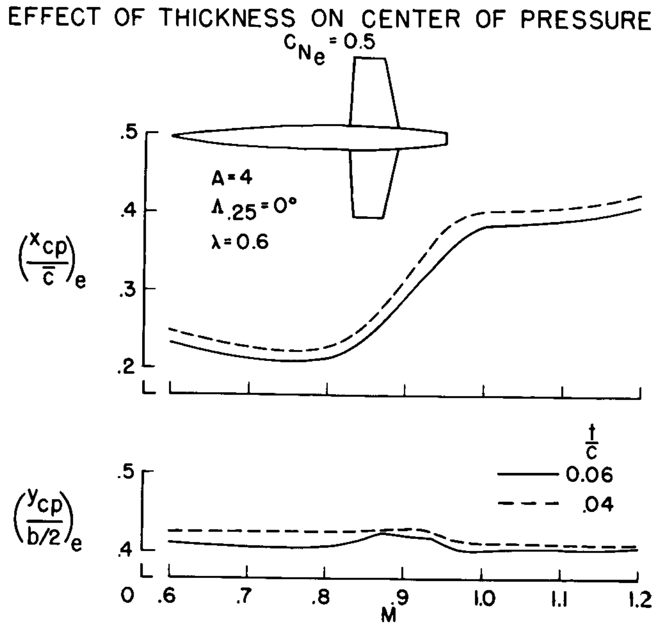

Figure 2

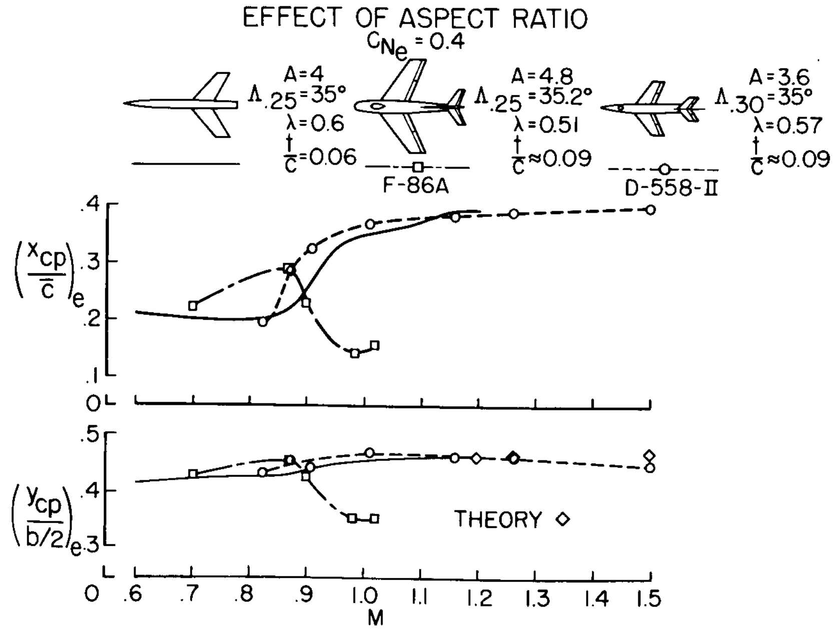

Figure 3

DECLASSIFIED

[redacted]

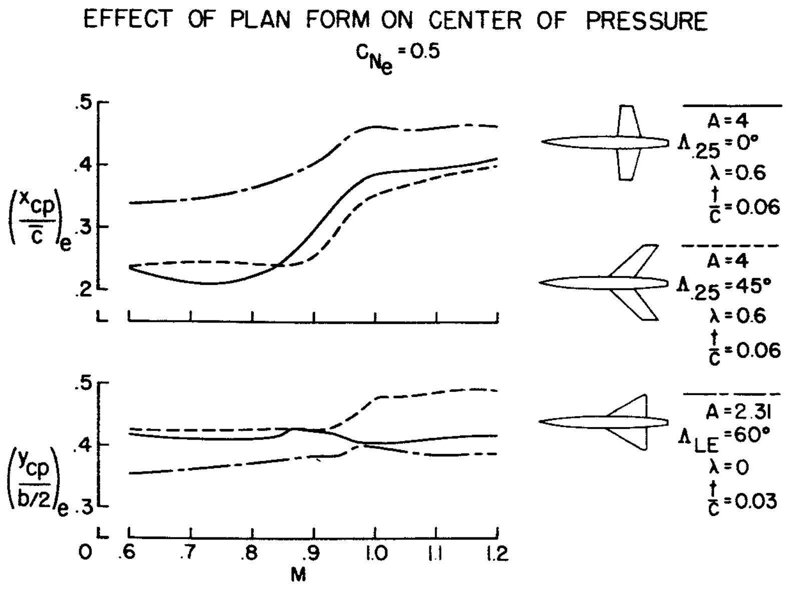

EFFECT OF PLAN FORM ON CENTER OF PRESSURE

$C_{N_e} = 0.5$

Figure 4

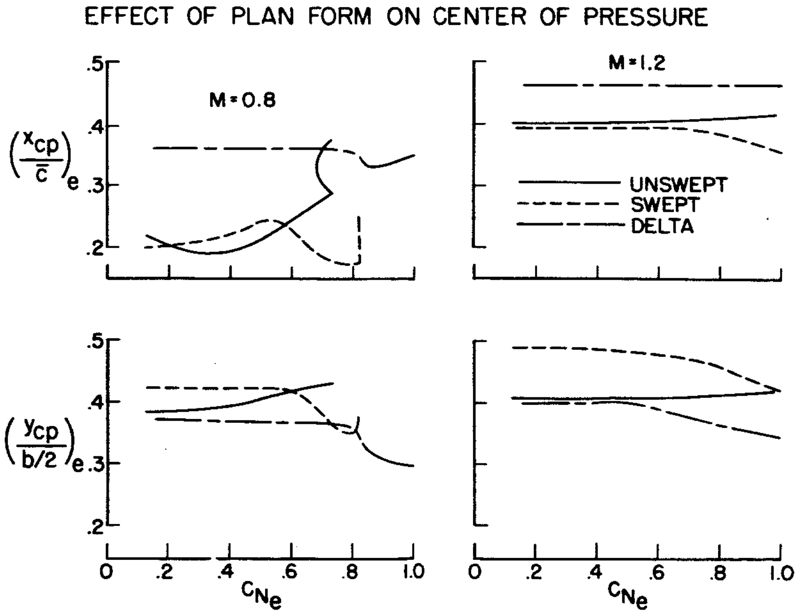

EFFECT OF PLAN FORM ON CENTER OF PRESSURE

Figure 5

[redacted]

[redacted]

EFFECT OF TAPER RATIO ON CENTER OF PRESSURE

$C_{N_e} = 0.4$

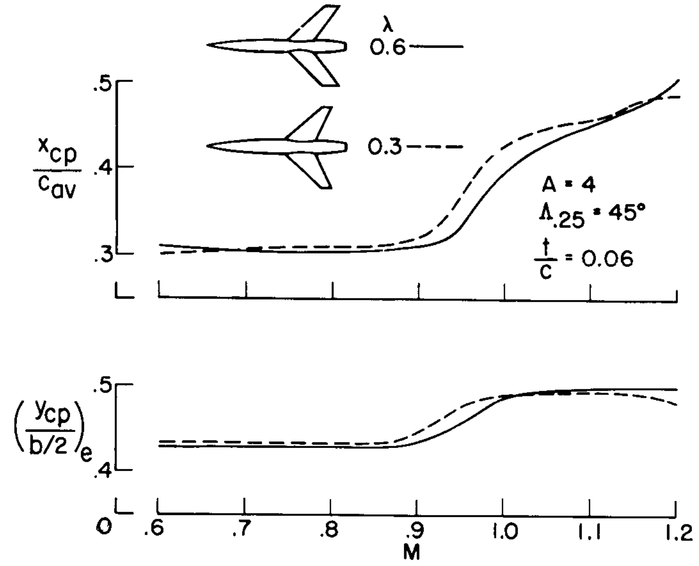

Figure 6

EFFECT OF BODY INDENTATION ON CENTER OF PRESSURE

$C_{N_e} = 0.4$

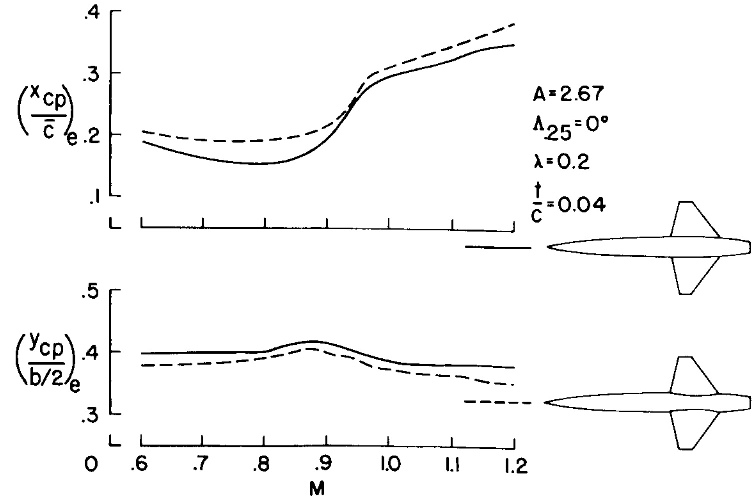

Figure 7

[redacted]

[redacted]

EFFECT OF DROOPED LEADING EDGE ON PRESSURES

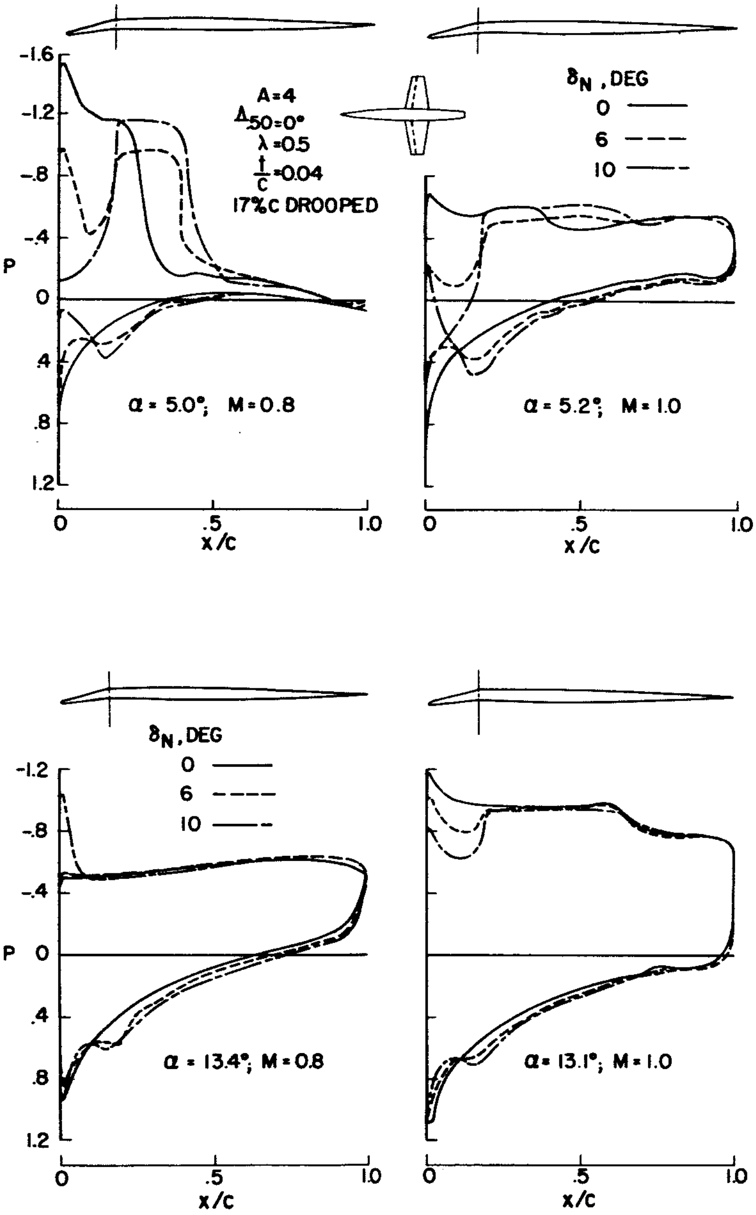

Figure 8

[redacted]

[redacted]

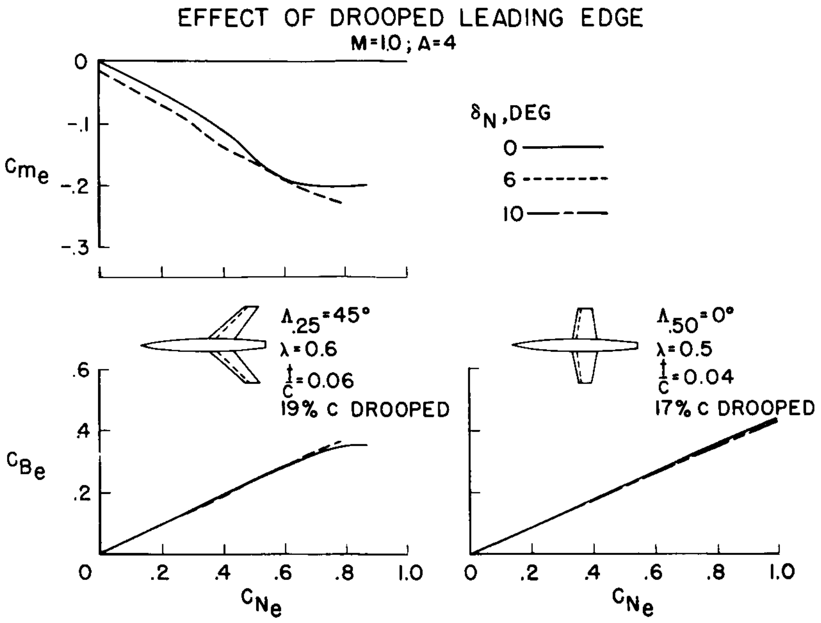

Figure 9

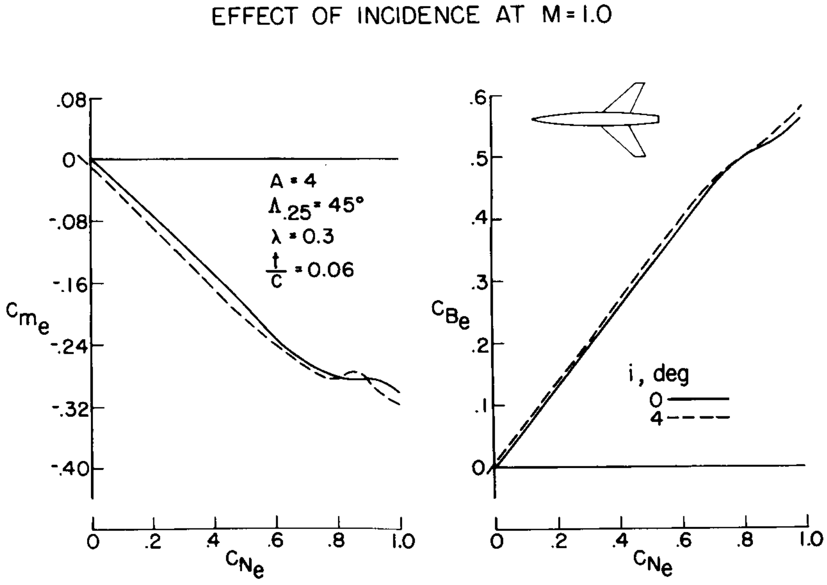

Figure 10

[redacted]

DECLASSIFIED [redacted]

EFFECT OF BODY INDENTATION ON BODY LOADS AND THE DIVISION OF LOADS AT TRANSONIC SPEEDS

By Thomas C. Kelly

Langley Aeronautical Laboratory

INTRODUCTION

One of the problems associated with the structural design of airplanes is the estimation of the load division between components of various configurations. Simplified theoretical methods are available (refs. 1 and 2) which permit the load division to be estimated readily at subsonic, transonic, and supersonic speeds for wing-body and wing-body-tail combinations having wings with rectangular, trapezoidal, and delta plan forms. Unfortunately, the simplified methods do not apply for wings having sweptback trailing edges. In addition to the theoretical methods, experimental data which indicate the effects of many variables on the division of loads (refs. 3 to 6, for example) are available.

Because of the recent emphasis placed upon body contouring as a means for reducing drag at transonic and supersonic speeds (see refs. 7 and 8), it becomes important to determine the effects that these modifications may have upon wing and body loads and the division of loads. The previous paper by Don D. Davis, Jr., and Gerald Hieser has indicated the effects of body indentation on the wing center-of-pressure locations. The purpose of the present paper is to present division-of-load information for three wing-body combinations having wings with trapezoidal, swept, and delta plan forms and to show for each plan form the effect of body indentation on the load division.

DISCUSSION

Figure 1 illustrates the combinations which are considered. The solid and dashed lines shown in the vicinity of the wing root represent outlines of the basic and indented bodies. Both force tests and pressure distribution tests at transonic speeds have been made for the trapezoidal- and swept-wing combinations. Complete-model force tests and measurements of the wing forces in the presence of the body have been obtained for the delta-wing configuration and for a group of other swept and unswept wings. Some of these data are available (ref. 9).

[redacted]

[redacted]

Figure 2 shows the effect of body indentation on the division of loads for the trapezoidal wing-body combinations. The wing had an unswept three-quarter chord line, an aspect ratio of 2.61, and a ratio of maximum body diameter to wing span of 0.179. Results are shown as the ratio of body normal-force coefficient $\left(C_N\right)_B$ to wing-body normal-force coefficient $\left(C_N\right)_{WB}$ plotted against wing-body normal-force coefficient. In all cases, the body normal-force coefficients were measured in the presence of the wing. This ratio represents simply the percentage of the total load carried by the body of the combination. Results are shown at Mach numbers of 0.80 and 1.12 for the basic and indented configurations. The quantity $1 - \frac{S_e}{S}$, where S_e is the exposed wing area and S, the total wing area, represents the percentage of the total wing area which is blanketed by the body. Theoretical values, which are shown in figure 2, were obtained for the basic-body configuration by using Nielson's method (ref. 1).

At a Mach number of 0.80, the experimental and theoretical results show excellent agreement at low normal-force coefficients where the theoretical method applies. At normal-force coefficients above about 0.50 for the basic-body combination, the body loads begin to increase noticeably from the original value of about 21 percent. This increase in body load is a result of the loss in wing lift associated with separation. A similar increase in body load occurs for the indented-body configuration which is carrying about 5 percent less load at this Mach number as a result of the increase in exposed wing area. Although the area ratio $1 - \frac{S_e}{S}$ gives a poor approximation of the portion of the total load carried by the body, the difference in the basic- and indented-body loads shown by this ratio (about 3 percent) are in good agreement with the experimental differences (approximately 4 percent).

At a Mach number of 1.12, the percent load carried by the body has increased somewhat and there is only a slight indication of an increase in body load associated with wing separation at the highest total normal-force coefficients. Here again, the theory is in excellent agreement with the experimental results for the basic-body combination, and the experimental increment in the percent loads carried by the basic and indented bodies is close to the increment shown by the area ratios.

In figure 3, division-of-load data are presented in the same manner for the swept-wing combination. The wing, which was cambered, had 45° sweepback of the quarter chord, an aspect ratio of 4, and a ratio of body diameter to wing span of 0.113. The percent load carried by the basic body at a Mach number of 0.80 is low, on the order of 11 to 12 percent at low normal-force coefficients; again, the data indicate an increase in body loads at the higher normal-force coefficients. The low values of

[redacted]

body loads would be expected when the ratio of the body maximum diameter to wing span of 0.113 is considered; the value of this parameter gives a good approximation of the body load for this particular configuration. As was shown in the case of the trapezoidal wing, the experimental increment between the percent body loads for the basic and indented configurations is close to the increment shown by the ratios of $1 - \frac{S_e}{S}$ for the two configurations.

Similar results are seen at a Mach number of 1.12, the only apparent difference in the two Mach numbers being a delay in wing separation indicated by the fairly rapid increase in body loads at $M = 0.80$ at the higher normal-force coefficients and a tendency for the body loads to maintain a straight-line variation at the higher Mach number.

Results are shown in figure 4 for the delta-plan-form combinations that had a wing with a 60° sweptback leading edge, an aspect ratio of 2.31, and a ratio of body diameter to span of 0.206. For this case, the Mach numbers are 0.80 and 1.2. Because of strain-gage balance limitations, the data are restricted to a low normal-force-coefficient range and are presented as a matter of interest.

At a Mach number of 0.80, agreement of the experimental and theoretical basic-body load percentages is fair, the experimental value being about 19 percent and the theoretical, 24 percent. At the higher Mach number, the load carried by the body has increased to approximately 23 percent and the agreement in theory and experiment is good for the basic-body configuration.

For these basic and indented combinations, the change in the load division resulting from indentation was much greater than the change in the ratios based on exposed wing area.

The preceding figures have indicated the division of loads for the various configurations. Figures 5 and 6 have been prepared in order to show the effect of indentation on the body loads themselves. Results are shown as the variation of body pressure coefficient P with percent body length x/L for the 45° swept wing-body configurations. Data are shown at an angle of attack of 8° and at Mach numbers of 0.80 and 1.12 for the basic body in the presence of the wing (shown by the solid line), the indented body in the presence of the wing (shown by the dashed line), and for the basic body alone (shown by the long and short dashes). These pressure distributions were obtained from orifice rows which extended along the top and bottom of the body at the plane of symmetry as shown in the sketch. For purposes of orientation, the location of the wing on the bodies is shown, and pressure coefficients corresponding to a Mach number of 1.0 are shown as P_{sonic}.

[redacted]

At both Mach numbers and for both upper and lower orifice rows, the effects of indentation on the body pressures are similar. These effects are an initial acceleration of the flow at the start of the indentation followed by a fairly abrupt deceleration and finally a second acceleration at the rearward part of the indentation. Peak pressures over the upper surface are slightly reduced at a Mach number of 0.80; at a Mach number of 1.12, these peak pressures are almost unchanged.

CONCLUSIONS

These results have indicated that agreement in theoretical and experimental values of load division for the basic-body configurations was excellent for the trapezoidal plan form and fair to good for the delta-wing configuration. Although the simplified theoretical methods do not apply for the swept-wing case, the ratio of maximum body diameter to wing span gave a good estimate of the load division for this particular combination.

For the trapezoidal- and swept-wing combinations, the ratios based upon the change in exposed wing area provided a good approximation of the change in load division resulting from indentation. For the delta-wing combinations, the change in the load division was much greater than the change in the area ratios.

The main effects of indentation on body pressures appear in the form of local accelerations and decelerations of the flow in the vicinity of the indentation.

[redacted]

DECLASSIFIED

[redacted]

REFERENCES

1. Nielson, Jack N., Kaattari, George E., and Anastasio, Robert F.: A Method for Calculating the Lift and Center of Pressure of Wing-Body-Tail Combinations at Subsonic, Transonic, And Supersonic Speeds. NACA RM A53G08, 1953.

2. Tucker, Warren A.: A Method for Estimating the Components of Lift of Wing-Body Combinations at Supersonic Speeds. NACA RM L52D22, 1952.

3. Gillis, Clarence L.: A Summary of Data on the Division of Loads for Various Wing-Fuselage Combinations. NACA RM L53E08. 1953.

4. Loving, Donald L.: The Effect of a Change in Body Shape on the Loading of a 45° Sweptback Wing-Body Combination at Transonic Speeds. NACA RM L54B09, 1954.

5. Robinson, Harold L.: The Effects of Wing Incidence on the Aerodynamic Loading Characteristics of a Sweptback Wing-Body Combination at Transonic Speeds. NACA RM L54G23b, 1954.

6. Williams, Claude V.: An Investigation of the Effects of a Geometric Twist on the Aerodynamic Loading Characteristics of a 45° Sweptback Wing-Body Configuration at Transonic Speeds. NACA RM L54H18, 1954.

7. Whitcomb, Richard T.: A Study of the Zero-Lift Drag-Rise Characteristics of Wing-Body Combinations Near the Speed of Sound. NACA RM L52H08, 1952.

8. Whitcomb, Richard T., and Fischetti, Thomas L.: Development of a Supersonic Area Rule and an Application to the Design of a Wing-Body Combination Having High Lift-to-Drag Ratios. NACA RM L53H31a, 1953.

9. Delano, James B., and Mugler, John P., Jr.: Transonic Wind-Tunnel Investigation of the Effects of Taper Ratio and Body Indentation on the Aerodynamic Loading Characteristics of a 45° Sweptback Wing in the Presence of a Body. NACA RM L54L28, 1955.

[redacted]

[redacted]

DECLASSIFIED

[redacted]

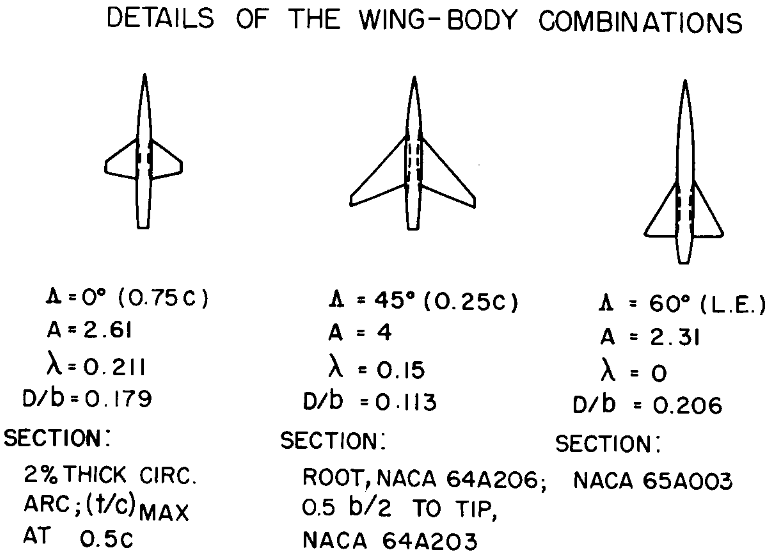

Figure 1

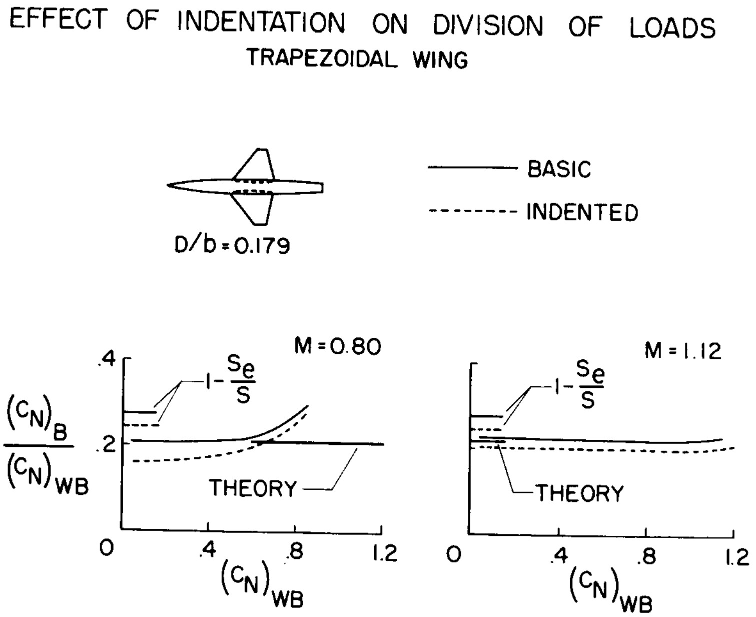

Figure 2

[redacted]

[redacted]

DECLASSIFIED [redacted]

EFFECT OF INDENTATION ON DIVISION OF LOADS
45° SWEPT WING

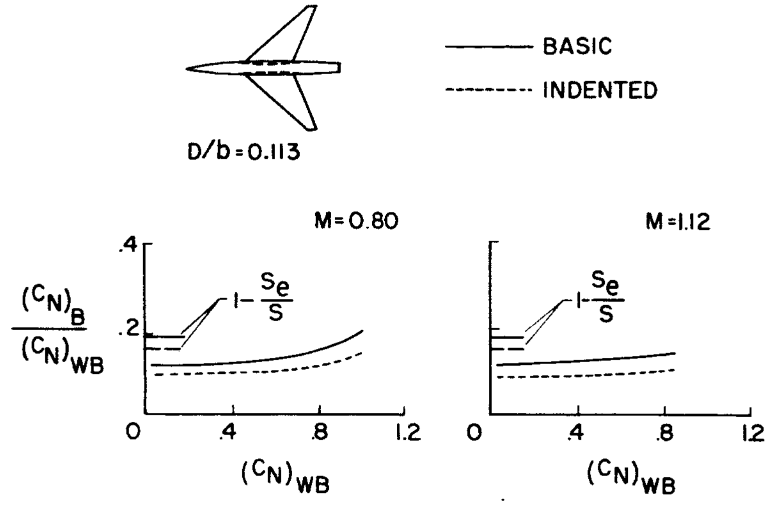

Figure 3

EFFECT OF INDENTATION ON DIVISION OF LOADS
60° DELTA WING

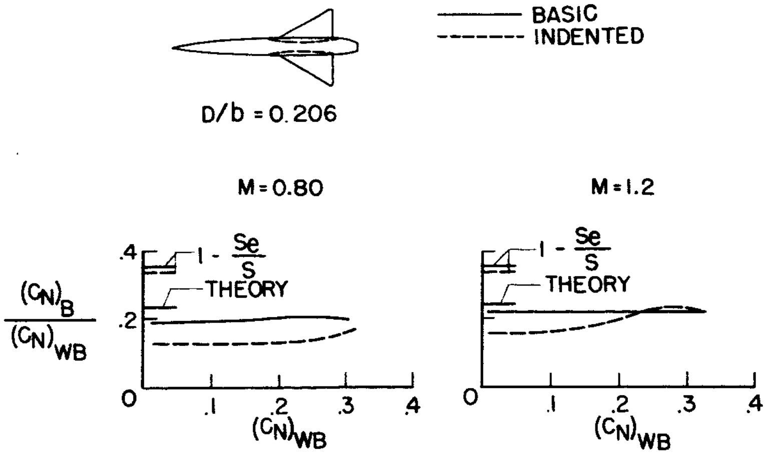

Figure 4

[redacted]

[redacted]

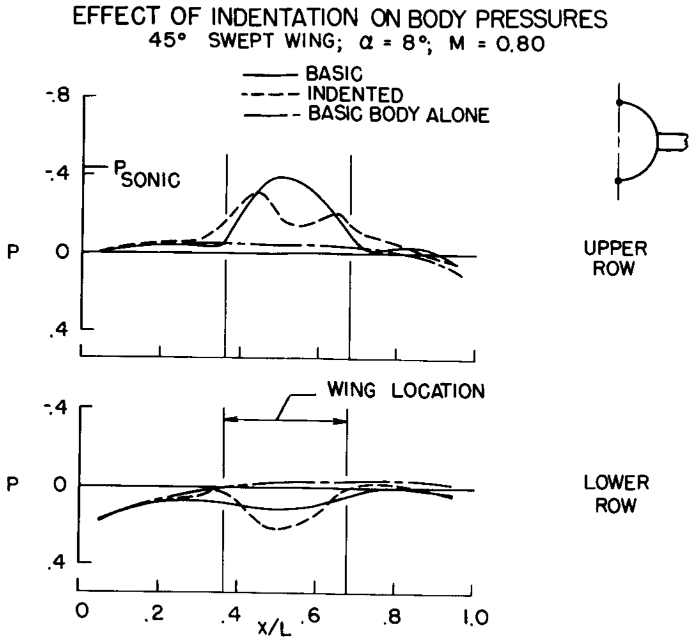

Figure 5

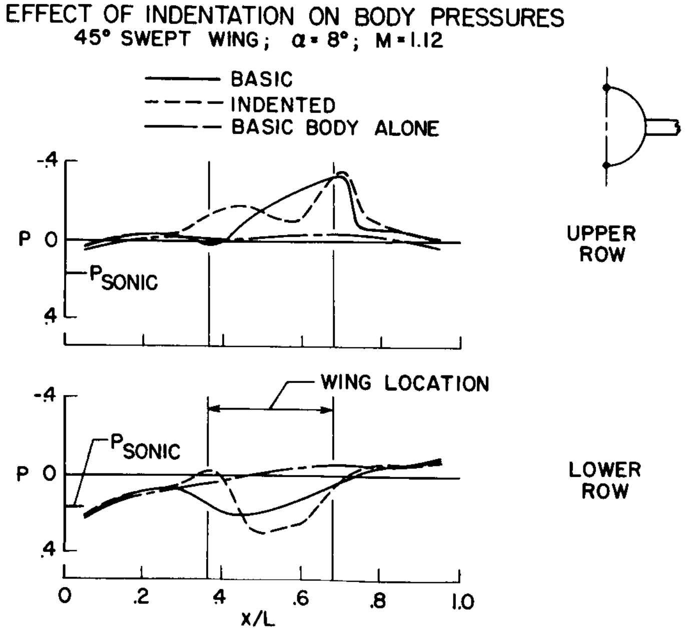

Figure 6

[redacted]

DECLASSIFIED

[redacted]

SOME RESULTS FROM LOAD AND DEFLECTION MEASUREMENTS ON THE BOEING B-47 AIRPLANE

By Paul W. Harper and Alton P. Mayo

Langley Aeronautical Laboratory

In one phase of a recently completed flight-test program on the Boeing B-47 airplane, strain-gage measurements of shear, moment, and torque and photographic measurements of wing deflection were obtained at a number of stations along the span.

Aside from obtaining specific data on the effects of aeroelasticity on wing loading, one of the primary aims of the program was to check current methods of computing span loading for swept flexible wings.

The strain-gage and deflection measurements are related to each other and to the span loading by successive integration utilizing the wing-stiffness characteristics. The two types of measured quantities were obtained independently and, therefore, permitted independent correlations with theoretical span loadings, as well as correlation with each other. Thus, methods of computing and utilizing the wing-stiffness characteristics could be checked directly without recourse to the span-load theory.

Analysis of the strain-gage data is currently in progress, and analysis of the wing-deflection measurements for symmetrical loading conditions has recently been published (ref. 1).

Some of the results thus far obtained are presented in the following figures.

Figure 1 illustrates the wing plan form and shows positions of strain-gage and target-deflection stations. Center lines are drawn on the wing at the front- and rear-spar locations.

Optigraph-target light positions are given by the circular symbols. Targets were mounted on both spars at four stations on the left wing. Targets were duplicated on the right wing at the two outboard stations. The deflection of these targets was recorded by an optigraph camera installed within a canopy above the fuselage. Note that targets are alined streamwise so as to indicate directly the net streamwise twist due both to the bending deflection along the beam (or elastic axis) and to twist about the elastic axis.

[redacted]

Strain-gage bridges were mounted on both spars at four span stations on the left wing (see fig. 1) and at the root of the right wing. The gages were calibrated in a manner similar to that described in reference 2 to give the net or structural shear load acting outboard of each gage station and the moment and torque associated with this load. Note that the two inboard gage stations would respond to wing plus (inboard) nacelle loads.

Time histories of the air loads and moments were obtained by combining the structural loads with the inertia loads at various instants of time during a maneuver. Because of the motion or flapping of the wings it was necessary to measure vertical accelerations at a number of span positions in order to obtain the inertia loading.

In analyzing these time histories it was desired to evaluate the effect of each of the various pertinent flight parameters on the wing loading. Ideally, this would be accomplished by varying but one parameter at a time; but this procedure, as is generally known, is rarely feasible in flight testing.

In a roller-coaster maneuver, for example, the speed could usually be held relatively constant, but changes in wing load did occur because of the effects of other parameters in addition to the load factor. Some of these parameters were wing flapping, pitching velocity and acceleration, and aileron movement. It was necessary, therefore, to resort to a least-squares procedure wherein the measured load (or deflection) at a particular wing station was simultaneously related to each of the variables.

This procedure utilized equations of the form shown in figure 2. At the top is shown an equation for deflection at any target. At the bottom are shown equations, of identical form, for aerodynamic shear, bending moment, and torque at any station. In these equations the quantities in brackets (not matrix notation) are the unknown coefficients, whereas the remaining portions are derived from measured quantities.

Consider the shear equation, for example. The measured shear load at a particular station is assumed to consist of a contribution from the basic or zero-lift loading given by the S_0 term; a fraction A_S of the total wing-fuselage additional loading given by the second term where n is the load factor, W is the gross weight, and L_T is the tail load - also obtained with strain gages; a contribution due to airplane pitching acceleration given by the $\ddot{\theta}$ term; and similar terms for each pertinent parameter which changed during the maneuver. Four to seven terms were usually required.

[redacted]

A set of simultaneous shear equations was formed by using simultaneous values of the shear, $nW - L_T$, and $\ddot{\theta}$ obtained at each of from 20 to 50 different instants of time selected during a maneuver. When normalized and solved, the A_S coefficient, for example, gave the fraction of the total wing-fuselage additional load which was carried on the wing area outboard of a particular gage station. From a similar solution for bending moment at this particular station, the A_M coefficient gave the bending moment associated with this fraction of load, and the ratio of A_M to A_S gave the spanwise distance to the center of the load. The streamwise distance to the load center could likewise be obtained from the A coefficient in the torque-equation solution. The A_D coefficient in the deflection equation gave the deflection due to both the additional air loading and that part of the inertia loading which was caused by this additional loading.

In connection with the coefficients in the brackets, it should be emphasized that the A coefficient in the shear equation, for example, gave the change in shear which would appear at a particular gage station if only the $nW - L_T$ term were to change while each of the other terms remained constant. A parallel reasoning applies to the coefficients for each of the other parameters.

Solutions of this type were obtained for deflection, aerodynamic shear, moment, and torque at each station for each of a number of maneuvers performed at various altitudes, Mach numbers, and weight conditions. Some of the results obtained for the additional loading, that is, results based on the A coefficients, are presented in the subsequent figures. These results are presented and referred to as deflection per g or load per g.

In figure 3 some wing-deflection results are plotted against the dynamic pressure q. These deflections are presented on an incremental or per g basis for a gross weight of 126,000 pounds and for a constant altitude of 30,000 feet so that the Mach number also changes with the dynamic pressure.

Deflections are shown for four stations on the left wing and begin at the top for the tip station. The solid-line curves and square symbols denote the theoretical and experimental rear-spar deflections, and the broken-line curves and the circular symbols denote front-spar deflections.

In order to obtain the calculated deflections, theoretical span loadings were computed by the method of reference 3, which includes (among others) consideration of the effects of fuselage interference, compressibility, and wing deformation. The deflections were then derived from these loadings by means of influence coefficients. In this connection it might be mentioned that influence coefficients calculated for this wing structure agreed very closely with those obtained experimentally by applying point loads at a number of positions on the wing.

The calculated curves give $1\frac{1}{2}$ to 2 inches greater deflection than the experimental values; but since four integrations are required to convert a loading curve to a deflection curve, the two curves may be considered to be in good agreement.

The difference between front- and rear-spar deflection in figure 3 indicates negative per g changes in local streamwise twist. The deflections per g become smaller as q increases and denote a reduction in tip loading or inboard shift of the additional load center. Considerably higher deflections would be obtained for higher gross-weight conditions, and the values would show a correspondingly greater change with q than do these values.

The magnitude of this indicated load shift is shown by some center-of-pressure results in figure 4. These results apply to the additional load acting outboard of the root gage station. In the upper part of the figure the spanwise distance to the air-load center from the gage station is given in percent of the portion of span outboard of the gage station. At the bottom of the figure is shown the streamwise location with respect to the mean aerodynamic chord of the wing area outboard of the gage station. The circular symbols denote left-wing values and the square symbols, right-wing values. The calculated variation is given by the sloping lines and applies roughly to the range of Mach number and gross weight covered by the test values.

The values plotted are for random Mach numbers and gross weights and, although an insufficient amount of data have been analyzed to isolate the effects of these variables, the relative lack of scatter would indicate a rather small overall effect.

The shift of the center of pressure with increasing q is seen to be inboard (parallel to the quarter-chord line, incidentally) and forward in a destabilizing direction, and also substantially in agreement with that calculated. The magnitude of this shift is perhaps more important from the viewpoint of stability or tail loads than in connection with wing design. Over the maximum operating q range of the B-47, which is larger than that shown here, this load shift would amount to about a 15-percent change in root moment for a given constant shear load.

The actual location of these centers of pressure on the wing plane can be seen from figure 5. All the center-of-pressure values obtained for the root gage station fall within the envelope drawn at the intersection of the quarter-chord line and the mean aerodynamic chord. Results obtained for the other three gage stations are also shown here. For example, the center-of-pressure values obtained for the load acting outboard of the gage station nearest the wing tip all fall within the area of the small envelope drawn near the wing tip, those for the wing area outboard from the midsemispan station fall within the next envelope, and for the station near the nacelle the values fall within the third envelope from the tip.

The small vertical arrows indicate calculated center-of-pressure locations for a rigid-wing loading. The experimental values for the root station are seen to fall inboard from the rigid-wing position, whereas those for the outer stations are just about on the rigid-wing positions and do not change by more than about 1 percent of the semispan. Examination of a number of calculated flexible-wing span loadings for various values of q has shown essentially this same pattern. These results were obtained for a range of Mach number up to 0.81 but for gross weight and q ranges much below the maximum ranges for this airplane. Nevertheless, the rather small area covered by each envelope would indicate that these parameters have - relatively speaking - a small overall effect.

It will be remembered that wing-plus-nacelle loads were measured at the two inboard stations. Qualitatively speaking, if loads and moments on the nacelle were subtracted out to obtain wing-alone loads, then the center-of-pressure envelope obtained for the gage station near the large nacelle would be shifted toward the quarter-chord line, and that for the root station would not change very much.

Although a detailed discussion of nacelle loads is not within the scope of this paper, it may be said that wind-tunnel results do indicate a rather large local interference effect because of the nacelle presence, but this effect is found primarily in the basic loading rather than in the wing lift-curve slopes or additional loading, except in the high or nonlinear C_N range. Although data for power-off conditions were not obtained from the tests, the effect of thrust on the additional loading is likewise considered to be small.

In figures 6 to 9, results from a theoretical span loading are compared with both the strain-gage and the deflection results obtained from a specific flight maneuver. For these comparisons the theoretical span loading was converted by successive integration to span curves of shear, moment, torque, and wing deflection.

In figure 6 the comparison is shown for the spanwise distribution of aerodynamic shear for a 1 g incremental load at a Mach number of 0.66,

[redacted]

a dynamic pressure of 244 pounds per square foot, and a gross weight of 112,000 pounds. In figure 7 are shown the associated bending-moment and torque distributions. In these two figures the solid theoretical curves apply to the actual flexible-wing case. The broken-line curves for the rigid-wing case have been added to indicate the order of magnitude of the change due to wing deformation for this flight condition. The symbols designate the experimental values for four span stations. Although the experimental values were obtained for a particular maneuver performed at the specified conditions, values from other maneuvers made in this approximate q range but for somewhat different values of Mach number and weight fall also within the areas of the symbols.

It is evident that the theory adequately predicts the load distribution for this case. Other comparisons of this type are contemplated for various other symmetrical and unsymmetrical loadings.

The wing deflections obtained for this maneuver are shown in figure 8, where spar deflections in inches for the 1 g loading are plotted along the semispan.

The rear-spar deflections are shown theoretically by the upper curve and experimentally by the square symbols at the four span stations. The front-spar deflections are shown by the bottom curve and by the circular symbols. The calculated deflections may be seen to average about an inch higher along the span, but the agreement here also may be considered good.

In any event, changes in wing-load distribution are produced by the difference between front- and rear-spar deflections in figure 8 rather than by the deflections themselves. The net effect of this "difference deflection" on the wing angle-of-attack distribution is shown in figure 9.

In figure 9 the local streamwise angle of attack in degrees is plotted along the semispan. The solid curve is the calculated distribution which for the theoretical case will produce a 1 g increment in load and is associated with the deflections given in figure 8. The local angle-of-attack change caused by the wing deformation is essentially the difference between the solid curve and the horizontal broken line which is drawn at the level of the root angle of attack. The experimental values are also those associated with the deflections given in figure 8.

The previously mentioned figures have roughly outlined the current status of one phase of the flight investigation. Within the limitations of the results thus far obtained it would appear that current methods of predicting the flexible-wing aerodynamic load may be used with confidence in the subsonic Mach number range.

[redacted]

REFERENCES

1. Mayo, Alton P., and Ward, John F.: Flight Investigation and Analysis of the Wing Deformations of a Swept-Wing Bomber During Push-Pull Maneuvers. NACA RM L54K24a, 1954.

2. Skopinski, T. H., Aiken, William S., Jr., and Huston, Wilber B.: Calibration of Strain-Gage Installations in Aircraft Structures for the Measurement of Flight Loads. NACA TN 2993, 1953. (Supersedes NACA RM L52G31.)

3. Gray, W. L., and Schenk, K. M.: A Method for Calculating the Subsonic Steady-State Loading on an Airplane With a Wing of Arbitrary Plan Form and Stiffness. NACA TN 3030, 1953.

[redacted]

LOCATION OF STRAIN GAGES AND OPTIGRAPH TARGETS

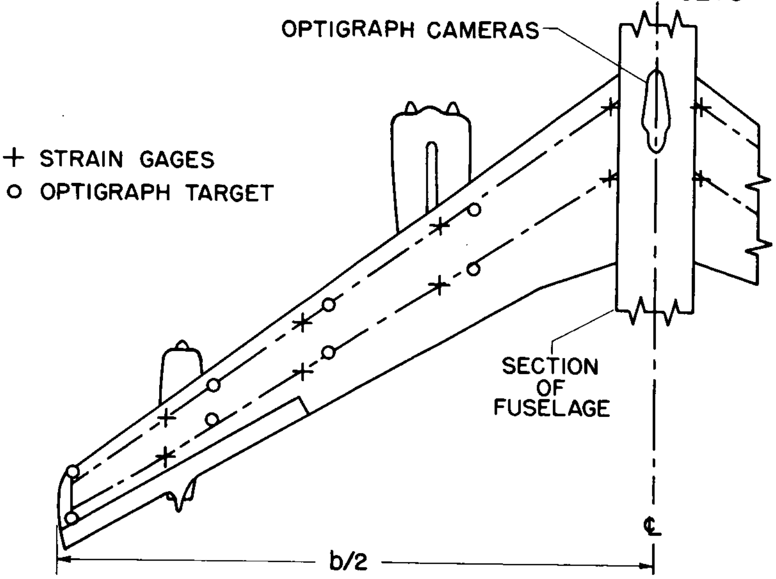

Figure 1

EQUATION FORM FOR LEAST-SQUARES SOLUTIONS

$$\begin{array}{rl}
\text{DEFL.} = & \underbrace{[D_0]}_{\text{BASIC}} + \underbrace{[A_D](nW-L_t)}_{\text{ADDITIONAL}} + \underbrace{[B_D](\ddot{\theta})}_{\text{ANGULAR ACCEL.}} + \underbrace{----}_{\text{OTHER PARAMETERS}} \\
\text{SHEAR} = & \overbrace{[S_0]} + \overbrace{[A_S](nW-L_t)} + \overbrace{[B_S](\ddot{\theta})} + \overbrace{----} \\
\text{BENDING MOMENT} = & [\quad] + [\quad](\qquad) + [\quad](\;) + ---- \\
\text{TORQUE} = & [\quad] + [\quad](\qquad) + [\quad](\;) + ----
\end{array}$$

Figure 2

[redacted]

[redacted]

EFFECT OF DYNAMIC PRESSURE ON WING DEFLECTION

W=126,000 LB; H=30,000 FT

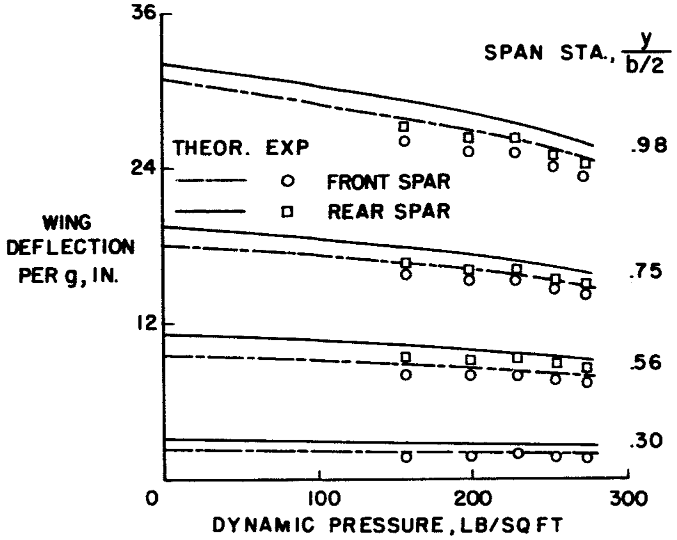

Figure 3

EFFECT OF DYNAMIC PRESSURE ON AIR-LOAD CENTER

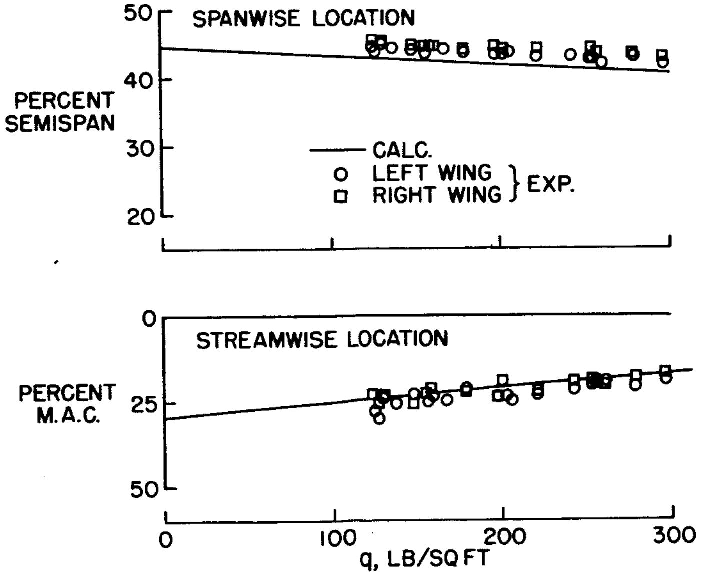

Figure 4

[redacted]

LOCATION OF AIR-LOAD CENTERS

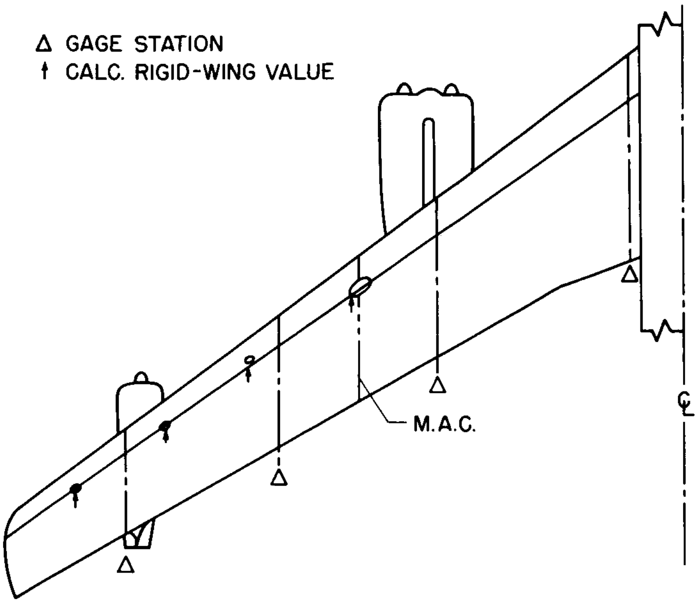

Figure 5

DISTRIBUTION OF AERODYNAMIC SHEAR

M=0.66; q=244 LB/SQ FT; W=112,000 LB

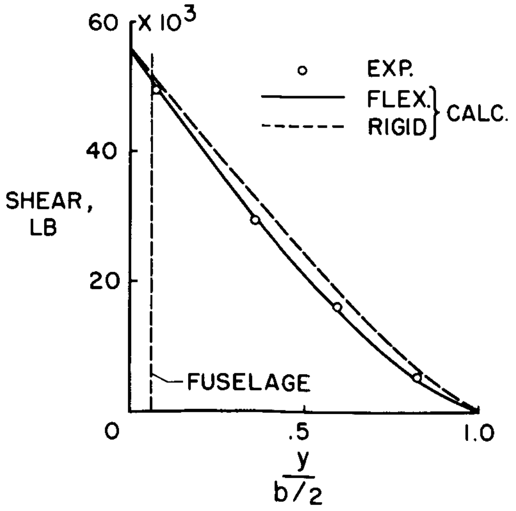

Figure 6

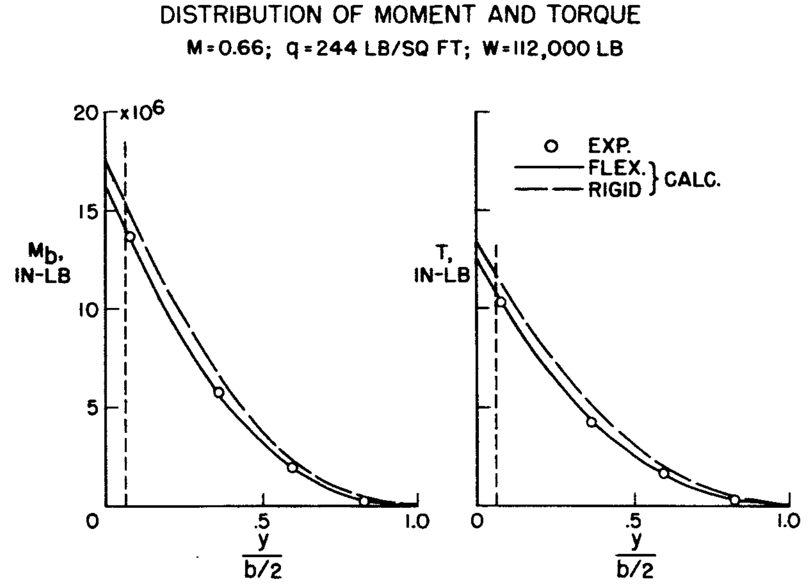

Figure 7

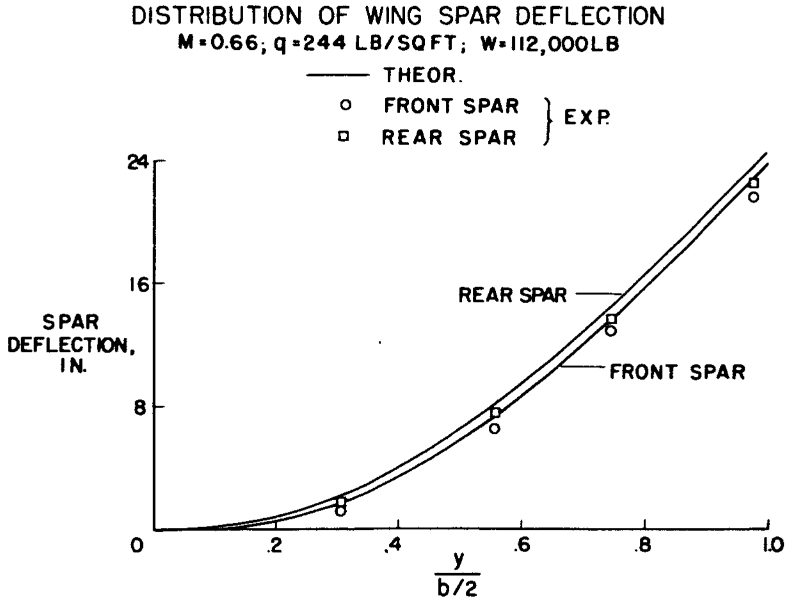

Figure 8

[redacted]

[redacted]

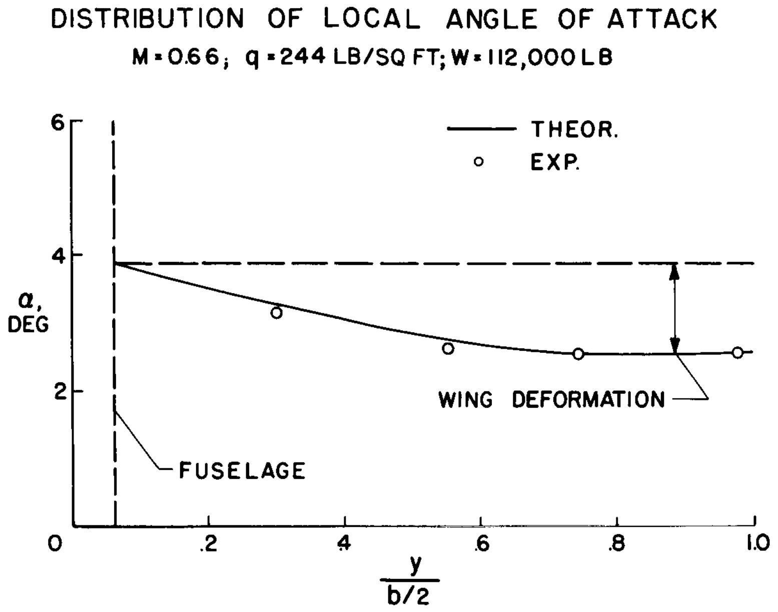

Figure 9

[redacted]

DECLASSIFIED

[redacted]

COMPARISON OF CALCULATED AND EXPERIMENTAL SPAN-LOAD DISTRIBUTIONS ON WINGS UP TO $M = 1.0$

By John L. Crigler

Langley Aeronautical Laboratory

INTRODUCTION

The problem of span loading always arouses considerable interest in calculation methods; in particular, the distribution (or shape) of the span loading is of interest. The object of this paper is to investigate to what degree such distributions can be calculated by linear theory, particularly in the speed ranges approaching sonic conditions. In this study, the calculated span-load distributions are compared with experimentally measured distributions obtained on wings discussed in reference 1, which are thin wings designed to operate effectively in this speed range.

METHOD

A number of methods have been developed for predicting the span loading on arbitrary wings, but most of these methods are based on incompressible flow and have been extended to the compressible case by use of the Gothert rule, which makes use of affine transformations that involve the Mach number relation $\frac{1}{\sqrt{1 - M^2}}$. At $M = 1$, these transformations cease to be affine, and, therefore, this method breaks down.

The method used in making calculations for the present study is similar to that used by Falkner (ref. 2) for the incompressible case, except that the present method directly relates the downwash velocity to the left on the wing in a compressible medium for any Mach number. The expression is exact on the basis of linearized theory but does not take into account flow separation or shock waves. The method may be explained briefly as follows:

Figure 1 shows a wing diagram, and the equation relating a known local downwash velocity w to an unknown local lift L of the wing is as follows:

[redacted]

[redacted]

$$w(x_a,y_a) = \frac{1}{4\rho\pi}\iint_S L(x_n,y_n)K(x_a - x_n,y_n - y_a,M)dx_n\,dy_n \qquad (1)$$

where

$$L(x_n,y_n) = \sqrt{b^2 - y_n^2}\Big[\cot\frac{\theta}{2}(a_{0,0} + a_{0,1}y_n + a_{0,2}y_n^2 + \ldots) +$$

$$\sin\theta(a_{1,0} + a_{1,1}y_n + a_{1,2}y_n^2 + \ldots) +$$

$$\sin 2\theta(a_{2,0} + a_{2,1}y_n + a_{2,2}y_n^2 + \ldots)\ldots\Big] \qquad (2)$$

and

$$\cos\theta = \frac{2x}{c} \qquad (3)$$

The function K appearing in this integral represents the known downwash at any point (x_a,y_a) due to a pressure doublet at any other point (x_n,y_n). This expression, which is derived in reference 3, is found to be a simple function of the distances $(x_a - x_n)$, $(y_n - y_a)$, and the Mach number M. For arbitrary wings it does not appear possible to obtain exact solutions to this integral equation, so that approximate methods must be resorted to in order to obtain solutions. The method employed is to assume that the lift L can be expressed in the form of a series of terms as shown in equation (2). This series has often been used to obtain a solution for the incompressible case and, as shown here, is for subsonic flow. The significant features of this series are that it involves the elliptic type of loading, implied by the term $\sqrt{b^2 - y_n^2}$ where b is the wing semispan and y_n is the lateral position on the semispan, but the elliptic loading is modified by other terms involving y_n. The $\cot\frac{\theta}{2}$ term implies a singularity of $\frac{1}{\sqrt{x}}$ type at the leading edge, and all of the trigonometric terms imply that the loading goes continuously to zero at the trailing edge. This type of loading is assumed only for the subsonic case. Other types of load distribution are required for other flow regimes. For example, for the sonic case the leading-edge singularity is

[redacted]

still required but the loading need not necessarily go continuously to zero at the trailing edge. In general the integration involving the product of this series and the function K cannot be carried out in closed form. These integrations can be performed by approximate or numerical procedures, however, as accurately as one may desire; that is, for any preassigned values of $\left(x_a,y_a\right)$. If the downwash velocity $w\left(x_a,y_a\right)$ is assumed to be known, it may be seen that after the integrations are performed, the equations for $w\left(x_a,y_a\right)$ are obtained in terms of the unknown coefficients a appearing in the lift distribution. Thus, by assuming the downwash to be known at an appropriate number of points, a system of linear algebraic equations is obtained from which the values of a can be determined. The a's now depend not only on plan form and aspect ratio but also implicitly on the Mach number and on the form of the series chosen to represent the lift. Thus, a simple transformation cannot be expected to give results for one Mach number from that for another. Unfortunately, separate and complete calculations must be made for each plan form, aspect ratio, and Mach number.

In the present work the body is assumed to be represented by an infinite cylinder and the treatment is similar to that proposed in reference 4.

RESULTS

Results of calculations showing the effect of the body are first presented, and then calculated results on the wing-body configuration are compared with experimentally measured results. Figure 2 shows a comparison of the calculated spanwise lift distribution of the wing alone with that of the same wing in combination with a body for incompressible flow ($M = 0$). The wing parameters and the wing-body configurations are shown in the figure. The only significant effect of the body is to reduce the loading on the wing adjacent to the body. The loadings on the more important outboard sections are not significantly affected. In all remaining calculations the effect of the body is included. For these calculations the wing is assumed to have a fixed geometry; that is, no deflection or bending under load, which is inherently included to some extent in the experimental results, has been considered. However, the effects of the wing deflections have been evaluated for these wings and in all cases the effects were found to be small.

Figure 3 shows a comparison of the calculated and experimentally measured spanwise loading plotted against the wing semispan for several subsonic Mach numbers and for Mach number 1.0, for the same configuration as shown in figure 2. These data are for an angle of attack of 4.0°. The spanwise distribution of lift or shape of the loading on which the

[redacted]

wing shear and bending moments depend are generally in good agreement. It may be noted that, for $M = 1.0$, there is a drop in lift adjacent to the body and also an increase near the tip which results in a change in shape of the loading curve; that is, a shift of lateral center of pressure shown in the experimental results is not found in the calculated results.

Figure 4 shows results for the same wing as in figure 3 except that in this case the wing had a twist of 4.0° from the fuselage boundary to the wing tip. The agreement of theory and experiment for the wing with twist is somewhat better than that shown in figure 3 for the wing without twist, and the same trends with Mach number are noted. It thus appears that the effects on span loading of twist due to wing deflections can be predicted by theory at these Mach numbers.

Figure 5 shows calculated and experimental spanwise loading coefficients for another 45° sweptback wing, the significant changes in this wing being that it is more highly tapered and the wing sections are cambered. The wing parameters are shown in the figure. This wing is one of the most effective wings tested in reference 1 for use in the transonic speed range. For this wing the favorable center-of-pressure characteristics at transonic speeds were mentioned in reference 1. The curves at the bottom of this figure for Mach numbers of 0.8 and approximately 1.0 show the loading at an angle of attack of 0° and give the effect of camber. The curves at the top of the figure show the loading for an angle of attack of approximately 4°. This wing was not tested experimentally at $M = 1.0$ but the general shape at $M = 0.98$ for angles of attack of both 0° and 4° is still in close agreement with the calculated results at $M = 1.0$.

In many cases the distribution of the spanwise loading is of primary importance and the curves in figure 5 have been normalized for equal lift on figure 6 for Mach numbers of 0.8 and approximately 1.0. When made on the basis of the same total loading, the load distribution for this wing even at $M = 1.0$ is still in good agreement. It thus appears that the effects on span loading of camber as well as twist for these high-speed wings can be calculated with reasonable accuracy up to sonic speeds. This result is of interest for the determination of aeroelastic effects as well as design camber and twist in the wing.

CONCLUDING REMARKS

From the limited number of cases that have been calculated, it may be concluded that the magnitude and the distribution of spanwise loading calculated for these thinner wings are in good agreement with experiment up to a Mach number of 0.95, and for the highly tapered wing the agreement of the calculated spanwise load distribution with the experimental distribution is still good up to a Mach number of approximately 1.0.

[redacted]

[redacted]

REFERENCES

1. Davis, Don D., Jr., and Hieser, Gerald: Loads on Thin Wings at Transonic Speeds. (Prospective NACA paper.)

2. Falkner, V. M.: The Calculation of Aerodynamic Loading on Surfaces of Any Shape. R. & M. No. 1910, British A.R.C., Aug. 1943.

3. Watkins, Charles E., Runyan, Harry L., and Woolston, Donald S.: On the Kernel Function of the Integral Equation Relating the Lift and Downwash Distributions of Oscillating Finite Wings in Subsonic Flow. NACA TN 3131, 1954.

4. Zlotnick, Martin, and Robinson, Samuel W., Jr.: A Simplified Mathematical Model for Calculating Aerodynamic Loading and Downwash for Wing-Fuselage Combinations With Wings of Arbitrary Plan Form. NACA TN 3057, 1954. (Supersedes NACA RM L52J27a.)

[redacted]

[redacted]

[redacted]

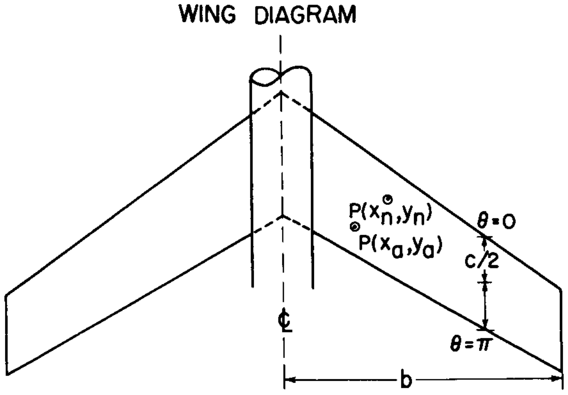

Figure 1

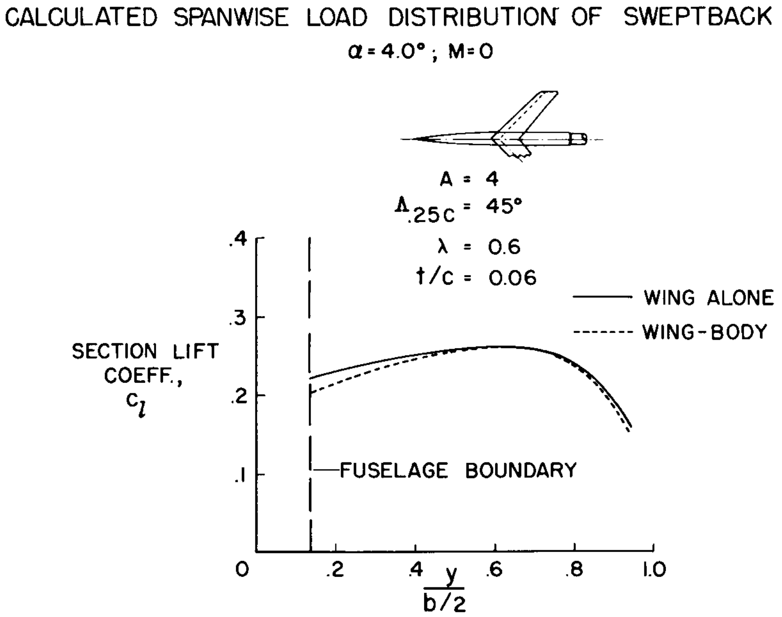

Figure 2

[redacted]

[redacted]

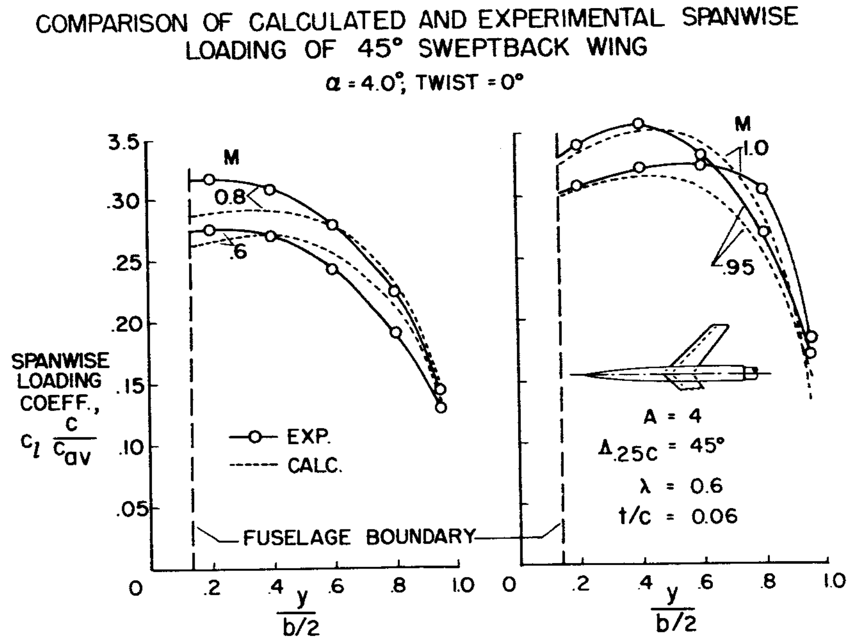

Figure 3

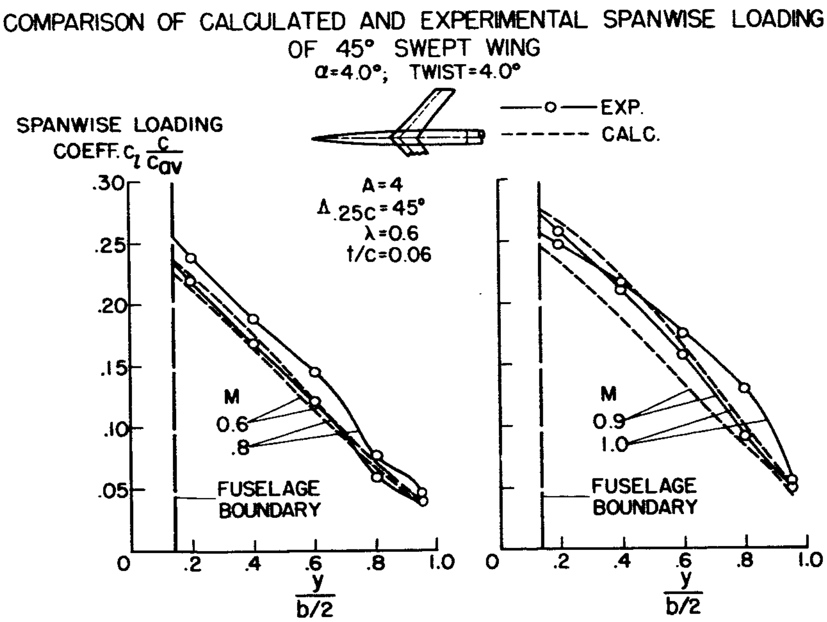

Figure 4

[redacted]

[redacted]

COMPARISON OF CALCULATED AND EXPERIMENTAL SPANWISE LOADING OF 45° SWEPTBACK WING

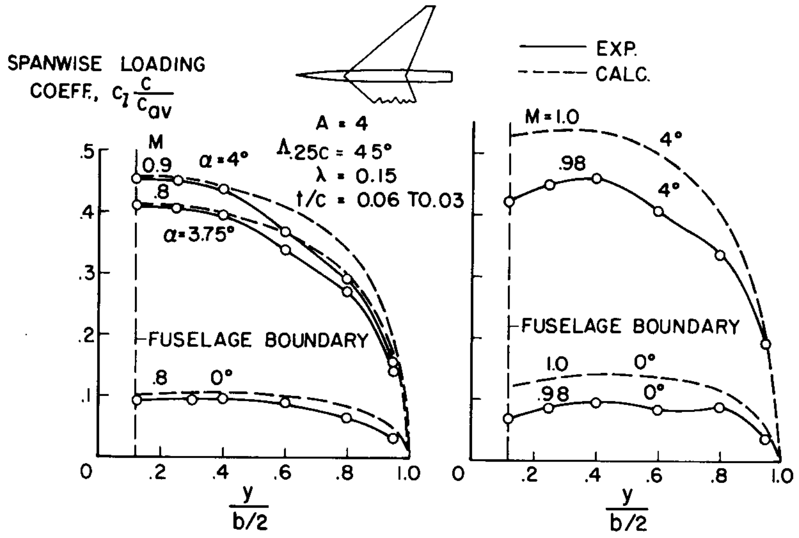

Figure 5

COMPARISON OF CALCULATED AND EXPERIMENTAL SPANWISE LOADING OF 45° SWEPTBACK WING

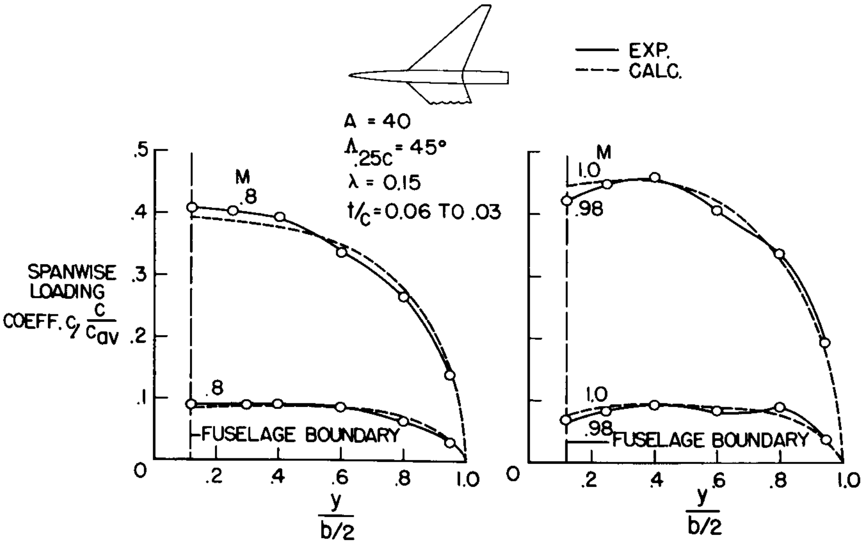

Figure 6

[redacted]

UNCLASSIFIED [redacted]

LOADS ON EXTERNAL STORES AT TRANSONIC AND SUPERSONIC SPEEDS

By Lawrence D. Guy

Langley Aeronautical Laboratory

SUMMARY

Results of recent wind-tunnel investigations of the loads on external stores at transonic and supersonic speeds have shown that the most critical store loading appears to be that due to the store side force, both because of its magnitude and because the force acts in the direction of the least structural strength of the pylon.

The magnitude of the side forces is determined principally by angle of attack, store position, and Mach number. Angle of attack and store positions are inextricably related since the rate of change of side force with angle of attack, which can be very large, is primarily a function of position. Also, at moderate angles of attack, the rate of increase of side-force coefficient with angle of attack for a given store position is essentially constant with Mach number. The effects of Mach number are shown principally in the values of the coefficient at small angles of attack. These values are strongly influenced by local flow angularities and the changes in flow behavior that occur at transonic and supersonic speeds.

INTRODUCTION

In providing for the use of external stores on high-speed aircraft the designer is faced with the problem of determining what factors exert the greatest influence on the development of critical store loading conditions and how the character of the loading conditions varies as the speed is increased from subsonic to supersonic Mach numbers.

Theoretical treatment of the problems is difficult because of the complexity of the flow field about an aircraft-store configuration. The initial approach, therefore, has of necessity been experimental. Until recently such experimental results have been, for the most part, for specific design problems or for a limited range of variables such as angle of attack and Mach number.

[redacted]

The purpose of this paper is to show the relative importance of some of the factors which influence the development of critical loading conditions on external stores. Principally, the effects of angle of attack, Mach number, and to some extent store position for various wing plan forms will be examined in the speed range from subsonic to supersonic Mach numbers near 2.0.

The greater part of the data to be presented in this paper were obtained in the Langley 9- by 12-inch blowdown tunnel. Some results obtained in flight tests will, however, be presented.

SYMBOLS

C_Y	store side-force coefficient, $\frac{\text{Store side force}}{qS_S}$
C_n	store yawing-moment coefficient referred to $0.4l_S$, $\frac{\text{Store yawing moment}}{qS_S l_S}$
q	free-stream dynamic pressure
S_S	maximum frontal area of external store
l_S	closed length of store
$\bar{c}$	mean aerodynamic chord of wing
c	local wing chord
A	aspect ratio of wing
$b/2$	semispan of model
λ	taper ratio of wing
$\Lambda_{\frac{c}{4}}$	sweepback of wing quarter-chord line
β	angle of sideslip for complete airplane measured with respect to free stream, or angle of skew of external store measured with respect to model plane of symmetry as shown in figure 5

[redacted]

α angle of attack measured with respect to free stream

M Mach number

RESULTS AND DISCUSSION

Figure 1 shows the geometry of the wing models and the store locations for which experimental data have been obtained at Mach numbers from 0.7 to 1.96. The Reynolds number based on store length was about 2.2×10^6. The store was tested at each of two spanwise positions on both the unswept and sweptback wings and two chordwise positions on the 60° delta wing. Only the more significant results of these tests have been selected for presentation.

The semispan wing models were cantilevered from a five-component strain-gage balance set flush with the tunnel wall. The store, which had a Douglas store shape and a fineness ratio of 8.6 based on the closed length, was cut off at 80 percent of its length to permit installation of an internal sting-supported balance. As shown by the cross-sectional views in figure 1, the pylons or struts were attached to the wings and separated from the store by an extremely small gap which is exaggerated in the figure. This gap was maintained constant while the angle of attack of the store and wing varied from -3° to 12°. Four components of the forces and moments on the store were measured simultaneously with measurements of the loads on the wing. Only the store loads, however, will be discussed in this paper.

Examination of the data indicated that the most severe problems were associated with side-force loads. Figure 2 illustrates the build-up of the side forces with angle of attack and with Mach number. The examples chosen represent practical store locations on each of two wings and illustrate the size of the forces that may very well be encountered. The side forces and yawing moments have been scaled up from the measured data to correspond to a 400-gallon store at an altitude of 40,000 feet. Loads are shown at angles of attack of 0° and 10°.

It should be pointed out that an angle of attack of 10° at $M = 2.0$ represents a $5\frac{1}{2}$g maneuver condition with a wing loading of 75 pounds per square foot. Such an acceleration is less than that which may be required of a fighter-type aircraft.

Figure 2 shows that in either example very large side forces are incurred at an angle of attack of 10° and supersonic Mach numbers. The magnitude of these forces presents a very serious problem since the

[redacted]

[redacted]

direction of the force is in the direction of the least structural strength of the pylon.

The importance of yawing moments in establishing critical loads is not clear cut since the support stresses involved may be pretty much a function of the geometry of the configuration. It is worth noting, however, that for the largest yawing moments (which occurred at an angle of attack of 10° for the store in the presence of the delta wing) the center of pressure is three-tenths of the store length behind the store nose.

The normal forces, which are not shown, show only small variation with either angle of attack or Mach number and even at supersonic speeds are considerably less than the weight of the full fuel tank. It appears that the inertia forces in maneuvering flight will considerably outweigh the aerodynamic normal forces. In any event, providing structure for their support is much less difficult than in the case of the side forces.

Because of their magnitude and direction, the side forces will be treated exclusively in the balance of this paper.

Figure 3 shows the variation with angle of attack of store side-force coefficient based on store frontal area. Data are shown at Mach numbers of 0.75, 1.05, and 1.62 for each of two store locations in the presence of the unswept, sweptback, and delta wing.

This figure shows very large increases in the outward side force with increasing angle of attack for stores in the presence of all three wing plan forms. At moderate angles of attack, the curves are linear and for a given store position the slopes of the curves show remarkably small effects of Mach number even at transonic speeds. The effect of Mach number is shown principally at small angles of attack by the intercept variation. Note, for example, that, for the stores in the presence of the sweptback wing, the value of the intercept increases between Mach numbers 0.75 and 1.05 and then is negative at Mach number 1.62. Also, at small angles of attack, nonlinearities are evident in many of the curves. The most pronounced nonlinearity is shown in the curves for the delta-wing stores. The nonlinearities and values of the coefficient at small angles of attack are strongly influenced by local flow angularities and by changes in flow behavior that occur at transonic and supersonic speeds. Details of the effect of flow angularities and the interferences of the wing flow field on store loads at subsonic speeds are given in reference 1. The nonlinear nature of the curves at low angles indicates considerable care must be exercised in using data obtained at low angles of attack to predict the side forces at higher angles of attack.

Large effects of store position on the side forces at moderate angles of attack are shown. In the case of the unswept wing, moving the store outboard greatly increases va[redacted]efficient at angle of attack for all Mach numbers. This is because the relieving effect of the wing

[redacted]

tips on the pressure field under a wing in a lifting condition inclines the flow in the direction of the tips. The lateral component of the inclined flow increases in velocity as the tip is approached and, consequently, lateral forces on objects near the tips will be greater than on objects near the plane of symmetry. In fact, data presented at Mach numbers up to 0.9 in reference 2 have indicated that side forces on a store at 95 percent of the semispan may be twice as great as those indicated here.

Moving the store outboard on the sweptback wing shows the same general trends as for the unswept wing although the effects of spanwise position are somewhat obscured by the change in chordwise position relative to the wing itself.

Chordwise effects can be quite large as is shown for the delta wing. For stores located some distance below the wing without pylons or supporting structure, the side forces on stores in the forward position are considerably less. This indicates that there are powerful effects of blocking the laterally inclined flow between the store and wing surface just back of the wing leading edge.

It is interesting to note (see fig. 3) that although moving the store inboard reduces the rate of buildup of side force with angle of attack, the installation drag of the store is increased. Reference 3 has shown that the most favorable drag characteristics at supersonic speeds were obtained with the store located near the wing tip. However, of the two store positions shown for the 60° delta wing, the store at the rearward position showed the smallest installation drag (ref. 4) and also, as figure 3 shows, the smallest side-force loads at angle of attack.

More complete treatment of the effects of store position on store loads at supersonic speeds is given in reference 5.

The data presented so far have shown important effects of angle of attack, store position, and Mach number on store side forces. Details of the store installation and supports, however, are also important.

The store installations considered so far have been for stores located immediately adjacent to the wing lower surface. Figure 4 shows data for three configurations: a short pylon, a long pylon, and a condition with no pylon. Side-force and yawing-moment coefficients (based on the store frontal area and store closed length) for the store in the presence of the sweptback wing are plotted against angle of attack for three Mach numbers: 0.75, 1.41, and 1.96. For the store adjacent to both the short pylon and the long pylon, very little difference in the curves was found except at Mach numbers near 1.4. Similarly, in reference 2, at Mach numbers up to 0.9, increases in pylon length for stores as much as 1.6 diameters below the wing had only minor effects on the

[redacted]

side-force variation with angle of attack. Figure 4 shows that removing the pylon, however, greatly reduced the rate of increase of side-force coefficient with angle of attack throughout the entire Mach number range. Similar effects of extending the pylon length and of removing it altogether have been found for the store at 0.80b/2 on the unswept wing. It appears that there is a big aerodynamic effect on store side forces due to the pylon. The reasons for such a large effect are only partially understood and further investigation is necessary to clarify the problem.

One way of reducing the side-force loads on a store for a given angle of attack would be to skew the store relative to the wing plane of symmetry. The results of this approach are shown in figure 5. Here side-force coefficient is plotted against angle of attack for three Mach numbers for the store in the presence of the sweptback wing. Data are shown for 0° and 5° angle of skew (as is defined in the upper left-hand corner of fig. 5). As might be expected, skewing the store 5°, nose inboard, resulted in a displacement of the curves at all Mach numbers but had no appreciable effect on the rate of increase of side-force coefficient with angle of attack.

It may be noted that between Mach numbers of 1.41 and 1.96 considerable displacement of the curves is shown for both the skewed and unskewed store. The reasons for this large change with Mach number are not fully understood, although a third of the displacement can be accounted for by the effects of the shock wave from the nose of the fuselage (which was considerably foreshortened in this particular model). Incidentally, this variation has been confirmed by repeat tests. Although such variation may cause some difficulty, it still appears that side forces at a given angle of attack may be reduced over a large range of Mach numbers by skewing the store.

So far, only the effects on side forces of angle changes in the pitching plane have been considered. The more direct effects of sideslip angle when the complete aircraft as well as the store is yawed are also of interest. Figure 6 shows some information on these effects that were obtained in flight tests of an F-86 airplane. The store, which had a fineness ratio of 5, is shown in the upper part of this figure. The coefficients were obtained by integration of the pressure distributions on both store and pylon and are based on the store frontal area. The data shown for zero sideslip angle are given in reference 6 whereas the other results are unpublished.

Side-force coefficient is plotted against angle of attack on the left-hand plot of figure 6 and against sideslip angle on the right-hand plot for a Mach number of approximately 0.6. It can be seen that the rate change due to angle of attack and angle of sideslip are about the same at 10° angle of attack and 4° angle of sideslip, respectively. It is well to remember that the increase in side force with angle of

[redacted]

attack becomes larger as the store is moved outboard. The increase with sideslip angle, however, may become larger as the store is moved inboard since the fuselage interference can considerably increase the loading due to sideslip angle.

It is worth mentioning that in these flight tests the effects of yawing, pitching, and rolling velocities on the aerodynamic store loads were determined. These effects, however, were small relative to the effects of the changes shown for angles of attack and sideslip.

The side forces on the pylon at both angle of attack and sideslip are much smaller than for the store. However, considering the size of the pylon relative to the store, they indicate that the forces on a larger pylon may be quite substantial.

CONCLUDING REMARKS

The results that have been presented have indicated the following conclusions:

The most critical loading on external stores at transonic and supersonic speeds appears to be that due to the store side force, both because of its magnitude and because the force acts in the direction of the least structural strength of the pylon.

The magnitude of the side forces is determined principally by angle of attack, store position, and Mach number. Angle of attack and store positions are inextricably related since the rate of change of side force with angle of attack, which can be very large, is primarily a function of position. Also, at moderate angles of attack, the rate of increase of side-force coefficient with angle of attack for a given store position is essentially constant with Mach number. The effects of Mach number are shown principally in the values of the coefficient at small angles of attack. These values are strongly influenced by local flow angularities and the changes in flow behavior that occur at transonic and supersonic speeds.

[redacted]

[redacted]

REFERENCES

1. Alford, William J., Jr.: Effects of Wing-Fuselage Flow Fields on Missile Loads at Subsonic Speeds. (Prospective NACA paper.)

2. Silvers, H. Norman, and King, Thomas J., Jr.: Investigation at High Subsonic Speeds of Bodies Mounted From the Wing of an Unswept-Wing–Fuselage Model, Including Measurements of Body Loads. NACA RM L52J08, 1952.

3. Jacobsen, Carl R.: Effects of Systematically Varying the Spanwise and Vertical Location of an External Store on the Aerodynamic Characteristics of an Unswept Tapered Wing of Aspect Ratio 4 at Mach Numbers of 1.41, 1.62, and 1.96. NACA RM L52F13, 1952.

4. Jacobsen, Carl R.: Effects of the Spanwise, Chordwise, and Vertical Location of an External Store on the Aerodynamic Characteristics of a 60° Delta Wing at Mach Numbers of 1.41, 1.62, and 1.96. NACA RM L52H29, 1952.

5. Smith, Norman F., and Carlson, Harry W.: Some Effects of Configuration Variables on Store Loads at Supersonic Speeds. (Prospective NACA paper.)

6. O'Bryan, Thomas C.: Flight Measurements of Aerodynamic Loads and Moments on an External Store Mounted Under the Wing of a Swept-Wing Fighter-Type Airplane. NACA RM L53G22, 1953.

[redacted]

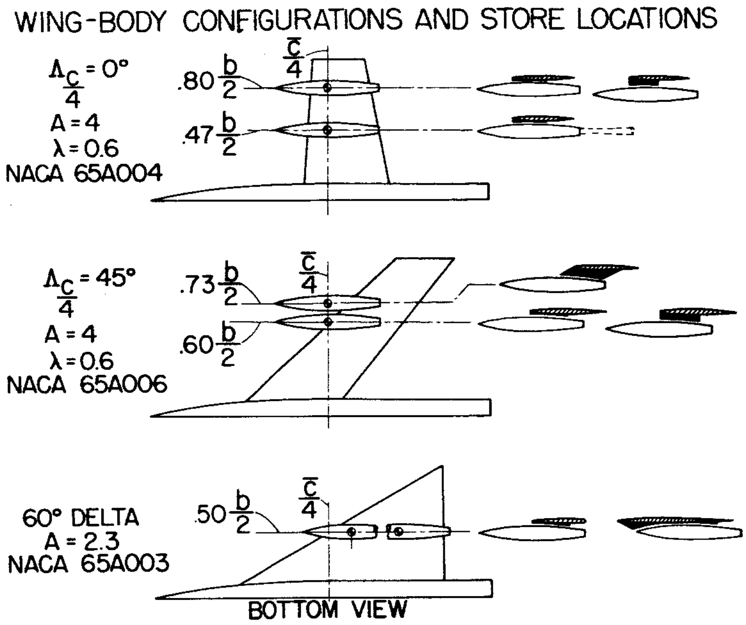

Figure 1

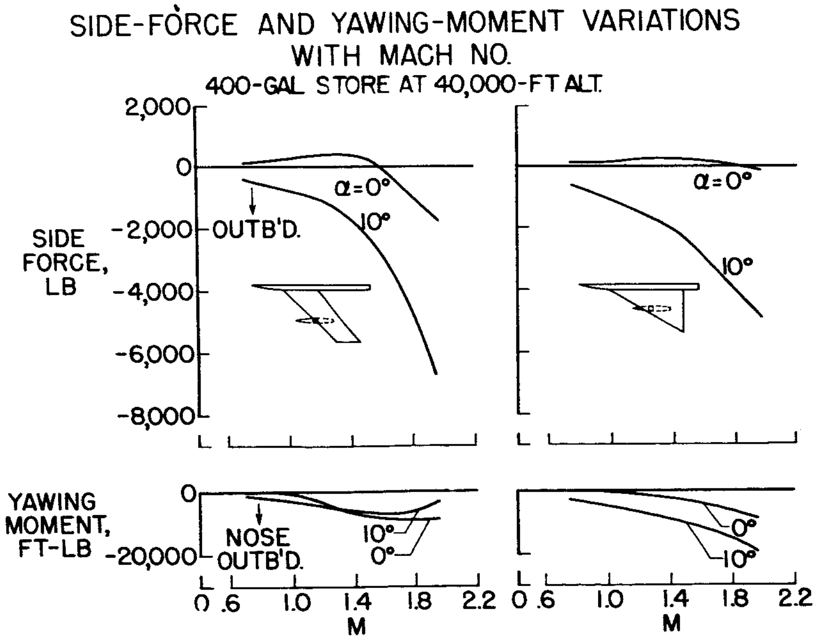

Figure 2

[redacted]

SIDE-FORCE VARIATION WITH ANGLE OF ATTACK

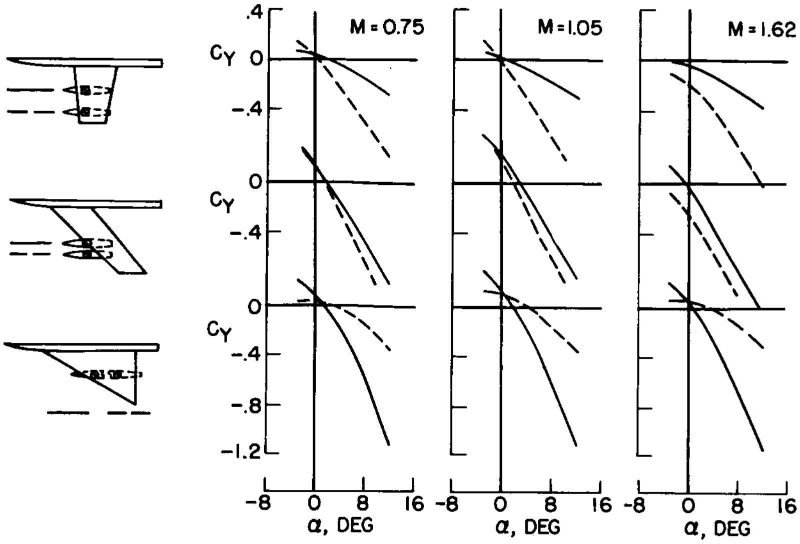

Figure 3

EFFECT OF STORE VERTICAL POSITION AND SUPPORT PYLON

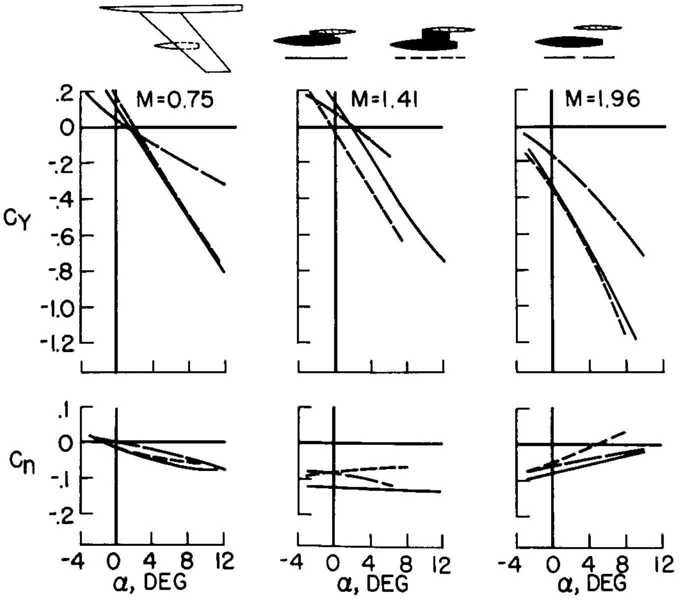

Figure 4

[redacted]

SIDE-FORCE VARIATION WITH ANGLE OF ATTACK AND SKEW

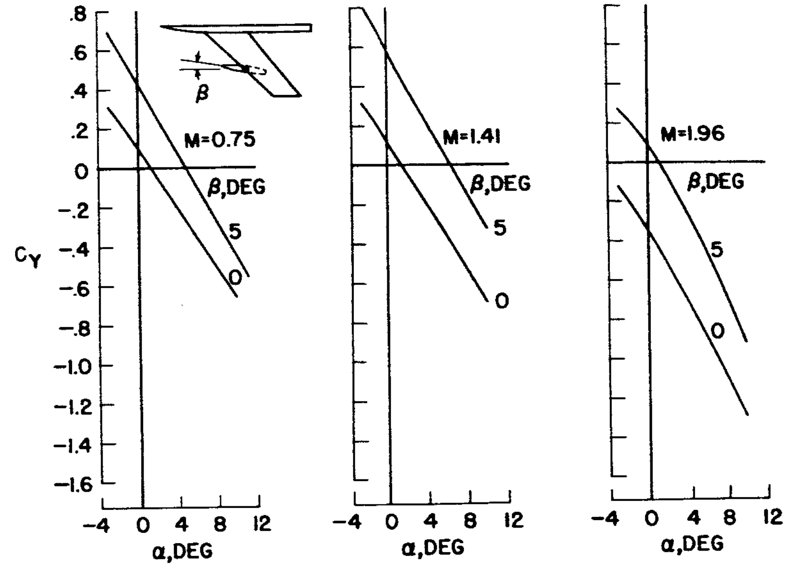

Figure 5

SIDE-FORCE VARIATION WITH ANGLE OF ATTACK AND SIDESLIP
M≈0.6

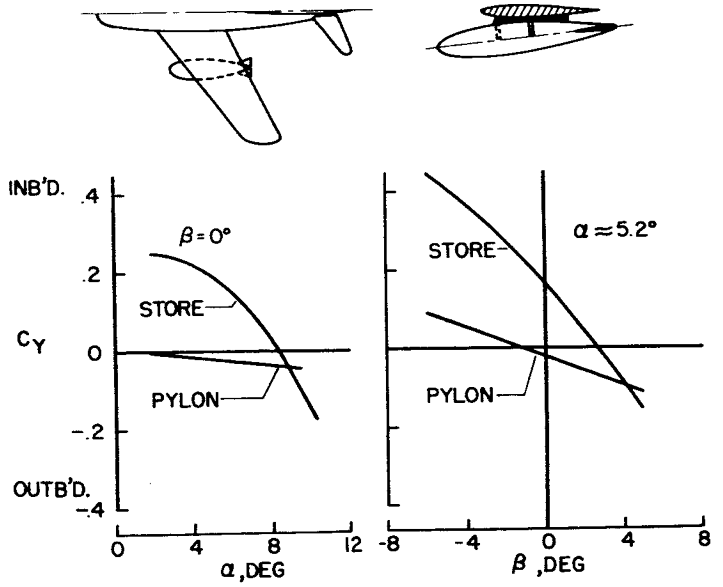

Figure 6

[redacted]

D[redacted]SSIFIED

EFFECTS OF WING-FUSELAGE FLOW FIELDS ON MISSILE LOADS AT SUBSONIC SPEEDS

By William J. Alford, Jr.

Langley Aeronautical Laboratory

SUMMARY

The flow-field characteristics around a swept-wing airplane model at low subsonic speed are described, and the loads induced on a typical missile model while operating within these flow fields are presented. In addition, theoretical flow fields are compared with experiment and are used in first-order estimations of the resulting induced missile loads.

INTRODUCTION

The loading problems associated with the external storage of tanks, bombs, nacelles, and missiles have become increasingly serious with increase in airspeed, and knowledge of these loads is desirable in the design of the store-supporting members. A study of available data from wind-tunnel tests (refs. 1 to 3), in conjunction with theory (refs. 4 and 5), has indicated that these loads are primarily due to the nonuniform flow field generated by the airplane.

The purpose of this paper is to describe these flow fields at low subsonic speeds and to indicate the magnitude of missile loads that may result because of the nature of these flow fields. In addition, comparisons of theoretical flow fields with experiment are presented. These flow fields, both theoretical and experimental, are used in first-order estimations of the resulting missile loads.

SYMBOLS

α	angle of attack, deg
α_l	local angle of attack between xy-plane and local flow direction, $\alpha - \epsilon$, deg (see ref. 1)
ϵ	angle of downwash, deg
β	angle of sideslip, deg

[redacted]

[redacted]

β_l	local angle of sideslip between xz-plane and local flow direction, $\beta + \sigma$, deg (see ref. 1)
σ	angle of sidewash, deg (see ref. 1)
Λ	angle of sweepback, deg
M	Mach number
A	aspect ratio
λ	taper ratio
c	local wing chord, ft
x	longitudinal distance, ft
y	lateral distance, ft
z	vertical distance, ft
V_0	free-stream velocity, ft/sec
q_0	free-stream dynamic pressure, lb/sq ft
q_l	local dynamic pressure, lb/sq ft
l	missile length, ft
b	wing span, ft
$\bar{x}$	longitudinal location of chordwise vortices (fig. 8), ft
Γ	circulation
n	chordwise vortex index
m	spanwise vortex index
u	longitudinal perturbation velocity parallel to free-stream direction (fig. 8), ft/sec
u'	perturbation velocity normal to spanwise line of constant sweep, ft/sec

[redacted]

Subscripts:

c/4	at quarter chord
c/2	at midchord
CG	missile center-of-gravity position

TEST CONFIGURATIONS

Presented in figure 1 are configurations used in investigations, made at low speed in the Langley 300 MPH 7- by 10-foot tunnel, in which flow-field surveys were made using the survey rake shown in the center of the figure. This rake consisted of six probes, each of which was instrumented to measure local pitch and sideslip angularities and dynamic pressure. These surveys were made under the fuselage and at each one-quarter semi-span location of the swept-wing–fuselage combination and at the one-half semispan location of the unswept-wing–fuselage combination. The range of vertical, spanwise, and chordwise position investigated is indicated by the dots, which represent the leading edge of the survey rake.

Static force and moment measurements were obtained on a typical missile model, shown in the center of figure 2, for various locations within the wing-fuselage flow fields. The range of missile center-of-gravity location investigated are shown by symbols at the data points.

The results of these investigations indicated that the induced longitudinal characteristics were, in general, qualitatively similar for both the swept and unswept configurations, whereas the induced lateral characteristics were considerably more seriously affected for the swept-wing configuration. In view of this result, the discussion deals hereinafter with the swept configuration.

MEASURED FLOW FIELDS

In defining a flow field, or velocity distribution, it is necessary to know both the direction and magnitude of the local velocity vectors. For convenience, the flow directions are expressed as vertical and lateral inclinations and the magnitudes are expressed as dynamic pressure.

The local angles of attack as measured about the one-half semispan location of the swept-wing–fuselage combination are presented in figure 3. The conditions depicted, which are for an angle of attack of 8° and zero sideslip, are equivalent to the 6g service load limit of a typical fighter

[redacted]

airplane for a velocity of 430 mph at an altitude of 20,000 feet. These data are presented in contour form; that is, as lines of constant angularity for the physical space surrounding the airfoil profile. The missile outline is superimposed on the contours to show its size relative to the local wing chord and to indicate the angularity gradients to which it is subjected. Regions where the local angles are greater than 8° indicate an upflow and regions where these angles are less than 8° are indicative of downflow. The angularity variation along the center line of the missile, which in this case was 15 percent of the local wing chord below the wing chord plane, are presented in the lower portion of figure 3. Two missile center-of-gravity locations are shown to indicate both the angularity magnitudes and the angularity gradient that exist along the missile center line. For the chordwise range indicated, the local angles of attack vary from 5° to 12°, a gradient of 7° along the missile center line extended.

Presented in figure 4, for the same vertical plane, are the local sideslip angles. It should be noted that the perturbation velocities which generate these lateral angularities are in a plane normal to the plane of the figure. The local sideslip angles below the wing chord plane represent an outflow direction (toward the wing tip), and the angles above the chord plane indicate an inflow (toward the plane of symmetry). The sideslip angles that exist along the missile center line are presented in the lower graph and indicate a gradient of 6° along the center line extended. Comparison of these sideslip gradients with angle-of-attack gradients of figure 3 shows that they are of the same magnitude and could be considerably more important since the supporting pylon would have its least structural strength in the lateral direction.

The local dynamic pressures referenced to free-stream conditions are presented in figure 5. The effects of the induced longitudinal velocities are as would be expected, since the dynamic pressures are increased above and decreased below the wing chord plane. Sizeable gradients are again in evidence over the length of the missile center line extended. These data also indicate that, for positive angles of attack, the dynamic pressure can effect load reductions but, for negative angles of attack, would cause large load increases.

MEASURED MISSILE LOADS

The preceding discussion has attempted to define and illustrate the flow phenomenon existing around the airplane. Having shown that the missile is forced to operate in regions of adverse flow, it would be desirable to correlate the flow characteristics with the loads induced on the missile.

[redacted]

The total missile normal forces, in pounds, for a free-stream dynamic pressure of 445 pounds per square foot are presented in figure 6. These data were obtained by assuming a full-scale missile to be stored externally on a typical fighter airplane at a velocity of 430 mph at an altitude of 20,000 feet. The effects of compressibility are absent since the missile loads data were obtained at low speed. The normal-force load center, in percent of the missile length from the missile nose, is also presented. These parameters are given for various locations of the missile center of gravity in fractions of the local wing chord, relative to the leading edge of the local wing chord. For comparison, the isolated missile characteristics, at an identical attitude, are shown by the dashed lines. The two missile center-of-gravity locations (fig. 6) indicated by the solid symbols are identical to those shown in the lower graph of figure 3. It should be noted that the total normal forces are a result of an integration of the angularities (fig. 3) and dynamic pressures (fig. 5) over the length of the missile. Considering the rearward location of the missile center of gravity ($x/c \approx 0.45$), the missile is seen to be operating in a region of reduced angularity and consequently experiences a reduced normal force when compared to the isolated missile. Further examination shows that the tail is operating in a slightly higher angular region than the missile wing (fig. 3) and consequently the load center is drawn aft. When the missile center of gravity is in the forward position ($x/c \approx -0.75$), the missile is experiencing higher angularities (fig. 3) and the resulting normal forces are considerably increased (fig. 6). For the range of missile center-of-gravity location investigated, the normal forces are initially decreased approximately 30 percent and later increased about 50 percent with a total load-center travel of approximately 10 percent of the missile length.

Presented in figure 7 are the total missile side forces and side-force load centers as a function of missile center-of-gravity location. Recalling that the airplane-missile combination is at zero sideslip, the comparable isolated-missile characteristics would be zero. In order to show the relative magnitude of these side loads, the isolated-missile characteristics at 6° sideslip are shown as the dashed lines. Once again the solid symbols represent the missile center-of-gravity locations shown in the lower graph of figure 4. Since the missile was below the wing, the local sideslip angles are in an outward direction (fig. 4) and cause negative side forces (force directed toward the wing tip, fig. 7). The side loads and load centers are as would be expected since, when the missile wings are in the highest angular region (fig. 4, $x/c \approx 0.50$), the load center moves forward (fig. 7) and when the tail ($x/c \approx -0.75$) is in the highest angular region the load center moves rearward with a total load-center travel of 30 percent missile length for the chordwise range indicated. The region of greatest side load is encountered when the missile wings are in the highest angular region.

THEORETICAL FLOW FIELDS

Once a problem has been defined and shown to exist, it then becomes desirable to have, or to formulate, procedures by which the individual components of the system can be studied.

In the present instance, the chief difficulty appears to be in the severe angular gradients that are generated by the airplane. The mathematical models used to calculate these flow fields assumed a simulated lifting surface (fig. 8), the appropriate airfoil-section singularity distribution (by method of reference 6), and simple sweep theory (fig. 8). The simulated lifting surface, shown in figure 8, approximated both the spanwise and chordwise distributions of vorticity by discrete horseshoe vortices. The spanwise vorticity distribution was represented by 10 horseshoe vortices and the chordwise distribution was represented by four vortices of equal strength, the chordwise locations of which were determined from the familiar two-dimensional circulation distribution shown in figure 8. The nonlifting (thickness) effects were determined from the source-sink distribution that satisfied the two-dimensional airfoil-section boundary conditions (ref. 6) and were corrected by simple sweep theory (fig. 8) to account for wing sweep.

Typical results of these calculations compared with experiment are presented in figures 9 and 10. Figure 9 presents the local angles of attack and figure 10 presents the local angles of sideslip for the one-half semispan location $\left(y/\frac{b}{2} = 0.5\right)$ of the swept-wing–fuselage combination. The experimental data are shown as the symbols and the theory is shown as the solid-line curves. As is seen, the agreement is poor for $\alpha = -8^{\circ}$. This disagreement is presumed to be due to the fact that the flow on the suction side of the airfoil assumes characteristics that are nonpotential. The agreement is good between theory and experiment (figs. 9 and 10) for $\alpha = 0^{\circ}$ and for all positive angles of attack up to $\alpha = 24^{\circ}$, where theory then overestimates the local angles of attack. This is rather surprising from consideration of the nonpotential nature of the flow on the suction side of the wing surface. Calculations made for the three-quarter semispan location have shown that theoretical values obtained by using the theoretical span-load distribution overestimate the experimental values.

ESTIMATED MISSILE LOADS

With the flow-field characteristics known, the next step is to use them, in conjunction with the missile component characteristics, to estimate the airplane induced missile loads. This estimate has been made and figures 11 and 12 present sample comparisons of theory and experiment.

Presented in figure 11 are the estimated normal forces and normal-force load centers. Experimental loads are again represented by the symbols. The estimation obtained by using the experimental flow fields is shown as the solid curves and the estimation by using the theoretical flow fields is shown as the dashed curves. Good agreement in estimating the normal forces is obtained by both estimates over the rear portion of the chord, with evidence that theory gives values too low ahead of the leading edge. The load centers are also seen to be well predicted.

In the case of the estimated side forces (fig. 12) both estimates are low, although the side-force load centers are well predicted. The reason for the lack of agreement for the side forces is not completely understood.

The data that have been presented were obtained at low speed in order to permit convenient examination of the nature of the complex flow that exists around airplanes. The use of a missile as the store configuration was for illustrative purposes, and the approach utilized should be equally valid for other external stores, although such application has not, at present, been adequately demonstrated.

The results of a brief theoretical study have indicated that the effects of compressibility, for subcritical Mach numbers, are to generate larger flow distortions and consequently larger induced missile loads, although the flow structure remains similar to that of an incompressible nature.

CONCLUDING REMARKS

In summary, these results have shown that the flow fields in regions beneath the one-half semispan location of a swept-wing airplane model can be calculated. These flow fields can then be used in first-order estimations of the loads experienced by a missile while operating in these flow fields.

REFERENCES

1. Alford, William J., Jr., Silvers, H. Norman, and King, Thomas J., Jr.: Preliminary Low-Speed Wind-Tunnel Investigation of Some Aspects of the Aerodynamic Problems Associated With Missiles Carried Externally in Positions Near Airplane Wings. NACA RM L54J20, 1954.

2. Alford, William J., Jr., Silvers, H. Norman, and King, Thomas J., Jr.: Experimental Aerodynamic Forces and Moments at Low Speed of a Missile Model During Simulated Launching From the Midsemispan Location of a 45° Sweptback Wing-Fuselage Combination. NACA RM L54K11a, 1954.

3. Alford, William J., Jr.: Experimental Static Aerodynamic Forces and Moments at Low Speed on a Canard Missile Model During Simulated Launching From the Midsemispan and Wing-Tip Locations of a 45° Sweptback Wing-Fuselage Combination. NACA RM L55A12, 1955. (Prospective NACA paper.)

4. Luce, R. W., Jr., and Velton, E. J.: Investigation of the Aerodynamic Interference of a Launching Aircraft on the Sparrow II Missile. Rep. No. SM-14383 (Bur. Aero. Contract NOa(s)51-252, Douglas Aircraft Co., Inc., Oct. 29, 1952.

5. Evans, K. E., and Freeman, P. A.: Launch Study Supplement XAAM-N-4 (Oriole) Launching Dispersions Including the Effects of the Airplane Wing and Pylon on the Flow Field Around the Missile. Eng. Rep. No. 5058 (Contract NOa(s)51-194-C), The Glenn L. Martin Co., Apr. 1952.

6. Smith, R. H.: Aerodynamic Theory and Test of Strut Forms - I. NACA Rep. 311, 1929.

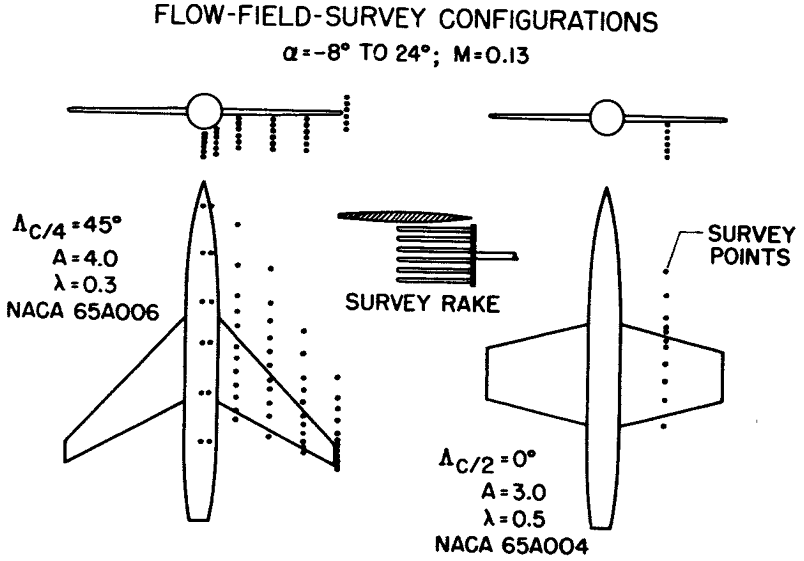

Figure 1

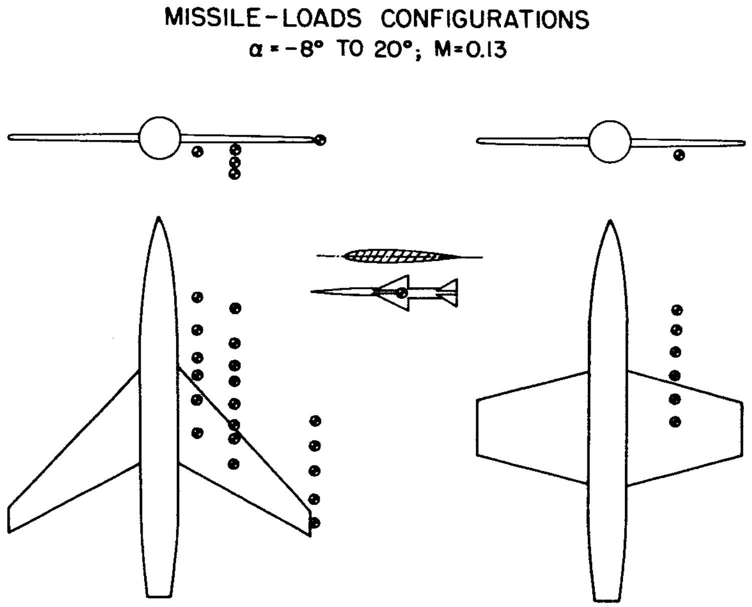

Figure 2

[redacted]

[redacted]

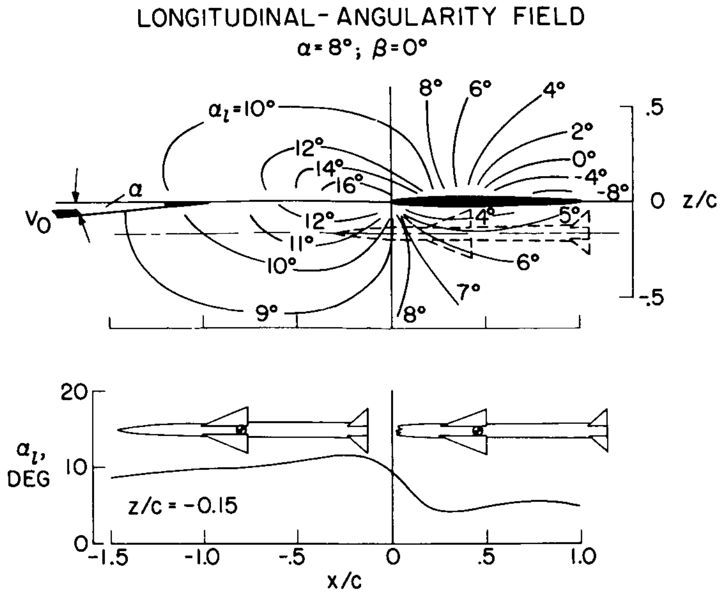

Figure 3

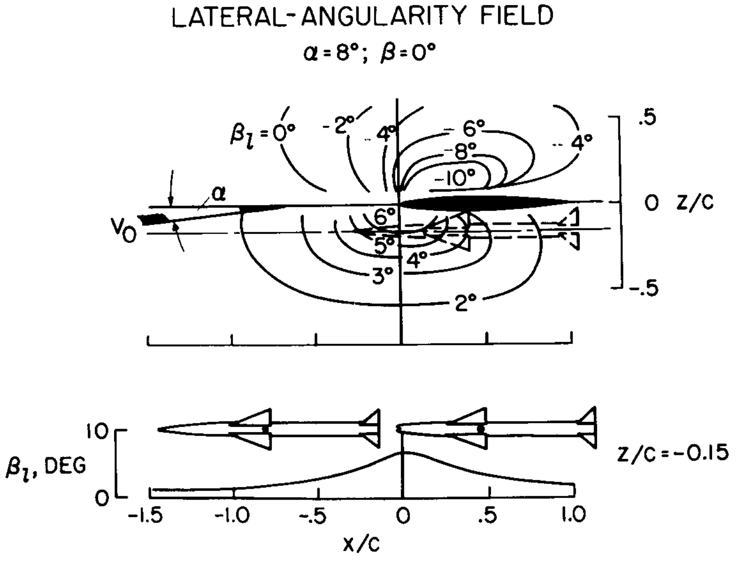

Figure 4

[redacted]

[redacted]

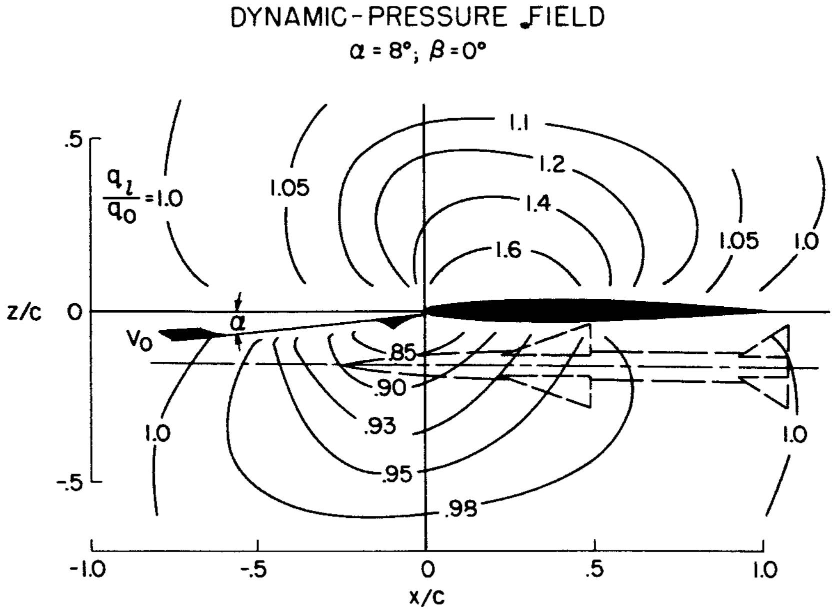

Figure 5

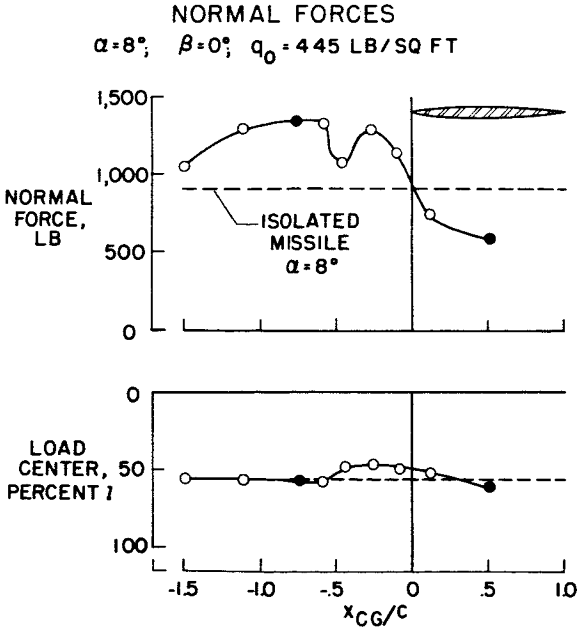

Figure 6

[redacted]

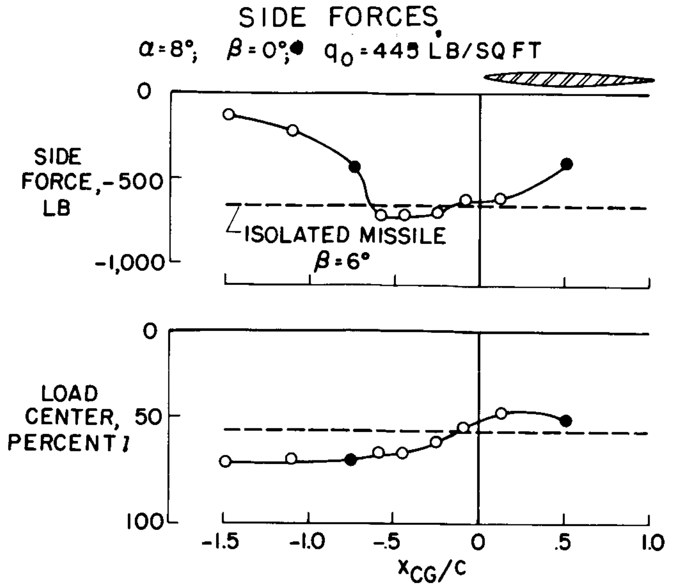

Figure 7

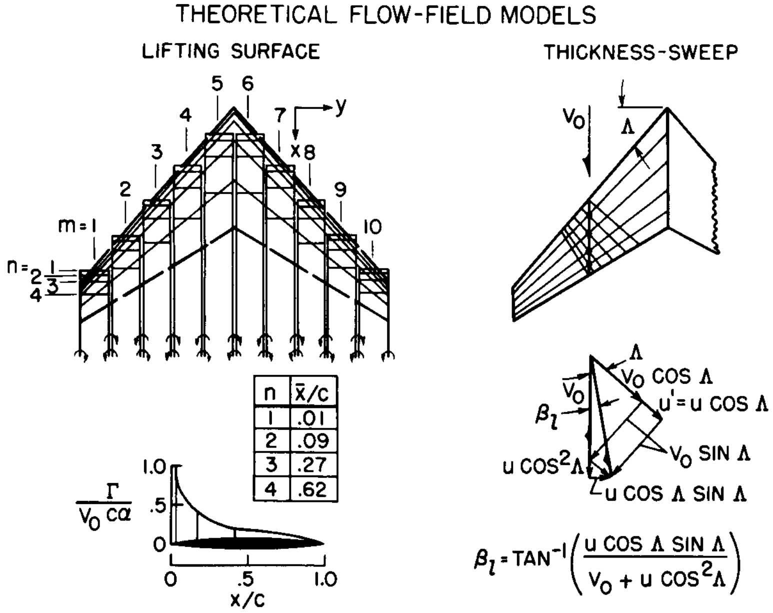

Figure 8

[redacted]

D[redacted]SSIFIED

PREDICTION OF LONGITUDINAL ANGULARITIES

$\frac{y}{b/2} = 0.5$; $z/c = -0.15$

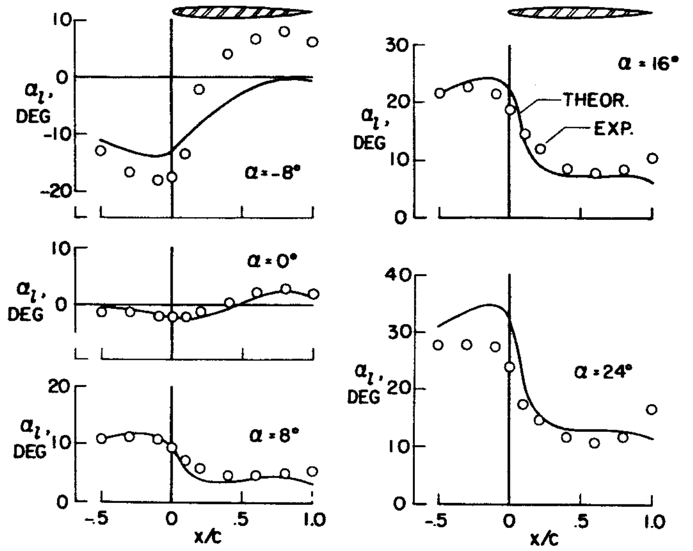

Figure 9

PREDICTION OF LATERAL ANGULARITIES

$\frac{y}{b/2} = 0.5$; $z/c = -0.15$; $\beta = 0°$

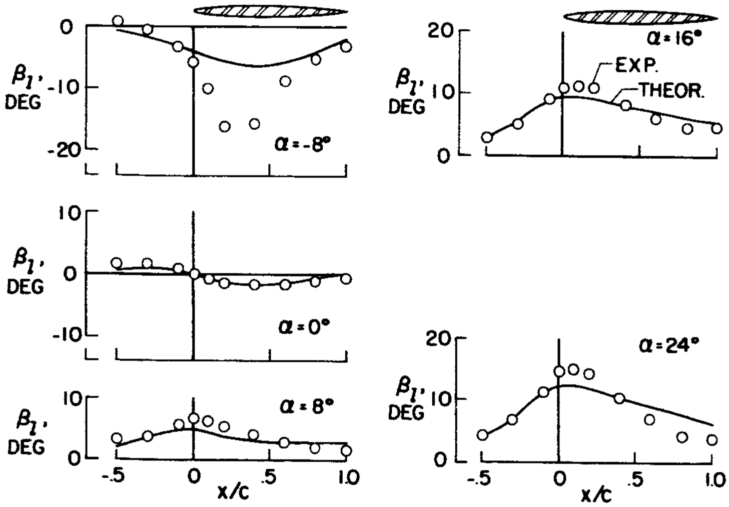

Figure 10

[redacted]

[redacted]

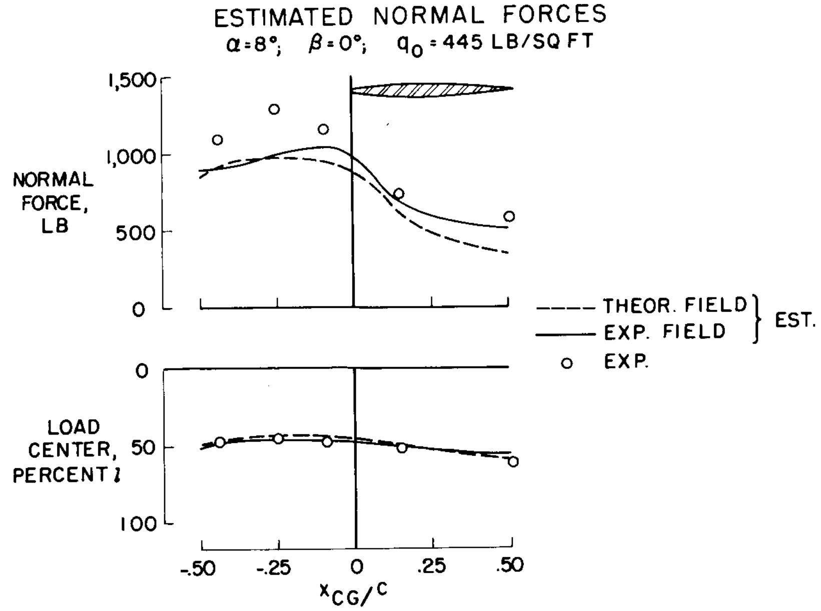

Figure 11

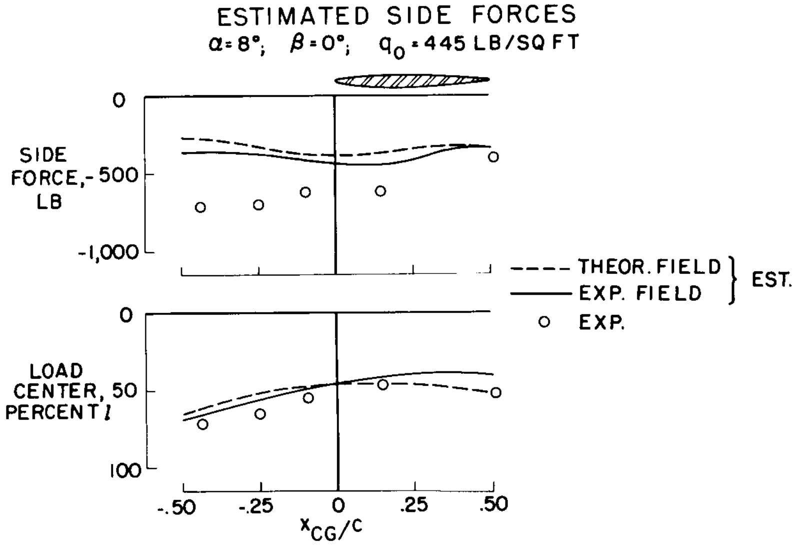

Figure 12

[redacted]

D[redacted]SSIFIED

SOME EFFECTS OF CONFIGURATION VARIABLES ON STORE LOADS AT SUPERSONIC SPEEDS

By Norman F. Smith and Harry W. Carlson

Langley Aeronautical Laboratory

SUMMARY

A large volume of data from several recent stores-research programs has been examined and analyzed and is sampled and illustrated in this paper. Comprehensive coverage of the important configuration variables, obtained by measurements of separate forces and moments on stores in a large number of positions, is shown to give an improved understanding of the factors affecting store loads.

INTRODUCTION

The many store and nacelle investigations which have been performed to date have demonstrated the large and important performance and load problems that can be incurred. Although these investigations have yielded valuable information for the specific configurations tested, they contributed little toward obtaining a basic understanding of this interference phenomenon, particularly at supersonic speeds. This is true because of the large number of configuration variables which affect store loads. It is the purpose of this paper to discuss and evaluate the effects of some configuration variables on store loads at supersonic speeds.

In view of the fact that a very wide range of store locations are in use or under consideration today, any treatment of the store problem must cover a large number of store positions. A recent wind-tunnel investigation, which will be the principal source of the data presented in this paper, accomplishes this and, in addition, treats a number of the configuration variables involved. Figure 1 shows the models and test "grid" for this investigation in the Langley 4- by 4-foot supersonic pressure tunnel at supersonic speeds. The model store was separately sting supported on a strain-gage balance which measured six components. The half-model of fuselage, wing, or wing-fuselage combination was mounted on a four-component balance in the tunnel boundary-layer bypass plate. The test grid through which the store was moved involved 8 fore-and-aft positions and 11 spanwise positions for a total of 88 store positions at each of several store vertical heights. Not

[redacted]

all these test positions represent practical store positions, of course, but were included in order to make possible interference mapping of the entire area, with an eye toward an improved understanding of the source and distribution of the interferences. The angles of attack of only the wing and fuselage were varied up to 4°, the store remaining at 0° throughout. Several store shapes and sizes and several wing and fuselage configurations were investigated. (The delta wing is shown by dashed lines in fig. 1.) All the data from the Langley 4- by 4-foot supersonic pressure tunnel are for a store tested in the absence of a pylon.

With this equipment rather extensive work has been done; although much has been learned, there are many questions yet unanswered, particularly with regard to store loads. The data presented are the first results obtained with this technique and are useful in themselves as well as forming a guide for future work. A large volume of data has been examined and analyzed and will be sampled and illustrated in this paper. Store side force is used extensively because it has been shown to be generally the important load from the standpoint of pylon or support design. The other loads will be found in NACA reports on this work (for example, refs. 1 and 2).

RESULTS AND DISCUSSION

Figure 2 shows the store side force in the presence of the wing-fuselage combination at an angle of attack of 0° at $M = 1.6$. Force data from about 30 store positions were used to make this contour map. The lines show positions of the store midpoint for constant values of store side-force coefficient. For the store position shown, for example, the value of C_Y is 0.04. The shaded areas signify regions in which the store side force (for the store shown) is negative or toward the tip, whereas the unshaded areas signify regions in which the store side force is positive or toward the root. Note that the store side-force coefficient changes rapidly from -0.08 to 0.12 in a fairly short region of usable store positions and that the values change from peak maximum to zero or less in less than one wing-chord length. The value of C_Y of 0.12 corresponds to the side force developed by the isolated store at 4° of yaw. Note that the side-force values shown are for the store only; these data are for conditions with no pylon present except when specifically stated.

One of the first things to be considered in the problem of sorting out the important variables and understanding their influence is the matter of the relative contribution of the configuration components themselves. The results of some of the configuration breakdown tests are shown in figure 3. In this figure, the store side force and store normal force are plotted for an inboard, a midspan, and an outboard station in the presence of the wing and wing-fuselage combination. The squares in the upper plots are the same data included in the contour plot of figure 2. It can be seen from the C_Y curves for the inboard station that the contribution of both fuselage and wing to store side force in this position is important, mutual interference probably further confusing the effects. For the outboard station, the influence of the fuselage (as shown by the difference between the curves) has diminished but is still felt. In the case of normal force (lower half of fig. 3), the influence of the fuselage appears to be relatively unimportant for all store positions because the store lift in the presence of the wing-fuselage combination is almost exactly equal to the store lift in the presence of the wing alone. Data similar to these covering the other forces and moments are presented in references 1 and 2.

It might be pointed out in passing that the magnitudes of the variations in C_Y and C_N shown here are comparable with those measured for the other forces and moments (the store drag, yawing moment, and pitching moment). This condition applies to all the configurations but, since these effects are not fully understood, it is not known whether this result is general.

In order to determine the more important variables involved in the store-loads problem, it is necessary to eliminate some of the less important ones. One of these is vertical displacement between wing and store. Shown in figure 4 is a plot of store side force against store longitudinal position x for three spanwise stations: inboard, midspan, and tip. The data with the circle symbols is for a large space between wing and store and corresponds to the data previously shown in the contour plot (fig. 2). The effect of decreasing the vertical height is to increase the magnitude of the side-force variations, especially in the inboard position. Outboard, the effect of vertical height is smaller, and the character of the curves is essentially the same. The overall effect of vertical height is thus shown to be small within the range tested.

Another minor variable, the effect of store size on side force, is shown in figure 5. Although the character of the C_Y curves tends to be similar, some shifting is in evidence and very much larger values of maximum side-force coefficient were measured for the small store than for the large store. This phenomenon is explained by the fact that the small store can become more completely submerged in a region in which side force is generated (because of a pressure gradient or flow deviation or both) in one direction, either inward or outward. The large store, on the other hand, tends to extend through several such regions so that a lower peak value of side-force coefficient results.

It is significant to note that the slope of the curve of side-force coefficient with angle of attack C_{Y_α} (lower curves of fig. 5) is not appreciably affected by store size. This phenomenon is not fully understood, and it is not known whether this result applies outside the range of sizes tested in this investigation.

From the data shown in figure 2 and similar data for $\alpha = 2^\circ$ and 4°, the slope of side force with angle of attack has been obtained and is shown in contour-map form in figure 6. It can be seen that the slopes vary greatly with store location and that for some store locations the slopes are so great that very high loads may be encountered at high angles of attack for these locations. The store side-force coefficient C_{Y_α} increases toward the wing tip as would be expected from the fact that the sidewash increases as the tip is approached and as the lift is increased. Large changes in C_{Y_α} can also be experienced in moving the store from the leading edge of the wing to the trailing edge of the wing near the midspan. These data were taken by changing the wing-fuselage angle of attack, as mentioned earlier. The fact that the store remained at $\alpha = 0^\circ$ affects the store normal force but not to any appreciable extent the store side force. The effect of the small change in vertical displacement between wing and store which occurs when the wing-fuselage angle of attack is changed is, as has been shown previously, small and unimportant compared with the effects now being considered.

This C_Y contour map was prepared from data limited to an angle of attack of 4°. For many conditions, angles considerably higher are of interest and may, as suggested by the data shown here, be a design or limiting condition for store loads. Some data from an investigation in the Langley 9- by 12-inch blowdown tunnel involving similar tests of two store positions up to higher angles of attack provide some information on this point. Figure 7 shows the variation of C_Y with α for a store at midspan position up to an angle of attack of 12°. Shown for comparison are curves taken from the mapped data of figures 2 and 6 for a comparable (midspan) store position and two others - one inboard and the other near the wing tip. It will be noted from the configuration sketches labeling the curves that configuration differences exist. The configuration on which the high angle-of-attack data were obtained involves a smaller store, a shorter fuselage nose, and a lower wing taper. The effects of these differences are measurable but, as was shown previously for the case of store size and the effect of the fuselage, are not important for the comparisons made here. The side-force data chosen from some of the mapped data shown previously for a comparable store location agree well with the data from the blowdown tunnel. This agreement lends credence to the extrapolation of the mapped data to reasonably high angles of attack. The curves shown for the inboard and tip, however, are greatly different and show the important effect of store position on the maximum side-force loads which can be encountered. In the absence of adequate mapped data at higher angles of attack, it appears that the data available for a limited number of store positions from the Langley 9- by 12-inch blowdown tunnel might be used as a guide for judicous extrapolation of the mapped data as shown in figure 6.

Turning now to the effects of another variable, the wing plan form, figure 8 shows a contour map of C_{Y_α} for the delta wing for comparison with the same data for the swept wing (fig. 6). The highest values are obtained at the tip, as in the case of the swept wing, but the chordwise variation of C_{Y_α} is essentially zero in the case of the delta wing, in contrast with the considerable variation shown for the swept wing.

These data, like the swept-wing data shown previously, are limited to an angle of attack of 4°. Again, these data can be correlated with the blowdown tunnel data on a similar delta-wing configuration. Figure 9 shows the variation of C_Y with α for this configuration (shown shaded) up to $\alpha = 12^\circ$. Shown for comparison is a curve for the same store position from the mapped data for the delta-wing configuration tested in the Langley 4- by 4-foot supersonic pressure tunnel. These data agree well as to general slope and values of side force indicated up to 12°. Also shown in figure 9 are curves from the mapped data for a store at an inboard position and at a tip position. Again, as in the case of the swept wing, the effect of store position is shown to be important. Extrapolation of the mapped data to higher angles of attack, using the data from the Langley 9- by 12-inch blowdown tunnel as a guide, also appears to be feasible in the case of the delta wing.

The foregoing data involve only the load on the store and do not consider either the load on the pylon itself or the effect of the pylon on the store loads. Unfortunately, little or no data exist at present on pylon loads. Some information is available, however, on the effect of a pylon on store loads. Figure 10 shows the data from the Langley 9- by 12-inch blowdown tunnel for the variation of store side force with angle of attack, the space between store and wing being open and this space being filled with an unswept support pylon (as shown in the sketch in fig. 10). The pylon is attached to the wing but does not touch the store. It can be seen that the large store side force which is produced as the angle of attack is increased is more than doubled when the pylon is present. Since these large loads added to the unknown but undoubtedly large load on the pylon are somewhat terrifying, it is of interest to speculate a bit as to whether these limited data are showing a general situation.

[redacted]

Since the store in this position is experiencing a high side load, it is probable that the pylon is also in a region of high side load. The pylon-store combination can be considered to be comparable to a wing-tip-store configuration under lifting conditions. It has been shown that at angle of attack a tip store experiences an interference lift because of the presence of the wing which is dependent on the angle of attack and on the wing plan form and may be influenced by other factors. Location of the pylon in a region of lower side loads could be expected to reduce the loads induced on the store and on the pylon. A change in pylon plan form could also be expected to affect these loads.

From an examination of this and other limited data by using the above assumptions, it is believed that the increment in side force due to the pylon shown in figure 10 is an extreme case. Further research is needed on the effect of pylons and on pylon loads themselves.

All the previous figures have pertained to store or nacelle configurations having no tail fins. The effect of tail fins on a large store is shown in figure 11. In figure 11, the side force C_Y and the slope of side force with angle of attack C_{Y_α} are plotted against store chordwise position x for three spanwise positions. The C_Y curves for stores with and without fins undulate in similar fashion, but the peak value (both positive and negative) of C_Y attained is larger for the finned store in all cases. The actual value of C_Y for any one store position may be either higher or lower. These effects are the result of the presence of the fins in regions of strong crossflow or pressure gradients.

Figure 11 appears to indicate that the regions of inward and outward force which exist are strong and relatively sharply defined. It is apparent that the effect of adding fins to a store can be known only if specific test data are available or if very detailed information on the flow field is available.

The data presented herein are consequently being analyzed with the aim of providing an improved understanding of the flow field. A useful picture of the flow field has been formulated in the case of drag, where simple buoyancy concepts were found to explain the drag interference between components (ref. 1). The buoyancy concept was found inadequate in dealing with other forces, however, because flow angularity is important, if not predominant, in the production of these forces. Other approaches are being attempted, based upon the large amount of mapped force data available.

[redacted]

CONCLUDING REMARKS

In recent research, sufficient coverage of important variables has been included to give an improved understanding of the factors affecting store loads. For a given wing plan form, store position and configuration angle of attack have been shown to be the two most important parameters in the evaluation of store side force, and these two items are so intertwined as to require careful consideration of both. The effects of other variables such as store size, vertical displacement, and fins have been illustrated.

The effect of a supporting pylon has been shown to be large and important, although the factors governing the effects of pylons are not fully understood and more work is needed on both the effect of pylons and on the pylon loads themselves.

REFERENCES

1. Smith, Norman F., and Carlson, Harry W.: The Origin and Distribution of Supersonic Store Interference From Measurement of Individual Forces on Several Wing-Fuselage-Store Configurations. I. - Swept-Wing Heavy-Bomber Configuration With Large Store (Nacelle). Lift and Drag; Mach Number, 1.61. NACA RM L55A13a, 1955.

2. Smith, Norman F., and Carlson, Harry W.: The Origin and Distribution of Supersonic Store Interference From Measurement of Individual Forces on Several Wing-Fuselage-Store Configurations. II. - Swept-Wing Heavy-Bomber Configuration With Large Store (Nacelle). Lateral Forces and Pitching Moments. (Prospective NACA paper.)

MODELS AND TEST GRID

EACH + INDICATES A STORE MIDPOINT LOCATION

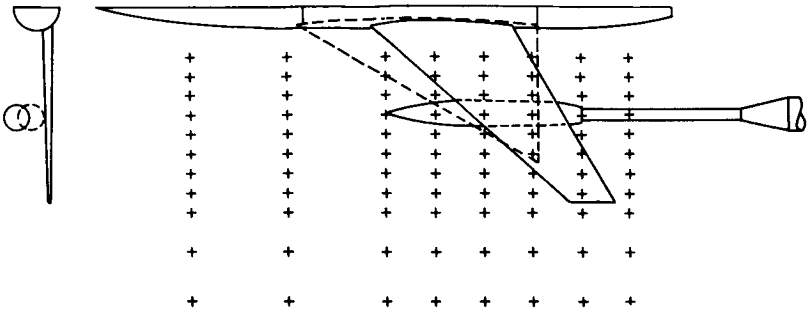

Figure 1

STORE SIDE-FORCE COEFFICIENT

SWEPT WING; $M = 1.6$; $\alpha = 0°$

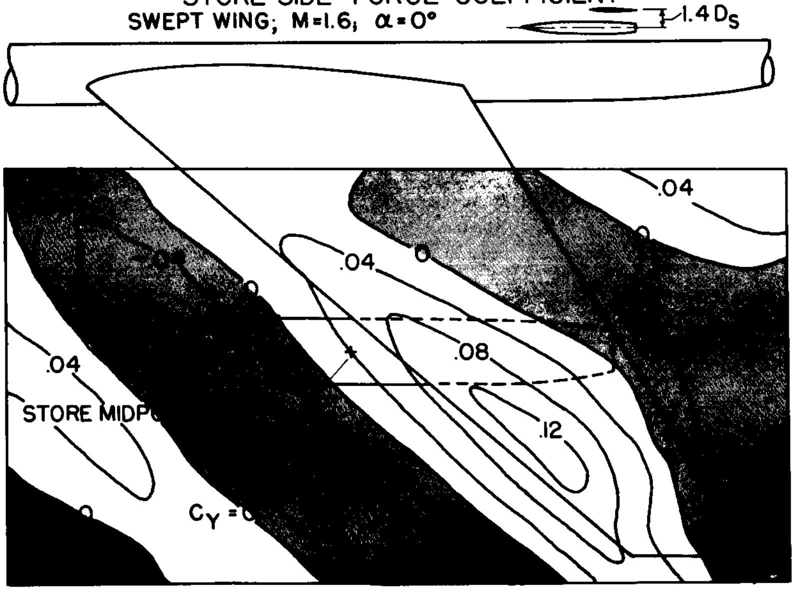

Figure 2

[redacted]

DECLASSIFIED [redacted]

CONTRIBUTION OF COMPONENTS IN PRODUCING STORE FORCES

M=1.6; α=0°

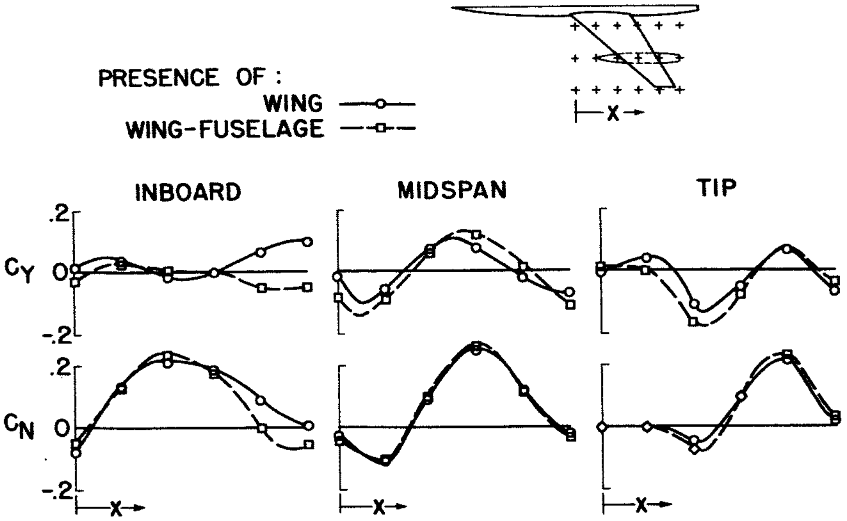

Figure 3

EFFECT OF STORE VERTICAL LOCATION ON C_Y

M=1.6 ; α=0°

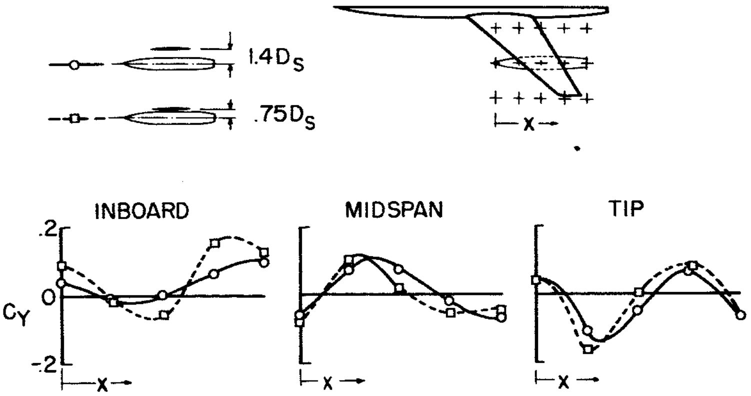

Figure 4

[redacted]

[redacted]

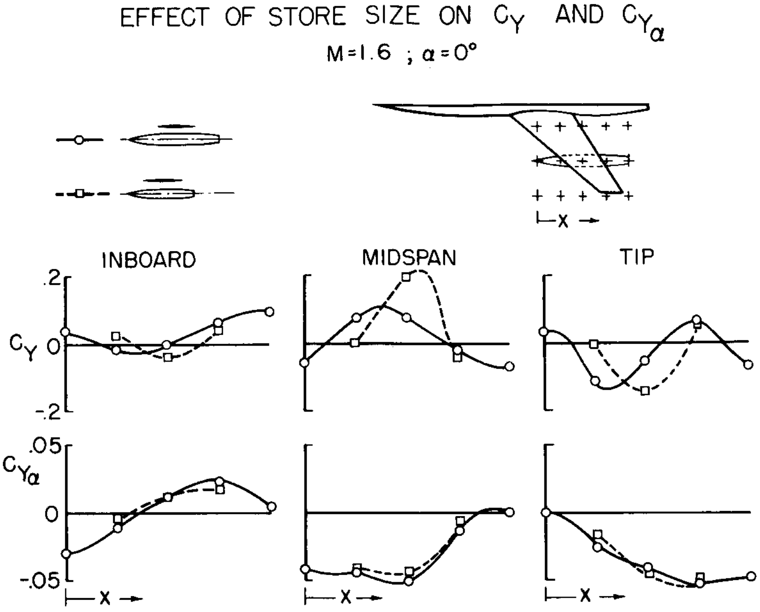

Figure 5.

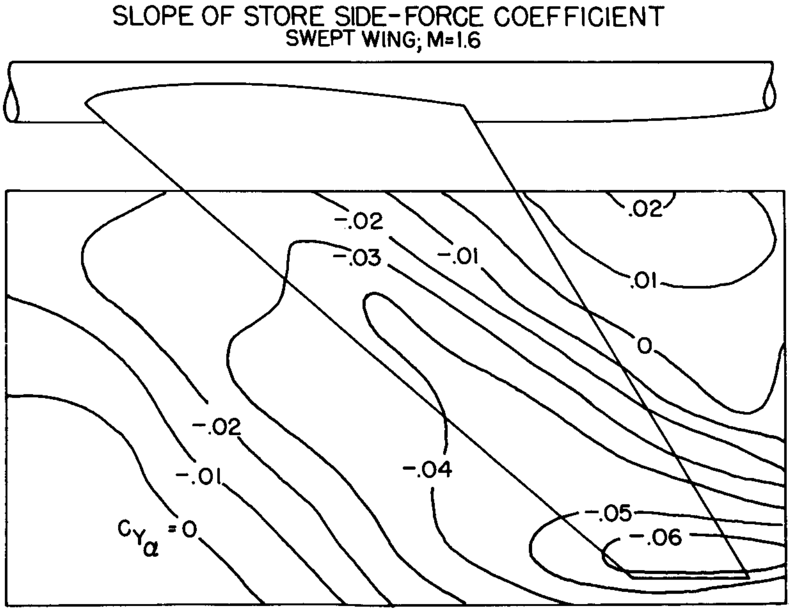

Figure 6.

[redacted]

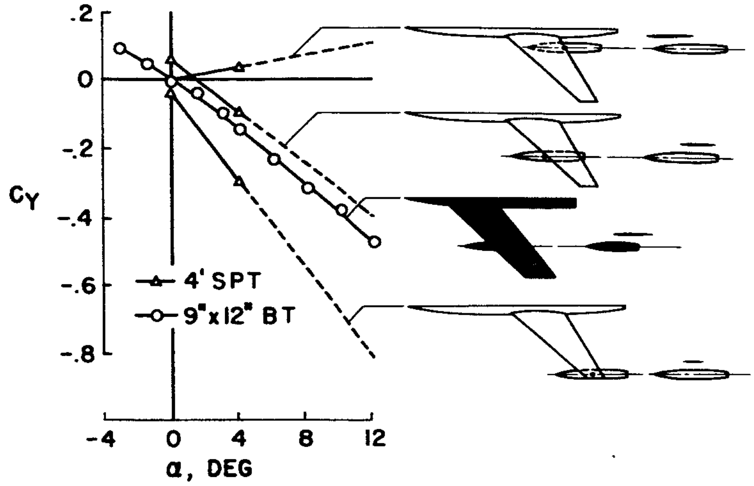

EFFECT OF STORE LOCATION AND ANGLE OF ATTACK ON C_Y

SWEPT WING; M ~ 1.6

Figure 7

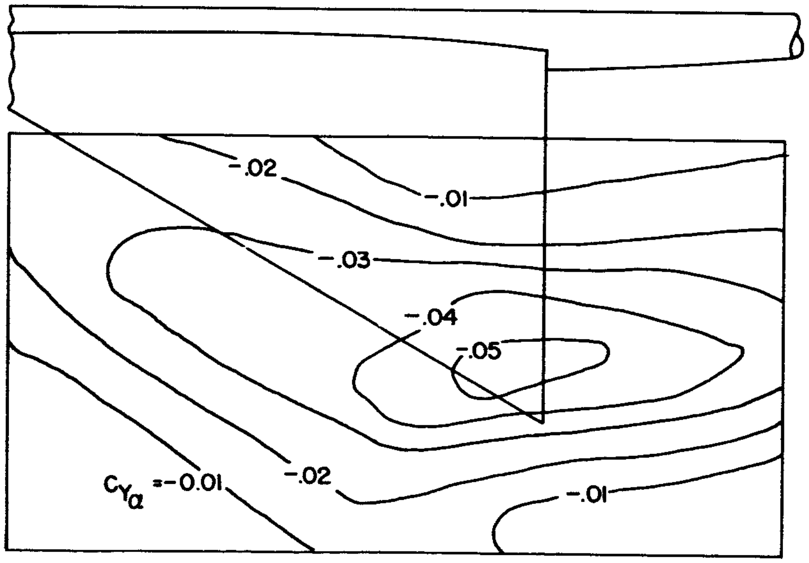

SLOPE OF STORE SIDE-FORCE COEFFICIENT

DELTA WING; M=1.6

Figure 8

[redacted]

EFFECT OF STORE LOCATION AND ANGLE OF ATTACK ON C_Y

DELTA WING ; $M \approx 1.6$

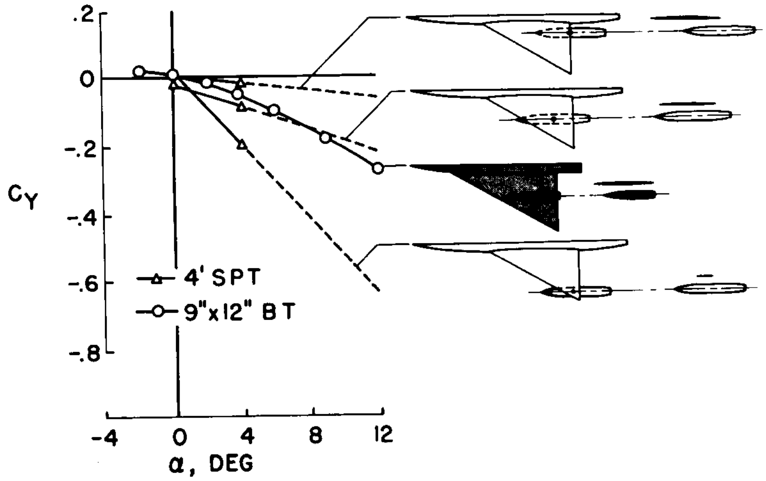

Figure 9

EFFECT OF PYLONS ON C_Y

9" x 12" BT; $M \approx 1.6$

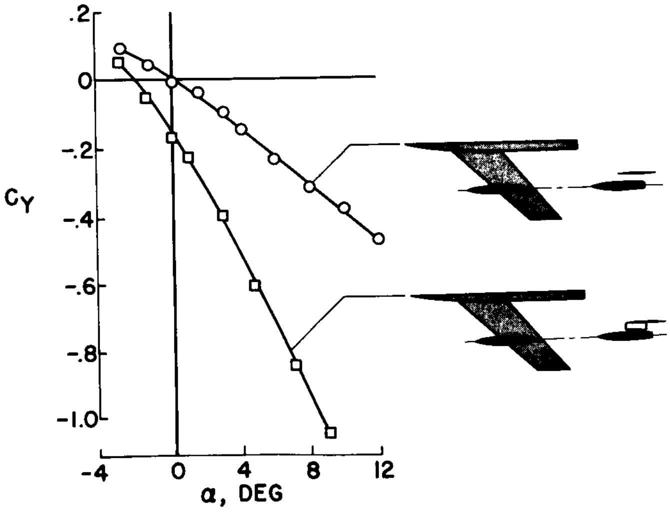

Figure 10

[redacted]

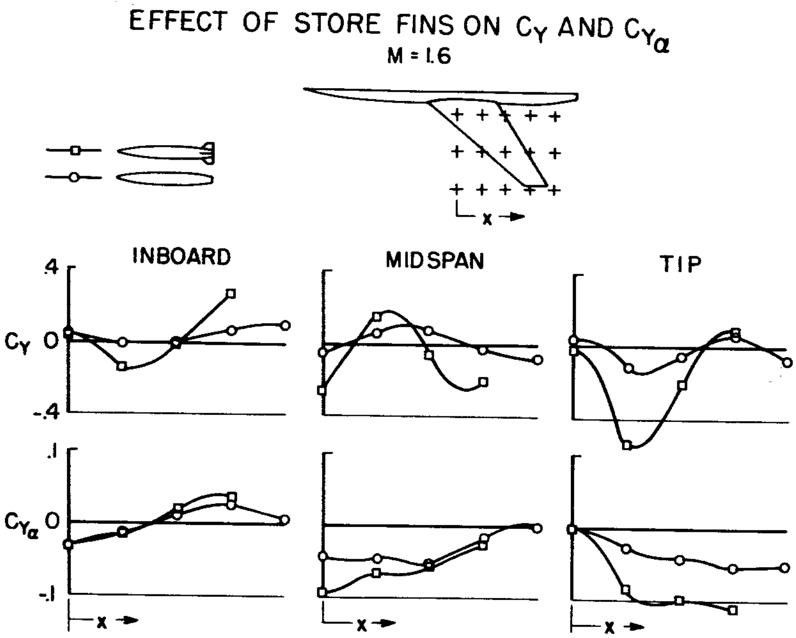
EFFECT OF STORE FINS ON C_Y AND C_{Y_α}
M = 1.6
INBOARD
MIDSPAN
TIP
.4
C_Y 0
-.4
.1
C_{Y_α} 0
-.1
x →
x →
x →
x →

Figure 11.

UNCLASSIFIED [redacted]

AN INVESTIGATION OF JET EFFECTS ON ADJACENT SURFACES

By Walter E. Bressette and Maxime A. Faget

Langley Aeronautical Laboratory

SUMMARY

The steady pressure loads as well as the temperature change on adjacent surfaces due to the presence of a propulsive jet at subsonic speeds is shown to be insignificant. Whereas at supersonic speeds the temperature effect might be expected to remain insignificant, the steady pressure loads were shown to increase greatly on surfaces downstream of the propulsive jet exit.

INTRODUCTION

In the past few years an investigation has taken place in the preflight blowdown tunnel at the Langley Aeronautical Laboratory to determine the jet effects on surfaces located in the near vicinity and downstream of a propulsive jet exit. The purpose of this paper is to supplement information already published at Mach number 2.00 with information obtained at other Mach numbers. The jet effects discussed are the steady pressure loads produced on a flat-plate wing due to the presence of a propulsive jet, the heating of the wing surface by the propulsive jet, and the fluctuating pressure frequency spectra superimposed on the wing steady pressures from the propulsive jet.

SYMBOLS

D_j	diameter of sonic exit
D_{j_*}	diameter of sonic throat
ΔC_N	incremental normal-force coefficient, $\frac{\Delta N_{total}}{qS_{j_*}}$
H_j	total pressure at exit of nacelle
M_o	free-stream Mach number

[redacted]

[redacted]

ΔN	incremental normal force, $(\text{Normal force})_{\text{jet on}} - (\text{Normal force})_{\text{jet off}}$
P	wing pressure coefficient, $\frac{p_w - p_o}{q}$
ΔP	incremental pressure coefficient, $P_{\text{jet on}} - P_{\text{jet off}}$
p_w	wing static pressure
p_o	free-stream static pressure
$\bar{p}$	overall acoustic pressure fluctuations
q	free-stream dynamic pressure
S_{j_*}	area of sonic throat
T_{wing}	static temperature on wing
T_{s_o}	free-stream stagnation temperature
V_e	velocity at the nacelle exit
x	chordwise distance on wing from nacelle exit (downstream positive)
y	spanwise distance on wing from nacelle center line

RESULTS AND DISCUSSION

Presented in figure 1 is a three-dimensional sketch of the test setup showing a small-scale nacelle mounted below a flat-plate wing at the exit of the preflight blowdown tunnel. The general airplane configurations in the figure are the type of airplane configurations that this test setup would apply to. The shaded areas on the configurations are the areas most likely to experience the type of jet effects that are discussed in this paper.

Presented in figure 2 is a side view of the test setup showing the small-scale nacelle, having a 5° boattail angle, mounted at $3.35D_j$ below the flat-plate wing at the exit of the preflight blowdown tunnel. Although more than one vertical position was tested in this investigation,

[redacted]

a vertical position of $3.35D_j$ was selected for this paper in order to correlate the additional data with an exact position that has already been published at a Mach number of 2.00 (ref. 1). The nacelle at this position was tested with two types of exit nozzles, a convergent nozzle called a sonic exit and a convergent-divergent nozzle called a supersonic exit, both having the same size sonic throat.

Figure 3 shows the location from the nacelle exit of 47 static-pressure orifices on the wing as well as the high-frequency pressure pickup and a thermocouple plate with 24 thermocouples that was installed in a similar wing.

The pressure field on the wing with nacelle jet off is presented in figure 4 and shows the nacelle wake which is responsible for the formation in the free-stream flow of a jet-off trailing wake shock wave. In the jet-off operation, the pressure is negative downstream of the nacelle exit because of the presence of the nacelle boattail angle and rises to a positive pressure further downstream because of the intersection on the flat-plate wing of the jet-off trailing wake shock wave.

In figure 5 is presented a typical nacelle jet-on pressure field on the wing showing the propulsive jet issuing from the exit of the nacelle and flowing downstream below the flat-plate wing. In the jet-on operation, a shock wave (called the primary shock wave) forms at the exit of the nacelle, and the impingement on the wing of this shock wave is responsible for the formation of the first positive pressure in the field. This positive pressure gradually falls off in pressure until a second positive pressure rise occurs, which is less intense than the first one. This second positive pressure rise is caused by the intersection on the wing of a second jet-on shock wave (called the secondary shock wave) that is formed in the propulsive jet wake downstream of the nacelle exit.

Presented in figure 6 is the axial pressure distribution downstream of the nacelle exit for both jet on and jet off at the same value of H_j/p_o for M_o of 1.40, 1.80, and 2.00. The first positive pressure rise on the wing with jet on moves farther to the rear of the nacelle exit with an increase in M_o. This effect is the result of decreasing the primary shock-wave angle when M_o is increased at a constant value of H_j/p_o.

Because all pressures on the wing vary with nacelle-exit jet off depending upon the general configuration of the nacelle, the pressure on the wing also varies with the nacelle jet on; but the increment of pressure between jet on and jet off, or the pressure on the wing due to the presence of the propulsive jet, should remain the same. Therefore, all discussion of pressures and loads that follow in this paper will be in the form of incremental pressures and incremental loads.

[redacted]

Shown in figure 7 is the incremental pressure field due to the nacelle jet wake for a sonic exit and a supersonic exit at the same H_j/p_o.

When jet-on and jet-off wing pressure data were combined to form the incremental pressure data, positive incremental pressure resulted immediately behind the intersection on the wing of the primary shock wave. This positive incremental pressure gradually decreased until it became negative in the vicinity of the intersection on the wing of the jet-off trailing wake shock and it remained negative to the end of the wing.

The primary shock-wave angle was lower in angle for the supersonic exit than it was for the sonic exit. Therefore, the positive pressure behind the shock wave as well as the area upon which it acts was reduced.

From an integration of these chordwise incremental pressure profiles, the spanwise incremental wing loading can be obtained. In figure 8 the relative spanwise incremental wing loading is presented for a sonic exit with $H_j/p_o = 6$ for M_o of 1.40, 1.80, and 2.00.

With an increase in M_o, the spanwise distance from the nacelle-exit center line upon which the loads act is decreased. This is a result of decreasing the primary shock-wave angle by increasing M_o. Also shown is a subsonic test made at $M_o = 0.80$ and $H_j/p_o = 3.37$. From this test, slight negative pressures on the wing were obtained. From an integration of the spanwise wing loading, ΔC_N can be obtained.

Figure 9 presents the variation of ΔC_N with H_j/p_o for a nacelle sonic exit at M_o of 1.40, 1.80, 2.00, and 0.80. The value of ΔC_N at a constant value of H_j/p_o in the supersonic range is decreased with an increase in M_o; but with the ΔC_N curves tending to increase with an increase in H_j/p_o and with present-day turbojet engines indicating that a maximum value of H_j/p_o of 5 will be produced at $M_o = 1.40$, of 9 at $M_o = 1.8$, and of 10 at $M_o = 2.00$, then a nearly constant ΔC_N is indicated from this flat-plate-wing analysis for maximum cruising operation.

In figure 10 is presented the variation of ΔC_N with H_j/p_o for a nacelle sonic exit and a nacelle supersonic exit at $M_o = 1.40$. The value of ΔC_N was reduced at all H_j/p_o tested by using a nacelle supersonic exit.

Presented in figure 11 is the variation of the ratio of ΔN to thrust with H_j/p_o for a nacelle sonic exit at all free-stream supersonic Mach numbers tested. As can be seen in the figure there is little difference in the ratio of ΔN to thrust with a decrease in M_o, and a mean lower value of 0.6 was obtained at a nacelle-exit pressure ratio of 7. Although ΔN increased with an increase in H_j/p_o, this figure shows that it did not increase as rapidly as the thrust did.

In figure 12 is presented the axial temperature distribution downstream of the nacelle exit at $M_o = 0.80$ with nacelle jet on and nacelle jet off. The ordinate of the curves is the ratio of the temperature as measured on the wing during steady-state conditions divided by the free-stream stagnation temperature. A nacelle jet temperature of 1,500° F with $H_j/p_o = 4$ was obtained for the jet-on tests by burning hydrogen in air at a low fuel-air ratio. The broken lines show the temperature distribution with nacelle jet off. The solid lines show the temperature distribution with the nacelle jet on at two vertical positions from the wing, the higher one being at $1.7D_j$ from the wing and the lower one being at $3.35D_j$ from the wing. The maximum difference between jet-off temperature and jet-on temperature is less than 10° F indicating very little heating due to the presence of the propulsive jet. It should be noted that the hot exhaust gas in the propulsive jet wake did not penetrate the free-stream flow to the wing surface in a distance of $6D_j$ downstream of the nacelle exit.

Presented in figure 13 is the frequency spectra of $\bar{p}$ that were obtained at a point immediately behind the intersection on the wing of the primary shock wave, whereas H_j/p_o was varied from 7 to 2 at $M_o = 1.80$ for a nacelle sonic exit and a nacelle supersonic exit. These data were preliminary and were obtained with a specially designed pickup using a small-scale nacelle having a sonic throat of 0.72 inch in diameter. These data show that $\bar{p}$ is greater for the supersonic exit than it was for the sonic exit. Also, the range of pressures is essentially in agreement with that obtained by Lassiter and Hubbard (ref. 2), for a sonic jet with no free-stream flow.

CONCLUDING REMARKS

The steady pressure loads as well as the temperature change on adjacent surfaces due to the presence of a propulsive jet at subsonic speeds is shown to be insignificant. Whereas at supersonic speeds the temperature effect might be expected to remain insignificant, the steady pressure loads were shown to increase greatly on surfaces downstream of the propulsive jet exit.

REFERENCES

1. Bressette, Walter E.: Investigation of the Jet Effects on a Flat Surface Downstream of the Exit of a Simulated Turbojet Nacelle at a Free-Stream Mach Number of 2.02. NACA RM L54E05a, 1954.

2. Lassiter, Leslie W., and Hubbard, Harvey H.: The Near Noise Field of Static Jets and Some Model Studies of Devices for Noise Reduction. NACA TN 3187, 1954.

APPLICATION OF JET EFFECTS

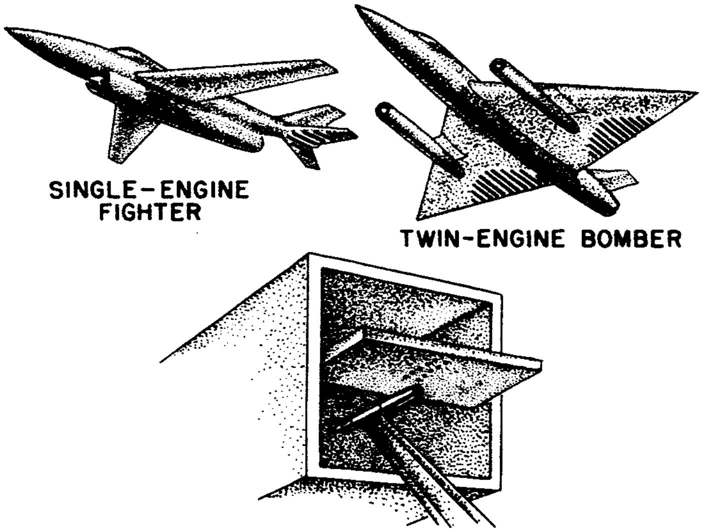

Figure 1

TEST SETUP
(SIDE VIEW)

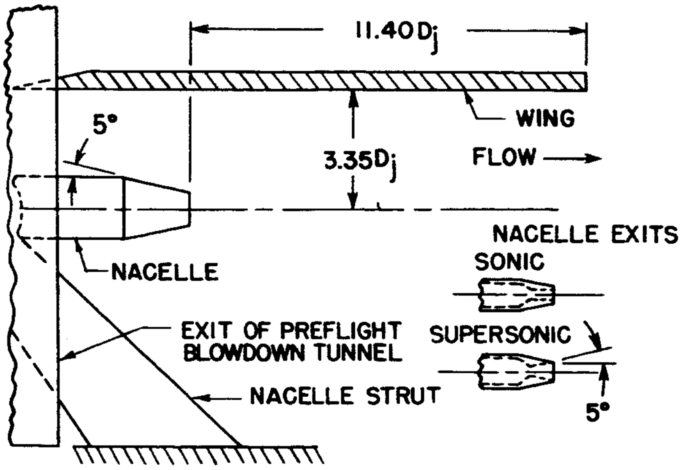

Figure 2

[redacted]

LOCATION OF WING INSTRUMENTATION
(BOTTOM VIEW)

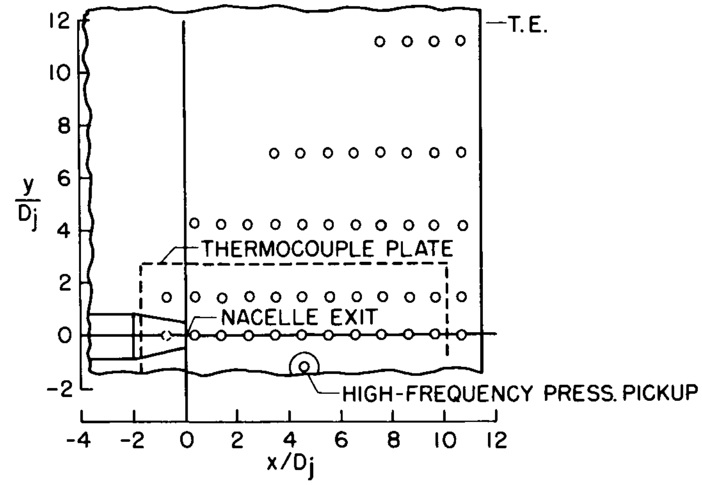

Figure 3

PRESSURE FIELD ON WING WITH JET OFF

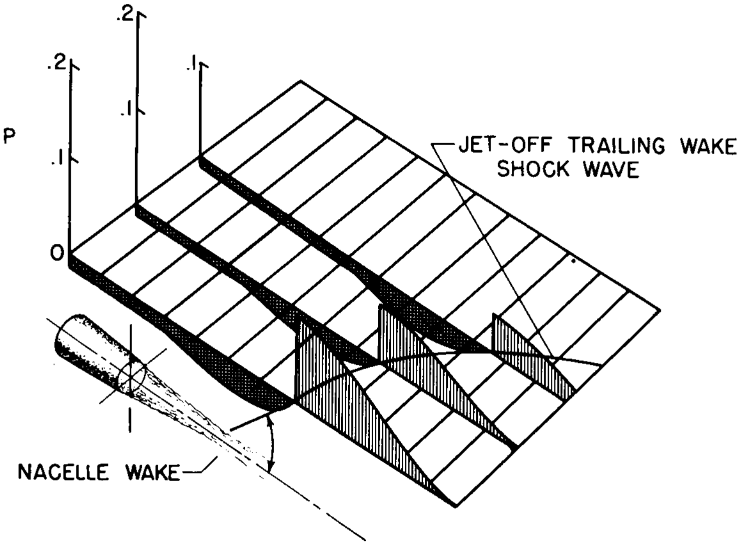

Figure 4

[redacted]

PRESSURE FIELD ON WING WITH JET ON

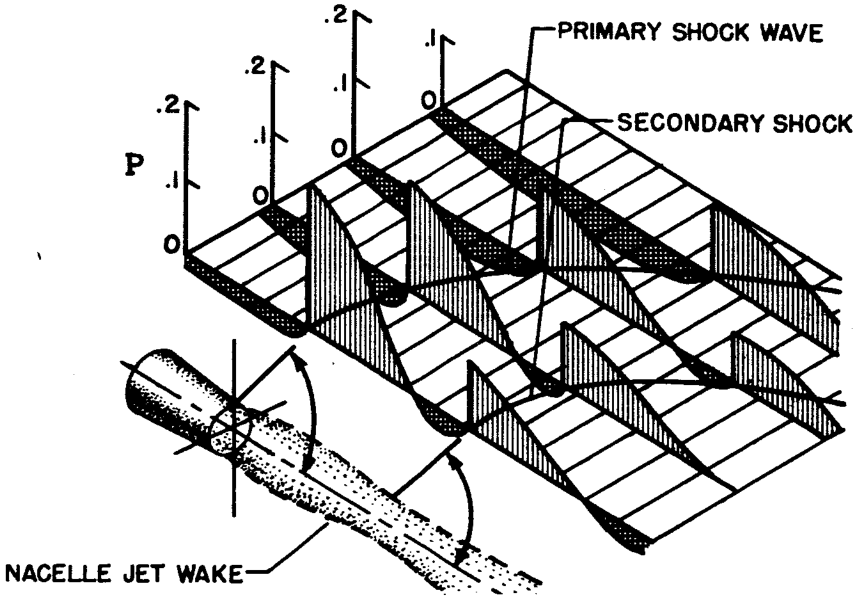

Figure 5

AXIAL PRESSURE DISTRIBUTION DOWNSTREAM OF NACELLE EXIT

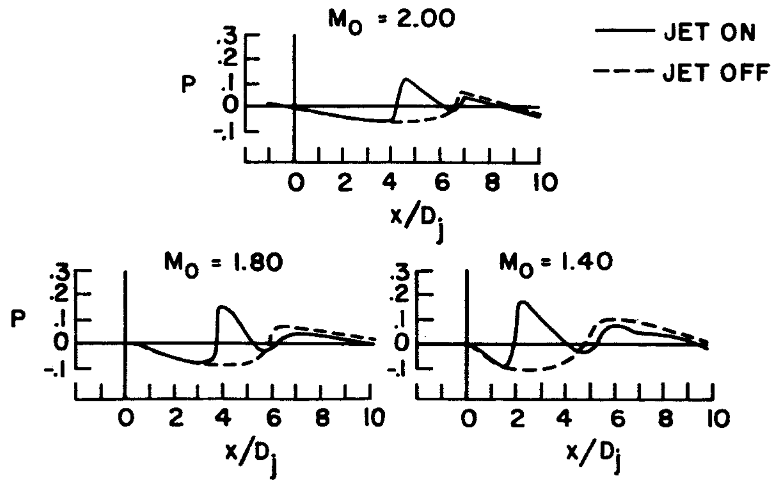

Figure 6

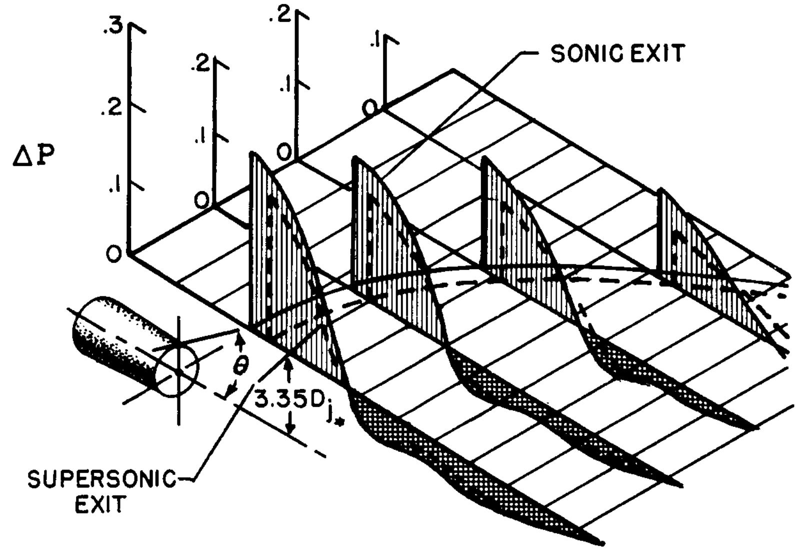
PRESSURE FIELD ON WING DUE TO NACELLE JET WAKE

Figure 7

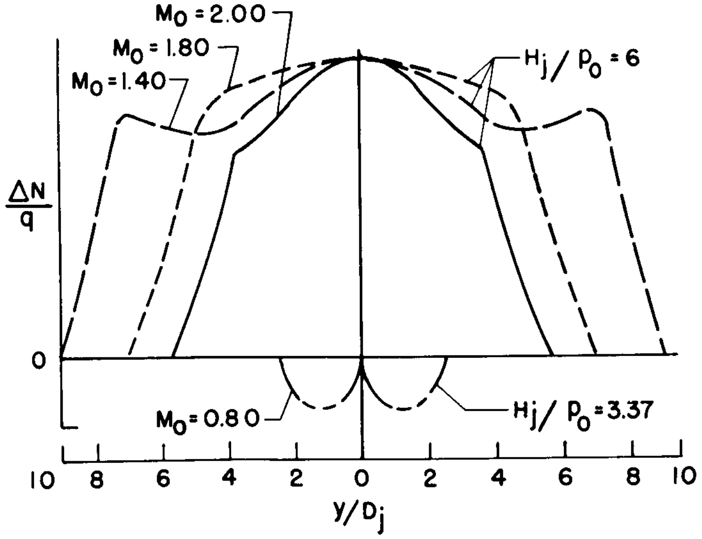
RELATIVE SPANWISE WING LOADING

SONIC EXIT; WING TRAILING EDGE 9 Dj DOWNSTREAM

Figure 8

[redacted]

VARIATION OF NORMAL-FORCE COEFFICIENT
SONIC EXIT; WING TRAILING EDGE $9D_j$ DOWNSTREAM

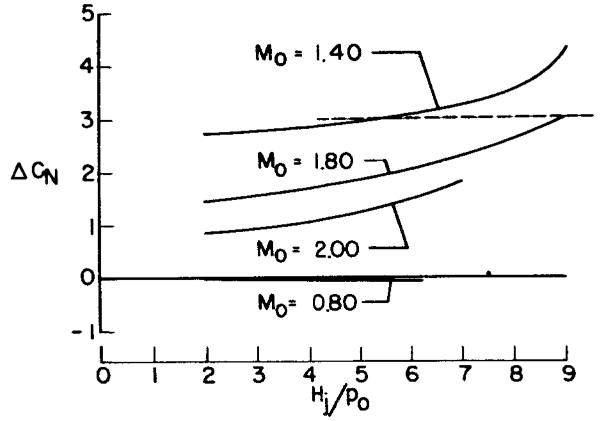

Figure 9

NORMAL-FORCE COEFFICIENT FOR
SONIC AND SUPERSONIC NACELLE EXITS
$M_0 = 1.40$

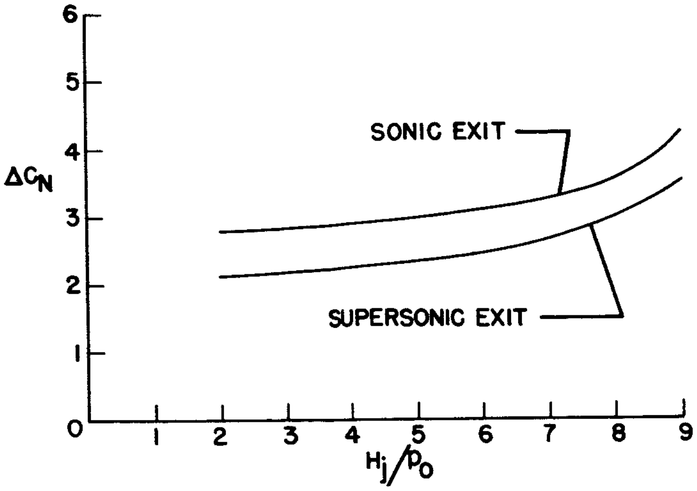

Figure 10

[redacted]

[redacted]

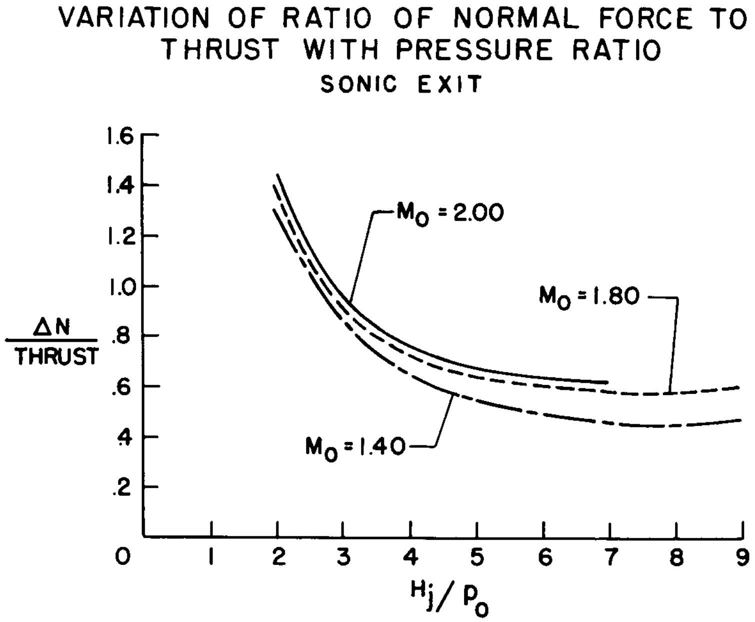

Figure 11

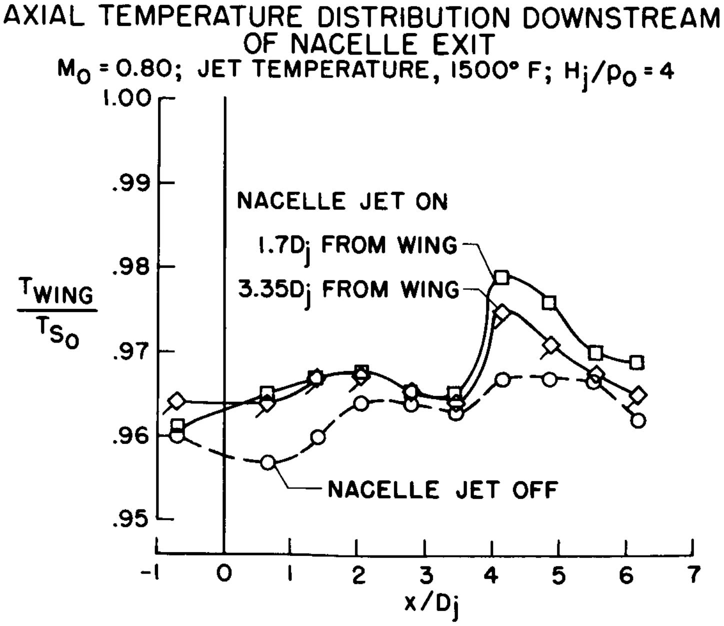

Figure 12

[redacted]

[redacted]

FREQUENCY SPECTRA OF PRESSURE FLUCTUATIONS

$M_0 = 1.8$; 300-CPS-BANDWIDTH FILTER; $(H_j/p_0)_{MAX} = 7$

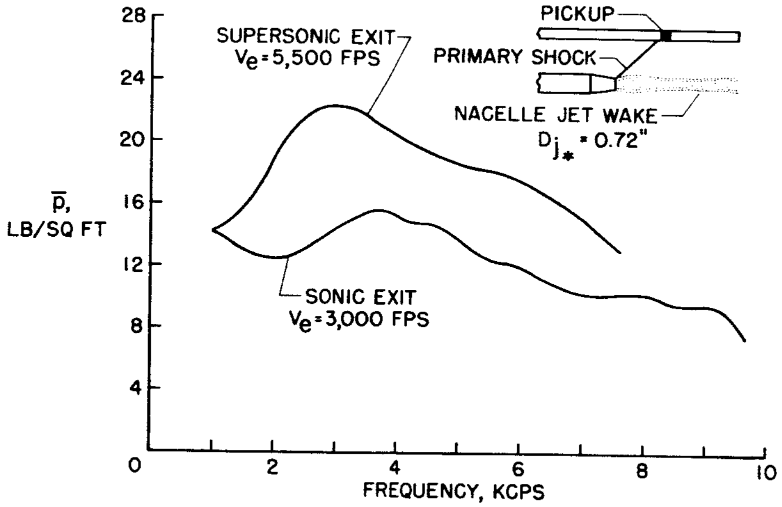

Figure 13

[redacted]

[redacted]

AN INVESTIGATION OF LOADS ON AILERONS AT TRANSONIC SPEEDS

By Jack F. Runckel and W. H. Gray

Langley Aeronautical Laboratory

RUNCKEL & GRAY

SUMMARY

Some aileron load characteristics for three thin wings varying in sweep have been presented for Mach numbers from 0.80 to 1.05. For the transonic Mach number range, shock effects exert a large influence on the loading, but the exact location of each shock for a specific wing design cannot be catalogued at the present time. It is shown, however, that the aileron loading, although greater in magnitude than at subsonic speeds, nevertheless varies in as uniform a fashion as at subsonic speeds.

INTRODUCTION

Limited information obtained from unpublished data for investigations at the Langley Aeronautical Laboratory has indicated that loading on flap-type controls may change in a nonuniform fashion in the transonic range. The purpose of this paper is to present a few loading characteristics of typical wing-aileron configurations which have recently been obtained in the Langley 16-foot transonic tunnel.

SYMBOLS

A	aspect ratio
b	wing or aileron span
c	wing chord
$\bar{c}$	average aileron chord
C_N	aileron normal-force coefficient
c_r	root chord

[redacted]

M	Mach number
N	normal force
P	pressure coefficient
x/c	fraction of wing chord
$x/\bar{c}$	fraction of aileron average chord
y/b	fraction of aileron span
α	angle of attack
δ	aileron deflection
Λ	angle of sweepback
λ	taper ratio

DESCRIPTION OF MODELS

The plan forms of the configurations tested are shown in figure 1. Three wing-body combinations having unbalanced ailerons were investigated: a 4-percent-thick unswept wing, a 4-percent-thick swept wing, and a 3-percent-thick triangular wing. The unswept wing had outboard ailerons extending over 40 percent of the wing semispan with a chord of 25 percent of the wing chord. The swept wing had centrally located ailerons also extending over 40 percent of the semispan with the aileron chord 30 percent of the wing chord. The triangular wing had an outboard aileron of 37 percent semispan extent with a constant chord of 10 percent of the wing root chord. Other characteristics of the configuration, including the location of the inboard end of each aileron, are noted in figure 1. Loads information on the ailerons of the unswept and swept wings was obtained from two-component strain-gage balances located inside the wings. Pressure-distribution measurements were, however, also obtained for the undeflected-aileron case for the entire chord at each of three spanwise stations on the unswept wing and six spanwise stations on the swept wing. The loading on the triangular-wing aileron was determined from pressure-distribution measurements at two spanwise stations over the aileron out of the six available stations over the wing.

DISCUSSION

Because shock formations occur at transonic speeds, it was reasonable to expect that the formation and movement of the shocks would introduce nonlinearities in control loads. The most predominant shocks for the three representative wings with undeflected controls are illustrated in figure 2 for what may be characterized as the Mach numbers for which the shocks would be expected to exert the greatest influence over the control area. The observations which follow would necessarily be modified somewhat for deflected flaps.

The flow-field shock is a normal shock and its rapid axial movement across and off the wing with increasing angle of attack at a given Mach number is responsible for a change in the pressure-distribution shape from triangular to generally rectangular which will be shown to cause some nonlinearities in loading characteristics. Examples of typical pressure-distribution changes are illustrated in figure 2.

At moderate and high angles of attack the wing leading-edge and trailing-edge shocks develop, but as they are relatively weak in the case of thin wings and are restricted in movement to portions of the wing, one would not expect them to cause severe loading changes. These latter shocks may, however, induce high fluctuating loads and further studies are being made of this aspect. Although there are similarities in the shock patterns in the transonic range between different wing designs, the exact location of each shock for a specific wing is unpredictable at the present time.

Typical effects of Mach number and deflection on the aileron loading characteristics of the three representative wings will now be discussed.

Several loading variations obtained on the aileron of the unswept wing are shown in figure 3. Aileron normal-force coefficient is plotted against angle of attack for three nominal control deflections, -10°, 0°, and 10°. The characteristics at a Mach number of 0.8 which is representative of the high subsonic speed variation are shown with the broken lines, and the variation at a Mach number of 0.94 which is typical of the transonic range is indicated by the solid line.

At a Mach number of 0.80 the aileron is ineffective in developing normal-force load with change in angle of attack up to angles of about 8° which represents the approximate maximum lift for the wing at this Mach number. Above 8° the loading over the control changes from triangular to trapezoidal in shape and the loading increases with angle of attack.

At a Mach number of 0.94 the aileron becomes effective in producing increased loading with angle-of-attack change at much lower angles and the increase in load is generally greater than at the lower Mach numbers.

[redacted]

The rate of increase in loading at low angles of attack contrasted with high angles of attack is directly related to the change in pressure distribution from triangular to rectangular (fig. 2) which in turn is influenced by the shock pattern. At transonic Mach numbers from 0.92 to 1.05, the values of aileron normal-force coefficient lie very close to those shown for 0.94 Mach number.

For the test speed range, which was from a Mach number of 0.70 to 1.05, the spread in magnitude of load carried at the positive and negative aileron deflections remains approximately constant with angle-of-attack change.

Figure 4 shows similar information obtained with the 45° swept-wing aileron. The nominal control deflections are now 15° and -15° instead of 10°. Again the Mach numbers illustrated are 0.8 and 0.94. Here again the data shown for a Mach number of 0.94 is typical of the results obtained at Mach numbers from 0.92 to 1.05.

There are several differences between this aileron and the unswept-wing aileron. In the first place, the effect of Mach number on the load carried by the aileron (compare the values of load coefficient at 12° angle of attack) is not as great as that on the unswept-wing aileron. Secondly, the spread in magnitude of load for positive and negative deflections does not remain constant with angle of attack for the swept wing. It may also be noted that the swept wing with 15° aileron deflection carried about the same unit load at the lower angles of attack as the unswept-wing aileron with 10° deflection (fig. 3).

The loading characteristics of the outboard aileron on the triangular wing are shown in figure 5. The aileron load variations with angle of attack at Mach numbers of 0.80 and 0.98 are presented for nominal control deflections of 0°, 15°, and -15°.

Several predominant characteristics of this control should be noted. The magnitude of the unit load carried by the triangular-wing aileron for the same control deflections is generally greater than that of the swept-wing aileron; the transonic variation in aileron loading with angle of attack is more uniform than at high subsonic speeds; the effect of Mach number on the load carried by the aileron is greater at zero and positive deflections than at negative control deflections.

Some variation of aileron center-of-load location with Mach number for the three ailerons tested is shown in figure 6. Chordwise center of load referenced to the average chord of the aileron $\bar{c}$ and spanwise center of load referenced to the span of the aileron b are plotted on the vertical scales with Mach number on the horizontal axis. The center-of-load locations for approximately comparable deflections for the three controls are illustrated in this figure. An attempt has been made to indicate typical locations of center-of-load travel for constant angles of attack and varying control deflection, and constant control deflection with changing angle of attack. The center-of-load locations may, however, vary over greater limits than those shown in the case where the load or moments approach zero.

The chordwise center-of-load location of the unswept-wing aileron generally remains between the 20- and 50-percent-aileron-chord locations through most of the angle-of-attack range for all control deflections tested. The spanwise center-of-load location is near the midspan of the aileron.

The chordwise center-of-load travel of the swept-wing aileron is somewhat greater than that for the unswept-wing aileron, generally extending from the 20- to 60-percent-chord points for the deflections tested. Again the spanwise center of load remains at about the center of the aileron.

The chordwise center-of-load location on the aileron of the triangular wing also generally lies between the 20- and 60-percent-chord stations and the spanwise location is usually somewhat more inboard than for the other two ailerons, being near the 45-percent-span station of the aileron.

CONCLUDING REMARKS

Some aileron load characteristics for three thin wings varying in sweep have been presented for Mach numbers from 0.80 to 1.05. For the transonic Mach number range, shock effects exert a large influence on the loading, but the exact location of each shock for a specific wing design cannot be catalogued at the present time. It is shown, however, that the aileron loading, although greater in magnitude than at subsonic speeds, nevertheless varies in as uniform a fashion as at subsonic speeds.

[redacted]

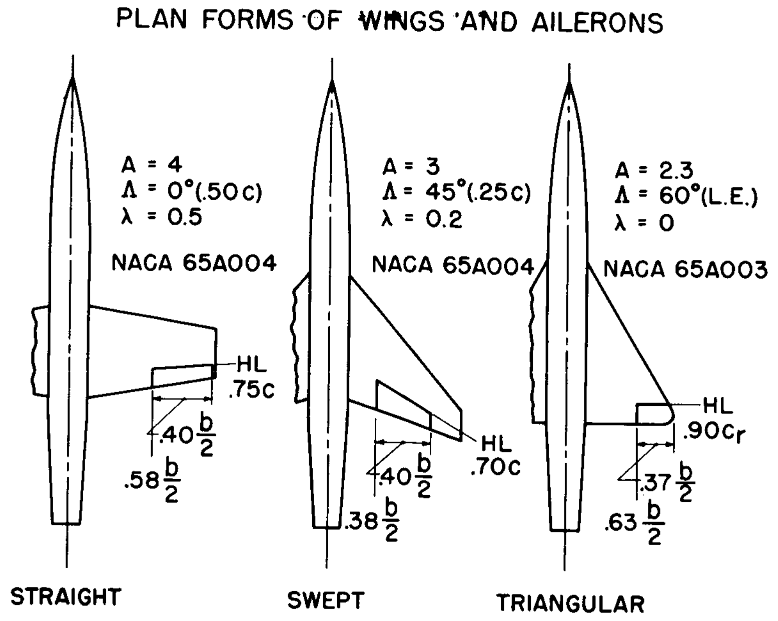

Figure 1

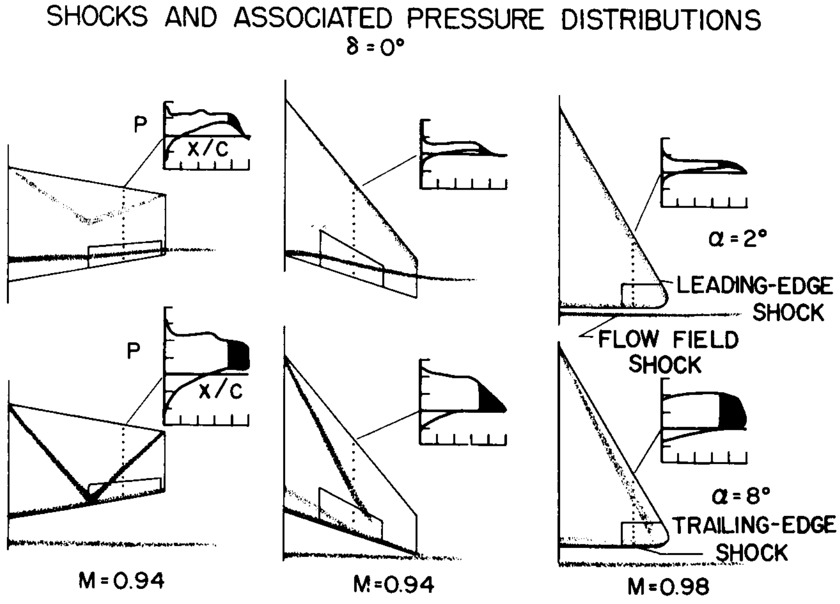

Figure 2

[redacted]

[redacted]

[redacted]

AILERON NORMAL-FORCE COEFFICIENT CHANGE WITH α
UNSWEPT WING

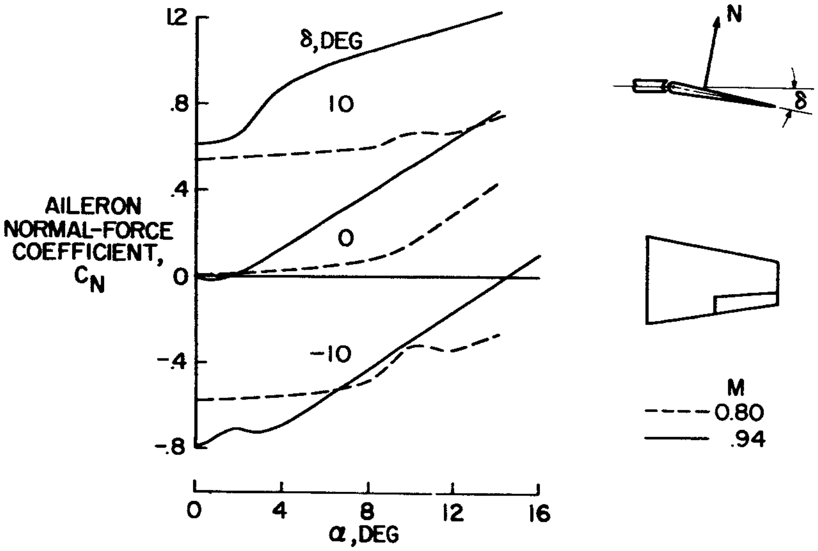

Figure 3

AILERON NORMAL-FORCE COEFFICIENT CHANGE WITH α
SWEPT WING

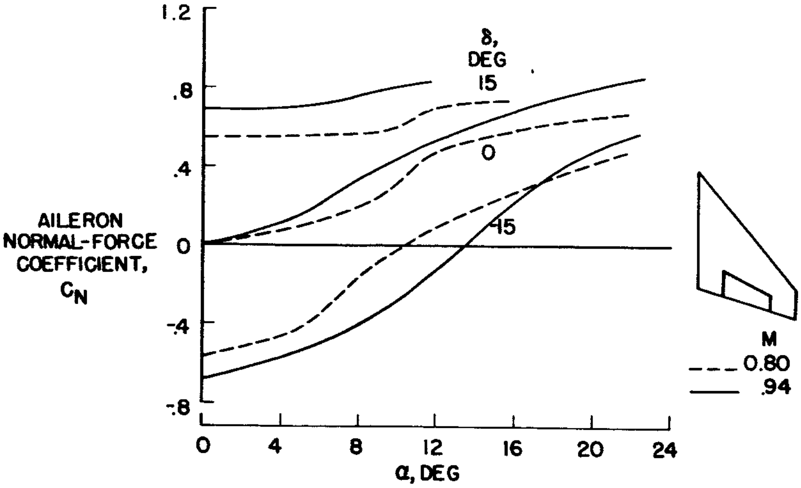

Figure 4

[redacted]

[redacted]

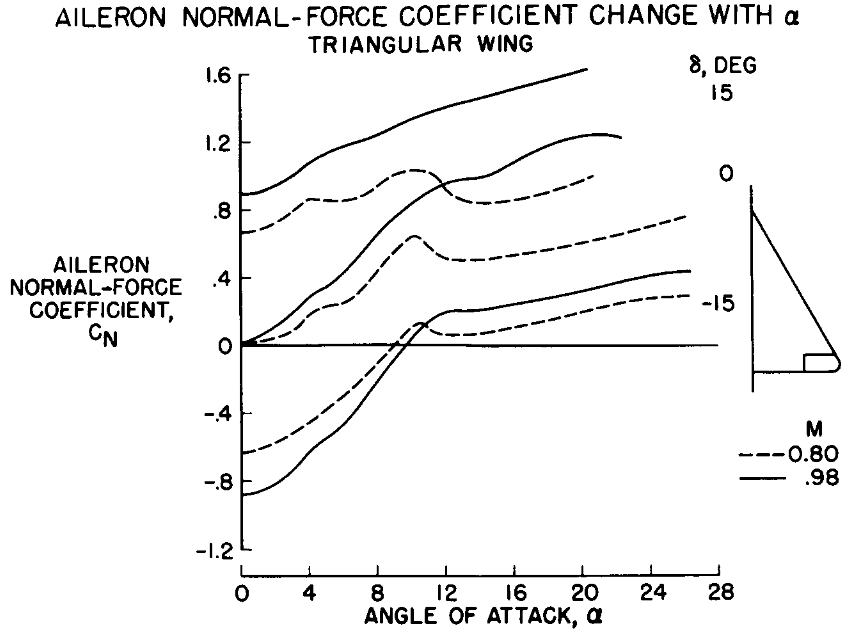

Figure 5

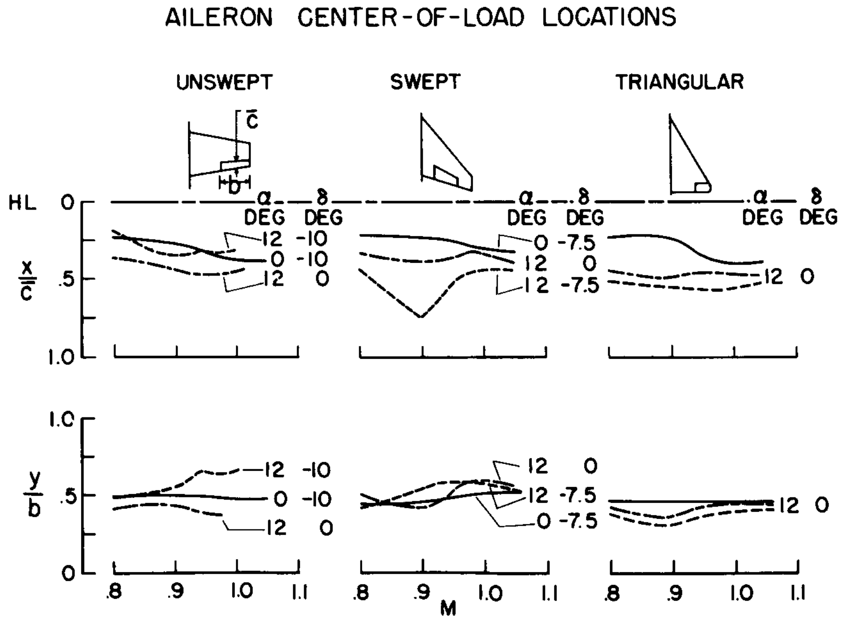

Figure 6

[redacted]

[redacted]

SIMPLIFIED PROCEDURES FOR ESTIMATING FLAP-CONTROL LOADS AT SUPERSONIC SPEEDS

By K. R. Czarnecki and Douglas R. Lord

Langley Aeronautical Laboratory

SUMMARY

An investigation has been made to determine the possibility of using simplified procedures for the estimation of control loads at supersonic speeds. The results of the investigation indicate that relatively simple procedures are possible for the estimation of loadings on flap-type controls at supersonic speeds for the case where no flow separation occurs ahead of the hinge line. For tip-type controls, the simplified procedures have been tested only in a few cases and need further development. For controls with swept hinge lines, experimental data are lacking, but it is anticipated that the procedures developed for the unswept hinge-line controls will apply provided that there is no flow separation at the hinge line or that the sweep angle is not too large. In general, the loadings predicted by the simplified procedures are in better agreement with experiment than is unmodified three-dimensional linear theory.

INTRODUCTION

The estimation of control loads at supersonic speeds from linear theory or other available techniques has proved to be rather complicated and tedious. In particular, there is a need for rapid methods of predicting control loads with reasonable accuracy for preliminary design. The objective of this paper is to present such a technique. Of course, it should be stressed that simplicity is often achieved only at a sacrifice in ultimate accuracy. Another restriction that has been imposed in this paper is that the boundary layer on the wing is turbulent.

CZARNECKI & LORD

SYMBOLS

b	wing span
c	local chord
p	static pressure

[redacted]

P	pressure coefficient, $\frac{p_l - p}{q}$
q	dynamic pressure
M	free-stream Mach number
y	spanwise distance
α	angle of attack, deg
δ	control deflection, deg
Δc_{n_f}	increment in section normal force on control
Δc_{n_w}	increment in section normal force on wing plus control
Δc_{m_f}	increment in section pitching moment due to load on control
Δc_{m_w}	increment in section pitching moment due to load on wing plus control
K	constant

Subscripts:

l	local
1	ahead of control hinge line
2	behind control hinge line
av	average
cr	critical

TRAILING-EDGE CONTROLS

Basic Flow Types

In figures 1 and 2 are depicted two basic types of flow over a flap-type control. Figure 1 shows a flow that adheres closely to the airfoil surface. This type of flow occurs only at relatively low angles of attack and control deflection. Some theoretical and experimental chordwise pressure distributions characterized by this type of flow are indicated in the lower part of figure 1. These results were obtained at a Mach number of 1.61 on an essentially two-dimensional station on a trapezoidal wing having a hexagonal section. The symbol P denotes the usual pressure coefficient and x/c, the chordwise station in terms of the local chord. The agreement between linear theory and experiment is seen to be good except that experimentally the flow does not expand as much around the corner just ahead of the control hinge line as is indicated by theory and the load over the control is only about 70 percent of the theoretical load.

The sketch in the upper part of figure 2 illustrates conditions where the flow is separated up to the hinge line on the control low-pressure surface and on the main wing ahead of the hinge line on the side of the control high-pressure surface. Separated flows such as these occur when the angles of attack and control deflection are large enough to produce very strong shocks at the control trailing edge or hinge line. These strong shocks cause the boundary layer on the wing or control to separate. The plot in the lower part of figure 2 shows the corresponding pressure distributions. Obviously, the agreement between theory and experiment is not good; on the control upper surface, theory even indicates a pressure lower than absolute vacuum.

In this paper it is impossible to discuss thoroughly all the types of flow illustrated in figures 1 and 2. Experience has shown, however, that separation from the control low-pressure surface occurs first, is generally restricted to the control itself, and has a relatively small effect on the control aerodynamic characteristics. The chordwise pressure distribution in such a separated-flow region is usually uniform as indicated for the control upper surface in figure 2. Thus, for conditions where flow separation does not occur ahead of the hinge line, the control chordwise loadings closely resemble the uniform loading shown for an unseparated-flow condition in figure 1 even though the loading may be asymmetrical between the upper and lower surfaces. In this paper the discussion of flap-type controls will be limited to conditions where flow separation may be present on the control itself but does not occur ahead of the control on the main wing.

Method of Approach

As was mentioned previously, within the limitations just described the control chordwise loadings resemble the one shown in figure 1. The crux of the situation lies in this uniform loading; for if this loading is always a constant percentage of the theoretical value, the loading per unit degree of angle of attack or control deflection can be readily estimated from simple two-dimensional considerations by taking the proper proportion of the linear theory loading given by $4/\sqrt{M^2 - 1}$. This ratio of experimental to theoretical loading is defined as K and, as indicated by the results in figure 1, is equal to about 0.7. Thus, if it can be shown that effects of α and δ can be considered independently of one another, that the span loading is uniform, and that the constant K always remains about 0.7, then a simple procedure for estimating control span loadings becomes available. Before proceeding with these discussions, however, it is desirable first to indicate the manner in which the limiting-flow conditions can be determined and the effect of Mach number.

Flow-Separation Parameters

In figure 3 are presented two criteria to aid in determining the limiting conditions of flow separation ahead of the control hinge line. At present, it is not known which is the better criterion. In figure 3 on the left, $(p_1/p_2)_{cr}$ relates the static pressures ahead of and behind the hinge line for the initial appearance of separation. In figure 3 on the right $\left(\frac{p_2 - p_1}{q_1}\right)_{cr}$ describes the pressure rise in terms of the local dynamic pressure ahead of the shock required for flow separation. The local flow Mach number ahead of the control surface is M_1. The experimental data are from control tests on a trapezoidal wing at $M = 1.61$ and 2.01. The data are compared with the results compiled by Bogdonoff and Kepler (ref. 1) and by Lange (ref. 2). Agreement is only fair in both cases. It is suggested that an average value indicated by the present experimental results be used to determine the limiting control angle. In general, for the usual type of control configuration with sharp trailing edge, the limiting δ will tend to approach 20°. For controls with thickened trailing edges and for controls operating at free-stream Mach numbers at or below 1.6 at fairly high angles of attack, where the local Mach number becomes low and shock detachment becomes imminent for small pressure-rise ratios as indicated by the plots in figure 3, the limiting angles decrease.

Effect of Mach Number

Figure 4 shows the effect of Mach number on the chordwise pressure distributions. The sketch at the top of figure 4 indicates that the data were obtained on an essentially two-dimensional station on a trapezoidal wing at Mach numbers of 1.61 and 2.01. The ordinate is the normalized pressure coefficient and x/c, the station in terms of the local wing chord. Two angle-of-attack and control-deflection conditions, as

[redacted]

indicated, are shown. The results for the two test Mach numbers are seen to be in very good agreement despite the fact that flow separation has already occurred ahead of the control at $M = 1.61$ on the side of the control high-pressure surface (indicated by the square and diamond symbols) and the control angle therefore is somewhat beyond the limit previously described. On the basis of other results it appears that this type of correlation should be possible to considerably higher Mach numbers than indicated here, perhaps to $M = 3.5$ or 4.0.

Spanwise Loadings

The use of the previously suggested uniform-loading procedure in determining the span-load distributions for a full-span flap-type control is illustrated in figure 5 for a Mach number of 1.61. The control is denoted by the shaded area in the sketch in the upper part of the figure. The wing shown, incidentally, has 23° sweep at the leading edge, and thus the control is influenced by conical flow across nearly the entire span. In the plot on the left of figure 5 are presented the section normal-force parameters for the load on the control due to α against the semispan distance parameter $\frac{y}{b/2}$. On the right-hand side of figure 5 are shown the section normal-force parameters for the load on the control due to δ. The dashed lines indicate span loadings computed from linear theory. The experimental points in the plot on the left-hand side of the figure cover a range of α from 0° to 15°, whereas the experimental points in the plot on the right-hand side cover a δ range from -20° to 20°. The solid lines represent the span loadings obtained by assuming a uniform loading both chordwise and spanwise with a point value of $0.7 \times 4/\sqrt{M^2 - 1}$ for both the angle-of-attack and control-deflection cases. A comparison of the results indicates that the experimental spanwise loadings are in good agreement with the span loadings computed simply on the basis of uniform loading and the aforementioned point-loading parameter. The agreement is considerably better than that between experiment and the unmodified linear theory. It should also be noted that the effects of the wing tip and control tip were relatively small and can be neglected to a first order. For the case of uniform loading the center of pressure for the complete control is predicted to be at the control center of area; the experimental spanwise center-of-pressure results are in good agreement with this prediction.

Figure 6 shows the application of the simplified technique for estimating span loadings to a partial-span control. The control is indicated by the sketch at the top of figure 6. Ordinates and abscissas are as in figure 5 except that the incremental wing-span loading parameter is used to show the effects of control deflection on wing carryover. The flap

[redacted]

section normal force is equal to the wing section normal force within the span covered by the control when there is no flow separation ahead of the hinge line, as is the case here. Linear theory, uniform loading calculations, and experimental results are indicated by dashed lines, solid lines, and experimental points, respectively. The agreement between the uniform-loading span-load distribution and experiment is seen to be again considerably better than that between unmodified linear theory and experiment. The experimental spanwise center of pressure for the control is also very close to the center of control area as predicted by uniform-loading calculations.

Figure 7 has been prepared to illustrate how closely the spanwise distribution of chordwise pitching moment due to the loads on the control can be predicted. These results are for the same control configuration shown in figure 6. The same line and symbol code applied except that the ordinates in this figure are the increments in section wing pitching moments contributed by the flap from the loading due to α or δ. The moments are taken about the center of the mean aerodynamic chord or about the 0.564 root-chord station, as indicated in the sketch. Again, the simple uniform load predictions are in good agreement with experiment; thus, the experimental chordwise loadings are uniform and the experimental control longitudinal center of pressure is near the center of control area.

For controls operating in a strongly conical flow field, such as on a highly swept delta wing, the problem of estimating the spanwise control loading due to α becomes more complex and the procedure must be modified. This condition is shown in figure 8 for a full-span flap-type control on a 60° delta wing at a Mach number of 1.61. For the loading due to control deflection, the uniform-loading procedure presented in previous figures still applies. The loading on the control due to α, however, increases across the span to a peak at about the 87-percent semispan station. Inasmuch as the form of this loading is dependent upon the relationship between the Mach line from the wing apex and the wing leading edge and must be preserved, the following technique was evolved. The chordwise loading at any spanwise station is assumed to be constant and equal to the three-dimensional linear-theory value at the flap midchord point multiplied by $K = 0.7$. The spanwise variation in loading is thus introduced by the spanwise variation in the midchord point loading.

The agreement between these constant-chord-load calculations and experiment is good. Although the data are not shown, the agreement between the calculated spanwise variation of pitching moment and experimental results is equally good.

The exact region where the uniform-loading procedure should give way to this modified procedure is difficult to define because of the gradual transition from one type of loading to the other. In general, however, the modified procedure should be used when the Mach line from the wing apex begins to approach the wing leading edge and the edge tends to become sonic or subsonic.

TIP CONTROLS

Basic Problems

The problem of estimating loadings on tip controls is considerably more complex than that of the flap-type control and the simplified methods of estimating the loadings have not been as fully developed. Although tip-control configurations generally are not afflicted with hinge-line separation, they are affected by additional variables such as leading-edge separation and shock detachment and are considerably more sensitive to control section and wing-control parting-line effects. Consequently, the chordwise loadings can change rapidly with changes in any one of these variables and the loading often has no resemblance to that predicted by linear theory. It appears, however, that, despite all these complications, it may eventually be possible to develop a relatively simple procedure for estimating the loadings on at least certain types of tip controls.

Typical Spanwise Loading

Figure 9 shows the results of some such simple calculations for a half-delta tip control. The control is depicted by the shaded area in the sketch of the wing. The ordinate is the section pitching moment due to α or δ taken about the middle of the mean aerodynamic chord or the 2/3 station of the root chord. Linear theory is indicated by the dashed lines and the uniform loading predictions by the solid line. The first thing to notice is that a K-factor of 0.70 no longer always guarantees good agreement between the uniform-loading calculations and experiment, as exemplified by the control-deflection case. In order to overcome this deficiency, the constant K was modified to give a good fit between calculated and experimental section normal-force parameters, which are not shown here. The resultant values of K were 0.85 for the loading due to α and only 0.44 for the loading due to δ. This large decrease for the control-deflection case is to be expected because of the strongly three-dimensional flow over a very low-aspect-ratio shape. The calculated section pitching-moment parameters for these modified values of K are in fair agreement with experiment for the loading due to δ but tend to be somewhat high for the loading due to α. Better agreement as regards both magnitude and shapes of the curves can be obtained in the latter case by assuming a trapezoidal rather than uniform chordwise loading.

The assumption of uniform spanwise pressure appears to be reasonably adequate, as does the assumption of no wing carryover of the control load due to δ.

At present, these simplified procedures for estimating loads on tip controls have been applied to only a limited number of cases. Indications are that the value of K may be dependent upon control configuration and Mach number. Obviously, further analysis of available data must be made before final recommendations can be given.

CONTROLS WITH SWEPT HINGE LINES

At present, there is a lack of experimental data on which to develop simple procedures for estimating loadings on controls with swept hinge lines. On the basis of available knowledge, however, it may be anticipated that the procedures described previously should apply provided there is no hinge-line separation, the sweep angle is not too high, and the normal component of the velocity at the hinge line is used.

CONCLUDING REMARKS

In conclusion, it may be stated that simplified procedures have been developed for the estimation of control loadings on flap-type controls at supersonic speeds for the case where no flow separation occurs ahead of the hinge line. For tip-type controls, the simplified procedures have been tested only in a few cases and need further development. For controls with swept hinge lines, experimental data are lacking, but it is anticipated that the procedures developed for the unswept hinge-line controls will apply provided that there is no flow separation at the hinge line or the sweep angle is not too large. It might also be mentioned that, in general, the loadings predicted by the simplified procedures are in better agreement with experiment than the unmodified three-dimensional linear theory is.

REFERENCES

1. Bogdonoff, Seymour M., and Kepler, C. Edward: The Separation of a Supersonic Turbulent Boundary Layer. Preprint No. 441, S.M.F. Fund Paper, Inst. Aero, Sci., Jan. 25-29, 1954.

2. Lange, Roy H.: Present Status of Information Relative to the Prediction of Shock-Induced Boundary-Layer Separation. NACA TN 3065, 1954.

[redacted]

[redacted]

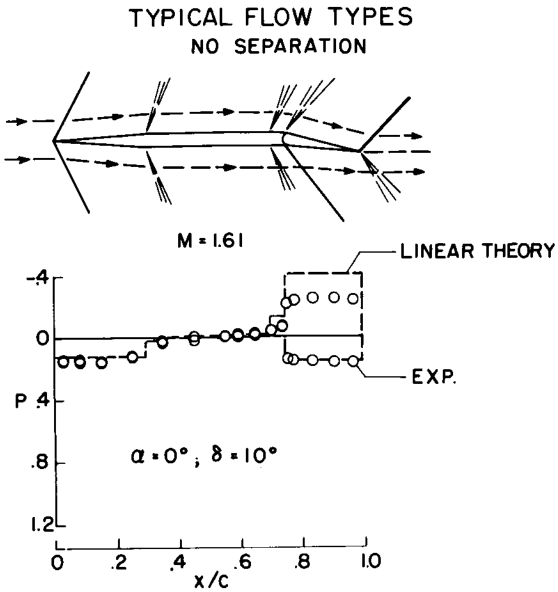

Figure 1

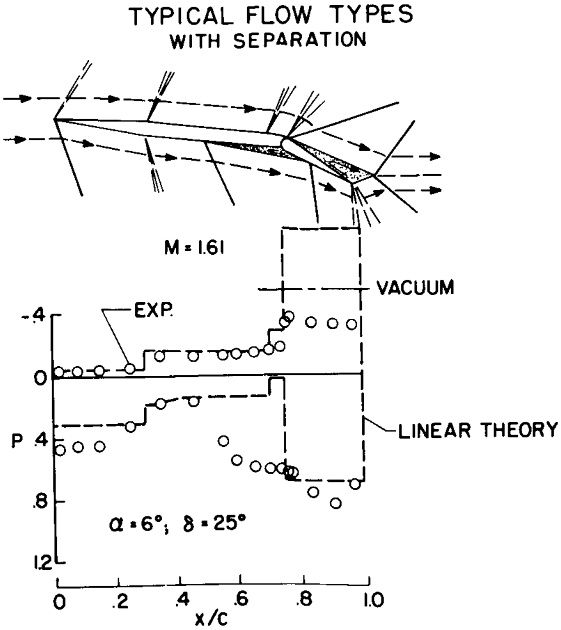

Figure 2

[redacted]

[redacted]

[redacted]

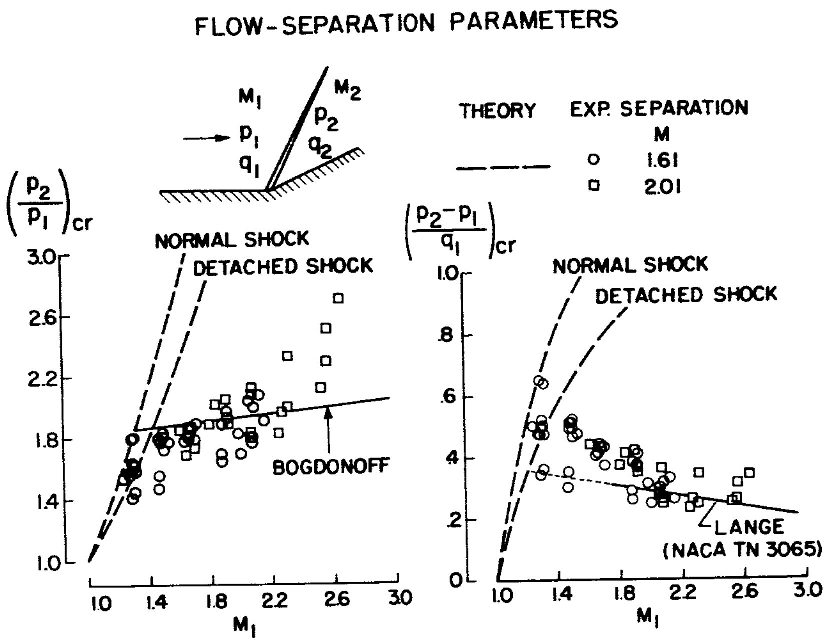

Figure 3

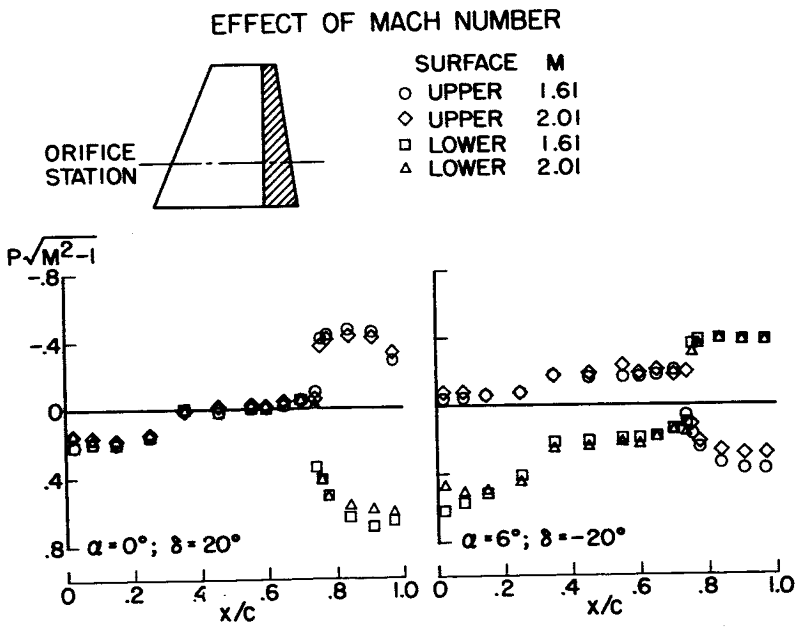

Figure 4

[redacted]

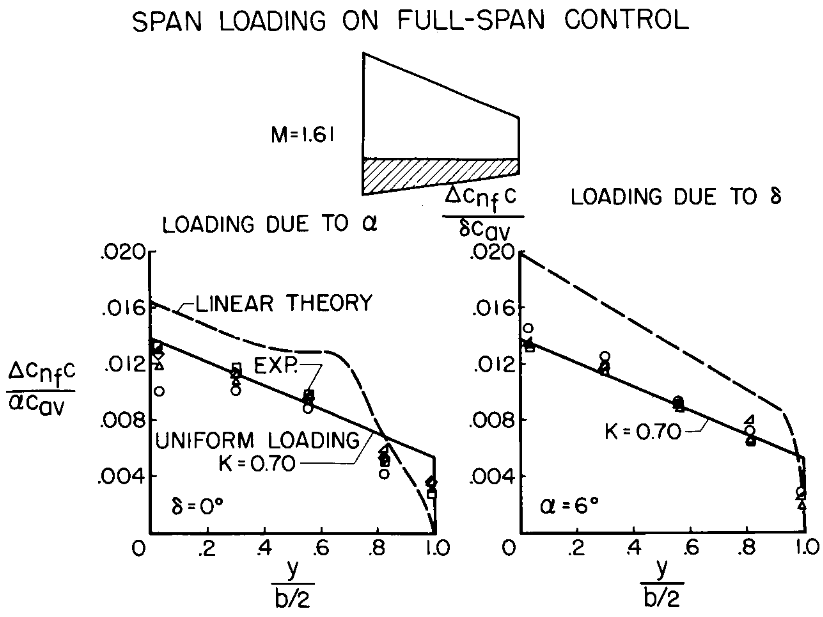

Figure 5

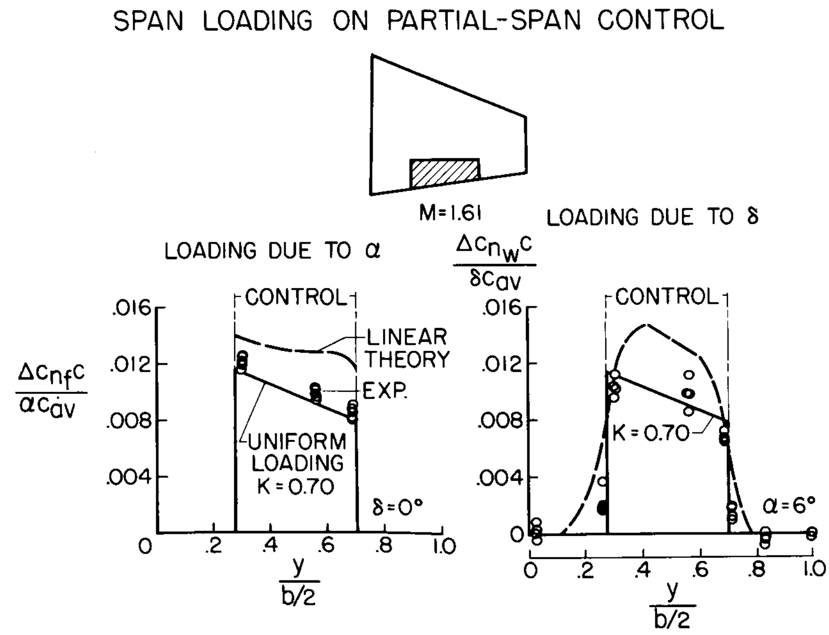

Figure 6

[redacted]

[redacted]

PITCHING-MOMENT DISTRIBUTION ON PARTIAL-SPAN CONTROL

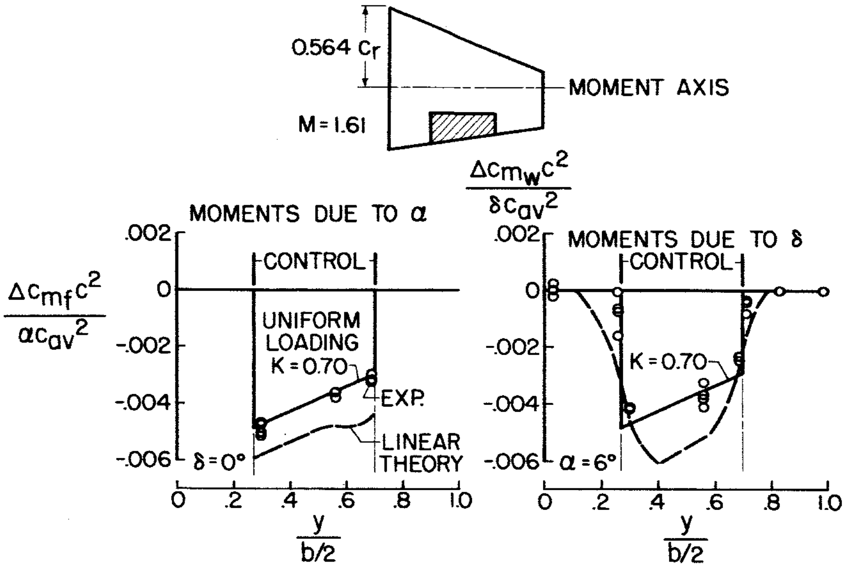

Figure 7

EFFECT OF LARGE SWEEP ON SPAN LOADING

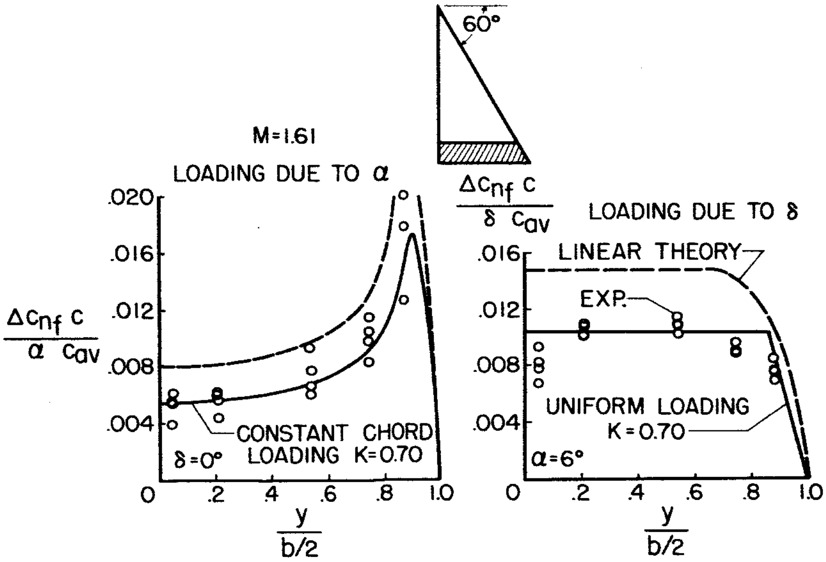

Figure 8

[redacted]

PITCHING-MOMENT DISTRIBUTION FOR TIP CONTROL

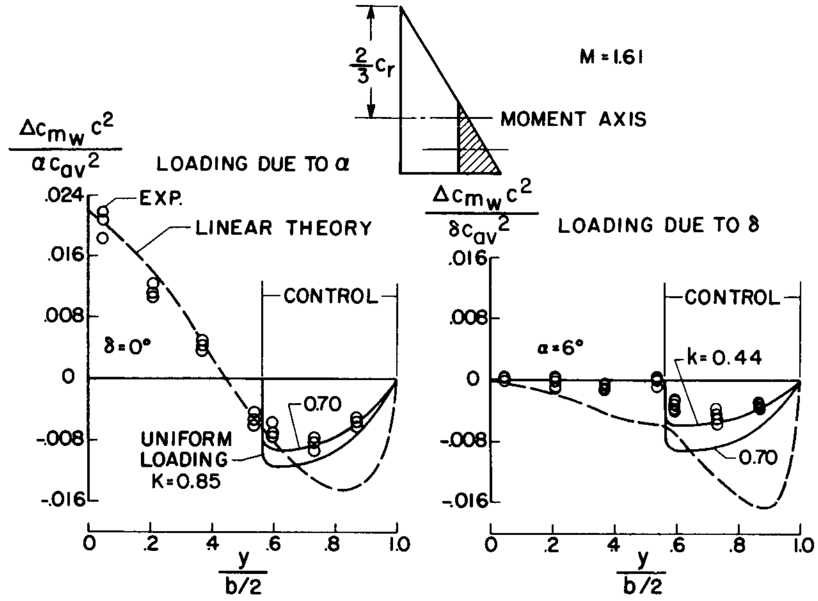

Figure 9

[redacted]

[redacted]

LOADS ON WINGS DUE TO SPOILERS AT SUBSONIC AND TRANSONIC SPEEDS

By Alexander D. Hammond

Langley Aeronautical Laboratory

SUMMARY

Some of the results of several of the more recent investigations made in the Langley 7- by 10-foot tunnels are presented to illustrate the magnitude and distribution of the additional loads on wings resulting from projection of spoiler-type controls. The results show that, although there is no known pure theoretical method for determining the magnitude or the point of application of the additional load due to spoiler projection on a given wing, wind-tunnel test data on wings close to the desired configuration can be used to estimate with a fair degree of accuracy the additional loads associated with spoiler-type controls.

INTRODUCTION

The spoiler is being used more and more on present-day aircraft for lateral control. In order to illustrate the variation of the magnitude and distribution of the additional loads on wings resulting from spoiler projection with changes in angle of attack, speed, and geometry of the wing and spoiler, some of the results of several of the more recent investigations made in the Langley 7- by 10-foot tunnels will be presented.

COEFFICIENTS AND SYMBOLS

c_n	section normal-force coefficient, $\dfrac{\text{Normal force}}{qc}$
C_N	wing normal-force coefficient, $\dfrac{\text{Wing normal force}}{qS}$
C_B	wing bending-moment coefficient, $\dfrac{\text{Wing bending moment}}{q\frac{S}{2}\frac{b}{2}}$

[redacted]

[redacted]

P_R	resultant pressure coefficient, $\left(\frac{p - p_o}{q}\right)_u - \left(\frac{p - p_o}{q}\right)_l$
A	aspect ratio, b^2/S
b	wing span, ft
c	local wing chord measured in planes parallel to wing plane of symmetry, ft
c_{av}	average wing chord, $\frac{c_r + c_t}{2}$, ft
c_f	flap chord, ft
M	Mach number
p	static pressure, lb/sq ft
p_o	free-stream static pressure, lb/sq ft
q	free-stream dynamic pressure, $\frac{1}{2}\rho V^2$, lb/sq ft
S	wing area, sq ft
t	wing maximum thickness, ft
V	free-stream air velocity, ft/sec
x	chordwise distance from wing leading edge, ft
Δx_{cp}	chordwise distance of center of pressure resulting from control deflection from wing leading edge, ft
y	spanwise distance from plane of symmetry, ft
Δ	increment resulting from control deflection
α	angle of attack of wing, deg
δ	control deflection
Λ	sweep angle, deg
λ	taper ratio; ratio of tip chord to root chord, c_t/c_r

[redacted]

ρ	mass density of air, slugs/cu ft

Subscripts:

cp	center of pressure
d	deflector
f	flap
u	upper wing surface
l	lower wing surface

DISCUSSION

In figure 1 are shown the model configurations and test conditions for the investigations made in the Langley 7- by 10-foot tunnels. A pressure-distribution investigation utilizing a 30° sweptback-wing-fuselage model (model A) having an aspect ratio of 3, a taper ratio of 0.5, and NACA 65A004 airfoil section parallel to the plane of symmetry was made at a Mach number of 0.26 for an angle-of-attack range from -4° to 24°. The right wing of the model was equipped with two of the more common types of spoiler controls, a plain spoiler and a spoiler slot deflector. These controls were tested for a range of spoiler projection from 0 to 12 percent of the local chord and a range of deflector projection from 0 to 9 percent of the local chord. The results of this investigation are unpublished.

Force tests were made on model B, an unswept semispan wing having an aspect ratio of 4, a taper ratio of 0.6, and NACA 65A006 airfoil sections parallel to the plane of symmetry, through a Mach number range from 0.62 to 1.20 for angles of attack from -4° to 20°. Model B was equipped with a plain spoiler and a spoiler slot deflector, extending from the 40- to the 97-percent-semispan stations; tests were made for spoiler projections from 0 to 10 percent of the local chord and for deflector projections from 0 to 7.5 percent of the local chord. The results of this investigation are published in reference 1.

Force tests were also made on a series of unswept untapered semispan wings, represented by model C, having aspect ratios from 1 to 6 and two airfoil sections, NACA 65A004 and NACA 65A006, parallel to plane of symmetry. A plain flap-type spoiler projected to a height of 7.5 percent chord was tested along the 40-, 60-, 80-, and 100-percent-chord lines of the wings through a Mach number range from 0.6 to 1.1 at angles of attack from -10° to 25°. These tests are also unpublished.

The results of the pressure-distribution measurements taken at the six spanwise stations on the right wing of model A are used to show, in figure 2, the variation of the wing-section normal-force coefficient c_n with spanwise position $y/b/2$ from the wing-fuselage junction to the wing tip for the plain wing at angles of attack of 2° and 8°. The spoiler was projected to 12 percent of the local chord and the deflector was projected to 9 percent of the local chord. At both angles of attack (2° and 8°), projection of the spoiler slot deflector considerably decreased the loading over that portion of the wing span covered by the control.

Inasmuch as the incremental loads due to spoiler projection, that is, the differences between the plain-wing curves and the curves for the spoiler slot deflector, are of primary interest, the incremental loadings obtained from plots similar to figure 2 have been normalized and replotted in figure 3 to show the variation of the incremental section normal-force coefficient per unit incremental wing normal-force coefficient $\frac{\Delta c_n c}{\Delta C_N c_{av}}$ with spanwise location from the wing-fuselage junction to the wing tip. The theoretical curve was obtained by the method of DeYoung outlined in references 2 and 3 for flap-type controls having the same span as the spoilers of model A on a wing having the same geometric characteristics as the wing of model A. Since the spoilers are deflected only on the right wing of model A, the theoretical curve is the average between the curve obtained for symmetrically deflected flaps and unsymmetrically deflected flaps from references 2 and 3, respectively. The experimental points denoted by the circled symbols were for an angle-of-attack range from -4° to 6°.

At the top of figure 3 are curves of the variations of the incremental wing normal-force coefficient ΔC_N and incremental wing bending-moment coefficient ΔC_B with angle of attack for the spoiler slot deflector projected to heights of 12 and 9 percent of the local chord. In the angle-of-attack range from -4° to 6°, there is an increase in both the incremental normal force and bending moments with increase in angle of attack although there is little change of the distribution of this load with change in angle of attack and the experimental and theoretical span load distributions are in good agreement (fig. 3). At angles of attack above about 6°, there is separation in the flow over the wing near the wing tip and the inboard end of the spoiler, and the experimental distributions would not be expected to agree with theory.

The chordwise load distribution resulting from spoiler projection will now be considered. The results of the pressure-distribution measurements made at the midsemispan station of model A have been used to show, in figure 4, the chordwise resultant pressure distribution due to two types of spoiler controls. Figure 4 gives the variation of the

[redacted]

incremental resultant pressure coefficient ΔP_R with chordwise location $\Delta x/c$ expressed in terms of the local chord for plain spoilers (denoted by solid curves) and for spoiler slot deflectors (denoted by the dashed curves). These data were for an angle of attack of 0°. The projection chosen for the two types of spoiler controls was such that they gave approximately equal section normal-force coefficients. Because of the load carried on the deflector itself (fig. 4), which is located well back on the wing, the center of pressure for the spoiler slot deflector is behind the center of pressure for the plain spoiler. Figure 5 shows the variation of the center-of-pressure location of the section incremental normal force $\frac{\Delta x_{cp}}{c}$ with span for a plain spoiler projected to a height of 12 percent chord and for a spoiler slot deflector projected to heights of 12 and 9 percent chord on model A at an angle of attack of 0°. The center of pressure for the spoiler slot deflector lies along approximately the 43-percent-chord line across the wing span and the center of pressure for the plain spoiler is from 10 to 30 percent further forward on the wing.

Although there were no pressure-distribution measurements made on model B to obtain the variation of the center-of-pressure location across the wing span, the results of the force tests on model B have been used to show (fig. 6) the variation of the center-of-pressure location of the incremental wing normal force with angle of attack at Mach numbers of 0.84 and 1.20. The spoiler was deflected to 10 percent chord (see solid curves); the spoiler slot deflector was projected to 10 and 7.5 percent chord (see dashed curves).

The results shown in figure 6 indicate that the center-of-pressure locations of the incremental wing normal force are about 10 percent further forward on the wing for the plain spoiler than the center-of-pressure locations of the spoiler slot deflector at all angles of attack at the Mach numbers shown. There are variations in the centers of additional load with angle of attack; however, the trends of this variation for the two types of spoilers are similar at the Mach numbers shown and at the other Mach numbers investigated. It then follows that the results of force tests on plain spoilers can be used to determine the center-of-pressure location of the incremental normal force resulting from projection of spoiler slot deflectors.

Results of the investigation made on the unswept wings denoted by model C can be used to show the changes in the chordwise position of the center-of-pressure location with such variables as wing thickness, wing aspect ratio, and spoiler chordwise position. The data for the aspect-ratio-6, 6-percent-thick wing have been used to show (fig. 7) the variation of the center-of-pressure location of the incremental section normal force with Mach number at an angle of attack of 0° for spoilers

[redacted]

projected to 7.5 percent chord and located along the 40-, 60-, 80-, and 100-percent-chord lines and, for comparison, data on a 23-percent-chord flap-type control are also presented (dashed curve).

As the spoilers move rearward on the wing, the center-of-pressure location moves toward the wing trailing edge at all Mach numbers tested. Although there is little variation in the center of additional load with Mach number for spoilers located along the 80-percent-chord line, spoilers located along 100-percent-chord line have centers of pressure that are located near the wing trailing edge at transonic Mach numbers as does the plain flap-type control. In order to show the variation of the center-of-pressure location with Mach number at other angles of attack, the data for the spoilers located along the 80-percent-chord line have been plotted on the right-hand side of figure 7 for angles of attack from 0° to 10°. At all Mach numbers investigated, the center-of-pressure location moves toward the wing trailing edge with increase of angle of attack up to 10°, and limited data indicate that the centers of additional load move back toward the wing leading edge with further increase in angle of attack.

The trends shown for the aspect-ratio-6, 6-percent-thick wing of the variation of the center-of-pressure location with Mach number are similar to the trends found for other wings of this series. The variation of the center-of-pressure location of the incremental wing normal-force coefficient with aspect ratio at an angle of attack of 0° is shown in figure 8 for spoilers located along the 60-, 80-, and 100-percent-chord lines of the 4- and 6-percent-thick wings at a Mach number of 0.80. The dashed curves are for the spoilers on the 4-percent-thick wings and the solid curves are for the spoilers on the 6-percent-thick wings. At all aspect ratios investigated, moving the spoilers rearward on the wing moves the center-of-pressure location toward the wing trailing edge. Although there is little variation of the center-of-pressure location with aspect ratio for spoilers located along the 80-percent-chord line on either the 4- or 6-percent-thick wings, the center-of-pressure locations for spoilers on the 4-percent-thick wings are approximately 8 to 10 percent further forward on the wing than are the center-of-pressure locations for spoilers on the 6-percent-thick wings. In order to show the variation of the center-of-pressure location with aspect ratio at angles of attack other than 0°, the data for spoilers located along the 80-percent-chord line on the 6-percent-thick wings have been plotted on the right-hand side of figure 8 for angles of attack from 0° to 10°. At this Mach number there is very little variation of the center-of-pressure location with aspect ratio at any angle of attack up to 10°, although the center of pressure generally moves forward on the wing with increase in angle of attack for the spoiler on wings having aspect ratios from 1 to 5.

[redacted]

CONCLUDING REMARKS

It should be pointed out that there is no known pure theoretical method for determining either the magnitude or the point of application of the additional load due to spoiler projection on a given wing. However, if force tests on configurations close to the desired configuration are used to estimate the magnitude of the additional load and its point of application, and if this load is distributed according to the theoretical load distribution of flap-type controls of the same span, the additional root bending moment and wing twisting moment can be determined in the subsonic and transonic speed range at low angles of attack with a fair degree of accuracy.

REFERENCES

1. Vogler, Raymond D.: Wind-Tunnel Investigation at Transonic Speeds of a Spoiler-Slot-Deflector Combination on an Unswept NACA 65A006 Wing. NACA RM L53J21, 1953.

2. DeYoung, John: Theoretical Symmetric Span Loading Due to Flap Deflection for Wings of Arbitrary Plan Form at Subsonic Speeds. NACA Rep. 1071, 1952. (Supersedes NACA TN 2278.)

3. DeYoung, John: Theoretical Antisymmetric Span Loading for Wings of Arbitrary Plan Form at Subsonic Speeds. NACA Rep. 1056, 1951. (Supersedes NACA TN 2140.)

[redacted]

[redacted]

[redacted]

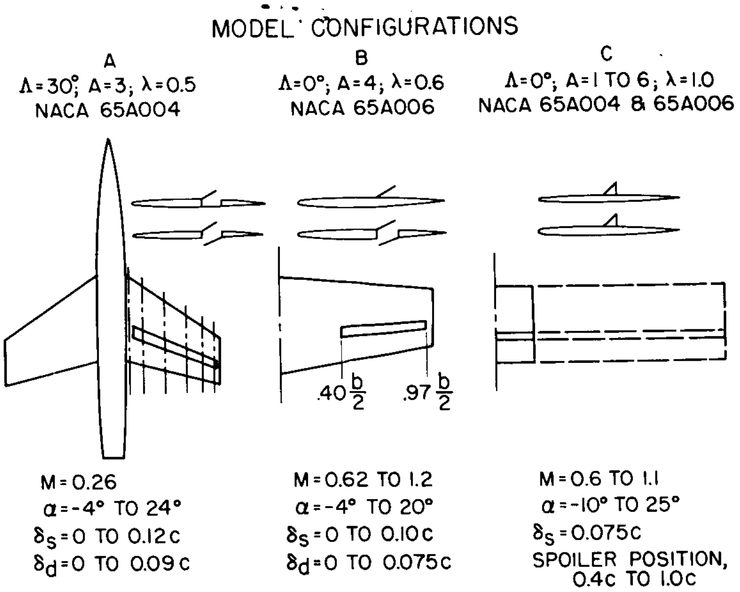

Figure 1

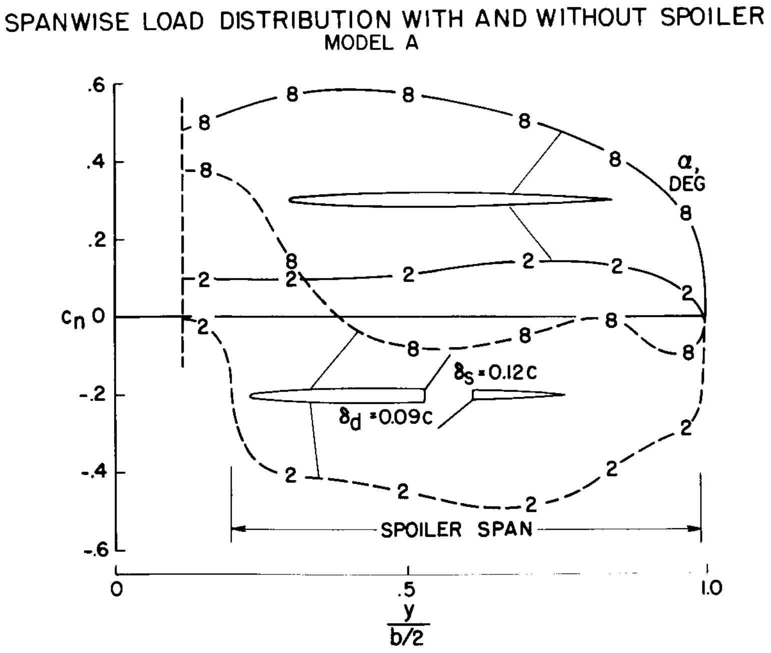

Figure 2

[redacted]

[redacted]

[redacted]

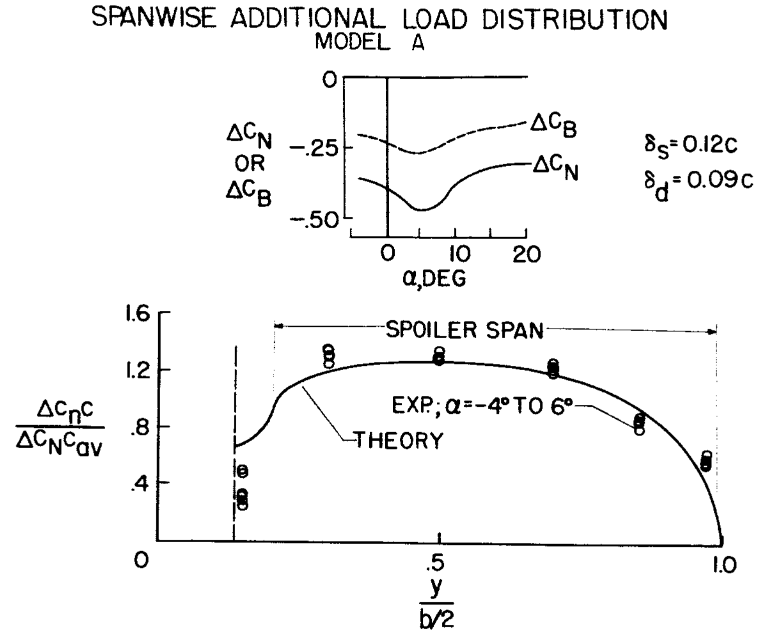

Figure 3

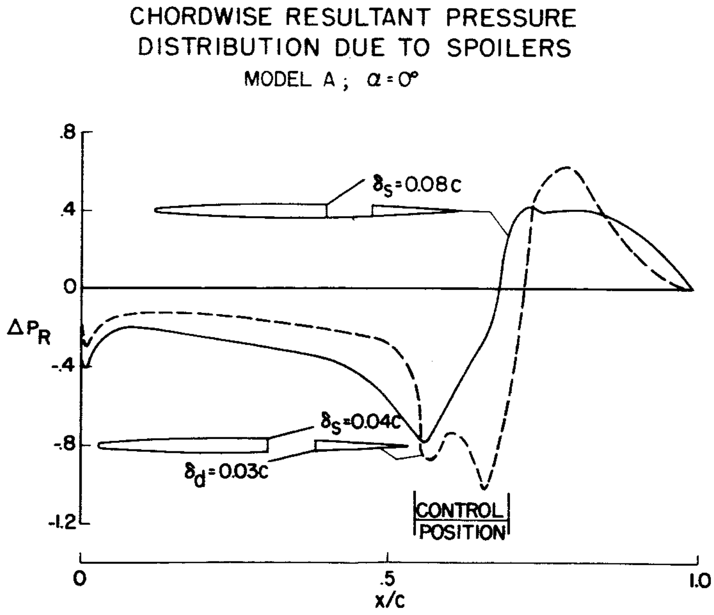

Figure 4

[redacted]

[redacted]

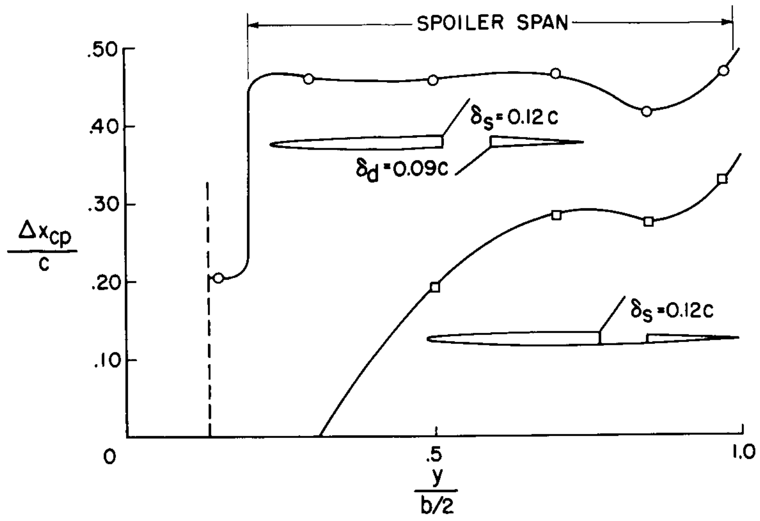
VARIATION OF LOCAL CHORDWISE CENTERS OF PRESSURE
MODEL A; $\alpha = 0°$

Figure 5

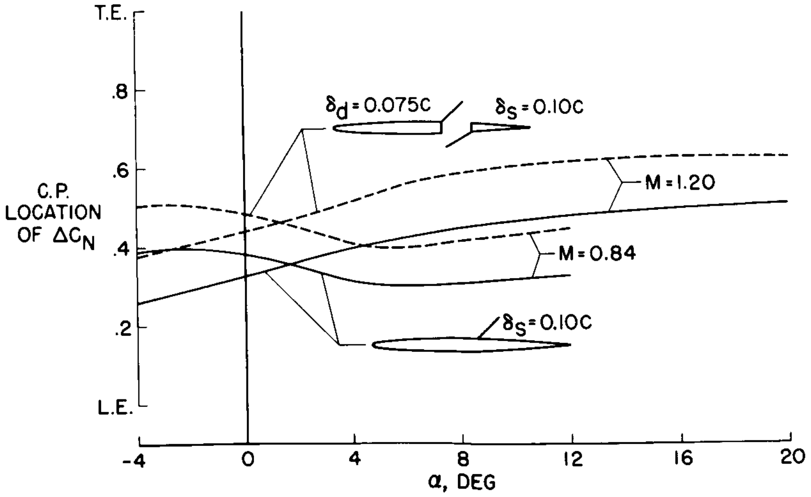
VARIATION OF CHORDWISE CENTERS OF ADDITIONAL LOAD
WITH ANGLE OF ATTACK

MODEL B

Figure 6

[redacted]

[redacted]

VARIATION OF CHORDWISE CENTERS OF ADDITIONAL LOAD WITH MACH NUMBER

MODEL C; A = 6; t/c = 0.06

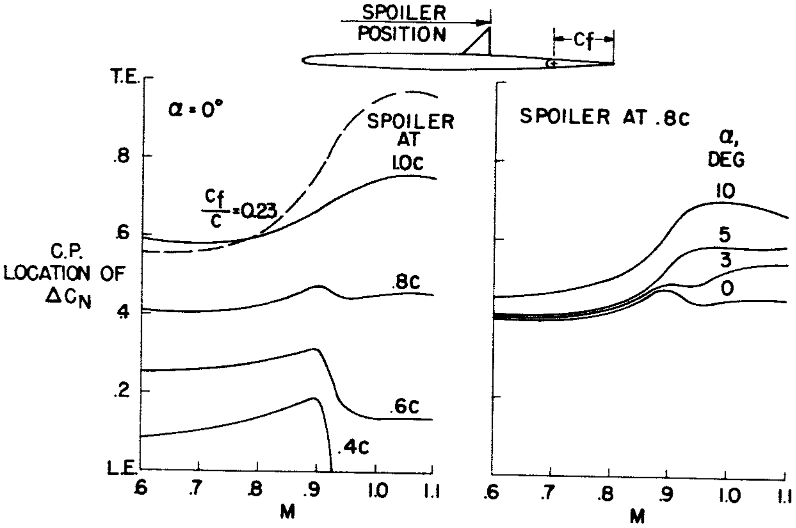

Figure 7

VARIATION OF CHORDWISE CENTERS OF ADDITIONAL LOAD WITH ASPECT RATIO

MODEL C, M = 0.8

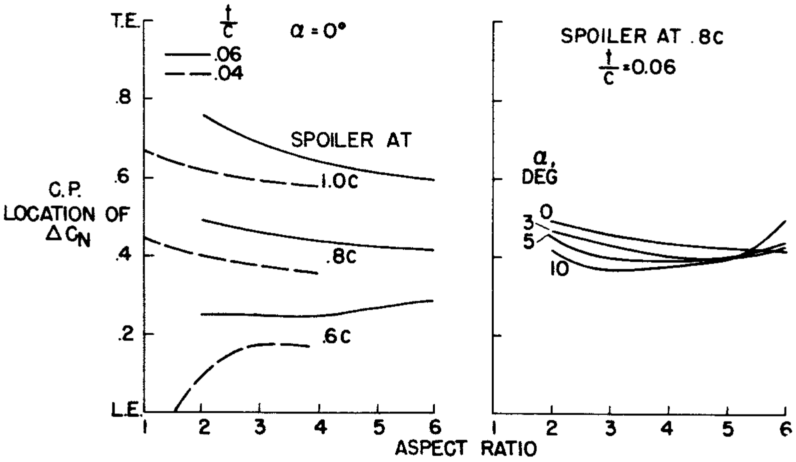

Figure 8

[redacted]

[redacted]

LOADS ASSOCIATED WITH SPOILERS AT SUPERSONIC SPEEDS

By Douglas R. Lord and K. R. Czarnecki

Langley Aeronautical Laboratory

SUMMARY

The available information concerning the loads associated with spoilers at supersonic speeds has been reviewed and the effect of some of the more important variables in the problem has been considered. Although a large proportion of the data now available are fundamental in nature, they lend considerable basic knowledge to the study of spoiler loadings and permit some estimations to be made.

This paper presents typical data available for various spoiler installations and presents an approximation method for estimating the loadings caused by an unswept spoiler. Some preliminary data and discussion are also presented for spoilers yawed to the main flow.

INTRODUCTION

At the present time there is available only a limited quantity of experimental data concerning the loads associated with spoilers in supersonic flow. During the past few years, however, several tests of a fundamental nature have been made which give some insight into the loadings caused by spoilers and enable a better understanding of the flow phenomena involved. The majority of the data obtained to date are for spoiler installations in what might be termed idealized conditions, and the application of these results to three-dimensional lifting wings with their attendant spanwise variations will undoubtedly introduce new complications. The present results are, however, a vital first step in understanding the flow characteristics and in developing methods for predicting the spoiler loads for an actual installation. The purpose of this paper is to present typical data from some of the most recent tests and to discuss the conclusions which have been reached to date. All data presented are for turbulent boundary layers.

SYMBOLS

M	stream Mach number
M_l	local Mach number

[redacted]

p	stream static pressure
p_l	local static pressure
q	stream dynamic pressure
P	pressure coefficient, $\frac{p_l - p}{q}$
δ_{sep}	effective angle of flow separation ahead of spoiler
l	horizontal distance from top of spoiler to point of flow separation
h	spoiler height
Λ	sweep angle
D	spoiler section drag
c_d	spoiler section drag coefficient, D/qh
H	spoiler section moment about base of spoiler
c_h	spoiler section hinge-moment coefficient, H/ql^2

MODELS AND TESTS

Figure 1 illustrates the testing techniques which have been used in studying this problem. Although some of the tests were initiated as part of shock—boundary-layer interaction programs, they are inherently suited for studying the loadings ahead of spoilers. On each of the sketches shown, the horizontal lines above and below the diagram define the location of the tunnel walls. In the upper left sketch of the figure, the two-dimensional step technique, used both at the David Taylor Model Basin (ref. 1) and at Princeton University (ref. 2), is shown. Orifices ahead of and on the front face of the spoiler were used to determine the loadings.

The collar-on-a-tube technique, illustrated in the top middle sketch of figure 1, was employed in tests in a blowdown jet of the Langley Gas Dynamics Branch (ref. 3). Here again, a single row of orifices was used to obtain pressures along the tube and on the front face of the collar.

[redacted]

Tests were made in the Langley 9-inch supersonic tunnel (ref. 4) on a two-dimensional airfoil (as shown in the upper right sketch of fig. 1) in which spoilers of various heights were mounted at three chordwise locations on the airfoil upper surface. A single row of orifices along the surface measured the pressures both ahead of and behind the spoiler.

The three techniques shown so far have been used primarily to study the effect of spoilers placed normal to the flow. In order to study the loadings caused by a spoiler in the yawed condition such as would be encountered on a swept-wing spoiler installation, with the simplifying condition of uniform flow ahead of the spoiler, the technique shown in the lower left sketch of figure 1 was used in the Langley 4- by 4-foot supersonic pressure tunnel. Spoilers of varying height, span, and deflection angle were mounted on a turntable in a flat boundary-layer bypass plate. The turntable was instrumented with approximately 260 orifices located so that, as the turntable was rotated to obtain various sweep angles, rows of orifices were always so alined as to give detailed pressure distributions in the streamwise direction. Pressures were obtained ahead of and behind the spoilers as well as on the front and rear faces of the spoiler itself.

In the lower right-hand corner of figure 1 is a plan view of the three-dimensional semispan-wing model which was tested in the 4- by 4-foot supersonic pressure tunnel with various spoiler installations. A typical location for a full-span spoiler is shown, in addition to the five rows of orifices located across the wing span. Some of the variables investigated in these tests were spoiler height, span, chordwise location, and sweep.

DISCUSSION

Unswept Spoilers

In figure 2 the typical loadings caused by an unswept spoiler in supersonic flow are illustrated. In the left part of the figure the pressure distributions ahead of and behind three spoilers have been superimposed. Two of the spoilers were vertical spoilers of different heights and the third was a flap-type spoiler deflected 45° to the surface. As has been previously demonstrated at subsonic speeds, when the loadings are plotted as a function of distance from the top of the spoiler in terms of the actual spoiler height above the surface, the loadings are nearly identical. Further investigations have shown that this remains true with reductions in spoiler height until the height becomes of the same order of magnitude as the boundary-layer thickness.

[redacted]

DECLASSIFIED [redacted]

Since it was found that, at this Mach number, the spoiler caused the flow to separate approximately $5\frac{1}{2}$ spoiler heights ahead of the spoiler top, a simple approximation to the loading can be obtained, as shown, by following these rules: First, drawing a line from the separation point to the top of the spoiler determines the angle through which the flow must turn and, therefore, the average pressure in the forward dead-air region can be calculated. Further, from examining the pressure distributions, it appears that at the spoiler top the flow expands through an angle approximately three times the value of the separation angle just determined. By calculation then, it is possible to get the pressure immediately downstream of the spoiler. It would ordinarily be anticipated that this pressure would remain constant until the flow impinged on the surface and again had to be turned to realine with the stream. Experience has shown, however, that the compression takes place in a gradual manner and is approximately completed at a point downstream of the spoiler the same distance as the separation occurred upstream. A straight line connecting the last computed pressure point with the proper distance along the axis in the downstream direction, therefore, completed the approximation.

On the right-hand side of figure 2 are shown the loadings on the front and rear faces of the three spoilers depicted. The vertical spoilers exhibit marked pressure increases on the front face near the bottom and top of the spoiler which indicate stagnation of the local flow at these points. The 45° spoiler has its highest pressure at about 80 percent of its height, followed by a rapid expansion. These variations are caused by the circulatory flow in the dead-air region ahead of the spoiler. On the rear faces of the spoilers, there appears to be little effect of spoiler height or deflection angle, and indications of any circulation are lacking. At the present time, no technique has been obtained for estimating the distribution of pressures along the front face of a spoiler; however, the uniform pressure on the rear face may be approximated by using the pressure obtained just after the expansion of the main flow at the spoiler top.

If the experimental pressures are known on the wing surface immediately ahead of and behind the spoiler, a good approximation of the average loads on the spoiler can be obtained by assuming that these pressures apply uniformly over the adjacent spoiler faces.

Since, in the discussion of the technique used in estimating the loadings caused by a spoiler, it was necessary to first know the extent of the separated region, the obvious question which follows is how to determine this distance. In figure 3 the separation distance from the spoiler in terms of the height is plotted against Mach number. All the data on this figure were determined from the tests discussed in figure 1. The two-dimensional results are shown as symbols, whereas the results from the only available three-dimensional tests are shown as a shaded area.

[redacted]

The data for any one family of test points in which there was a Mach number variation indicate a decreasing trend with Mach number. From consideration of the scatter of the available results, it appears that the assumption of a constant separation distance of $5\frac{1}{2}$ spoiler heights as shown by the dashed line would be satisfactory for estimating loadings in the Mach number range from 1.6 to 3.0.

Effects of Sweep

Up to now, only unswept spoilers have been discussed. Figure 4 illustrates the changes in upstream influence of a spoiler caused by increasing the spoiler sweep from 0° to 60°. In considering the effects of spoiler sweep, a new phenomenon is involved: The flow not only must be deflected by a shock from the surface to surmount the spoiler height, but a new shock is necessary to turn the flow along the surface - thus allowing the flow to move parallel to the face of the spoiler.

It can be seen from figure 4 that, for an unswept spoiler, there is relatively little effect of the spoiler tips on the upstream influence of the spoiler within its spanwise boundaries. As the spoiler is swept, the curve of initial disturbance assumes the position of a detached shock about the upstream tip of the spoiler.

This interaction is illustrated better in figure 5, in which the effect of 45° sweep on the pressure distributions in streamwise rows at two stations along the spoiler span is shown. The upper diagrams show the loadings ahead of, behind, and on the spoiler at station 1; whereas the lower diagrams show the same variations at a station considerably closer to the spoiler tip. At 0° sweep, the loadings are almost identical at the two stations shown. When the sweep is increased to 45°, the compression ahead of the spoiler occurs in two steps and is separated by an expansion region. At station 1, the change in sweep from 0° to 45° increases considerably the upstream influence of the spoiler. At station 2, nearer the tip, the initial compression occurs much closer to the spoiler than it does at station 1; however, the peak of the expansion region appears to be about the same distance from the spoiler at both stations. The final compression ahead of the spoiler is much greater at station 2 and is also illustrated by the higher pressure along the front face of the spoiler at this station. The pressures in the region downstream of the spoiler are generally more negative at station 2 for this sweep condition.

Since the variation in loading along the span has been shown, it follows that the integrated lift and pitching moment caused by the spoiler will also vary spanwise. Because of the limited number of stations across the span and the relatively low spoiler span-to-height ratio for these tests, it is impossible to give a complete picture of the spanwise variations of lift and pitching moment caused by a swept spoiler. Indications are, however, that when a spoiler having a sweep of 45° or greater is used, there is a strong tendency for reversal in lift and reduction in pitching moment within approximately 10 spoiler heights of the upstream tip. These indications have been borne out by correlations obtained between data from these tests and data from three-dimensional tests in the Langley 16-foot transonic tunnel (ref. 5) on a 45° swept-wing—spoiler combination in which the local wind velocities ahead of the spoiler were supersonic.

In accordance with the discussion of the effects of spanwise location on the changes with sweep, figure 6 shows the variations in spoiler section drag and flap-type spoiler section hinge-moment coefficients along the span for various angles of sweep. At 0° sweep, the drag and hinge moments are constant along the span insofar as was investigated. As the spoiler is swept to 60°, the drag and hinge moment first fall off on the downstream portion of the spoiler and then fall off all along the span.

CONCLUDING REMARKS

Considerable information of a fundamental nature is now available on the status of research on loadings caused by spoilers at supersonic speeds. Estimations can be made very simply to determine the loadings caused by unswept spoilers in uniform flow fields. The effects of sweep, though understood somewhat, are still too complex to permit any simple approximation techniques to be demonstrated. It is anticipated that further analysis of the available information should clarify this problem; however, detailed loading investigations of spoiler installations on three-dimensional lifting wings will be needed for a complete solution to the problem.

[redacted]

REFERENCES

1. Patterson, R. T.: The Characteristics of Trailing-Edge Spoilers. Part II - The Effects of Gap, Flap Deflection Angle, Thickness, and Sweep Angle on the Aerodynamic Characteristics of Two-Dimensional Spoilers, and the Pressure Distribution Near the Tip of a Partial-Span Trailing-Edge Spoiler, at a Mach Number of 1.86 - TED No. TMB DE-3109. Aero Rep. 827, David W. Taylor Model Basin, Navy Dept., Dec. 1952.

2. Bogdonoff, S. M., and Kepler, C. E.: Separation of a Supersonic Turbulent Boundary Layer. Rep. 249 (Contract No. N6-onr-270), Princeton Univ., Dept. Aero. Eng., Jan. 1954.

3. Lange, Roy H.: Present Status of Information Relative to the Prediction of Shock-Induced Boundary-Layer Separation. NACA TN 3065, 1954.

4. Mueller, James N.: Investigation of Spoilers at a Mach Number of 1.93 To Determine the Effects of Height and Chordwise Location on the Section Aerodynamic Characteristics of a Two-Dimensional Wing. NACA RM L52L31, 1953.

5. Hallissy, Joseph M., Jr., West, F. E., Jr., and Liner, George: Effects of Spoiler Ailerons on the Aerodynamic Load Distribution Over a 45° Sweptback Wing at Mach Numbers From 0.60 to 1.03. NACA RM L54C17a, 1954.

[redacted]

[redacted]

[redacted]

TEST CONFIGURATIONS

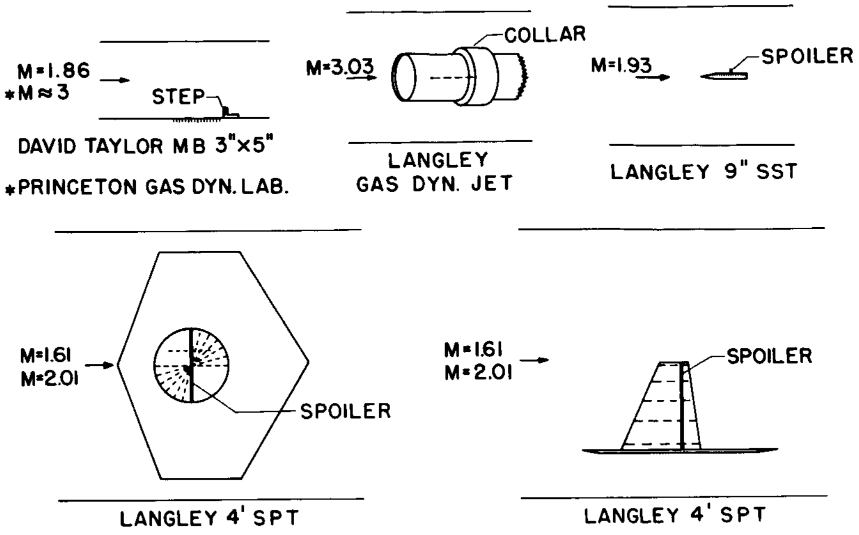

Figure 1

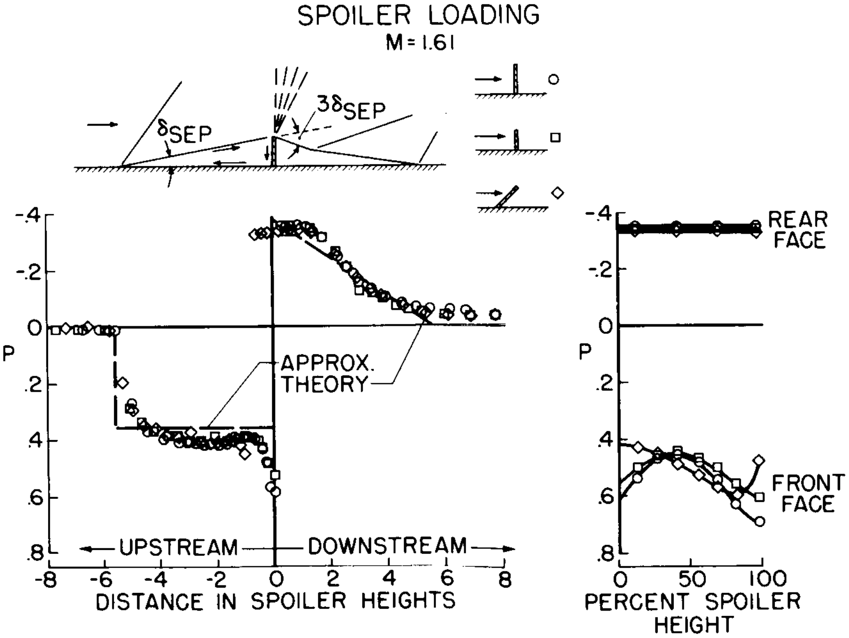

Figure 2

[redacted]

[redacted]

[redacted]

EFFECT OF MACH NUMBER ON SEPARATION

Λ = 0°

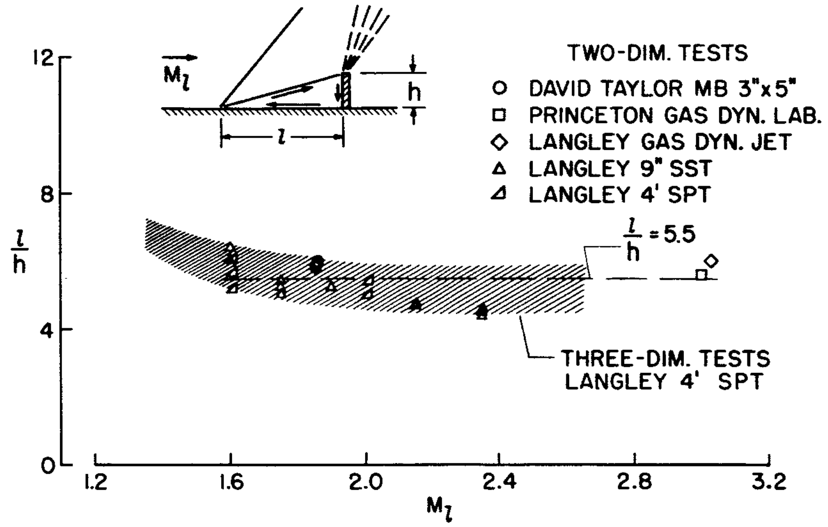

Figure 3

UPSTREAM INFLUENCE OF SPOILER

M=1.61

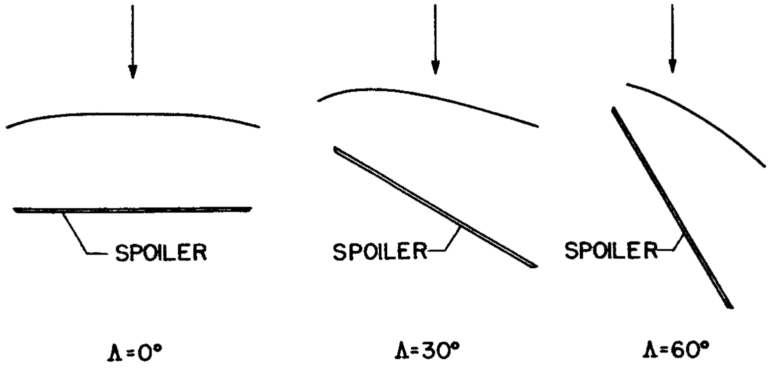

Figure 4

[redacted]

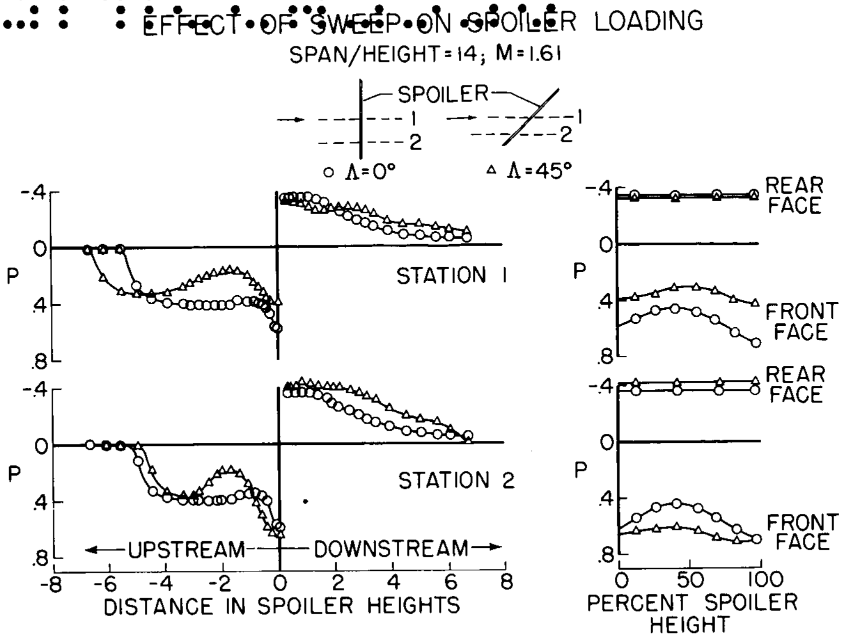

EFFECT OF SWEEP ON SPOILER LOADING

SPAN/HEIGHT = 14; M = 1.61

Figure 5

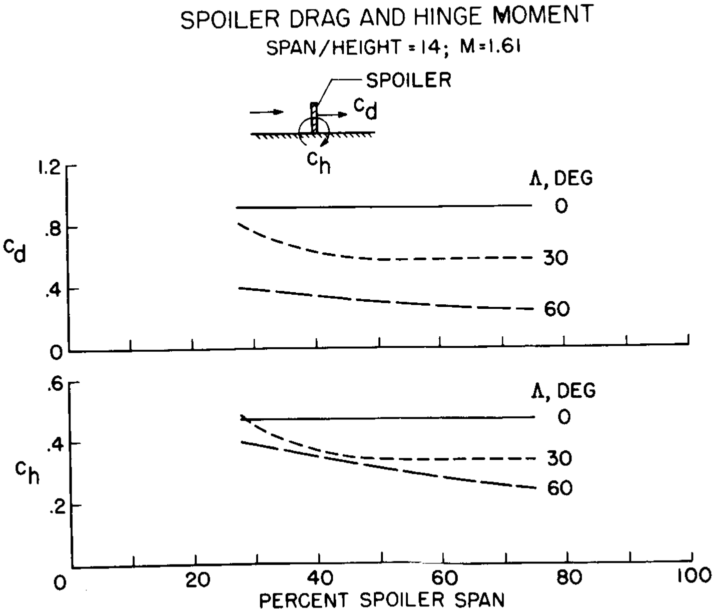

SPOILER DRAG AND HINGE MOMENT

SPAN/HEIGHT = 14; M = 1.61

Figure 6

[redacted]

[redacted]

SOME INTERFERENCE EFFECTS THAT INFLUENCE VERTICAL-TAIL LOADS AT SUPERSONIC SPEEDS

By S. Sherman Edwards

Ames Aeronautical Laboratory

INTRODUCTION

In order to develop loads on the vertical tail, it is necessary for the airplane to be at an angle of sideslip. The purpose of the vertical tail, of course, is to limit the sideslip angle to which the airplane yaws and to balance the tail-off yawing moments which generally are unstable at supersonic speeds.

The yawing motion of an airplane is considered in figure 1. It might be expected that the load on the vertical tail would be directly proportional to its size. In reference 1 the importance of examining the motions of the airplane in determining vertical-tail loads was discussed and the sideslip angles associated with deficiencies in directional stability were shown to lead to large vertical-tail loads. For example, a large tail on the airplane (on the left in fig. 1) may provide sufficient directional stability so that the maximum sideslip angle to which the airplane yaws in a given maneuver is limited to a small value. If the vertical-tail size were reduced, the airplane would attain much larger sideslip angles in the same maneuver as shown on the right in figure 1 and a larger load, therefore, could be developed on the smaller tail. The directional stability is the important parameter determining the sideslip angles which will occur in maneuvering conditions. This paper will consider, therefore, vertical-tail loads in relationship to their influence upon the directional stability of several supersonic airplanes. It will be confined, primarily, to a general discussion of the aerodynamic interference effects which have been observed to be contributing to deficiencies in vertical-tail effectiveness with increasing angle of attack and increasing supersonic Mach numbers.

RESULTS AND DISCUSSION

The variation of the directional stability (or the yawing moment due to sideslip C_{n_β}) with angle of attack at two Mach numbers for a swept-wing airplane is presented in figure 2. The results for this model show a substantial decrease in directional stability with angle of attack and also with Mach number. In fact, a Mach number of 1.9 is well into the speed

[redacted]

[redacted]

range in which danger of directional divergence exists. The vertical-tail contribution is the difference between the data for the tail-off and complete configurations. At both Mach numbers, the decrease in the yawing moment due to sideslip with increasing angle of attack is caused by a corresponding decrease in vertical-tail effectiveness. The magnitude of the unstable yawing moment due to sideslip shown for the tail-off configuration illustrates why an efficient vertical tail is needed. For this airplane, the decreased effectiveness of the vertical tail as the angle of attack increases means that to avoid critical tail loads accompanying directional divergence, the size of the surface must be larger than that necessary at small angles of attack.

What are the aerodynamic conditions that combine to rob the vertical tail on this model of its effectiveness as a stabilizing surface? The effect of Mach number is explained adequately by the decreased lift effectiveness of the vertical tail with increasing Mach number. There are, however, three possible explanations of the angle-of-attack effect. Sidewash effects of the wing may be unfavorable. Examination of the increment in C_{n_β} between the results for the body-tail and complete comfigurations indicates, however, that the addition of the wing seems to increase rather than decrease the vertical-tail loading at a given angle of sideslip. The second possibility is that the sweepback of the vertical tail is effectively increased with angle of attack and tends to reduce the effectiveness of the vertical tail because it is known that the lift-curve slope decreases with increasing sweepback. The magnitude of the decrease in vertical-tail effectiveness is much larger than can be traced to this simple explanation. The third possibility is indicated by a study of the body-tail results. Note the marked decrease in the vertical-tail effectiveness with increasing angle of attack. This decrease has been traced to an induced effect of the fuselage in the lifting condition.

With regard to the third possibility, the nature of the induced flow field in the tail region of this model is shown in figure 3 for the fuselage alone at an angle of sideslip of 5° and two angles of attack. These photographs were obtained by means of the vapor-screen technique in the Ames 1- by 3-foot supersonic tunnel No. 1. The darkened spots on the vapor screen near the tail of the body are caused by regions of concentrated vorticity associated with the fuselage loading. The spinning action of the vortices forces moisture particles outward from the center of rotation. Innermost areas of the vortices, therefore, are devoid of moisture particles capable of reflecting light and hence these vortex regions appear as dark spots on the vapor screen. Note that in figure 3 the upper vortex appears to be in the plane of the vertical tail, the position of which is shown in the sketch at the top of figure 2. As the angle of attack was increased from 8° to 16°, this vortex moved upward to approximately the top of the vertical tail.

[redacted]

In figure 4, a similar study of the swept wing in combination with the fuselage is shown. The vantage point from which the vapor screen is observed in this case is located inside the wind tunnel with the model upstream of this point. The light screen is projected from the left in these pictures; consequently, a shadow of the model is cast to the right. In addition to the wing-tip vortices which appear, body vortex regions in the vicinity of the tail locations are shown. Again, a strong vortex appears in this case somewhat to the right of the plane of the vertical tail. As the angle of attack is increased, this vortex seems to keep approximately the same lateral location with respect to the position of the vertical tail. Forward movement of the vapor screen to the mid-point of the body shows that at this point one of the two body vortices is located under the left wing; the other is above the wing. The marked asymmetry in the body vortex flow, therefore, is readily apparent.

The manner in which these vortices influence the vertical-tail loading is not known quantitatively. Several qualitative statements can be made, however, regarding these vortices and their relationship to the vertical-tail loads: (1) The vertical tail in sideslip is not lifting in a uniform stream and both chordwise and spanwise variations in the loading caused by localized vorticity should be expected. (2) The marked decrease in vertical-tail load with angle of attack of the body-tail combination appears to be related to the fact that, as shown in figures 3 and 4, the vortex coming from the right side of the fuselage (looking forward) actually intersects the vertical tail and hence has maximum influence. The point of intersection moved almost to the top of the tail at the maximum angle of attack so that the induced effects would be expected to decrease at larger angles. (3) The vertical movement of this vortex (that is, the one from the right side of the fuselage) is somewhat restricted by the presence of the wing; it seems, also, to have moved away from the vertical tail. Consequently, its influence is diminished and the complete configuration has slightly more directional stability throughout the angle-of-attack range.

The effect of an unswept wing upon the results presented in figure 2 is shown in figure 5. This wing had the same span and aspect ratio as the unswept wing. (See fig. 2.) The vertical tail also was changed to an unswept design; however, results for this tail when tested on the original swept-wing model showed an almost identical variation of the vertical-tail effectiveness with angle of attack and with Mach number as that of the original swept tail. The effect of the vortices that were observed in the vapor-screen tests therefore must have been about the same for the two tails when the fact that the height, area, and chord at the fuselage juncture was kept the same is considered. In figure 5 the data for the unswept-wing model show that the directional stability is maintained and actually increases at moderate angles of attack. The high level as compared with the original airplane is caused by the fact that it was necessary to shift the center of gravity forward slightly to accommodate the more forward position of the unswept-wing center of pressure. For both configurations, the same static margin at a Mach number of 1.5 was maintained. It was estimated that the effect of the straight wing was negligible on the tail-off results shown in figure 2; therefore, it was concluded that the maintenance of directional stability with angle of attack was caused almost entirely by an increase in the vertical-tail effectiveness at high angles of attack.

Again, vapor-screen tests provided an explanation for the results. The vortex coming from the right side of the fuselage looking forward (see fig. 4) was pronouncedly influenced by the unswept wing. In the presence of this wing, this vortex was much more diffuse in nature, tended to cling closer to the fuselage, and was even farther away from the vertical tail than the position shown in figure 4. The increased effectiveness of the vertical tail on this airplane at large angles of attack, therefore, is attributed to a reduction in the influence of the fuselage vortices.

A different type of interference effect upon vertical-tail effectiveness has been observed for configurations similar to that shown in figure 6. The increment in the C_{n_β} parameter between the tail-off and complete-model results shows again in this case a decrease in the vertical-tail contribution to the directional stability with increasing angle of attack and increasing Mach number. Although the possibility of vortices associated with the lift of the fuselage forward of the wing is not discounted in this case, it is believed that the major factor contributing to this result is the unusually far forward location of the vertical tail. More specifically, as the angle of attack of this model is increased, the stream following the wing-leading-edge shock wave expands to higher than free-stream Mach numbers across the top of the wing. The vertical tail on this model is in this higher Mach number region. The reduction in the load on the vertical tail caused by the decreased dynamic pressure associated with this expansion reduces the directional stability of the airplane as the angle of attack increases.

Most of the vertical tail of the swept-wing model previously discussed is downstream of the flow region influenced by expanding flow above the wing at Mach numbers lower than 1.9; therefore, a similar type of interference effect was not mentioned as a major contributing factor to the vertical-tail loads. At higher speeds, of course, this effect would become of increasing importance for that configuration.

Another interference effect differing from those previously discussed was observed for the model shown in figure 7. Notice that the increment in C_{n_β} between the tail-off results and the curve for the complete model shows a nonlinear variation of the tail contribution to the directional stability with Mach number. This nonlinearity disappeared when the nacelles were removed or when the outboard nacelles were placed on pylons below the

[redacted]

wing. Expansion waves from the nacelles impinge upon the vertical tail in this arrangement and cause both chordwise and spanwise variations in the loading on the vertical tail and a general decrease in its effectiveness. The nonlinear increase in effectiveness with Mach number is caused by the rearward movement of pressure waves from the nacelles along the vertical tail. This effect causes the directional stability of the complete model to approach the nacelles-off results at a Mach number of 1.9. An important consideration for an airplane having nacelles in this position from the standpoint of vertical-tail design would be the sudden loss of thrust in one of the outboard engines. This condition could result in large differences in the pressure waves impinging on the two sides of the vertical tail and could cause large sideslip angles and large loads on the tail.

SUMMARY OF RESULTS

In summary, it is pointed out that a deficiency in directional stability permits the airplane to develop large angles of sideslip and hence large vertical-tail loads. The tail-off yawing moments for each of the models considered were markedly unstable. The vertical tail on the swept-wing model provided adequate directional stability at low angles of attack; however, vorticity associated with the lift of the fuselage decreased the vertical-tail effectiveness as the angle of attack increased. When the wing on this model was changed to an unswept design, the effectiveness of the vertical tail was maintained with increasing angle of attack. This result was believed to be caused by the fact that the unswept wing altered the position of vortices originating from the fuselage ahead of the wing and caused a decrease in the adverse sidewash at the vertical tail.

For the triangular-wing model, a decrease in vertical-tail effectiveness with angle of attack also occurred; this decrease was caused by the location of the tail in a region of reduced dynamic pressure associated with expansion of the flow over the wing. For both airplanes, large vertical tails are necessary to avoid directional divergence and hence excessive tail loads.

An interference effect of a different nature influenced the vertical-tail loads on the model with nacelles located on the wing. In this case, pressure waves from the nacelles impinged on the vertical tail. At moderate supersonic Mach numbers, these waves influenced the vertical-tail loads in sideslip and caused a nonlinear variation of the directional stability with Mach number.

REFERENCE

1. Weil, Joseph, Gates, Ordway B., Jr., Banner, Richard D., and Kuhl, Albert E.: Flight Experience of Inertia Coupling in Rolling Maneuvers. (Prospective NACA paper.)

[redacted]

[redacted]

[redacted]

VERTICAL - TAIL LOADS IN SIDESLIP

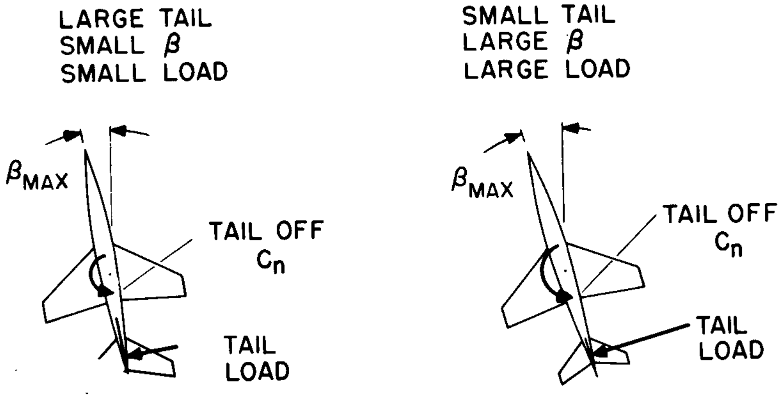

Figure 1

VERTICAL-TAIL EFFECTIVENESS FOR A SWEPT-WING AIRPLANE

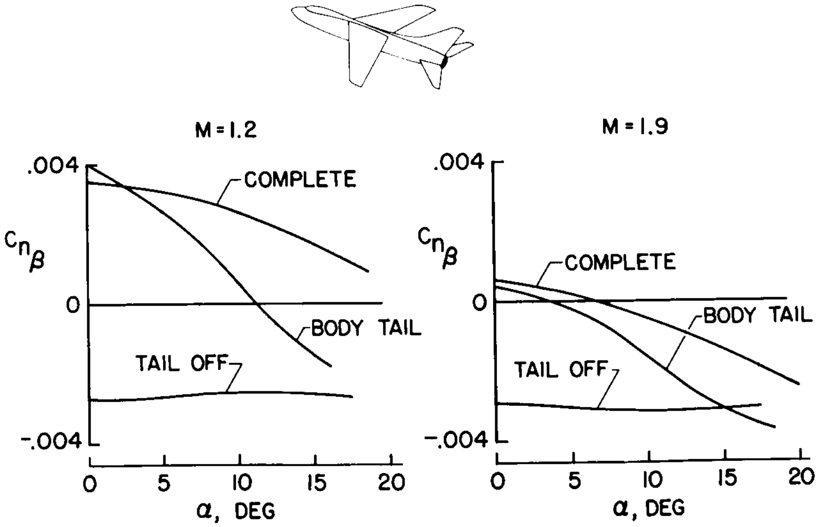

Figure 2

[redacted]

[redacted]

[redacted] DECLASSIFIED

VAPOR-SCREEN PHOTOGRAPHS OF FUSELAGE VORTICES IN THE TAIL REGION

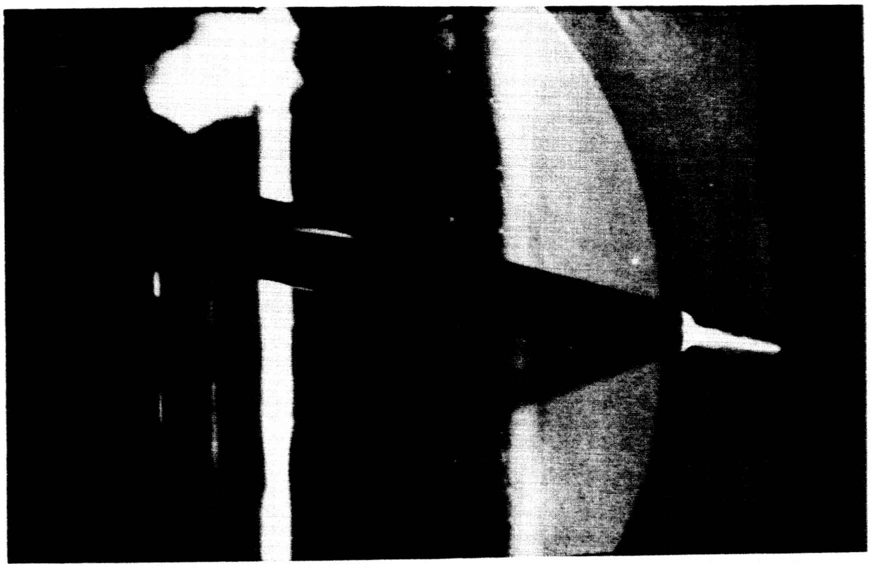

$\alpha = 8°$, $\beta = 5°$, $M = 1.9$

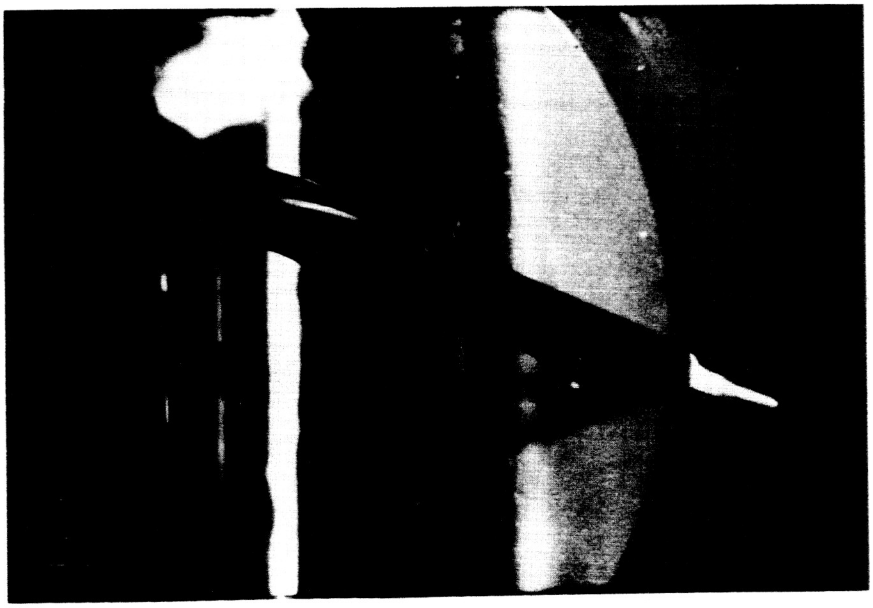

$\alpha = 16°$, $\beta = 5°$, $M = 1.9$

Figure 3

[redacted]

EFFECT OF THE WING ON FUSELAGE VORTICES VIEWED DIRECTLY UPSTREAM

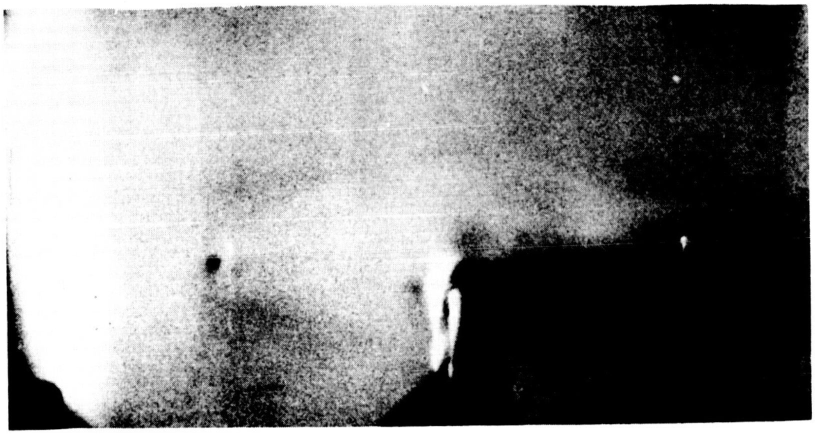

$\alpha = 6°$, $\beta = 5°$, M = 1.9

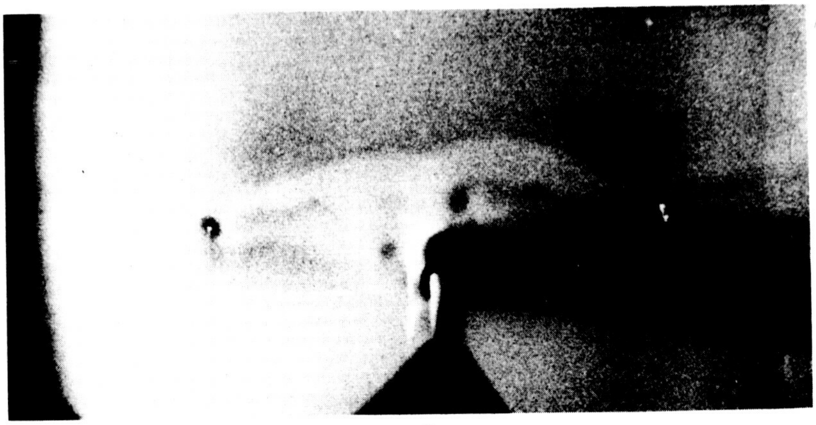

$\alpha = 12°$, $\beta = 5°$, M = 1.9

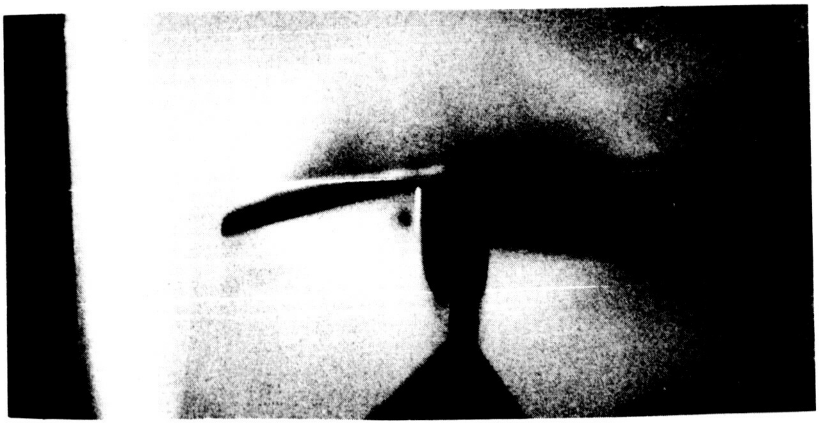

$\alpha = 12°$, $\beta = 5°$, M = 1.9

VAPOR SCREEN FORWARD TO MIDPOINT OF BODY

Figure 4

[redacted]

EFFECT OF AN UNSWEPT WING

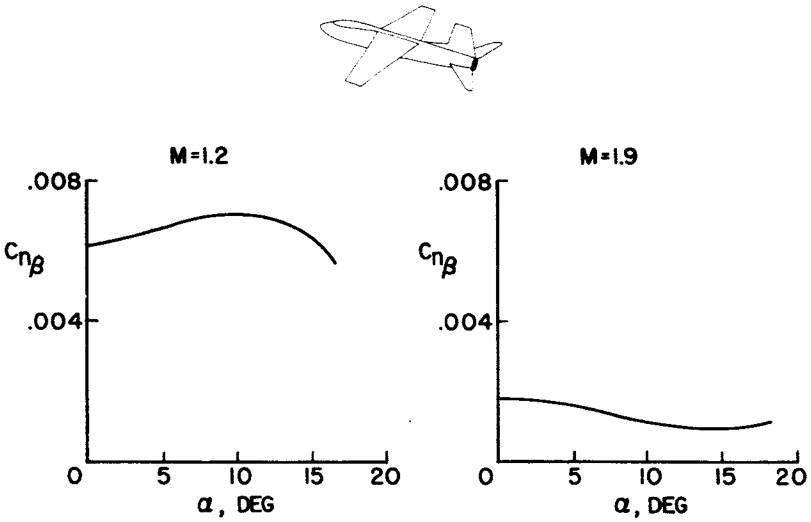

Figure 5

VERTICAL-TAIL EFFECTIVENESS FOR A TRIANGULAR-WING AIRPLANE

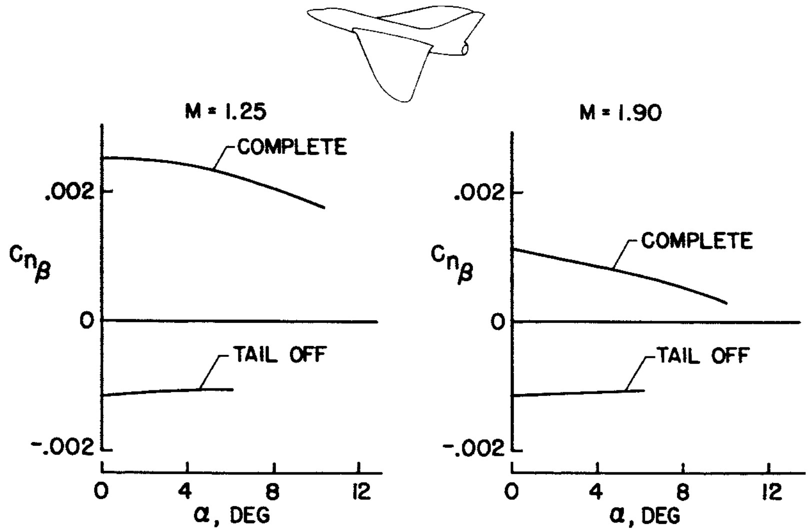

Figure 6

[redacted]

EFFECT OF NACELLES ON VERTICAL-TAIL EFFECTIVENESS

$\alpha = 0°$

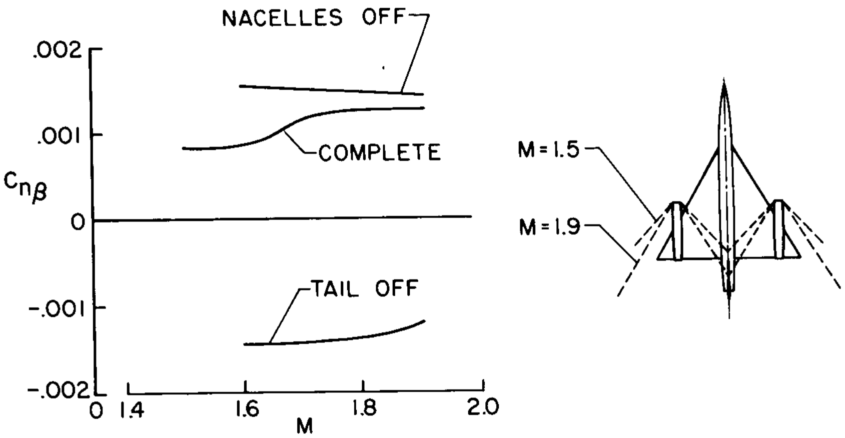

Figure 7

[redacted]ASSIFIED

A DISCUSSION OF RECENT WIND-TUNNEL STUDIES RELATING TO THE PROBLEM OF ESTIMATING VERTICAL- AND HORIZONTAL-TAIL LOADS

By Richard E. Kuhn, Joseph M. Hallissy, Jr.,
and Ralph W. Stone, Jr.

Langley Aeronautical Laboratory

SUMMARY

Some of the effects of angle of attack, sideslip, Mach number, and airplane configuration on the vertical-tail loads and, to a lesser extent, horizontal-tail loads have been discussed. In addition, the division of load between the exposed vertical tail and the fuselage has also been considered. It has been shown that at low angles of attack, in both the subsonic and supersonic speed ranges, adequate predictions of the vertical-tail loads can be made. At angles of attack at which the flow begins to separate from the wing and fuselage, however, large rolled-up vortices appear in the flow in the region of the tail assembly and large changes in both vertical- and horizontal-tail loads result.

It has been shown that the effects of these vortices on the tail loads can be calculated if the strength and position of all vortices are known. For practical configurations with their complex fuselage shapes, however, it appears that, at present, some type of flow-visualization studies to indicate the vortex positions and some indication of the loads on the fuselage to estimate the vortex strength are necessary in order to estimate the tail loads.

INTRODUCTION

When an airplane is disturbed from equilibrium (as discussed in refs. 1 and 2), loads are developed on the tail surfaces of the airplane and usually act to oppose the motion of the airplane, that is, tend to bring the airplane back into equilibrium. The designer is interested in estimating these loads throughout the attitude range expected for the airplane in connection with both the stability of the configuration and the structural design of the tail surfaces themselves.

The present paper examines some recent wind-tunnel data on loads on vertical and horizontal tail surfaces of complete configurations in order

[redacted]

[redacted]

to point out some of the factors influencing the loads at high angles of attack. The data and discussion presented are limited to sideslip angles of the order of 4° or 5°.

SYMBOLS

C_N	normal-force coefficient, N/qS_v
C_B	bending-moment coefficient, $\dfrac{B}{q\,\dfrac{S_h}{2}\,\dfrac{b_h}{2}}$
N	vertical-tail normal force, lb
B	root bending moment of horizontal-tail semispan, ft-lb
q	dynamic pressure, $\rho V^2/2$, lb/sq ft
ρ	mass density, slugs/cu ft
V	free-stream velocity, ft/sec
M	Mach number
S_v	area of exposed vertical tail, sq ft
S_h	area of horizontal tail, sq ft
b_v	span of exposed vertical tail, ft
b_h	span of horizontal tail, ft
z	distance from fuselage—vertical-tail juncture to center of load on exposed vertical tail, ft
L	lift on wing; or lift on fuselage alone, lb
l	effective span of wing; or effective diameter of fuselage, ft
Γ	circulation, sq ft/sec
c_l	local section lift coefficient
c	local chord
c_{av}	average chord

[redacted]

RESULTS AND DISCUSSION

Vertical-Tail Loads at Low Angles of Attack

Procedures and data that can be used in estimating the loads on most tail configurations at both subsonic and supersonic speeds and at low angles of attack are available in the literature. References 3 to 13, for instance, present studies relating specifically to tail assemblies, and references such as 14 and 15, which relate to the lift-curve slope of lifting surfaces, can also be used provided the end-plate effect of the fuselage is properly accounted for. A comparison between the experimental and calculated vertical-tail normal-force coefficient at low angles of attack is presented in figure 1. The data presented were obtained by subtracting the measured side force on the model with the vertical tail removed from the measured side force on the complete model. Thus the results shown represent the total tail load which included both the normal force carried on the vertical tail and the additional increment of normal force that the vertical tail induced on the fuselage. The data were obtained from tests of the models at sideslip angles of the order of 4°.

In the supersonic speed range, the calculated variation, from reference 11, is in very good agreement with the experimental data which were obtained from an unpublished investigation. A rather complete discussion of the procedures for calculating the forces on the tail assembly of a complete configuration at supersonic speeds is included in reference 16.

References 14 and 17 were used for the calculations in the subsonic speed range. In making these calculations, the effective aspect ratio of the vertical tail was increased by the empirical relationship presented in reference 17 to account for the end-plate effect of the fuselage. The end-plate effect of the fuselage can also be treated by procedures such as those outlined in references 18 to 21. The experimental data shown at subsonic Mach numbers were obtained from reference 22. It should be remembered that the coefficients presented in the present paper are based on the exposed area of the vertical tail rather than on the area extended to the fuselage center line as is used in many of the references.

Vertical-Tail Loads at High Angles of Attack

Experience has indicated that the methods of calculation used at low angles of attack do not hold throughout the angle-of-attack range because, at high angles of attack, the vertical tail is operating in the disturbed flow field from the wing and fuselage. Any attempt to calculate the tail loads at high angles of attack should be based on an understanding of the flow at the tail.

Flow field at tail.- At subsonic speeds, an idea of the nature of the flow at the location of the vertical tail can be obtained by means of the tuft-grid technique as discussed in references 23 and 24. The setup used in obtaining tuft-grid pictures is illustrated in figure 2. The tail surfaces are removed from the model and replaced by wires to indicate the location of the vertical tail and three possible horizontal-tail locations. The tuft grid is mounted immediately behind the model and is made of closely spaced vertical and horizontal wires with a tuft tied at each intersection. The camera views the tufts from a point on the axis of the tunnel far downstream of the model. If the flow is disturbed, as by a vortex trailing from a wing tip, the tufts will follow the local flow direction and a projection of the tuft will be seen. The orientation of the tuft will give an indication of the local sidewash and downwash.

A tuft-grid picture of the flow behind a model at an angle of attack of 10° and a sideslip angle of 25° is shown in figure 3. The model was painted black so as to make the tufts easier to see, and as a result the model itself is rather indistinct. The heavy white lines are the wires which indicate the location of the vertical tail and three possible horizontal-tail locations. The picture shows the system of vortices from the wing and fuselage. The fuselage vortex was found to originate at the nose of the fuselage.

In this case, a high sideslip angle was chosen so as to make the fuselage vortex more distinct. At smaller sideslip angles, the vortex would be less intense but would also be much closer to the vertical tail. Fuselage vortices have also been shown to exist at supersonic speeds, as shown in references 25 to 27. For these investigations the vapor-screen technique was used to obtain a picture of the flow.

The presence of these vortices at both subsonic and supersonic speeds is not surprising because their strength depends on the crossflow velocity (component of velocity perpendicular to the fuselage axis), and as long as the crossflow Mach number remains subcritical the strength of the vortices and their position would be expected to be relatively independent of Mach number effects.

The effect that a single vortex can have on the distribution of load on the vertical tail is illustrated in figure 4. Above the vortex, the sidewash from the vortex increases the local angles of attack on the vertical tail and thus increases the load. Below the vortex, the reverse is true, and the load is decreased.

Method of calculation.- Any procedure for estimating the effects that the vortices from the wing and fuselage have on the vertical-tail loads at high angles of attack should take into account the effects of all the vortices trailing from the wing and fuselage. It is necessary to know both the position and strength of each vortex.

The system used in this paper (fig. 5), although somewhat arbitrary, was deduced from inspection of tuft-grid and vapor-screen pictures and was selected from among the arrangements tried because it appeared to give reasonable agreement with experiment. It is presented here as an example of the type of vortex system which exists behind some configurations; however, it may not hold for all configurations.

A vortex from each wing was assumed to trail streamwise from the quarter-chord line of the wing. For the calculations in this paper, their lateral positions were judged by inspecting measured span load distributions on a wing of similar plan form. If vapor-screen or tuft-grid pictures of the flow behind the configuration in question are available, it would, of course, be preferable to use the positions indicated in these pictures. For the case of the wing vortices, tuft-grid or vapor-screen pictures at the Mach number in question will probably be necessary to locate accurately the vortices because the stall pattern on the wing and thus the positions of the vortices usually changes appreciably with Mach number. The strength of the vortices was determined from the vortex-lift equation

$$L = \rho V \Gamma l$$

where Γ is the vortex strength and l is the effective span of the wing over which the lift is assumed to be acting.

Two vortices were assumed to be shed by the fuselage and to be positioned as shown in figure 5. They were assumed to trail streamwise from the nose to the point of maximum fuselage cross-sectional area, from which point they were carried back parallel to the axis of the fuselage. This positioning was purely arbitrary but is seen to give reasonable agreement between calculated and measured vertical-tail loads for the configurations investigated. The radial positions of the vortices were determined by the orientation of the crossflow velocity, which is a function of both angle of attack and angle of sideslip, as shown in figure 5. The strength of the fuselage vortices was also determined on the basis of the above vortex-lift equation where, in this case, L is the combined components of the fuselage-alone lift and side force in the crossflow direction and the distance factor l was assumed to be the fuselage diameter.

For this paper, measured wing lift and measured lift and side-force data on the fuselage alone were used in computing the vortex strengths. Other papers which relate to the position and strength of vortices trailing from wing and fuselage shapes are listed as references 23 to 34.

Comparison of calculated and experimental total tail loads.- A comparison of the vertical-tail loads calculated by this procedure with measured loads for a high-wing and a low-wing model is shown in figure 6.

[redacted]

The data presented represent total tail loads as obtained from the difference between tail-on and tail-off tests. The agreement between the calculated and measured data indicates that these variations of total vertical-tail load apparently do result from a system of vortices similar to that assumed, although the strength and/or position of the vortices assumed for the high-wing configuration apparently were not exactly correct.

For these.calculations, the effect of the vertical position of the wing on the sidewash at the vertical tail was accounted for by the procedure of reference 35. References 36 to 38 also give information relative to the effect of wing position on the sidewash at the vertical tail and thus on the tail loads.

As might be expected, the fuselage vortices were found to have the greatest effect on the vertical-tail loads. It would be expected, then, that the shape of the fuselage could also have a significant effect on the sidewash at the tail and thus on the tail loads.

The effect of fuselage shape on the vertical-tail loads is illustrated in figure 7. These data also represent the total tail load as obtained from the difference between tail-on and tail-off tests. Note the extreme variation of tail load for the square-fuselage configuration. This extreme variation is probably due to an appreciable increase in the strength of the vortices shed from the fuselage resulting from the square corners of the fuselage. The corners in this case were not sharp but had a radius of about 10 percent of the fuselage width. Lift data on the square fuselage alone were not available to use in estimating the strength of the fuselage vortices. It was necessary then to estimate the lift of the square fuselage, and this was done by increasing the viscous lift of the round fuselage by the ratio of the drag of a square rod to that of a round rod perpendicular to the wind. The positions of the vortices were assumed to be the same as those for the round fuselage.

The designer seldom has such simple fuselage shapes to deal with, however. A practical fuselage usually provides space and protuberances for such things as air intakes for the engines, radar domes, and the canopy for the pilot. The variation of total tail load with angle of attack for such a complex fuselage shape is also shown in figure 7. Fuselage-alone data were available for this configuration, but apparently there are other factors affecting the strength and/or position of the vortices at the intermediate angles of attack that were not considered.

The low value of vertical-tail load per degree of sideslip at high angles of attack, of course, does not necessarily indicate low overall tail loads because this low level also indicates that the configuration would have poor directional stability and under these conditions large sideslip angles might be expected. As a result, the tail loads at the high angles of attack may be more critical than at the lower angles of attack.

[redacted]

Division of load.- The data presented in figures 1, 6, and 7 represent the total vertical-tail load as determined from the difference between tail-on and tail-off tests and include both the load on the exposed part of the vertical tail and the load that the tail induces on the fuselage. These data are primarily of interest in connection with the stability of the airplane. For structural design the designer also would like to know the division of load between the fuselage and the exposed vertical tail. Recently two models have been instrumented with strain-gage balances in order to obtain some information on the breakdown in load between the exposed tail and the fuselage. One of these models is shown in figure 8. The strain-gage balance installed in the fuselage measured the load on the exposed part of the tail and the root bending moment about the dotted line. The model could be equipped with two alternate horizontal-tail configurations, one on the fuselage center line and one on top of the vertical tail in a T-configuration.

The division of load between the exposed tail and the fuselage for this model with the horizontal tail in the low position is shown in figure 9. The effect of relocating the horizontal tail from the low to the high position is shown in figure 10, and the effective position of the center of pressure of the load on the exposed vertical tail is presented in figure 11. This is referred to as an effective position of the center of pressure because it was obtained by dividing the measured root bending moment by the measured normal force, and, in the case of the high-horizontal-tail configuration, the measured root bending moment of the vertical tail included the rolling-moment couple that the horizontal tail imposes on the vertical tail. These data (figs. 9, 10, and 11) were obtained from tests at sideslip angles of $\pm 4^\circ$.

The calculated division of load between the exposed tail and the fuselage was obtained by calculating the span load distribution over the vertical tail by the procedure of reference 6 and integrating the loading over the appropriate part of the tail span. Contrary to the method of reference 6, wherein the entire fuselage load is estimated, the present paper deals only with the load induced on the fuselage by the vertical tail. The calculations were made, therefore, by assuming that the vertical tail was at an angle of incidence equal to the angle of sideslip and that the fuselage was at zero sideslip.

At the higher angles of attack the local angle-of-attack distribution over the vertical tail was modified by the sidewash from the system of vortices assumed (fig. 5) and the calculated load distribution was modified by a strip-theory analysis. The resulting modified load distribution (similar to fig. 4) was then integrated again over the appropriate percentage of tail span to obtain the division of load (fig. 9). The calculated center-of-pressure travel was also obtained from these calculations (fig. 11). Again the agreement is good, and in particular the calculated center-of-pressure variation indicates that the assumed vortex positions are approximately correct for this model.

Placing the horizontal tail atop the vertical tail (fig. 10) effectively increases the aspect ratio of the vertical tail and thus increases the load on the vertical tail. The estimated increment of vertical-tail load shown was obtained from reference 39 and was added to the angle-of-attack variation throughout the angle-of-attack range. Additional information on the effect of the horizontal tail, in any position, on the vertical-tail loads can be found in references 3, 4, 6 to 9, and 40.

The effect of Mach number in the transonic range on the division of load is illustrated in figure 12. The instrumentation of this model was similar to that for the model shown in figure 8. In general, the effects of Mach number are small, with the exception of the data for an angle of attack of 13°. References 14 and 17 were used in making the calculations shown. In making these calculations the effective aspect ratio of the vertical tail was increased (ref. 17) to account for the end-plate effect of the fuselage.

Horizontal-Tail Loads

Examination of tuft-grid pictures, such as figure 3, indicates that the horizontal tail can also be significantly affected by the system of vortices trailing from the wing and fuselage. In figure 3, the fuselage vortex is in a position to have serious effects on the load on a horizontal tail placed in the middle position. At higher angles of attack, the wing vortices can also have serious effects, because as the angle of attack is increased the wing tips begin to stall, and as the stall progresses the trailing vortices from the wing move in and approach the tail. If, in addition, the airplane is at an angle of sideslip, one tip of the tail moves toward the vortex. The effect that a single vortex can have on the load distribution on the horizontal tail is illustrated by the calculated load distributions in figure 13. The vortex has the greatest effect on the load distribution when it has moved inboard from the tip of the horizontal tail. Inboard of the vortex, the local angles of attack are decreased and the load is reduced. Outboard of the vortex the local angles and the load are increased.

Similar effects are shown in the experimental load distributions and root bending-moment coefficients shown in figure 14. The measured load distributions were obtained with the horizontal tail set at zero incidence. Note the rapid increase in the difference between the root bending-moment coefficient of the right and left semispans of the horizontal tail at the highest angles of attack ($M = 0.8$). This trend is apparently due to the effects of the trailing vortex from the right wing as shown by the measured span load distribution.

At a Mach number of 0.98 these large changes in load are apparently not present in the angle-of-attack range tested, because at this Mach number the stall pattern of the wing has changed and the trailing vortices from the wing have not moved in. References 31, 32, 41, and 42 also deal with the problem of asymmetric loads on the horizontal tail or the effects of trailing vortices. There are other factors, such as the fuselage vortices and the load that the vertical tail induces on the horizontal tail, that are affecting the measured load distribution shown in figure 14. These factors were not considered in the calculated load distributions shown in figure 13.

CONCLUDING REMARKS

Some of the effects of angle of attack, sideslip, Mach number, and airplane configuration on the vertical-tail loads and, to a lesser extent, horizontal-tail loads have been discussed. In addition, the division of load between the exposed vertical tail and the fuselage has also been considered. It has been shown that at low angles of attack, in both the subsonic and supersonic speed ranges, adequate predictions of the vertical-tail loads can be made. At angles of attack at which the flow begins to separate from the wing and fuselage, however, large rolled-up vortices appear in the flow in the region of the tail assembly and large changes in both vertical- and horizontal-tail loads result.

It has been shown that the effects of these vortices on the tail loads can be calculated if the strength and position of all vortices are known. For practical configurations with their complex fuselage shapes, however, it appears that, at present, some type of flow-visualization studies to indicate the vortex positions and some indication of the loads on the fuselage to estimate the vortex strength are necessary in order to estimate the tail loads.

REFERENCES

1. Zimmerman, Charles H.: Recent Stability and Aerodynamic Problems and Their Implications as to Load Estimation. (Prospective NACA paper.)

2. Weil, Joseph, Gates, Ordway B., Jr., Banner, Richard D., and Kuhl, Albert E.: Flight Experience of Inertia Coupling in Rolling Maneuvers. (Prospective NACA paper.)

3. Queijo, M. J., and Riley, Donald, R.: Calculated Subsonic Span Loads and Resulting Stability Derivatives of Unswept and 45° Sweptback Tail Surfaces in Sideslip and in Steady Roll. NACA TN 3245, 1954.

4. Riley, Donald R.: Effect of Horizontal-Tail Span and Vertical Location on the Aerodynamic Characteristics of an Unswept Tail Assembly in Sideslip. NACA Rep. 1171, 1954. (Supersedes NACA TN 2907.)

5. Lyons, D. J., and Bisgood, P. L.: An Analysis of the Lift Slope of Aerofoils of Small Aspect Ratio, Including Fins, With Design Charts for Aerofoils and Control Surfaces. R. & M. No. 2308, British A.R.C., 1945.

6. Wiley, Harleth G., and Riley, Donald R.: An Experimental and Theoretical Investigation at High Subsonic Speeds of the Effects of Horizontal-Tail Height on the Aerodynamic Characteristics in Sideslip of an Unswept, Untapered Tail Assembly. NACA RM L53J19, 1953.

7. Wiley, Harleth G., and Moseley, William C., Jr.: An Investigation at High Subsonic Speeds of the Pressure Distributions on a 45° Sweptback Vertical Tail in Sideslip With and Without a 45° Sweptback Horizontal Tail Located on the Fuselage Center Line. NACA RM L54H23, 1954.

8. Wiley, Harleth G., and Moseley, William C., Jr.: Investigation at High Subsonic Speeds of the Pressure Distribution on a 45° Sweptback Vertical Tail in Sideslip With a 45° Sweptback Horizontal Tail Mounted at 50-Percent and 100-Percent Vertical-Tail Span. NACA RM L54I08, 1954.

9. Wiley, Harleth G., and Moseley, William C., Jr.: An Investigation at High Subsonic Speeds of the Effects of Horizontal-Tail Height on the Aerodynamic and Loading Characteristics in Sideslip on a 45° Sweptback, Untapered Tail Assembly As Determined From Force Tests and Integrated Vertical-Tail Span Loadings. (Prospective NACA paper.)

10. Bobbitt, Percy J.: Theoretical Calculations of the Lateral Stability Derivatives for Triangular Vertical Tails With Subsonic Leading Edges Traveling at Supersonic Speeds. NACA TN 3240, 1954.

11. Martin, John C., and Malvestuto, Frank S., Jr.: Theoretical Force and Moments Due to Sideslip of a Number of Vertical Tail Configurations at Supersonic Speeds. NACA TN 2412, 1951.

12. Malvestuto, Frank S., Jr.: Theoretical Supersonic Force and Moment Coefficients on a Sideslipping Vertical- and Horizontal-Tail Combination With Subsonic Leading Edges and Supersonic Trailing Edges. NACA TN 3071, 1954.

13. Margolis, Kenneth: Theoretical Calculations of the Pressures, Forces, and Moments Due to Various Lateral Motions Acting on Thin Isolated Vertical Tails With Supersonic Leading and Trailing Edges. NACA TN 3373, 1955.

14. DeYoung, John, and Harper, Charles W.: Theoretical Symmetric Span Loading at Subsonic Speeds for Wings Having Arbitrary Plan Form. NACA Rep. 921, 1948.

15. Polhamus, Edward C.: A Simple Method of Estimating the Subsonic Lift and Damping in Roll of Sweptback Wings. NACA TN 1862, 1949.

16. Margolis, Kenneth, and Bobbitt, Percy J.: Theoretical Calculations of the Stability Derivatives at Supersonic Speeds for a High-Speed Airplane Configuration. NACA RM L53G17, 1953.

17. Queijo, M. J., and Wolhart, Walter D.: Experimental Investigation of the Effect of Vertical-Tail Size and Length and of Fuselage Shape and Length on the Static Lateral Stability Characteristics of a Model with 45° Sweptback Wing and Tail Surfaces. NACA Rep. 1049, 1951. (Supersedes NACA TN 2168.)

18. Michael, William H., Jr.: Investigation of Mutual Interference Effects of Several Vertical-Tail—Fuselage Configurations in Sideslip. NACA TN 3135, 1954.

19. Zlotnick, Martin, and Robinson, Samuel W., Jr.: A Simplified Mathematical Model for Calculating Aerodynamic Loading and Downwash for Wing-Fuselage Combinations With Wings of Arbitrary Plan Form. NACA TN 3057, 1954. (Supersedes NACA RM L52J27a.)

20. Robinson, Samuel W., Jr., and Zlotnick, Martin: A Method for Calculating the Aerodynamic Loading on Wing—Tip-Tank Combinations in Subsonic Flow. NACA RM L53B18, 1953.

21. Lawrence, H. R., and Flax, A. H.: Wing-Body Interference at Subsonic and Supersonic Speeds – Survey and New Developments. Jour. Aero. Sci., vol. 21, no. 5, May 1954, pp. 289-324.

22. Kuhn, Richard E., and Wiggins, James W.: Static Lateral Stability Characteristics of a $\frac{1}{10}$ - Scale Model of the X-1 Airplane at High Subsonic Mach Numbers. NACA RM L51F01a, 1951.

23. Bird, John D., and Riley, Donald R.: Some Experiments on Visualization of Flow Fields Behind Low-Aspect-Ratio Wings by Means of a Tuft Grid. NACA TN 2674, 1952.

24. Michael, William H., Jr.: Flow Studies in the Vicinity of a Modified Flat-Plate Rectangular Wing of Aspect Ratio 0.25. NACA TN 2790, 1952.

25. Seiff, Alvin, Sandahl, Carl A., Chapman, Dean R., Perkins, E. W., and Gowen, F. E.: Aerodynamic Characteristics of Bodies at Supersonic Speeds. A Collection of Three Papers. NACA RM A51J25, 1951.

26. Perkins, Edward W., and Kuehn, Donald M.: Comparison of the Experimental and Theoretical Distributions of Lift on a Slender Inclined Body of Revolution at $M = 2$. NACA RM A53E01, 1953.

27. Allen, H. Julian, and Perkins, Edward W.: Characteristics of Flow Over Inclined Bodies of Revolution. NACA RM A50L07, 1951.

28. Bollay, William: A Non-Linear Wing Theory and Its Application to Rectangular Wings of Small Aspect Ratio. Z.f.a.M.M., Bd. 19, Nr. 1, Feb. 1939, pp. 21-35.

29. Brown, Clinton E., and Michael, William H., Jr.: On Slender Delta Wings With Leading-Edge Separation. NACA TN 3430, 1955.

30. Spreiter, John R.: Downwash and Sidewash Fields Behind Cruciform Wings. NACA RM A51L17, 1952.

31. Rogers, Arthur W.: Application of Two-Dimensional Vortex Theory to the Prediction of Flow Fields Behind Wings of Wing-Body Combinations at Subsonic and Supersonic Speeds. NACA TN 3227, 1954.

32. Lomax, Harvard, and Byrd, Paul F.: Theoretical Aerodynamic Characteristics of a Family of Slender Wing-Tail-Body Combinations. NACA TN 2554, 1951.

33. Landahl, Mårten T.: Analysis of Some Wing-Body-Vertical Tail Interference Problems for Non-Symmetric Steady Flow Using Slender-Body Theory. KTH-Aero TN 32, Roy. Inst. of Tech., Div. of Aero. (Stockholm, Sweden), 1953.

34. Spahr, J. Richard: Longitudinal Aerodynamic Characteristics to Large Angles of Attack of a Cruciform Missile Configuration at a Mach Number of 2. NACA RM A54H27, 1954.

35. Goodman, Alex, and Thomas, David F., Jr.: Effects of Wing Position and Fuselage Size on the Low-Speed Static and Rolling Stability Characteristics of a Delta-Wing Model. NACA TN 3063, 1954.

36. Multhopp, H.: Aerodynamics of the Fuselage. NACA TM 1036, 1942.

37. House, Rufus O., and Wallace, Arthur R.: Wind-Tunnel Investigation of Effect of Interference on Lateral-Stability Characteristics of Four NACA 23012 Wings, an Elliptical and a Circular Fuselage, and Vertical Fins. NACA Rep. 705, 1941.

38. Goodman, Alex: Effects of Wing Position and Horizontal-Tail Position on the Static Stability Characteristics of Models With Unswept and 45° Sweptback Surfaces With Some Reference to Mutual Interference. NACA TN 2504, 1951.

39. Brewer, Jack D., and Lichtenstein, Jacob H.: Effect of Horizontal Tail on Low-Speed Static Lateral Stability Characteristics of a Model Having 45° Sweptback Wing and Tail Surfaces. NACA TN 2010, 1950.

40. Katzoff, S., and Mutterperl, William: The End-Plate Effect of a Horizontal-Tail Surface on a Vertical-Tail Surface. NACA TN 797, 1941.

41. Braun, Winfried: Asymmetric Tailplane Loads Due to Sideslip. Tech. Note No. Structures 81, British R.A.E., Jan. 1952.

42. Cooney, T. V.: The Unsymmetrical Load and Bending Moment on the Horizontal Tail on a Jet-Powered Bomber Measured in Sideslipping Flight. NACA RM L51J24, 1952.

[redacted]

[redacted]

[redacted]

TOTAL VERTICAL-TAIL LOADS AT SMALL ANGLES OF ATTACK

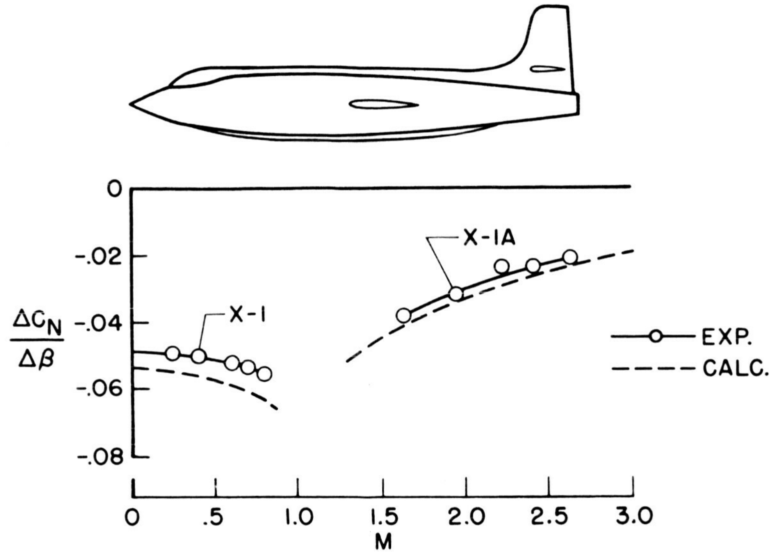

Figure 1

SETUP FOR FLOW SURVEY WITH TUFT GRID

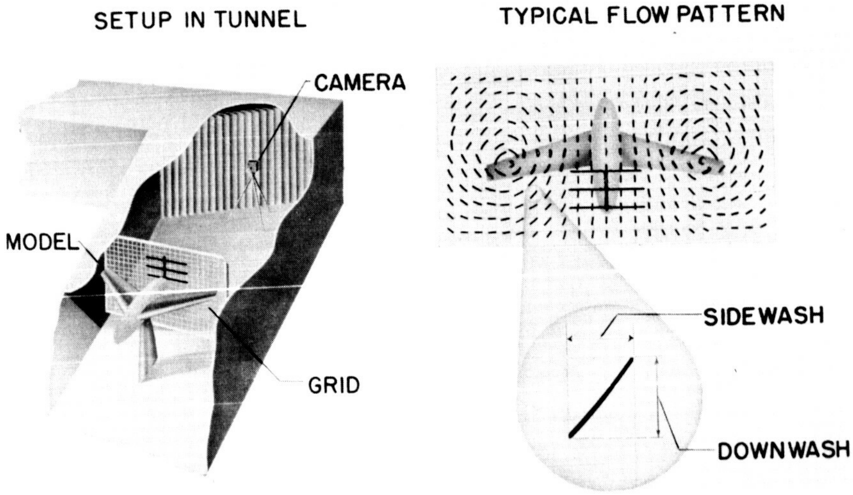
SETUP IN TUNNEL

TYPICAL FLOW PATTERN

Figure 2

[redacted]

[redacted]

FLOW FIELD BEHIND MODEL
$\alpha = 10°$; $\beta = 25°$

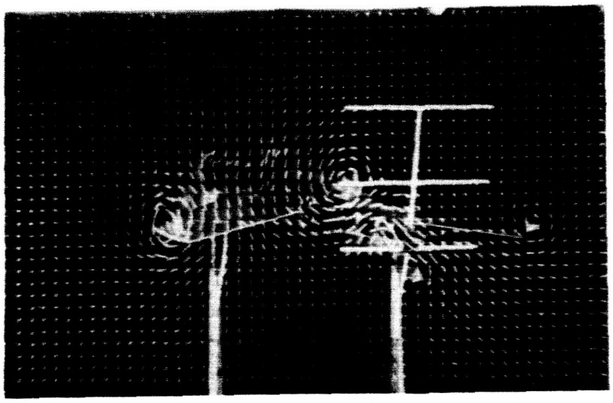

Figure 3

EFFECT OF FUSELAGE VORTEX ON VERTICAL-TAIL LOAD DISTRIBUTION

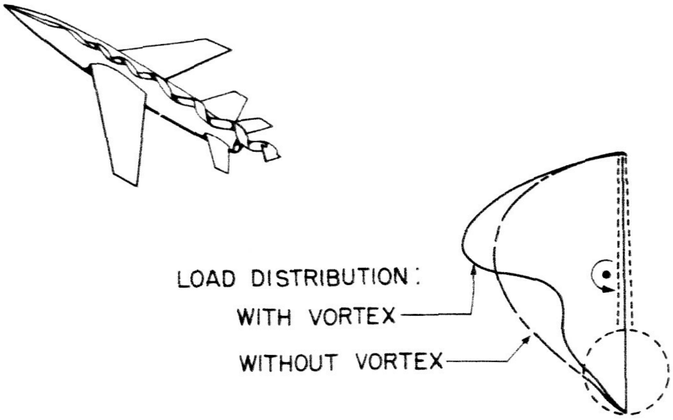

Figure 4

[redacted]

[redacted]

[redacted]

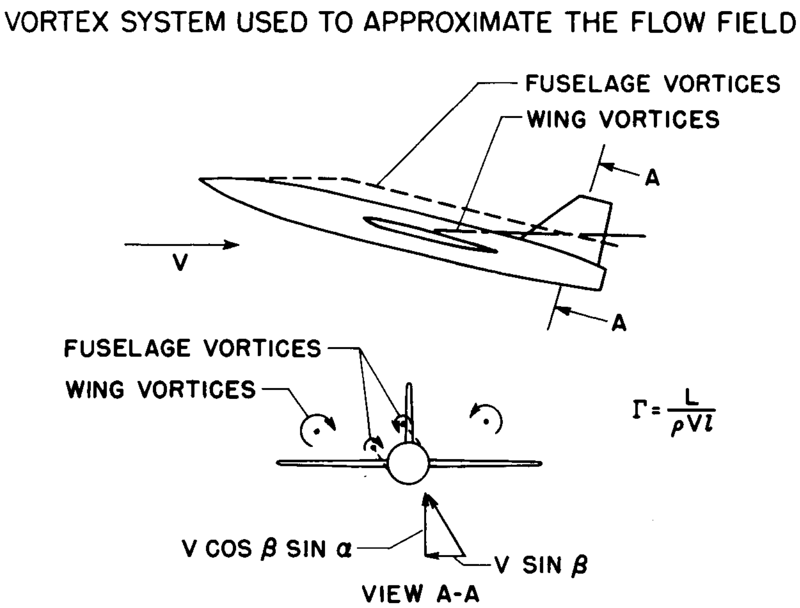

Figure 5

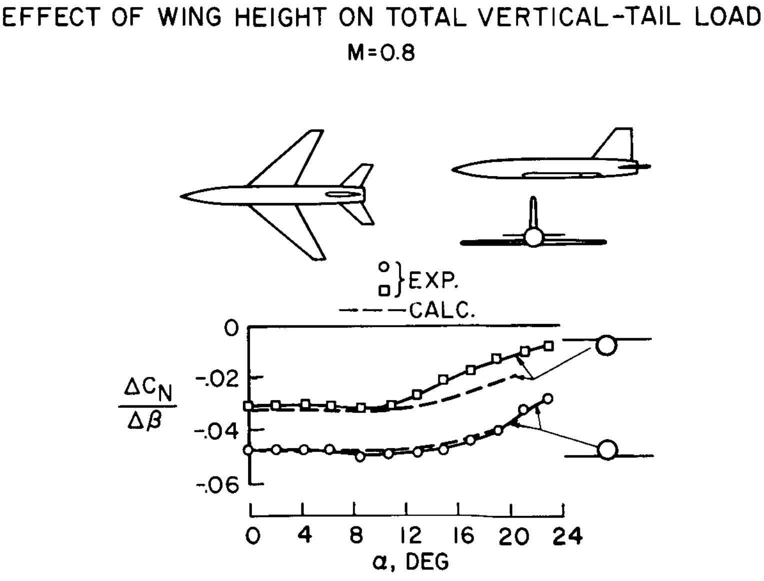

Figure 6

[redacted]

[redacted]

EFFECT OF FUSELAGE SHAPE

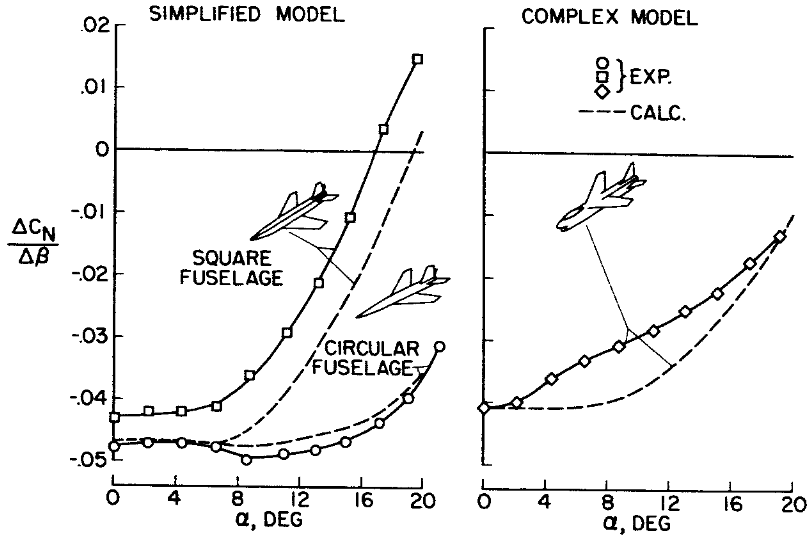

Figure 7

MODEL USED IN INVESTIGATIONS OF LOAD ON EXPOSED VERTICAL TAIL

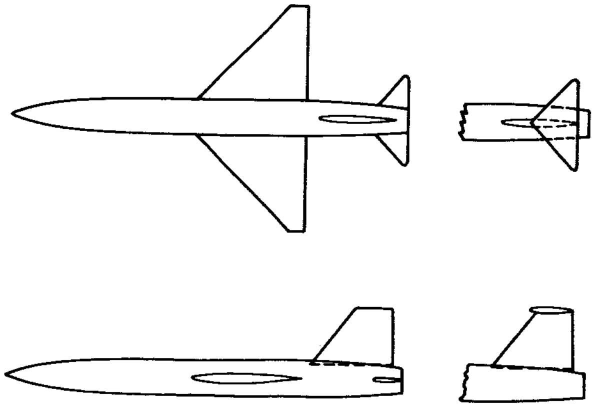

Figure 8

[redacted]

[redacted]

COMPARISON OF TOTAL VERTICAL—TAIL LOAD AND LOAD ON EXPOSED TAIL

M = 0.80 ; LOW HORIZONTAL TAIL

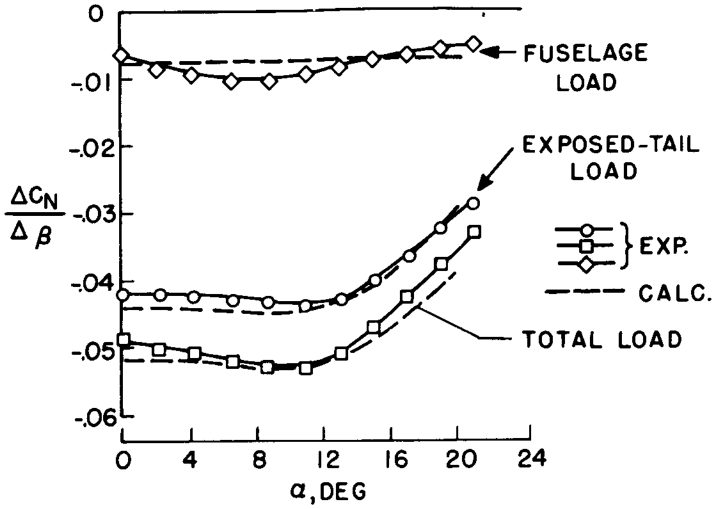

Figure 9

EFFECT OF HORIZONTAL-TAIL POSITION ON EXPOSED-VERTICAL-TAIL LOAD

M = 0.8

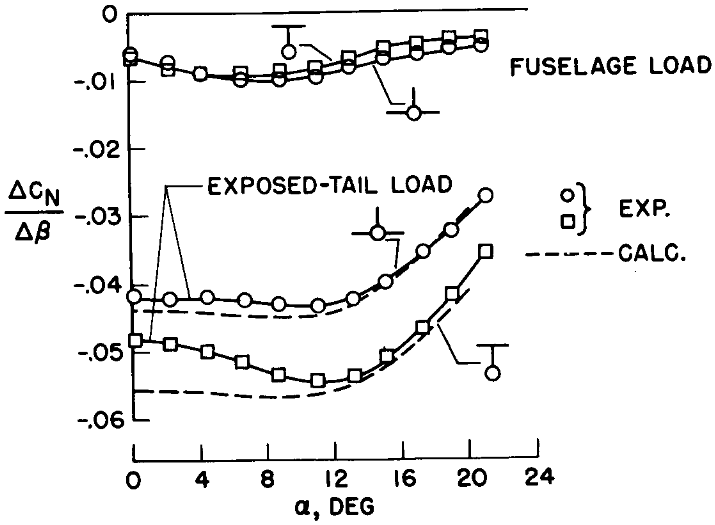

Figure 10

[redacted]

EFFECTIVE SPANWISE POSITION OF LOAD ON EXPOSED TAIL

M = 0.80

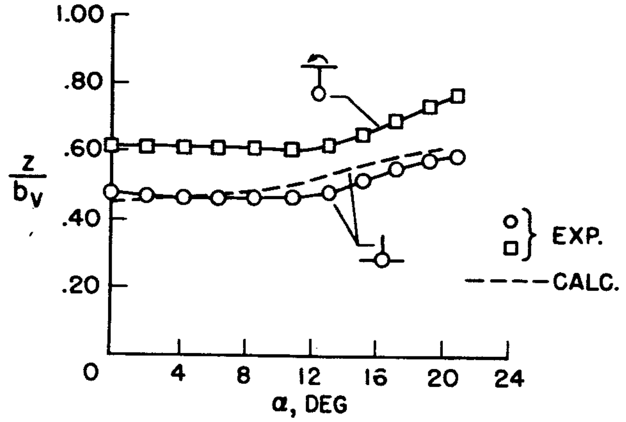

Figure 11

EFFECT OF MACH NUMBER ON TAIL LOAD

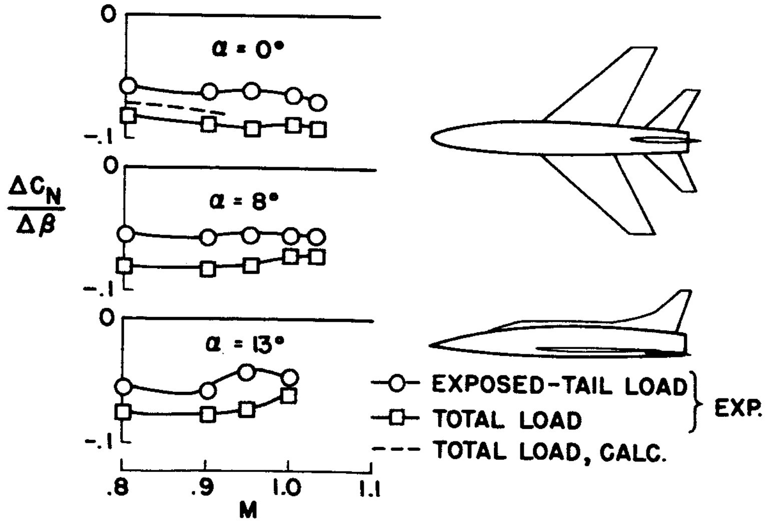

Figure 12

[redacted]

WING-VORTEX EFFECT ON HORIZONTAL-TAIL LOAD DISTRIBUTION
CONSTANT TOTAL LOAD

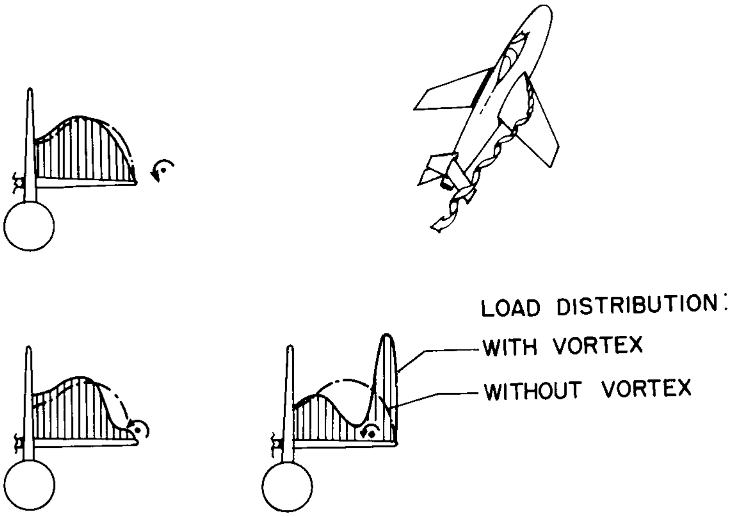

Figure 13

HORIZONTAL-TAIL LOADS IN SIDESLIP
$\beta = 5°$

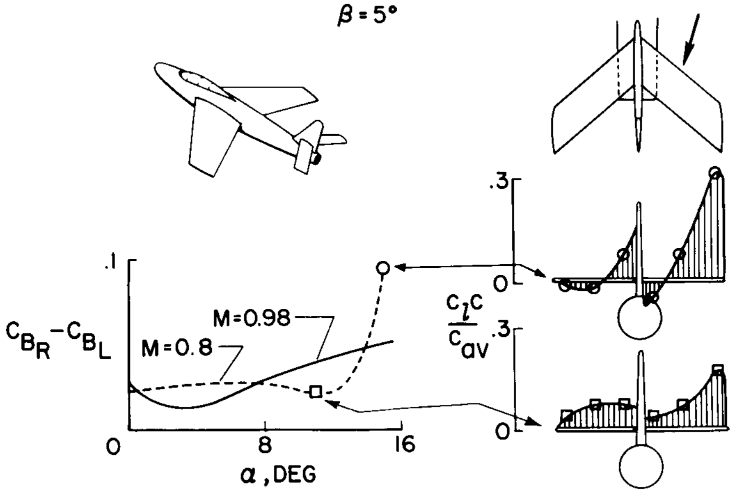

Figure 14

[redacted]

[redacted]ASSIFIED

A REEVALUATION OF GUST-LOAD STATISTICS FOR APPLICATIONS IN SPECTRAL CALCULATIONS

By Harry Press

Langley Aeronautical Laboratory

INTRODUCTION

During the last 20 years, a considerable body of statistical data on the gust and load experience of airplanes in transport operations and in special flight tests has been collected by the National Advisory Committee for Aeronautics. These data have, in the past, for simplicity been reduced on the basis of simple airplane gust-response theory and the so-called "effective gust velocities" determined. In the last few years, it has been considered desirable to redefine these gust velocities in order to account more fully for the variations with altitude in the airplane response to gusts. The term "derived gust velocities" (ref. 1) has been applied to these redefined values and the conversion of the gust data into this form is now largely completed (see, for example, refs. 2, 3, and 4). Some new results obtained in the conversion of thunderstorm gust data into this form, which are of current interest, are included in the appendix of this paper. The gust data in this form have been analyzed in detail, and the airplane gust experience for various types of operations and for various flight altitudes and weather conditions have been established (ref. 5). These results are finding useful application in the calculation of gust loads for arbitrary flight plans.

Even more recently, it has been desirable in many gust-response problems both to account explicitly for the continuous character of atmospheric turbulence and to account in greater detail for the airplane dynamics. For this purpose, the techniques of generalized harmonic analysis or spectrum analysis appear particularly appropriate and they are finding increasing application (refs. 6 to 16). The application of these techniques to the gust-load design problem requires detailed information on the spectral characteristics of atmospheric turbulence. The purpose of this paper is to describe the information available on the spectral characteristics of atmospheric turbulence and, in particular, to adapt the large amount of statistical data on gust loads already available into a form suitable for use in spectral calculations. First, the available measurements of the spectrum of atmospheric turbulence will be reviewed. Then, a technique for the reevaluation of the gust statistics is outlined and some results obtained by the application of this technique are presented.

[redacted]

SPECTRAL CHARACTERISTICS OF ATMOSPHERIC TURBULENCE

Figure 1 contains a summary of most of the available airplane measurements of the power spectrum of atmospheric turbulence. The first of these measurements was made by Clementson at the Massachusetts Institute of Technology (ref. 6) and subsequent measurements were made by the National Advisory Committee for Aeronautics (refs. 10 and 11), the Douglas Aircraft Company, Inc. (ref. 12), and Summers at the Massachusetts Institute of Technology (ref. 13). The curves shown represent the various power spectra and were obtained under different weather conditions. The abscissa is the frequency argument Ω which has the dimensions of radians per foot and is equal to 2π divided by λ, the gust wavelength. (The data shown cover a range of gust wavelengths from about 10 feet to 3,000 feet.) The ordinate is the power density normalized to the power-density values at $\Omega = 0.01$. This normalized ordinate is used in order to facilitate comparison of the various spectral shapes.

The spectra in all but one case are for the vertical component of the turbulence. In one case marked by the letter H, the spectrum is for the horizontal or longitudinal component of turbulence. Examination of these results indicates that the spectral shapes appear relatively consistent; in all cases, the power decreases rapidly with increasing frequency. In fact, in most cases, the spectra appear inversely proportional to the square of the frequency. This spectral shape of $1/\Omega^2$ is in reasonable agreement with theoretical results obtained for the spectral shape at the higher frequencies in the theory of isotropic turbulence. At the lower frequencies, the situation is not so clear, few measurements being available for frequencies of $\Omega < 0.005$. Some additional measurements obtained at the Cornell Aeronautical Laboratory (ref. 16) do cover these lower frequencies and indicate a flattening of the spectrum in this frequency region.

In addition to these variations in spectral shape, the various measurements also differed in turbulence intensity. The individual root-mean-square values are estimated to vary from roughly 1.5 to perhaps 4 feet per second, which, as will be seen, represent the relatively lighter levels at atmospheric turbulence.

Another source of information on the spectral characteristics of atmospheric turbulence is the measurements made by meteorologists at the lower altitudes from towers. A large number of such spectral measurements have now been obtained. A few representative measurements from reference 17 are shown in figure 2 and were obtained at an elevation of about 300 feet and for various conditions of average wind speed V as shown in figure 2. These measurements extend to lower frequencies (longer gust wavelengths) than the available airplane measurements. At the higher frequencies these results approximate the same $1/\Omega^2$ form characteristic of the airplane measurements. In addition, at the lower frequencies, a definite tendency toward a flattening of the spectra can be noted. The variation in the spectrum intensity with wind speed should also be noted.

Because of the general characteristics of these spectral measurements, it has been convenient in theoretical studies to use the following analytical expression for the turbulence spectrum

$$\Phi(\Omega) = \sigma_U{}^2 \frac{L}{\pi} \frac{1 + 3\Omega^2 L^2}{(1 + \Omega^2 L^2)^2} \tag{1}$$

where $\Omega = 2\pi/\lambda$ and λ is the gust wavelength. This expression has been useful in wind-tunnel studies of turbulence and, as will be seen, has the general characteristics of the measured spectra of atmospheric turbulence. The equation has two parameters, the mean-square gust velocity $\overline{\sigma_U{}^2}$ which describes the overall intensity, and the so-called scale of turbulence L which, in a rough sense, can be considered to be proportional to the average eddy size. Curves for this expression are shown in figure 3 for values of L of 200, 600, and 1,000 feet. At higher frequencies, these curves all approach a shape of $1/\Omega^2$ but differ in the frequency at which the flattening occurs. For increasing values of L, the curves flatten out at lower frequencies. Comparison of these curves with those of figures 1 and 2 and other measurements of the spectrum for atmospheric turbulence has suggested that representative values of L for atmospheric turbulence are at least several hundred feet to over 1,000 feet.

For design purposes, the overall gust experience in operations is of concern. Presumably, the overall experience consists of various exposure times to each of the spectra shown in figures 1 and 2 as well as to other spectra associated with different weather conditions. It thus appears important to determine the proportion of flight time spent under these various conditions of turbulence. In the remainder of this paper, some results derived from available gust statistics on this problem will be described. The basic approach used is described in detail in reference 14 and will only be outlined for present purposes.

[redacted]

RELATIONS BETWEEN PEAK COUNTS AND SPECTRA

It will be recalled that available gust-load statistical data are normally given in the form of counts of acceleration peaks exceeding given values. It is therefore necessary to relate such peak counts to the spectra of the turbulence. For this purpose, it appears necessary and reasonable to make some simplifying assumptions. First, it will be assumed that the turbulence for a given weather condition is a Gaussian process. This assumption implies that the turbulent velocity fluctuations and also the airplane response for linear systems have a normal or Gaussian probability distribution; this distribution appears from available measurements to be a reasonable approximation. The Gaussian character for the turbulent velocity fluctuations for a given weather condition will be used as a building block to construct the operational load history which covers many weather conditions and, in the overall, is far from a simple Gaussian process. Secondly, it appears necessary to make some simplifying assumptions on the form of the power spectrum of the gust velocity. On the basis of the available measurements, it appears reasonable to assume that the spectral form is given by equation (1). These assumptions and available relations between peak counts and spectra for the Gaussian case provide the basis for the analysis to be presented.

Homogeneous case.- For a Gaussian process $y(t)$, the number of peak (maxima) values $N(y)$ per second exceeding given values (for large values of y) is given by the following relation (ref. 18)

$$N(y) = \frac{1}{2\pi}\left[\frac{\int_0^\infty \omega^2\Phi(\omega)\,d\omega}{\int_0^\infty \Phi(\omega)\,d\omega}\right]^{1/2} e^{-y^2/2\sigma^2} \qquad (2)$$

where

y a random variable

ω frequency, radians/sec

$\Phi(\omega)$ power spectrum of y

σ root-mean-square value of y

When this relation is applied to the acceleration history of an airplane in homogeneous turbulence, the spectrum of normal acceleration for a

[redacted]

linear system is, in turn, related to the spectrum of atmospheric turbulence by the relation

$$\Phi_a(\omega) = \Phi_U(\omega)T^2(\omega) \tag{3}$$

where $\Phi_a(\omega)$ and $\Phi_U(\omega)$ are the power spectra of the normal acceleration and vertical gust velocity, respectively, and $T(\omega)$ is the amplitude of the airplane acceleration response to unit sinusoidal gusts encountered at frequency ω. Equations (2) and (3) thus relate the number of peak accelerations per second exceeding given values to the spectrum of the turbulence. When these relations are applied to an airplane in flight through turbulence of a given spectrum (which in the present application can be considered to be given by equation (1)), the number of peak accelerations per second exceeding given values of acceleration a, as illustrated by the sketch on the upper left of figure 1, may be expressed as

$$N(a) = N_0 e^{-a^2/2\sigma_a{}^2} \tag{4}$$

where

$$N_0 = \frac{1}{2\pi}\left[\frac{\int_0^\infty \omega^2\Phi_U(\omega)T^2(\omega)\,d\omega}{\int_0^\infty \Phi_U(\omega)T^2(\omega)\,d\omega}\right]^{1/2} \tag{4a}$$

When equation (1) is substituted for $\Phi_U(\omega)$ in equation (4a), the quantity N_0 may be seen to depend upon the value of L, the scale of turbulence, and the airplane transfer function but is readily seen to be independent of the turbulence intensity or root-mean-square gust velocity. Thus, for a given airplane and a given value of L, N_0 is a constant independent of turbulence intensity. The quantity N_0 has the dimensions of a frequency and can be considered to be a characteristic frequency of the airplane response to the given turbulence. In addition, the number of peaks $N(a)$ is seen from equation (3) to depend also on the acceleration level a and the root-mean-square acceleration σ_a which, as will be seen, depends directly on the turbulence intensity.

Composite case.- So far, the turbulence has been assumed to be homogeneous and Gaussian. Now, if the airplane is assumed to fly for given flight times t_1, t_2, and t_3 through turbulence of different intensities but of the same spectral form, the acceleration histories for each flight time would differ in intensity or in root-mean-square acceleration value as indicated by the sketches on the lower left of figure 4. Equation (4) may be extended for this composite case in order to obtain the overall average number of peaks exceeding given values as follows:

$$N(a) = N_0\left[\frac{t_1}{t_T} e^{-a^2/2\sigma_{a_1}{}^2} + \frac{t_2}{t_T} e^{-a^2/2\sigma_{a_2}{}^2} + \frac{t_3}{t_T} e^{-a^2/2\sigma_{a_3}{}^2}\right] \tag{5}$$

where

$$t_T = t_1 + t_2 + t_3$$

Equation (4) is essentially a sum of terms of the form of equation (4) weighted by the relative exposure times $\frac{t_1}{t_T}$, $\frac{t_2}{t_T}$, and $\frac{t_3}{t_T}$.

Continuous case.- If the airplane is now assumed to encounter turbulence of all intensities (continuous variations in the root-mean-square gust velocity) but of the same spectral shape (fixed value of L for present applications), equation (4) may be extended for the continuous case to yield the following relation

$$N(a) = N_0 \int_0^\infty f(\sigma_a) e^{-a^2/2\sigma_a{}^2} d\sigma_a \tag{6}$$

In this case the sum of the terms of equation (5) becomes a continuous integral. The expression for the continuous case contains the same characteristic frequency N_0, which is independent of the turbulence intensity, the same exponential term as the earlier expressions but, in addition, contains the function $f(\sigma_a)$. This function is the counterpart of the ratios $\frac{t_1}{t_T}$, $\frac{t_2}{t_T}$, and $\frac{t_3}{t_T}$ in equation (5) and is the probability distribution of σ_a which can be considered to define the proportion of total flight time spent at values of σ_a between σ_a and $\sigma_a + d\sigma_a$. A sketch of $f(\sigma_a)$ is shown in figure 5. The total area under the curve is, of course, equal to one with the percentage of the total time between any two values given by the area under the curve between the two values as indicated by the hatched area.

Equation (6) relates the probability distribution of the root-mean-square acceleration to the overall number of peak accelerations per second. Since gust-load statistical data are usually summarized in the form of number of peak accelerations per unit time (or distance) exceeding given values, this relation may be used to determine the appropriate distribution of the root-mean-square acceleration $f(\sigma_a)$ from the available data without recourse to the reevaluation of the original records.

For a given airplane, the root-mean-square acceleration is also simply related to the root-mean-square gust velocity. This relation may be expressed simply as

$$\sigma_a = \bar{A}\sigma_U \tag{7}$$

where $\bar{A}$ may be considered a transfer function between root-mean-square gust velocity and root-mean-square acceleration and for a given case is a constant depending upon the gust spectrum and the airplane response characteristics. For the gust spectrum used in the present analysis, $\bar{A}$ is given by the following integral

$$\bar{A} = \left[\frac{L}{\pi}\int_0^\infty \frac{1 + 3\Omega^2L^2}{\left(1 + \Omega^2L^2\right)^2} T^2(\Omega)\,d\Omega\right]^{1/2} \tag{8}$$

The value of $\bar{A}$ for this case is seen to depend only upon the value of L and the airplane transfer function. Thus, the root-mean-square values of acceleration for a given airplane and a given value of L may be used directly to determine the root-mean-square gust velocities.

Equation (7) may be applied directly to determine the distribution of root-mean-square gust velocity for a given distribution of root-mean-square acceleration. The relation between these distributions is given by

[redacted]

$$\hat{f}(\sigma_U) = \bar{A}f(\sigma_a) \tag{9}$$

where $\sigma_a = \bar{A}\sigma_U$. Thus, the final result desired, the distribution of the root-mean-square gust velocity, may be obtained by the solution of equation (6) for $f(\sigma_a)$ and the application of equation (9).

These relations can, of course, also be used to calculate the number of peak loads for a given operation, if the probability distribution of the root-mean-square gust velocity $f(\sigma_U)$ is known. In terms of the distribution of root-mean-square gust velocity, the number of peak accelerations per second exceeding given values is given by

$$N(a) = N_o\int_0^\infty \hat{f}(\sigma_U)e^{-(\bar{A}a)^2/2\sigma_U^2}d\sigma_U \tag{10}$$

where N_o is given by equation (4a). Thus, in this approach, the probability distribution of the root-mean-square gust velocity is the fundamental quantity and takes the place in spectral calculations of the counts of gust peaks used in the discrete gust calculations.

SOME RESULTS OBTAINED IN THE REEVALUATION OF GUST DATA

In this section, the results obtained by the application of the relations derived in the preceding section to available statistical data on gust loads are presented. Three principal problems are encountered in such applications and involve the choice of an appropriate value of the scale of turbulence L, the determination of the airplane acceleration transfer function for gusts $T(\omega)$ (or more particularly, the value of $\bar{A}$), and the determination of the value of the characteristic frequency N_o. The value of L chosen for present purposes was 1,000 feet which, on the basis of available data, appears to be a reasonable estimate for an average value for atmospheric turbulence. In the determination of the airplane transfer function and the values of $\bar{A}$ for the various airplanes involved, the airplane accelerations were assumed to be due entirely to the vertical gusts and the airplane was assumed to respond in vertical motion only (no pitch, rigid-body condition). A justification for this restriction to the one-degree-of-freedom response for this purpose is given in reference 14. Finally, it was found simple and expedient to obtain good estimates of the characteristic frequency N_o directly from the flight records of acceleration for the various airplanes in accordance with the method gi[redacted]ence 14.

2V

Variation with type of operation.- In reference 14, the foregoing techniques were applied to derive estimates of the distribution of root-mean-square gust velocity $f(\sigma_U)$ from data for eight transport operations. As might be expected, little difference was noted in this distribution for similar types of operation. A distinctive difference was noted, however, between the results for a feeder-line low-altitude operation and the normal higher altitude transport operations, as might be expected. The results obtained for the feeder-line operation and one of the more normal transport operations are compared in figure 6 in order to illustrate the type of variations in the distribution. The feeder-line operation consisted of short-haul, low-altitude flights over the rough terrain in the western part of the United States and was known to spend much time in rough air. The other operation was a four-engine transcontinental operation mostly flown at moderate altitude and was known to be a relatively smooth operation. In each case, the results are shown for a range of values of σ_U from 0 to 20 feet per second. Since the individual gust peaks in rough air of a given root-mean-square value can be three or four times the root-mean-square value, the results shown cover peak gust velocities up to perhaps 80 feet per second.

The curves both indicate a rapid decrease in the probability with increasing root-mean-square value. It is clear that the transcontinental operation includes more time at very low values of σ_U, less time at the moderate values of σ_U, and perhaps more time at the very large values of σ_U. However, since the proportion of flight time between given root-mean-square values is given by areas under the curves, the significant areas are distorted by the logarithmic plot and direct comparison of the curves is made difficult. For this reason, the significant points obtained from these curves are summarized in the table on the upper right-hand side of figure 6. The table gives the percent flight time for the two operations in smooth air $(\sigma_U < 1$ foot per second), and in moderate to severe rough air $(\sigma_U > 5$ feet per second). The table clearly indicates that the transcontinental operation is a much smoother operation with almost twice the percentage time of the feeder-line operation in smooth air and only about one-eighth the percentage time in moderate to severe turbulence. At the very high values of root-mean-square gust velocity, there is some indication that the transcontinental operation may encounter very severe turbulence, associated with the more violent thunderstorms, more frequently than the feeder-line operation. The time above 20 feet per second is small, however, being only about 1/100,000 of the total flight time.

The description of the gust experience in this form is directly applicable to load calculations for other airplanes in similar types of operation by reversing the procedures used in obtaining these results. However, direct application of these results would only apply to operations having the same type of flight plan. In order to obtain results

[redacted]

that are more flexible and applicable to arbitrary flight plans, it would be desirable to determine the variations in these distributions with altitude, weather condition, and perhaps geography. Efforts in this direction are being made.

Variation with altitude.- In order to arrive at some rough estimates of the variation of $\hat{f}(\sigma_U)$ with altitude, use was made of the summary of gust statistics given in reference 5. Figure 6 of reference 5 presents estimates of the average gust experience at various altitudes that are representative of contempory types of transport operations. In order to estimate the associated distributions of root-mean-square gust velocity, these results which are in terms of derived gust velocities were, for convenience, first converted to accelerations by using the characteristics of a representative transport airplane. The charts of reference 14 were then used to estimate the appropriate distribution form and scale value for the root-mean-square gust velocity. It was found that, for each altitude bracket, the number of peak accelerations for the various altitude brackets could be approximated by the following distributions for $\hat{f}(\sigma_U)$:

$$\hat{f}(\sigma_U) = \frac{1}{1.8} e^{-\sigma_U/1.8}$$

for the altitude bracket of 0 to 10,000 feet,

$$\hat{f}(\sigma_U) = \frac{1}{2(0.34)^2} e^{-\sqrt{\sigma_U}/0.34}$$

for the altitude bracket 10,000 to 40,000 feet, and

$$\hat{f}(\sigma_U) = \frac{1}{2(0.31)^2} e^{-\sqrt{\sigma_U}/0.31}$$

for the altitude bracket 40,000 to 50,000 feet. These distributions are shown in figure 7.

The results in figure 7 indicate that, except for the lowest altitude bracket, little difference exists in the distribution of σ_U

[redacted]

at the higher altitudes. Perhaps the most important points, which are obscured by the logarithmic scale, are the relatively large amount of time spent at essentially smooth air ($\sigma_U < 1$ foot per second) at the higher altitudes and the relatively large amount of time spent in moderate to severe turbulence ($\sigma_U > 5$ feet per second) at the lowest altitude bracket. The time spent above 5 feet per second for the lowest altitude bracket is roughly five times as great as that for the higher altitude bracket.

It should be remembered that these results are in terms of true gust velocity. If equivalent gust velocities which are more directly related to the airplane response are used, the decrease in turbulence intensity with altitude would, of course, be even more pronounced than is indicated here.

As a check on the consistency of these results, the acceleration histories were calculated for two hypothetical operations, a moderate-altitude transport operation and a high-altitude operation perhaps representative of jet transport operations. In the calculation of the value of $\overline{A}$, theoretical results for a single degree of freedom (vertical motion only) (ref. 9) were used. The results obtained in this manner were roughly equivalent to those obtained by discrete gust calculations which would be expected for this single-degree-of-freedom case.

The method of application of these results to the calculation of load histories for arbitrary flight plans is parallel to that used for the discrete gust case described in reference 5. The sequence of steps involves: (1) The appropriate distribution of $\hat{f}(\sigma_U)$ is selected for each altitude bracket. (2) The values of $\overline{A}$ are determined for each significant portion of the flight plan in accordance with equation (8). (3) Each of the distributions of $\hat{f}(\sigma_U)$ are transformed in order to obtain the associated distributions of acceleration $f(\sigma_a)$ by the relation

$$f(\sigma_a) = \frac{1}{\overline{A}} \hat{f}(\sigma_U)$$

where

$$\sigma_U = \sigma_a / \overline{A}$$

(4) The values of N_0 are determined in accordance with equation (4a) or directly from flight records as described in reference 14. It should be noted that the value of N_0 [redacted] for the one-degree-of-freedom

[redacted]

case treated in reference 9 and therefore the results obtained in that analysis cannot be used for this purpose without some modification. For a rigid airplane, the value of N_0 appears to be larger but of the same order as the period of the longitudinal short-period oscillation. (5) The distributions of σ_a and the values of N_0 are then used in equation (6) to derive the number of peak accelerations per second or per mile for each condition. (These calculations can be facilitated by the use of charts such as given in ref. 14.) (6) The results obtained in step 5 are then weighted in accordance with the flight distance in each condition and then summed for all conditions in order to obtain the overall acceleration history.

Variation with weather condition.- In the preceding discussion, the variation in the gust experience with flight altitude was considered. Another breakdown of the gust experience which may be useful in some problems is the variation in gust experience with weather conditions. Figure 8 shows estimates of the variations in $\hat{f}(\sigma_U)$ that have been obtained for several types of turbulent weather conditions. The curve labeled "clear air turbulence" was based on data obtained in flight through clear and turbulent air at the lower altitudes. The curve labeled "cumulus clouds" was based on data obtained in flight under moderate convective conditions such as represented by bulging cumulus clouds. Finally, the curve labeled "thunderstorms" was based on data obtained in flight in the immediate vicinity and within severe thunderstorms. The distributions obtained appear to have the same general form but are seen to vary widely in intensity. A simple measure of the relative intensity of the turbulence for these conditions may be obtained by comparing the root-mean-square values at the lower probability levels. It will be noted that, at these probability levels, the values for the cumulus and thunderstorm conditions are roughly twice and three times the values of σ_U for the clear-air condition.

It has been estimated that contemporary transport operations spend about 10 percent of their flight time in this clear-air turbulence condition, 1 percent in the cumulus condition, and perhaps 0.05 percent in thunderstorms. These results may therefore find some application in evaluating the effects on the overall load experience of operational procedures which would tend to modify this weather experience. For example, the introduction of airborne radar for weather avoidance may be expected to reduce the exposure time to the severe turbulence conditions of thunderstorms. Also, high rates of climb and descent through the lower and more turbulent altitude layers may cause a drastic reduction in the 10 percent of the flight time attributed to clear-air-turbulence conditions and thereby cause a marked reduction in the overall gust experience.

[redacted]

CONCLUDING REMARKS

The foregoing analysis has served to demonstrate that the gust statistics may, under reasonable assumptions, be converted into a form appropriate for spectral-type calculations. The significant and fundamental quantity, for this purpose, appears to be the probability distribution of the root-mean-square gust velocity. The results obtained in defining the variations of this function with type of operation, flight altitude, and weather condition provide at least a starting basis for their application to response calculations in arbitrary operations. These results should serve to supplement the discrete-gust techniques in current use and be particularly appropriate in problems requiring a more detailed accounting for the airplane dynamics than is possible by discrete-gust techniques.

APPENDIX

VARIATION WITH ALTITUDE OF DERIVED GUST VELOCITIES IN THUNDERSTORMS

Because of the current interest in the gust standards for the higher altitudes, some results obtained on the variation with altitude of the intensity of turbulence in thunderstorms are appended to this paper. The available data on gust velocities in thunderstorms have, in the past (ref. 19), been presented in terms of effective gust velocities. As a result of the recent redefinition of the gust-response factor and the gust velocity (ref. 1) in order to account more fully for variations in the airplane response with altitude, it was of interest to determine what effect these changes might have on the indicated variation of turbulence intensity with altitude. The gust data obtained from the 2 years of flight operation of the U. S. Weather Bureau Thunderstorm Project and the earlier XC-35 airplane investigations have consequently been reevaluated and the "derived gust velocities" determined for each flight altitude. These data were summarized in order to obtain the average flight miles required to exceed given derived gust velocities for each of the flight altitudes. The overall results obtained on the variation of the turbulence intensity with altitude are summarized in figure 9. As a simple measure of the relative intensity of the turbulence at the various altitudes, the quantity used for the abscissa is the gust velocity exceeded once, on the average, in a given number of flight miles. The actual number of miles used for each of these sets of data shown in figure 9 was varied in order to obtain velocities that were of about the same magnitude for the three sets of data. The actual numbers used were about 100 miles for the Thunderstorm Project data and 25 miles for the XC-35 airplane data. The variations in gust velocity with altitude for other values of flight miles were essentially similar.

The solid points on the left-hand side of figure 9 are for the effective gust velocities U_e whereas the unshaded points on the right-hand side are for the corresponding "derived gust velocities" U_{de}. At the highest altitude (32,000 feet), two points each are shown for the U_e and U_{de} values. In each case, the point on the left represents all the flight data for the XC-35 airplane tests for this altitude. These results, however, cover some flight time in clear air and cirrus-cloud conditions, as indicated in reference 19. The points on the right were, therefore, obtained by considering only the data associated with thunderstorms. These points were based on 54 miles of flight test data out of the total of 117 miles flown in this altitude range.

Faired lines are shown in each case but because of the small amount of data and the uncertainty of the results at the highest altitude, the faired lines are dashed [redacted]eet. It may be seen that the

U_{de} values are in the overall about 50 to 60 percent higher than the corresponding U_e values at each altitude, the amount of increase varying somewhat with altitude - the smallest increase being at the highest altitude. Thus, the principal effect of the conversion is a substantial increase in the gust velocities. The variations with altitude have also, as can be seen, changed somewhat, with the U_{de} results showing a tendency to decrease with altitude above 20,000 feet.

[redacted]

REFERENCES

1. Pratt, Kermit G.: A Revised Formula for the Calculation of Gust Loads. NACA TN 2964, 1953.

2. Walker, Walter G.: Summary of Revised Gust-Velocity Data Obtained From V-G Records Taken on Civil Transport Airplanes From 1933 to 1950. NACA TN 3041, 1953.

3. Coleman, Thomas L., and Walker, Walter G.: Analysis of Accelerations, Gust Velocities, and Airspeeds From Operation of a Twin-Engine Transport Airplane on a Transcontinental Route From 1950 to 1952. NACA TN 3371, 1955.

4. Coleman, Thomas L., Copp, Martin R., Walker, Walter G., and Engel, Jerome N.: An Analysis of Accelerations, Airspeeds, and Gust Velocities From Three Commercial Operations of One Type of Medium-Altitude Transport Airplane. NACA TN 3365, 1955.

5. McDougal, Robert L., Coleman, Thomas L., and Smith, Philip L.: The Variation of Atmospheric Turbulence With Altitude and Its Effect on Airplane Gust Loads. NACA RM L53G15a, 1953.

6. Clementson, Gerhardt C.: An Investigation of the Power Spectral Density of Atmospheric Turbulence. Ph.D. Thesis, M.I.T., 1950.

7. Liepmann, H. W.: An Approach to the Buffeting Problem From Turbulence Considerations. Rep. No. SM-13940, Douglas Aircraft Co., Mar. 13, 1951.

8. Press, Harry, and Mazelsky, Bernard: A Study of the Application of Power-Spectral Methods of Generalized Harmonic Analysis to Gust Loads on Airplanes. NACA Rep. 1172, 1954. (Supersedes NACA TN 2853.)

9. Fung, Y. C.: Statistical Aspects of Dynamic Loads. Jour. Aero. Sci., vol. 20, no. 5, May 1953, pp. 317-330.

10. Press, Harry, and Houbolt, John C.: Some Applications of Generalized Harmonic Analysis to Gust Loads on Airplanes. Jour. Aero. Sci., vol. 22, no. 1, Jan. 1955, pp. 17-26.

11. Chilton, Robert G.: Some Measurements of Atmospheric Turbulence Obtained From Flow-Direction Vanes Mounted on an Airplane. NACA TN 3313, 1954.

12. Connor, Roger J., Hawk, John, and Levy, Charles: Dynamic Analyses for the C-47 Airplane Gust Load Alleviation System. Rep. No. SM-14456, Douglas Aircraft Co., July 29, 1952.

[redacted]

13. Summers, Robert A.: A Statistical Description of Large-Scale Atmospheric Turbulence. Sc. D. Thesis, M.I.T., 1954. (Also Rep. T-55, Instrumentation Lab., M.I.T.)

14. Press, Harry, Meadows, May T., and Hadlock, Ivan: Estimates of Probability Distribution of Root-Mean-Square Gust Velocity of Atmospheric Turbulence From Operational Gust-Load Data by Random-Process Theory. NACA TN 3362, 1955.

15. Diederich, Franklin W.: The Dynamic Response of a Large Airplane to Continuous Random Atmospheric Disturbances. Preprint No. 548, S.M.F. Fund Paper, Inst. Aero. Sci., Jan. 24-27, 1955.

16. Lappi, V. O., and Turner, W. N.: An Investigation of Airplane Accelerations Due to Large-Scale Turbulence and of the Power Spectral Densities of the Turbulence. Rep. No. CAL-41, Cornell Aero. Lab., Inc., Mar. 20, 1952.

17. Panofsky, H. A.: Statistical Properties of the Vertical Flux and Kinetic Energy at 100 Meters. Scientific Rep. No. 2 (Contract No. AF 19(604)-166), Division of Meteorology, Pa. State College, July 1, 1953.

18. Rice, S. O.: Mathematical Analysis of Random Noise. Pts. III and IV, Bell Syst. Tech. Jour., vol. XXIV, no. 1, Jan. 1945, pp. 46-156.

19. Tolefson, H. B.: An Analysis of the Variation With Altitude of Effective Gust Velocity in Convective-Type Clouds. NACA TN 1628, 1948.

[redacted]

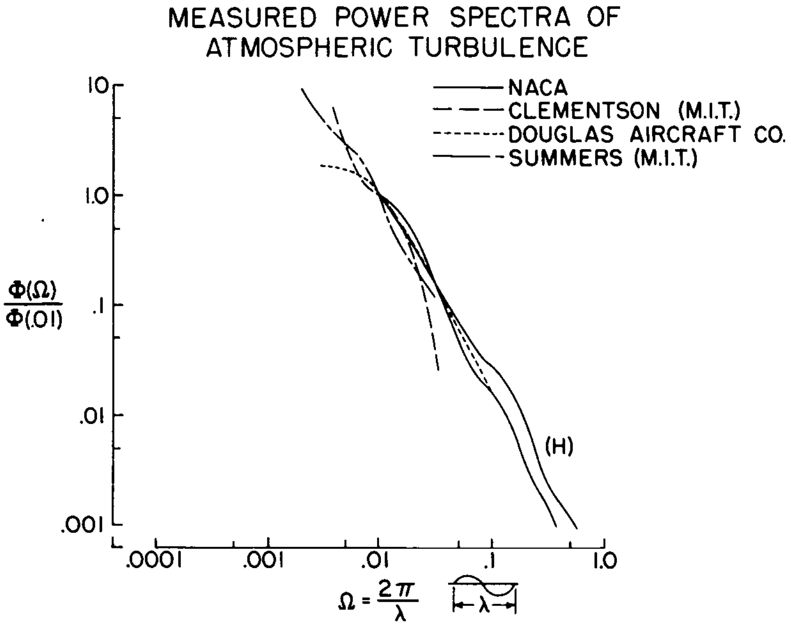

Figure 1

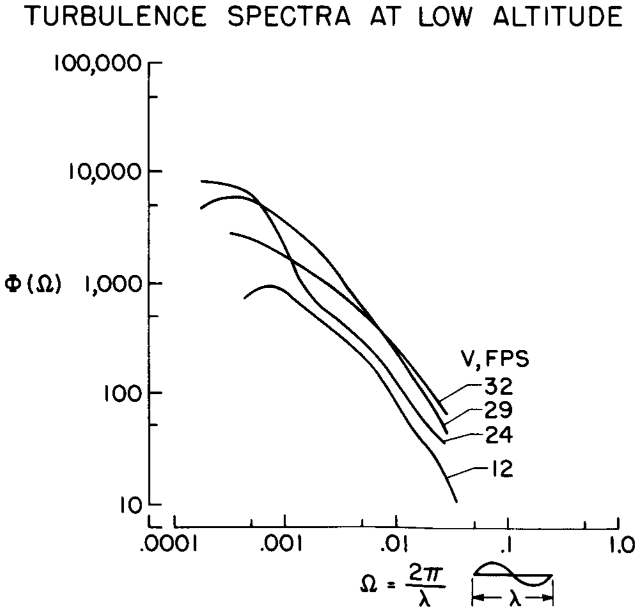

Figure 2

[redacted]

[redacted]

[redacted]

ANALYTIC REPRESENTATION OF TURBULENCE SPECTRA

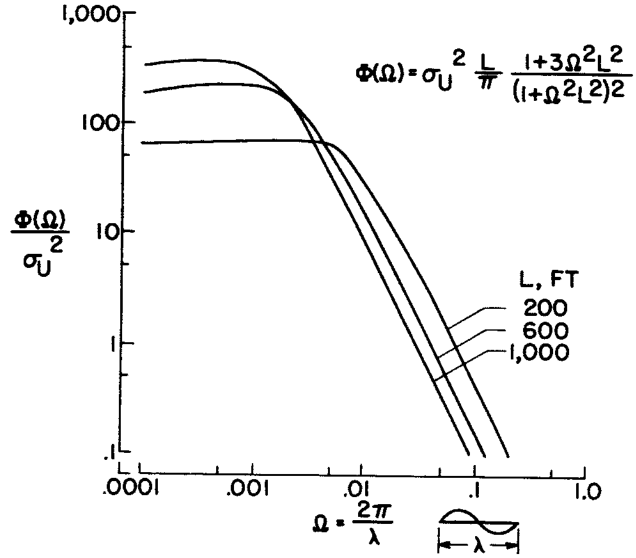

Figure 3

BASIC RELATIONS

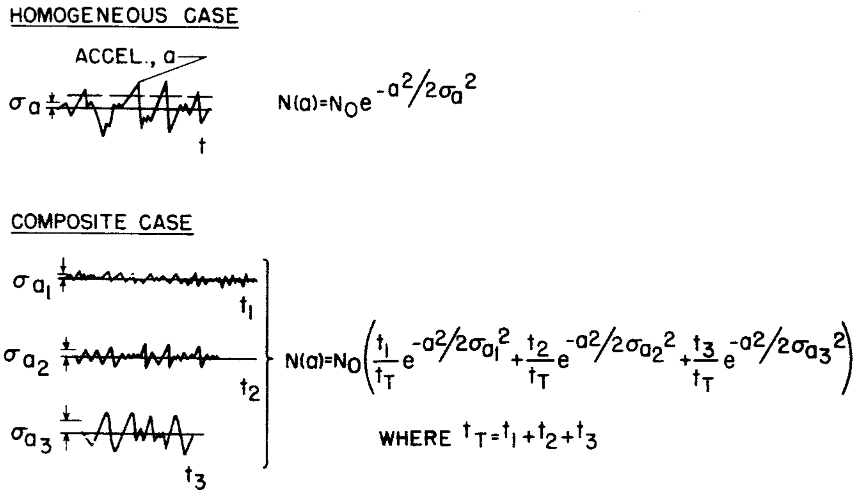

$$N(a)=N_0e^{-a^2/2\sigma_a^2}$$

$$N(a)=N_0\left(\frac{t_1}{t_T}e^{-a^2/2\sigma_{a_1}^2}+\frac{t_2}{t_T}e^{-a^2/2\sigma_{a_2}^2}+\frac{t_3}{t_T}e^{-a^2/2\sigma_{a_3}^2}\right)$$

WHERE $t_T=t_1+t_2+t_3$

Figure 4

[redacted]

[redacted]

BASIC RELATIONS

CONTINUOUS CASE

$$N(a) = N_0 \int_0^{\infty} f(\sigma_a)\, e^{-a^2/2\sigma_a^2}\, d\sigma_a$$

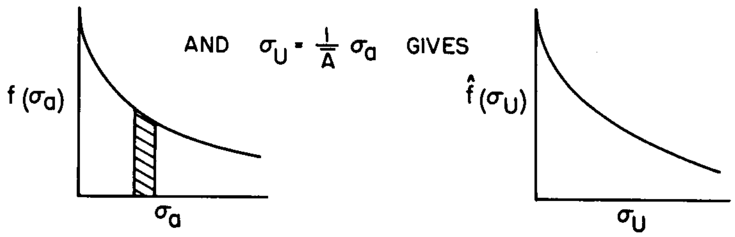

Figure 5

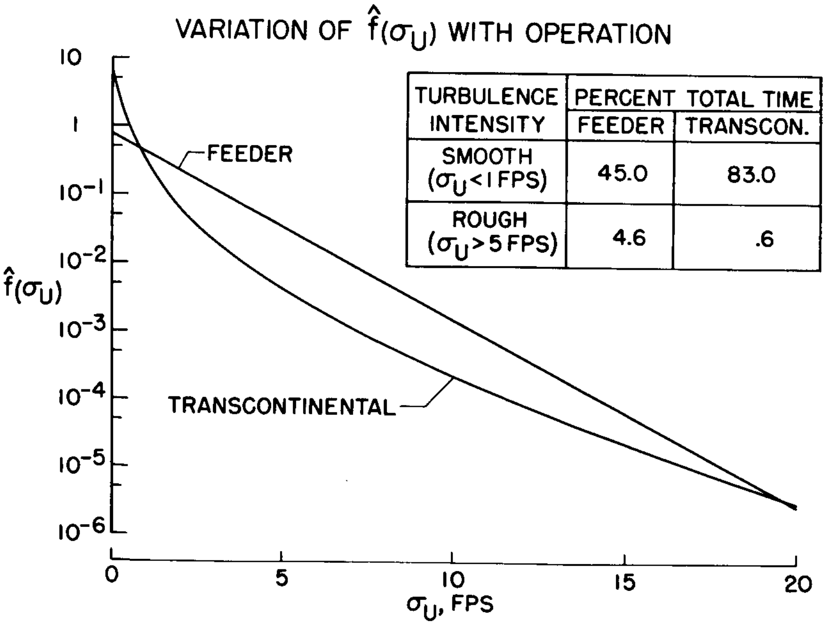

TURBULENCE INTENSITY	PERCENT TOTAL TIME	
	FEEDER	TRANSCON.
SMOOTH (σ_U<1 FPS)	45.0	83.0
ROUGH (σ_U>5 FPS)	4.6	.6

Figure 6

[redacted]

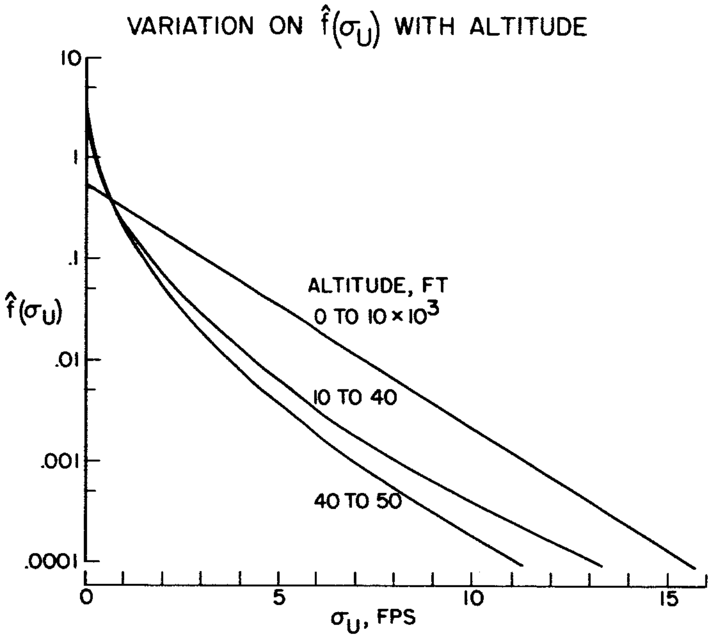

Figure 7

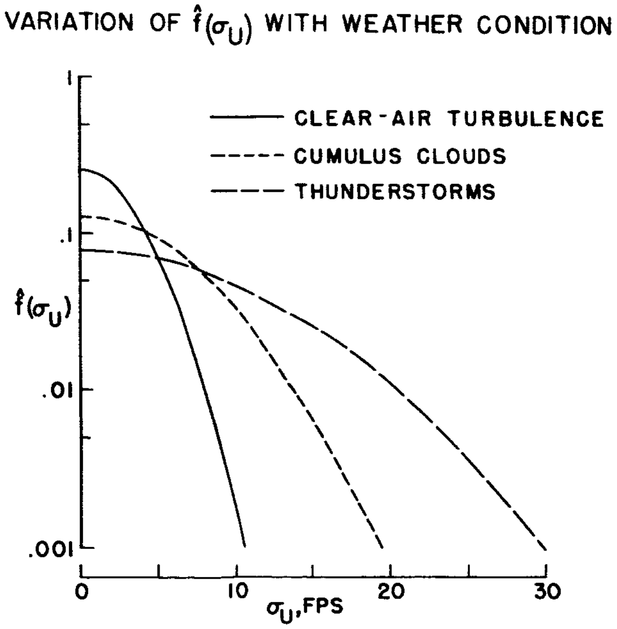

Figure 8

[redacted]

[redacted]

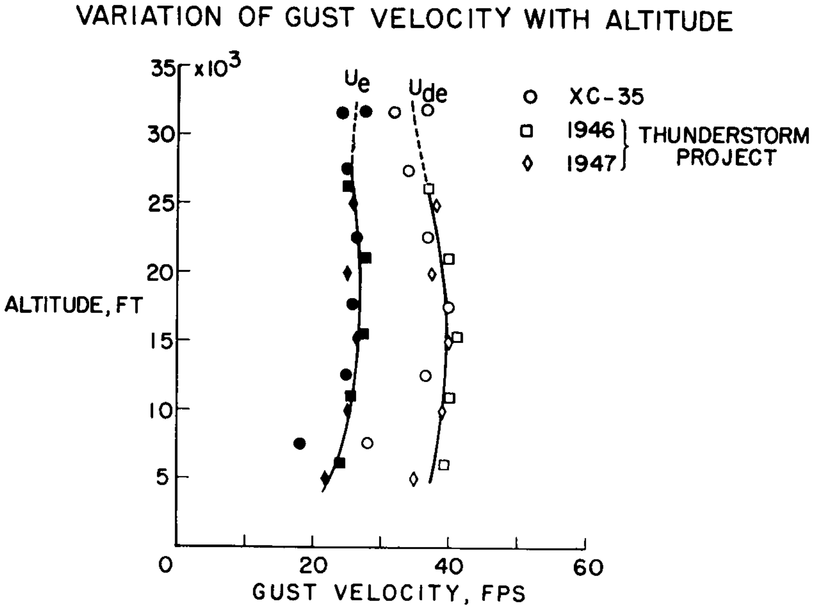

Figure 9

[redacted]

A DISCUSSION OF GUST LOADS AS INFLUENCED BY THE STABILITY OF THE AIRPLANE

By Clarence L. Gillis

Langley Aeronautical Laboratory

INTRODUCTION

Studies of aircraft motions in rough air, and the resulting loads, have received continuing attention at the NACA. The material presented herein does not represent one integrated study of such problems, but very briefly describes recent progress on several phases of the problem, which can generally be considered as dealing with the effects of airplane stability, both static and dynamic. Effects of changes in airplane characteristics, flight conditions, the addition of auxiliary damping, and the inclusion of more complete airplane dynamics and gust inputs are being investigated.

All of the studies included herein have utilized the method of generalized harmonic analysis to investigate loads in continuous rough air. Since many other recently published investigations (refs. 1 to 4) have used the same method, it is assumed that the method is fairly well known and requires no further explanation.

DISCUSSION

Previous limited experience (ref. 1) indicated that the normal-acceleration loads in rough air would be affected to only a small extent by the airplane static stability in the usual range, but would be greatly affected by the damping. Further extensive analytical studies are in progress to ascertain the validity of these conclusions over wide ranges of airplane stability characteristics and flight conditions.

A typical chart resulting from this study is shown in figure 1. The study is being made utilizing five nondimensional parameters involving turbulence scale, airplane geometry, damping and frequency, a mass parameter, and a root-mean-square acceleration ratio. For illustration purposes these have been converted to dimensional quantities in figure 1. The data shown are for an airplane having a wing loading of 48 lb/sq ft, a chord of 10 ft, and a wing plan form represented by the lift-curve slope of 5.0 per radian. The flight conditions are 400 mph at sea level and a turbulence scale, defined by the symbol L in the input spectrum,

GILLIS

of 1,000 ft. The values plotted are root-mean-square normal acceleration for a root-mean-square vertical gust velocity of 10 ft/sec. They are shown as a function of damped natural frequency of the short-period mode for various values of the time to damp to one-half amplitude. Note that the frequency scale is logarithmic. The handling-qualities requirement of damping to one-tenth amplitude in one cycle is shown by the long-dashed line with values to the left being satisfactory. The calculations include values in the unsatisfactory region but these are not shown in the figure for simplicity. It might be noted that when the damping is small a frequency of 0.2 cps represents a static margin of about 1 percent $\bar{c}$ whereas a frequency of 1.0 cps represents a static margin of about 30 percent $\bar{c}$ for this airplane. Thus, for purposes of this discussion, the region around a frequency of 0.5 cps is of primary interest. The results show that variations in static stability have relatively small effects on the normal accelerations whereas variations in time to damp have much larger effects. The same trends occur for all values of mass parameter included in the study and for all turbulence scales except the smallest.

The short-dashed line in figure 1 is the acceleration calculated for vertical motion only (ref. 2), and of course is independent of the stability. For well-damped airplanes the effect of adding freedom in pitch is to obtain an alleviation of normal accelerations, but for poorly damped airplanes the accelerations are amplified. The study showed that this effect becomes more pronounced as the mass parameter and turbulence-scale parameter increase.

Experimental data have been obtained, by means of rocket-propelled models flown in continuous rough air, which confirm these conclusions, at least qualitatively, and indicate the validity of the calculation method for several configurations (refs. 5 and 6). Shown in figure 2 are experimental and calculated root-mean-square normal accelerations for three swept-wing configurations over a Mach number range from about 0.8 to slightly over 1.0. These tests were made at essentially sea-level altitude so that this Mach number range includes a corresponding velocity range. All models had the same wing, and one was tailless, one had a conventional tail, and one a canard surface. The results shown have been corrected to the same wing loading and the same turbulence intensity. Shown also are the stability characteristics in terms of undamped natural frequency (dashed lines) and time to damp to one-half amplitude. The fact that the frequency for the tailless model is roughly twice as great as for the other two models means that the static margin is roughly four times as great; however, there is little difference in the general level of measured or calculated normal accelerations. It might be noted that in addition to the expected increases in calculated accelerations with Mach number caused by the increased velocity and lift-curve slope, the curves follow rather faithfully the changes in damping with Mach number, including the more rapid increase for the tailless model than for the other two, and the downward hook at high Mach numbers for the tailless and canard models.

Within the scatter of the experimental data, it can be said that the calculated and measured results are in fair agreement. The scatter is caused primarily by the inherent statistical errors resulting when only small data samples are available for analysis. In figure 3 are shown results for a tailless delta-wing model. This model had cruciform wings, and accelerations were measured normal to each set of wings. Making use of the assumption of isotropic turbulence, the accelerations measured in both planes over any given time interval can be considered together in the data-reduction procedure, which effectively doubles the sample size and increases the statistical reliability. Calculated damping and frequency are shown as obtained from wind-tunnel oscillation test data and the blank space around $M = 1.0$ is caused by lack of pitch-damping data in this region for the small amplitudes required. A sharp reduction in pitch damping above a Mach number of 0.9 is reflected in increased damping time and root-mean-square acceleration. The experimental data again show fair agreement with the calculated curves except for the highest point which indicates a greater rise at a lower Mach number than the calculated curve. This one test point is the average value obtained over a time interval while the model was decelerating from a Mach number of about 0.95 to 0.85 and thus includes the accelerations experienced at the higher Mach numbers where the damping is poor. Lack of suitable turbulence conditions at Wallops Island delayed the rocket-model flight test intended to obtain some experimental data at Mach numbers up to 2.0 on this configuration for comparison with the calculations shown.

Since the results discussed so far indicate that the short-period damping is of primary importance in determining the root-mean-square normal accelerations, the question arises as to how much benefit might be derived from adding auxiliary damping to the airplane by means of an automatic control system. An analytical investigation of this problem has been conducted (ref. 7) and the results are shown in figure 4. A large swept-wing airplane was used for the calculations, which were made at Mach numbers of 0.9, 1.0, and 1.1 at sea level using transonic wind-tunnel data on this configuration. Again, this change in Mach number includes a corresponding change in velocity. The calculations used two degrees of freedom of the rigid airplane and included the dynamics of the control system. The control system was actuated by signals proportional to pitching velocity as obtained from a rate gyro. The results are shown as root-mean-square values of normal acceleration, pitch angle, and elevator deflection. Introducing the auxiliary damping resulted in a reduction of about 25 percent in normal accelerations and about 75 percent in pitch angles. The indications are that even if all the pitching motion were removed only a little additional reduction in load could be realized. These reductions in normal acceleration and pitch angle were accomplished with root-mean-square elevator deflections varying from 0.3° at a Mach number of 0.9 to about 0.8° at a Mach number of 1.1. The rather small elevator deflections required at $M = 0.9$ suggests the possibility that any flexibility or play in the elevator control system which

[redacted]

permitted uncontrolled motions of this order of magnitude could result in significant increases or decreases in load depending on the phase relation between this motion and the airplane motion.

The subject of lateral motions and the resulting loads on airplanes in continuous rough air have received less attention in the past than have longitudinal motions. Some work is underway, however. Figure 5 illustrates an experimental and analytical investigation that has been made of the vertical tail loads on a jet-bomber-type airplane. This airplane has lightly damped directional oscillation characteristics. The power spectral density of the tail loads is plotted for one particular set of flight conditions. The calculations considered two degrees of freedom, yawing, and sideslipping, but neglected rolling effects. It was assumed that the vertical tail was the only component producing any lift or moment. The calculations (solid line) indicate a very sharp peak at the natural frequency which is characteristic of lightly damped systems. The experimental power estimates also show a peak at the natural frequency but this peak is much less sharp owing to the necessarily finite width of the effective filter applied to the experimental data in the data-reduction process. When the calculated curve was modified to include the effects of the experimental filter, as indicated by the dashed curve, the agreement between experiment and calculation was considerably better. It will be noted that the calculated root-mean-square load is about 20 percent less than the experimental value. This is due to the fact that the input turbulence scale was derived from fluctuating airspeed measurements, and theoretical considerations indicate that for the turbulence scale and the frequency range of importance here the lateral gust velocities which produce these tail loads will be about 20 percent greater than the longitudinal gust velocities which were used to obtain the input for the calculations.

Neglecting the rolling motion was apparently a valid approximation for the case just shown. For more recent and future airplane designs, which generally will have higher roll-to-yaw ratios, it may not be justifiable to neglect rolling motions. Complete three-degree-of-freedom lateral-response calculations will be required and a method for accomplishing this is currently being investigated.

CONCLUDING REMARKS

In summary, a number of investigations are underway, both experimentally and analytically to investigate effects of stability, flight conditions, and configuration changes on gust loads resulting from both longitudinal and lateral motions. With respect to normal accelerations, calculations indicate that, except under unusual conditions, static stability has only a small effect on loads, whereas dynamic stability has

[redacted]

a relatively large effect, which produces load alleviation for well-damped airplanes and load amplification for poorly damped airplanes. Experimental results obtained to date confirm these conclusions. Methods of predicting the lateral motions and loads are under investigation but little experimental data are available as yet. What data are available indicate good agreement with calculated results and also emphasize the importance of damping, as in the longitudinal case.

REFERENCES

1. Press, Harry, and Mazelsky, Bernard: A Study of the Application of Power-Spectral Methods of Generalized Harmonic Analysis to Gust Loads on Airplanes. NACA Rep. 1172, 1954. (Supersedes NACA TN 2853.)

2. Fung, Y. C.: Statistical Aspects of Dynamic Loads. Jour. Aero. Sci., vol. 20, no. 5, May 1953, pp. 317-330.

3. Press, Harry, and Houbolt, John C.: Some Applications of Generalized Harmonic Analysis to Gust Loads on Airplanes. Jour. Aero. Sci., vol. 22, no. 1, Jan. 1955, pp. 17-26.

4. Summers, Robert A.: A Statistical Description of Large-Scale Atmospheric Turbulence. Sc. D. Thesis, M.I.T., 1954. (Also Rep. T-55, Instrumentation Lab., M.I.T.)

5. Vitale, A. James, Press, H., and Shufflebarger, C. C.: An Investigation of the Use of Rocket-Powered Models for Gust-Load Studies With an Application to a Tailless Swept-Wing Model at Transonic Speeds. NACA TN 3161, 1954.

6. Vitale, A. James: Characteristics of Loads in Rough Air at Transonic Speeds of Rocket-Powered Models of a Canard and a Conventional-Tail Configuration. NACA RM L54L17, 1955.

7. Bridgland, T. F., Jr.: A Theoretical Investigation of the Effect of Auxiliary Damping on the Longitudinal Response of a Transonic Bomber Configuration in Flight Through Continuous Turbulence. NACA RM L54K15a, 1955.

[redacted]

[redacted]

[redacted]

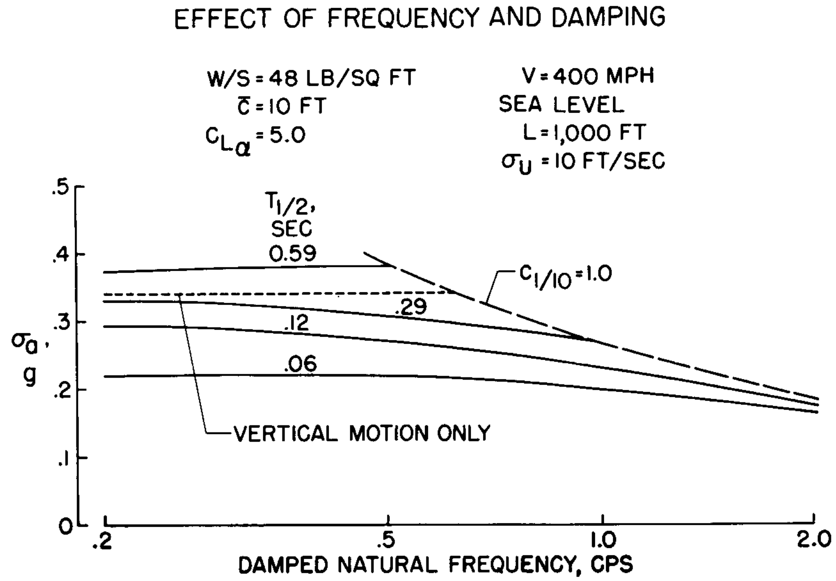

Figure 1

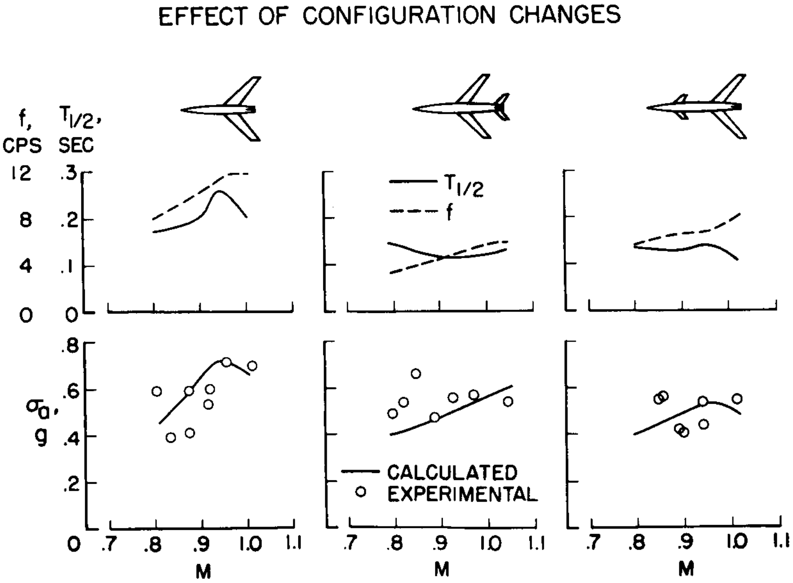

Figure 2

[redacted]

[redacted]

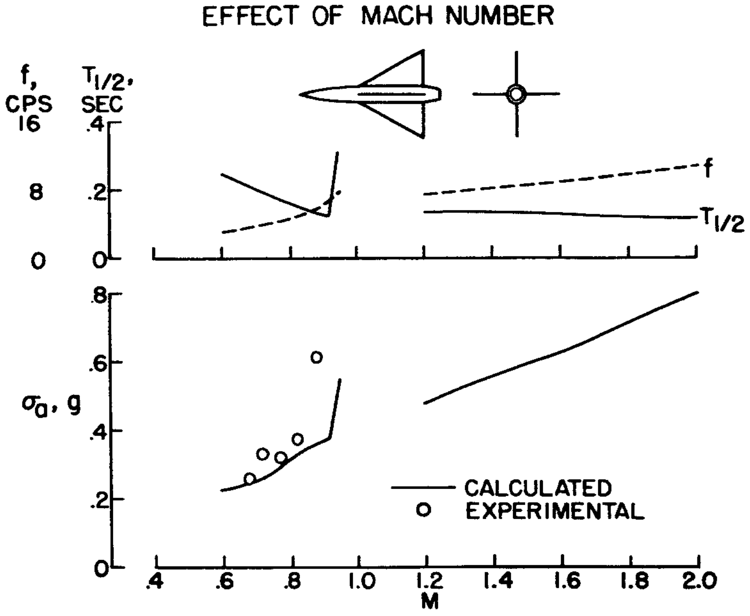

Figure 3

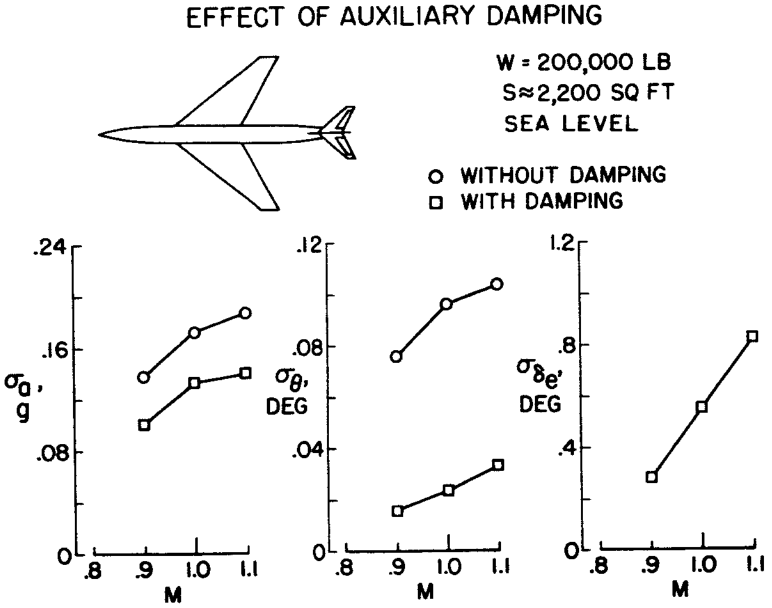

Figure 4

[redacted]

[redacted]

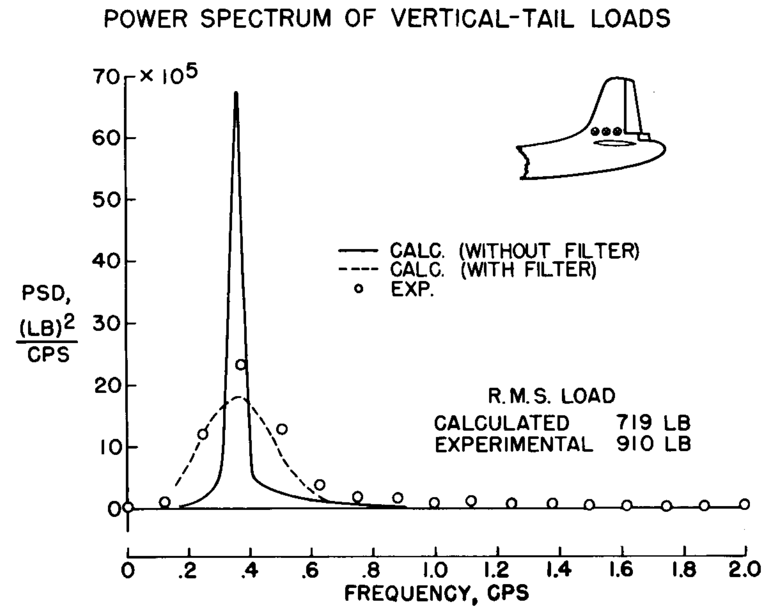

Figure 5

[redacted]

[redacted]

SCHNITZER

REDUCTION OF HYDRODYNAMIC IMPACT LOADS FOR WATERBORNE AIRCRAFT

By Emanuel Schnitzer

Langley Aeronautical Laboratory

SUMMARY

Recent NACA research aimed at the reduction of water loads on both hull and hydro-ski-equipped seaplanes is presented. It is shown that hull loads can be reduced by proper trim programming from elevator action and by use of high dead rise. For the hydro-ski-equipped seaplanes, loads are shown to be reduced by a decrease of ski beam or length and by mounting the ski on either conventional shock struts or on a new type of frequency-discriminating shock strut.

INTRODUCTION

The rough-water loads problem is one of the chief factors limiting greater use of the seaplane. Various means exist for reducing these loads such as control techniques, hull modifications, and auxiliary devices, particularly hydro-skis. This paper summarizes recent NACA research in these fields of water-load reduction. Earlier loads work on hydro-ski-equipped seaplanes has been reported and is summarized in reference 1 along with a fairly complete reference bibliography. The water-loads investigations covered in this paper are divided into two general groups, the first applying to the hull-type seaplane and the second, mainly to the hydro-ski-equipped seaplane. Under the heading of hulls, attitude control by elevator action and variations in bottom cross section (namely, dead rise) are considered. Under hydro-skis, beam loading, that is, hull loading based on the beam or width, plan-form proportions, and types of shock-strut mountings are considered. The shock mountings include the translating- and trimming-ski types and a frequency-discriminating oleo called the low-pass shock strut. A list of references is included which contains the published part of the material in this paper (refs. 2 to 4) and a bibliography of related work (refs. 5 to 29).

[redacted]

HULLS

Attitude Control

Model experiments.- The loads encountered in a water take-off or landing depend on the manner in which the airplane attitude or trim is varied during the run. In the past pilots have exerted some trim control during water operations. Recently, an attempt has been made to evaluate the amount of load alleviation possible by the use of various forms of such trim programming. In figure 1 is shown the effect of three different types of trim control, namely, fixed elevators, fixed trim, and automatically controlled elevators, on hull loads experienced in landings. These results were obtained in an experimental program conducted in the Hydrodynamics Division with a model flying boat landing in oncoming waves. All the experimental waves discussed in this paper were approximately sinusoidal in shape and occurred in a single train. The same critical wave condition was used throughout this trim-control investigation. Each point plotted gives the relative maximum vertical acceleration experienced during one landing and thus represents several impacts, since each landing or take-off consists of a series of bounces from wave to wave. Relative values of the vertical acceleration are shown on this and succeeding figures because the magnitudes of the loads do not necessarily represent those encountered in open-sea operations. The trends, however, are thought to be similar. The first cluster of points at the left represents recommended Navy practice for the average pilot in which the elevators are held fixed with the nose high. The spread of the data in this figure results from contacting at different positions on the waves at various flight conditions. The second cluster of points representing the fixed-trim condition, which to date has only been realized in laboratory tests, shows a possible reduction of 40 percent below the fixed-elevator case when the highest values of acceleration are compared. Possibly the fixed-trim condition could be achieved in practice by means of water elevators or vertical rockets. The short horizontal lines represent the acceleration levels exceeded during 10 percent of the landings. These levels are believed to give more realistic comparisons from a statistical point of view and are seen to yield the same qualitative conclusions obtained by comparing maximum accelerations. The third cluster of points represents an attempt to approach, as closely as possible, the fixed-trim condition in an actual flying boat by means of automatic elevator control. The control mechanism utilized for this test consisted of a combination of a trim-displacement control, which actuated the elevators to oppose a change in attitude, and a gyro-rate control, which actuated the elevators to oppose a trimming velocity of the flying boat. The elevator deflection speeds approximated conventional autopilot control rates. This control system gave a reduction in maximum vertical acceleration of 20 percent below the fixed-elevator case as shown, and an even greater reduction in angular acceleration of 40 percent (not shown). We may conclude from this material that proper programming of take-off and landing attitudes of flying boats can substantially reduce maximum water impact loads.

Narrow-body trimming theory.- It may be of some interest to note that there are theoretical methods available for determining the effects of different kinds of trim control on loads. In order to study trim-control techniques, the trimming case must first be defined accurately. During a seaplane take-off or landing the flight conditions of the airplane as it leaves one wave greatly influence the contact conditions on the next wave; thus the complete time history of the motions during any impact must be known. Previously, fixed-trim theory (ref. 1) was available for calculating maximum impact force, which was extended for the wide-float case to the entire time history (ref. 2). More recently, a quasi-steady trimming theory was developed to cover impact and planing of narrow hulls or hydro-skis undergoing pitching rotation. This theory is based on a dynamic-camber concept in which a pitching flat plate immersed in a streaming fluid is assumed to be replaced by a fictitious cambered plate fixed in space, for which the degree of camber at any instant is related to the pitching velocity of the original flat plate. In order to evaluate the effects of trimming motion during impact, this new theory is compared with the fixed-attitude narrow-body theory in figure 2. This figure shows a sample load time history of a rough-water impact of a large narrow flying boat. The solid line represents the dynamic-camber theory, and the line of long dashes represents the fixed-attitude theory. It appears from this figure that for the case considered the maximum accelerations are in close agreement, whereas during the remainder of the time histories the disagreement is increased. It should be borne in mind, however, that the angular motions are substantially different for the two theories. This means that, for a single impact for which the initial conditions are known, approximate calculations of maximum load by means of the fixed-attitude theory might suffice. However, since an actual seaplane landing involves the interplay of air and water forces through a sequence of impacts, any of which can be the worst one, calculations of complete time histories of water landings where the integrated effects of all the variables are critical, or in which pitching motion is important, will require the more exact theory which takes into account the effects of angular rotation. The line of short dashes represents an intermediate type of approximation which ignores the effects of rotation on the load distribution but extends the fixed-attitude theory by taking into account the velocity vector contributed by the pitching motion. This theory is probably adequate for a fairly large range of condition.

[redacted]

Cross Section

The degree of load alleviation attainable by sharpening up the bottom of the hull, that is, increasing its dihedral or dead rise in nautical terminology, is now considered. Although high dead rise, while reducing impact loads, is accompanied by increased water drag during take-off, this drag penalty is partially offset by the increased thrust available with modern engines.

The results of an experimental investigation of effects of dead rise are shown in figure 3. Tests were made with a dynamic scale model of a high-speed flying boat landing on waves 4 feet high and ranging from 180 feet to 320 feet in length. The data obtained in this investigation were cross-plotted to yield the relative values of maximum landing acceleration for a constant hull width or beam. From this figure we may observe that, for the range of wave length used, the maximum load decreases almost linearly with increasing dead rise, at least up to dead-rise angles of 60° for flying boats in free flight. This downward trend of load with increasing dead rise follows theoretical and experimental predictions based on fixed-trim landings in smooth water. It should perhaps be noted that some indications of directional instability for the 60° case occurred at low trims and are being investigated further. The effect of wave length is seen to decrease at the higher dead rises for the constant wave height tested, and, as may have been expected from geometric considerations involving the ratio of hull to wave length, the intermediate wave length of 230 feet is seen to give the highest loads. It may be concluded from these tests, therefore, that the high dead rises are very effective in reducing rough-water loads and in addition possess satisfactory hydrodynamic qualities with respect to spray and stability.

HYDRO-SKIS

Beam Loading

The next topic under consideration is the study of load alleviation by means of hydro-skis. The first hydro-ski parameter considered is the beam-loading coefficient usually denoted by C_Δ. This parameter is somewhat similar to wing loading in that it relates the weight of the aircraft to the dimension of the body. In the aerodynamic case, the entire area of the wing is significant because it is always completely immersed in the fluid, whereas, in the hydrodynamic case, beam loading relates the aircraft weight to the hydro-ski beam only because the wetted length of the ski bottom varies throughout the impact.

The effect of beam loading on water loads is illustrated in figure 4 which was constructed from the results of several hundred landings

[redacted]

[redacted]

of flat rectangular plates in the Langley impact basin. The flat plate was selected since it was believed to approximate the hydro-ski which usually has a fairly low dead rise. The sketch at the top of the figure identifies the model mass m, beam b, trim τ, initial flight-path angle γ, resultant velocity V, and water density ρ. The ranges of variables tested include beam-loading coefficients from 1 to 134, trim angles from 3° to 45°, and flight-path angles from 2° to 22°. When these data are plotted in the nondimensional form shown in this figure, all the data condense within the envelope included by the shaded area. If dead-rise data were plotted in this figure, these data would probably group below the flat-plate data, the degree of separation depending on the dead rise and possibly also on the beam loading tested. From this plot we can see that the impact lift coefficient C_L can be approximated by a simple linear function of the product of the flight-path angle at contact γ times the cube root of the beam-loading coefficient C_{Δ}. Since an increase in beam loading is associated with either an increase in weight or a reduction in beam, it is evident that, when the nondimensional parameters are defined, the maximum impact force varies directly with the beam and the cube root of the weight. Thus, it turns out that higher beam loadings reduce impact accelerations although they are usually associated with more severe spray conditions. The spread of the data in the envelope results principally from the effect of trim. We may conclude from the wide ranges of the variables tested that for load estimation the trim effect can be neglected, the effect of flight path can be taken as a linear function, and the beam-loading effect can be closely represented by the cube-root function.

In order to estimate maximum impact force from this plot a straight line has been faired through the data, the equation of which yields the impact lift coefficient. (Note that γ is expressed in degrees in this equation.) The maximum impact force can be calculated from the equation for F_{MAX} also given in the figure. With this information the designer can approximate for his particular airplane the impact-load reductions possible through manipulation of weight, beam, and flight-path angle.

Plan Form

Reductions in impact acceleration can be achieved for the hydro-ski by increasing its beam loading as has been demonstrated. Another parameter investigated was the proportioning of the hydro-ski plan form. The plan-form investigation was carried out in the Langley tank no. 1 with a dynamic model of a hydro-ski-equipped flying boat. In these tests the model was landed on waves having a height of 4 feet and 4 different lengths. The initial conditions of impact were made as nearly alike as practicable.

[redacted]

[redacted]

Figure 5 illustrates the effect on loads of variations of the hydro-ski plan form pictured, where each point represents a considerable number of landings. The values plotted represent the accelerations exceeded for the ski in 10 percent of the landings relative to the acceleration for the hull alone. Only the length and width of the skis have been varied. The effect of ski length on loads is obtained directly from the line connecting the three skis of equal beam identified by the solid points. The load is seen to increase with ski length. Even though the beam of the hull was equal to the beam of the ski on the extreme left of figure 5, use of skis is seen to reduce greatly the load. The effect of beam can also be seen on this plot if the two models of almost equal length are compared; the narrower ski gives the smaller load as predicted by the previous figure on beam loading. From figure 5 the general conclusion drawn is that the smaller the ski length, or beam, the lower the load. Since too small a ski allows the hull to contact the water and receive large subsequent impacts, a compromise must be made between the ski area and the length of the strut supporting it. Too long a strut creates a take-off problem with respect to drag loads.

Theoretical considerations show that the beam should be more powerful than the length as a load-controlling parameter. The data shown here tend to substantiate the theory if the three upper hydro-skis at the left of the figure which have the same plan-form area are considered. From these three points the load is seen to decrease even if the ski length increases. Since the increase in length for a given ski area must be accompanied by a proportional decrease in beam, the conclusion that the beam has the main effect on loads is verified.

Shock Mountings

Translating ski.- Water loads have been shown to be reduced by the use of hydro-skis. How additional load reductions could be achieved by mounting hydro-skis on shock struts has also been demonstrated in the past by means of theoretical calculations (ref. 3). Since that time, landing tests with dynamic scale models have been made in the tanks to verify these calculations for the translating type of shock mounting, as shown in figure 6. These experimental results are presented in reference 4. With this type of mounting, the ski is not permitted to trim relative to the seaplane during the impact. Figure 6 presents a typical load time history of one of these impacts for a rough-water landing of a large jet hydro-ski seaplane. The theory is represented by the lower solid line and the corroborating experimental data, by the circled points. As a matter of interest the load for the same seaplane landing at the same initial conditions but with the shock strut locked out of action is presented by the upper solid line. For this case the load reduction achieved by the shock strut is 40 percent.

[redacted]

[redacted]

Trimming ski.- In addition to the translating type of mounting, several other methods of shock-mounted hydro-skis have been considered. In one of these methods, the hydro-ski was allowed to trim relative to the aircraft during compression of the shock strut. A computational method has been evolved by utilizing the dynamic-camber theory mentioned earlier in this paper, which enables the loads on these trimming hydro-skis to be calculated. A typical load time history computed by this method is presented in figure 7 by the lower line, which represents a rough-water landing of a fighter aircraft equipped with pivoted shock-mounted hydro-skis. Comparisons were not made with the translating-ski case because the time histories are drastically different and depend on the values selected for the many independent parameters.

In order to estimate roughly the load reduction achieved by this pivoted-ski arrangement, the load for the same aircraft landing at the same initial conditions but with the shock strut locked out of action is presented by the upper line of figure 7. The load reduction for the pivoted ski is seen to be about 26 percent with the rate of application of loading somewhat reduced. Notice that area on this slide is proportional to vertical impulse or momentum change. Since the area under the trimming ski curve is smaller than for the fixed-ski curve it may be concluded from this figure, and probably also from complete time histories for the preceding figure, that the vertical rebound velocity is reduced by the shock-strut action, which results in much milder initial conditions for the next impact. From a practical point of view, the pivoted-ski mounting has the advantage of keeping the bending moments which may produce serious frictional loads out of the shock strut.

Low-pass shock strut.- When a conventional oleo strut is used with the types of shock mountings considered, load reductions can be expected during rough-water operations as long as the bumps or waves encountered by the aircraft are long and smooth. For short steep bumps, however, especially at high speeds, conventional oleos tend to become quite rigid and transmit the full shock loads to the aircraft. In order to overcome this difficulty, a new type of filter-action oleo, the low-pass shock strut, was conceived. This strut tends to filter out the rapidly applied loads from steep bumps while acting as a conventional oleo for smooth hills or swells.

In figure 8 simplified versions of the conventional oleo at the left and the low-pass strut at the right are compared. Usually, the conventional oleo is equipped with a fixed metering pin which can vary the size of the orifice in the piston only as a function of the strut telescoping displacement. Thus, when the lower end of the strut is forced upward, the rate of flow of fluid up through this orifice, which regulates the applied force, is controlled only by the strut telescoping displacement. Since the load developed in the strut is proportional to the square of the telescoping velocity, the steeper the slope of the

[redacted]

[redacted]

bump encountered by the landing gear, the more rigid the strut becomes, until for very steep bumps it is practically a rigid bar. The low-pass strut, on the other hand, has a movable metering pin which varies the orifice size as a function of the rate of loading and which is actuated by a special frequency-sensitive piston in the control cylinder shown at the top of the strut. For very steep bumps, however, the rapid increase of pressure in the lower cylinder is communicated through the large-diameter tube at the left to the under side of the control piston. This piston snatches the metering pin upward by opening wide the orifice, allowing the strut to telescope easily, and thereby reducing the load. For slowly applied loads of either small or large magnitude, the metering pin remains in the equilibrium position shown so that a conventional fixed orifice strut is approximated.

In order to assess the effectiveness of the low-pass strut as applied to seaplanes, the results of theoretical calculations which have been made for a hydro-ski seaplane operating in rough water are shown in figure 9.

This figure is concerned with the loads experienced during high-speed operation on a complex sea made up of small steep waves superposed on large swells. Both wave trains are sinusoidal in shape and oriented in the same direction. The hydro-ski is assumed to penetrate the water so that the actual waves can be considerably higher than the magnitudes shown in the lower figure, which represents the hydro-ski motion only. The upper figure shows that the conventional shock strut develops large loads for the high-frequency waves or in the region of the steep wave fronts, whereas the low-pass strut greatly reduces these loads.

CONCLUSIONS

The various methods which have been shown to be effective in reducing water loads are as follows:

For the flying boat,

Trimming restraint by elevator control
Increased bottom dead rise

For the hydro-ski,

Reduction of the beam
Reduction of length
Shock mounting on conventional oleos for slowly applied loads and on low-pass shock struts for all rates of load application.

[redacted]

All these methods, either singly or in combination, can be used to effect load reductions during water operations.

REFERENCES

1. Schnitzer, Emanuel: Estimation of Water Landing Loads on Hydro-Ski-Equipped Aircraft. NACA RM L53D29, 1953.

2. Miller, Robert W.: Theoretical Analysis of Hydrodynamic Impact of a Prismatic Float Having Freedom in Trim. NACA TN 2698, 1952.

3. Schnitzer, Emanuel: Water-Impact Theory for Aircraft Equipped With Nontrimming Hydro-Skis Mounted on Shock Struts. NACA RM L54H10, 1954.

4. Hoffman, Edward J., and Fisher, Lloyd J.: Model Investigation of the Effect of Mounting Hydro-Skis on Shock Absorbers. NACA RM L54L02, 1955.

5. Mayo, Wilbur L.: Hydrodynamic Impact of a System With a Single Elastic Mode. I - Theory and Generalized Solution With an Application to an Elastic Airframe. NACA Rep. 1074, 1952. (Supersedes NACA TN 1398.)

6. Miller, Robert W., and Merten, Kenneth F.: Hydrodynamic Impact of a System With a Single Elastic Mode. II - Comparison of Experimental Force and Response With Theory. NACA Rep. 1075, 1952. (Supersedes NACA TN 2343.)

7. Miller, Robert W.: Water-Landing Investigation of a Flat-Bottom V-Step Model and Comparison With a Theory Incorporating Planing Data. NACA TN 2932, 1953.

8. Miller, Robert W.: Comparison of Experimental Hydrodynamic Impact Loads and Motions for a V-Step and a Transverse-Step Hydro-Ski. NACA RM L53K20a, 1954.

9. Milwitzky, Benjamin: Generalized Theory for Seaplane Impact. NACA Rep. 1103, 1952.

10. Schnitzer, Emanuel: Theory and Procedure for Determining Loads and Motions in Chine-Immersed Hydrodynamic Impacts of Prismatic Bodies. NACA Rep. 1152, 1953. (Supersedes NACA TN 2813.)

[redacted]

11. Sims, Joseph L., and Schnitzer, Emanuel: A Theoretical Investigation of the Effect of Partial Wing Lift on Hydrodynamic Landing Characteristics of V-Bottom Seaplanes in Step Impacts. NACA TN 2815, 1952.

12. Schnitzer, Emanuel, and Hathaway, Melvin E.: Estimation of Hydrodynamic Impact Loads and Pressure Distributions on Bodies Approximating Elliptical Cylinders With Special Reference to Water Landings of Helicopters. NACA TN 2889, 1953.

13. Smiley, Robert F.: Water-Pressure Distributions During Landings of a Prismatic Model Having an Angle of Dead Rise of $22\frac{1}{2}^\circ$ and Beam-Loading Coefficients of 0.48 and 0.97. NACA TN 2816, 1952.

14. Carter, Arthur W., and Butler, Roger V.: Experimental Investigation of the Flow Field Behind an Aspect-Ratio-10 Hydrofoil Near the Water Surface. NACA RM L52L11, 1953.

15. Fisher, Lloyd J., and Hoffman, Edward L.: A Brief Hydrodynamic Investigation of a Navy Seaplane Design Equipped With a Hydro-Ski. NACA RM L53F04, 1953.

16. Wadlin, Kenneth L.: Considerations Affecting Hydro-Ski Airplane Design. NACA RM L53I28b, 1953.

17. McGehee, John R., Weinflash, Bernard, and Pelz, Charles A.: The Hydrodynamic Planing Lift of Four Surfaces as Measured in a 200-FPS Free Jet. NACA RM L54F01, 1954.

18. Weinflash, Bernard, and Fontana, Rudolph E.: The Hydrodynamic Force Characteristics of Streamline Bodies of Revolution Having Fineness Ratios of 6, 9, and 12 With and Without Chine Strips. NACA RM L54K22, 1955.

19. Olson, Roland E., and Bielat, Ralph P.: An Aerodynamic and Hydrodynamic Investigation of Two Multijet Water-Based Aircraft Having Low Transonic Drag Rise. NACA RM L55A11a, 1955.

20. Mottard, Elmo J., and Loposer, J. Dan: Average Skin-Friction Drag Coefficients From Tank Tests of a Parabolic Body of Revolution (NACA RM-10). NACA Rep. 1161, 1954. (Supersedes NACA TN 2854.)

21. Chambliss, Derrill B., and Boyd, George M., Jr.: The Planing Characteristics of Two V-Shaped Prismatic Surfaces Having Angles of Dead Rise of 20° and 40°. NACA TN 2876, 1953.

[redacted]

22. Weinstein, Irving, and Kapryan, Walter J.: The High-Speed Planing Characteristics of a Rectangular Flat Plate Over a Wide Range of Trim and Wetted Length. NACA TN 2981, 1953.

23. Kapryan, Walter J., and Boyd, George M., Jr.: The Effect of Vertical Chine Strips on the Planing Characteristics of V-Shaped Prismatic Surfaces Having Angles of Dead Rise of 20° and 40°. NACA TN 3052, 1953.

24. Wadlin, Kenneth L., Ramsen, John A., and Vaughan, Victor L., Jr.: The Hydrodynamic Characteristics of Modified Rectangular Flat Plates Having Aspect Ratios of 1.00 and 0.25 and Operating Near a Free Water Surface. NACA TN 3079, 1954.

25. Coffee, Claude W., Jr., and McKann, Robert E.: Hydrodynamic Drag of 12- and 21-Percent-Thick Surface-Piercing Struts. NACA TN 3092, 1953.

26. Carter, Arthur W., and Woodward, David R.: Static Properties and Resistance Characteristics of a Family of Seaplane Hulls Having Varying Length-Beam Ratio. NACA TN 3119, 1954.

27. Shuford, Charles L., Jr.: A Review of Planing Theory and Experiment With a Theoretical Study of Pure-Planing Lift of Rectangular Flat Plates. NACA TN 3233, 1954.

28. Ramsen, John A., and Vaughan, Victor L., Jr.: The Hydrodynamic Characteristics of an Aspect-Ratio-0.125 Modified Rectangular Flat Plate Operating Near a Free Water Surface. NACA TN 3249, 1954.

29. Ramsen, John A., and Vaughan, Victor,L., Jr.: Hydrodynamic Tares and Interference Effects for a 12-Percent-Thick Surface-Piercing Strut and an Aspect-Ratio-0.25 Lifting Surface. NACA TN 3420, 1955.

[redacted]

[redacted]

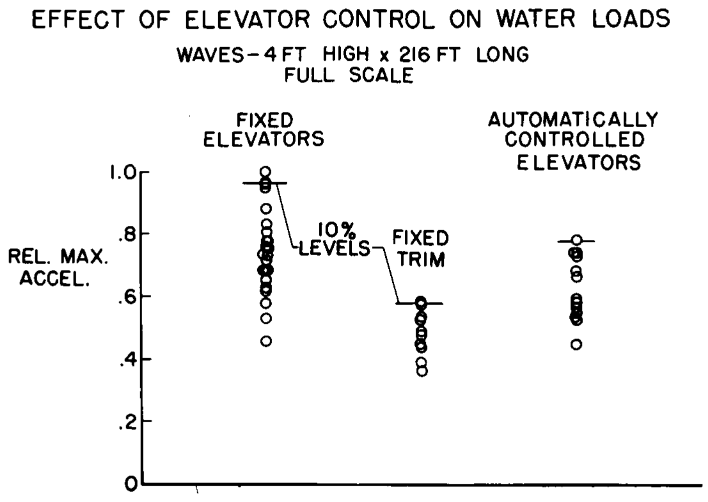

Figure 1

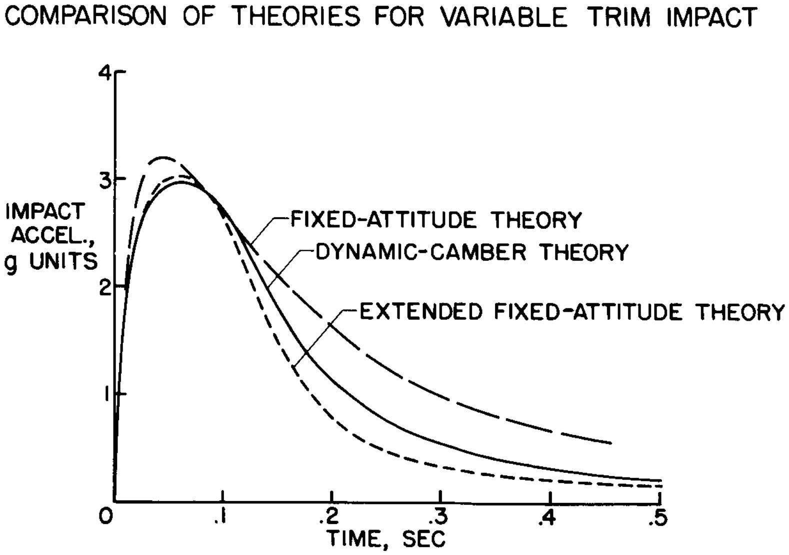

Figure 2

[redacted]

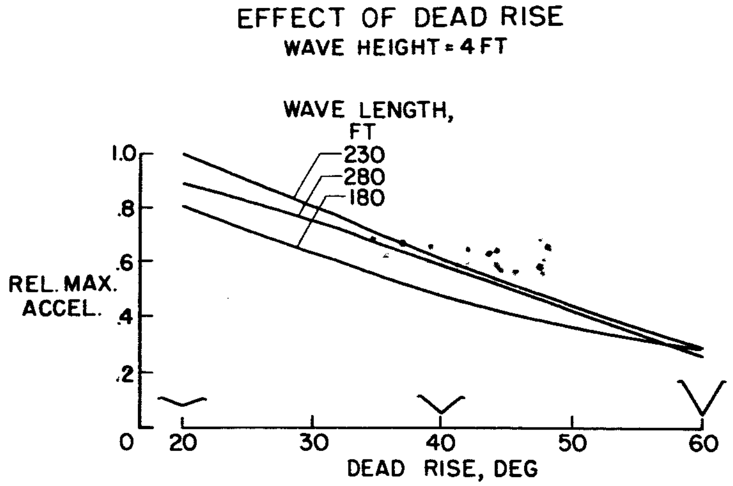

Figure 3

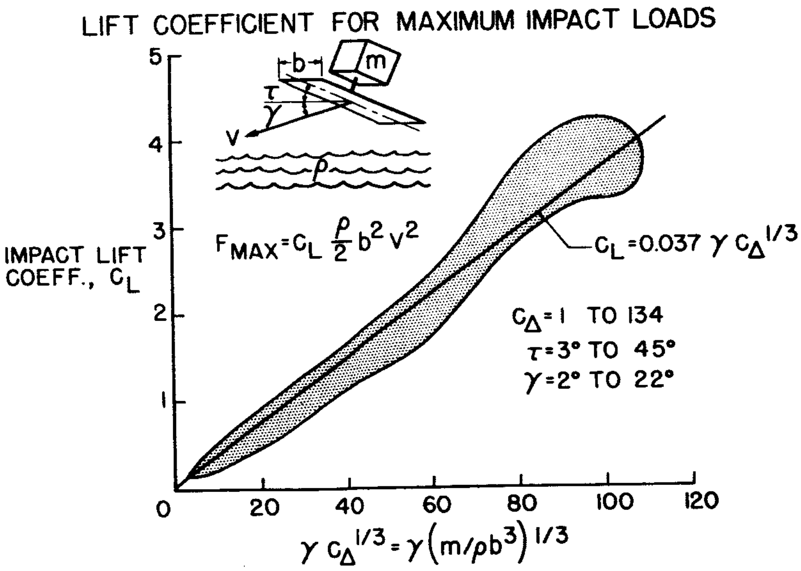

Figure 4

[redacted]

[redacted]

EFFECT OF HYDRO-SKI PLAN FORM
WAVES 4FT × 180 TO 270 FT

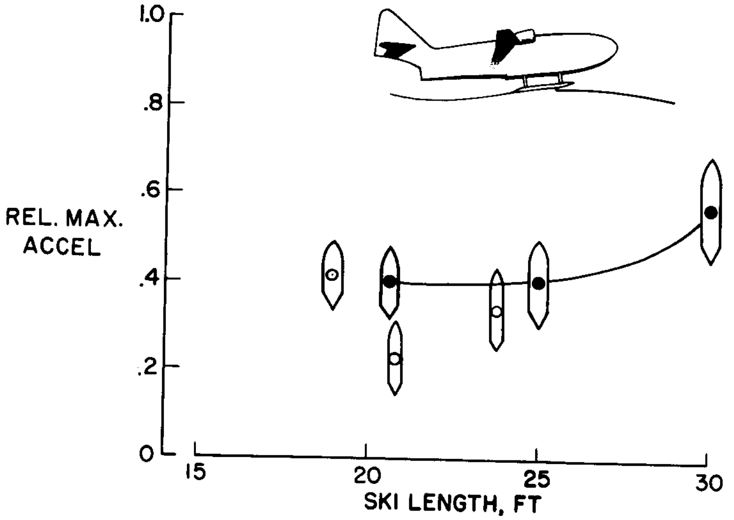

Figure 5

IMPACT LOADS FOR TRANSLATING SHOCK-MOUNTED HYDRO-SKI

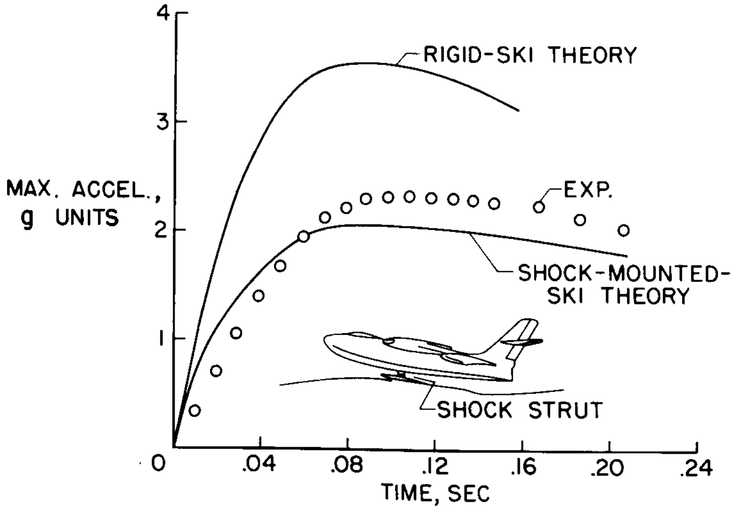

Figure 6

[redacted]

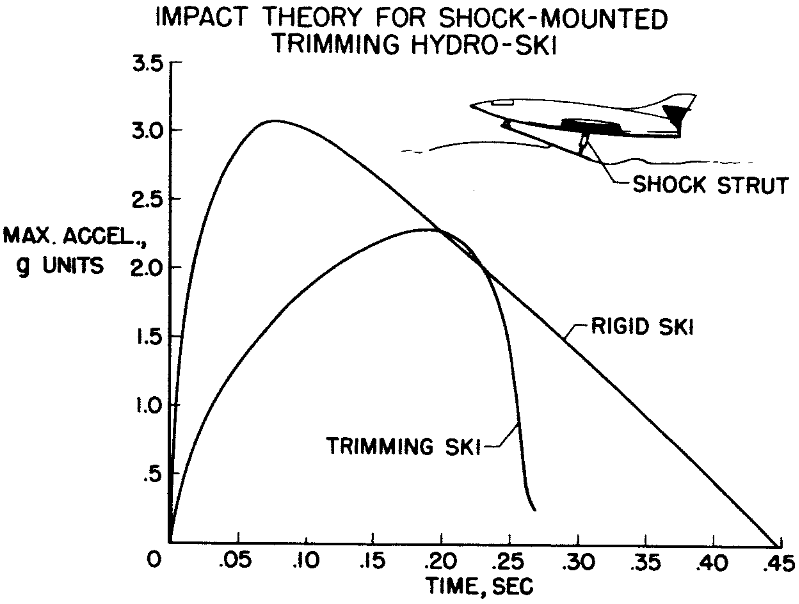

Figure 7

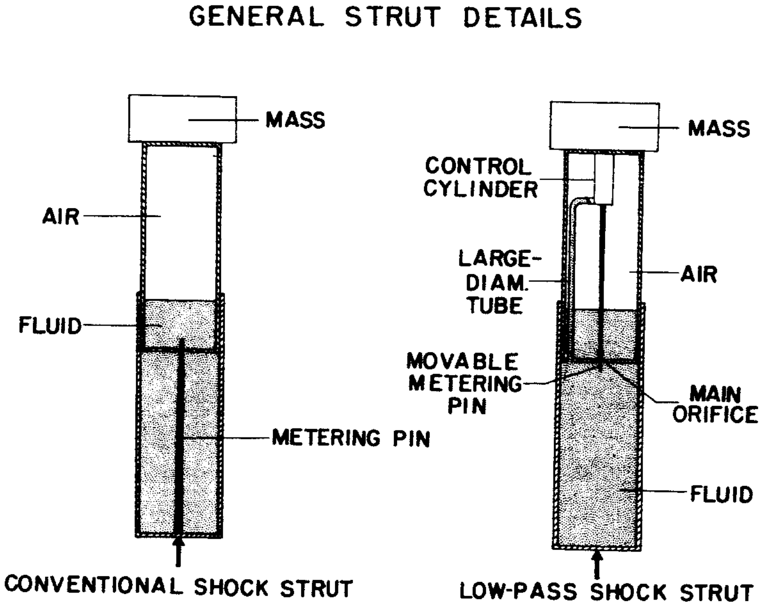

Figure 8

[redacted]

[redacted]

TAXIING ON A COMPLEX SEA

SPEED, 120 KNOTS

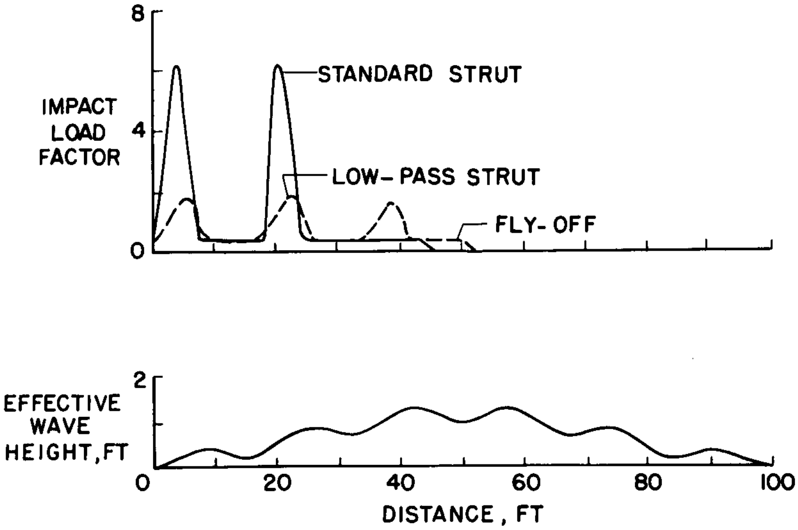

Figure 9

[redacted]

[redacted]

LANDING CONDITIONS FOR LARGE AIRPLANES IN ROUTINE OPERATIONS

By Norman S. Silsby and Eziaslav N. Harrin

Langley Aeronautical Laboratory

SUMMARY

Measurements have been obtained by means of a specially developed photographic method of landing contact conditions of some commercial transports, the Boeing KC-97 tanker, the Boeing B-47 jet bomber, and the Convair B-36 bomber. From these measurements, vertical velocities and airspeeds at contact have been evaluated and a brief statistical analysis of the results, including the effect of horizontal gusts on the landing conditions for the transports, has been made.

The analysis indicates that one out of 1,000 landings will equal or exceed a vertical velocity of 3.5 fps and 4.7 fps for the nongusty and gusty conditions, respectively, or an increase of about 25 percent due to gustiness. It appears likely, however, that on the average the curves for the condition without gusts represents the more probable condition. The relative frequency of occurrence of gusts to no gusts was found to be 1 to 20 for a 5-year period at the Langley Air Force Base.

The values of vertical velocity likely to be equaled or exceeded once in 1,000 landings of routine operations of tankers and bombers were 5.5 fps for the KC-97 tankers, 6 fps for the B-47 jet bombers, and 7 fps for the B-36 bombers. These results are comparable to the transport probability curve for the condition without gusts, which indicated that an average vertical velocity for all transports of about 3.5 fps would be equaled or exceeded once in 1,000 landings.

The analysis of airspeed at contact indicated that one out of 1,000 landings will equal or exceed an airspeed of 50 percent above the stall for the B-36 airplane, 60 percent above the stall for the transports, and about 70 percent above the stall for the B-47 airplane.

INTRODUCTION

In order to aid in the development of more rational landing-loads design requirements and procedures, the National Advisory Committee for Aeronautics has been conducting a project to obtain statistical measurements of landing contact conditions for various types of airplanes during routine daytime operations. The technique for obtaining the statistical measurements empl[redacted]y developed photographic method which requires no instrument installation in the aircraft and permits rapid data reduction together with good accuracy. (See ref. 1.)

Previous preliminary results on some landing contact conditions obtained by this method were presented for commercial transport airplanes during routine daytime operations at the Washington National Airport (ref. 2). The project has been continued, and the number of measurements has been increased to what appears to be a sufficiently large sample in order to allow some separation of data for investigating the influence of certain factors on the contact conditions (ref. 3). In addition to the data for the transports, measurements have been obtained for Boeing B-47 jet bombers and Boeing KC-97 tankers at Barksdale Air Force Base and for Convair B-36 bombers at Carswell Air Force Base, which were obtained with the cooperation of the Strategic Air Command.

RESULTS AND DISCUSSION

The measurements in most cases included vertical velocity, forward speed, bank angle, and rolling velocity at the instant before landing contact. The discussion will be confined to vertical velocity and forward speed since these quantities have the most direct influence on the vertical and drag loads produced in the landing gear.

Effects of Gusts

One factor which was believed to be important in its effect on the contact conditions was the turbulence of the air. Figure 1 shows the results obtained by separating the center-of-gravity vertical-velocity data for the transport airplanes according to whether the wind was gusty or not gusty. The gusty condition is defined by the U. S. Weather Bureau as sudden intermittent increases in speed with at least a 10-mph variation between peaks and lulls, the peaks reaching at least 18 mph and the average time interval between peaks and lulls usually not exceeding 20 seconds. The figure shows curves of the probability of equaling or exceeding given center-of-gravity vertical velocities obtained by fitting Pearson Type III probability curves to the measured data.

The mean vertical velocities $\bar{V}_V$ were 1.22 fps without gusts and 1.50 fps with gusts, and this difference is statistically significant. Comparison of the gusty and nongusty condition indicates that for a given number of landings the vertical velocity likely to be equaled or exceeded is about 25 percent greater for the condition with gusts than for the condition without gusts. The values of vertical velocity likely to be equaled or exceeded in 1,000 landings are 3.5 fps and 4.7 fps for the nongusty and gusty conditions, respectively.

[redacted]

Inasmuch as the tests were conducted during clear weather conditions, the gust effect shown is due to gust intensities occurring in clear air at the ground and does not include the extreme gust intensities associated with squalls and other storm conditions. On the average, the high relative frequency of occurrence of gusts and no gusts, indicated by the number of landings for the two conditions during the tests, was much greater than would normally be expected. An analysis of the hourly sequence reports of the U. S. Weather Bureau at Langley Air Force Base for a 5-year period indicated that the relative frequency of occurrence of the gusty condition was about 1 to 20. Thus, over a long period of time, for instance, the life of a given airplane, the solid curve for the condition without gusts is the one to be considered as representative of the condition likely to be encountered about 95 percent of the time and the dashed curve for the gusty condition, the other 5 percent. The number of landings are given for the probability curves as an indication of their reliability. A comparison of the probability curves of vertical velocity determined from the data of the first 60 landings for all airplanes, and then successively for 126, 243, and 478 landings as more landings were photographed, indicated that possibly on the order of 200 landings are required to establish a probability curve which will have a practical degree of reliability.

Comparison of Vertical Velocities at First and Second Contacts

Although the vertical velocity of the center of gravity of an airplane generally characterizes the severity of the landing, most landings are not symmetrical and the load produced in the landing gear is dependent on the vertical velocity at the landing gear itself. A theoretical study contained in reference 4 indicated that there could be substantial differences in the vertical velocity of the first gear truck to contact and in subsequent contacts by the other trucks depending on the attitude and angular velocities of the airplane, on the amount of lift, and on the configuration and inertia characteristics.

One factor involved is the ratio of the semitread to the rolling radius of gyration. Presented in figure 2 is a comparison of the vertical-velocity probability curves obtained from the measured data for the first and second truck contacts for the transport landings, separated into four-engine and two-engine categories, since the values of the ratio of semitread y_t to rolling radius of gyration k_X of 0.7 to 0.8 for the four-engine airplane and 1.0 to 1.2 for the two-engine airplane are appreciably different for these airplane types. The theoretical analysis of reference 4 indicated that, other factors being the same, the ratio of vertical velocities for the second wheel to contact to the first wheel to contact should vary approximately as this parameter $\frac{y_t}{k_X}$. Thus, for the four-engine airplane, the vertical

[redacted]

CONCLUDING REMARKS

The statistical analysis of the transport landings indicated that the gusty wind condition had a significant effect in increasing the vertical velocity likely to be equaled or exceeded in a given number of landings. One out of 1,000 landings will equal or exceed a vertical velocity of 3.5 fps and 4.7 fps for the nongusty and gusty conditions, respectively, or an increase of about 25 percent due to gustiness. It appears likely, however, that on the average the curves for the condition without gusts represents the more probable condition. The relative frequency of occurrence of gusts to no gusts was found to be 1 to 20 for a 5-year period at the Langley Air Force Base.

The values of vertical velocity likely to be equaled or exceeded once in 1,000 landings of routine operations of tankers and bombers were 5.5 fps for the KC-97 tankers, 6 fps for the B-47 jet bombers, and 7 fps for the B-36 bombers. These results are comparable to the transport probability curve for the condition without gusts, which indicates that an average vertical velocity for all transports of about 3.5 fps would be equaled or exceeded once in 1,000 landings.

The analysis of airspeed at contact indicated that one out of 1,000 landings will equal or exceed an airspeed of 50 percent above the stall for the B-36 airplane, 60 percent above the stall for the transports, and about 70 percent above the stall for the B-47 airplane.

REFERENCES

1. Rind, Emanuel: A Photographic Method for Determining Vertical Velocities of Aircraft Immediately Prior to Landing. NACA TN 3050, 1954.

2. Silsby, Norman S., Rind, Emanuel, and Morris, Garland J.: Some Measurements of Landing Contact Conditions of Transport Airplanes in Routine Operations. NACA RM L53E05a, 1953.

3. Silsby, Norman S.: Statistical Measurements of Contact Conditions of 478 Transport-Airplane Landings During Routine Daytime Operations. NACA TN 3194, 1954.

4. Yntema, Robert T., and Milwitzky, Benjamin: An Impulse-Momentum Method for Calculating Landing-Gear Contact Conditions in Eccentric Landings. NACA TN 2596, 1952.

[redacted]

[redacted]

[redacted]

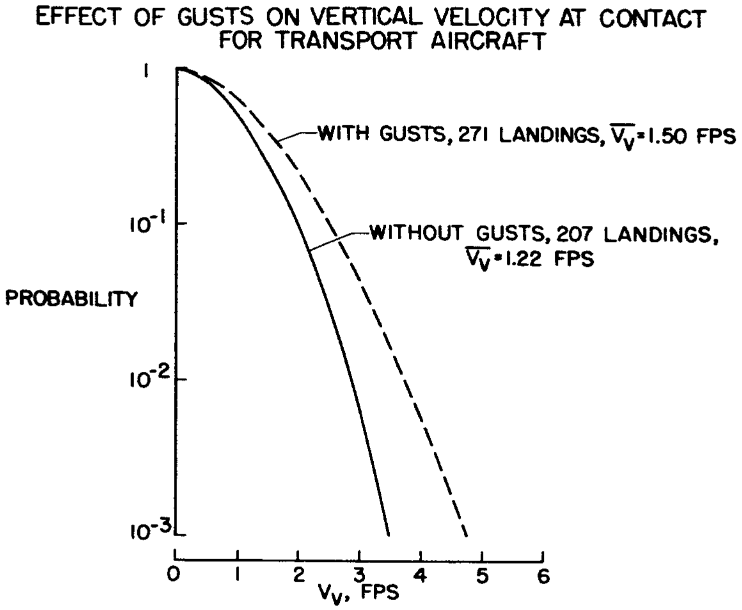

EFFECT OF GUSTS ON VERTICAL VELOCITY AT CONTACT FOR TRANSPORT AIRCRAFT

Figure 1

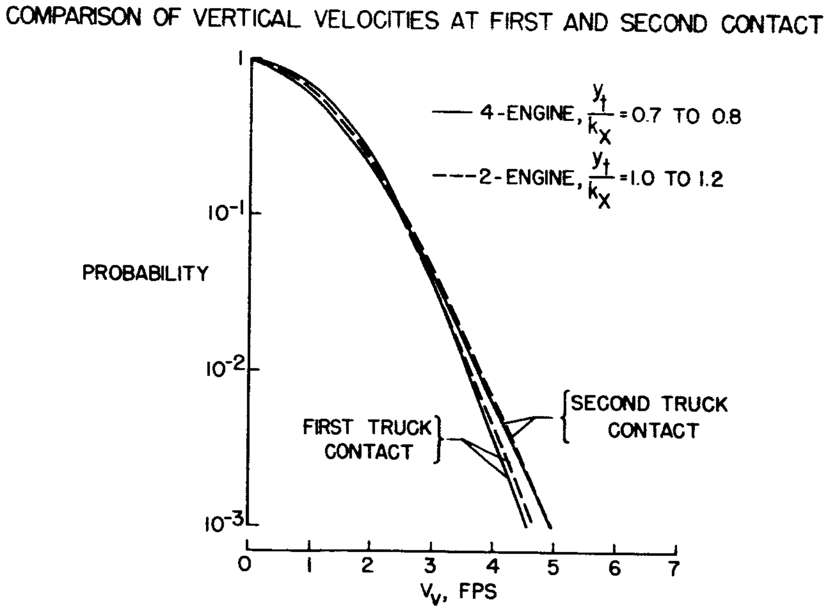

COMPARISON OF VERTICAL VELOCITIES AT FIRST AND SECOND CONTACT

Figure 2

[redacted]

[redacted]

PROBABILITY CURVES FOR MILITARY OPERATIONAL LANDINGS

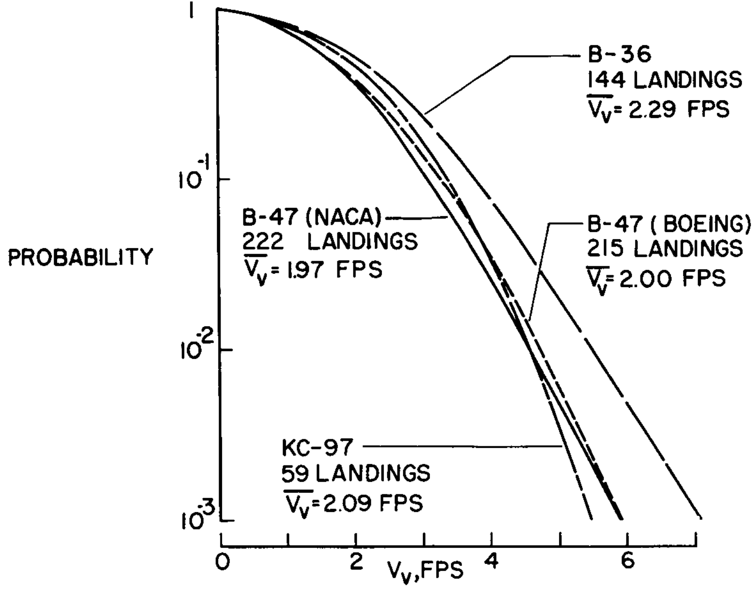

Figure 3

PROBABILITY CURVES FOR VARIOUS TYPES OF AIRCRAFT

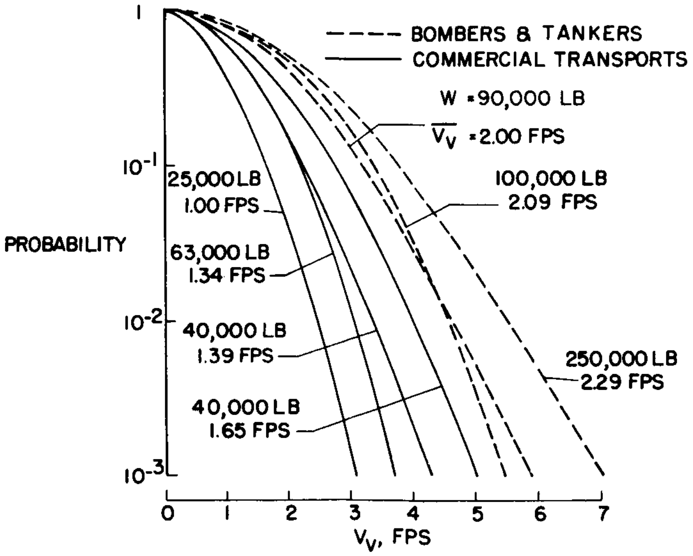

Figure 4

[redacted]

[redacted]

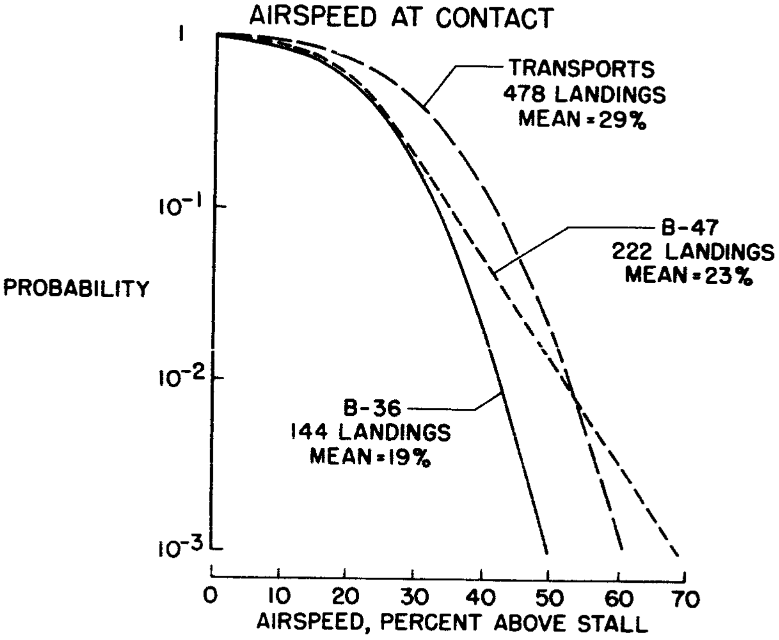

Figure 5

[redacted]

8V

[redacted]

VERTICAL AND DRAG GROUND-REACTION FORCES DEVELOPED IN LANDING IMPACTS OF A LARGE AIRPLANE

By Richard H. Sawyer

Langley Aeronautical Laboratory

SAWYER

SUMMARY

Tests were conducted on a large bomber-type airplane to determine the ground reactions imposed on the landing gear under actual landing conditions. The program covered landings made at vertical velocities up to 8.5 feet per second and forward speeds at contact from 95 to 120 miles per hour. Landings were made on both wet and dry concrete runways. Results are presented of the effects of vertical velocity at contact and the effects of runway surface condition (wet and dry) on the vertical and drag ground reactions obtained during the landing impact.

INTRODUCTION

In recent years, considerable interest has arisen in the problem of obtaining a more rational understanding of the ground-reaction forces applied to the airplane in landing and taxiing because of structural failures that have arisen from these forces. Prediction of the dynamic structural forces causing these failures is possible by use of existing dynamic-analysis methods, but the methods require knowledge of the forcing functions, that is, of the ground-reaction forces. At present, only a limited amount of reliable experimental results defining the ground-reaction forces under actual flight conditions or under conditions duplicating flight conditions is available.

An experimental investigation has therefore recently been conducted on a large bomber-type airplane to obtain information, applicable to large airplanes, on the ground reactions imposed on the landing gear under actual landing conditions. The investigation included study of the interrelations of the ground reactions, as well as the relationship of the ground reactions to landing-approach conditions and to landing-gear and airplane characteristics.

The results presented in the phase of the investigation reported herein are limited to the effects of vertical velocity and the effects of surface condition (wet and dry) on the vertical and drag ground reactions obtained during the landing impact.

[redacted]

DECLASSIF[redacted]

TESTS AND INSTRUMENTATION

The test program covered landings of a large bomber at vertical velocities ranging up to 8.5 feet per second and forward speeds at contact from 95 to 120 miles per hour with various drift and roll attitudes at contact at two airplane weights. Most of the landings were made on dry concrete, but in one flight six landings were made on a runway wetted down by fire hoses to simulate a heavy rain.

A complete list of the quantities measured for the purpose of defining both the landing-approach conditions and the impact and spin-up phenomena is tabulated, as follows:

Approach
Center-of-gravity acceleration
Airspeed
Pitch attitude
Pitching velocity
Roll attitude
Rolling velocity
Yaw angle
Yawing velocity
Drift angle
Pilot's control motions

Impact
Wheel vertical reaction
Wheel drag reaction
Truck side reaction
Truck yawing moment
Truck vertical velocity
Tire deflection
Wheel rotational velocity
Oleo displacement
Nose-gear trail angle

The present paper is limited to the vertical and drag ground-reaction results obtained on the main wheels of the landing gear.

Figure 1 illustrates the general arrangement of one of the dual-wheel main landing-gear trucks of the airplane with one of the wheels removed. The weight of the airplane for these tests was approximately 100,000 pounds, necessitating a tire pressure of about 75 pounds per square inch in the 56-inch-diameter tires. The shock strut shown has an overall telescoping action of 12 inches. Also illustrated is the instrumentation pertinent to the results given in this paper. The dynamic vertical and drag reactions imposed on each wheel during the landing impact and wheel spin-up were obtained from measurements made with the strain gages and linear accelerometers shown. As a check, the drag reaction was also obtained on one wheel (from consideration of the torque applied to the wheel by the drag reaction) by means of measurements of wheel rotational acceleration and measurements of tire deflection with the trailing arm shown. The trailing arm included instrumentation to give the vertical velocity of the truck at instant of contact. The rotational speed of each wheel was determined by a tachometer fastened to the outer brake shoe and geared to the wheel.

[redacted]

RESULTS AND DISCUSSION

Vertical and Drag-Reaction Time Histories

Figure 2 illustrates a time history of the vertical and drag reactions on one wheel experienced in a landing at a vertical velocity of 5.5 feet per second on dry concrete. The upper curve shows the buildup of the vertical reaction during the impact and its decay as the wheel starts to rebound. The two lower curves show the buildup of the drag reaction as the wheel is spinning up, the sudden decay of the reaction to about zero as the wheel fully spins up and the oscillatory nature of the reaction as the wheel springs forward and rearward after spin-up. The good agreement throughout the spin-up of the results from the two methods of measuring the drag reaction is shown. Following spin-up, the drag reaction from the strain-gage linear accelerometer measurements is not believed to be as reliable as that from the angular accelerometer tire-deflection measurements because of nonlinearities and hysteresis effects due to the axle arrangement which were amplified by the rapid changes in the drag reaction. It is interesting to note that spin-up of this relatively large wheel for the impact shown was completed in a little over 0.1 second corresponding to about one-third of a revolution of the wheel.

Wet and Dry Surface Conditions

Figure 3 shows a comparison of time histories (similar to the one shown in figure 2) for landings on both wet concrete and dry concrete at vertical velocities V_V of 2.5 and 5.5 feet per second. Several basic effects can be observed from this figure. An increase in the maximum vertical load with increase in vertical velocity for both wet and dry conditions is evident. For the lower vertical velocity, the maximum vertical load is about the same for the wet-runway condition as for the dry-runway condition. At the higher vertical velocity, the maximum vertical reaction is slightly higher for the dry condition than for the wet condition; however, this result was not consistently obtained, as will be shown later. For the wet-runway condition, it is evident that the coefficient of friction between the tire and runway (the instantaneous ratio of the drag reaction to the vertical reaction) is less than that for the dry condition. As would be expected from impulse-momentum considerations, the time to reach maximum drag reaction is greater and the value of the maximum drag reaction is less for the wet condition than for the dry condition. The maximum drag load for the wet condition is decreased both by the lower coefficient of friction and by the delay of the maximum drag load to a time where the vertical load has decreased.

Maximum Vertical Reactions

In figures 4 and 5, the effect of vertical velocity on the maximum vertical reactions measured for a number of landings is shown. Figure 4 shows the maximum vertical reactions measured on a truck (the sum of the loads on both wheels of a truck). Results are given for both left and right trucks for landings on dry and wet concrete. Examination of the results showed no apparent effect of the sequence of impact; that is, for a given vertical velocity of a truck the resulting vertical reaction was about the same whether the truck was the first or second to make contact. Inspection of the results obtained from the landings on wet concrete shows no consistent effect of the greatly reduced friction coefficient present in these tests on the maximum vertical reactions. This last result is in contrast to results reported in reference 1 which showed, for the bomber airplane used in those tests, an appreciable reduction in the maximum structural vertical load when the structural drag force was reduced by prerotation of the wheels, apparently because of reduced friction in the shock strut. The rather high values of the maximum vertical reaction shown at low vertical velocities apparently result from the fact that a vertical reaction averaging about 24,000 pounds had to be developed, because of the air pressure in the strut and the strut static friction, before the telescoping action of the shock strut started. Thus, up to this "breakout" force, the variation of the maximum vertical reaction with vertical velocity apparently had a rather steep slope determined by the load-deflection characteristics of the tires. The breakout force was about the same for both wet and dry conditions; consequently, this force was apparently unaffected by the lower drag reaction in the wet condition.

For correlation with the experimental results shown in figure 4, some values of the maximum vertical reactions have been calculated by use of the method described in reference 2. To date, for the assumed case of a rigid airplane in a symmetrical landing but with use of the actual tire and shock-strut characteristics of the airplane, the calculated results obtained show the same trend with vertical velocity as the experimental results but with values 10 to 15 percent higher.

For comparative purposes, design limits for the test airplane reduced to the weight used in these tests are shown. The upper limit represents the maximum vertical load for the case of zero drag load while the lower limit is for the case of drag load equal to the vertical load.

In figure 5 the maximum vertical reaction measured on the first wheel of a truck to make contact is shown - for example, in a landing in which the left truck contacts first, the results shown are for the left outboard wheel and the right inboard wheel. The dashed curve shown is one-half the value of the faired truck reaction (fig. 4). It can be

[redacted]

seen that, if an average is considered, the maximum vertical reaction on the first wheel of a truck to contact is somewhat greater than one-half the value for the truck, and therefore the average maximum vertical reaction on the other wheel of a truck is less by the same amount. Although all factors which cause the differences in reactions on the two wheels of a truck are not yet understood, it is believed that the differences for the most part arise from factors which affect the roll angle of the truck with respect to the ground, so that one wheel makes contact first and has a greater tire deflection and consequently a greater reaction than the other throughout the impact. Examination of the airplane roll attitude at contact indicated that, if an average is taken, a roll attitude of about 1° existed in such a direction as to cause this effect. This roll attitude used with the known force-deflection characteristics of the tires gave computed differences in the reactions of the wheels of about 2,500 pounds at low vertical velocities and about 4,500 pounds at the higher vertical velocities. These computed values, however, account for only about one-half the differences in the reactions on the two wheels.

Variation of Coefficient of Friction

The variation of the coefficient of friction with the instantaneous skidding velocity of the wheel during the spin-up period is shown in figure 6. The spin-up occurs from right to left, the highest skidding velocity occurring at the instant of impact and zero skidding velocity occurring when the wheel attains the fully rolling condition. Results are shown for a typical landing on dry concrete and for a typical landing on wet concrete. In each case the highest skidding velocity shown by the data is about 3 percent less than the horizontal velocity at initial contact because the measured loads for a small interval after contact are so small that errors in the measurements are significant in computing the friction coefficient. At skidding velocities near zero, data is not presented because the sudden decay of the drag load at this time prevented accurate determination of the coefficient of friction. In figure 7, the variation of the same quantities for both wet and dry conditions are shown for a number of landings as shaded regions. These regions represent the overall variation of the faired values of the individual landings. The variations in the results among landings is believed to be caused primarily by differences in the condition of the runway surface - for example, in the dry condition the presence of skid marks, oil, dirt, etc., and in the wet condition by these same effects and the amount of water present on the runway. The friction coefficient for the dry condition is seen to increase from values of 0.36 to 0.50 at nearly full sliding to 0.68 to 0.85 at incipient skidding. For the wet condition, the values of friction coefficient range from 0.10 to 0.20 at nearly full sliding to 0.28 to 0.47 at incipient skidding. Results are also shown from impacts

[redacted]

with forward speed and from impacts with both forward speed and reverse rotation of a small wheel on dry concrete in the Langley Impact Basin (ref. 3). The results agree well with the present results near spin-up, but the trends with skidding velocity appear to be in disagreement, probably as a result of the effects of different impact conditions, especially different slip ratios, where the slip ratio is defined as the ratio of the skidding velocity to the forward speed of the wheel. The ratio of the maximum structural drag load to the structural vertical load obtained in the bomber landing tests of reference 1 attained values as high as 0.8, although the majority of the results were considerably lower, probably because the runways used in these tests were still partly covered with a camouflage material consisting of sawdust spread on an asphalt binder.

The present results indicate that, for landings on dry concrete, the maximum drag reaction will be of the order of 80 percent of the vertical reaction at spin-up. It also appears that, for estimation of the variation of the drag reaction during spin-up for use in dynamic-analysis methods, consideration should be given to the variation of the coefficient of friction from the full-sliding value to the incipient-skidding value. The considerably lower values of the coefficient of friction on the wet concrete surface suggest the possibility of reducing drag loads in the landing impact by artificial lubrication of the tire or runway during the wheel spin-up period.

SUMMARY OF RESULTS

The principal results presented are summarized as follows:

1. The maximum vertical reaction on a truck, or on the first wheel of a truck to make ground contact, appeared to be primarily a function of the truck vertical velocity and to be unaffected by the sequence of impact.

2. The maximum vertical reaction was apparently unaffected by the greatly reduced friction coefficient present in the landings on wet concrete.

3. The first wheel of a landing-gear truck to make contact was found to have a maximum vertical reaction somewhat greater than that of the other wheel of the truck. The difference in the reactions on the two wheels of a truck is believed to arise primarily from factors which affect the roll angle of the truck, which causes one wheel to have a greater tire deflection and, consequently, a greater reaction than the other throughout the impact.

[redacted]

4. The coefficient of friction between the tire and the runway for both dry and wet surface conditions was found to increase considerably as the wheel progressed from the full-sliding condition to the incipient-skidding condition in the wheel spin-up process.

REFERENCES

1. Westfall, John R.: Measurements of Landing-Gear Forces and Horizontal-Tail Loads in Landing Tests of a Large Bomber-Type Airplane. NACA TN 1140, 1946.

2. Milwitzky, Benjamin, and Cook, Francis E.: Analysis of Landing-Gear Behavior. NACA Rep. 1154, 1953.

3. Milwitzky, Benjamin, Lindquist, Dean C., and Potter, Dexter M.: An Experimental Investigation of Wheel Spin-Up Drag Loads. NACA TN 3246, 1954.

ARRANGEMENT AND INSTRUMENTATION OF MAIN GEAR TRUCK

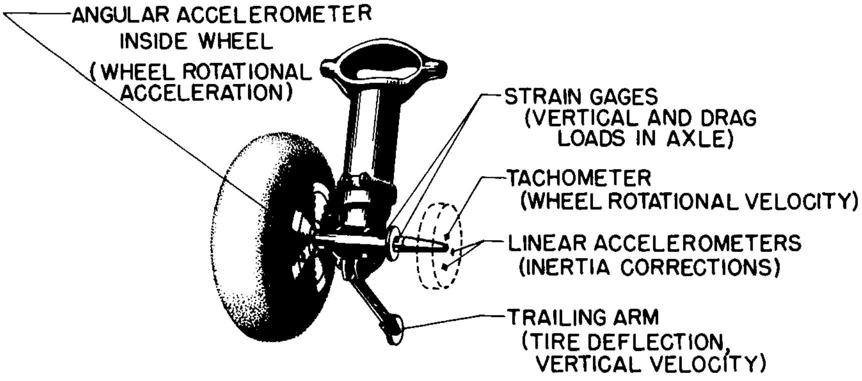
ANGULAR ACCELEROMETER INSIDE WHEEL (WHEEL ROTATIONAL ACCELERATION)
STRAIN GAGES (VERTICAL AND DRAG LOADS IN AXLE)
TACHOMETER (WHEEL ROTATIONAL VELOCITY)
LINEAR ACCELEROMETERS (INERTIA CORRECTIONS)
TRAILING ARM (TIRE DEFLECTION, VERTICAL VELOCITY)

Figure 1

GROUND REACTIONS ON WHEEL IN LANDING

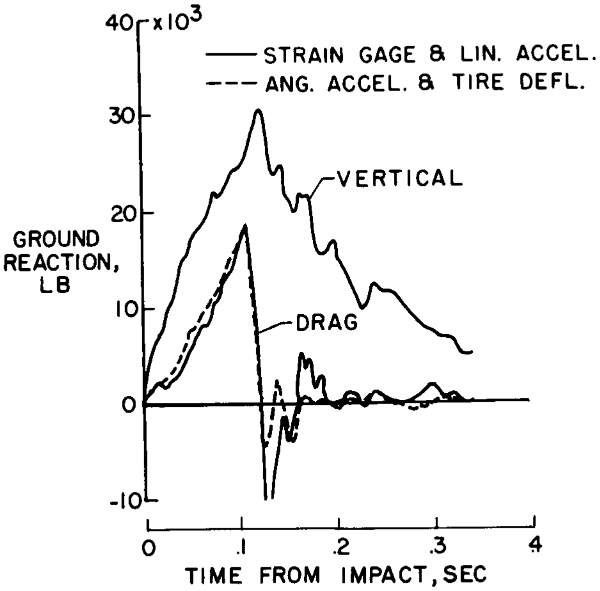

Figure 2

[redacted]

[redacted]

[redacted]

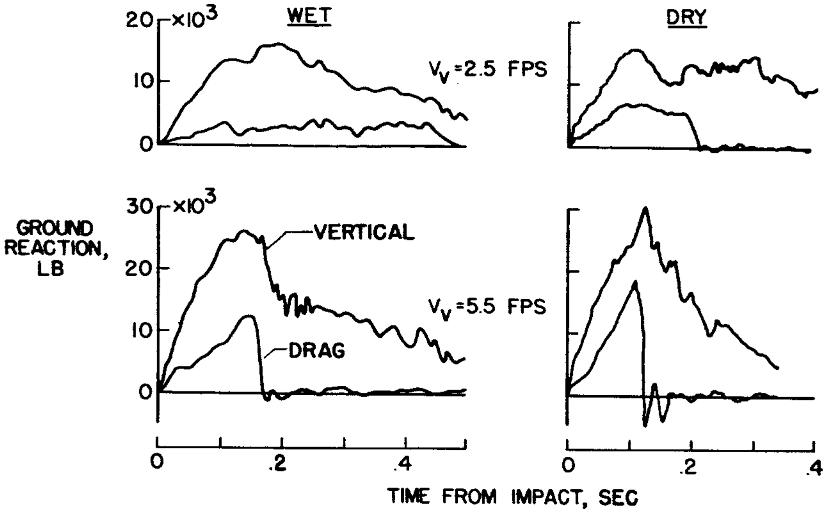
GROUND REACTIONS

Figure 3

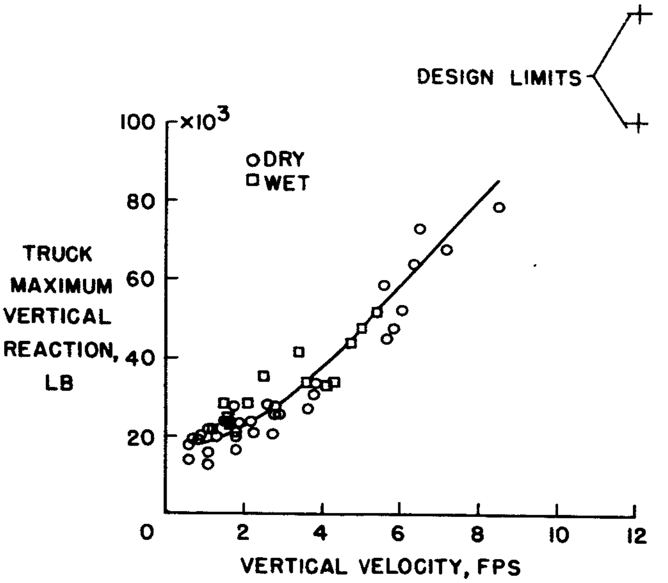
MAXIMUM VERTICAL GROUND REACTION ON TRUCK

Figure 4

[redacted]

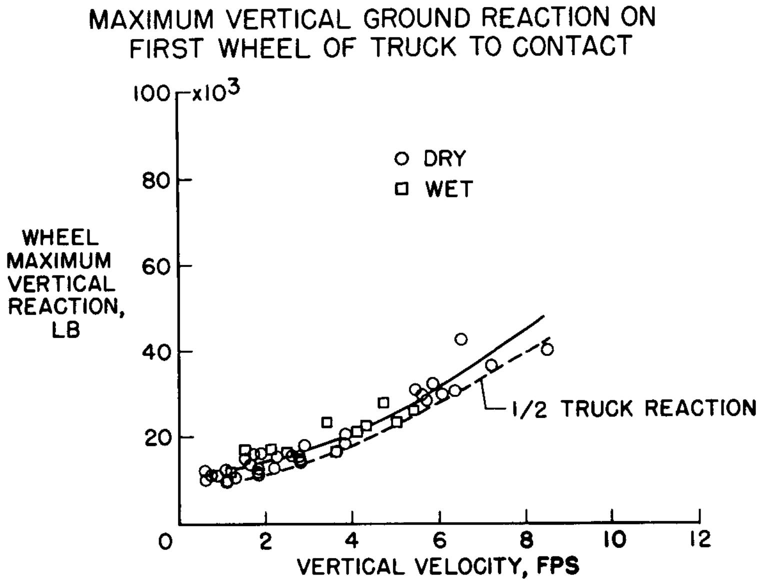

Figure 5

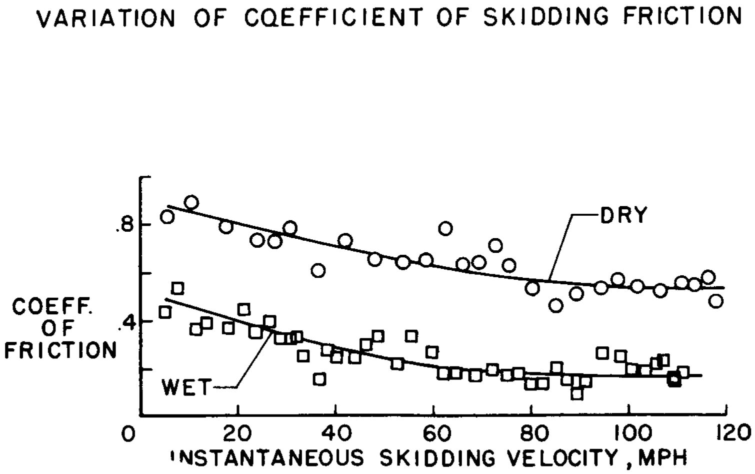

Figure 6

[redacted]

VARIATION OF COEFFICIENT OF SKIDDING FRICTION

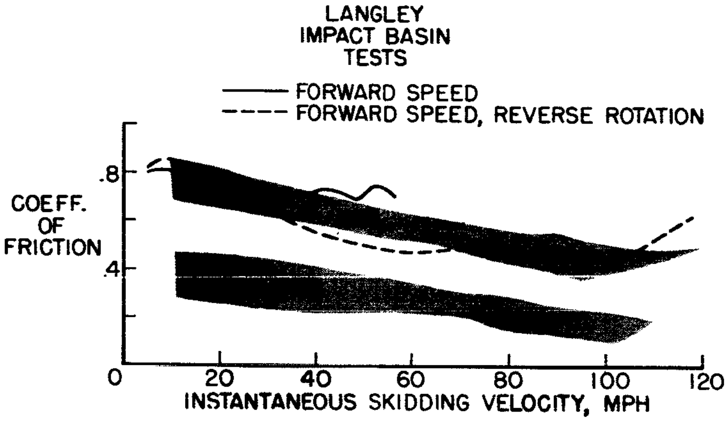

Figure 7

[redacted] 1228J039

ON SPECTRAL ANALYSIS OF RUNWAY ROUGHNESS AND LOADS DEVELOPED DURING TAXIING

By John C. Houbolt, James H. Walls, and Robert F. Smiley

Langley Aeronautical Laboratory

SUMMARY

The application of the techniques of generalized harmonic analysis to the airplane taxiing problem is considered in a cursory manner in this paper. Some previous results on runway roughness are reviewed, and some results obtained from taxiing tests of a large airplane are given.

It is indicated that an extrapolation by elementary means of results from low taxiing velocities to higher taxiing velocities would lead to conservative results. Oleo-strut friction is shown to be a very important factor in the taxiing problem. With regard to the load-prediction phase of taxiing loads by spectral techniques, much additional work is required, especially with respect to the treatment of the transfer functions.

INTRODUCTION

The purpose of this paper is to review some previous runway-roughness measurements and to present some results obtained from taxiing tests of a Boeing B-29 airplane. Besides the results themselves, the chief concern is a preliminary evaluation of how well the techniques of generalized harmonic analysis apply in the analysis of the taxiing problems. There is no intent in the paper to make a comprehensive study of the problem or even to evaluate in detail some of the points covered. This paper is to be regarded as being introductory in nature.

RUNWAY-ROUGHNESS STUDIES

A brief review of an earlier runway-roughness study is given in this section. Measurements of elevation were made by means of a surveyor's level and rod on two runways at Langley Field, Va. The spacing of the measurements was taken as 2 feet. These measurements and the power spectra of roughness obtained from them have been previously published in reference 1. The power spectra are reproduced in figure 1 where the

[redacted]

DECLASSIF [redacted]

ordinate $\Phi_h(\Omega)$ is the power spectrum of runway elevation h and the abscissa Ω is a spacial frequency which is inversely related to the length L of the harmonic components as indicated in the figure. The curve labeled "smooth" applies to one of the Langley runways in routine use. The curve labeled "rough" applies to a runway which is now used only for parking.

From these results three significant points may be drawn: (1) The use of power-spectral analysis seems to be a very concise way of presenting runway characteristics and gives at a glance the manner in which the roughness is distributed to the various frequency components. (2) A means is suggested for establishing a criterion for judging the severity of runway roughness. Thus, it is conceivable that, by compiling the spectra of many different satisfactory runways, a spectrum may be established within whose limits all new runways must be built or all old runways maintained in order to insure satisfactory operation. And (3) as an extension of the second point, a "design spectrum" might also conceivably be established which provides the basis for a rational requirement in the design for taxi loads.

It is realized at present that the question of whether a runway is rough is largely a subjective one; it depends on pilot interpretation, his experience, what type of operations are being performed, and other considerations. From the information that could be gathered, it is judged that the rough runway dealt with in reference 1 is a borderline case. Thus, tentatively the experimental spectrum for this runway might be regarded as an upper limit of acceptable roughness, or as a lower limit of runways which are too rough.

LOAD PREDICTION AND RESULTS OF TAXIING STUDIES

The problem of predicting loads in an airplane from spectra of roughness is now considered. For the airplane with pneumatic tires, nonlinear struts, and many degrees of freedom, the problem is extremely difficult; in fact, it is not known whether a solution is possible. However, the remainder of this paper does present a few observations pertinent to a solution of this problem which have been gathered largely from taxi tests with a Boeing B-29 airplane. By way of introduction, consider what elementary theory would predict. As a first approximation, the runway-roughness spectrum may be expressed by a simple expression of the form $\Phi_h(\Omega) = C/\Omega^2$, where C is a constant. In terms of the frequency argument $\omega = V\Omega$, where ω is frequency in radians per second, the roughness spectrum would be $\Phi_h(\omega) = CV/\omega^2$. If a linear system is assumed, then the following input-output relation applies

[redacted]

[redacted]

$$\Phi_o(\omega) = T^2(\omega)\Phi_h(\omega)$$

where $\Phi_o(\omega)$ is the output spectrum and $T(\omega)$ is the amplitude of the frequency-response function. With the previous approximate input expression, the output would be

$$\Phi_o(\omega) = V \frac{CT^2(\omega)}{\omega^2}$$

Now, if the further assumption is made that T is independent of airplane velocity when expressed in terms of the frequency argument ω, it is seen that the output spectrum should be linearly proportional to V. This suggests that the mean-square output, which is the area under the output spectrum, is proportional to V.

This relation was tested by means of the B-29 taxi tests and the results are shown in figure 2, where ${\sigma_a}^2$ is the mean-square value of center-of-gravity vertical acceleration. It is seen that the results are surprisingly linear for the lower velocities. There is, however, a marked dropoff in the mean-square acceleration for high velocities; an explanation for this is offered in the subsequent discussion.

Next, the distribution of mean-square acceleration to the various frequency components is considered. Figure 3 shows the B-29 output spectra, in terms of the spectrum of center-of-gravity vertical acceleration, plotted as a function of frequency ω in radians per second. Curves are shown for three different velocities. First, note the rather pronounced peaks in the spectra. These peaks may be identified with certain natural frequencies. The first peak is associated with the vibration of the airplane on its tires; the second, with fundamental wing bending; and the third, with fuselage bending. Next, note that at the higher frequencies there is an orderly increase in the spectra height with velocity, consistent with the result derived on an elementary basis. At the lower frequencies, however, where there is the most power, there is first an increase and then a decrease as the velocity increases. As was previously mentioned, the areas under these curves equal the mean-square accelerations. It can, thus, be seen that the area would not increase linearly with velocity; but more specifically it can be seen that the departure from linearity is due largely to the dropoff of the spectra at high velocities in the lower range of frequency, where the roughness is most severe.

An explanation of why this dropoff occurred can be made by examining the behavior of the main oleo struts, which is shown in figure 4. This

[redacted]

[redacted]

figure presents reproduced oscillograph traces of oleo-strut motion which show two important points: (1) At 10 mph, there is no strut motion; and (2) at other velocities, strut motion is only in the form of random step functions, the number and severity of these step functions increasing as the velocity increases. Both these points indicate the presence of a very sizable friction force in the struts. In fact, at 10 mph, the taxiing loads evidently never exceeded the friction force; and, therefore, the airplane behaved like a flexible structure on elastic tires only. At higher taxiing speeds the strut releases momentarily and then seizes as the taxiing loads occasionally exceed the friction force, and the number of such occurrences increases with velocity as might be expected. This inherent load-limiting action seems to account for the dropoff in the output spectra at the higher velocities. To see this erratic behavior take place, however, is somewhat disconcerting, since it appears that such factors have to be included in the treatment of the problem.

In the treatment of this problem by spectral techniques, the determination of the frequency response or transfer function is of primary interest. It has been suggested that perhaps the frequency-response function of the airplane could be deduced from the response that is obtained by taxiing over rectangular bumps, thereby obviating all the assumptions and restrictions that would have to be made in attempting to derive these functions analytically. Therefore, some taxiing runs over rectangular planks were included in the B-29 taxi tests. Figure 5 shows three of the time histories of center-of-gravity acceleration that were obtained. It is noted that these curves resemble the damped 10 cps sine wave which is shown also for comparison. This 10 cps frequency is very much higher than the predominating characteristic frequencies that are present in the output spectra of figure 3, which were on the order of 2 to 3 cps. The impulsive loads received from the planks evidently excite a very high frequency component which completely dominates the lower frequencies of concern in continuous roughness studies. In addition, there was a very pronounced oleo movement in these tests. Thus, not only are different frequencies excited but also the system behaves differently than it does in the normal taxiing operations. There is, therefore, no point in trying to derive the frequency-response functions from these impulse responses, since there is essentially no low frequency power coming through. The conclusion drawn is that presumably a more appropriate type of test would be to taxi over a corrugated surface having long wavelengths.

The final aspect in this paper deals with the computation of the frequency response or transfer function. As yet it is not known whether it is possible to pursue the course of action where an equivalent linear system is found which will yield results characteristic of the actual system, or whether it is necessary to go to a more involved nonlinear treatment. Many of the remarks made thus far concerning the several structural degrees of freedom and the erratic behavior of the oleo as

[redacted]

brought about by strut friction - not to mention the inherent nonlinear characteristics - suggest some of the factors that undoubtedly have to be included in this consideration. As an example of another factor which has to be included, figure 6 presents theoretically derived transfer functions for the case where the airplane is considered rigid and the landing struts are replaced by linear undamped springs. The point to note is that the transfer function at 80 mph is slightly different than at 10 mph, thereby indicating a slight velocity dependence, which is contrary to the assumption made in the elementary consideration at the beginning of this paper. Thus, velocity is another factor which must be considered. The manner in which velocity enters is connected with the bumps and valleys of the curves in figure 6. The first two peaks are associated with a structural type of resonance; the other peaks, however, are associated with a geometric type of resonance. These later peaks correspond roughly to the condition where the wavelengths of the ground roughness are direct multiples of the distance between the main and nose landing gears. For these conditions, both main and nose landing gears rise and fall together; hence, the individual effects of the two gears on the center-of-gravity acceleration are additive. The later valleys on the curves correspond roughly to those ground wavelength conditions where the motions of the two gears are the most out of phase, such that the main gear is rising when the nose gear is falling. Hence, one gear tends to produce positive center-of-gravity acceleration, while the other one tends to produce negative acceleration - the net center-of-gravity acceleration being the difference of these two accelerations as compared to the sum for the case where the two gear motions are in phase.

CONCLUSIONS

From an investigation of runway roughness and loads developed during taxiing of a large flexible airplane, the following conclusions are presented:

1. The use of spectral techniques seems to be a rather concise way of presenting the characteristics of runway roughness.

2. An extrapolation by elementary means of results from low taxiing velocities to higher taxiing velocities would lead to conservative results.

3. Oleo-strut friction is an important factor in the behavior of airplanes while taxiing.

4. With regard to the load-prediction phase of taxiing loads by spectral techniques, much additional work is required, especially with respect to the treatment of the transfer function.

[redacted]

[redacted]

REFERENCE

1. Walls, James H., Houbolt, John C., and Press, Harry: Some Measurements and Power Spectra of Runway Roughness. NACA TN 3305, 1954.

[redacted]

[redacted]

ELEVATION SPECTRA

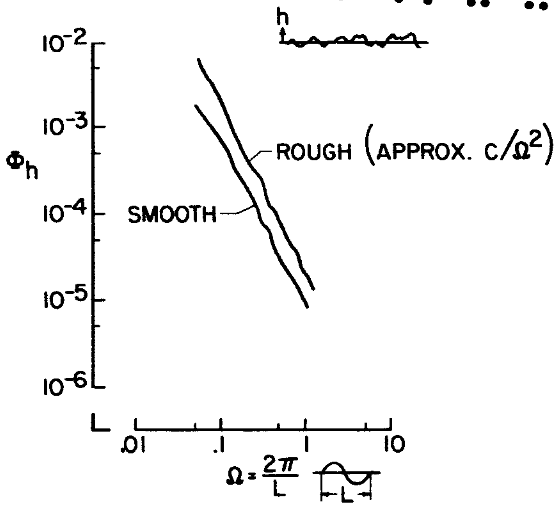

Figure 1

MEAN SQUARE C.G. ACCELERATION

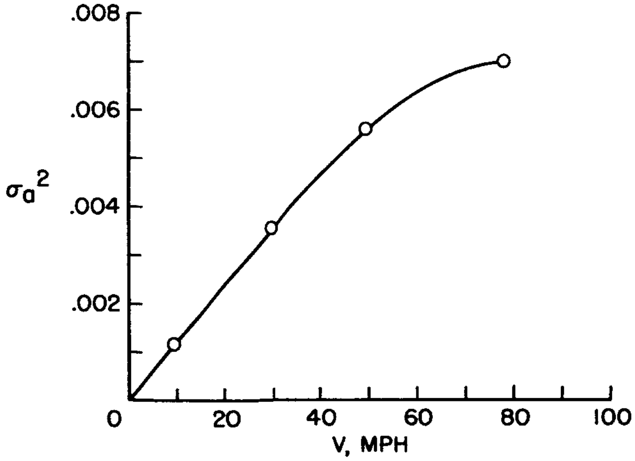

Figure 2

[redacted]

[redacted]

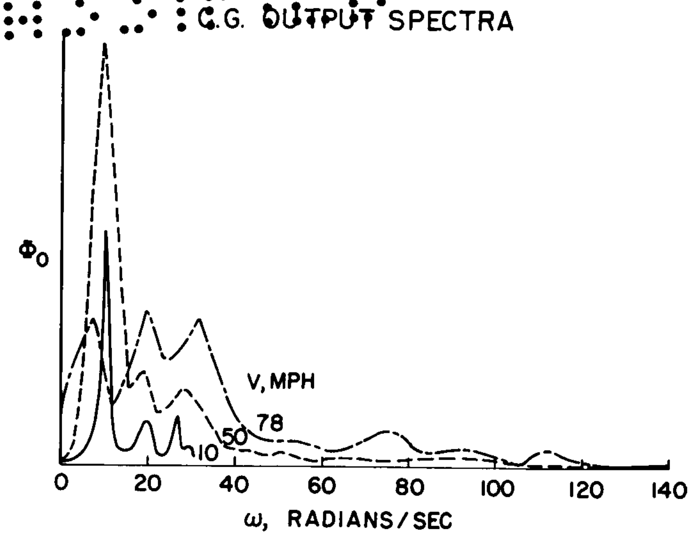

Figure 3

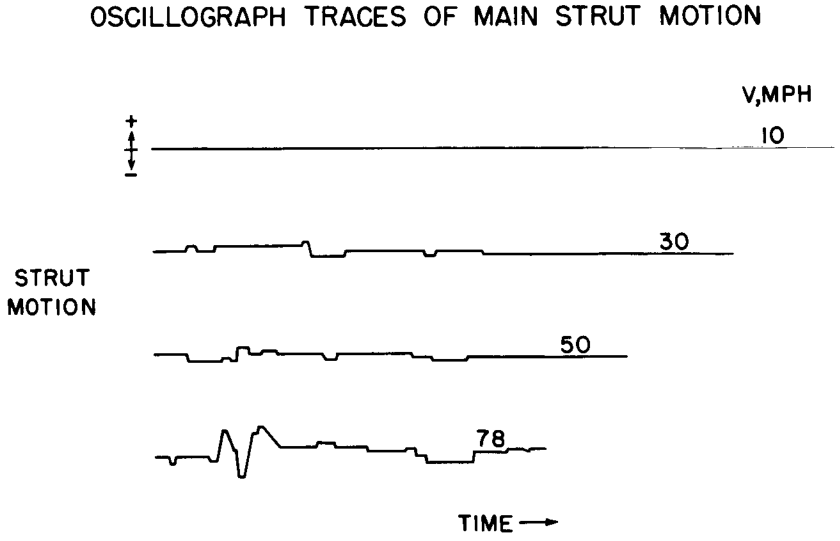

Figure 4

[redacted]

[redacted]

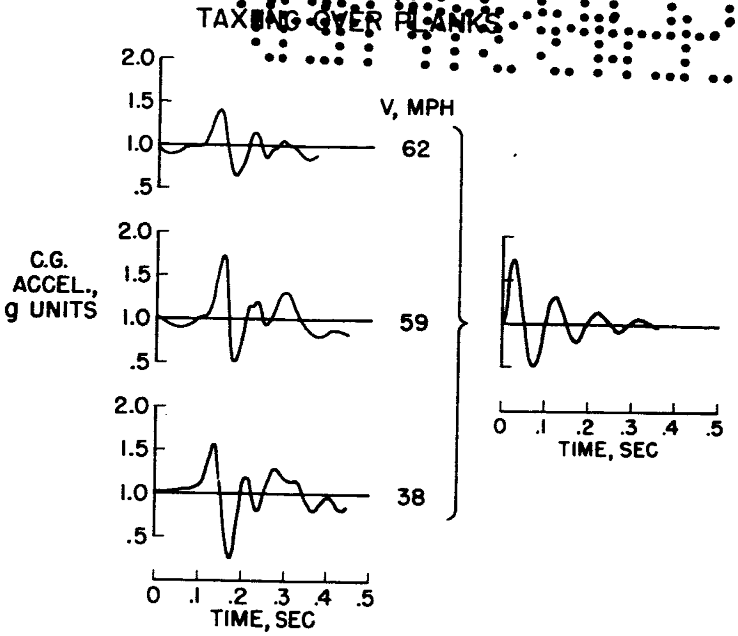

Figure 5

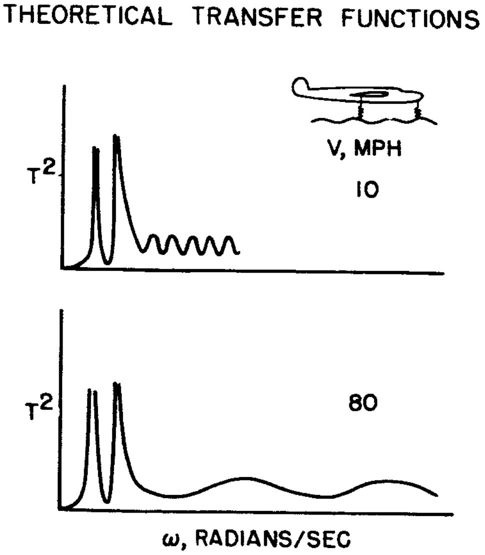

Figure 6

[redacted]

FLUTTER AND BUFFETING

1fv

[redacted]

A STUDY OF THE CORRELATION BETWEEN FLIGHT AND WIND-TUNNEL BUFFETING LOADS

By Wilber B. Huston, A. Gerald Rainey, and Thomas F. Baker

Langley Aeronautical Laboratory

SUMMARY

Comparison of the buffet loads measured on wind-tunnel models with loads measured in flight indicates that, during the course of the regular wind-tunnel testing program on a model, a simple strain-gage measurement can be made which can be used to predict the wing buffet loads on the airplane. The comparison is made for airplanes with swept and with unswept wings. The relation between buffet loads on a model and buffet loads on an airplane in flight is discussed from the standpoint of the input-output relationships of generalized harmonic analysis. The analysis of buffet load measurements on a statistical basis is outlined.

INTRODUCTION

In several of the wind tunnels, experiments have been under way to see whether some simple measurement could be made, preferably in the course of the regular wind-tunnel testing program, which would predict the buffeting loads encountered on the airplane. This paper is in the nature of a progress report on this investigation.

In a study of this sort it has been necessary to find a measure of the loads which despite the fluctuating character of buffeting would permit comparison of model and airplane results. The instrumentation has been based on electrical strain-gage bridges mounted at the wing root of both model and airplane. Statistical procedures have been used in the data reduction and some of the quantities used are illustrated in figure 1.

SYMBOLS

$A^2(\omega)$	admittance of elastic system
b	wing span

[redacted]

[redacted]

c	chord
C_L	lift coefficient
C_{L_α}	effective slope of lift curve under condition of separated flow
C_M	bending-moment coefficient
C_N	normal-force coefficient
f	frequency
q	dynamic pressure
t	time
T	time interval
c_n	section normal-force coefficient
$L^2(\omega)$	power spectral density function of buffet force
p	static atmospheric pressure
V	airspeed
y	spanwise coordinate
y_g	location of strain-gage station
F_s	a structural factor
S	area
S_1	effective area in bending
S_2	effective area in bending
M_w	mass of wing
M_1	effective mass of wing in bending
$w_1(y)$	normalized shape of first bending mode
M_{m_1}	effective moment of wing mass outboard of strain-gage station

[redacted]

σ	standard deviation, or root-mean-square value
γ	ratio of damping to critical damping
ω	circular frequency

Subscripts:

L	shear
M	moment

ANALYSIS OF FLUCTUATING DATA

The wavy line in figure 1 is a portion of a strain-gage record taken during buffeting. Maximum peak-to-peak values have been used in the past as a measure of magnitude, but this measure suffers from a number of disadvantages. If the fluctuations y_B are taken as variations about the mean line (dashed), a number of studies under constant conditions of lift and Mach number both in wind tunnels and in flight show that the fluctuations are normally distributed. In other words, buffeting is a particular type of a random process, a Gaussian process. For such a process a natural measure and one which is of a much more stable nature than a peak-to-peak value is the root-mean-square value or the standard deviation σ. In the tunnels, this measure is easily obtained from a strain-gage output with standard electrical techniques. In flight, buffeting is frequently encountered during maneuvers, and the buffeting intensity may change with flight condition. For the analysis of flight records, where as here the maneuver component is changing, it has been found feasible to separate the two components by using numerical methods (see ref. 1), break the buffet component into a series of short intervals of say 1/2 second, determine the root-mean-square value over each as defined by the formula, and use it as a measure of intensity. Flight-load data obtained in this way have been used for comparison with the wind-tunnel data.

SCALING OF BUFFET LOADS

For comparison of flight and model loads, some sort of scale factor is required. For dynamic analyses, the complexity of this scale factor would depend upon the complexity of the dynamic systems involved. Although airplanes exhibit complex vibration patterns, there are indications that, in some instances at least, simplification is permissible for the analysis of buffeting. Shown in figure 2 are frequency analyses of the wing-root bending moments obtained on three different airplanes: the Douglas X-3 with unswept wing, the Douglas D-558-II with swept wing, and the Convair XF-92A with delta wing. The ordinate is the power spectral density of the wing bending moment as obtained by Tukey's numerical procedures (see ref. 2) or the equivalent electrical techniques. Each spectrum is characterized by a single large peak and is similar to the response of a lightly damped single-degree-of-freedom system. In each case this peak is that associated with first symmetrical wing bending. Other modes are excited but to a very much lesser extent and it appears that a dynamic analysis based on a single degree of freedom should at least take care of first-order effects.

A simple basis for scaling buffet loads, and one which has been frequently used for the analysis of buffet data may be termed the static analogy. Just as static forces such as lift or bending moment are defined by dimensionless coefficients C_L and C_M in the equations

$$L = C_L q S \tag{1}$$

$$M = C_L q \frac{b}{2} S \tag{2}$$

the root-mean-square shear σ_L or root-mean-square bending moment σ_M could be expressed by similar buffeting coefficients

$$\sigma_L = C_{L_B} q S \tag{3}$$

$$\sigma_M = C_{M_B} q \frac{b}{2} S \tag{4}$$

The dynamic analysis of buffeting has been considered in some detail in references 3 to 5. The method, that of generalized harmonic analysis, is illustrated in some detail in reference 5 which has provided the basis for the present study. The input force, the admittance of the elastic system, and the aerodynamic damping all vary with frequency. Lift fluctuations associated with the separated flow over the wing are expressed in terms of their frequency content by means of a spectrum which is a function not only of frequency but of reduced frequency $\omega c/V$,

$$L^2(\omega) = q^2 c^2 \frac{c}{V} c_n\left(\frac{\omega c}{V}\right) \tag{5}$$

The admittance is that for a single-degree-of-freedom system,

[redacted]

$$A^2(\omega) = \frac{1}{\left(1 - \frac{\omega^2}{\omega_1{}^2}\right)^2 + \left(2\gamma \frac{\omega}{\omega_1}\right)^2} \tag{6}$$

The damping expressed in terms of critical damping is aerodynamic of the sort which is proportional to the angle-of-attack changes induced by the velocity of the bending vibrations and is specified by an effective slope of the lift curve C_{L_α} which is also a function of reduced frequency

$$\gamma(\omega) = \frac{qc}{2m\omega_1 V} c_{l_\alpha}\left(\frac{\omega c}{V}\right) \tag{7}$$

These relationships may be used to compute the root-mean-square bending moment at the wing root

$$\sigma_M = \left[\omega_1 \frac{b}{2}\sqrt{\bar{c}SM_W}\right]\sqrt{q}\, F_S\left[\frac{C_N\left(\frac{\omega_1\bar{c}}{V}\right)}{C_{L_\alpha}\left(\frac{\omega_1\bar{c}}{V}\right)}\right]^{1/2} \tag{8}$$

In this expression (eq. (8)), the many parameters which enter have been grouped in several related terms. The first term in brackets includes the principle physical characteristics of the wing (natural frequency, span, chord, and mass). The operating conditions are represented by the square root of q. The quantity F_S is a dimensionless structural factor which reduces the actual values of wing area, mass, and moment arm to their effective values in the vibrating system. For a wing with spanwise chord distribution $c(y)$ the area S and two effective areas S_1 and S_2 are given by the expressions

$$S = \int_{-b/2}^{b/2} c(y)\,dy \tag{9}$$

$$S_1 = \int_{-b/2}^{b/2} c(y)w_1(y)\,dy \tag{10}$$

$$S_2 = \int_{-b/2}^{b/2} c(y)w_1{}^2(y)\,dy \tag{11}$$

where $w_1(y)$ is the shape of the fundamental wing-bending mode (taken as unity at the wing tips, $y = \pm b/2$). For a spanwise mass distribution $m(y)$, the wing mass M_W and an effective mass M_1 are defined by the integrals

$$M_W = \int_{-b/2}^{b/2} m(y)\,dy \tag{12}$$

$$M_1 = \int_{-b/2}^{b/2} m(y) w_1^2(y)\,dy \tag{13}$$

The effective moment of the mass outboard of the point y_g at which the strain-gage station is located is

$$M_{m_1} = \int_{y_g}^{b/2} (y - y_g) m(y) w_1(y)\,dy \tag{14}$$

and the structural factor F_S is given by the equation

$$F_S = \frac{M_{m_1}}{M_1 \frac{b}{2}} \sqrt{\frac{\pi}{8} \frac{S_1^2}{S_2 S} \frac{M_1}{M_W}} \tag{15}$$

The second term in brackets (eq. (8)) represents the magnitudes of the input spectrum and the damping at the particular value of reduced frequency corresponding to the fundamental bending frequency, the average chord, and the flight speed.

One simple basis for dynamic scaling is evident in equation (8). For both an airplane and its model, the factor F_S, depending primarily on plan form and mode shape would be the same. If the reduced frequency of the model in the tunnel can be arranged to be the same as the flight value, the second term in brackets would also be the same. Thus in the ratio of the root-mean-square bending moment in flight to that of the model, the primary factor is the group of parameters included in the first bracket.

[redacted]

On the other hand, a more elaborate study could evaluate the reduced frequency function (second term in brackets) and it could be used as the basis for scaling. This parameter has been used in the flutter-tunnel study described subsequently.

One important distinction between the static and dynamic bases for scaling lies in the forms q and $\sqrt{q}$. An example of the use of statistical procedures for the analysis of flight buffeting loads which appears to discriminate neatly between the static and dynamic case is provided by a recently completed analysis of some buffeting data on the North American F-86A, some of which are shown in figure 3.

CORRELATION OF BUFFET LOAD WITH FLIGHT CONDITION

Shown on the left-hand side of figure 3 are the values of C_N and Mach number during a typical gradual turn into buffeting. The circles represent conditions at successive one-second intervals. Also reproduced are half-second samples of an oscillograph record of a wing-root-strain-gage bridge sensitive in this case primarily to shear. The arrows run to the average flight condition during the sample; the numbers 10 to 340 are the values of root-mean-square shear. There is a strong correlation between values of σ and C_N for this maneuver, as indicated by the plot on the right. This maneuver was performed at 35,000 feet. Similar data exist for a number of runs at this altitude at $M = 0.8$ and also at 45,000 feet. For wing-root bending moments, there are data at 20,000, 35,000, and 45,000 feet, some of which are shown in figure 4, where a comparison is made between the buffet loads at three different altitudes at $M = 0.8$. The root-mean-square bending moment is plotted against the static pressure on a log-log scale. The values and trends shown here, which are for a C_N of 0.65, are typical of those obtained with both shear and bending moment at other values of C_N. Straight lines with slopes proportional to p and $\sqrt{p}$ have been placed on the plot. Since Mach number is constant, these lines are also proportional to q and $\sqrt{q}$. The agreement shown with the $\sqrt{q}$ relationship confirms for a swept wing at transonic speeds the indications from an unswept wing reported in reference 5 and lends strong support to the validity of the dynamic approach to buffet scaling.

COMPARISON OF WIND-TUNNEL AND FLIGHT-TEST RESULTS

In figure 5 some buffet loads are given for a 1/16-scale model of the Douglas D-558-II measured in the Langley 7- by 10-foot tunnel. Shown are results for four different Mach numbers. The root-mean-square bending moment measured near the wing root at the 50-percent chord line has been measured with a strain-gage bridge and is plotted against lift coefficient. Circles represent runs made at the start of a general program on the model; squares represent a check run made at the middle of the general program; both show a good order of consistency. Straight lines have been faired through the data to represent what appear to be three typical characteristics. A low-level portion at low lift showing no change with lift occurs first; then there is a sharp increase with lift; and at the higher Mach numbers there is a further change in slope at still higher values of lift.

The low-level portion is believed to be associated with the residual tunnel turbulence. These tests were made following the installation of screens in the tunnel, a change which considerably improved the dynamic response of models although no change in static aerodynamic characteristics was noted. The increase in level is similar to that noted in flight on the F-86A. The change in slope was not noted on the F-86A tests but it occurs at values of lift which are higher than those reached in that study.

An important difference between the loads measured on the model in buffeting and those on the airplane is apparently associated with the model support system. The model was sting supported, the actual connection between sting and model being a six-component strain-gage balance. A frequency analysis of the model wing-root bending moment in buffeting is shown in figure 6. For the model as for the airplane, the bending moments in buffeting are largely associated with response in the first symmetrical wing bending mode, in this case centered on 196 cps, but another mode, which is a rocking motion of the model as a whole about the balance, is also present at about 80 cps. This physical restraint of roll by the balance represents a constraint and a vibrational mode which have no real counterparts in the buffet response of the airplane. The meter used to record the wing-root strain-gage output recorded the mean square of all components above about 5 cycles per second. Frequency analyses (of which figure 6 is typical) have been made of a few oscillograph records obtained during the tests at $M = 0.9$. These analyses indicate that roughly one-half of the mean-square bending moment is associated with the symmetrical bending mode. That is, on a square-root basis, the data of figure 5 at $M = 0.9$ are roughly 30 percent high when comparison with flight is contemplated. It also appears that a simple correction could be made or a high pass filter could be used to separate the symmetrical bending mode. Sufficient data are not now available, however, to adjust these data at all Mach numbers so that, for an extension to flight-test conditions, the faired lines were used to represent the wind-tunnel data, the low-level portion being ignored.

Shown in figure 7 is a comparison of the model loads (fig. 5) scaled to the D-558-II airplane and compared with the root-mean-square bending moments measured in two gradual turns into buffeting at the average Mach numbers shown. The reduced frequencies of both model and airplane are nearly the same; the lines represent the 1/16-scale-model loads scaled to the flight conditions on the basis of the dynamic analysis incorporated in equation (8). The agreement between the scaled and flight data is considered to be encouraging.

In connection with figures 5 and 6, it was stated that the wind-tunnel data at $M = 0.9$ were of the order of 30 percent high because of the presence of model response in modes (especially the rocking mode at 80 cps) which have no counterpart in flight. The shaded area on the right-hand side of figure 7 is used to indicate where the model tests would fall if a simple correction were made for this effect. This comparison with flight loads is considered to be promising, especially when coupled with the results of a study under way in the Langley flutter tunnel shown in figures 8 and 9.

In figure 8 the ordinate is the value of root-mean-square bending moment in buffeting expressed in terms of the reduced frequency buffeting parameter discussed in connection with the dynamic analysis

$$\left[\frac{C_N\left(\frac{\omega_1\bar{c}}{V}\right)}{C_{L_\alpha}\left(\frac{\omega_1\bar{c}}{V}\right)}\right]^{1/2}$$

The abscissa is the reduced frequency $\omega_1\bar{c}/V$ where ω_1 is the frequency of fundamental bending and $\bar{c}$, the average chord. These tests were run on a family of related unswept wings of the same geometry and airfoil section which differed only in stiffness and natural frequency and thus in the product $\omega_1\bar{c}$ shown. Each point represents a value of reduced frequency corresponding to a different speed. These data are for an angle of attack of 12°; data have been obtained for a number of different angles of attack. The variation with reduced frequency is typical. It is well represented by a mean line at higher values of $\omega_1\bar{c}/V$; the separation at lower values is believed to be a Mach number effect and is the subject of further investigation involving tests in both air and Freon.

These tests were made on semispan models rigidly mounted on the tunnel wall. The lowest identifiable frequency in the strain-gage output is that of fundamental bending and the buffeting should therefore be comparable to that in flight. A comparison with flight has been made by using the data of figure 9 and that of other angles of attack; the range of reduced frequencies covered in the comparison is indicated by the mean line. The wind-tunnel data were used to estimate the buffet loads on the X-3 airplane. The results are shown in figure 9. The circles represent values of root-mean-square bending moment measured during a 1 g stall at constantly decreasing airspeed plotted against angle of attack. The change in Mach number during the run is indicated by the arrows. The wind-tunnel results have been scaled on a dynamic basis. The comparison again is considered to be promising.

CONCLUDING REMARKS

The present study has summarized the available data on the use of model tests as an indicator of the magnitude of buffet loads. The strain-gage technique, applied to both an unswept and a swept configuration, appears promising, and its use appears to be indicated in those wind tunnels with suitable flow characteristics.

Statistical concepts provide a valuable guide in the analysis of flight-test data and scaling of the wing loads on a simple dynamic basis, which employs the methods of generalized harmonic analysis, appears to be feasible.

REFERENCES

1. Huston, Wilber B., and Skopinski, T. H.: Some Statistical Analyses of Buffeting. (Prospective NACA paper.)

2. Press, Harry, and Houbolt, John C.: Some Applications of Generalized Harmonic Analysis to Gust Loads on Airplanes. Preprint No. 449, S.M.F. Fund Preprint, Inst. Aero. Sci., Jan. 25-29, 1954.

3. Liepmann, H. W.: On the Application of Statistical Concepts to the Buffeting Problem. Jour. Aero. Sci., vol. 19, no. 12, Dec. 1952, pp. 793-800, 822.

4. Miles, John W.: An Approach to the Buffeting of Aircraft Structures by Jets. Rep. No. SM-14795, Douglas Aircraft Co., Inc., June 1953.

5. Huston, Wilber B., and Skopinski, T. H.: Measurement and Analysis of Wing and Tail Buffeting Loads on a Fighter-Type Airplane. NACA TN 3080, 1954.

[redacted]

QUANTITATIVE EVALUATION OF BUFFETING

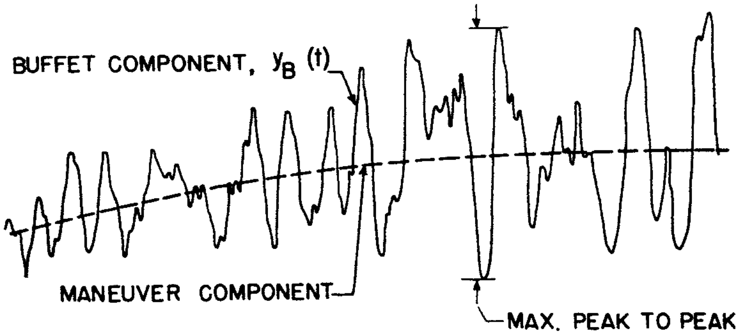

$$\sigma(t) = \left[\frac{1}{2T} \int_{t-T}^{t+T} y_B^2(t)\,dt \right]^{1/2}$$

Figure 1

FREQUENCY CONTENT OF WING BUFFET LOADS

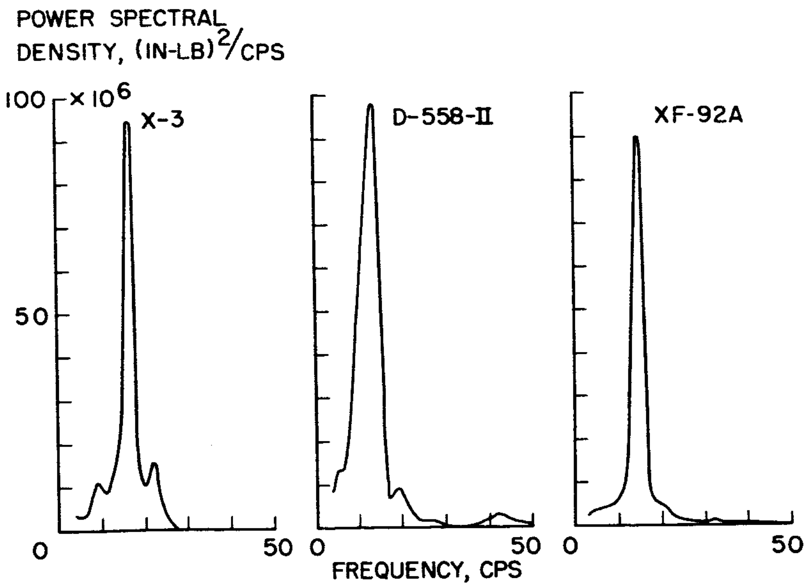

Figure 2

[redacted]

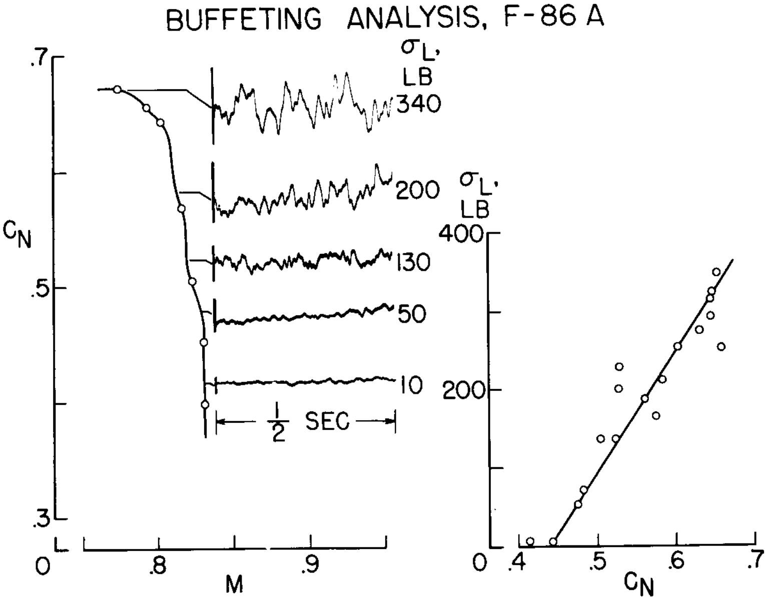

Figure 3

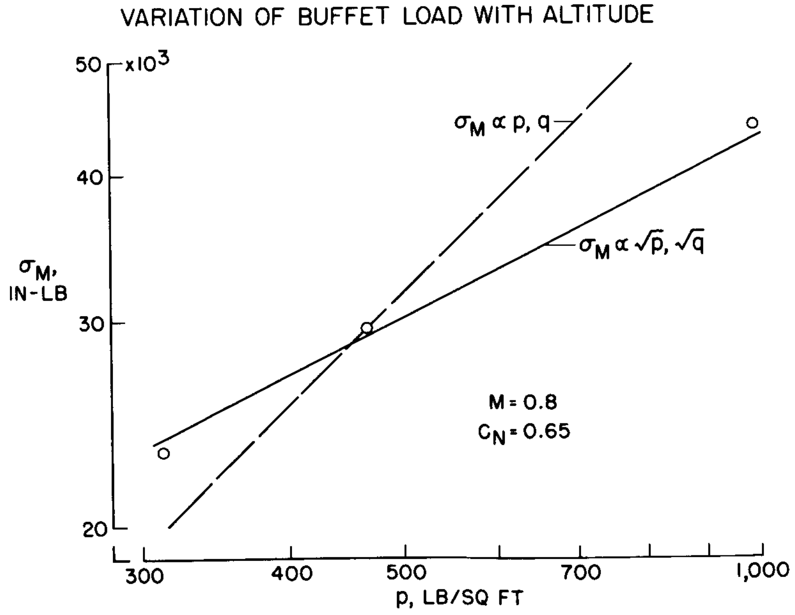

Figure 4

[redacted]

[redacted]

WING-ROOT BENDING MOMENTS, D-558-II
1/16-SCALE MODEL; LANGLEY 7'x10' TUNNEL

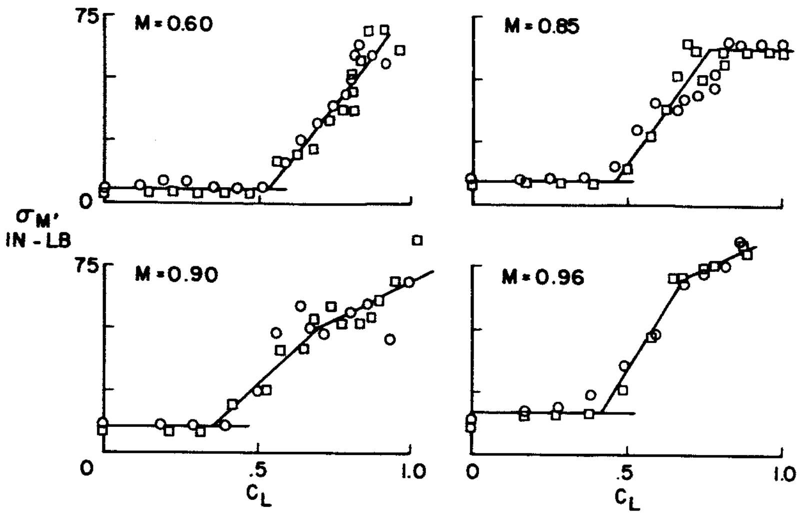

Figure 5

FREQUENCY CONTENT OF MODEL WING ROOT BENDING MOMENT

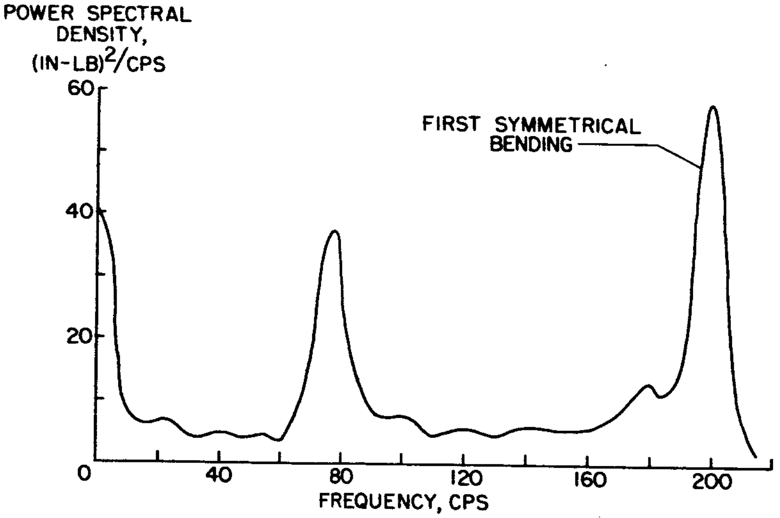

Figure 6

[redacted]

DECLASSIFIED

[redacted]

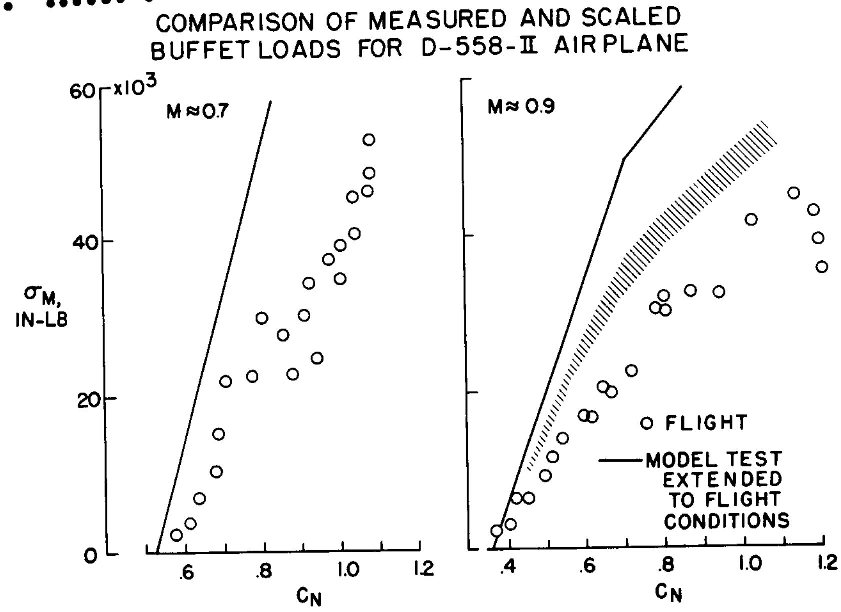

Figure 7

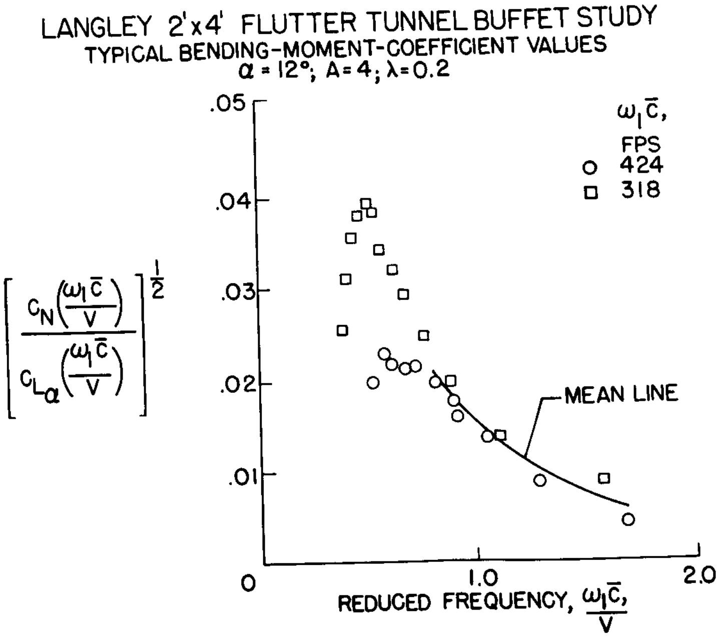

Figure 8

[redacted]

COMPARISON OF MEASURED AND SCALED BUFFET LOADS FOR X-3 AIRPLANE

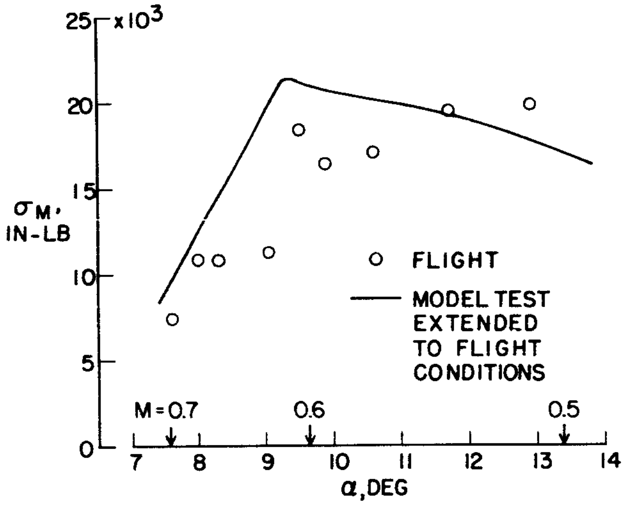

Figure 9

[redacted]

[redacted]

A STUDY OF THE RESPONSE OF PANELS TO RANDOM ACOUSTIC EXCITATION

By Robert W. Hess, Leslie W. Lassiter,
and Harvey H. Hubbard

Langley Aeronautical Laboratory

SUMMARY

An application is made of the method of generalized harmonic analysis to the problem of prediction of stresses in airplane-skin panels due to excitation by jet noise. The concepts of the theory are reviewed briefly and some of the significant parameters are evaluated in the tests. Measurements of stresses in some panels due to random acoustic excitation are presented and are found to be in general agreement with calculated results.

INTRODUCTION

It is well known that jet noise has in many instances caused fatigue failures of airplane-skin panels in proximity to the jet-engine exhaust stream. These failures have been mainly on the fuselage or the wings, depending on the type of engine installation. Some configurations having the engine exits relatively far aft have also experienced damage to panels in the tail assembly.

Very few data are available which would permit a designer to estimate dynamic stresses in panels exposed to a given random excitation. As a result, "ad hoc" modifications, such as an increase of skin gage or the addition of stiffeners or both, have frequently been necessary after construction of the airplane in order to alleviate fatigue problems. Thus, there is serious need for a means of predicting in the design stage the dynamic stresses of a panel subjected to a given random excitation.

In reference 1, the techniques of generalized harmonic analysis have been applied to a theoretical treatment of this problem, and it appears that these techniques may afford a relatively simple approach to the problem. Therefore, the main purpose of the present paper is to determine how well this type of analysis applies in predicting panel stresses.

[redacted]

Although the discussion is mainly concerned with the problem of jet-noise excitation, certain of the results will be shown to apply to the case of propeller-noise excitation as well.

METHOD OF ANALYSIS

The concepts involved in analysis of the panel-response problem are illustrated in figure 1, which is a schematic illustration of the input-output relationships involved. The top sketch in figure 1 represents the spectrum of jet noise which is causing the vibration of the panel. The second sketch is the panel transfer function, or the square of the frequency-response quantity of interest – whether it be displacement or stress. This transfer function is necessary in relating the output to the input. The curve may have several peaks corresponding to the various modes of vibration but, for simplicity, only the first-mode response is shown. The bottom sketch is the output-response spectrum and is the product of the input function and the panel transfer function. If the panel transfer function is expressed in terms of stress per unit input, as in this case, then this output curve is the stress-response spectrum of the panel.

A useful index of the overall response of the panel is the mean-square stress, and this is the area under the output curve in figure 1. For the case where the input function varies only slowly with frequency and the panel-response curve is sharp, reference 1 shows that the expression for the mean-square stress σ^2 takes the simplified form

$$\sigma^2 \approx \frac{\pi}{4\delta}\omega_0 S_0{}^2 \phi_N(\omega_0) \qquad (1)$$

Thus, the stress in the panel is a function of four parameters, one associated with the input and three with the panel structural characteristics. These parameters are: (1) ω_0, the panel natural frequency, (2) $\phi_N(\omega_0)$, the input noise at the panel natural frequency, (3) S_0, the the static stress per unit pressure, and (4) the damping of the panel given as percent of critical damping and designated as δ. This damping factor δ is a measure of the sharpness of the response curve, denoted either by its width or by its height. Perhaps another form of this equation, utilizing panel dimensions, is of more practical interest. Thus, if the product $\omega_0 S_0{}^2$ is substituted for in terms of panel length (or width) a and panel thickness t, the proportionality relation

$$\sigma \propto \frac{\left[\phi_N(\omega_0)\right]^{1/2} a}{\delta^{1/2} t^{3/2}} \qquad (2)$$

[redacted]

is obtained from equation (1), where $\left[\phi_N(\omega_0)\right]^{1/2}$ has the dimension of acoustic root mean square of pressure per unit band width. The latter form is noted to apply to the root-mean-square stress.

RESULTS AND DISCUSSION

The rest of the present paper is devoted to an evaluation of how well equation (1) and expression (2) apply to stress predictions in panels exposed to jet noise. To make this evaluation, some flat panels measuring 11 inches by 13 inches were tested with a 4-inch air jet.

Noise Input

A typical spectrum of the jet noise is shown in figure 2. The main reasons for presenting these data are to point out again that, in the analysis, only the value of the input at the natural frequency of the panel is of interest and to indicate that these tests deal with overall noise levels of approximately 130 decibels. The frequency at which the spectrum is a maximum will vary with location in the noise field as well as with the size and velocity of the jet. Hence, the noise from a full-scale engine would probably be somewhat different from that for the example shown in figure 2. Therefore, no special significance is attached to the ordinate numbers in figure 2 except that they may be useful in checking the method of calculation of the present paper.

Panel Structural Characteristics

The means used to obtain the response and the damping characteristics of the test panels are illustrated in figure 3. The panels were exposed to the periodic noise from a laboratory siren which could be operated in such a manner as to vary both the fundamental frequency of the noise and its intensity. The siren output was not sinusoidal, as would be desired in the ideal case, but contained a few harmonics of relatively low intensity. This particular study was concerned only with the fundamental frequency, and the root-mean-square pressure P_1 of this component is used as a measure of the acoustic input to the panels. To avoid excitation from both sides, the panels were mounted on a rigid chamber which was acoustically insulated and vented so as to minimize the load on the back of the panel.

A sample frequency-response curve for a 0.040-inch aluminum-alloy panel is shown on the left side of figure 3, where the stress amplitude σ_{MAX} in pounds per square inch is plotted as a function of frequency for constant input pressure P_1. The panel is seen to have a very sharp response at its resonant frequency. The slight skewness of the curve is believed to be due to nonlinearities of the system. Experimental determination of the unstable part of the curve is somewhat difficult and, for that reason, this portion of the curve is shown as a broken line. Because of this difficulty, measurements of damping were based on the height of the response curves rather than on the width. By definition, δ is equal to the ratio $\frac{\sigma_{st}}{2\sigma_{MAX}}$ where σ_{st} is the stress amplitude at zero frequency. This static stress is obtained experimentally by evacuating the chamber to a static pressure corresponding to $\sqrt{2}$ times the value P_1 of the dynamic tests.

Values of damping corresponding to the appropriate input pressures of the tests were determined with the aid of figure 3 for the calculations of this paper. It should also be noted that the damping values of figure 3 apply directly to the case of pure frequency excitation. Hence, for the case of excitation by the random spectrum of the jet, some account must be taken of the effective band width of the panel. This band width can be shown to be approximately equal to $2\delta\omega_0$.

By the means just discussed, evaluations of the three structural parameters necessary for a stress calculation were made. These parameters are: the resonant frequency ω_0, the panel damping δ, and the static stress per unit pressure S_0, which equal to $\sigma_{st}/\sqrt{2}\,P_1$.

Panel Response

Before considering the measured stresses of the present tests, it is helpful to study some of the qualitative results. Characteristic time histories of the response of a panel to both periodic and random excitations are shown in figure 4. At the top of the figure is shown the panel response to a periodic excitation which in this case is the noise from a siren. It can be seen that the panel response is uniform and has a definite frequency. This frequency is the frequency of the periodic input function.

At the bottom of figure 4 is shown the panel response to a random excitation which in this case is the noise from the 4-inch air jet. Again, the panel response has a definite frequency but, in this case, it is the first-mode resonant frequency of the panel. It will also be noted that pronounced beats are apparent in the response. This type of response is characteristic of a sharply tuned system with low damping and is an ample justification for studying only the first-mode response characteristic, as has been done in these tests.

The results of the siren tests of figures 3 and 4 would apply directly to the case of excitation by propeller nose; for this case, the panel would respond mainly to that noise frequency at or near its first mode of vibration. Because of the sharp panel-response curve, it can be anticipated that a small change in the propeller revolutions per minute would markedly change the panel stresses even though the noise-input level were unchanged.

COMPARISON OF THEORY AND EXPERIMENT

Some stress calculations by the simplified equation, equation (1), given in the analysis section of the paper have been made by using the values of S_0, ω_0, and δ determined in the experiments. In figures 5 and 6 these calculations are compared with measured stresses obtained when the panels were placed in the near-noise field of the 4-inch air jet. Figure 5 gives the results obtained from a 0.040-inch panel located at various axial and radial distances from the jet. In the plot on the lower left-hand side of figure 5, stress data are shown as a function of x/D, where x is the axial distance from the nozzle to the center of the panel and D is the jet diameter. The radial distance d is held constant at 1.75 diameters. It can be seen from this figure that the theory and experiment are in very good agreement. Likewise, good agreement is indicated in the plot on the lower right-hand side of figure 5, where radial distance was varied and the axial distance held constant at 6.4 diameters.

Figure 2 indicated that the overall noise levels for these tests were in the range of 130 decibels. Since jet-engine noise levels may be of the order of 150 decibels or perhaps even higher, it can be anticipated that the associated stresses will be considerably higher than those measured in the present tests. If the assumption is made that the shape of the spectrum from an engine is the same as that from the 4-inch air jet used in these tests, then an increase of 20 decibels in the overall noise level would result in an increase in the stresses by a factor of approximately 10.

Figure 6 gives results for the case where panel thickness is varied and input pressure is held constant. The root-mean-square stress is plotted as a function of panel thickness for a range of thickness from 0.020 inch to 0.081 inch. The panel natural frequencies ranged from 78 cycles per second for the 0.020-inch thickness to 250 cycles per second for the 0.081-inch thickness. According to expression (2),

[redacted]

stress should vary inversely as the thickness to the 3/2 power, as is indicated by the dashed curve. The measured points tend to bear out this relation fairly well.

From the good agreement between theory and experiment shown in figures 5 and 6, it can be concluded that the method of generalized harmonic analysis is particularly well suited to this problem and that equation (1) applies well for the conditions of these tests.

CONCLUDING REMARKS

Some preliminary measurements of the response of aircraft-skin panels to a random acoustic excitation have been presented and were found to be in general agreement with the results of an approximate analysis. These panels were noted to have very low damping and to vibrate mainly in their first modes in response to a random-noise input. Root-mean-square stresses were noted to be proportional to the sound pressure per unit band width at the natural frequency of the panel and were higher for panels of less thickness.

REFERENCE

1. Miles, John W.: On Structural Fatigue Under Random Loading. Jour. Aero. Sci., vol. 21, no. 11, Nov. 1954, pp. 753-762.

[redacted]

PANEL EXCITATION BY JET NOISE

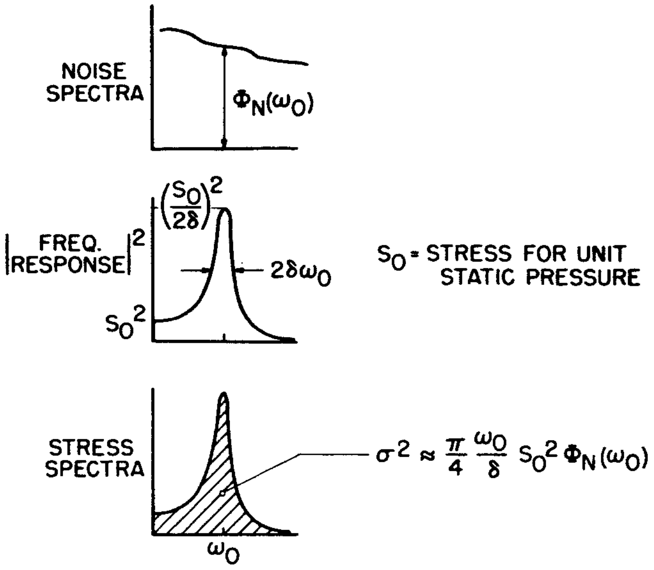
NOISE SPECTRA
$\Phi_N(\omega_0)$
|FREQ. RESPONSE|^2
$\left(\frac{S_0}{2\delta}\right)^2$
$2\delta\omega_0$
S_0^2
S_0 = STRESS FOR UNIT STATIC PRESSURE
STRESS SPECTRA
$\sigma^2 \approx \frac{\pi}{4}\frac{\omega_0}{\delta} S_0^2 \Phi_N(\omega_0)$
ω_0

Figure 1

SAMPLE NOISE INPUT
4" AIR JET

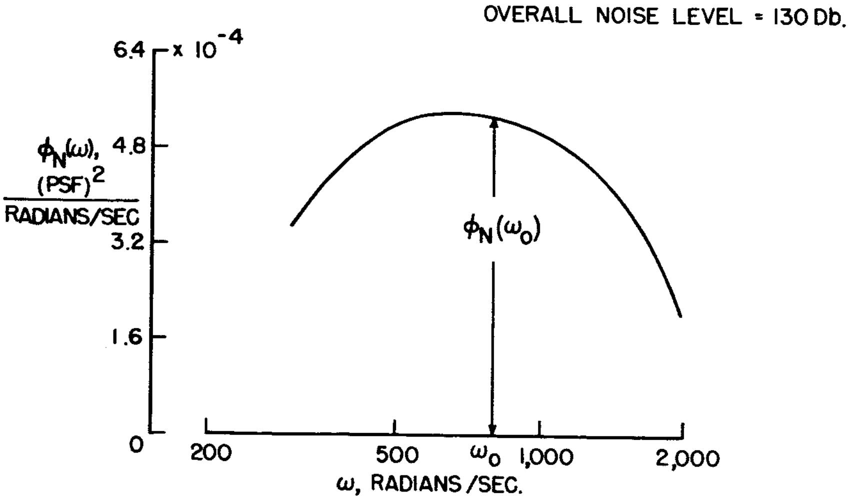

Figure 2

[redacted]

PANEL DYNAMIC CHARACTERISTICS

t=0.040"

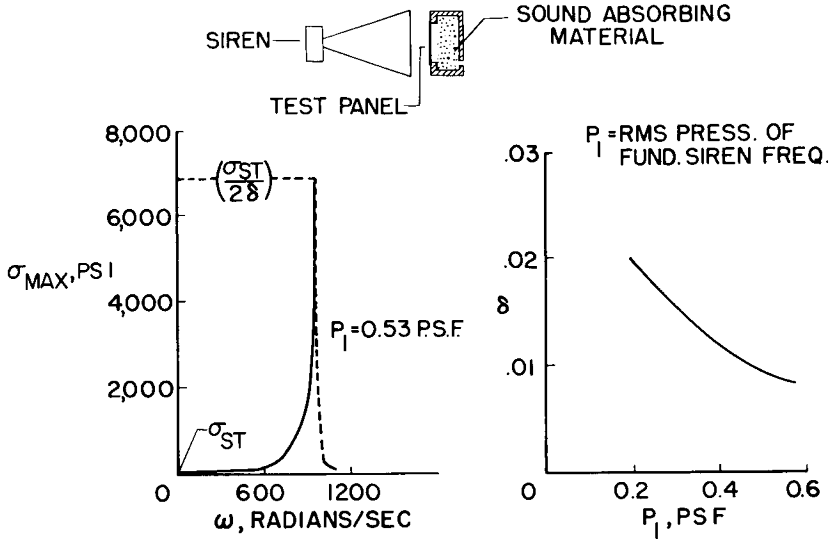

Figure 3

RESPONSE OF PANEL

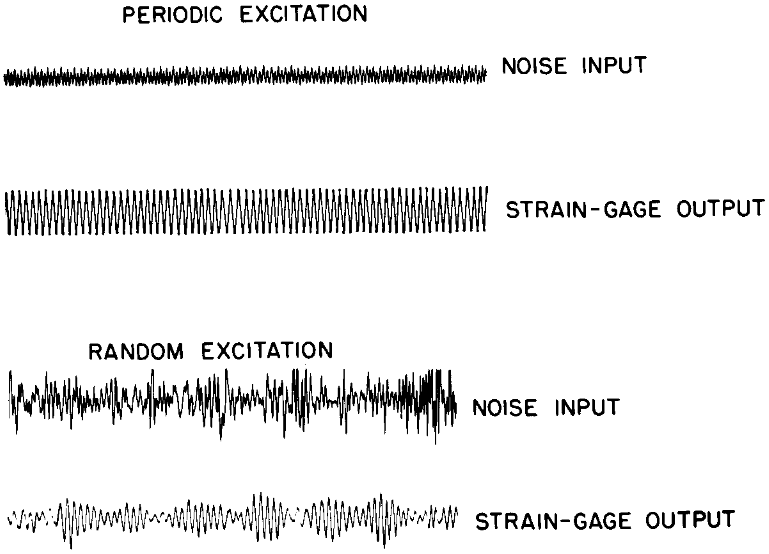

Figure 4

[redacted]

14V

[redacted]

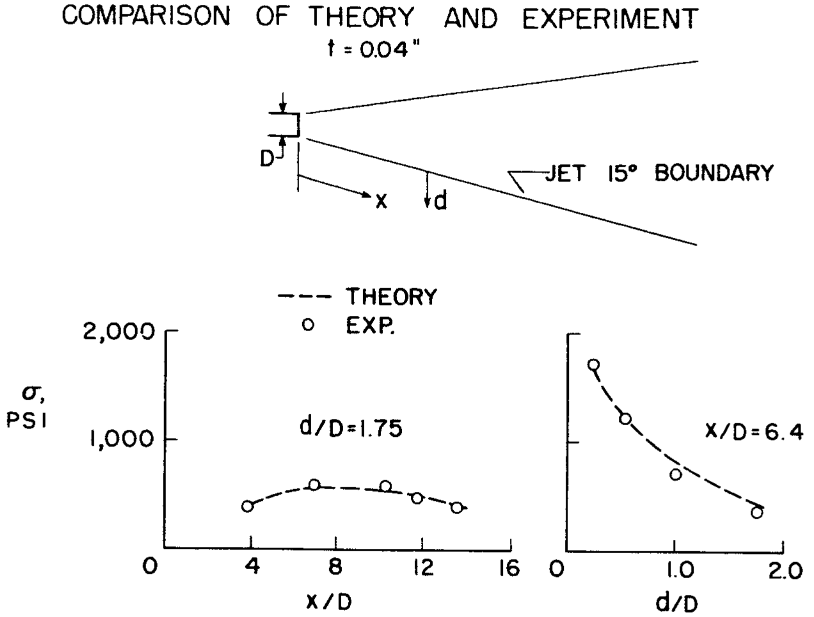

Figure 5

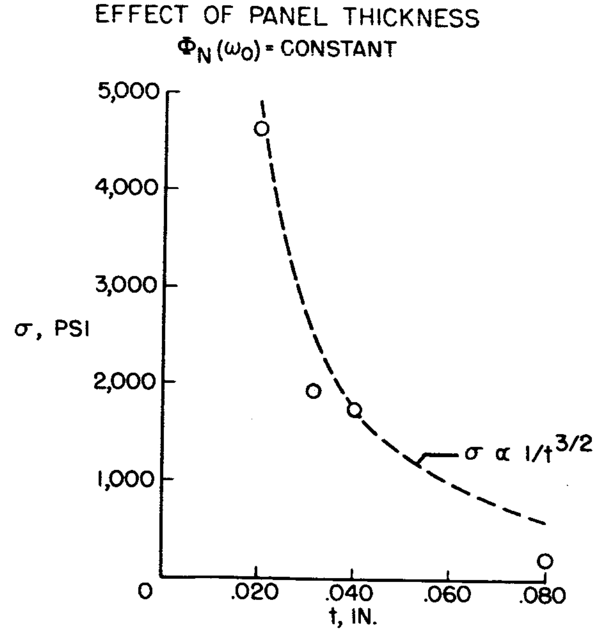

Figure 6

[redacted]

[redacted]

RECENT RESULTS OF THE CALCULATION OF AERODYNAMIC LOADING AND FLUTTER OF SEVERAL WINGS AT SUBSONIC AND SONIC SPEEDS

By Harry L. Runyan and Donald S. Woolston

Langley Aeronautical Laboratory

INTRODUCTION

If one examines the status of theoretical work on oscillating air forces for flutter, it is seen that the two-dimensional theory is rather well developed throughout the Mach number range but that the three-dimensional theory is not satisfactory, particularly with regard to the high subsonic and sonic speeds. Recently a method has been developed at the Langley Laboratory for calculating the forces on a finite wing which is oscillating harmonically in subsonic and sonic flow. The purpose of this paper is to present a brief description of the method and to show some results. The usual assumptions of linearized flow have been made. Basic to the method is the development and treatment of a kernel function of an integral equation which for subsonic flow has been treated in reference 1. The development of the kernel function for the supersonic case has recently been completed and is presented in reference 2.

There exists an alternative approach which is based on the classical method of separation of variables and which has been proposed by Kuessner (ref. 3) for general use. However, the method is limited to certain general plan forms such as the circular or elliptic plan form and some of the functions necessary for solution have neither been studied nor tabulated.

However, with the relatively recent development of high-speed computing devices, laborious computing procedures which formerly were not deemed practical and which may lend themselves to systematization are now practical. It is into this class of computing problems that the lifting-surface calculations based on an integral equation may be placed.

METHOD

An indication of the method is given in the following paragraph. The equation

$$\Delta w(x,y) = \Sigma K \, \Delta A$$

[redacted]

states that the downwash or vertically induced velocity Δw is equal to the product of the aerodynamic load L which is acting over an area ΔA times a kernel function K. The physical meaning of this equation is best seen by referring to the sketch. If a loading L is assumed to be acting over an area ΔA, then the induced vertical velocity at any other point on the wing, for example, at $P(x,y)$, is the product of L times K. It is apparent then that the kernel function represents the vertical induced velocity at a point on a wing due to a unit loading at another point on the wing and may thus be termed an aerodynamic influence coefficient. By summing the effect of the entire area of the wing on the point P, the total induced velocity is obtained and thus the integral equation

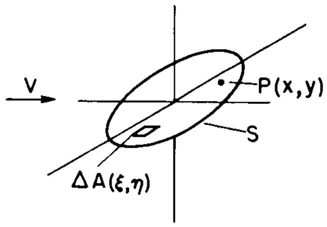

$$w(x,y) = \iint_S LK \, d\xi \, d\eta$$

is obtained. The similarity to the structural deflection problem is readily apparent. The downwash w corresponds to the wing deflection, L to the structural loading, and the kernel function K to the structural influence coefficients. Thus the problem is to devise a practical means for solving this equation. If the loading L is known, then the problem is simply to perform the double integration from which the deformation of the wing is determined. However, if the deformation or downwash w is known but not the loading L, then the problem becomes more complicated and an integral equation must be solved since the unknown appears under the integral sign. It is the latter problem which is of interest since, in most cases, the loading is not known but the motion of the wing is known.

The loading L is approximated by a series as

$$L = C\sqrt{1 - \eta^2}\Big[\cot\frac{\theta}{2}(a_{00} + a_{01}\eta + \ldots) + \sin\theta(a_{10} + a_{11}\eta + \ldots) + \sin 2\theta(a_{20} + a_{21}\eta + \ldots) + \ldots\Big]$$

where θ is a chordwise coordinate, η is a spanwise coordinate, and the a's are unknown. This form has been used in many steady-state solutions. The series satisfies the wing edge conditions and is useful for all subsonic Mach numbers. For the sonic condition a slight modification of the chordwise terms is necessary. The kernel K is a complicated but known function and is discussed in reference 1. The wing is divided in many small areas and the double integration over each area is accomplished by numerical procedures with the aid of the mean-value theorem. The downwash at a point P is then determined by summing the

[redacted]

increments of downwash due to all the areas on the wing surface. By selecting other positions P on the wing for calculation of the downwash, a set of simultaneous equations is obtained from which the a's of the loading series may be calculated. As mentioned previously, the downwash w is usually known since the motion of the wing is known and the air forces for any deformed wing mode may be calculated with no more difficulty than for a rigid pitching or translating wing.

With regard to the time required for calculating the forces on a wing, it takes about 1 week with the computing equipment available at the Langley Aeronautical Laboratory. With the latest computing equipment now commercially available, this might be cut to 1 to 2 days.

RESULTS

This section is concerned with presenting some results of applying the procedure of this paper to some specific examples.

In figure 1 the lift and moment and corresponding phase angles are plotted against the reduced-frequency parameter $k = b\omega/V$ where b is the wing semichord, ω the angular frequency, and V the stream velocity. The results are for a rectangular wing of $A = 2$ at $M = 0$ and for a rigid wing which is oscillating in pitch about the midchord. The results of the present analysis are compared with the results of Lawrence and Gerber (ref. 4), and it is seen that the two methods agree rather well. Although the present method may be used for sonic or subsonic Mach numbers, comparison is made with Lawrence and Gerber's results, which is restricted to the incompressible case, in order to show the agreement with a published method. Inasmuch as different types of approximations have been made in the two analyses, it is remarkable that the agreement is so good, and one can surmise that the physical problem has been adequately represented in both analyses.

In figure 2, the variation of the lift and moment coefficient for a rectangular wing of $A = 2$, oscillating in pitch at a constant reduced frequency $k = 0.22$ about the midchord line are plotted against Mach number. The results up to and including $M = 1$ were obtained using the method of this paper, and the supersonic coefficients were obtained from existing published results and are shown by the solid line. It is believed that this is the first time that calculated results have been obtained for the oscillating finite wing throughout the complete subsonic Mach number range including $M = 1$. As may be expected, the lift and moment coefficients increase with M up to the vicinity of $M = 1$ and decrease on the supersonic side. Comparison with other methods is not possible since none exists for this Mach number range; however, the two-dimensional coefficients are included, as shown by the dashed line. It

[redacted]

is interesting to note that the rule for aspect-ratio correction $\frac{A}{A + 2}$, which for this case is 1/2, is generally applicable up to $M = 0.7$ to 0.8.

In figure 3, the corresponding phase angles between the wing position and the force or moment are shown for the same case as in figure 2. It is here that the attempts to obtain simple factors relating the two-dimensional coefficients to the three-dimensional coefficients fail since no relation seems to exist between the two-dimensional and three-dimensional phase angles. Thus it appears that up to certain Mach numbers, the magnitude of the force might be adjusted for aspect ratio; whereas the time at which the force acts during the cycle of oscillation cannot be so easily corrected.

In figure 4 is shown the lift and associated phase angles plotted against the reduced-frequency parameter $k = b\omega/V$ for a delta wing of $A = 4$. The wing is oscillating in pitch about the midchord. Results of the present analysis as shown by the solid line and those of Lawrence and Gerber as shown by the dashed line are compared with some experimental results of Leadbetter and Clevenson (ref. 5) indicated by the circles. The results of the two analyses agree rather well with regard to both lift and magnitude and phase angles. The agreement with experiment, especially with regard to the phase angle, indicates that the theories are adequate.

In figure 5, the moment and the corresponding phase angles are shown for the same wing under the same conditions as in figure 4, plotted against the reduced frequency k. Results of both analyses are in substantial agreement with respect to the magnitude of the moment, but the slope is less than the experiments indicate. Insofar as the phase angles are concerned, the first difference between the two theories arises, although both theories indicate the same trend. The reason for this difference cannot be explained at the present time and will have to be resolved by further calculations and experiments.

The results shown in figures 1 to 5 were for rigid wings. The remainder of the paper is concerned with the flexible case. In figure 6 are shown the magnitude of the lift and the phase angles along the semispan for an untapered, rectangular wing oscillating in a torsion mode. The experimental results, as indicated by the circles, were obtained from reference 6. Three theories are shown. The two-dimensional results were obtained by multiplying the two-dimensional air forces by the mode shape, which is the usual practice when using two-dimensional coefficients. The lift as calculated by the theory of Reissner and Stevens (ref. 7) is shown, and the lift as calculated by the method of the present analysis is also shown. The aspect ratio for the experimental and Reissner and Stevens' result was 5. For the present analysis

[redacted]

[redacted]

the results are for $A = 4.53$, since calculations had already been made for this aspect ratio for other purposes, and this small difference in aspect ratio should not affect the forces. As would be expected, the two-dimensional theory predicts a much larger force for practically the whole semispan. The two finite-span theories are in reasonable agreement with experiment. Reissner and Stevens' analysis overpredicts the force for most of the outboard region. The present theory slightly overpredicts the force at the inboard position. With regard to the phase angles, both finite-span theories are in good agreement with experiment.

In figure 7 are shown the results of making flutter calculations using both two-dimensional theory and the present three-dimensional theory for a rectangular unswept wing. The flutter-speed parameter $V/b\omega_\alpha$ (where V is the stream velocity, b the semichord, and ω_α the uncoupled torsional frequency) is plotted against Mach number. Calculations were made for an untapered rectangular wing of $A = 4.53$. The wing center of gravity was at the midchord and the elastic axis at 34 percent of the chord. Two uncoupled deformation modes of torsion and bending of a uniform cantilever wing were used in both analyses. The three-dimensional results including $M = 1$ were obtained by use of the present analysis, and the supersonic results were obtained from reference 8. It is seen that for both the two- and three-dimensional calculations, the flutter-speed parameter drops with Mach number up to $M = 1$ and increases with M on the supersonic side. Two experimental points are shown. One, a flutter point at $M = 1.3$, was reported in reference 9, where very good agreement was found. A no-flutter point on the subsonic side is indicated by the open test point. An attempt was made to flutter the model that had been previously fluttered at supersonic speeds in a subsonic tunnel, and no flutter was obtained up to the Mach number and $V/b\omega_\alpha$ indicated. Due to limitations of tunnel power at the proper air density, the model did not flutter. However, the value reached in the tests was well above the range predicted for flutter by the two-dimensional results but not up to the values predicted by the three-dimensional theory. Going back to the calculated results, an unexpected large aspect-ratio effect is seen in the subsonic range. It should be pointed out, however, that the calculations for the entire Mach number range were made at the same air density that was reached in the supersonic tests, which corresponded to an altitude of about 40,000 feet. Calculations for a higher density or lower altitude bring the two- and three-dimensional results closer together.

A problem that has been of concern to designers for some time has been the question of the existence of single-degree-of-freedom bending flutter of a swept wing. In the absence of three-dimensional theory, two-dimensional air-force coefficients have been used and it has been found that, theoretically, a bending type of flutter was possible, because, even though the wing is bending, there is an effective angle of attack due to the sweep which is not present in an unswept wing.

[redacted]

[redacted]

In figure 8 are shown the results of both two- and three-dimensional calculations for a 45° swept uniform wing oscillating in bending for a free-stream Mach number of 1. The damping-force coefficient is plotted against the reduced velocity $1/k$. It is seen that the damping-force coefficient changes sign for the two-dimensional case, as shown by the dashed line, at $1/k = 8$, thus indicating the possibility of an unstable condition. The results of some calculations using the present three-dimensional method is shown by the solid line, and it is seen that a stable condition is indicated. It may thus be concluded that the effect of aspect ratio is to greatly reduce, if not eliminate, the possibility of single-degree-of-freedom bending flutter of a swept wing. Results for the incompressible case (ref. 10) also support this statement.

In conclusion, a method has been presented for calculating the air forces on oscillating wings of finite plan form for subsonic and sonic Mach numbers. The method is adaptable to the calculation of the loading on deformed wings, and comparisons with experiment and other theory seem to indicate that the results may be used with confidence.

[redacted]

REFERENCES

1. Watkins, Charles E., Runyan, Harry L., and Woolston, Donald S.: On the Kernel Function of the Integral Equation Relating the Lift and Downwash Distributions of Oscillating Finite Wings in Subsonic Flow. NACA TN 3131, 1954.

2. Watkins, Charles E., and Berman, Julian H.: On the Kernel Function of the Integral Equation Relating Lift and Downwash Distributions of Oscillating Wings in Supersonic Flow. NACA TN 3438, 1955. (Prospective NACA paper.)

3. Kuessner, H. G.: A General Method for Solving Problems of the Unsteady Lifting Surface Theory in the Subsonic Range. Jour. Aero. Sci., vol. 21, no. 1, Jan. 1954, pp. 17-26, 36.

4. Lawrence, H. R., and Gerber, E. H.: The Aerodynamic Forces on Low Aspect Ratio Wings Oscillating in an Incompressible Flow. Jour. Aero. Sci., vol. 19, no. 11, Nov. 1952, pp. 769-781. (Errata issued, vol. 20, no. 4, Apr. 1953, p. 296.)

5. Leadbetter, Sumner A., and Clevenson, Sherman A.: Some Measurements at Subsonic Speeds of the Aerodynamic Forces and Moments on Two Delta Wings of Aspect Ratios 2 and 4 Oscillating About the Midchord. NACA RM L53J26a, 1953.

6. Wilson, Leo E.: The Measurement of Nonstationary Airload Distributions on a Straight Flexible Wing Oscillating in a Subsonic Wind Stream. Rep. No. P245C-27 (Contract No. AF 33(616)-176), Southwest Res. Inst., Sept. 22, 1954.

7. Reissner, Eric, and Stevens, John E.: Effect of Finite Span on the Airload Distributions for Oscillating Wings. II - Methods of Calculation and Examples of Application. NACA TN 1195, 1947.

8. Nelson, Herbert C., Rainey, Ruby A., and Watkins, Charles E.: Lift and Moment Coefficients Expanded to the Seventh Power of Frequency for Oscillating Rectangular Wings in Supersonic Flow and Applied to a Specific Flutter Problem. NACA TN 3076, 1954.

9. Tuovila, W. J., Baker, John E., and Regier, Arthur A.: Initial Experiments on Flutter of Unswept Cantilever Wings at Mach Number 1.3. NACA TN 3312, 1954. (Supersedes NACA RM L8J11.)

10. Peloubet, Raymond P.: Aspect Ratio Effects on Single Degree of Freedom Bending Flutter. Tech. Note WCLS 53-62, Wright Air Dev. Center, U. S. Air Force, Apr. 1954.

[redacted]

[redacted]

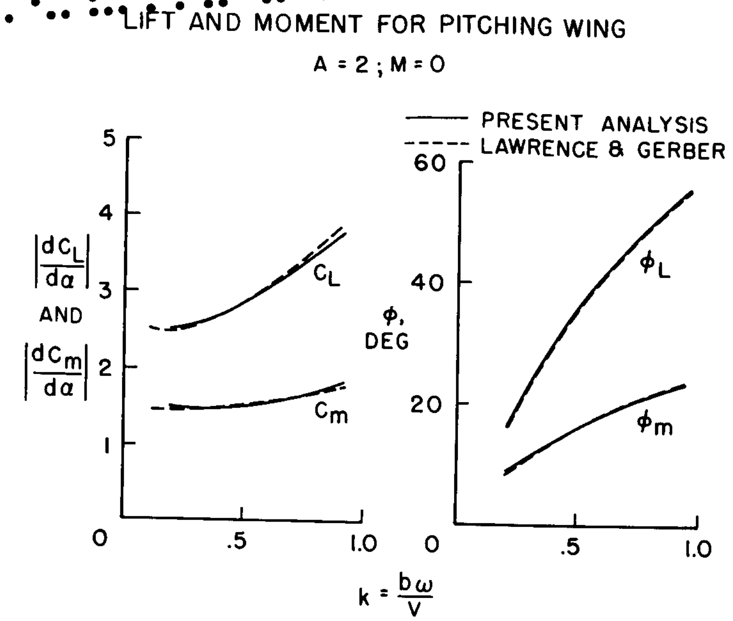

Figure 1

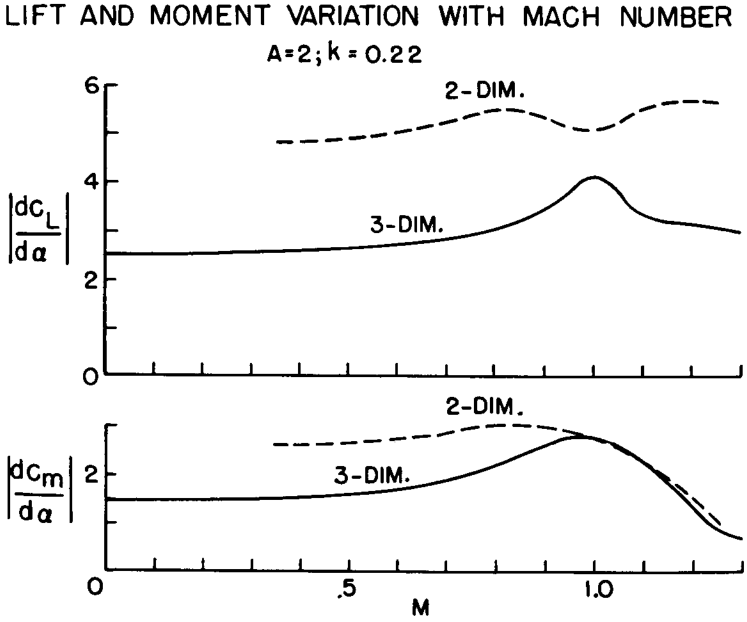

Figure 2

[redacted]

[redacted]

[redacted]

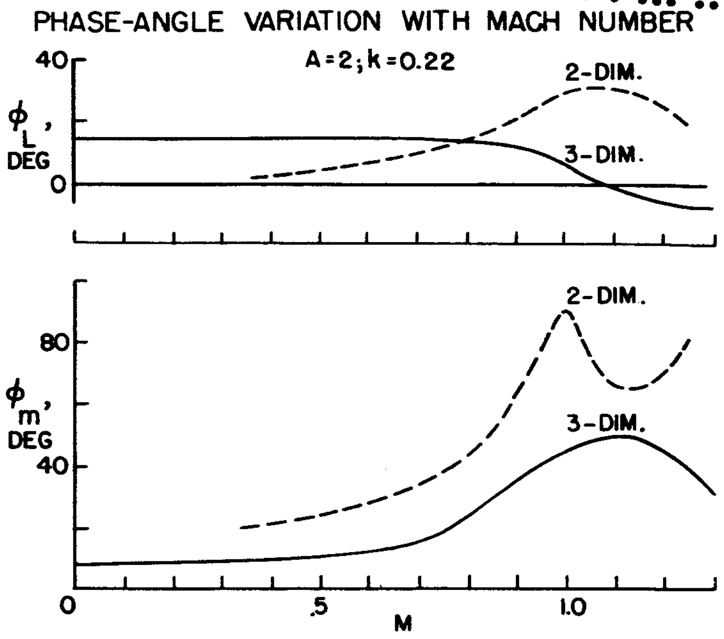

Figure 3

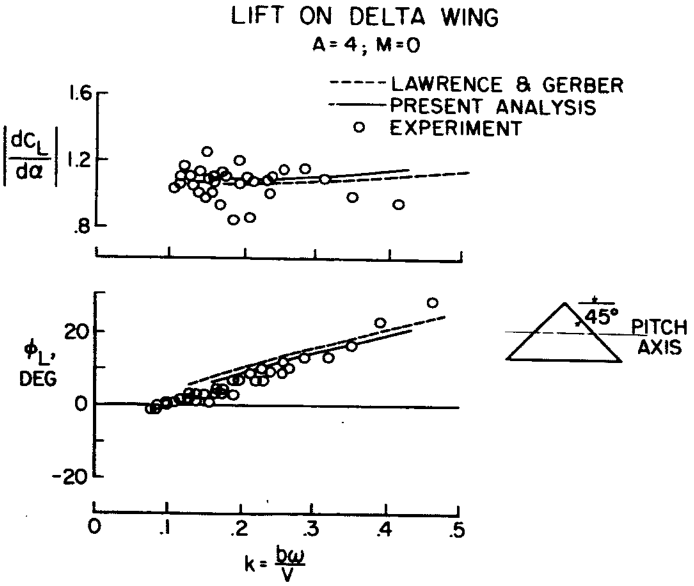

Figure 4

[redacted]

[redacted]

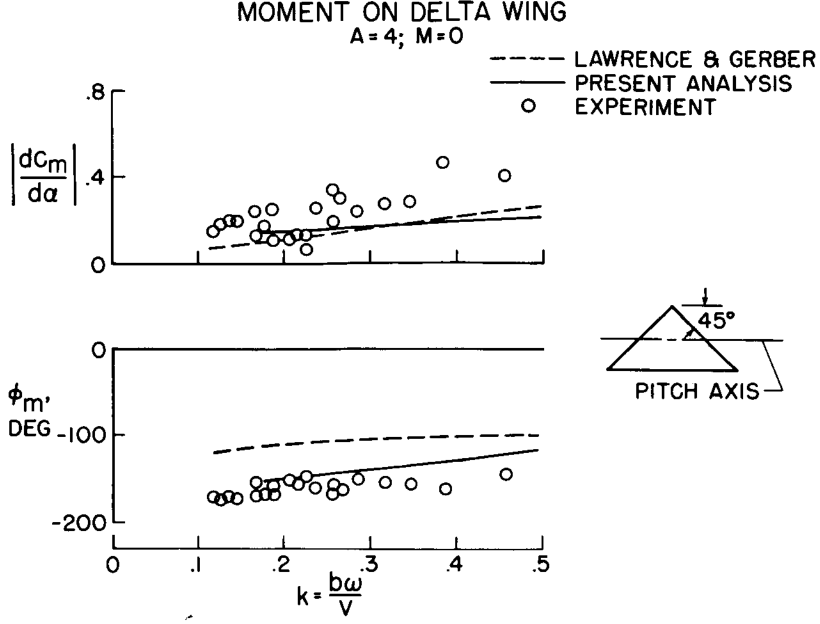

Figure 5

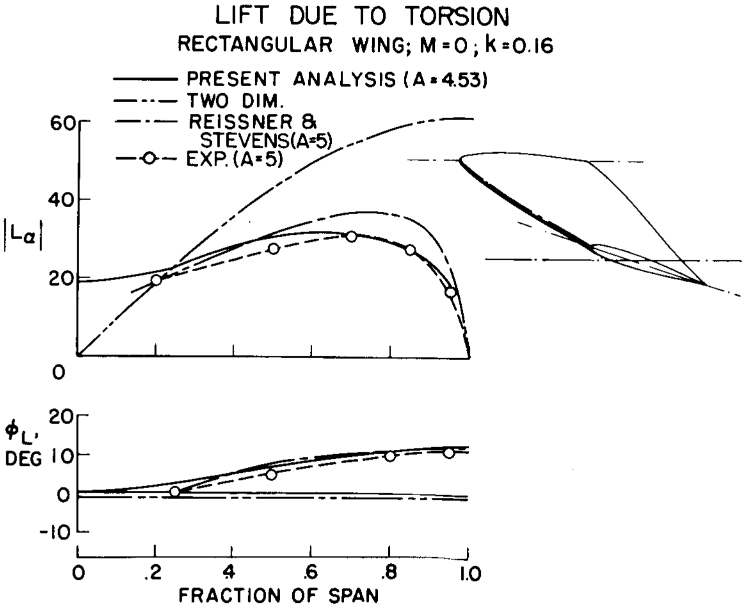

Figure 6

[redacted]

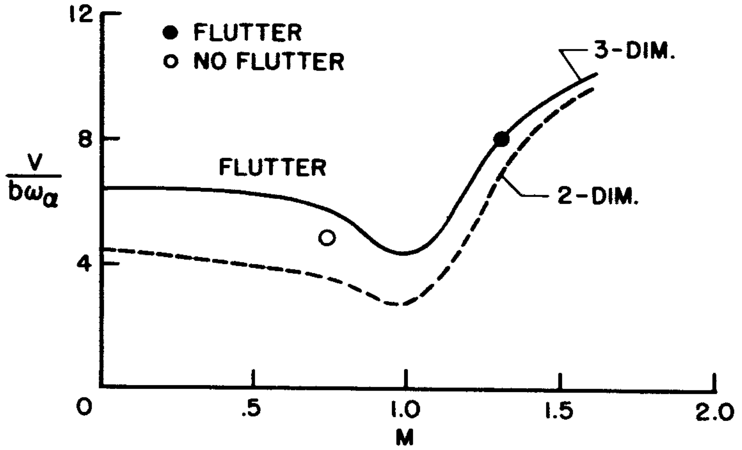
FLUTTER OF AN UNSWEPT WING

A = 4.53

Figure 7

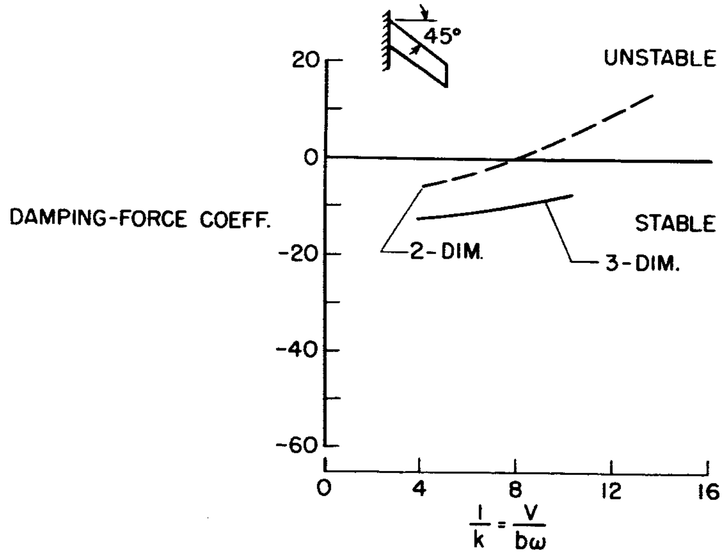
SINGLE-DEGREE-OF-FREEDOM DAMPING FORCE ON A SWEPT WING

M = 1

Figure 8

SOME RECENT EXPERIMENTAL DATA ON THREE-DIMENSIONAL OSCILLATING AIR FORCES

By Sumner A. Leadbetter and Sherman A. Clevenson

Langley Aeronautical Laboratory

SUMMARY

The status of oscillating air forces is indicated. Forces, moments, and their respective phase angles are shown for a 45° swept wing of aspect ratio 2 and for two bodies of revolution, one a streamline body and the other, an open tube. For comparison, derivatives based on available analyses were shown for these three configurations. Damping-moment derivatives were given for a tank located over the end of a wing and indicated the effect of the presence of a fin on the tank. In-phase and damping-moment derivatives were presented for a wing-tank combination with the fin location either inboard or outboard. It was indicated that the inboard location increased the aerodynamic damping in the torsional mode and an outboard position would tend to increase the divergent speed.

INTRODUCTION

The accuracy of predicting the limiting flutter speeds of aircraft depends on how well the component forces which appear in a flutter analysis are known, that is, how well the aerodynamic, elastic, and inertia forces are known. Regarding knowledge of the aerodynamic forces of flutter, theory has contributed much, but many uncertainties still exist. It becomes necessary to rely on experiment to check the various theories as well as to handle cases which are too complex for theoretical analysis. Considerable work on some of the analytical aspects of the oscillating air-force problem is currently being done by Harry L. Runyan and Donald S. Woolston of the Langley Aeronautical Laboratory. It is the purpose of this paper to indicate the status of available experimental data on oscillating air forces, and to present some current results of experiments in the Langley 2- by 4-foot flutter research tunnel on wings and bodies. Some of the current experimental results are compared with the results of analyses. The configurations discussed are swept wings, bodies at the end of struts, and wings with tip tanks with and without fins.

SYMBOLS

c	chord of wing in stream direction, ft
k	reduced-frequency parameter, $\frac{c\omega}{2V}$
L	length of body, ft
M	Mach number
q	dynamic pressure, lb/sq ft
S	plan-form area, sq ft
V	wind velocity, ft/sec
α	angular displacement, radians
ϕ_L	phase angle by which the lift vector leads the angular displacement, deg
ϕ_M	phase angle by which the moment vector leads the angular displacement, deg
ω	circular frequency of oscillation, radians/sec
c/2, L/2	subscripts referring to the midchord and midlength positions

RESULTS AND DISCUSSION

Status of Experimental Oscillating Air Forces

Before presenting the three-dimensional oscillating air-force derivatives for the aforementioned configurations, it is appropriate to illustrate briefly the status of experimental oscillating air forces, indicating in what regions experimental data are available. Figure 1 shows the ranges in which data are available for five configurations. The ordinates of each figure is the conventional flutter parameter k which is the oscillation frequency times a reference chord divided by twice the velocity. The abscissa is Mach number. The black areas indicate regions for which oscillating air-force data are available and may be found in references 1 to 17, whereas the cross-hatched areas indicate regions in which data have been obtained and are available in this paper. Data are available for rectangular wings of low aspect ratio,

[redacted]

swept wings, delta wings, wing tank over the end of a wing of aspect ratio 2, and two bodies of revolution - one an open circular tube and the other a streamline body, each at the end of a small round tapered strut. All models were oscillated in pitch about an axis of rotation as indicated. Some data are also available for other rigid body modes such as vertical translation and rolling motion and for some flexible modes in limited areas of the black regions. The following discussion and presentation of oscillating aerodynamic derivatives will concern some recent representative experimental data on a 45° swept wing oscillating about its root-midchord axis, two bodies of revolution - an open tube and a streamlined body - at the ends of short struts, and a wing-tip-tank combination with and without fins.

45° Swept Wing of Aspect Ratio 2

The oscillating air-force and moment derivatives for a 45° swept wing of aspect ratio 2 are shown in the figure 2. The ordinates are ϕ_L, and ϕ_M, the angles by which the lift and moment lead the angular position, and the lift and moment derivatives, where q is the dynamic pressure, S is the plan-form area, α is angular displacement, and $c/2$ is the half chord measured in the stream direction. The sketch in the upper right-hand corner indicates three dimensionally how a half wing was mounted on a plate and oscillates with the plate. A small gap separates the plate from the tunnel wall. The solid symbols are for the moment data and the open symbols are for lift data. For comparison, experimental data obtained from integrated pressure distribution at the Massachusetts Institute of Technology (ref. 8) are shown as squares. All moment data are referred to the 50-percent root-chord station. As a matter of interest, theory for a two-dimensional 45° swept wing (ref. 2) is included and shown as the solid and dashed curves - the solid curves for the lift derivative and lift phase angle, the dashed curves for the moment derivative and moment phase angle. It may be seen that the theory for the lift and moment phase angles agree rather well with the experimental data. However, theory for the lift derivative underestimates the experimentally determined lift derivatives, and theory for the moment derivatives overestimates the experimentally determined values. Thus, as might be expected, two-dimensional theory is inadequate for predicting the oscillatory lift and moment derivatives on a 45° swept wing of aspect ratio 2.

Bodies of Revolution

The use of large external stores attached to wings raises the question as to the oscillating air forces on these bodies. Two bodies of fineness ratio 7 have been oscillated in pitch about their midlengths, and sets of derivatives and phase angles have been determined. The first configuration is a streamlined body supported by a single strut as indicated in figure 3. In the upper right-hand corner is a sketch indicating how the strut is mounted on the end plate. The ordinates are as shown in figure 2: ϕ_L, ϕ_M, and lift or moment derivative. The experimental lift and lift phase angles are indicated by circles and the moments and moment phase angles are indicated by squares. Shown for comparison are the results of an analysis based on slender-body theory presented in reference 5 for a streamlined body. Since this theory is based on potential flow, it should not be expected to predict the results of the experiment. For instance, at $k = 0$ the experimental lift derivative is 0.06π whereas the analyses predicted it to be zero and the corresponding experimental moment derivative was 0.08π compared to the analytical value of over 0.12π. The moment phase angles appear to have some agreement but the analytical lift phase angles differ greatly from those obtained experimentally. This lack of agreement between analysis and experiment is not unexpected considering that the analysis does not account for boundary-layer separation or viscosity effects on the body.

The second body upon which oscillating air forces have been determined was an open tube - similar to a stove pipe - as shown in figure 4. This tube could be considered as a simplified ramjet minus the internal mechanisms. The tube was mounted on the same strut as the streamlined body and has the same ratio of length to maximum diameter and was oscillated at approximately the same frequency. Thus forces on the tube are directly comparable to the measured forces on the streamlined body. It may be noted that for the open tube the lift derivatives are considerably greater and the moment derivatives are slightly greater than for the streamlined body. The lift phase angles are similar and the magnitudes of the moment phase angles are larger for the open tube than for the streamlined body. For comparison with this experimental data, curves of theory were determined from reference 5 for the open tube and are shown as the solid curves. The trends of the theoretical phase angles agree with experimental trends as does the trend of the lift derivatives. The experimental moment derivatives tend to indicate that the moment derivative is independent of k although the theory indicates that the moment should increase with k. Although the preceding data may not be directly applicable to a flutter analysis, they do give some insight as to the oscillating air forces present on bodies by themselves.

Wing With Tip Tank

The last configuration for which data will be presented is a tip tank over the end of a wing of aspect ratio 2. The addition of a fin in the plane of the wing on a tip tank is of interest from a flutter

[redacted]

standpoint. Some data have been obtained over a small k range on the damping moment contributed by a tank of fineness ratio 5.7 over the end of a wing of aspect ratio 2 and are presented in figure 5. The sketch in the upper right-hand corner illustrates in plan form the wing with the tip tank attached. In order to find an effect of fin shape, a trapezoidal and a delta fin were used as indicated. The tank was mounted on strain beams such that the forces measured are the forces on the tank alone. The ordinate of the graph is the damping-moment derivative where S is the plan-form area of the tank. The abscissa is the usual flutter parameter k. The circles represent the no-fin condition, the squares the delta fin, and the triangles represent the trapezoidal fin. From a comparison of the square and triangle, it may be seen that the damping-moment derivative on the tank is essentially the same regardless of which fin is used. However, all of these moments are less than the no-fin condition. It may be noted that, although all the magnitudes of the damping derivatives are very small, under 0.06π in this low k range, the addition of a fin in this position decreases the damping moment on the tank for the torsional mode and may be detrimental from a flutter standpoint. A possible explanation of this decrease in damping is that the fin, placed in an outboard position on the tank, is in the upwash of the tip vortex. Thus the presence of the fin on the tank in the upwash reduced the damping contributed by the tank rather than increasing the damping as may have been expected.

Experimental moment derivatives for the wing-tank combination instead of the tank alone are given in figure 6. In addition to the data for the trapezoidal fin in the outboard position, derivatives are presented for the fin in the inboard position, shown dotted in the sketch. The effects of a fin being in the downwash as well as the upwash of the tip vortex will be indicated. The upper graph shows the in-phase moment derivatives as a function of k and the lower graph shows the damping-moment derivatives as a function of k. These derivatives are for the combined moments for the wing and tank together. The S used in these derivatives is the plan-form area of the combination wing and tank, or wing, tank, and fin as the case may be. It may be noted in the lower figure that the damping derivatives for the fin in the outboard position and for the no-fin condition are practically the same, whereas for the fin in the inboard position the damping derivatives are greater. Thus from considerations of damping in the torsional mode, it would be better to have the fin inboard. However, the detrimental effect of the inboard fin is indicated in the upper figure. It is seen that the in-phase moment derivatives for the inboard fin or no-fin condition are about the same. The outboard-fin condition results in a much smaller value of in-phase moment derivative at the lower values of k. It must be remembered that a larger value of in-phase moment results in a lower divergence speed. The lower value of in-phase moment as shown by the fin in the outboard position is beneficial from a viewpoint of divergence in that it would cause the divergence speed to be higher than that which would result from no fin or fin in the inboard position. It may be concluded that the fin located in an inboard position may be of some benefit regarding flutter since it caused an increase in damping in the torsional mode, whereas the fin located in an outboard position would be of benefit regarding divergence.

CONCLUDING REMARKS

This paper has dealt with the status of oscillating air forces, indicating regions of available data and regions for which data is presented in this paper. Forces, moments, and their respective phase angles were shown for a 45° swept wing of aspect ratio 2 and for two bodies of revolution, one a streamline body and the other, an open tube. For comparison, derivatives based on available analyses were shown for these three configurations. Damping-moment derivatives were given for a tank located over the end of a wing and indicated the effect of the presence of a fin on the tank. In-phase and damping-moment derivatives were presented for a wing-tank combination with the fin location either inboard or outboard. It was indicated that the inboard location increased the aerodynamic damping in the torsional mode and an outboard position would tend to increase the divergent speed.

REFERENCES

1. Ashley, H., Zartarian, G., and Neilson, D. O.: Investigation of Certain Unsteady Aerodynamic Effects in Longitudinal Dynamic Stability. USAF Tech. Rep. No. 5986. (Contract No. AF 33(038)-11668, RDO No. R458-414b), Wright Air Dev. Center, U. S. Air Force, M.I.T., Dec. 1951.

2. Barmby, J. G., Cunningham, H. J., and Garrick, I. E.: Study of Effects of Sweep on the Flutter of Cantilever Wings. NACA Rep. 1014, 1951. (Supersedes NACA TN 2121.)

3. Beam, Benjamin H.: The Effects of Oscillation Amplitude and Frequency on the Experimental Damping in Pitch of a Triangular Wing Having an Aspect Ratio of 4. NACA RM A52G07, 1952.

4. Clevenson, Sherman A., Leadbetter, Sumner A., and Tuovila, Weimer J.: Discussion of Three-Dimensional Oscillating Air Forces Based on Wind-Tunnel Measurements. NACA RM L53E18a, 1953.

5. Clevenson, S. A., Widmayer, E., Jr., and Diederich, Franklin W.: An Exploratory Investigation of Some Types of Aeroelastic Instability of Open and Closed Bodies of Revolution Mounted on Slender Struts. NACA TN 3308, 1954. (Supersedes NACA RM L53E07.)

6. Goodman, Alex, and Brewer, Jack D.: Investigation at Low Speeds of the Effect of Aspect Ratio and Sweep on Static and Yawing Stability Derivatives of Untapered Wings. NACA TN 1669, 1948.

7. Henderson, Arthur, Jr.: Investigation at Mach Numbers of 1.62, 1.93, and 2.41 of the Effect of Oscillation Amplitude on the Damping in Pitch of Delta-Wing—Body Combinations. NACA RM L53H25, 1953.

8. Laidlaw, W. R.: Theoretical and Experimental Pressure Distributions on Low Aspect Ratio Wings Oscillating in an Incompressible Flow. Tech. Rep. 51-2 (Contract NOas 52-576-c, Bur. Aero.), Aeroelastic and Structures Res. Lab., M.I.T., Sept. 1954.

9. Leadbetter, Sumner A., and Clevenson, Sherman A.: Some Measurements at Subsonic Speeds of the Aerodynamic Forces and Moments on Two Delta Wings of Aspect Ratios 2 and 4 Oscillating About the Midchord. NACA RM L53J26a, 1953.

10. Mollo-Christensen, Erik L., and Lewis, S. Dean: An Exploratory Investigation of Unsteady Transonic Flow. Part II - Experimental Results. TACP Rep. 6 (Contract No. AF 33(038)-22184), Aero. Eng. Dept., M.I.T., Aug. 1954.

11. Rainey, A. Gerald: Preliminary Study of Some Factors Which Affect the Stall-Flutter Characteristics of Thin Wings. NACA RM L52D08, 1952.

12. Scruton, C., Woodgate, L., and Alexander, A. J.: Measurements of the Aerodynamic Derivatives for an Arrowhead and a Delta Wing of Low Aspect Ratio Describing Pitching and Plunging Oscillations in Incompressible Flow. S. & C. 2810, British N.P.L. (Rep. No. 16,210, A.R.C.), Oct. 1953.

13. Scruton, C., Woodgate, L., and Alexander, A. J.: Measurements of the Aerodynamic Derivatives for a Clipped Delta Wing of Low Aspect Ratio Describing Pitching and Plunging Oscillations in Incompressible Flow. S. & C. 2719, British N.P.L. (Rep. No. 15,499, A.R.C.), Dec. 1952.

14. Tobak, Murray: Damping in Pitch of Low-Aspect-Ratio Wings at Subsonic and Supersonic Speeds. NACA RM A52L04a, 1953.

15. Tobak, Murray, Reese, David E., Jr., and Beam, Benjamin H.: Experimental Damping in Pitch of 45° Triangular Wings. NACA RM A50J26, 1950.

16. Widmayer, Edward, Jr., Clevenson, Sherman A., and Leadbetter, Sumner A.: Some Measurements of Aerodynamic Forces and Moments at Subsonic Speeds on a Rectangular Wing of Aspect Ratio 2 Oscillating About the Midchord. NACA RM L53F19, 1953.

17. Wilson, Leo E.: The Measurement of Nonstationary Airload Distributions on a Straight Flexible Wing Oscillating in a Subsonic Wind Stream. Rep. No. P245C-22 (Contract No. AF 33(616)-176), Southwest Res. Inst., May 1954.

[redacted]

STATUS CHART OF THREE-DIMENSIONAL OSCILLATING AIR FORCES IN PITCH

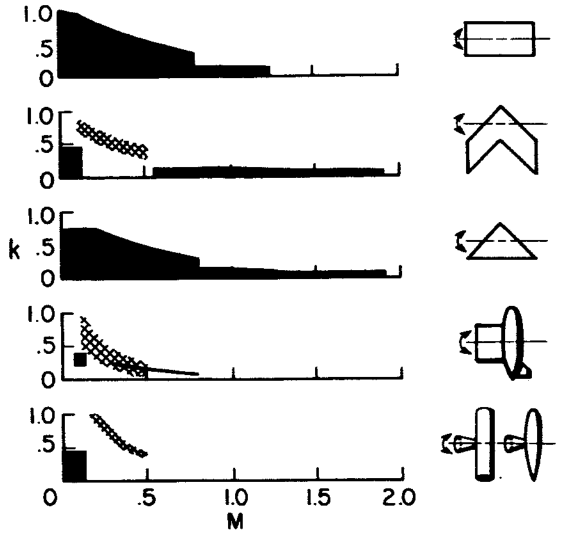

Figure 1

AERODYNAMIC DERIVATIVES FOR A=2, 45° SWEPT WING

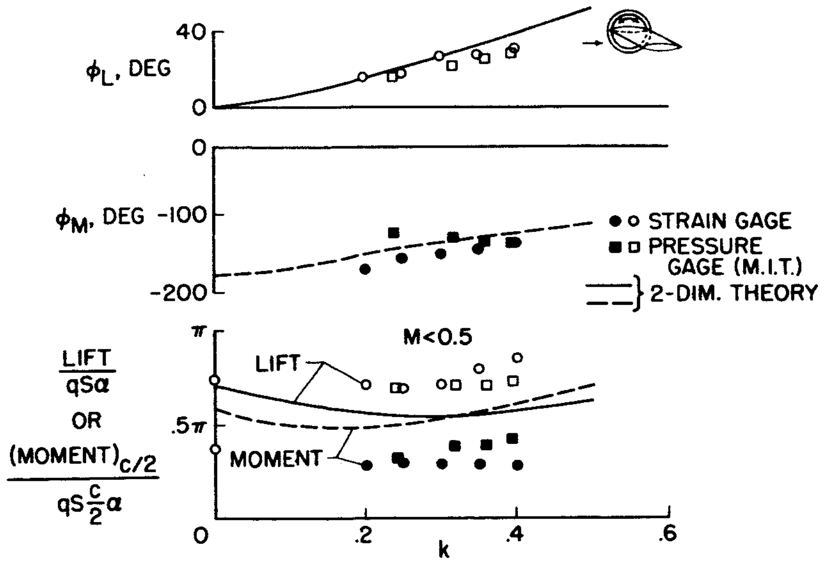

Figure 2

[redacted]

AERODYNAMIC DERIVATIVES FOR A STREAMLINE BODY AT THE END OF A CIRCULAR STRUT

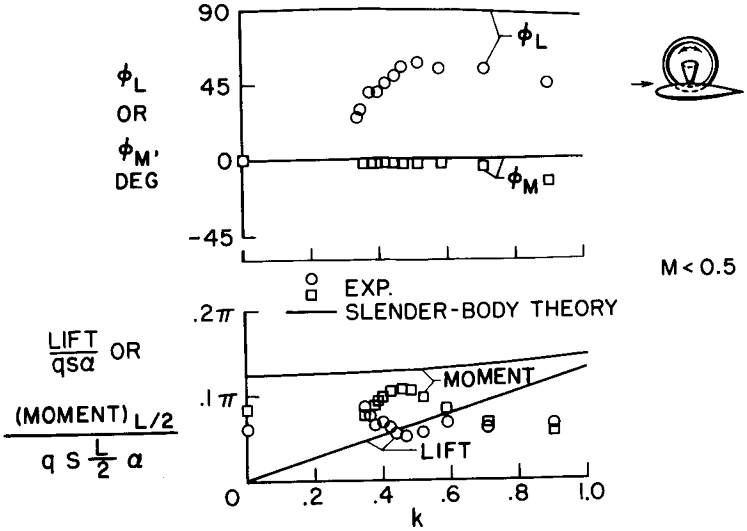

Figure 3

AERODYNAMIC DERIVATIVES FOR AN OPEN TUBE AT THE END OF A CIRCULAR STRUT

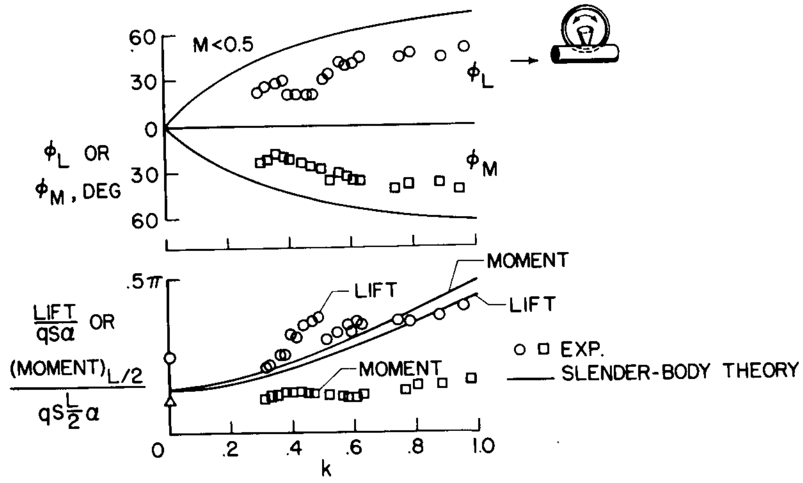

Figure 4

[redacted]

EFFECT OF FIN ON DAMPING-MOMENT DERIVATIVE ON TIP TANK IN PRESENCE OF WING

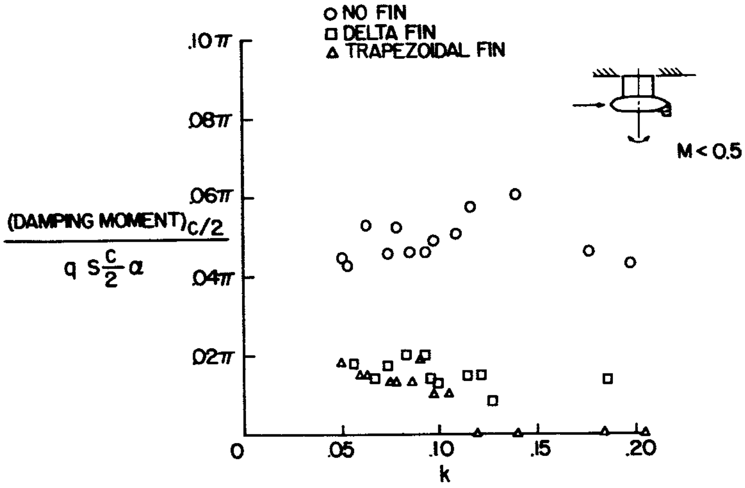

Figure 5

EFFECT OF FIN LOCATION ON MOMENT DERIVATIVES ON A WING – TANK COMBINATION

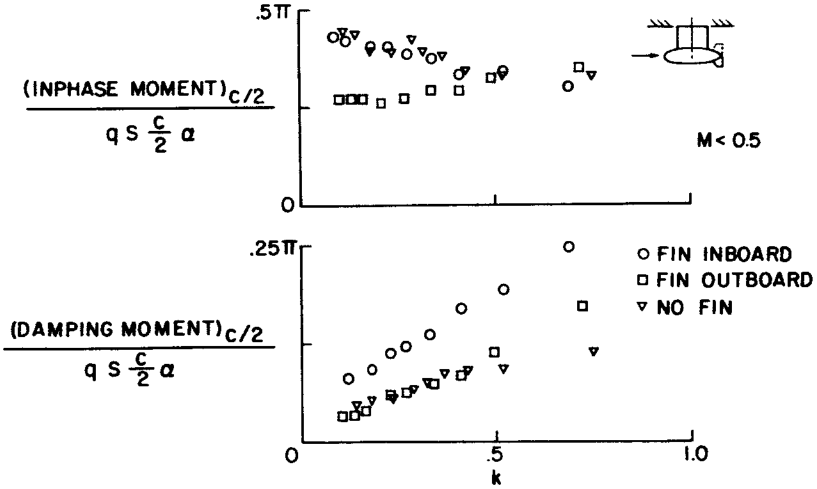

Figure 6

[redacted]

[redacted]

EXPLORATORY INVESTIGATION OF THE MOMENTS ON OSCILLATING CONTROL SURFACES AT TRANSONIC SPEEDS

By Dennis J. Martin, Robert F. Thompson, and
C. William Martz

Langley Aeronautical Laboratory

SUMMARY

Control hinge-moment data have been obtained for oscillating trailing-edge controls on unswept, swept, and delta wings through the use of wind-tunnel and rocket test models.

It has been found that a range of unstable damping occurs at transonic speeds for each configuration tested. Examination of the results indicates the importance of several parameters. However, it would appear that the transonic control-instability problem might be considerably alleviated by structural modifications such as increased stiffness and damping or by aerodynamic configuration changes.

INTRODUCTION

One of the most difficult problems that has arisen as flight speeds have increased into the transonic and supersonic speed range is concerned with control-surface flutter. Flutter troubles on control surfaces have been the rule rather than the exception on most configurations. Broadly speaking, there are two types of flutter involving control surfaces that have been of concern. One is coupled flutter that involves an interaction between control-surface motion and one or more other degrees of freedom of the airplane. Adjusting the mass balance, for example, as directed by theory has usually proved adequate to correct this coupled control-surface flutter. However, even though the coupled flutter is eliminated, another type of flutter involving only the degree of freedom of the control surface is frequently encountered. (See refs. 1 to 9.) This single-degree-of-freedom control-surface flutter is generally not sensitive to mass balance. However, like most single-degree-of-freedom types of flutter, it is very sensitive to damping.

To determine the amount of damping necessary to prevent this single-degree type of flutter, a number of experimental measurements have recently been made at transonic speeds of the hinge moments on control surfaces on swept, unswept, and delta wings. Presenting some preliminary results of these investigations is the primary purpose of this paper.

MARTIN, THOMPSON,
& MARTZ

[redacted]

DECLASS[redacted]

SYMBOLS

M_δ	aerodynamic hinge moment on control per unit deflection, positive trailing edge down, ft-lb/radian
q	free-stream dynamic pressure, lb/sq ft
M'	area moment of aileron area rearward of and about hinge line, ft^3
c_a	mean geometric control chord, ft
c_w	mean geometric wing chord, ft
ω	angular frequency of oscillation, radians/sec
k_a	aileron reduced frequency, $\frac{\omega c_a}{2V}$
k_w	wing reduced frequency, $\frac{\omega c_w}{2V}$
V	free-stream velocity, ft/sec
M	Mach number
C	equivalent viscous-damping coefficient, $\frac{\text{ft-lb}}{\text{radians/sec}}$
δ	control-surface deflection, positive trailing edge down, radians
$1 - x_1$	ratio of control chord to wing chord
M_3, M_4, N_5, N_6 M_3', M_4', N_5', N_6'	flutter derivatives as used, for example, in reference 10
L	control span, ft

$$C_{h_\delta} = \frac{\text{Real part of } M_\delta}{2M'q}$$

$$C_{h_{\dot{\delta}}} = \frac{\text{Imaginary part of } M_\delta}{2M'qk_a}$$

[redacted]

DISCUSSION OF PARAMETERS

The hinge moment existing on an oscillating control is not necessarily in phase with the control position and may be represented in complex notation by the relation

$$\frac{M_\delta}{2M'q} = C_{h_\delta} + ik_aC_{h_{\dot\delta}}$$

The part C_{h_δ} is the component in phase with the displacement and is commonly called the inphase or spring moment, whereas $k_aC_{h_{\dot\delta}}$ is the component that is 90° out of phase with displacement, that is, in phase with the velocity. This part is called the quadrature or damping moment. Negative values of C_{h_δ} oppose the displacement and hence act as an aerodynamic spring and result in an increase in the stiffness or an increase in the natural frequency of a control surface. Likewise, negative values of $C_{h_{\dot\delta}}$ oppose the velocity and hence indicate stable damping; that is, a free oscillation of a control surface would damp out. Positive values of $C_{h_{\dot\delta}}$ then would indicate an unstable aerodynamic damping moment, and an oscillation would increase in amplitude unless structural damping or a control-surface damper provided damping moments greater than the unstable aerodynamic moments. The value of equivalent viscous damping required of the damper to overbalance the unstable aerodynamic moment is given by the expression

$$C = \frac{qM'c_aC_{h_{\dot\delta}}}{V}$$

where C is the damper hinge moment in foot-pounds per angular velocity required of the damper.

The data presented in this paper are in the form of the stability coefficients C_{h_δ} and $C_{h_{\dot\delta}}$; the expressions relating these values to commonly used coefficients in flutter analysis are

$$C_{h_\delta} = -\frac{c_a{}^2k_a{}^2LM_3}{M'} = -\frac{c_a{}^2k_w{}^2LN_5}{(1 - x_1)^2M'}$$

and

$$C_{h_{\dot{\delta}}} = -\frac{c_a{}^2 k_a I M_4}{M'} = -\frac{c_a{}^2 k_w L N_6}{(1 - x_1)^3 M'}$$

For the special case of a rectangular control hinged at the leading edge,

$$C_{h_{\delta}} = -2k_a{}^2 M_3{}' = -\frac{2k_w{}^2 N_5{}'}{(1 - x_1)^2}$$

and

$$C_{h_{\dot{\delta}}} = -2k_a M_4{}' = -\frac{2k_w N_6{}'}{(1 - x_1)^3}$$

THEORETICAL CONSIDERATIONS

It may be of interest to see just what the theory predicts for the control-surface damping moments throughout the transonic speed range. Figure 1 shows theoretical values of $C_{h_{\dot{\delta}}}$, the control damping coefficient, as a function of Mach number for three values of reduced frequency based on control chord. These values have been obtained from references 10, 11, and 12 for the subsonic, sonic, and supersonic ranges. All calculations are for a 20-percent-chord control hinged at its leading edge. No two-dimensional coefficients are tabulated between $M = 0.8$ and 1.0, and hence the curves have been arbitrarily faired between the subsonic and sonic theories. Theory shows that for the lower range of reduced frequencies there is an abrupt loss in stable damping and that the damping becomes unstable and remains unstable up to supersonic speeds. Theory further indicates that at the higher reduced frequencies the instability does not exist throughout the speed range. This has been confirmed by experience inasmuch as it has generally been found that, if it is possible to make the control-surface frequency high enough, the troubles have been cured or avoided. When an excessive penalty must be paid to achieve a sufficiently high frequency, it has been necessary to provide dampers to absorb the unstable aerodynamic damping that remains.

[redacted]

DISCUSSION OF RESULTS

Now that the predictions of the idealized theory have been considered, some experimental results in the transonic speed range are discussed. Experimental data are somewhat difficult to correlate because of nonlinearities that are encountered on control surfaces. One nonlinear effect is illustrated in figure 2, which shows the experimental variation of the damping-moment coefficient $C_{h_{\dot{\delta}}}$ with the amplitude through which the control is oscillating. These data are for an unswept, semispan model which was tested in the Langley high-speed 7- by 10-foot tunnel at a Reynolds number of about 2×10^6 based on wing chord. The 30-percent-chord aileron had 20-percent aerodynamic balance and was not sealed. It can be seen that at these Mach numbers there is a nonlinear variation of damping-moment coefficient with amplitude. Further, for this particular case the maximum unstable damping appears to occur at some intermediate amplitude, and it is possible that, combined with some level of structural damping, this could explain some of the limited-amplitude flutter obtained in many cases of control-surface flutter. These nonlinear variations with amplitude, however, make evaluations of the effects of other parameters, such as Mach number, difficult.

In order to obtain some idea of Mach number effects, a constant amplitude of oscillation was chosen near the maximum unstable damping, around 2.5°, and the damping coefficients for this amplitude were plotted as a function of Mach number. Figure 3 shows the experimentally determined damping-moment coefficients at angles of attack of 0° and 6° for the same configuration, and the dashed curve indicates the values predicted by two-dimensional subsonic, sonic, and supersonic theories. The theoretical values presented in this figure as well as subsequent figures were calculated for a 20-percent-chord control hinged at the leading edge. It can be seen from the curves through the data points that there is an abrupt change from stable to unstable damping, and it has been found that the Mach number at which this change takes place depends upon many things, for example, airfoil thickness, angle of attack, or amplitude of oscillation.

Of immediate importance to the transonic and supersonic airplane designer is the magnitude of the maximum unstable damping that is likely to be encountered over the entire Mach number range. It can be seen that theory, which is the idealized two-dimensional theory, predicts some of the trends but is inadequate in predicting the magnitudes. The magnitude thus depends upon oscillation amplitude as was seen in figure 2 and, to a lesser extent, angle of attack as indicated in figure 3.

The aerodynamic profile of the control is known to have an effect on aileron buzz, and figure 4 shows the effect of control-surface trailing-edge thickness on the damping-moment coefficient. Control surfaces with thickened trailing edges have been found in some cases to be less susceptible to control-surface buzz, and the results of this figure show that the control surface with a thickened trailing edge had smaller unstable damping moments than the one with a sharp trailing edge. Maximum values of $C_{h_{\dot{\delta}}}$ over an amplitude range of ±10° at zero angle of attack were used for this comparison.

Also of interest to the airplane designer is the aerodynamic inphase or spring moment, and figure 5 shows the inphase moment coefficient plotted against Mach number for the same two aileron profiles as in figure 4. The coefficient C_{h_δ} is the inphase aerodynamic moment coefficient, and negative values, it may be recalled, indicate a stiffening or spring effect. It is seen that C_{h_δ} is negative throughout the Mach number range, and it is of interest in comparing the effect of the control profile that the magnitudes of the inphase moments are increased when the trailing edge is thickened, whereas the damping moments are decreased; this would indicate a large reduction in the phase angle of the moment vector as the trailing edge is thickened. Theory again follows the general trend but predicts too large a magnitude. However, the theory shown was for a two-dimensional control with a sealed gap and hinged at the leading edge, whereas the control for this experiment permitted flow through the gap and had 20-percent aerodynamic balance.

Swept-wing controls have also encountered control-surface instabilities, and figure 6 presents the damping-moment coefficients on a swept-rudder configuration having a 25-percent-chord control hinged at the leading edge. These data were obtained from tests of a 5-percent-thick semispan model in the Langley 8-foot transonic pressure tunnel. The data are representative of oscillation amplitudes of ±1°, zero angle of attack, and Reynolds numbers of about 6×10^6. These tests extended to supersonic speeds of about $M = 1.12$ and again indicate an abrupt loss in damping, as in the case of the unswept configuration. The theory and experiment are for a constant value of reduced frequency of 0.048 and the experimental curve is obtained from cross plots of data. The theory is based on the component flow Mach number perpendicular to the hinge line. Although the trend of the instability seems to be predicted by theory, the crossover points and the magnitudes are in error. The unstable damping region obtained experimentally occurs at a slightly higher Mach number than that for the unswept wing, although, as mentioned, not as high as that predicted by the component flow Mach number theory.

The inphase hinge moments for the same configuration as in figure 6 are shown in figure 7, and a very good if not coincidental agreement is noted with theory.

[redacted]

Although control-surface instabilities on delta wings have not been as documented as those for other types of configurations, experimental hinge-moment measurements have been obtained for oscillating delta-wing controls and the damping-moment components are shown in figure 8. Some data are shown for a full-span model tested in the Ames 6- by 6-foot supersonic tunnel (ref. 13 and unpublished data) for a control with a sharp trailing edge. These data were obtained at zero angle of attack, oscillation amplitudes of ±1°, a Reynolds number of 2.4×10^6 based on wing mean aerodynamic chord, and reduced frequencies up to 0.03. Additional data are shown for a rocket model launched by the Langley Pilotless Aircraft Research Division at zero angle of attack with a full-span constant-chord unbalanced control having a thickened trailing edge. Reduced frequency for this test was about 0.05 and Reynolds number based on the mean wing chord was about 3×10^6. The damping-moment coefficients for the delta wing also show a loss in stable damping at transonic speeds, and stable damping appears to be regained at supersonic speeds, depending upon the amplitude of oscillation. The rocket model encountered control-surface flutter in the range of Mach numbers indicated by the hatched area and appeared to become stable above a Mach number of about 1.3. The control remained stable up to the maximum speed of the flight around $M = 2.0$, although a failure in the oscillating mechanism precluded obtaining damping coefficients in this range. Stiffness coefficients C_{h_δ} were obtained for the same configurations and are shown in figure 9. The measured stiffness coefficients increase as sonic speeds are approached and decrease at supersonic speeds in much the manner that theory predicts. The theory is for a sealed gap, whereas the tunnel experiments permitted some flow.

CONCLUDING REMARKS

The results of the investigations thus far have indicated that the airplane designer has several measures at his disposal for solving the problem of single-degree-of-freedom control-surface flutter. Aerodynamic modifications appear to offer some promise but require considerably more study to establish trends that will be practical for design. Structural modifications that increase the stiffness and hence frequency of the control appear to be straightforward, although there are limits to the amount by which the control-surface frequency can be increased before excessive weight penalties or other complications are encountered. The addition of control-surface dampers appears to offer another means of eliminating the control-surface instabilities and some of the data of this paper may be useful for this purpose. Of course, each basically different configuration will require separate study. It must be pointed out that, if the control-surface frequency is low, the size of the damper required to overcome the large aerodynamic unstable damping encountered at the low reduced frequencies may impose restrictions on the rate at which the pilot may control the airplane. Hence, it appears that some kind of a compromise may be necessary between control-surface stiffness and damper size.

REFERENCES

1. Erickson, Albert L., and Stephenson, Jack D.: A Suggested Method of Analyzing for Transonic Flutter of Control Surfaces Based on Available Experimental Evidence. NACA RM A7F30, 1947.

2. Smilg, Benjamin: The Prevention of Aileron Oscillations at Transonic Airspeeds. AAF TR No. 5530, Material Command, Army Air Forces, Dec. 24, 1946.

3. Erickson, Albert L., and Robinson, Robert C.: Some Preliminary Results in the Determination of Aerodynamic Derivatives of Control Surfaces in the Transonic Speed Range by Means of a Flush-Type Electrical Pressure Cell. NACA RM A8H03, 1948.

4. Clevenson, Sherman A.: Some Wind-Tunnel Experiments on Single Degree of Freedom Flutter of Ailerons in the High Subsonic Speed Range. NACA RM L9B08, 1949.

5. Thompson, Robert F.: Investigation of a 42.7° Sweptback Wing Model To Determine the Effects of Trailing-Edge Thickness on the Aileron Hinge-Moment and Flutter Characteristics at Transonic Speeds. NACA RM L50J06, 1950.

6. Levy, Lionel L., Jr., and Knechtel, Earl D.: Experimental Study of the Effect of Sweepback on Transonic Aileron Flutter. NACA RM A51E04, 1951.

7. Wyss, John A., and Sorenson, Robert M.: An Investigation of the Control-Surface Flutter Derivatives of an NACA 65_1-213 Airfoil in the Ames 16-Foot High-Speed Wind Tunnel. NACA RM A51J10, 1951.

8. Runyan, Harry L.: Single-Degree-of-Freedom-Flutter Calculations for a Wing in Subsonic Potential Flow and Comparison With an Experiment. NACA Rep. 1089, 1952. (Supersedes NACA TN 2396.)

9. Henning, Allen B.: Results of a Rocket-Model Investigation of Control-Surface Buzz and Flutter on a 4-Percent-Thick Unswept Wing and on 6-, 9-, and 12-Percent-Thick Swept Wings at Transonic Speeds. NACA RM L53I29, 1953.

[redacted]

10. Huckel, Vera, and Durling, Barbara J.: Tables of Wing-Aileron Coefficients of Oscillating Air Forces for Two-Dimensional Supersonic Flow. NACA TN 2055, 1950.

11. Anon.: Tables of Aerodynamic Coefficients for an Oscillating Wing-Flap System in a Subsonic Compressible Flow. Rep. F.151, Nationaal Luchtvaartlaboratorium Amsterdam, May 1954.

12. Nelson, Herbert C., and Berman, Julian H.: Calculations on the Forces and Moments for an Oscillating Wing-Aileron Combination in Two-Dimensional Potential Flow at Sonic Speed. NACA Rep. 1128, 1953. (Supersedes NACA TN 2590.)

13. Reese, David E., Jr.: An Experimental Investigation at Subsonic and Supersonic Speeds of the Torsional Damping Characteristics of a Constant-Chord Control Surface of an Aspect Ratio 2 Triangular Wing. NACA RM A53D27, 1953.

THEORETICAL DAMPING COEFF. AS FUNCTION OF MACH NO. AND REDUCED FREQUENCY

2-DIM. COMP.-FLOW THEORY

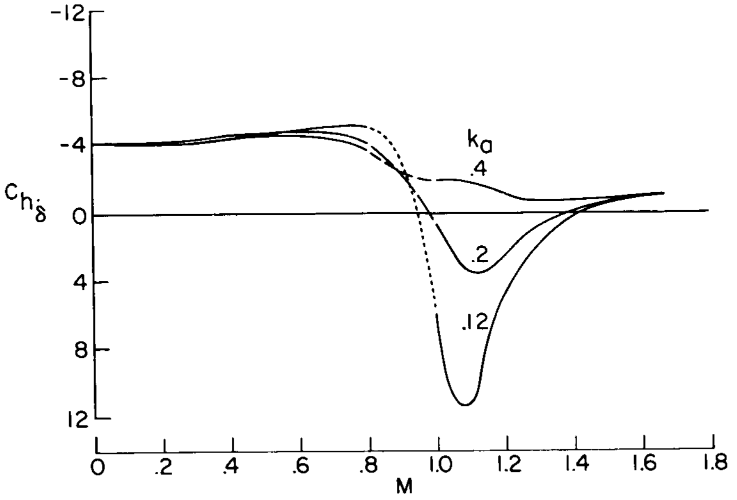

Figure 1

EFFECT OF AMPLITUDE ON CONTROL-SURFACE DAMPING COEFFICIENT

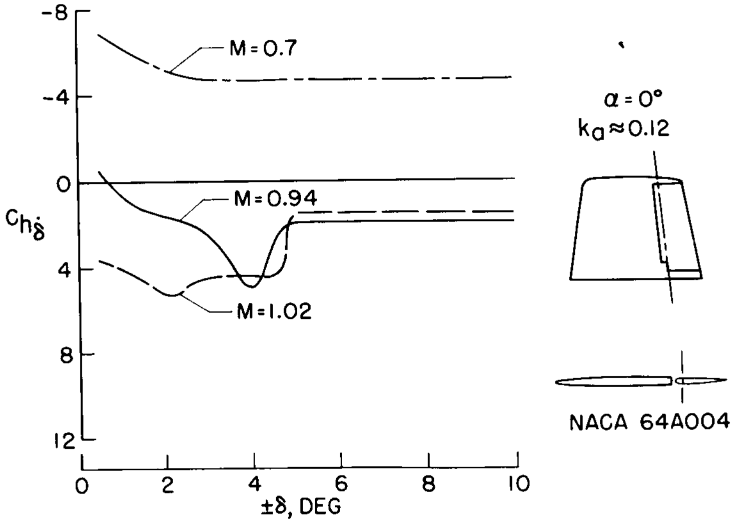

[redacted]

[redacted]

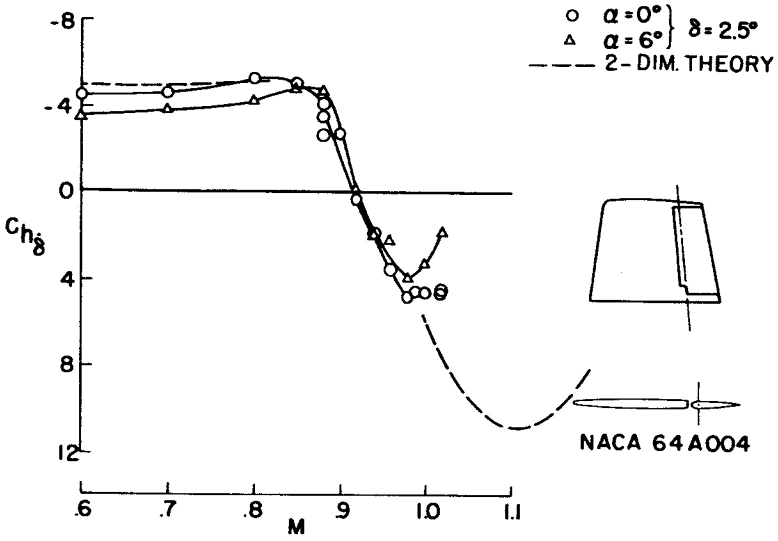

DAMPING COEFFICIENT FOR UNSWEPT WING

$k_a \approx 0.12$

Figure 3

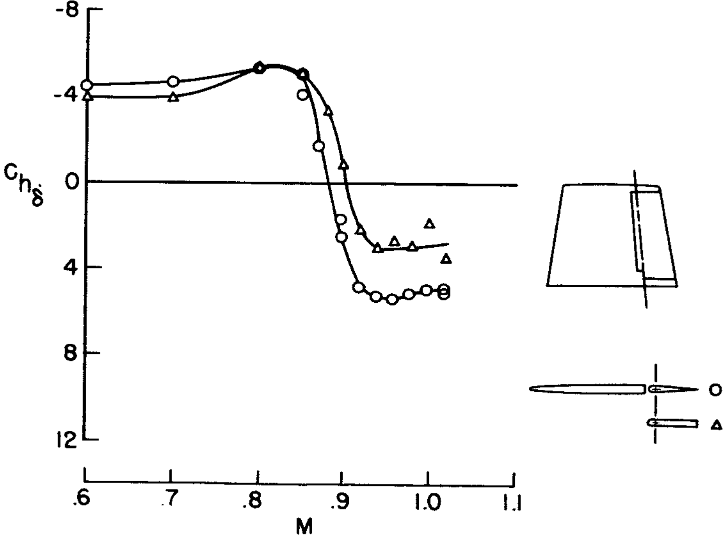

DAMPING COEFFICIENT FOR UNSWEPT WING

α = 0°; $k_a \approx 0.12$

Figure 4

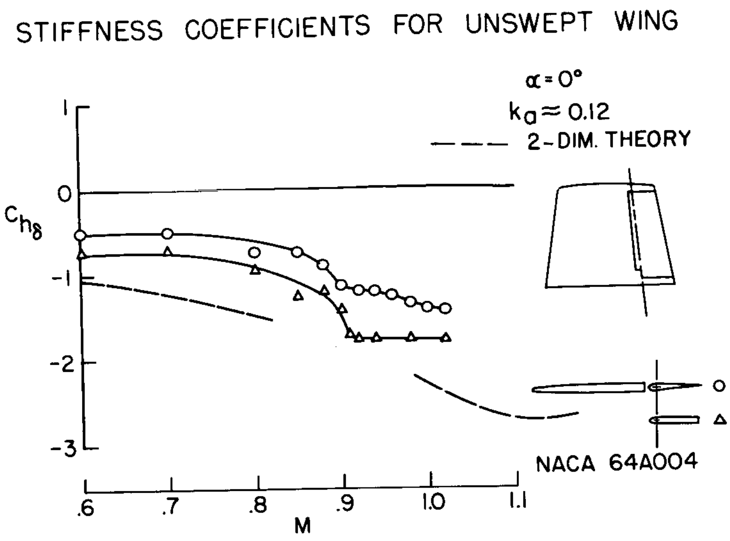

Figure 5

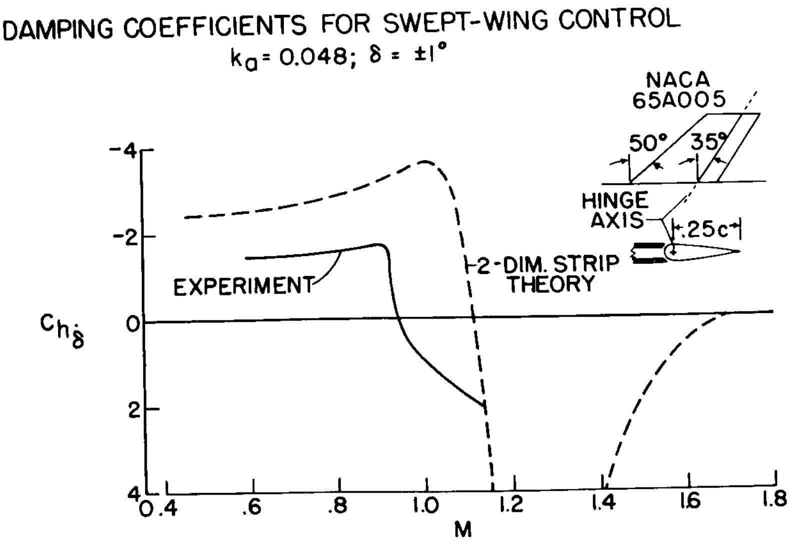

Figure 6

[redacted]

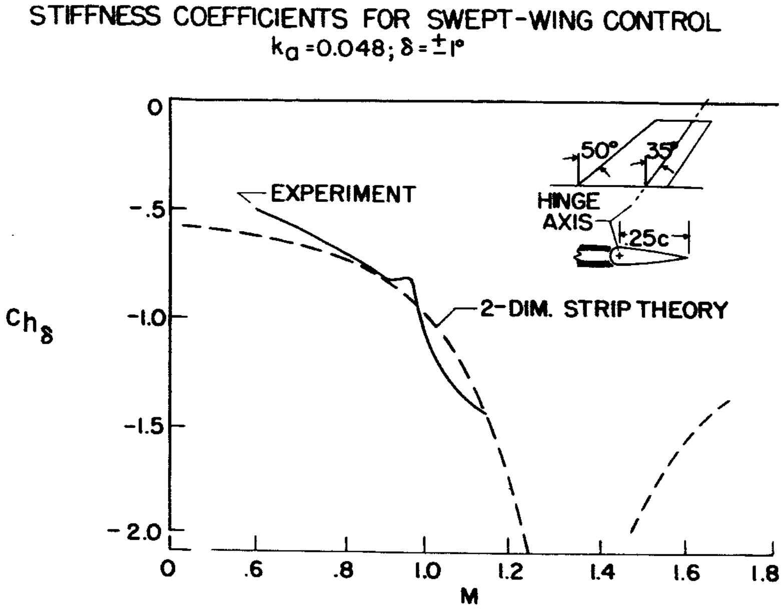

Figure 7

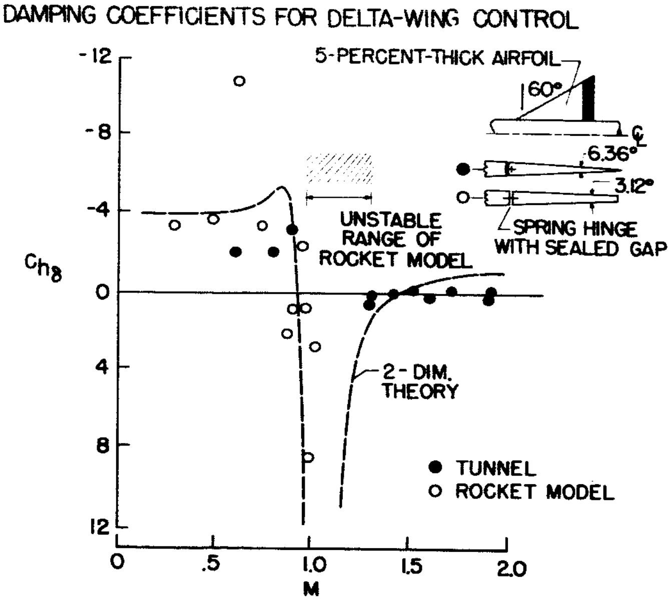

Figure 8

STIFFNESS COEFFICIENTS FOR DELTA-WING CONTROL

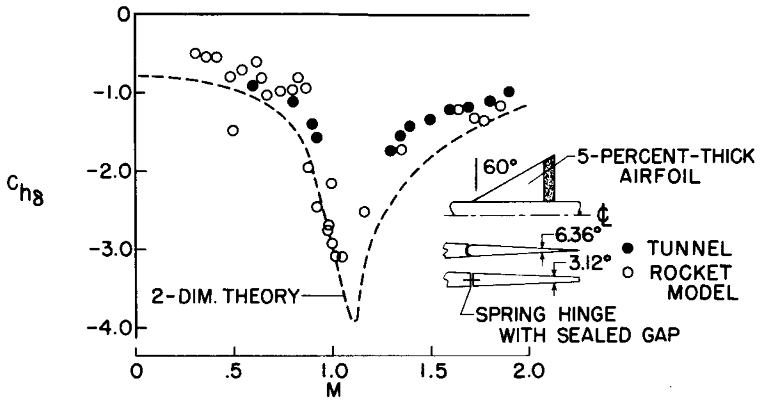

Figure 9

[redacted]

time variation of the angle of attack and the fluctuating load can be represented by rotating vectors shown in the left part of the figure, it is possible to resolve the fluctuating load into two parts - a component in phase with airfoil angular position and a component out of phase with angular position. The in-phase component corresponds to the stiffness terms in the flutter equations, whereas the out-of-phase component corresponds to the damping terms, which are, of course, in phase with the airfoil angular velocity.

In figure 3, data on the fluctuating loads for NACA 65A-series airfoils of 3 different thickness ratios are presented. The in-phase component shown in the upper part of figure 3 has been defined in figure 2. The out-of-phase component, also defined in figure 2, is shown in the lower part of figure 3. The dashed theoretical curves were derived from a report by Neumark (ref. 9) and are for $M = 0.8$. These data are for Mach numbers equal to or less than the Mach number for lift divergence and pertain to a reduced frequency of 0.06. It is apparent that the experimental trends are predicted by theory for both the in-phase and out-of-phase components of the fluctuating loads. The agreement between theory and experiment is not surprising in view of the flow conditions which existed. Neither shock waves nor separation occurred, with the result that the pressure fluctuations were of a sinusoidal nature.

When the Mach number is increased above that for lift divergence, however, the flow field is of an entirely different nature, and large changes in the fluctuating-load distributions are to be expected. This point is illustrated in figure 4, where it is observed that the fluctuating loads are altered substantially over the rear portion of the airfoils where shock waves are known to occur. In the case of the 12-percent- and 8-percent-thick airfoils, these alterations appear as an actual change in the direction of the loading. The magnitude of the alteration is comparable to the large loadings in the vicinity of the leading edge of the airfoil.

A similar comparison of results for Mach numbers less than and greater than lift divergence are shown in figures 5(a) and 5(b), respectively, for higher reduced frequencies than in figures 3 and 4.

There is then, the not altogether surprising indication that shock waves strongly influence the distribution of fluctuating loads on airfoils at supercritical speeds. It is well known, however, that the location of shock waves on airfoils is strongly dependent upon the location of the maximum thickness. It seems appropriate, therefore, to compare the fluctuating loads on airfoils having the same thickness ratios but different maximum-thickness positions. For this purpose, figures 6(a) and 6(b) are presented which show the fluctuating loads on three

[redacted]

[redacted]

A STUDY OF THE FLUCTUATING LOADS ON OSCILLATING AIRFOILS IN SUPERCRITICAL FLOW

By John A. Wyss

Ames Aeronautical Laboratory

This paper is concerned with the air loads acting on two-dimensional airfoils which were driven in harmonic motion at subcritical and supercritical speeds. An increase in Mach number so that the flow becomes supercritical is known to have large effects on steady-state aerodynamic characteristics. That large effects also occur to the nonsteady aerodynamic characteristics has also been shown in previously published papers (e.g., refs. 1, 2, and 3). In order to achieve a better understanding of these effects, a study has been made of the chordwise distribution of the fluctuating loads. Some of the typical results of this study will be shown by first comparing experimental and theoretical results for flow conditions where the theory would be expected to apply. In this manner, some indication of the validity of the experimental measuring technique can be indicated. Results will then be shown for flow conditions where shock waves have a strong influence on the results.

Figure 1 shows a diagrammatic sketch of the drive system. The airfoil was mounted between two walls which formed a two-dimensional channel. The walls were about 16 feet high and 20 feet long. The chord of the airfoil was 2 feet. The drive rod and sector arm attached to the airfoil were contained in one of the walls which formed the two-dimensional channel. The airfoils were driven in sinusoidal motion in pitch about the quarter-chord line at frequencies up to 40 cycles per second and at an amplitude of $\pm 1^{\circ}$. Reynolds number varied from 3×10^{6} to 8×10^{6}. Since the data were obtained in a closed-throat wind tunnel, it was necessary to disregard results near the tunnel resonant frequency in order to minimize the possible effects due to the presence of the wind-tunnel floor and ceiling (refs. 4, 5, and 6).

The data were obtained by means of pressure cells (see refs. 7 and 8) mounted flush with the upper and lower surfaces of the airfoils at several chord stations. Figure 2 illustrates the method of analysis for one chord station. The dashed line indicates the sinusoidal time variation of angle of attack; the solid line, the time variation of the loading coefficient, representing the fundamental component obtained from an harmonic analysis. It may be noted that the pressure coefficient represents the pressure difference between the upper and lower surfaces at each chord station and, therefore, represents the fluctuating load at each chord station. The small arrow over the symbol indicates that it pertains only to the fluctuating part of the air loads on the airfoil. By assuming that the

[redacted]

symmetrical airfoils oscillating about 0° angle of attack. Specifically, the in-phase and out-of-phase components are shown for 8-percent-thick airfoils with their maximum thickness at 16, 42, and 63 percent of the chord. The circular symbols are for a low reduced frequency of 0.05 corresponding to an actual frequency of 8 cycles per second. The square symbols are for the high reduced frequency of 0.25 corresponding to an actual frequency of about 40 cycles per second. The solid lines represent the static loading on the airfoils at the angle of attack, namely 1°, corresponding to the maximum amplitude of oscillation. It is observed again that the fluctuating loads tend to peak in the region where shock waves are known to occur. Also, high pressure peaks are observed to occur at the leading edge of the airfoils having smaller leading-edge radii. Evidently then, both leading-edge radius and maximum-thickness location on an airfoil significantly influence the distribution of the fluctuating loads at low and high reduced frequencies.

Another interesting feature of the data is the apparent relationship between static and fluctuating loads. For example, it is observed that the in-phase component of fluctuating load has much the same trend with chordwise position on the airfoil as the static load. Also, the static-load distribution provides an indication of the location of the peak values of the out-of-phase component. These observations suggest the possibility that the fluctuating loads can be related to the static loads.

It is also of interest to indicate the chordwise regions which contribute to a destabilizing damping moment, as illustrated in figure 7. The chordwise region which contributes a destabilizing damping moment is indicated by the shaded areas. Whether the moment is stable or unstable is determined not only by the sign of the fluctuating load, but also its fore-and-aft location with respect to the axis of rotation. As the point of maximum thickness is moved aft, the magnitude of the unstable fluctuating loads decreases. It is obvious, therefore, that shock waves have a large effect on the damping.

The results may be summarized as follows:

At Mach numbers less than that for lift divergence, the chordwise distribution of the fluctuating loads on the oscillating airfoils were indicated by the theory.

At Mach numbers greater than that for lift divergence, the general chordwise trends of the fluctuating loads were indicated by static-load distributions. Also, the chordwise location of the shock waves had a large effect on the aerodynamic damping.

REFERENCES

1. Wyss, John A., and Monfort, James C.: Effects of Airfoil Profile on the Two-Dimensional Flutter Derivatives for Wings Oscillating in Pitch at High Subsonic Speeds. NACA RM A54C24, 1954.

2. Wyss, John A., and Herrera, Raymond: Effects of Angle of Attack and Airfoil Profile on the Two-Dimensional Flutter Derivatives for Airfoils Oscillating in Pitch at High Subsonic Speeds. NACA RM A54H12, 1954.

3. Monfort, James C., and Wyss, John A.: Effects of Rigid Spoilers on the Two-Dimensional Flutter Derivatives of Airfoils Oscillating in Pitch at High Subsonic Speeds. NACA RM A54I22, 1954.

4. Runyan, Harry L., and Watkins, Charles E.: Considerations on the Effect of Wind-Tunnel Walls on Oscillating Air Forces for Two-Dimensional Subsonic Compressible Flow. NACA Rep. 1150, 1953. (Supersedes NACA TN 2552.)

5. Runyan, Harry L., Woolston, Donald S., and Rainey, A. Gerald: A Theoretical and Experimental Study of Wind-Tunnel-Wall Effects on Oscillating Air Forces for Two-Dimensional Subsonic Compressible Flow. NACA RM L52I17a, 1953.

6. Woolston, Donald S., and Runyan, Harry L.: Some Considerations on the Air Forces on a Wing Oscillating Between Two Walls for Subsonic Compressible Flow. Jour. Aero. Sci., vol. 22, no. 1, Jan. 1955, pp. 41-50.

7. Erickson, Albert L., and Robinson, Robert C.: Some Preliminary Results in the Determination of Aerodynamic Derivatives of Control Surfaces in the Transonic Speed Range by Means of a Flush-Type Electrical Pressure Cell. NACA RM A8H03, 1948.

8. Wyss, John A., and Sorenson, Robert M.: An Investigation of the Control-Surface Flutter Derivatives of an NACA 65_1-213 Airfoil in the Ames 16-Foot High-Speed Wind Tunnel. NACA RM A51J10, 1951.

9. Neumark, S.: Two-Dimensional Theory of Oscillating Aerofoils, With Application to Stability Derivatives. Rep. No. Aero 2449, British R.A.E., Nov. 1951.

DIAGRAMMATIC SKETCH OF WING DRIVE SYSTEM

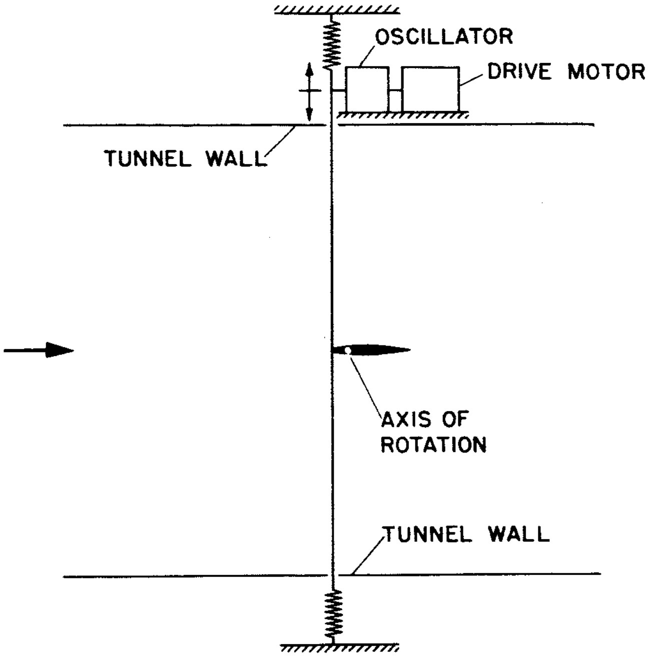

Figure 1

METHOD OF ANALYSIS

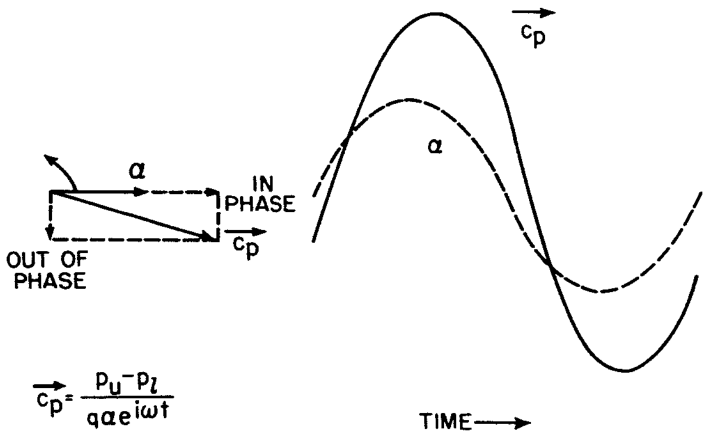

Figure 2

[redacted]

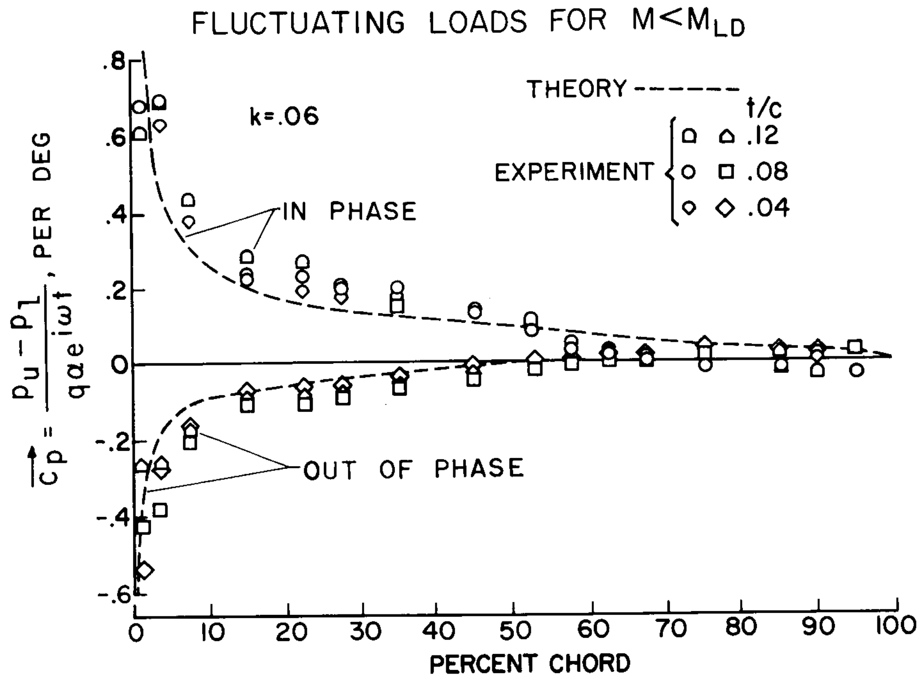

Figure 3

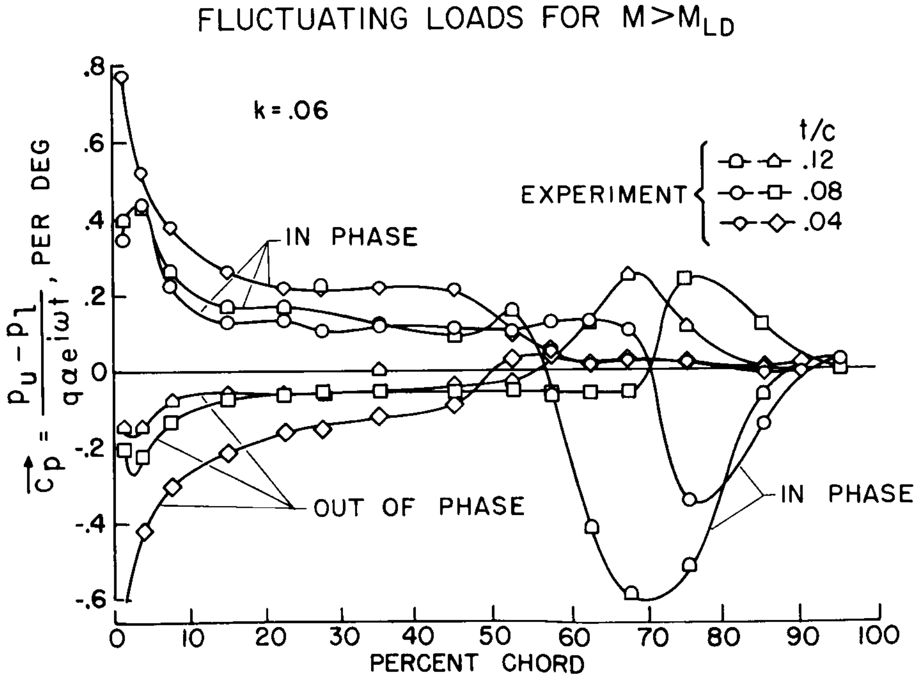

Figure 4

[redacted]

[redacted]

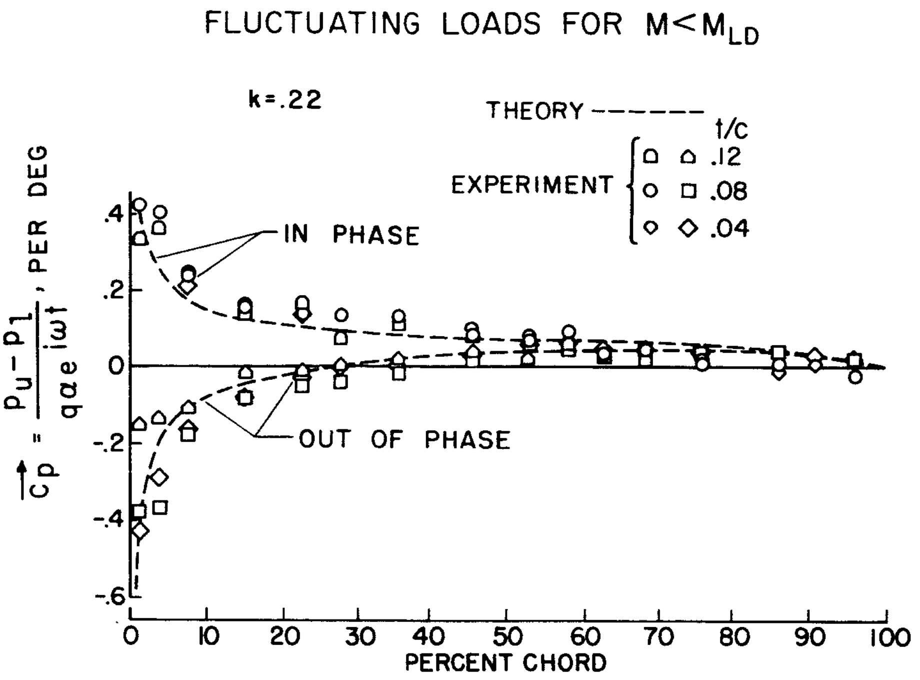
FLUCTUATING LOADS FOR $M<M_{LD}$

Figure 5(a)

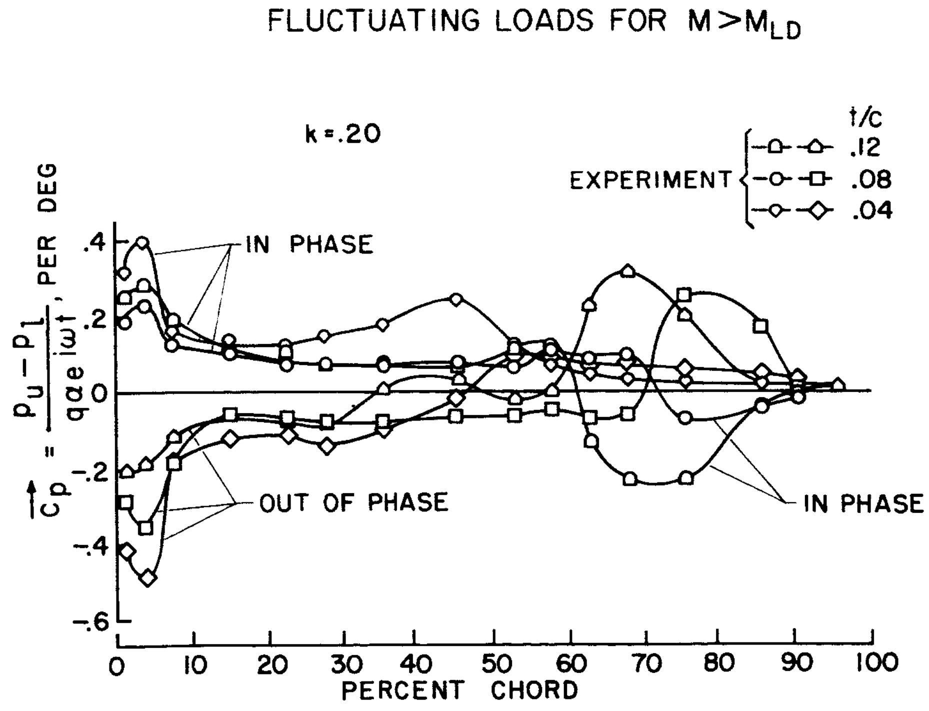
FLUCTUATING LOADS FOR $M>M_{LD}$

Figure 5(b)

[redacted]

UNCLASSIFIED [redacted]

FLUCTUATING LOADS AS AFFECTED BY PROFILE FOR $M>M_{LD}$

IN-PHASE COMPONENT

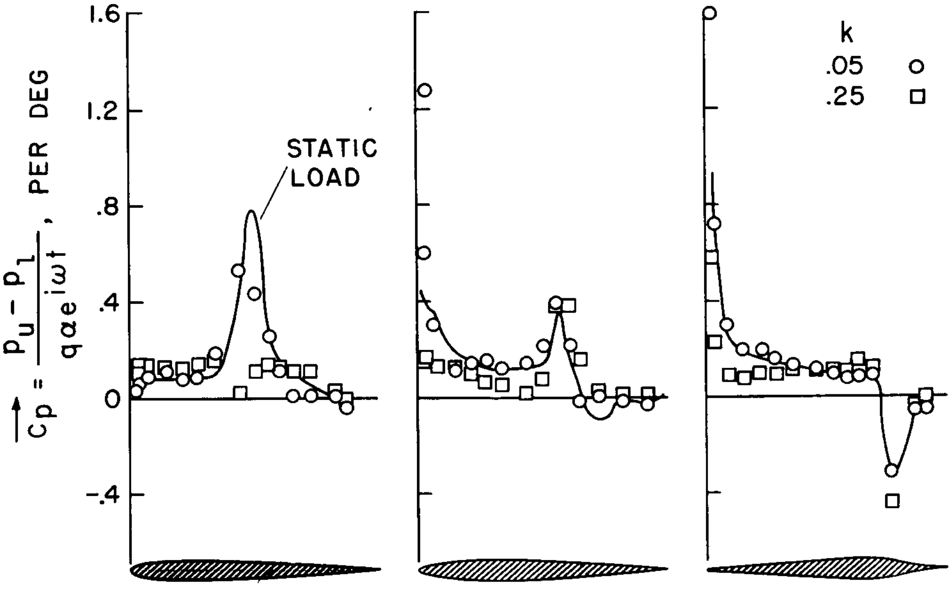

Figure 6(a)

FLUCTUATING LOADS AS AFFECTED BY PROFILE FOR $M>M_{LD}$

OUT-OF-PHASE COMPONENT

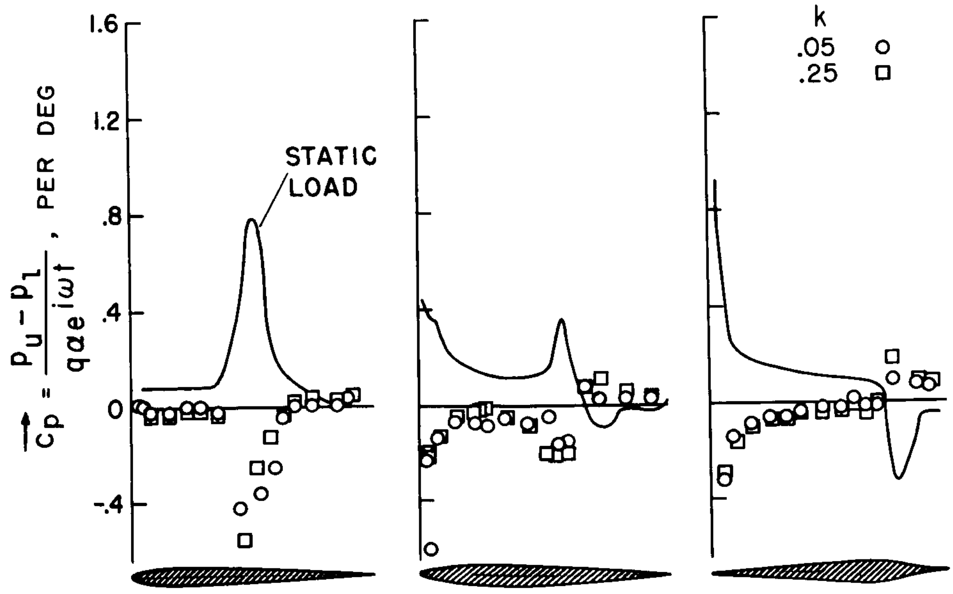

Figure 6(b)

[redacted]

FLUCTUATING LOADS AS RELATED TO
AERODYNAMIC TORSIONAL DAMPING
OUT-OF-PHASE COMPONENT

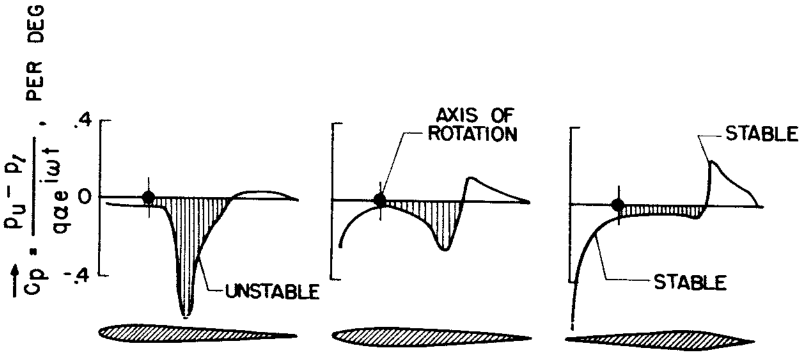

Figure 7

[redacted]

FLUTTER CHARACTERISTICS OF SWEPT WINGS AT TRANSONIC SPEEDS

By Laurence K. Loftin, Jr.

Langley Aeronautical Laboratory

SUMMARY

An experimental study of the flutter characteristics of swept wings is being made in the Langley transonic blowdown tunnel. The purpose of this work is to determine the important effects of some of the plan-form variables and to provide the basis for a means of flutter prediction at transonic speeds. The investigations have consisted of studies of the effects of variations in sweepback angle, aspect ratio, and taper ratio through a Mach number range extending from about 0.8 to 1.35. The investigations have shown that although some further work is no doubt required, the basic effects of these plan-form variables are fairly well defined. Variations in the center-of-gravity position have been shown to have an important effect on flutter at transonic speeds. A method of analysis has been developed which accounts for the effect of center-of-gravity position and which indicates the important aerodynamic parameters influencing flutter of a certain class of wings at transonic speeds.

INTRODUCTION

An experimental study of the flutter characteristics of swept wings is being made in the Langley transonic blowdown tunnel. The purpose of this work is to determine the important effects of some of the plan-form variables and to provide the basis for a means of flutter prediction at transonic speeds. The investigations have consisted of studies of the effects of variations in sweepback angle, aspect ratio, and taper ratio through a Mach number range extending from about 0.8 to 1.35. The variations in the individual plan-form parameters were chosen with a view toward bracketing the range of practical interest and consisted of sweepback angles from 0° to 60°, aspect ratios from 2.0 to 6.0, and taper ratios from 1.0 to 0.2. The effects of variations in certain wing mass parameters have also been briefly studied. Some of the results of these investigations have been reported (refs. 1, 2, and 3), whereas other more recent data are not yet generally available. The present paper will attempt to summarize and correlate some of the trends shown by the results. The experimental techniques

[redacted]

employed in the investigations are fully described in references 2 and 3 and will not be discussed here.

SYMBOLS

Λ	sweep angle of wing quarter-chord line
A	wing aerodynamic aspect ratio
λ	wing taper ratio
M	Mach number
$\frac{V_{EXP}}{V_{REF}}$	ratio of experimental to calculated flutter speeds
$\frac{V_{EXP}}{V_{REF'}}$	ratio of experimental to modified calculated flutter speeds
$\frac{\omega_{h_2}}{\omega_{\alpha_1}}$	ratio of measured coupled second bending frequency to first torsion frequency
C_{L_α}	lift-curve slope
$\frac{x}{c}$	distance along wing chord measured from leading edge, fraction of chord
c	wing chord length normal to quarter-chord line

Subscripts:

CG	center-of-gravity position
ac	aerodynamic-center position
M	Mach number
.8	stream Mach number of 0.8
N	direction normal to quarter-chord line

[redacted]

METHOD OF ANALYSIS

Before discussing the trends shown by the results for the various wings, a few remarks regarding the method of presentation and the definition of flutter speed may be appropriate. Some typical results for a swept wing are shown in figure 1. A definition of the exact plan form is not important in this case. The Mach number is plotted along the abscissa and the ratio of the experimental to a calculated, or reference, flutter speed is on the ordinate. The reference flutter speeds were determined from a Rayleigh type of analysis in which the flutter mode was represented by the superposition of the uncoupled modes of a cantilever beam and in which the aerodynamic coefficients were two-dimensional, incompressible values taken normal to the quarter-chord line (ref. 4). The necessity of employing such a normalizing factor as V_{REF} in the presentation of experimental flutter results seems unavoidable because of the large number of mass, elastic, geometric, and aerodynamic variables involved. Thus, by use of a reference flutter speed, the mass and stiffness properties of the models and the air density, all of which have a profound effect on the actual flutter speed, do not appear explicitly in the comparison of the various wings but are implicit in the values of V_{REF}. Curves of $\frac{V_{EXP}}{V_{REF}}$ against Mach number, therefore, show the departure of the actual flutter speed from a known reference level as a function of Mach number.

In many of our tests, difficulty is experienced in selecting a unique boundary which separates a condition of flutter from a condition of no flutter. The data points through which the solid line is faired in figure 1 indicate a condition of continuous flutter. The cross-hatched area represents a region of doubt in which the behavior of the model is characterized by random oscillations and intermittent bursts of flutter. As can be seen, the region of intermittent flutter is primarily associated with the supersonic range, although this is not always the case. The significance of this region of doubt and the extent to which the bursts of intermittent flutter may be due to excitation by tunnel turbulence in a region of low, but not zero, aerodynamic damping are open to some question. In any case, the flutter boundaries to be presented in succeeding figures correspond to the condition of continuous flutter as illustrated by the solid line in figure 1.

RESULTS AND DISCUSSION

The results of the study of the effect of varying sweep angle are shown in figure 2 where the flutter-speed ratio $\frac{V_{EXP}}{V_{REF}}$ is plotted against

[redacted]

Mach number. The wings had an aspect ratio of 4.0, a taper ratio of 0.6, and were about 4 percent thick in the streamwise direction. The sweep angles are seen to be 0°, 30°, 45°, 52.5°, and 60°. In the Mach number range below about 0.9, the agreement between experimental and calculated flutter speeds is very good, in spite of the oversimplified representation of the aerodynamic forces in the calculations. As indicated in the key of the figure, only two modes were employed in the calculations for the wings of 0° and 30° sweep. These were the uncoupled first torsion and first bending modes of a uniform cantilever beam. In addition to these modes, the second uncoupled bending mode was employed in the calculations for the other wings. The necessity for employing a third mode was found to be closely connected with the value of the ratio of second bending to first torsion frequency. The frequencies forming this ratio were the measured coupled values. The third mode appeared to be necessary in order to obtain good agreement between calculated and experimental flutter speeds when the ratio of second bending to first torsion frequency was in the vicinity of, or below, 1.0.

For Mach numbers greater than about 0.9, the value of the flutter-speed ratio increases with Mach number by an amount which depends on the sweep angle. Very little increase is noted for the 60° swept wing, with progressively more increase accompanying decreases in the sweep angle from 60° to 30°. An inversion in this trend is noted in the curve for the unswept wing which falls below the curves for the 30° and 45° swept wings. No entirely convincing reason for this behavior is apparent at the present time, although one possibility suggests itself. Difficulties with static divergence were experienced with some of the unswept-wing modes. These divergent tendencies may have, in some way, obscured the true zero-angle-of-attack flutter boundary. In any case, investigations are now being made of wings of about 10° sweepback angle in an effort to clarify these results.

Some effects of aspect ratio are shown in figure 3 in which the flutter-speed ratio $\frac{V_{EXP}}{V_{REF}}$ is again plotted as a function of Mach number. The data shown are for 45° sweptback wings having aspect ratios of 2, 4, and 6. The taper ratio is 0.6 and the airfoils are 4 percent thick. The calculated and experimental flutter speeds agree quite well at subsonic speeds for the wings having aspect ratios of 4 and 6. The calculated flutter speeds for the wing of aspect ratio 2 are, however, considerably lower than the experimental values at subsonic Mach numbers. The discrepancy between experimental and calculated flutter speeds in this case is perhaps due to the inadequacy of the two-dimensional aerodynamic coefficients employed in the calculation. At supersonic speeds, all three wings are characterized by values of the flutter-speed ratio which increased with increasing Mach number. The shape of the curves is, however, somewhat different for the three wings.

[redacted]

Some indication of the effect of taper ratio is provided in figure 4 in which the flutter-speed ratio is plotted against Mach number for 45° sweptback wings having taper ratios of 1.0, 0.6, and 0.2. The aspect ratio was 4.0 for all three wings and the airfoils were 4 percent thick. At subsonic Mach numbers, the agreement between calculated and experimental flutter speeds is seen to be good for the wings with taper ratios of 0.6 and 1.0. The calculations for the wing with a taper ratio of 0.2, however, give a flutter speed which is too low by about 20 percent. The flutter mode for these wings was characterized by high frequencies, between the still-air coupled second bending and torsion values, with large tip deflections. The first and second uncoupled bending and first uncoupled torsion mode shapes of a beam with a taper ratio of 0.2 were employed in the calculations. The flutter mode shape, however, may not have been adequately represented. Also, the still-air vibration modes for the wings having a taper ratio of 0.2 were highly coupled, which raises some question as to the approximate method employed for deducing the uncoupled torsion frequency from the coupled values. Consequently, the subsonic level of the $\frac{V_{EXP}}{V_{REF}}$ curve for the plan form with a taper ratio of 0.2 is not too well established. The data show, however, that the $\frac{V_{EXP}}{V_{REF}}$ curve tends to rise more steeply with increasing Mach number as the taper ratio decreases.

The results presented in the preceding three figures all show an increase in the flutter-speed ratio $\frac{V_{EXP}}{V_{REF}}$ as the Mach number increases into the supersonic range. The fact that the agreement between calculated and experimental flutter speeds becomes poorer as the Mach number increases is not surprising because no account was taken in the V_{REF} calculations of the effects of compressibility on the aerodynamic characteristics. The changes in aerodynamic characteristics with Mach number would seem to be primarily a function of wing-plan-form shape. An important question arises, however, as to whether the curves of $\frac{V_{EXP}}{V_{REF}}$ against Mach number are a function only of wing plan form or whether these curves may be altered by variations in some of the mass and elastic properties of the wing which are hidden in the V_{REF} calculation. Some understanding of the important aerodynamic parameters affecting the flutter speed may be obtained from the simple flutter formula given by Theodorsen and Garrick in reference 5. This empirical formula is based on the results of low-speed studies of two-dimensional wing flutter and is applicable to cases in which the ratio of first bending to first torsion frequency is small. A consideration of only those elements of the formula which contain the aerodynamic characteristics of the wing indicates the following important proportionality:

$$V \propto \sqrt{\frac{1}{C_{L_\alpha}\left[\left(\frac{x}{c}\right)_{CG} - \left(\frac{x}{c}\right)_{ac}\right]}} \tag{1}$$

where the symbols have the following meaning:

V	flutter speed
C_{L_α}	lift-curve slope
$\left(\frac{x}{c}\right)_{CG}$	section center-of-gravity position
$\left(\frac{x}{c}\right)_{ac}$	section aerodynamic-center position

The assumption is now made that the departure of the curves of $\frac{V_{EXP}}{V_{REF}}$ from 1.0 as the Mach number increases is a function only of the well-known rearward shift in the aerodynamic center and reduction in lift-curve slope. On the basis of this assumption and with the use of the relation (1), the following expression for the flutter-speed ratio is obtained:

$$\frac{V_{EXP}}{V_{REF}} = \sqrt{\frac{\left(C_{L_\alpha}\right)_{.8}}{\left(C_{L_\alpha}\right)_{M}} \frac{\left[\left(\frac{x}{c}\right)_{CG} - 0.25\right]_{.8}}{\left[\left(\frac{x}{c}\right)_{CG} - \left(\frac{x}{c}\right)_{ac}\right]_{M}}} \tag{2}$$

The subscript $.8$ refers to a Mach number of 0.8 for which the flutter-speed ratio $\frac{V_{EXP}}{V_{REF}}$ is usually about 1.0 and the corresponding aerodynamic center is near the 25-percent-chord station assumed in the V_{REF} calculation. The subscript M refers to some Mach number higher than 0.8. Equation (2) clearly shows that the reduction in lift-curve slope and rearward movement of the aerodynamic center which accompany an increase in Mach number beyond 1.0 should cause an increase in the flutter-speed ratio $\frac{V_{EXP}}{V_{REF}}$. Equation (2) also shows that the magnitude of the effect of rearward movements in the aerodynamic center on the flutter-speed ratio depends upon the position of the section center of gravity.

In order to obtain some indication of the correctness of these ideas, a short experimental investigation was made of three wings having identical plan forms but different section center-of-gravity positions. The wings had a sweep angle of 45°, an aspect ratio of 4.0, a taper ratio of 0.6, and 4-percent-thick airfoil sections. The wings had section center-of-gravity positions of 34, 45, and 57 percent chord. The results of the investigation are shown in figure 5 in which the flutter-speed ratio $\frac{V_{EXP}}{V_{REF}}$ is plotted as a function of Mach number. For any given supersonic Mach number, the value of $\frac{V_{EXP}}{V_{REF}}$ is seen to increase with forward movements of the center-of-gravity position. In fact, the wing with the most forward center-of-gravity position could not be fluttered at all, within the operating limits of the tunnel, above a Mach number of approximately 1.2. No-flutter points for this wing are indicated by solid symbols. The higher values of $\frac{V_{EXP}}{V_{REF}}$ for the more forward center-of-gravity locations are entirely consistent with equation (2).

Equation (2) suggests certain possibilities for generalizing the data of figure 5 to include other center-of-gravity positions. The values of the lift-curve-slope ratio and the aerodynamic-center positions appearing in relation (1) are unknown and must be found. One possibility is to use overall wing lift-curve slopes and aerodynamic-center positions as determined from static aerodynamic tests of rigid wings. Such a procedure does not yield good results, however, because the deflection of the wing is not considered. Another possibility is to regard again the aerodynamic parameters appearing in equation (2) as lumped or integrated values and to determine these values with the use of the flutter data of figure 5 and equation (2). This procedure has been followed herein. The aerodynamic-center position and the lift-curve-slope ratio at any given Mach number are assumed to be a function only of the plan form and, hence, would be the same for the three 45° swept wings having different center-of-gravity positions. This assumption implies that the flutter mode shapes for the three wings are not markedly different. Equation (2) indicates that the difference in the curves of $\frac{V_{EXP}}{V_{REF}}$ at supersonic speeds for the three wings of figure 5 is expressed by the difference in value of the ratio

$$\sqrt{\frac{\left[\left(\frac{x}{c}\right)_{CG} - 0.25\right]_{.8}}{\left[\left(\frac{x}{c}\right)_{CG} - \left(\frac{x}{c}\right)_{ac}\right]_{M}}}$$

whereas the lift-curve-slope ratio

$$\sqrt{\frac{(C_{L_\alpha})_{.8}}{(C_{L_\alpha})_M}}$$

has the same effect on all three wings. On the basis of this synthesis of the effects of lift-curve slope and aerodynamic center, the faired curves of figure 5 for the three wings were cross-plotted in such a way as to determine the variation of the lumped, or effective, values of the aerodynamic-center position and lift-curve-slope ratio with Mach number. The resulting aerodynamic-center position is shown as a function of Mach number normal to the quarter-chord line in figure 6. The aerodynamic center is seen to shift from the 0.25c station to the 0.34c station as the normal Mach number varies from 0.55 to 0.95. These values appear quite reasonable. The variation of the lift-curve-slope ratio $\frac{(C_{L_\alpha})_{.8}}{(C_{L_\alpha})_M}$ with Mach number normal to the quarter-chord line is shown in figure 7. The ratio of the lift-curve slopes at stream Mach numbers of 0.9 and 1.2, as determined from some unpublished static aerodynamic tests of a rigid 45° sweptback aspect-ratio-4.0 wing, is shown by the symbol in this figure.

An indication of how well the deduced variations of aerodynamic-center position and lift-curve ratio describe the results obtained for the wings with different center-of-gravity positions is provided in figure 8. In this figure, the ratio $\frac{V_{EXP}}{V_{REF}'}$ is plotted against stream Mach number for the wings with different center-of-gravity positions. The values of V_{REF}' were determined from equation (2) by letting

$$\frac{V_{REF}'}{V_{REF}} = \sqrt{\frac{(C_{L_\alpha})_{.8}}{(C_{L_\alpha})_M} \frac{\left[\left(\frac{x}{c}\right)_{CG} - 0.25\right]_{.8}}{\left[\left(\frac{x}{c}\right)_{CG} - \left(\frac{x}{c}\right)_{ac}\right]_M}} \qquad (3)$$

and using the values of $\left(\frac{x}{c}\right)_{ac}$ and $\frac{(C_{L_\alpha})_{.8}}{(C_{L_\alpha})_M}$ as given in figures 6 and 7. The correlation is excellent, with no systematic trends evident for the wings with different center-of-gravity positions.

The variations of aerodynamic-center position and lift-curve-slope ratio shown in figures 6 and 7, respectively, were determined from flutter tests of a particular wing plan form. Application of the results to an arbitrary wing plan form is not, in general, permissible. For the restricted case in which the sweep angle is the only plan-form parameter varied, however, one might expect the values of aerodynamic-center position and lift-curve-slope ratio for one sweep angle to be roughly applicable to other sweep angles on the basis of equal Mach numbers normal to the quarter-chord line. On the basis of this rather crude assumption, the aerodynamic-center position and lift-curve-slope data of figures 6 and 7, together with the formula (3), have been used in an attempt to correlate the swept-wing data of figure 2. The results are presented in figure 9 in the form $\frac{V_{EXP}}{V_{REF}}$, as a function of Mach number normal to the quarter-chord line. Also included in figure 9 are the data for the 45° swept wings with center-of-gravity positions of 34 and 57 percent chord. The unswept-wing data of figure 2 are not included. For normal Mach numbers less than 0.7, the correlation is within the scatter of the data for individual wings. At higher Mach numbers, the correlation is not quite so good, with the maximum disparity between the data points and the line $\frac{V_{EXP}}{V_{REF}}$' = 1.0 being about 15 percent.

The correlation of figure 9 indicates that, at least for the class of wings considered, the aerodynamic center and lift-curve slope are the important aerodynamic characteristics controlling the variation of $\frac{V_{EXP}}{V_{REF}}$ with Mach number. The fact that the correlation, figure 9, was achieved without any consideration of the effect of compressibility on aerodynamic lag is perhaps also of some significance. The formula, equation (3), together with the values of aerodynamic-center position and lift-curve-slope ratio given in figures 6 and 7, respectively, may perhaps prove of some use in estimating the effect of variations in center-of-gravity position on the flutter speed of wing plan forms of the same general class as those considered. The generality of the method, in an absolute sense, is however difficult to access.

CONCLUDING REMARKS

Transonic flutter investigations have been made of swept wings having different sweep angles, aspect ratios, and taper ratios. Although some further work is no doubt required, the basic effects of these plan-form variables seem fairly well defined. Variations in the section center-of-gravity position have been shown to have an important effect on flutter at transonic speeds. A method of analysis has been

[redacted]

developed which accounts for the effect of center-of-gravity position and which indicates the important aerodynamic parameters influencing flutter of a certain class of wings at transonic speeds.

REFERENCES

1. Bursnall, William J.: Initial Flutter Tests in the Langley Transonic Blowdown Tunnel and Comparison With Free-Flight Flutter Results. NACA RM L52K14, 1953.
2. Jones, George W., Jr., and DuBose, Hugh C.: Investigation of Wing Flutter at Transonic Speeds for Six Systematically Varied Wing Plan Forms. NACA RM L53G10a, 1953.
3. Land, Norman S., and Abbott, Frank T., Jr.: Transonic-Flutter Investigation of a Fighter-Airplane Wing Model and Comparison With a Systematic Plan-Form Series. NACA RM L55B16, 1955.
4. Barmby, J. G., Cunningham, H. J., and Garrick, I. E.: Study of Effects of Sweep on the Flutter of Cantilever Wings. NACA Rep. 1014, 1951. (Supersedes NACA TN 2121.)
5. Theodorsen, Theodore, and Garrick, I. E.: Mechanism of Flutter - A Theoretical and Experimental Investigation of the Flutter Problem. NACA Rep. 685, 1940.

[redacted]

[redacted]

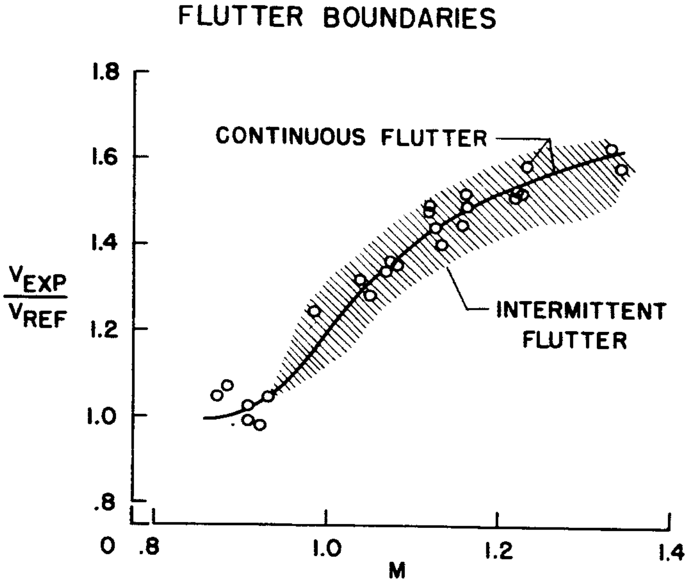

Figure 1

[redacted]

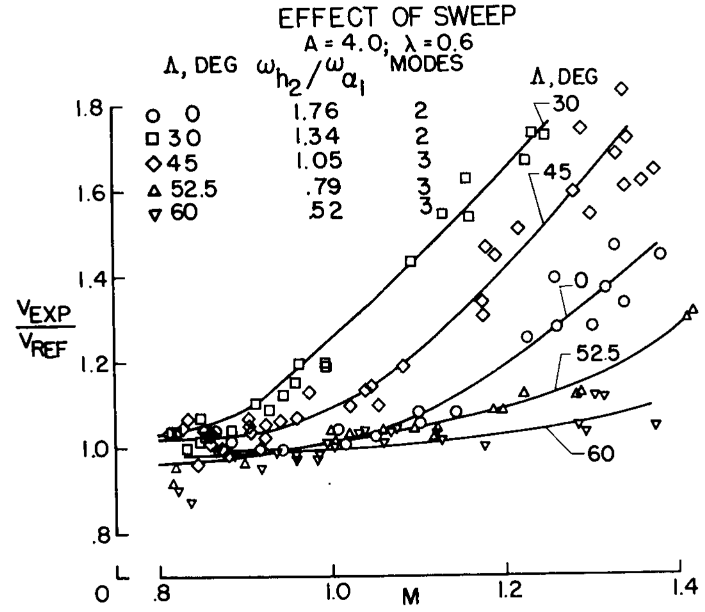

Figure 2

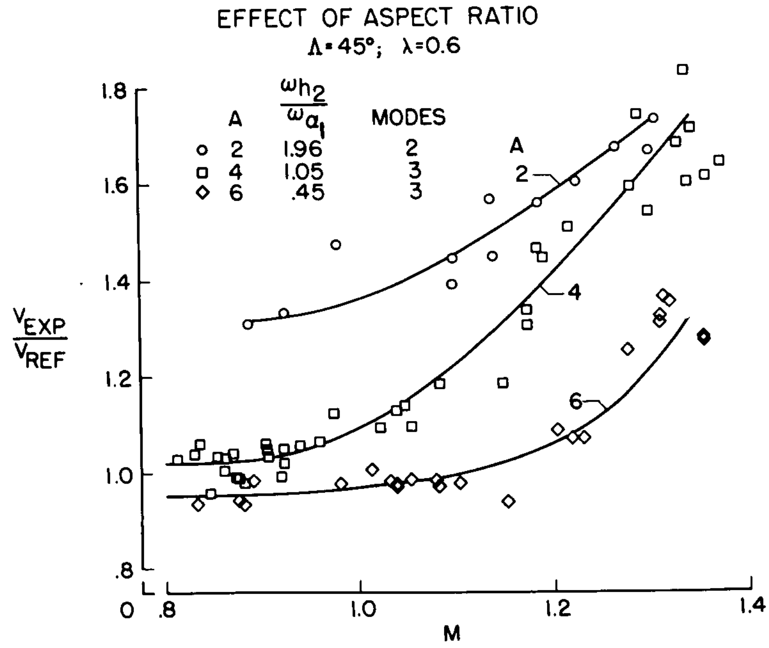

Figure 3

[redacted]

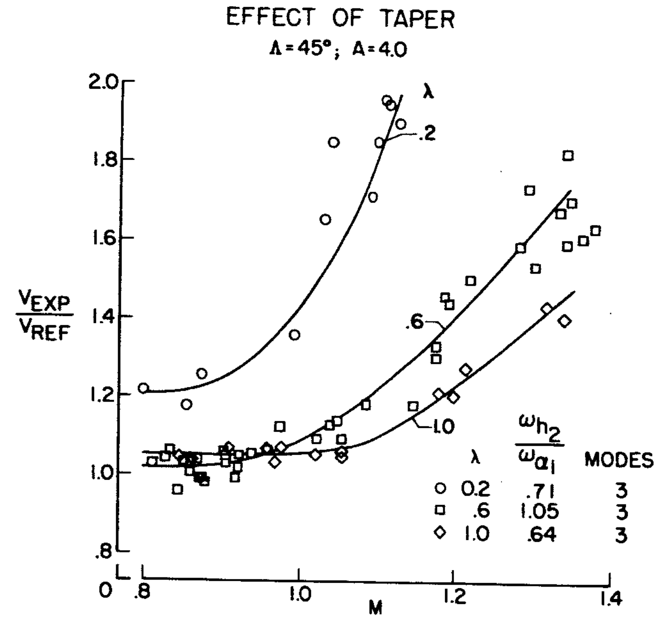

Figure 4

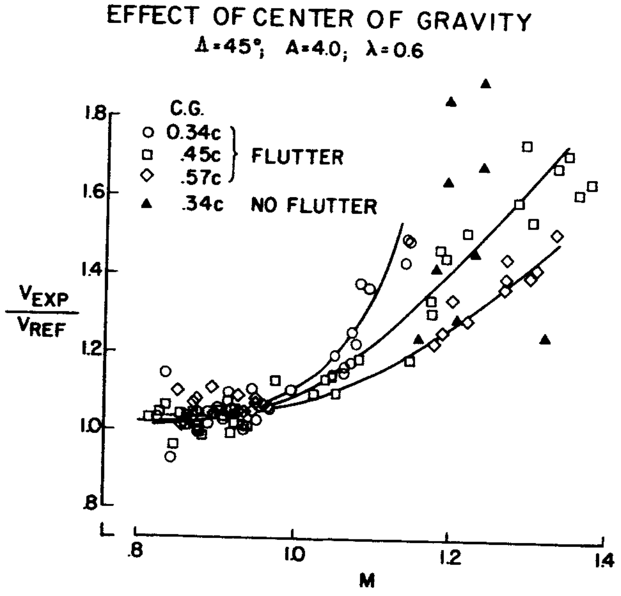

Figure 5

[redacted]

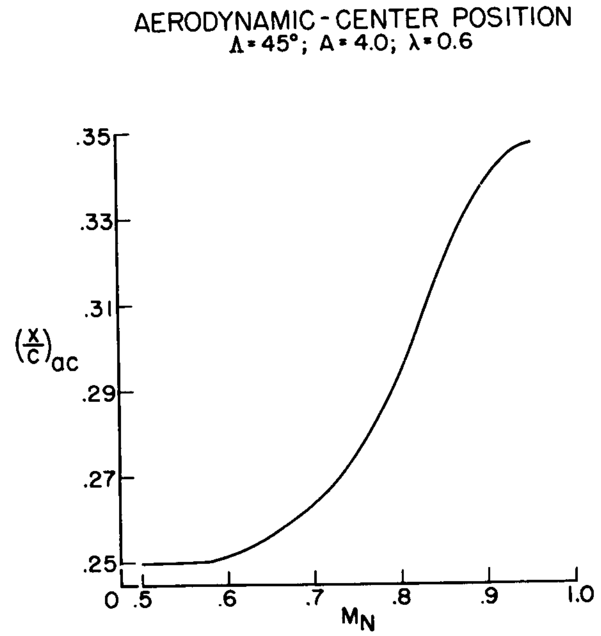

Figure 6

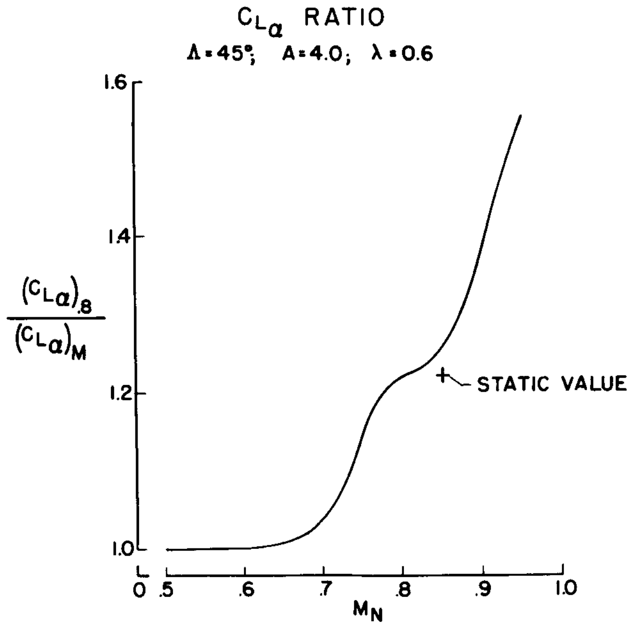

Figure 7

[redacted]

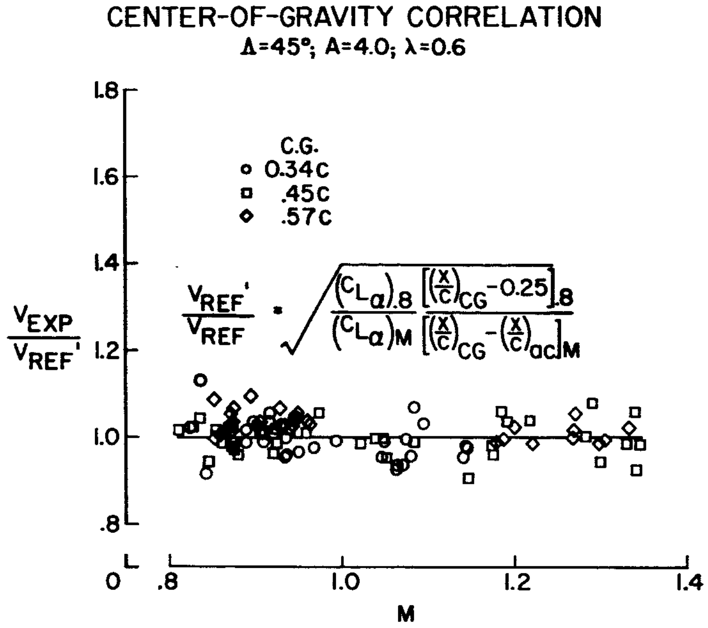

Figure 8

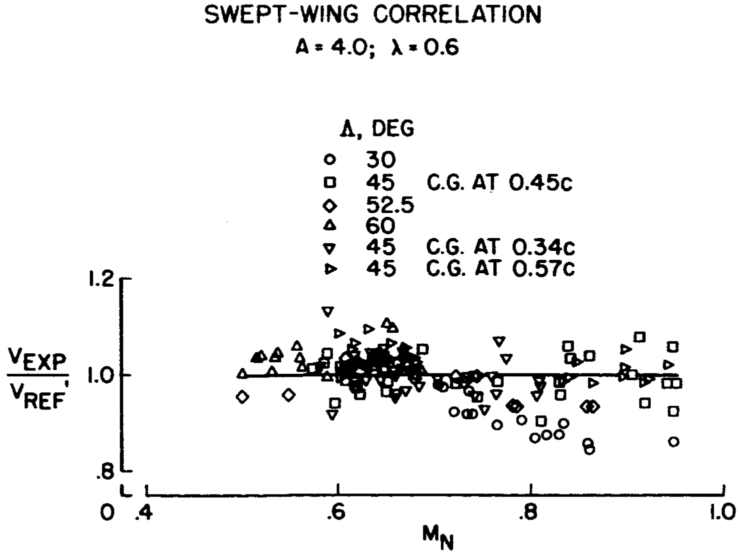

Figure 9

[redacted]

EXPERIMENTAL FLUTTER RESULTS FOR CANTILEVER-WING MODELS AT MACH NUMBERS UP TO 3.0

By W. J. Tuovila and John Locke McCarty

Langley Aeronautical Laboratory

SUMMARY

Experimental flutter tests have been made at Mach numbers up to 3.0 using cantilever-wing models with 0° to 60° sweepback and 45° and 60° delta-wing models. The effects of high Mach number and center-of-gravity location on the flutter trends are indicated. For wings with the center-of-gravity location ahead of the midchord and with small sweep angles, the stiffness requirements to prevent flutter at a given altitude are determined essentially at transonic speeds. For wings with rearward center-of-gravity locations and high sweep angles, the stiffness requirements continue to increase with increase in Mach number. Shifting the center-of-gravity location forward reduces the stiffness requirements to prevent flutter, particularly for wings of low sweep angle.

INTRODUCTION

One of the questions that arises when aircraft are being designed for high Mach number flight is whether or not there is still a serious flutter problem after the transonic range has been traversed. The trends as a function of Mach number have been fairly well defined for various configurations at transonic and low supersonic speeds. These data have been made available from free-flight rocket-model and wind-tunnel tests as indicated in references 1 to 5.

The available flutter data at the higher supersonic Mach numbers are very limited, especially for wing plan forms of current interest. Systematic wind-tunnel tests of two-dimensional wings at Mach numbers of 1.5 and 1.72 are reported in references 6 and 7, respectively, and comparisons with two-dimensional theory are given. Flutter data in free flight at Mach numbers up to approximately 2.1 have come mainly from isolated rocket-model tests, such as those described in references 8, 9, and 10, and pertain to 60° delta-wing plan forms.

The present paper extends the range of trend studies on cantilever-swept-wing and delta-wing plan forms up to a Mach number of 3.0. Part of these tests were made with the simple untapered models of reference 5 and

[redacted]

DECLAS[redacted]D

thus represent an extension of that work to higher Mach numbers. In addition, some data are presented on the effect of center-of-gravity location and taper on flutter at supersonic speeds.

SYMBOLS

A	aspect ratio
a	speed of sound
b	wing semichord measured parallel to airstream
c	chord
f	frequency
f_1, f_2, f_3	first three coupled frequencies
f_f	flutter frequency
f_α	assumed torsional frequency
l	semispan
M	Mach number
q	dynamic pressure referred to speed of sound
t	thickness of wing
V	free-stream velocity
Λ	sweepback angle
λ	taper ratio
μ	mass-density parameter
μ_o	reference value of μ
ρ	density of air
ω_α	wing torsional circular frequency

[redacted]

TEST APPARATUS AND MODELS

The flutter studies were made in the Langley supersonic flutter apparatus. This tunnel is an intermittent flow blowdown tunnel which operates at stagnation pressures up to about 80 pounds per square inch absolute using dried air. The testing technique used is described in reference 11.

The wing models that were tested are illustrated in figure 1. The untapered swept-wing models were cut from sheet metal and had the leading and trailing edge beveled 1/4 inch to form a hexagonal section shape. The chords of all these models were 2 inches measured perpendicular to the leading edge, and the thicknesses were all 0.041 inch. The 45° and 60° delta-wing models were cut from 0.034-inch sheet magnesium and the leading edges were beveled 1/8 inch. The tapered-wing models were made from wood and magnesium. The root chord for the models with taper ratio (λ) of 0.2 was 5 inches and for the models with taper ratio of 0.4 was 4.25 inches. The sweepback, aspect ratio, thickness ratio measured parallel to the airstream, and taper ratio of the models are given in the figure.

METHOD OF PRESENTING RESULTS

Some wing parameters and also the test conditions at flutter are presented in table I. The first three coupled frequencies and the flutter frequencies are listed along with the wing weights and air densities at flutter. The assumed torsional frequency is designated as f_{α}.

The results of these tests are presented in the form of a stiffness-altitude parameter $\frac{b\omega_{\alpha}}{a}\sqrt{\frac{\mu}{\mu_o}}$. (The symbol μ is the ratio of the mass of the wing to the mass of a cylinder of air of a diameter equal to the wing chord. The values of μ are based on the semichord b measured perpendicular to the leading edge for the untapered swept models; for the delta wings the mass of air is based on a cone with base parallel to the airstream and diameter equal to the root chord; for the tapered models the mass of air is based on a truncated cone with base perpendicular to the midchord line and base diameter equal to the wing chord where the midchord line intersects the root.) Part of this parameter represents the wing torsional stiffness and part refers to the altitude, hence, the name stiffness-altitude parameter. The $b\omega_{\alpha}$ part may be thought of as representing the wing torsional stiffness, and the speed of sound a and the mass-density parameter μ depend on the altitude. The stiffness-altitude parameter is effectively the torsional stiffness divided by q referred to speed of sound. It depends only upon the physical properties of the wing – in particular, the torsional stiffness – and upon the atmosphere in which it operates. Its value increases as the torsional stiffness increases and as the altitude increases.

RESULTS AND DISCUSSION

Untapered Swept Models

Figure 2 presents the results of the tests with the untapered swept wings. The altitude-stiffness parameter is plotted against test Mach number and the results are referred to a nominal value of $\mu = 50$ in order to eliminate the effect of differences in μ caused by flutter testing at varying densities. The flutter curves are the boundary between the flutter region, which is below the curves, and the no-flutter region above the curves. When the stiffness-altitude parameter for a particular wing lies above its flutter curve, the wing is free of flutter and thus the stiffness-altitude parameter may serve as a flutter criterion. For example, the dashed line represents a value of stiffness-altitude parameter which is sufficient to prevent flutter at all Mach numbers up to 3.0 for the 15° swept model. It is of interest to note the two different types of flutter curves. The curves for the 15° and 30° swept models rise to a maximum value at a Mach number of 1.2 and then drop off as the Mach number increases further, whereas the curves for the 45° and 60° models continue to rise as the Mach number increases. If the 15° and 30° swept models were designed to be free of flutter at Mach number 1.2, they would also be free of flutter at the higher Mach numbers at least up to 3.0. The 30° model would be near the flutter border, however, at the higher Mach numbers. If the 45° and 60° swept models are free of flutter up to a particular Mach number, any increase in Mach number requires an increase in stiffness or an increase in altitude. Subsonic points have been included to complete the flutter curves through the transonic range. The curves are dashed because the interpolations through the transonic range are based on previous flutter experience rather than on experiments of the present tests.

It should be noted that these results refer to the particular series of wings tested, and it is expected that the curves will vary as additional factors such as the center-of-gravity location, bending-to-torsion frequency ratio, aspect ratio, and sweepback are changed. For these models the center of gravity is located at 50 percent chord, the frequency ratios are near 0.2, and the aspect ratios vary from 5.35 to 1.39 as indicated.

Delta Models

Figure 3 shows flutter curves for the simple 45° and 60° delta-wing models. The first three coupled natural frequencies along with the range of flutter frequencies are indicated for each model. The assumed torsional frequency is indicated by f_{α}. On the basis of the interpolation, once the 45° delta-wing model passed a Mach number of 1.0 safely, it could go to almost 2.0 before any increase in stiffness or altitude would be needed. The 60° delta-wing model, however, needs considerable increase in stiffness or altitude to fly at increased Mach numbers.

Tapered Models

Figure 4 shows the effect of Mach number on the stiffness requirements for the series of tapered wings with center of gravity located at 46 percent chord and the mass-density ratio having a nominal value of 50. The 45° swept model with a taper ratio of 0.4 has a flutter curve which reaches a peak, according to the interpolation, near a Mach number of 1.0, and, if the transonic range is passed safely, the model is free of flutter up to a Mach number of 2.0. If the 60° model with a taper tatio of 0.2 is free of flutter at a Mach number of about 1.2, it is also free of flutter up to Mach number 2.0, but it is not far from the flutter boundary. The 60° model with a taper ratio of 0.4 requires increased stiffness for increased Mach numbers. Two of these models were also tested at Mach number 3.0, but no flutter was encountered probably because of the low densities available. For the 45° model, the lowest no-flutter point was at 0.29, and, for the 60° model with a taper ratio of 0.2, it was 0.34.

Effect of Center-of-Gravity Location

One of the important flutter parameters is the center-of-gravity location and figure 5 shows the effect of this location on the stiffness-altitude parameter for the simple swept-wing models at a Mach number of 2.0. Here, the stiffness-altitude parameter is plotted against the center-of-gravity location. These results have been referred to $\mu_o = 50$. Moving the center of gravity forward from 50 to 44 percent chord gives a pronounced reduction in the stiffness needed to prevent flutter. As the sweepback is increased, this effect is reduced. At 15° sweepback this decrease is about 30 percent whereas at 60° sweepback it is only about 10 percent. The influence of center-of-gravity location is illustrated in figure 6 for a tapered unswept model. This model was flown normally with the center of gravity at 46 percent chord and it was then reversed and flown backward with the center of gravity at 54 percent chord. The changes in airfoil shapes and sweep that occurred should not have had any appreciable additional effect on the flutter over the center-of gravity effect. At a Mach number of 2.0, there is a considerable reduction in the stiffness-altitude parameter as the center of gravity is shifted from 54 to 46 percent chord. At a Mach number of 1.3, the reduction is less. These curves also illustrate that the wing with a center-of-gravity location at 46 percent chord is free of flutter at least up to a Mach number of 2.0 if it is free of flutter in the transonic range. With a 54-percent-chord center-of-gravity location, however, any increase in Mach number requires an increase in stiffness or altitude. This effect of center-of-gravity location has been noted in reference 12.

SOME REMARKS ON COMPARISON WITH THEORY

Flutter analyses of wings in the subsonic and low supersonic range, based on two-dimensional air-force coefficients and a normal-flow concept usually results in flutter speeds which are lower than the measured ones. This previous experience was confirmed by a few calculations of the present tests at $M = 1.3$ in which values lower than experiment were also obtained. The fact that the theory is, in general, conservative, has made it useful for the subsonic and low supersonic range of flight speeds.

The limited experience to date in the higher supersonic range has indicated that the two-dimensional theory is no longer conservative and that it should be used with caution. Flutter calculations in references 6 and 7 show that at Mach numbers of 1.5 and 1.72 the calculations give higher values of flutter-speed coefficients than are measured. This type of result was also obtained for a limited number of cases treated in the present studies at Mach numbers of 2.0 and 3.0.

CONCLUDING REMARKS

The results of these experimental studies indicate that, for wings with center-of-gravity location ahead of the midchord and with small sweep angles, the stiffness requirements to prevent flutter at a given altitude are determined essentially at transonic speeds. For wings with rearward center-of-gravity location and high sweep angles, the stiffness requirements continue to increase with increase in Mach number. A forward shift of the center-of-gravity location has the effect of reducing the stiffness requirements to prevent flutter, particularly for wings of low sweep angle.

REFERENCES

1. Lauten, William T., Jr., and Barmby, J. G.: Continuation of Wing Flutter Investigation in the Transonic Range and Presentation of a Limited Summary of Flutter Data. NACA RM L9B25b, 1949.
2. Lauten, William T., Jr., and Teitelbaum, J. M.: Some Experiments on the Flutter of Wings With Sweepback in the Transonic Speed Range Utilizing Rocket-Propelled Vehicles. NACA RM L50C03a, 1950.
3. Tuovila, W. J.: Some Experiments of the Flutter of Sweptback Cantilever Wing Models at Mach Number 1.3. NACA RM L51A11, 1951.
4. Jones, George W., Jr., and DuBose, Hugh C.: Investigation of Wing Flutter at Transonic Speeds for Six Systematically Varied Wing Plan Forms. NACA RM L53G10a, 1953.
5. Tuovila, W. J.: Some Wind-Tunnel Results of an Investigation of the Flutter of Sweptback- and Triangular-Wing Models at Mach Number 1.3. NACA RM L52C13, 1952.
6. Pengelley, C. D., Benum, D., D'Ewart, B. B., Jr., and Blackwell, E.: Supersonic Flutter Model Tests at $M = 1.5$. AF Tech. Rep. No. 5793, Air Materiel Command, U. S. Air Force, Apr. 1951.
7. Andreopoulos, T. C., and Targoff, W. P.: Flutter at $M = 1.72$ - Two-Dimensional Model Tests. WADC Tech. Rep. 53-306, Wright Air Dev. Center, U. S. Air Force, Sept. 1953.
8. Judd, Joseph H., and Lauten, William T., Jr.: Flutter of a 60° Delta Wing (NACA 65A003 Airfoil) Encountered at Supersonic Speeds During the Flight Test of a Rocket-Propelled Model. NACA RM L52E06a, 1952.
9. Lauten, William T., Jr., and Mitcham, Grady L.: Note on Flutter of a 60° Delta Wing Encountered at Low-Supersonic Speeds During the Flight of a Rocket-Propelled Model. NACA RM L51B28, 1951.
10. Lauten, William T., Jr., and Judd, Joseph H.: Supersonic Flutter of a 60° Delta Wing Encountered During the Flight Test of a Rocket-Propelled Model. NACA RM L54D12a, 1954.
11. Tuovila, W. J., Baker, John E., and Regier, Arthur A.: Initial Experiments on Flutter of Unswept Cantilever Wings at Mach Number 1.3. NACA TN 3312, 1954. (Supersedes NACA RM L8J11.)
12. Garrick, I. E., and Rubinow, S. I.: Flutter and Oscillating Air-Force Calculations for an Airfoil in a Two-Dimensional Supersonic Flow. NACA Rep. 846, 1946. (Supersedes NACA TN 1158.)

DECLAS[redacted]ED

TABLE I.- FLUTTER PARAMETERS

(a) Untapered swept-wing models

[All models were 0.041 inch thick and had 2-inch chords measured perpendicular to leading edge]

	C.G. location, percent c	Wing weight, lb	Air density, ρ, slugs/cu ft	μ	M	V, fps	f_1, cps	f_2, cps	f_3, cps	f_α, cps	f_f, cps	Material
Λ = 15° 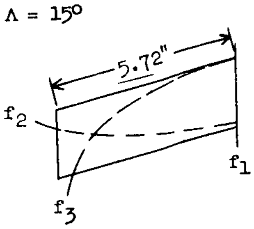	50	0.0257	0.00093	83	3.00	2,030	37	218	270	218	146	Magnesium
	50	.0257	.00053	146	2.00	1,680	35	205	234	205	134	Magnesium
	50	.040	.00049	244	1.30	1,280	36	210	254	210	102	Aluminum
	50	.040	.0023	52	.45	495	36	210	242	210	120	Aluminum
	44	.027	.00098	82	2.00	1,680	33	181	219	181	116	Magnesium
Λ = 30° 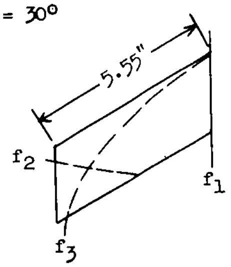	50	.0251	.00067	115	3.00	2,030	42	215	297	215	158	Magnesium
	50	.0251	.00043	180	2.00	1,680	38	210	261	210	142	Magnesium
	50	.0388	.00044	271	1.30	1,280	39	210	274	210	94	Aluminum
	50	.0388	.0023	52	.47	517	35	210	270	210	120	Aluminum
	44	.0264	.00064	126	2.00	1,680	37	178	256	178	132	Magnesium
Λ = 45° 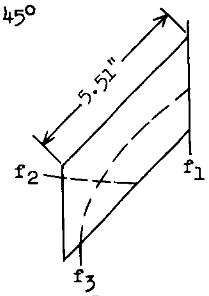	50	.0249	.00061	127	3.00	2,030	45	220	342	220	170	Magnesium
	50	.0249	.00044	176	2.00	1,680	43	206	310	206	148	Magnesium
	50	.0386	.00063	189	1.30	1,280	42	210	370	210	180	Aluminum
	50	.0386	.0023	52	.50	550	35	198	294	198	120	Aluminum
	44	.0262	.00056	143	2.00	1,680	41	180	298	180	140	Magnesium
Λ = 60° 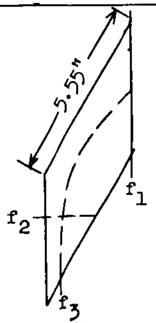	50	.0251	.00069	112	3.00	2,030	47	200	388	200	180	Magnesium
	50	.0251	.00072	107	2.00	1,680	45	199	354	199	166	Magnesium
	50	.0388	.0013	92	1.30	1,280	50	214	399	214	174	Aluminum
	50	.0388	.0022	54	.76	836	48	210	396	210	110	Aluminum
	44	.0264	.00080	100	2.00	1,680	52	190	360	190	170	Magnesium

[redacted]

[redacted]

TABLE I.- FLUTTER PARAMETERS - Continued

(b) Delta-wing models

[Models were 0.034 inch thick]

	C.G. location, percent c	Wing weight, lb	Air density, ρ, slugs/cu ft	μ	M	V, fps	f_1, cps	f_2, cps	f_3, cps	f_α, cps	f_f, cps	Material
45° delta 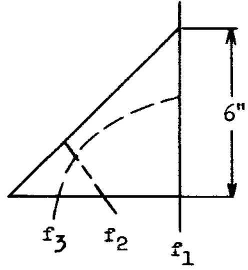	50	0.0391	0.00072	52	3.00	2,030	49	183	257	257	159	Magnesium
	50	.0391	.00070	53	2.00	1,680	50	185	261	261	159	Magnesium
	50	.0391	.00066	56	1.30	1,280	48	180	273	273	150	Magnesium
	50	.0391	.0023	16	.40	440	48	178	244	244	140	Magnesium
60° delta 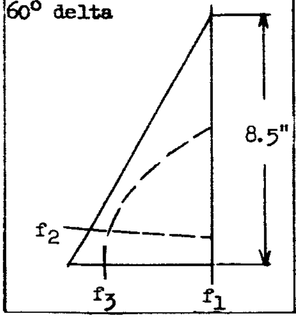	50	.0453	.00063	42	3.00	2,030	67	193	342	342	180	Magnesium
	50	.0453	.00070	38	2.00	1,680	66	200	341	341	170	Magnesium
	50	.0453	.00087	30	1.30	1,280	67	190	338	338	172	Magnesium
	50	.0453	.0023	12	.54	594	66	194	340	340	162	Magnesium

TABLE I.- FLUTTER PARAMETERS - Concluded

(c) Tapered wing models

[All models had 6-inch semispans measured perpendicular to root]

	C.G. location, percent c	Wing weight, lb	Air density, ρ, slugs/cu ft	μ	M	V, fps	f_1, cps	f_2, cps	f_3, cps	f_α, cps	f_f, cps	Material
Λ = 0°; λ = 0.2 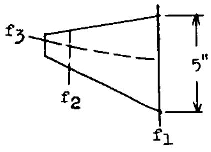	46	0.047	0.0025	21	2.00	1,680	120	360	505	505	433	Magnesium
	46	.047	.0014	37	1.30	1,280	120	360	480	480	420	Magnesium
Λ = 0°; λ = 0.2 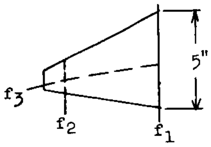	54	.047	.0012	44	2.00	1,680	121	360	520	520	431	Magnesium
	54	.047	.00096	55	1.30	1,280	120	344	495	495	384	Magnesium
	54	.047	.0023	23	.67	736	120	330	492	492	282	Magnesium
Λ = 45°; λ = 0.4 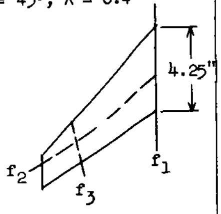	46	.030	.0011	45	2.00	1,680	93	320	405	320	276	Wood
	46	.030	.0013	39	1.30	1,280	100	344	408	344	212	Wood
	46	.030	.0023	22	.57	626	102	360	420	360	210	Wood
Λ = 60°; λ = 0.2 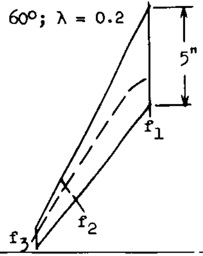	46	.033	.0012	55	2.00	1,680	68	207	420	420	378	Wood
	46	.033	.00080	82	1.30	1,280	68	217	420	420	288	Wood
	46	.033	.0023	29	.58	638	70	210	420	420	213	Wood
Λ = 60°; λ = 0.4 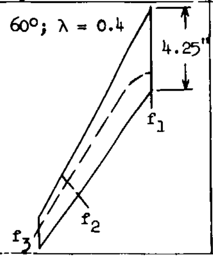	46	.030	.00048	152	2.00	1,680	42	154	320	320	180	Wood
	46	.030	.00049	148	1.30	1,280	41	152	315	315	144	Wood
	46	.030	.0023	32	.45	495	46	170	321	321	156	Wood

[redacted]

FLUTTER MODELS TESTED UP TO M = 3.0

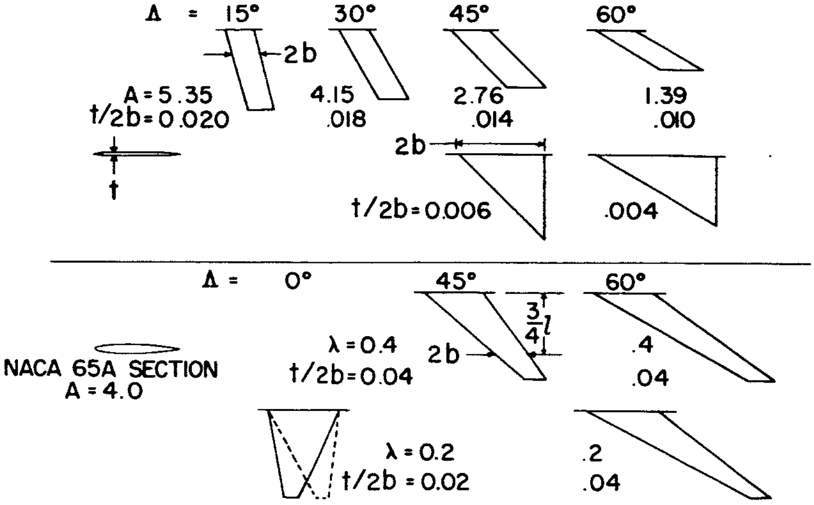

Figure 1

EFFECT OF MACH NUMBER

μ_0 = 50; C.G. LOCATION = 50% C

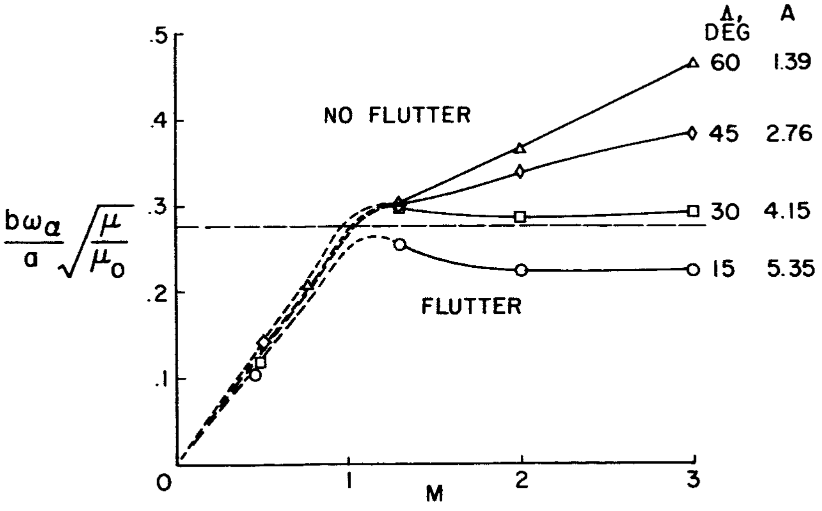

Figure 2

DECLA[redacted]ED

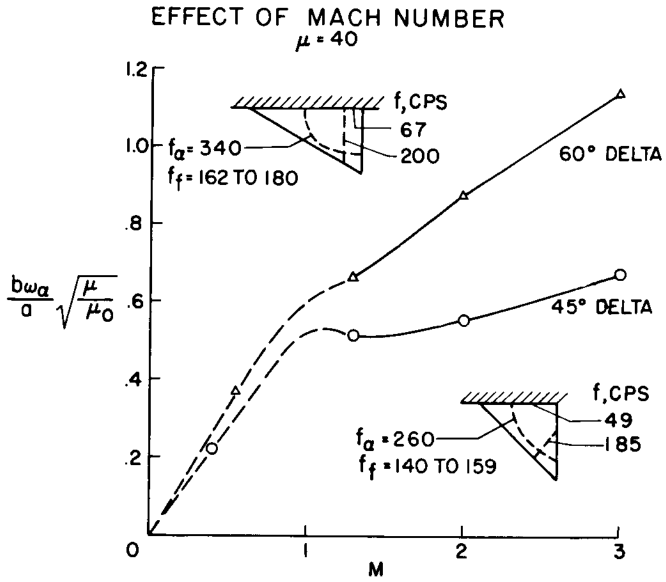

Figure 3

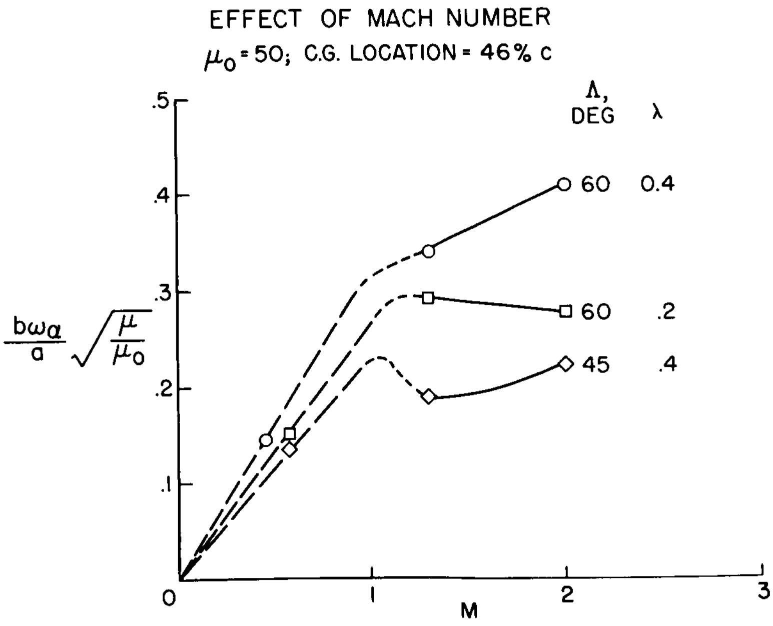

Figure 4

[redacted]

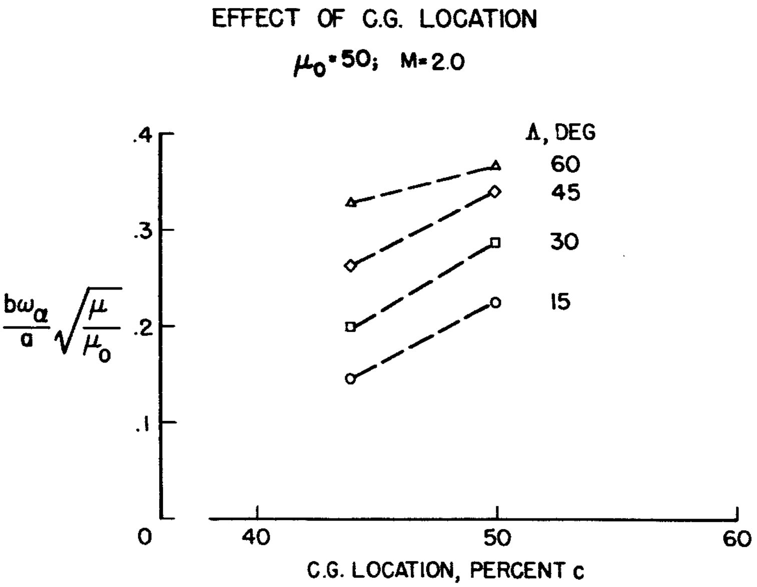

Figure 5

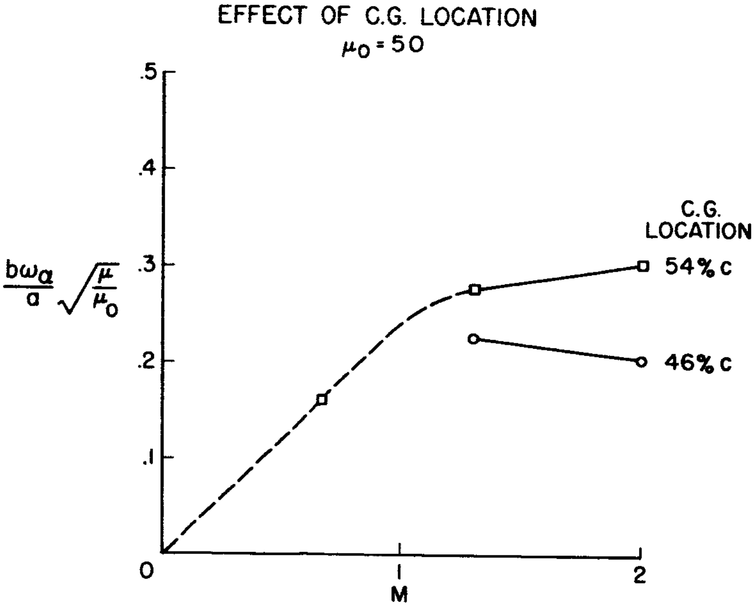

Figure 6

[redacted]

24V

[redacted]

AN INVESTIGATION OF THE EFFECTS OF SYSTEM NONLINEARITIES IN THE PROBLEM OF AIRCRAFT FLUTTER

By Donald S. Woolston, Harry L. Runyan,
and Thomas A. Byrdsong

Langley Aeronautical Laboratory

SUMMARY

This paper presents the results of a preliminary investigation of the effect of nonlinear structural terms on the flutter of a two-degree-of-freedom system. The three types of nonlinearities investigated were a flat spot, hysteresis, and a cubic spring. Calculations were made on an analog computer. For one case, the flat spot, an experimental investigation was also made and good correlation with theory was found.

In general it was found that the linear flutter speed did not change for small disturbance angles; however, for larger disturbance or input angles, the flutter speed usually decreased. One exception was the cubic hard spring, for which a limited-amplitude flutter was found to exist well above the linear flutter speed.

INTRODUCTION

Until fairly recently the problem of aircraft flutter has been treated analytically as a purely linear phenomenon. Potentially, however, many sources of nonlinearities exist and their possible effects are receiving more and more attention. It is thought, for example, that many of the limited-amplitude oscillations are associated with nonlinearities.

In the flutter problem three types of forces are involved. These are the inertia, the damping, and the elastic forces, and they may arise from either the aerodynamics of the problem or from the structure. Nonlinearities associated with the aerodynamics might arise, for example, from the effects of thickness or flow separation or from the variation in hinge moments with amplitude. Some aerodynamic effects of thickness have been studied analytically by Van Dyke (ref. 1). He has treated the case of two-dimensional, supersonic flow and has found, except near a Mach number of 1, that thickness effects for this case are moderate.

[redacted]

The structural side of the problem may also give rise to nonlinearities in the inertial, damping, and elastic forces. The present investigation is concerned with nonlinearities in the elastic forces, and three types of nonlinear springs have been considered. Their effects on flutter have been examined in the investigation of a two-dimensional, two-degree-of-freedom system.

SYMBOLS

f_h	natural frequency in translation, cps
f_α	natural frequency in pitch for basic linear system, cps
I_α	mass moment of inertia about elastic axis per unit length of span, slug-ft^2/ft
K_θ	spring constant of linear system, ft-lb/radian
M	moment, ft-lb
m	mass per unit length, slugs/ft
S_α	mass static unbalance per unit length, referred to elastic axis, slug-ft/ft
V/V_{LIN}	ratio of flutter speed to flutter speed of linear system
x_{cg}	coordinate of center of gravity measured from leading edge, percent chord
x_{ea}	coordinate of elastic axis measured from leading edge, percent chord
δ_T	angular free play, deg
θ	angle of rotation, deg unless indicated otherwise
ρ	fluid density, slugs/cu ft

TYPES OF NONLINEAR SPRINGS INVESTIGATED

Nonlinearities in the elastic forces can arise in many possible ways. An indication of some of these is given in figure 1. Three types of nonlinear springs have been considered, and their characteristics are shown as plots of the force or moment required to produce a given displacement.

Shown at the left of the figure is a flat spot. This may be considered to represent the condition of free play in the hinge or linkage of a control system.

At the right of the figure is one type of hysteresis. As force or moment is increased, displacement varies in a linear manner until a point is reached at which a jump occurs, after which the system is again linear. On the return path, a corresponding jump occurs at a negative value of the force. A nonlinearity of this type might occur in the case of a control surface with free play if friction exists at some point in the linkage, or it might occur through the action of power servos. In the case of a wing, this type of nonlinearity might represent the effect of rivet slip.

The third type of nonlinearity treated has been termed a cubic spring, where the force exerted depends on the usual linear power of the displacement and, in addition, on a term containing the cube of the displacement. This can be considered either as a hard spring, which becomes stiffer as displacement increases, as shown by the solid line, or as a soft spring, which becomes weaker as displacement increases, as shown by the dashed line. In the case of a control surface, a hard-spring effect might be associated with power controls. In the case of a structure, a hardening effect is found when a thin wing, or perhaps a propeller, is subjected to increasing amplitudes of torsion. A soft-spring effect may be associated with panel buckling.

EFFECTS OF NONLINEAR SPRINGS ON AIRCRAFT FLUTTER

These three types of nonlinearities have been considered in the flutter investigation of a two-dimensional, two-degree-of-freedom system, free to oscillate in translation and in pitch. The flutter characteristics of the system have been determined with an electronic analog computer, using incompressible, indicial air forces. The analog representation of the fundamental linear flutter equations was based on the work of Baird, Pines, and Winson (ref. 2). For the flat spot, in addition to the analog results, experimental results have been obtained in the Langley 2- by 4-foot flutter research tunnel. The physical characteristics of the systems treated for each of the three types of nonlinear springs are given in table I.

In the flutter results to be discussed, one of the variables to be employed is an input angle θ. The significance of this input angle is given in the following discussion.

In obtaining results with the analog computer for a particular case, a given value of velocity is selected, the system is given an initial displacement (for example, θ), and its response to this displacement is examined for stability. In general, the results to follow will show that the response of the system becomes unstable only when a sufficiently large initial displacement is imposed. In the physical system, this initial displacement corresponds to the effect of a gust or to an abrupt movement of the control stick.

Flutter Results With the Cubic Spring

In figure 2, analog results are shown for the cubic spring in the torsional degree of freedom. Results are shown in the form of the input angle θ required to induce flutter as a function of velocity. For this case, the relation between moment and displacement was arbitrarily assumed to be $M = 140.5\theta + 400\theta^3$, where M is the moment in foot-pounds and θ the torsional displacement in radians. The coefficient of the linear term in θ represents the spring constant in foot-pounds per radian of the linear system.

First, the flutter speed of the linear system was investigated and was found to be around 270 feet per second. Then, both hard and soft cubic springs were considered. Flutter boundaries are shown by the solid curve for the soft spring and by the dashed line for the hard spring. In both cases, the flutter region lies to the right of the boundary.

For the hard spring, the flutter boundary is a straight line at the flutter speed of the linear system. The soft spring in this case had a destabilizing effect in that flutter could be induced below the linear flutter speed by making the initial displacement sufficiently large. For the system treated herein, however, the deviation from the linear flutter speed occurs only at fairly high initial displacements.

It is also of interest to consider the flutter amplitudes associated with these results. For both the linear system and the soft spring, the flutter oscillation was highly divergent at any velocity above the flutter boundary. With the hard spring in the system, however, the flutter amplitude is self-limited. This limit amplitude is a function of velocity, however, and increases as velocity is increased beyond the flutter boundary.

[redacted]

In studying other configurations, cases have been found in which a hard spring can be destabilizing, and it appears that the effects produced by a cubic spring depend on the stiffnesses of the original linear system. Generally, flutter speed decreases as the bending-torsion frequency ratio approaches unity. If a cubic spring, whether hard or soft, tends to make this ratio approach unity, it will probably be destabilizing.

Flutter Results With the Flat Spot

The second type of nonlinearity to be considered is the flat spot and, as mentioned previously, both wind-tunnel and analog studies were made. The main features of the model used in the wind-tunnel tests are shown in figure 3. The sketch represents a two-dimensional model which completely spans the test section and which is free to oscillate in pitch and translation. The pitching degree of freedom is provided by a bearing-supported shaft located slightly behind the quarter chord. This system in turn is suspended between a pair of leaf springs on either side of the test section so that the entire mechanism is free to translate.

In translation the system is linear. The nonlinearity was introduced in the torsional degree of freedom in the manner shown in the detail sketch. A leaf spring is clamped to the end of the torsion axis and its free end extends upward between two set screws. The gap between the screws can be closed completely to give a linear torsion spring or opened to provide any desired amount of angular free play, giving the spring characteristic shown to the right in figure 3.

In figure 4, results obtained in the wind tunnel with this configuration are compared with analog results. The ordinate of the figure is again the input angle θ in degrees. The abscissa is a flutter-speed ratio V/V_{LIN}, where V_{LIN} is the flutter speed of the linear system, and it is immediately seen that the flutter speeds have been decreased. In the investigation the angular free play δ_T was kept constant at 0.5°. The solid curves and the regions labeled stable, mild flutter, and flutter refer to the analog results. The circles show wind-tunnel experimental points.

In both the experiment and the analog results, a preload was incorporated into the system. This preload was comparable in effect to a deflected tab and produced a moment which varied with the velocity. At equilibrium, therefore, the model was not centered in the flat spot but rather at some point on the linear arm of the diagram. This means that, for small displacements from equilibrium, the system moved only on this linear arm so that, at velocities below the linear flutter speed, the system was stable.

With displacements slightly greater than 0.5°, the effect of the flat spot began to enter the picture and a region of mild, limited-amplitude flutter was encountered. Here the system oscillated about its equilibrium position across only one knee of the flat spot and did not traverse the full flat-spot width.

As an example, at a value of the flutter-speed ratio of 0.6, the flutter amplitude in this region of mild flutter was about 1°. Such limited oscillations, when translated into the behavior of control surfaces in flight, might not be dangerous in themselves but could be significant from a fatigue standpoint.

As initial inputs were increased still further, a much more violent flutter was encountered in which the model oscillated completely through the flat spot with large amplitude. The experimental wind-tunnel points apply to this violent type of flutter and agreement with the analog results is fairly good. Although not shown in the figure, it should be noted that in the experimental tests, also, a region of mild flutter was encountered at initial displacements comparable to those indicated by the analog.

In obtaining these results, only a single value of the preload has been taken into account, and further studies in which the preload is varied would be desirable. The destabilizing effect of the flat spot in this case is probably associated with an effective reduction in torsional stiffness. In the absence of any preload, the torsional stiffness at equilibrium would be reduced to zero, and presumably then one would at least expect to encounter unstable oscillations in the region of the flat spot.

This system corresponds to the case of the all-movable control investigated experimentally by Hoffman and Spielberg (ref. 3). These investigators found that an increase in angular free play can greatly reduce the flutter speed of the system.

Flutter Results With Hysteresis

If, in addition to the free play, some source of static friction exists, the hysteresis phenomenon occurs. As mentioned previously, a hysteresis of the type described may arise in the case of friction in the hinge or linkage of a control surface or, in the case of a wing, might be associated with rivet slip.

Before considering the flutter results with hysteresis, some purely structural characteristics of the system with hysteresis should be examined. Shown in figure 5 is the response of a system with hysteresis at zero airspeed. The upper and lower traces represent, respectively, the displacement of the system and the variation in moment after release from the initial displacement from equilibrium. The indentations on the lower trace occur when the system passes through the flat spots of the hysteresis box.

The presence of this hysteresis in the system has two primary effects on the structural characteristics. One is the introduction of variable structural damping, shown by the lines drawn tangent to the upper trace. At high amplitudes, the rate of decay is relatively small. As the amplitude of the oscillation approaches the height of the hysteresis box, the damping is considerably greater. When the oscillation is contained within the box, the structural damping in this illustration is zero.

The second effect of the hysteresis on the structural properties of the system is not apparent in this figure but is the introduction of an effectively weaker spring. At high amplitudes the frequency of the oscillation is less than the frequency at low amplitudes where the system is linear.

Analog results for bending-torsion flutter with hysteresis in the torsional degree of freedom are shown in figure 6. Results are again presented in the form of the input angle θ plotted against flutter velocity. Two values of δ_T, the amount of free play in torsion or the width of the hysteresis box, were considered. These were δ_T of 0.2°, shown by the solid line, and $\delta_T = 0.4^\circ$, shown by the dashed line. The height of the hysteresis box was held constant. In these results, the flutter region lies above or to the right of the lines.

Consider first the results for δ_T of 0.2°, shown by the solid curve. For very small inputs, the system oscillates on a line through the center of the box with a linear spring constant, as shown by the dashed line in the spring diagram. For this reason, the flutter boundary at the highest velocity occurs at the flutter speed of the linear system.

This boundary continues straight upward until an initial displacement of 0.6° is imposed. Actually an initial displacement greater than 0.2° represents a displacement beyond the linear path within the hysteresis box. At low amplitudes, since the presence of the hysteresis introduces a large amount of structural damping, for inputs up to 0.6° the oscillation decays and the system oscillates at constant amplitude within the hysteresis box. For larger displacements at the linear flutter speed and at velocities above the linear flutter speed, the oscillation diverged rapidly.

As in the case of the flat-spot results, flutter could be induced at velocities below the linear flutter speed by making the initial displacements sufficiently large. At the larger displacements, the hysteresis damping is smaller and the presence of the free play in the system is producing an effectively weaker spring. Finally a velocity is reached below which the air forces will not sustain an oscillation regardless of the magnitude of the initial displacement. For all velocities below the linear flutter speed, the flutter is of limited amplitude.

Results for the wider hysteresis box exhibit the same trends. At velocities below the linear flutter speed, however, greater initial displacements are required to initiate flutter, since the wider hysteresis box introduces more damping. At the same time, the increased amount of free play reduces the effective spring constant even more, and the region of limited-amplitude flutter extends to a lower velocity.

CONCLUDING REMARKS

Little is known of the exact nature and magnitude of the nonlinearities which exist in actual aircraft. The purpose herein has been to take an initial look at the effects of some nonlinearities which might occur. The results shown are, of course, a function of the particular configurations treated and are perhaps most closely related to the problem of control-surface flutter. They indicate, however, that in some cases nonlinear effects can be large and can be destabilizing. The results indicate further that the stability of a nonlinear system can become a function of the magnitude of an external excitation; it is also indicated that, when a nonlinear system becomes unstable, its flutter may become less violent and self-limited.

REFERENCES

1. Van Dyke, Milton D.: Supersonic Flow Past Oscillating Airfoils Including Nonlinear Thickness Effects. NACA TN 2982, 1953.

2. Baird, Eugene F., Pines, Samuel, and Winson, Jonathan: The Solution of Two Problems of Four Degree of Freedom Flutter by Electronic Analogue Computation. Project Cyclone (Contract N6 ORI-128, Task Three - NR-725-001), Reeves Instrument Corp. (New York City), Feb. 1952.

3. Hoffman, Niles R., and Spielberg, Irvin N.: Subsonic Flutter Tests of an Unswept All-Movable Horizontal Tail. WADC Tech. Rep. 54-53, Wright Air Dev. Center, U. S. Air Force, Mar. 1954.

[redacted]

25V

[redacted]

TABLE I.- CHARACTERISTICS OF SYSTEMS

Parameter	Systems		
	Cubic	Flat spot	Hysteresis
Semichord, ft	0.5	0.5	0.5
x_{ea}, percent chord	23.0	29.7	23.0
x_{cg}, percent chord	25.6	31.8	25.6
m, slugs/ft	0.1489	0.2985	0.1489
S_α, slug-ft/ft	0.003871	0.0744	0.003871
I_α, slug-ft^2/ft	0.008934	0.01196	0.008934
f_h, cps	15	9.38	10.6
f_α, cps	20	12.93	20
ρ, slugs/cu ft	0.002378	0.00243	0.002378

[redacted]

[redacted]

TYPES OF NONLINEAR SPRINGS INVESTIGATED

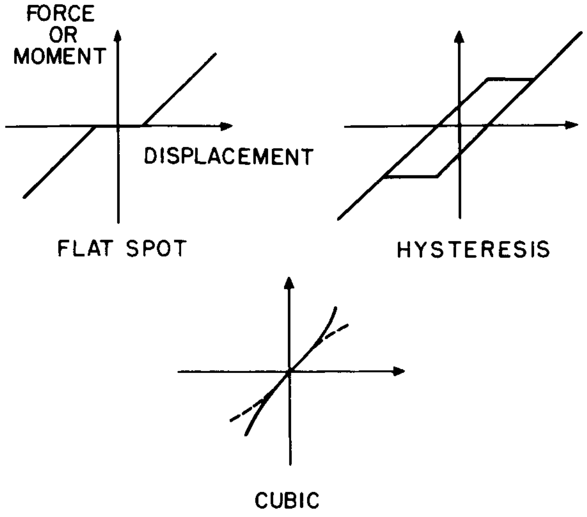

Figure 1

FLUTTER WITH CUBIC SPRING IN TORSION

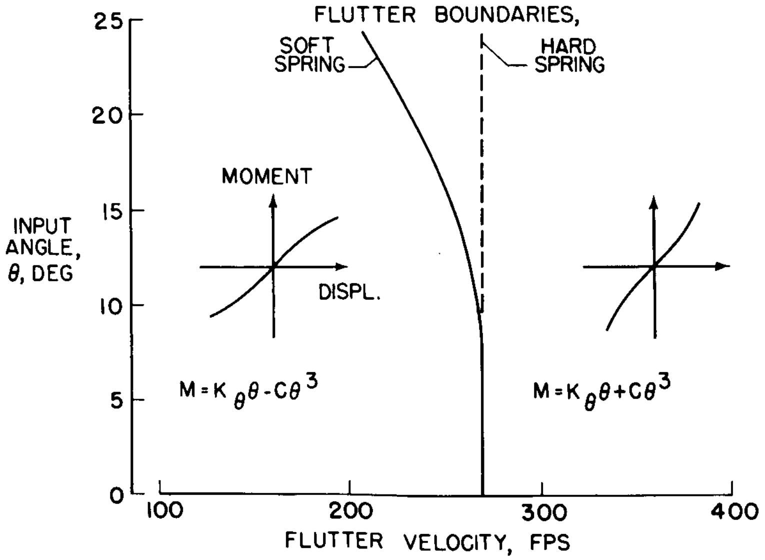

Figure 2

[redacted]

[redacted]

NONLINEAR FLUTTER MODEL

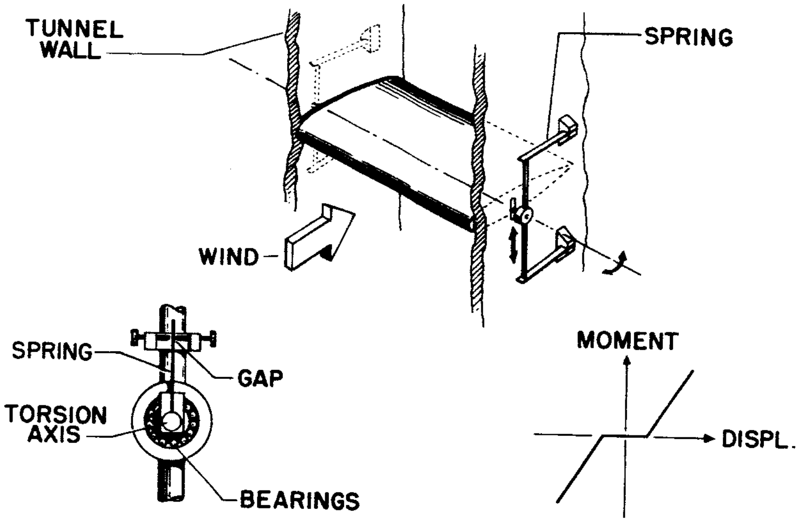

Figure 3

FLUTTER WITH FLAT SPOT IN TORSION

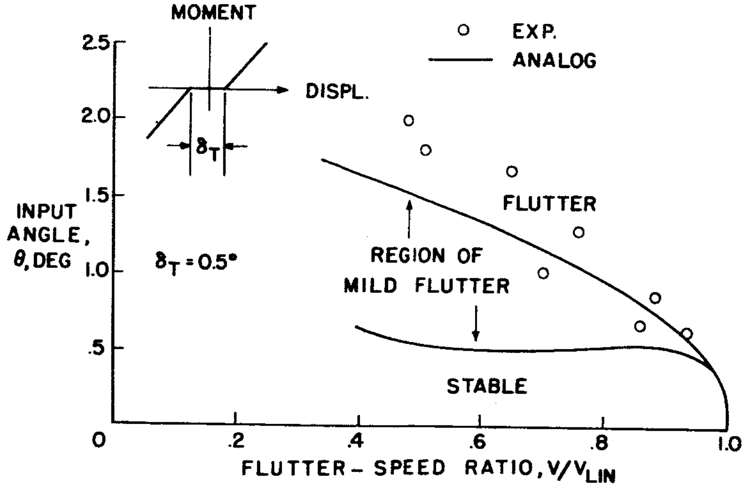

Figure 4

[redacted]

DAMPING ASSOCIATED WITH HYSTERESIS

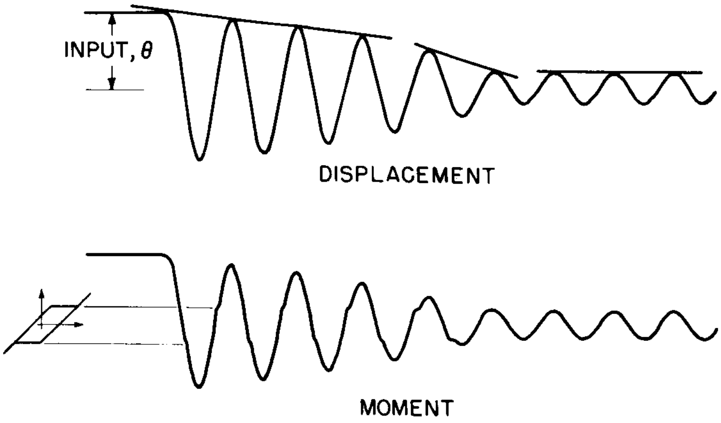

Figure 5

FLUTTER WITH HYSTERESIS IN TORSION

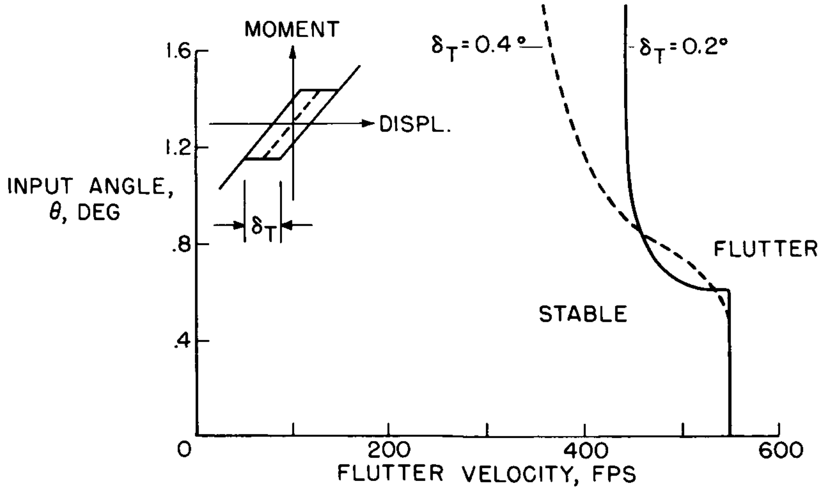

Figure 6

[redacted]

[redacted]

SOME EFFECTS OF FLUID IN PYLON-MOUNTED TANKS ON FLUTTER

By James R. Reese

Langley Aeronautical Laboratory

SUMMARY

Fluid-dynamics studies were made of a tank of fineness ratio 7.0 which was pylon mounted on a simplified two-dimensional flutter model in order to determine the effects of the fluid on flutter. The flutter speed was found experimentally for three cases as follows: with various amounts of water in the tank, with weights having the same mass and moment of inertia as the fluid considered to be a frozen solid, and with weights having the same mass and moment of inertia as the actual fluid. The results of the two methods of fuel representation were compared with the actual-fluid case, and it was concluded that, in flutter analyses and tests, the fuel in wing tanks must be represented by the effective-moment-of-inertia values. The damping action of the fluid was also studied, and it was found that sufficient damping was present to limit the amplitude of the flutter and that, at a frequency ratio near 1.0, the fluid damping may produce an increase in the flutter speed.

INTRODUCTION

The representation of the dynamic effects of large fuel masses carried in airplane wing tanks is of concern to the dynamicist. He may be aware that the fuel does not behave as a frozen solid, and, therefore, in order to represent it properly, he must know the effective pitching moment of inertia of the fuel. By effective moment of inertia of the fuel is meant the actual or true moment of inertia of the fuel, which is usually less than if the fuel were a frozen solid since a portion of the fluid does not partake of the pitching motion. Consider the cases of the tip- and pylon-mounted tanks which are represented in figure 1. The abscissa is the tank fullness, and the ordinate is the ratio of the effective moment of inertia of the fluid to the moment of inertia of the fluid considered to be a frozen solid. The data were obtained for a tank of fineness ratio 7.0. As the dashed curve in figure 1 shows, an important result of a previous investigation on centrally mounted tanks (ref. 1) is that the inertia ratio varies but little for a wide variation in tank fullness. This work on centrally mounted tanks has been extended recently to cover the case of pylon-mounted or offset tanks and to inclined and swept-wing tanks in reference 2. This reference gives effective-moment-of-inertia values and damping factors, and the lower curves are representative of

[redacted]

some of the moment-of-inertia values for the offset-tank case. Notice the large decrease in the inertia ratio of the partially full offset-tank configurations as compared with the centrally-mounted-tank case.

This large decrease in the inertia ratio may be explained as follows. When the tank is completely full, the fluid is forced to move with the boundaries of the tank and the inertia ratio is almost unity. As fluid is removed from the tank, the fluid then becomes free to move in a forward and rearward direction, and it is this horizontal translational freedom of the fluid which causes a reduction of the inertia ratio. When two solid baffles are added to the tank, the freedom of the fluid is somewhat restricted, and there is a slight increase in the inertia ratio of the partially full tank as shown by the curve passing through the triangles.

In reference 2, it was found that large decreases in the inertia ratio could result if the frequency of oscillation was close to the first natural frequency of the fluid in the tank. This condition was avoided in these tests by selecting springs which would avoid frequencies of this kind so that the inertia ratio remained essentially independent of frequency.

MODEL AND APPARATUS

In order to study some possible effects of fuel representation on flutter, use was made of the simplified two-dimensional flutter model shown schematically in figure 2. The arrows indicate the rotational and translational degrees of freedom. The model was equipped with a tank of fineness ratio 7.0, and this tank was offset beneath the axis of rotation, a distance of about $2\frac{1}{2}$ times the tank radius. Some physical parameters of the model are given in table I. The flutter speeds were found experimentally in the Langley 2- by 4-foot flutter research tunnel with air at atmospheric pressure for three different cases. First, the flutter speed was found with various amounts of water in the tank. Then the flutter speed was found by using weights having the same mass and moment of inertia as the fluid considered to be a frozen solid. The third series of tests were made with weights having the same mass and moment of inertia as the fluid, thus simulating the effective moment of inertia of the fluid.

RESULTS AND DISCUSSION

Some results of these tests are shown in figure 3, where the flutter speed is shown as a function of tank fullness for the three cases mentioned: the actual fluid, the frozen or solid fluid, and the simulated fluid. The values for the uncoupled bending-to-torsion frequency ratio ω_h/ω_α are

[redacted]

shown opposite each data point since these values are of significance in the discussion of the results. The actual flutter speeds obtained with fluid in the tank are shown by the solid curve passing through the circles. When the fluid was replaced with weights representing the frozen or solid moments of inertia, the flutter speeds are shown by the long- and short-dashed curve passing through the triangles. As can be seen they are considerably different from the speeds with the actual fluid and give both conservative and unconservative results; that is, for a given tank fullness, they may lie below or above the actual case. However, when the fluid was simulated by effective-inertia weights, good agreement with the actual case was obtained and is shown by the dashed curve passing through the diamonds. From these results it appears that the effective-inertia values are to be preferred. This is especially true in cases where the flutter speed is strongly affected by the moment of inertia or in cases where there is a large difference between the solid and effective moments of inertia of the fluid.

So far, the effects of inertia on flutter have been discussed. A few remarks about the effect of damping are now in order. Notice that the chief difference between the flutter speed obtained with actual fluid and the speed obtained with the effective-inertia weights occurred in this experiment at a frequency ratio near 1.0. This suggests that the damping of the fluid in the tank may produce an increase in the flutter speed near a frequency ratio of 1.0. As was shown in reference 1, fluid damping is generally quite low, g_α less than 0.01, for the first few cycles of oscillation. After the fluid breaks up into turbulent motion, the damping can become quite high, g_α reaching values of the order of 0.10 to 0.20, depending on the amount of fluid and the amplitude and frequency of oscillation. Thus it can be expected that the start of flutter will not be affected much by the fluid damping, except where the flutter speed is critically dependent on the damping, as is usually the case near a frequency ratio of 1.0.

If the amplitude of flutter builds up slowly enough, the fluid will break into turbulent motion, with resulting increases in damping which may limit the amplitude of the flutter. This occurred in this series of tests for all partially full configurations, and the results are shown in figure 4. Here the torsional flutter amplitude is shown as a function of the speed. The tank was equipped with two baffles, and each baffle had 13 evenly distributed 1/2-inch holes. For each amplitude, the value for the torsional damping factor g_α calculated from frequency-response curves obtained at zero airspeed is shown opposite each data point. The frequency-response curves were obtained by forcing the model at eight different amplitudes for each tank fullness studied. The figure shows that as the airspeed was increased the amplitude of the oscillations was increased and was limited by the effect of additional fluid damping since the damping of fluid in the tank increased with increased amplitude of oscillation.

CONCLUSIONS

These preliminary experiments indicate that, in flutter analyses and tests, the fuel in wing tanks must be represented by the effective-moment-of-inertia values. This is essential in cases where the flutter speed is strongly affected by the inertia of the fuel or where the effective moment of inertia of the fuel is considerably different from the solid inertia.

With regard to the damping action of the fluid, it was found that sufficient damping was present to limit the amplitude of the flutter, and at a frequency ratio near 1.0 the damping of the fluid in the tanks may produce an increase in the flutter speed.

REFERENCES

1. Widmayer, Edward, Jr., and Reese, James R.: Moment of Inertia and Damping of Fluid in Tanks Undergoing Pitching Oscillations. NACA RM L53E01a, 1953.
2. Reese, James R., and Sewall, John L.: Effective Moment of Inertia of Fluid in Offset, Inclined, and Swept-Wing Tanks Undergoing Pitching Oscillations. NACA TN 3353, 1955.

TABLE I

SOME PHYSICAL PARAMETERS OF THE MODEL

Wing span, ft	2
Wing chord, ft	1
Tank diameter, in.	4.25
Tank length, in.	30.0
Bending stiffness, lb/in.	168
Torsional stiffness, in-lb/radian	4,120
Bending damping coefficient, g_h, empty	0.009
Torsional damping coefficient, g_α, empty	0.018
Model weight, lb	
Empty	11.8
Full	21.7
Model moment of inertia, in-lb-sec^2	
Empty	0.103
Full	2.000
Model center-of-gravity location, percent chord	
Empty	43
Full	40
xis of rotation, percent chord	40

[redacted]

EFFECT OF TANK OFFSET ON MOMENT OF INERTIA
TANK FINENESS RATIO=7.0

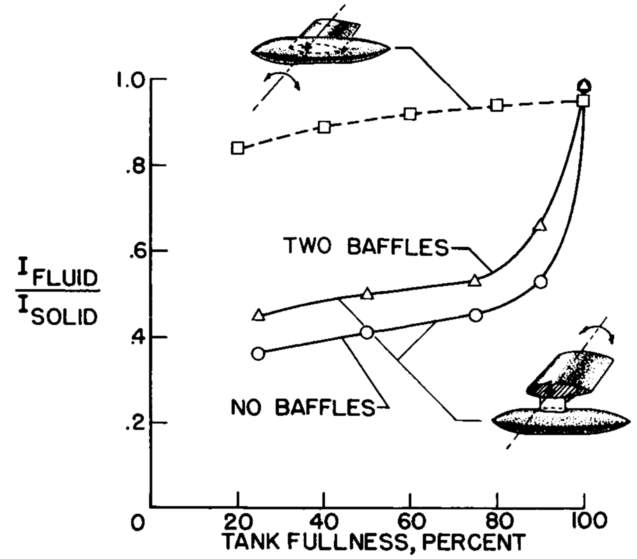

Figure 1

TWO-DIMENSIONAL FLUTTER MODEL AND APPARATUS

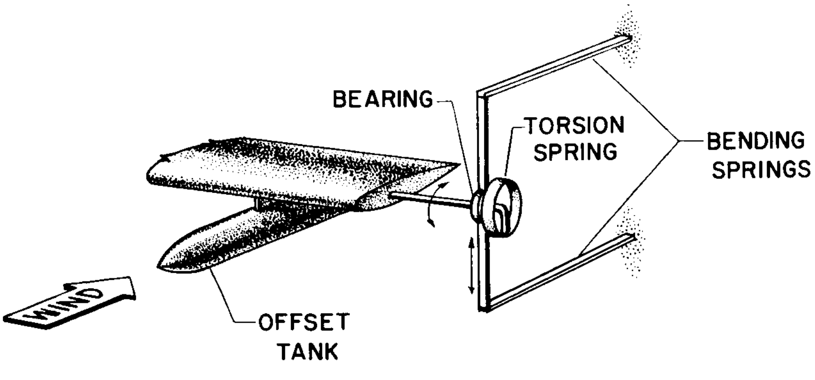

Figure 2

[redacted]

EFFECT OF FUEL REPRESENTATION ON FLUTTER

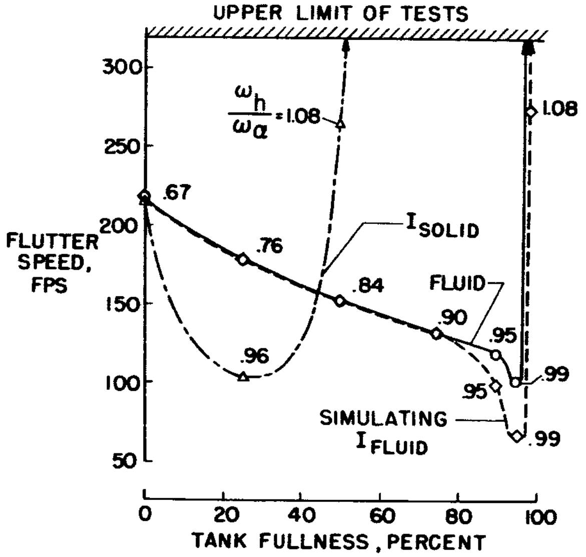

Figure 3

EFFECT OF FLUID ON FLUTTER AMPLITUDE

TANK CONTAINING BAFFLES WITH HOLES

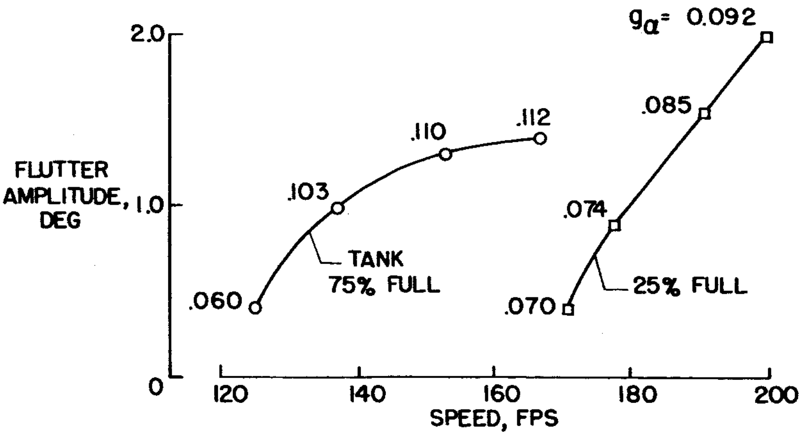

Figure 4

[redacted]

[redacted]

EXPERIMENTAL AND THEORETICAL STUDIES OF PANEL FLUTTER

By Maurice A. Sylvester, Herbert C. Nelson,
and Herbert J. Cunningham

Langley Aeronautical Laboratory

SUMMARY

Some theoretical and experimental flutter results for simplified panels clamped on front and rear edges are indicated and compared. The results of tests on buckled panels clamped on four edges show that, in general, their flutter characteristics cannot be predicted on the basis of the simplified theoretical or experimental results. An estimated flutter boundary is presented for buckled panels clamped on four edges and having various width-to-length ratios. A pressure differential is found to be effective in suppressing flutter. The results of the experimental tests indicate that panel flutter is probably of concern mainly from a fatigue standpoint.

INTRODUCTION

As more airplanes and missiles are being designed to operate at supersonic speeds, there is a continuing concern that portions of the skin coverings may be subject to flutter. Consequently, some experimental and theoretical studies have been made to evaluate some of the significant variables in the problem. The results of these studies may explain the causes of panel failures on some current high-speed airplanes and may also indicate sources of trouble on future airplane and missile designs.

The main purpose of this paper is to present the results of some recent panel-flutter experiments. In addition, a brief summary of some theoretical work on panel flutter is presented and a comparison is made between some of the theoretical and experimental results. The experiments extend previous work (ref. 1) to include greater ranges of Mach number, pressure differential across the panel, and ratios of panel width to length. Most of the tests were made with buckled rectangular panels clamped on either two or four edges and mounted as a section of the tunnel wall. The buckling forces were induced by thermal stresses or by a combination of thermal stresses and applied edge forces. The dynamic pressure was essentially constant (approximately 6.2 pounds per square inch) for most of the experimental tests.

[redacted]

SYLVESTER, NELSON,
& CUNNINGHAM

SYMBOLS

d	maximum depth of buckle
E	Young's modulus of elasticity
l	panel length in direction of flow
M	Mach number
q	dynamic pressure
t	panel thickness
V	stream velocity
w	panel width, perpendicular to flow

Subscript:

r	reference experimental conditions

RESULTS AND DISCUSSION

Panels Fastened on Front and Rear Edges

Summary of theory.- A summary of some recent theoretical work on panel flutter is shown in figure 1. Several investigators who have worked on panel flutter are listed, and the particular problems treated are indicated by the check marks. The panel configurations that were studied are the flat panel, the buckling panel, and the infinite flat panel on many supports. All the panels were considered two-dimensional both structurally and aerodynamically, and most of the work applied to supersonic speeds. Isaacs (ref. 2) treated the static stability of a buckled panel and, of course, used steady-state air forces. He advanced as plausible the concept that a buckled panel will flutter if it is not statically stable, and on this basis he obtained a design criterion $\left(\text{essentially } \left(\sqrt{M^2 - 1}\,\frac{E}{q}\right)^{1/3} \frac{t}{l} = 0.516\right)$. Hayes (ref. 3), in addition to considering the static stability, also treated qualitatively the dynamic stability of buckled panels, but used only steady-state air forces. Miles (ref. 4) studied the dynamic stability of both flat and buckled panels and used air forces that included first-order aerodynamic damping.

[redacted]

Shen (ref. 5) extended the work of Miles on flat panels by using exact unsteady air forces. Hedgepeth, Budiansky, and Leonard (ref. 6) analyzed the infinite flat panel on many supports and found that static divergence was of concern at subsonic speeds, and flutter was of concern at supersonic speeds. Fung (ref. 7) investigated the static stability of buckled panels and concluded that the height of the buckle was a significant parameter. Nelson and Cunningham (ref. 8) used exact unsteady air forces in their study of the dynamic stability of flat panels. This analysis appears to be the most general and flexible that is available for the single, flat, two-dimensional panel and included a study of the effect of such factors as Mach number, number of modes in the analysis, structural damping, and tension.

The analytical work has contributed to an understanding of the panel-flutter phenomenon, but further work is needed to extend the theories to more practical panels which are not two-dimensional and which may be either curved or buckled in a complex manner.

Comparison of theory and experiment.- Only Isaacs and Nelson and Cunningham obtained results for clamped-edge panels which correspond to those used in these experimental studies. Some experimental results are compared with these theoretical results in figure 2. This figure shows the thickness-to-length ratio required for flutter-free operation of aluminum panels as a function of Mach number. The data are for panels at an altitude of 25,000 feet since this is approximately the equivalent pressure altitude at which most of the experimental data were obtained. (Where necessary, the experimental data were adjusted to this pressure altitude with the relation $\frac{t}{l} = \left(\frac{t}{l}\right)_r \left(\frac{q}{q_r}\right)^{1/3}$. The subscript r refers to the experimental conditions.) The panels used in the experiments were 11.62 inches long and had a width-to-length ratio of 0.69. The boundary representing Isaacs' static stability or flutter criterion for buckled panels is shown, and the circular symbols are the corresponding experimental points. The boundary obtained from Nelson and Cunningham's two-dimensional flutter theory for flat panels is also indicated and the squares are the associated experimental results. The theoretical curves are shown to increase rather sharply at the lower Mach numbers. For Isaacs' results, the increase is due to the use of steady-state linearized air forces which become infinite at $M = 1$. For the curve of Nelson and Cunningham, the increase is due to a change in flutter mode and decreased aerodynamic damping. This latter curve would have a finite ordinate at $M = 1$. Figure 2 also shows that, in general, buckled panels appear to be more susceptible to flutter than flat panels.

Effect of altitude.- The results in figure 2 are for aluminum panels at an altitude of 25,000 feet. Since both experiment and theory indicate that the effect of decreasing the air density is beneficial, it is of interest to note the effect of altitude on panel flutter. Figure 3 shows the variation of the thickness-to-length ratio with altitude for buckled aluminum panels at Mach numbers of 1.2 and 3.0. The boundaries have been determined by adjusting the experimental results from figure 2 to the appropriate pressure altitude with the relation $\frac{t}{l} = \left(\frac{t}{l}\right)_r \left(\frac{q}{q_r}\right)^{1/3}$, which was indicated previously. Figure 3 shows that the thickness-to-length ratio to prevent flutter is reduced as the altitude is increased. Increasing the Mach number from 1.2 to 3.0 raises the boundary somewhat, indicating a slight adverse Mach number effect.

Effect of a pressure differential.- The results discussed so far have been for panels with zero pressure differential between the two surfaces. It was observed during the panel-flutter tests that a positive or negative pressure differential could be used to advantage in stopping or controlling the flutter. Since airplane and missile panels may be subjected to pressure differentials of various amounts, the effect of a pressure differential is of interest.

The effect of a pressure differential on the flutter of buckled panels clamped at the front and rear edges is indicated in figure 4. These results were obtained experimentally with aluminum-alloy, steel, magnesium, and brass panels having a length of 11.62 inches and a width-to-length ratio of 0.69. The ordinate is the nondimensional grouping of aerodynamic and stiffness parameters which was first suggested by Isaacs and which has been found useful in presenting the results of tests on this panel configuration for the range of Mach number tested ($M = 1.2$ to 3.0). The Mach number factor is based on steady-state linearized air forces and is, therefore, not valid near a Mach number of 1.0. The experimental data points indicate the pressure differential, measured in pounds per square inch, required to stop flutter at Mach numbers of 1.2, 1.3, 1.6, and 3.0. A conservative boundary is faired to contain the data points and represents the division between the flutter and no-flutter regions. Figure 4 shows that a pressure differential of the order of a few tenths of a pound per square inch was effective in eliminating flutter on all panels tested, and that the amount of pressure differential required to suppress flutter decreases as the value of the "flutter parameter" is increased. No flutter was obtained on these panels at a value of this parameter greater than approximately 0.46. Variations in the amount or depth of buckling did not appear to affect the results for the range of this variable studied (values of d/l from 0.003 to 0.009).

Panels Clamped on Four Edges

Comparison of experimental results.- Experimental studies on simplified panels clamped on the front and rear edges are useful in investigating flutter trends and in providing experimental verification of existing theories. However, results of tests on panels clamped on four edges are needed to determine the extent to which the results of studies on simplified panels may be applied to the more practical panel configurations.

The results of tests on two buckled panel configurations clamped on four edges are shown in figure 5, and the results are compared with the flutter boundary (reproduced from fig. 4) for panels of the same length (11.62 inches) clamped on the front and rear edges. The one- and two-half-wave types of buckling were easily obtained on the panels clamped on four edges which had width-to-length ratios of 0.83. The flutter parameter is again plotted against the pressure differential, and the boundary and data points indicate the pressure differential required to stop flutter on the panel configurations identified in figure 5. For instance, flutter was encountered on a given panel at values of the pressure differential less than that indicated by the data point and no flutter occurred for higher values of the pressure differential. Boundaries are not drawn for panels clamped on four edges because of the scatter in the limited data available. The data show, however, that panels with the two-half-wave type of buckling require a greater pressure differential to stop flutter than do panels buckled in one half-wave, and that panels clamped on four edges may be either less or more susceptible to flutter than panels clamped on the front and rear edges. In no case was the pressure differential required to stop flutter greater than approximately 0.87 pound per square inch. Increasing the amount of buckling or destroying the symmetry of the two-half-wave type of buckling appeared to have a stabilizing effect on the stiffer panels clamped on four edges.

The values of pressure differential, referred to in the discussion of figures 4 and 5, represent the approximate difference between the static pressure behind the panel and the effective static pressure acting on the surface exposed to the stream flow. Because of the scatter in the data, the general magnitude of this pressure differential and the trends shown should be emphasized rather than the exact values of the pressure differential.

Effect of panel width-to-length ratio.- Panel width-to-length ratios vary over a wide range, and it appears that the width rather than the length may be of more significance for long narrow panels. This observation is supported by the information in figure 6 which indicates the effect of panel width-to-length ratio and summarizes the present flutter experience on buckled panels clamped on four edges. Most of the data were obtained at a Mach number of 1.3 for panels which had no curvature prior to buckling. However, some data are presented for buckled panels with a slight initial curvature (radius of curvature approximately equal to 48 inches). The panels with width-to-length ratios of 0.20, 0.50, and 0.83 were 11.62 inches long and those with a width-to-length ratio of 2.0 were 5.81 inches long. The panels were buckled by thermal and applied edge forces, and, in general, the types of buckling modes formed were rather complex and strongly dependent on the panel width-to-length ratio as well as the ratio of applied edge forces in one direction to those in the perpendicular direction. The buckled modes usually consisted of a series of approximate half-waves running in the direction of the longer panel dimension and having a half-wave length roughly equal to the shorter panel dimension.

The ordinate of figure 6 is the previously presented panel-flutter parameter, and the abscissa is identical except that the length has been replaced by the width. The straight lines radiating from the origin are lines of constant width-to-length ratios. Moving away from the origin on these lines represents an increase in the panel thickness (or stiffness) since the dynamic pressure was essentially constant for these tests. The solid symbols represent flutter, the open symbols indicate no flutter, and the short dashes represent an estimated flutter boundary based on the experience with these panel configurations. Although additional data are needed to establish more definitely the flutter boundary, it is apparent that the panel width is significant when the panel width-to-length ratio is reduced sufficiently. For example, for panels with width-to-length ratios greater than approximately 0.8, decreasing the length is effective in eliminating flutter. However, for panels with width-to-length ratios less than approximately 0.5, decreasing the width appears to be a more effective method of reducing the possibility of flutter.

Panel flutter can occur throughout the unstable region as indicated by the data points. However, its occurrence may be of a somewhat statistical nature since such factors as variations in the type and amount of buckling and a small pressure differential may reduce or eliminate the unstable region. For instance, the flutter of relatively stiff panels with $w/l = 0.83$ occurred only when the panels were buckled predominantly in two half-waves. Observations of the flutter tests showed that when flutter does occur it is not necessarily immediately destructive but is probably of concern mainly from a fatigue standpoint. The flutter frequencies were predominantly in the 50 to 200 cps range.

As a matter of interest, some of the apparently more critical panels on the Bell X-1A research airplane would lie near the flutter boundary for flight at low supersonic Mach numbers at an altitude of 40,000 feet. A number of current high-speed airplanes have some panels which would plot well within the unstable region, and a few panel failures which have occurred may have been due to flutter.

[redacted]

CONCLUDING REMARKS

Some theoretical and experimental flutter results for simplified panels clamped on the front and rear edges have been indicated and compared. For these panel configurations, the thickness required for flutter-free operation is increased somewhat as the Mach number is increased from 1.2 to 3.0 (at constant density). Increasing the altitude is beneficial in that the panel thickness to prevent flutter is decreased.

The results of tests on buckled panels clamped on four edges have also been discussed, and it was shown that they may be either less or more susceptible to flutter than similar panels clamped only on the front and rear edges. A flutter boundary has been estimated for buckled panels clamped on four edges and having various width-to-length ratios. This boundary indicates that the panel width is probably of more significance than the length for panel width-to-length ratios less than approximately 0.5.

A pressure differential was found to be effective in eliminating flutter and for the panels tested did not exceed approximately 0.87 pound per square inch.

It was indicated that panel flutter is probably of concern mainly from a fatigue standpoint.

REFERENCES

1. Sylvester, Maurice A., and Baker, John E.: Some Experimental Studies of Panel Flutter at Mach Number 1.3. NACA RM L52I16, 1952.

2. Isaacs, R. P.: Transtability Flutter of Supersonic Aircraft Panels. U. S. Air Force Project RAND P-101, The Rand Corp., July 1, 1949.

3. Hayes, W. D.: A Buckled Plate in a Supersonic Stream. Rep. No. AL-1029, North American Aviation, Inc., May 10, 1950.

4. Miles, John W.: Dynamic Chordwise Stability at Supersonic Speeds. Rep. No. AL-1140, North American Aviation, Inc., Oct. 18, 1950.

5. Shen, S. F.: Flutter of a Two-Dimensional Simply-Supported Uniform Panel in a Supersonic Stream. Contract No. N5ori-07833, Office of Naval Res., Dept. Aero. Eng., M.I.T., Aug. 6, 1952.

6. Hedgepeth, John M., Budiansky, Bernard, and Leonard, Robert W.: Analysis of Flutter in Compressible Flow of a Panel on Many Supports. Jour. Aero. Sci., vol. 21, no. 7, July 1954, pp. 475-486.

7. Fung, Y. C.: The Static Stability of a Two-Dimensional Curved Panel in a Supersonic Flow, With an Application to Panel Flutter. Jour. Aero. Sci., vol. 21, no. 8, Aug. 1954, pp. 556-565.

8. Nelson, Herbert C., and Cunningham, Herbert J.: Theoretical Investigation of Flutter of Two-Dimensional Flat Panels With One Surface Exposed to Supersonic Potential Flow. (Prospective NACA paper.)

[redacted]

[redacted]

SUMMARY OF THEORETICAL WORK ON PANEL FLUTTER

PANEL CONFIGURATION	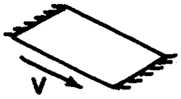 V		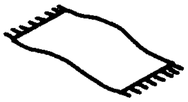		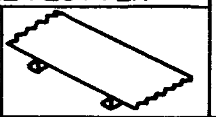	
TYPE OF ANAL. / ANALYST	STATIC	DYN.	STATIC	DYN.	STATIC	DYN.
ISAACS			✓			
HAYES			✓	✓		
MILES		✓		✓		
SHEN		✓				
HEDGEPETH, BUDIANSKY, AND LEONARD						✓
FUNG			✓			
NELSON AND CUNNINGHAM		✓				

Figure 1

THICKNESS-TO-LENGTH RATIO REQUIRED TO PREVENT FLUTTER
ALUMINUM-ALLOY PANELS AT 25,000-FT ALTITUDE

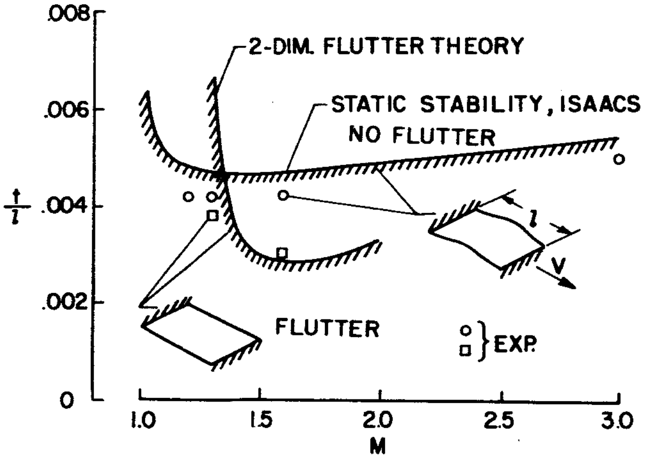

Figure 2

[redacted]

DECLA[redacted]D

EFFECT OF ALTITUDE, ALUMINUM PANELS

EXPERIMENTAL RESULTS ADJUSTED BY $\frac{t}{l} = \left(\frac{t}{l}\right)_r \left(\frac{q}{q_r}\right)^{\frac{1}{3}}$

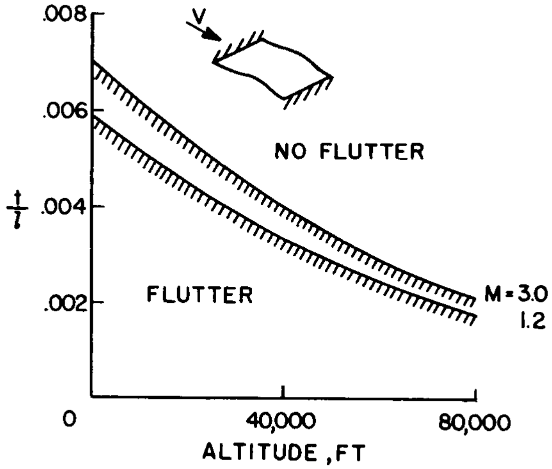

Figure 3

EFFECT OF A PRESSURE DIFFERENTIAL

$\frac{w}{l} = 0.69$

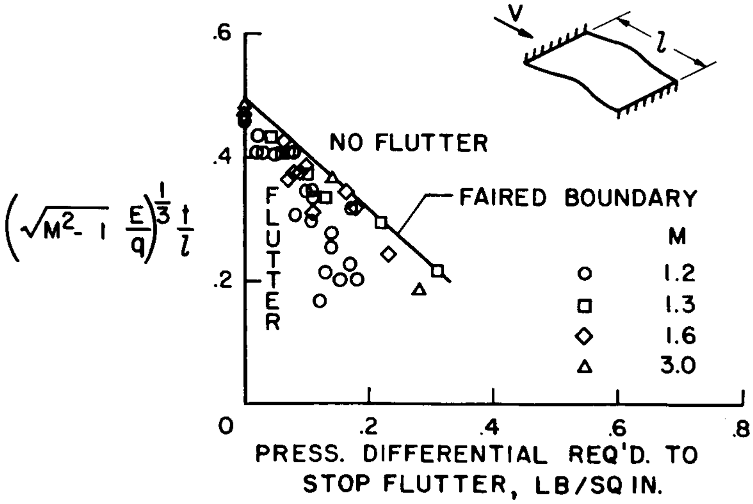

Figure 4

[redacted]

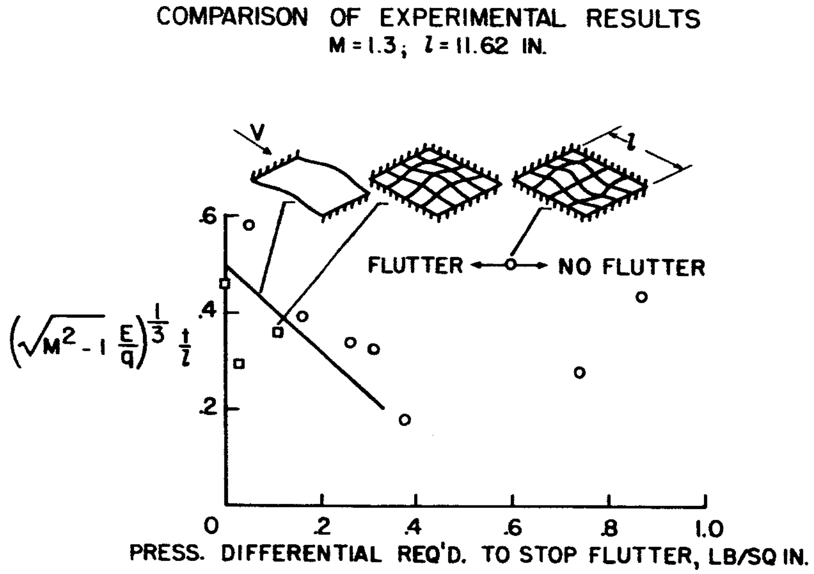

Figure 5

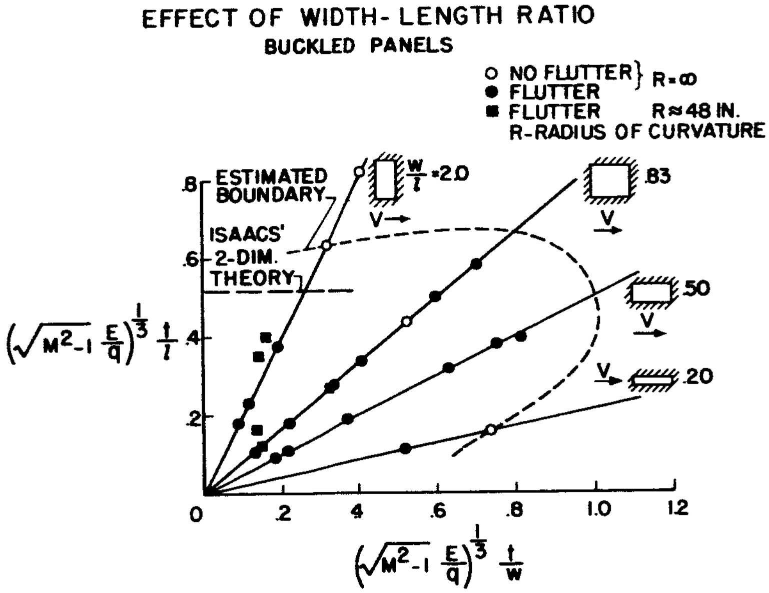

Figure 6

[redacted]

28V

STRUCTURES

[redacted]

INTRODUCTORY REMARKS ON THE STRUCTURAL EFFECTS OF AERODYNAMIC HEATING

By John E. Duberg

Langley Aeronautical Laboratory

INTRODUCTION

Aircraft that will fly at supersonic speeds will operate in an environment of aerodynamic heating that will have a profound effect on the design of the aircraft. In table I is shown a diagram of the paths by which aerodynamic heating can influence the design of the airframe. The most obvious and the most serious effect of high temperature is its depreciation of the materials of the airframe. Such effects are associated for the most part with the level of temperature. These changes in material properties carry over into the structure and determine its basic strength and stiffness. There is a direct effect of heating on the structure and this effect is associated more with the rate of heating than it is with the level of temperature. In an effort to alleviate the effect of heating on the airframe, devices and configurations will be considered which will have an effect on the final design of the airframe.

Before the effects on temperatures are discussed, the order of magnitude of aerodynamic heating should be considered. In figure 1 (solid line), the familiar plot of adiabatic wall temperature for the insulated plate plotted against Mach number is shown. At low temperatures at which radiation effects are not significant, this is almost the temperature that could be attained on the surface of aircraft. At higher temperatures, when radiation is significant, the equilibrium temperature is reached when the heat input from the boundary layer balances the heat output by radiation from the surface of the aircraft. For such a condition, the equilibrium temperatures depend first on the altitude, because the heat input for a given temperature potential varies directly as a power of the air density, and secondly, on the emissivity of the surface which determines how much heat can be radiated away. The dashed curves which have been calculated for the several altitudes have been obtained for black-body radiation, the highest possible, and indicate a considerable reduction in equilibrium temperature, particularly at high altitudes.

Whether the equilibrium skin temperatures shown in figure 1 are actually reached in a given flight depends on the heat capacity of the skin, the time history of the velocity, and the altitude of the aircraft. The heat capacity is proportional to the specific heat of the material and the thickness of the skin. The velocity and altitude establish the

[redacted]

[redacted]

adiabatic wall temperature and the heat-transfer coefficient. A rough idea of the times of flight required to reach equilibrium can be obtained from figure 2. Here are shown the time histories of the temperatures of a portion of aircraft skin made of 0.1-inch steel sheet when instantaneously accelerated to a Mach number of 4 at the three altitudes shown. The solid lines neglect radiation and the dashed lines are based on maximum radiation cooling. At an altitude of 50,000 feet, the rise in temperature is essentially completed in 3 minutes; at 100,000 feet, in 15 minutes; and at 200,000 feet, the time is of the order of hours.

Figures 1 and 2 have established limits on the magnitude of the temperature levels that can be expected in supersonic flight and the order of time required to reach them. The actual temperature histories will depend on the details of the flight plan. There will be as many characteristic temperature histories as there will be types of supersonic aircraft, but consider two possible ones which contain the significant features of a number of them. In figure 3 is shown the temperature history of an interceptor airplane which flies mostly subsonically; then, at an altitude of 50,000 feet, it accelerates rapidly to $M = 3$, remains there for 5 minutes, and then decelerates. If the skin of the wing of this airplane were 0.1-inch steel, its temperature would rise to 570°, almost the equilibrium temperature, and then on deceleration return to the ambient temperature. Such a temperature cycle would be expected to occur many times in the life of the aircraft.

In figure 4 is shown a flight history of a second type of vehicle which is launched at altitude, is boosted by rocket power to a higher altitude and Mach number of 6.2, and then coasts through an essentially ballistic path. The velocity of descent has been controlled by brakes. The temperatures on the wing rise rapidly during the boost period and reach a more or less steady state at high altitude where radiation is effective in restraining heating; then, as it descends into the denser atmosphere, the temperature rises rapidly because of the higher heat transfer and the resulting loss of effectiveness of radiation in lowering the temperature. At this time the wing of this aircraft is held at a small angle of attack and the increase in air density in the compressed region behind the shock on the lower side heats the lower surface to a peak of about 1,200° F. The upper surface is in a region of reduced density because of the expanded flow behind the shock and remains about 600° cooler.

It is apparent from figures 3 and 4 that supersonic aircraft of the forseeable future could experience peaks of temperatures that encompass the useful range of common aircraft materials, that these temperature peaks will be reached in times of the order of minutes, and that for some types of aircraft the cycles of heating may be repeated.

[redacted]

MATERIALS

Deterioration of Properties

The most serious effect of aerodynamic heating is its deterioration of the properties of the material of which the aircraft is made. Whereas in the past for subsonic aircraft material properties obtained at room temperature have sufficed to define a material for the purpose of predicting the static strengths of structures into which it is made, this simple situation no longer exists at high temperatures. Not only is it necessary to regard temperature as a parameter but also time. Materials exposed to a given temperature have different properties for each length of exposure, and materials exposed to a given temperature and then cooled also have different properties.

Creep

When load and high temperature are applied continuously, the material creeps, that is, elongates without change in load, and the usual stress-strain curve no longer provides a unique relationship between stress and strain. Although much creep information is available for the effects of steady loads and temperatures, only a relative small amount is available for cyclic variations in load and temperature which are the conditions which will exist for airframes. Since it is hopeless to attempt to get experimental creep data on all possible variations in load and temperature that may be experienced, the real value of cyclic-loading and heating tests lies in the possibility of their suggesting general laws of creep behavior under variable heating and loading.

STRUCTURES

Strength

Analogous to the problem of the prediction of the strength of the airframes at normal temperatures, there exists the same problem at elevated temperatures. The simplest problem is that of the prediction of the strength under rapid loading (but not so rapid as to develop inertia forces) of a uniformly heated structure. Sufficient evidence exists to indicate that this problem can be handled at elevated temperatures just as readily as it can be at room temperature and that, if the room-temperature strength and mode of failure are known, a rapid estimation of the effect of temperature can be made. The information that is required is contained in the stress-strain curves of the material obtained at the temperature time history of interest.

[redacted]

If the structure is required to support a given load at a given temperature for time of the order of hours, the possibility exists that it will collapse because of the creep of the material at a load lower than its rapid-loading strength. The time at load and temperature need not be continuous but can be made up of a sequence of short heatings and loadings.

Tests made on complete box beams of aluminum alloy have indicated that, if this failure is due to tensile-creep rupture, the failures correlate closely with tensile-rupture data for the material. Failures of some of these box beams, however, were due to collapse of the compression cover and, at the time of these tests, this problem which has been called creep buckling was little understood.

Thermal Stresses

The rapid heating experienced by supersonic aircraft gives rise to thermal stresses in the airframe. Although it is possible to conceive of circumstances under which thermal stresses can produce tensile failure of parts of an airframe, aircraft, however, are essentially shell structures and the more usual condition that exists is that aerodynamic heating induces compressive stresses in the skin which tend to buckle it and prevent any further increase in the tensile stresses in the cooler interior structure.

STIFFNESS AND DISTORTION

Structural stiffness is a primary design criterion for supersonic aircraft. There is a direct loss of stiffness of aircraft due to loss of the basic materials stiffness but, for the temperature range of applicability of the materials, stiffness losses are not as severe as are the losses of material strength.

Buckling

A more serious loss of stiffness of the shell structure can be attributed to thermal stresses which are induced by the high rates of heating. If these thermal stresses are severe enough, they can cause buckling of the plate elements of the aircraft. When so buckled, the effective stiffness of the entire structure is reduced.

[redacted]

Reduced Stiffness

Even without causing buckling, these thermal stresses tend to destabilize the plates of which the aircraft is made. The mechanism of this loss of stiffness is related to the effective loss of bending stiffness which occurs in a beam that is loaded axially by a thrust.

The strong effect of thermal stresses on stiffness makes it desirable to suppress these effects in supersonic aircraft, and, to some extent, the magnitudes of these stresses are under the controls of the designer who can detail internal structures that do not restrain the skin or offer a reduced amount of restraint.

Stress-Free Distortion

Whether large thermal stresses are induced in the airframe, unequal heating can cause distortion of the structure. The most serious occurrence of this is the unequal transient heating of thin supersonic wings that was illustrated in figure 4. By virtue of the unequal transient heating of top and bottom of the wing when at an angle of attack, wing bending can occur. The bending deflections can be substantial but it is not evident that these bending deflections can adversely affect the aircraft.

ALLEVIATION

It is clear from the many material and structures problems that arise from aerodynamic heating that it is desirable to find ways of alleviating them.

Insulation

The simplest idea which presents itself is to place between the structure and the airframe an insulator. Although efficient insulators exist, it is characteristic of aerodynamic heating that the surface of the insulator must follow instantaneously the full equilibrium temperature. Consequently, they have serious problems of thermal stressing and loss of strength with temperature.

Aerodynamics and Configuration

Some control of the heat input is possible by controlling the aerodynamics of the boundary layer. The laminar boundary layer has heat-transfer coefficients one-third to one-half of those of the turbulent

[redacted]

boundary layer; therefore, lower heat inputs can be obtained by those factors that encourage laminar flow, that is, favorable pressure gradients, cooled surfaces, and smooth surfaces. Blunted noses of bodies and rounded and swept leading edges also have reduced heat-transfer coefficients.

Cooling

A most effective way of reducing heat input to the airframe is the cooling of the boundary layer by introducing into it some fluid. Gases and liquids can be used, the liquids having the greatest capacity to cool by virtue of their heat of vaporization. Such schemes are mechanically complicated and can only be justified in special circumstances.

[redacted]

29V

[redacted]

TABLE I

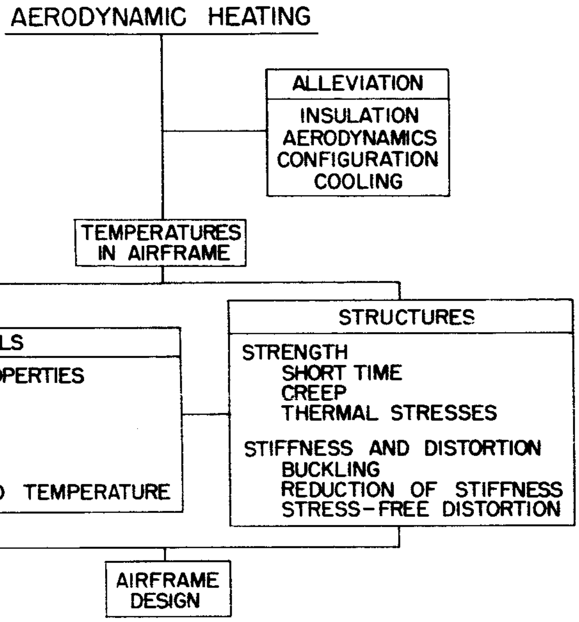

[redacted]

[redacted]

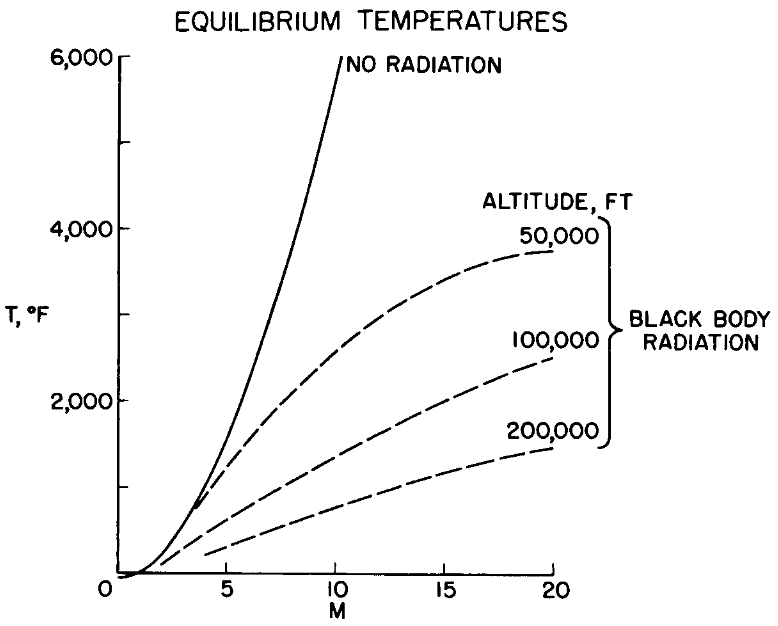

Figure 1

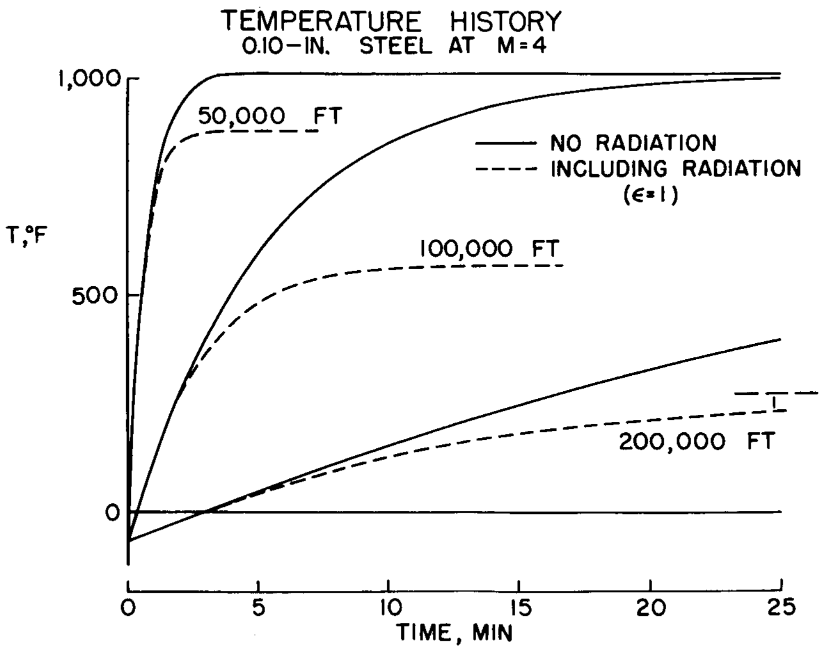

Figure 2

[redacted]

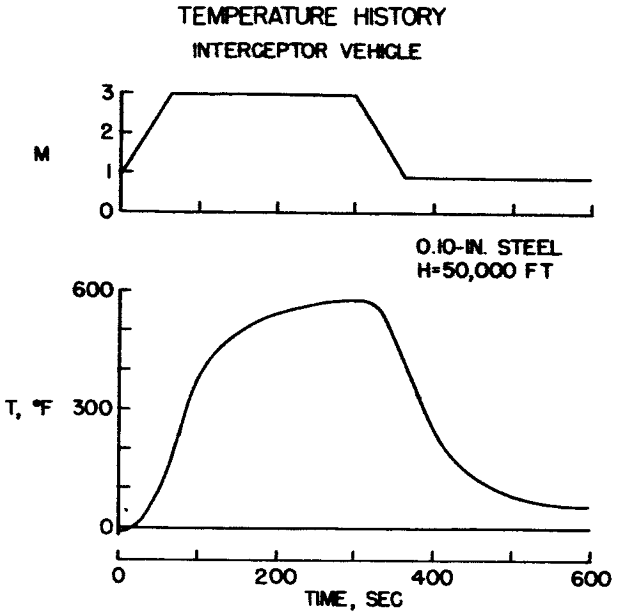

Figure 3

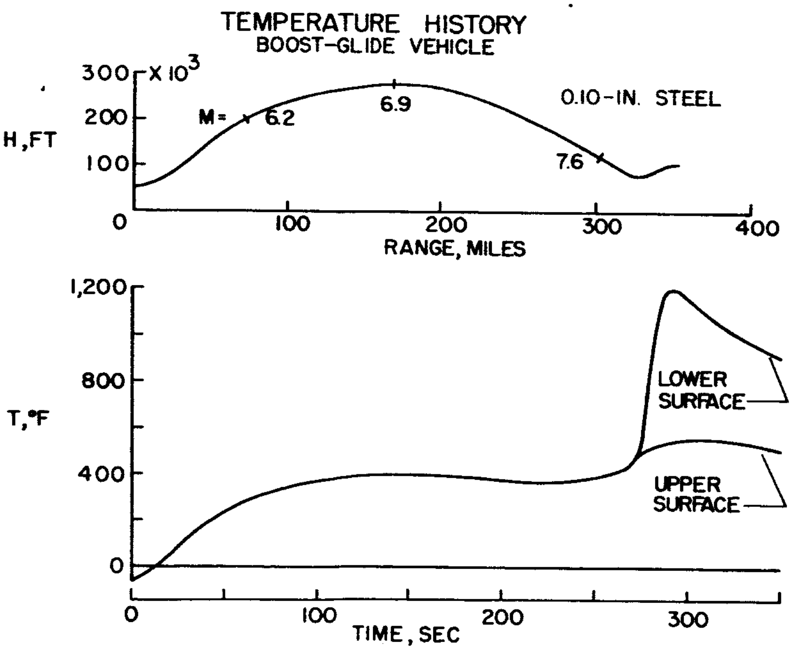

Figure 4

[redacted]

[redacted]

A DISCUSSION OF METHODS FOR REDUCING AERODYNAMIC HEATING IN SUPERSONIC FLIGHT

By A. J. Eggers, Jr.

Ames Aeronautical Laboratory

INTRODUCTORY REMARKS

Because of the seriousness of the structural and other problems introduced by aerodynamic heating, considerable effort has been devoted to finding methods of reducing heat transfer in supersonic flight. It is the purpose of this paper to describe some of the more promising of these methods which have been discovered to date.

RESULTS AND DISCUSSION

Aerodynamic heating is brought about primarily by the convection of heat from the boundary layer to the surface of a vehicle. The severity of the heating is strongly dependent upon the flow in the boundary layer. To illustrate this point, consider flow of the familiar laminar and turbulent types (see, e.g., refs. 1, 2, and 3). The friction coefficients for laminar flow are usually substantially less than those for turbulent flow, and according to Reynolds analogy (see, e.g., refs. 4 and 5) the heat-transfer coefficients should be reduced in about the same proportion. The magnitude of this reduction is indicated in figure 1 where the Stanton number, which is proportional to the heat-transfer coefficient, is shown as a function of Mach number for laminar and turbulent flow over a flat surface at a Reynolds number of 10^7. The surface is presumed to be at ambient air temperature. Under these circumstances, it can be seen that laminar heat-transfer coefficients vary from about one-fifth the turbulent value at a Mach number of 2 to about one-third the turbulent value at $M = 8$. According to Newton's law of cooling, the heat-transfer rate per unit area is equal to the product of the heat-transfer coefficient and the difference between the recovery temperature (corresponding to zero heat flow) and the wall temperature. It follows that the laminar heat-transfer rates should be less than turbulent in about the same proportion as the heat-transfer coefficients inasmuch as the recovery temperatures are about the same for both types of boundary layer, and the wall temperatures are, of course, presumed unchanged. It is indicated then that both local and overall heating of a vehicle can be reduced by increasing the amount of laminar flow. This observation raises the fundamental question - how

[redacted]

[redacted]

can the Reynolds number of transition from laminar to turbulent flow be increased?

Theoretical and experimental work to date (refs. 6 to 16) have indicated that there are three especially promising methods of increasing the transition Reynolds number in supersonic flight. One method is to cool the surface of the vehicle, another is to shape the surface to give decreasing pressures with distance aft on the vehicle, that is negative pressure gradients, and the third is to minimize surface roughness of the vehicle. The first two methods tend to stabilize the laminar boundary layer against disturbances which might otherwise cause transition to turbulent flow. The third method tends to eliminate one important source of these disturbances.

Some examples of the effects of surface temperature and pressure gradient on transition are shown in figure 2. First it is observed that cooling the surface from about 10 percent above to 10 percent below the recovery temperature increased the transition Reynolds number on a parabolic body of revolution from about 6×10^6 to 20×10^6 at a Mach number of 1.61 (ref. 12). In other words, the length of laminar run was increased by more than threefold. The effect of pressure gradient on transition Reynolds number (ref. 15) is also shown in this figure for the case of surface temperature equal to recovery temperature. The parabolic body, which has a negative pressure gradient for about three-fourths of its length, has about twice as long a laminar run as the ogive-cylinder which has a favorable gradient for only about the first quarter of its length. Similarly, the ogive-cylinder has about twice the laminar run of the cone-cylinder which has a negative pressure gradient only at its shoulder.

Pressure-gradient effects also become evident when cylindrical bodies fly at an angle of attack (ref. 11). This point is demonstrated in figure 3 where it is observed that the transition Reynolds numbers on the sheltered side of the body at an angle of attack are much smaller than those on the windward side. The effects shown can actually be correlated with a pressure-rise coefficient along a streamline passing from the windward to the sheltered side of the body. More generally, it can be said that all the experimental effects shown here and in figure 2 agree qualitatively with the results of boundary-layer stability theory (refs. 6 to 9).

The effect of distributed surface roughness on transition Reynolds number (ref. 11) is shown in figure 4. Here the transition Reynolds number on a model fired in a free-flight wind tunnel is plotted against the ratio of roughness height to the laminar-boundary-layer thickness at transition. The roughness height is the depth of the screw thread used to create the roughness. It is apparent that increasing the roughness moves transition forward for each of the length Reynolds numbers at which tests were conducted.

[redacted]

[redacted]

There are, then, several methods which individually and collectively offer promise of reducing heat transfer in supersonic flight by maintaining more laminar flow over a vehicle. At best, however, there are numerous disturbances such as those produced by shock waves, noise, and wakes, which can still cause transition and which cannot be easily eliminated. Accordingly, it is appropriate to consider next a method which appears especially suited to reducing heat transfer from a turbulent boundary layer to a surface. This method is termed transpiration cooling (see refs. 17 to 19).

With a transpiration cooling system, the coolant passes through the material to be cooled as shown in figure 5. The coolant may pass through as a gas, or as a liquid that would evaporate on the surface. A liquid has, of course, the advantage of absorbing the heat of vaporization during transpiration. In any event, the coolant leaves the surface as a gas and flows into the surrounding boundary layer. Naturally the outer skin of the aircraft would have to be porous. The porosity, however, introduces engineering problems of strength and of manufacture. Because of these and additional problems, consideration of transpiration cooling would only be made if it could be shown to be very effective. There are two reasons why a transpiration cooling system is thought to be effective. First, from a heat-exchanger viewpoint, a transpiration cooling system is efficient because it raises the temperature of the coolant to the temperature of the outer surface, where the highest temperature in the system exists. Thus, the coolant absorbs the maximum possible amount of heat. In addition, when the coolant leaves the surface as a gas, it reduces the shear in the boundary layer by tending to separate it from the wall. As a result the heat transfer to the body is reduced. These two attributes, utilizing the coolant to its fullest and reducing the amount of heat entering the aircraft, make a transpiration cooling system exceptionally effective. Some indication of the reductions in heat transfer obtainable by this method is shown in figure 6 for the case of flow over a flat plate at a Mach number of 2.6 and a length Reynolds number of 5×10^6. The ordinate is the ratio of heat-transfer coefficient with, to heat-transfer coefficient without transpiration. The abscissa represents the ratio of mass flow of air per unit area through the surface to the mass flow per unit area of the free stream. The important conclusion to be drawn from this figure is that according to both theory (ref. 18) and experiment, large reductions in heat transfer are obtained by transpiring relatively small amounts of air.

Up to this point, we have concerned ourselves primarily with overall heat transfer to a vehicle - local heat transfer has been discussed only in the sense that it contributes to overall heat transfer. It is appropriate now to view the local heating problem as it relates to the generation of "hot spots" on a vehicle. In this regard, it will be undertaken to consider only those spots which are more or less common

[redacted]

to all vehicles - namely, the nose of the body and the leading edge of the wing. (There may, of course, be other regions of this type - for example, the transition region - however, it is beyond the scope of the present paper to consider these possibilities.)

A nose or leading edge tends to become excessively hot for the following reason. The boundary layer is just beginning to form so it is still very thin and the rate of viscous shearing is very high. Accordingly, the local heat-transfer coefficients are very high. In the event a nose or leading edge is sharp, it is indicated by boundary-layer theory that the local heat-transfer coefficients take on prohibitively large values. For this reason, and because a sharp nose or leading edge has little capacity for absorbing heat, effects of bluntness on heat transfer have been a matter of some interest (see, e.g., refs. 20 and 21). Theoretical studies of the heat transfer from a laminar boundary layer to a hemispherical nose or a semicircular leading edge indicate that, all other things being the same, the heat-transfer coefficients should vary inversely with the square root of the radius of curvature of the surface (see refs. 22 to 26). Figure 7 compares this prediction with experimental data for transverse cylinders. The nominal test conditions were Mach number 9.8, stagnation temperature 2200° R, cylinder temperature 530° R, and cylinder Reynolds numbers from about 0.3×10^3 to 4.2×10^3. Variations in Re_D were obtained by varying cylinder diameter. For these tests, then, the dimensionless ordinate is proportional to heat-transfer coefficient while the abscissa is proportional to cylinder diameter. It is indicated that heat-transfer coefficients are substantially reduced by increasing the diameter, and essentially in the manner predicted by theory. Analogous results have been obtained for hemispherical noses (ref. 27). There is good reason to believe, then, that round noses and round leading edges are desirable from the standpoint of reducing the high rates of local heat transfer in these regions.

Now blunting the nose of a body in some cases actually reduces pressure drag. On the other hand, a substantial increase in pressure drag is almost inevitably associated with blunting the leading edge of a wing. Sweeping the leading edge is, of course, an effective means for minimizing this penalty (see, e.g., ref. 21). The question is then raised, however, as to what effect sweep has on heat transfer. Theory in this case has been worked out only for the stagnation region (ref. 26) and then only for the limited, although perhaps most practical, case of wall temperature that is low in comparison with stagnation temperature. Comparison of the predictions of this theory with experiments on heat transfer to swept cylinders is shown in figure 8. Specifically, there is shown the ratio of average heat-transfer rate at angle of sweep to average heat-transfer rate at zero sweep as a function of the angle of sweep. The experimental data are for Mach numbers of 9.8 and 6.9 and wall to stagnation temperature ratios of 0.24 and 0.48 to 0.84. The

[redacted]

[redacted]

theoretical prediction is shown only for the temperature ratio of 0.24, inasmuch as the theory is not applicable at the higher temperature ratios. It is encouraging to note that according to both theory and experiment, large reductions in heat-transfer rates are achieved by sweep. Sweepback, then, may prove as useful in reducing heat transfer and drag in flight at high supersonic speeds as it has been in reducing drag at low supersonic speeds.

So far in this discussion it has been presumed that the boundary layer is normal in the sense that it is laminar, transitional, or turbulent, and more or less steady. As a final point, however, I would like to depart from this presumption and consider a basically different flow (ref. 28) which offers promise of transferring less heat to a surface than the usual boundary layer. This flow is nonsteady, rather than steady, and it may be represented schematically as shown in figure 9. It differs from the normal boundary layer in one important respect - a large vortex exists in the boundary layer at short intervals along the surface. Now, assume that each vortex is made up of air from the main flow and, further, that the surface is at some reasonable temperature greater than ambient air temperature. It may be argued then that part of the heat convected to the surface in the region of the normal boundary layer should be convected from the surface in the region of a vortex since the peripheral portion of the vortex should be cooler than the surface. The cooling by the vortices should, of course, depend both upon their size and spacing.

It was undertaken to check the principle of this "boundary-layer-vortex" hypothesis using specially designed spike-nosed bodies of revolution. These bodies were employed simply because they are known to generate a high-frequency pulsating flow at supersonic speeds (ref. 29), and it seemed reasonable to expect that large-scale vortices would be discharged over the bodies with each pulsation. Visual flow studies (ref. 28) indicated that this was, in fact, the case. It was anticipated further that aerodynamic cooling by the vortices would reflect directly in the recovery temperatures of the surface. Some idea of the magnitude of this effect at zero angle of attack and a Mach number of 3.5 can be obtained from figure 10. Here the recovery factor at a representative point on the surface of a spike-nosed body is shown as a function of spike extension. The body consisted of a truncated cone with a conical spike and an annular cutout added to the front face of the cone. The purpose of this cutout is to produce stronger, better developed vortices during pulsation. For spike extensions up to about 0.4 inch the flow remained steady and the recovery factor remained at a rather high value characteristic of turbulent boundary layers. With further spike extension, pulsating flow occurred at the nose, and the bow shock oscillated between the front face of the model and the tip of the spike. Ring-shaped vortices were discharged over the model in concert with each pulsation, and as can be seen, substantial reductions

[redacted]

in recovery factor were obtained at spike extensions up to 2.2 inches. With further spike extension the pulsations tended to disappear, large vortices were no longer shed from the nose, and the recovery factor rose to values in the range of normal boundary layers. The maximum reduction in recovery factor due to spike extension was from about 0.91 to 0.68.

It is of interest now to see what the distribution of recovery factor is like on the spike-nosed body under conditions of pulsating flow. Figure 11 provides some information on this matter for a spike extension equal to about three-fourths of that for obtaining minimum recovery factors. It is observed first that the recovery factors rise from a relatively low value near the center of the spike to a high value near the annular cutout. On the afterbody something like the proposed boundary-layer-vortex flow was obtained and it is observed that the recovery factors are uniformly low, varying from about 0.72 to 0.75. These results and those of the previous figure indicate that recovery temperatures on the surface of a vehicle in flight at a Mach number of 3.5 in air at 40° F ambient temperature could be reduced from about 1150° F to as low as 870° F by using vortex cooling. Large vortices offer promise, then, of substantially reducing recovery temperatures in flight at high supersonic speeds.

It is appropriate to inquire next as to what effect the pulsating flow has on heat-transfer coefficients. Some idea of this effect can be obtained from figure 12 which shows indicated average heat-transfer coefficients as a function of the difference between indicated recovery and wall temperatures of a spike-nosed model and a truncated cone model. Each model was solid and made of duralumin. The term "indicated" is used because the temperatures were measured at the base of the models. There are two important things to be noted. First, the effect of pulsating flow on heat-transfer coefficients is rather small, in this case reducing the coefficient by perhaps 7 percent. Second, the heat-transfer coefficients for the pulsating flow are, as in the case of steady flow, more or less constant, independent of wall temperature.

The latter observation suggests that the measured recovery factors can be combined with the measured heat-transfer coefficients in order to estimate the effects of pulsating flow on average heat-transfer rates in flight. It seems unlikely that in practice these rates would exceed those corresponding to the case of wall temperature equal to ambient air temperature. For this particular case, the rate of heat transfer is simply proportional to the product of the heat-transfer coefficient and the recovery factor. But pulsating flow reduced the heat-transfer coefficient by about 7 percent and it reduced the recovery factor from 0.91 to about 0.77, or about 16 percent. The net reduction in maximum average heat-transfer rate is indicated, then, to be about 23 percent. For heat-transfer rates less than the maximum, the percentage reduction

[redacted]

associated with pulsing vortices over a body should be greater because the role played by recovery factor is of increased importance.

CONCLUDING REMARKS

In the light of these and the previous considerations, the following conclusions are reached regarding presently available methods of reducing aerodynamic heating in supersonic flight. First, since a laminar boundary layer convects heat to a surface much less rapidly than a turbulent boundary layer, it appears worthwhile to strive for larger amounts of laminar flow by employing smooth, cooled surfaces which are shaped to give favorable negative pressure gradients. In the event the turbulent boundary layer cannot be avoided, the resulting aerodynamic heating may be substantially reduced by using a transpiration cooling system. Excessive heating of the noses of bodies and leading edges of wings can be minimized by blunting or rounding these surfaces, and in the case of wings this local heating problem can be further alleviated by sweeping the leading edge. Finally, there is the encouraging possibility of reducing aerodynamic heating below that encountered with normal boundary-layer flows by employing vortex cooling.

REFERENCES

1. Klunker, E. B., and McLean, F. Edward: Laminar Friction and Heat Transfer at Mach Numbers From 1 to 10. NACA TN 2499, 1951.

2. Coles, Donald: Measurements in the Boundary Layer on a Smooth Flat Plate in Supersonic Flow - I. The Problem of the Turbulent Boundary Layer. Rep. No. 20-69 (Contract No. DA-04-495-Ord 18, Ord. Corps), Jet Propulsion Lab., C.I.T., June 1, 1953.

3. Sommer, Simon C., and Short, Barbara J.: Free-Flight Measurements of Turbulent-Boundary-Layer Skin Friction in the Presence of Severe Aerodynamic Heating at Mach Numbers From 2.8 to 7.0. NACA TN 3391, 1955.

4. Rubesin, Morris W.: A Modified Reynolds Analogy for the Compressible Turbulent Boundary Layer on a Flat Plate. NACA TN 2917, 1953.

5. Seiff, Alvin: Examination of the Existing Data on the Heat Transfer of Turbulent Boundary Layers at Supersonic Speeds From the Point of View of Reynolds Analogy. NACA TN 3284, 1954.

6. Lees, Lester, and Lin, Chia Chiao: Investigation of the Stability of the Laminar Boundary Layer in a Compressible Fluid. NACA TN 1115, 1946.

7. Lees, Lester: The Stability of the Laminar Boundary Layer in a Compressible Fluid. NACA Rep. 876, 1947. (Supersedes NACA TN 1360.)

8. Van Driest, E. R.: Calculation of the Stability of the Laminar Boundary Layer in a Compressible Fluid on a Flat Plate With Heat Transfer. Rep. No. AL-1334, North American Aviation, Inc., Sept. 3, 1951. (Rev. Feb. 14, 1952.)

9. Low, George M.: Cooling Requirements for Stability of Laminar Boundary Layer With Small Pressure Gradient at Supersonic Speeds. NACA TN 3103, 1954.

10. Sternberg, Joseph: A Free-Flight Investigation of the Possibility of High Reynolds Number Supersonic Laminar Boundary Layers. Jour. Aero. Sci., vol. 19, no. 11, Nov. 1952, pp. 721-733.

11. Jedlicka, James R., Wilkins, Max E., and Seiff, Alvin: Experimental Determination of Boundary-Layer Transition on a Body of Revolution at $M = 3.5$. NACA TN 3342, 1954.

[redacted]

12. Czarnecki, K. R., and Sinclair, Archibald R.: An Extension of the Investigation of the Effects of Heat Transfer on Boundary-Layer Transition on a Parabolic Body of Revolution (NACA RM-10) at a Mach Number of 1.61. NACA TN 3166, 1954. (Supersedes NACA RM L53B25.)

13. Higgins, Robert W., and Pappas, Constantine C.: An Experimental Investigation of the Effect of Surface Heating on Boundary-Layer Transition on a Flat Plate in Supersonic Flow. NACA TN 2351, 1951.

14. Eber, G. R.: Recent Investigation of Temperature Recovery and Heat Transmission on Cones and Cylinders in Axial Flow in the N.O.L. Aeroballistics Wind Tunnel. Jour. Aero. Sci., vol. 19, no. 1, Jan. 1952, pp. 1-6 and 14.

15. Hilton, John H., Jr., and Czarnecki, K. R.: An Exploratory Investigation of Skin Friction and Transition on Three Bodies of Revolution at a Mach Number of 1.61. NACA TN 3193, 1954.

16. Evvard, J. C., Tucker, M., and Burgess, W. C., Jr.: Statistical Study of Transition-Point Fluctuations in Supersonic Flow. NACA TN 3100, 1954.

17. Dorrance, William H., and Dore, Frank J.: The Effect of Mass Transfer on the Compressible Turbulent Boundary-Layer Skin Friction and Heat Transfer. Jour. Aero. Sci., vol. 21, no. 6, June 1954, pp. 404-410.

18. Rubesin, Morris W.: An Analytical Estimation of the Effect of Transpiration Cooling on the Heat-Transfer and Skin-Friction Characteristics of a Compressible, Turbulent Boundary Layer. NACA TN 3341, 1954.

19. Mickley, H. S., Ross, R. C., Squyers, A. L., and Stewart, W. E.: Heat, Mass, and Momentum Transfer for Flow Over a Flat Plate With Blowing or Suction. NACA TN 3208, 1954.

20. Allen, H. Julian, and Eggers, A. J., Jr.: A Study of the Motion and Aerodynamic Heating of Missiles Entering the Earth's Atmosphere at High Supersonic Speeds. NACA RM A53D28, 1953.

21. Eggers, Alfred J., Jr., Allen, H. Julian, and Neice, Stanford E.: A Comparative Analysis of the Performance of Long-Range Hypervelocity Vehicles. NACA RM A54L10, 1955.

22. Fluid Motion Panel of the Aeronautical Research Committee and Others: Modern Developments in Fluid Dynamics. Vol. II, S. Goldstein, ed., The Clarendon Press (Oxford), 1938, pp. 631.

23. Sibulkin, M.: Heat Transfer Near the Forward Stagnation Point of a Body of Revolution. Jour. Aero. Sci. (Readers' Forum), vol. 19, no. 8, Aug. 1952, pp. 570-571.

24. Cohen, Clarence B., and Reshotko, Eli: Similar Solutions for the Compressible Laminar Boundary Layer With Heat Transfer and Pressure Gradient. NACA TN 3325, 1955.

25. Cohen, Clarence B., and Reshotko, Eli: The Compressible Laminar Boundary Layer With Heat Transfer and Arbitrary Pressure Gradient. NACA TN 3326, 1955.

26. Eggers, A. J., Jr., Hansen, C. Frederick, and Cunningham, Bernard E.: The Effect of Yaw on Heat Transfer to a Cylindrical Stagnation Region in Hypersonic Flow. (Prospective NACA paper.)

27. Stalder, Jackson R., and Nielsen, Helmer V.: Heat Transfer From a Hemisphere-Cylinder Equipped With Flow-Separation Spikes. NACA TN 3287, 1954.

28. Eggers, A. J., Jr., and Hermach, C. A.: Initial Experiments on the Aerodynamic Cooling Associated With Large-Scale Vortical Motions in Supersonic Flow. NACA RM A54L13, 1955.

29. Beastall, D., and Turner, J.: The Effect of a Spike Protruding in Front of a Bluff Body at Supersonic Speeds. TN No. Aero. 2137, British R.A.E., Jan. 1952.

[redacted]

[redacted]

LOCAL HEAT TRANSFER FROM LAMINAR AND TURBULENT BOUNDARY LAYERS TO A FLAT SURFACE

$Re_x = 10^7$, $T_W = T_\infty$

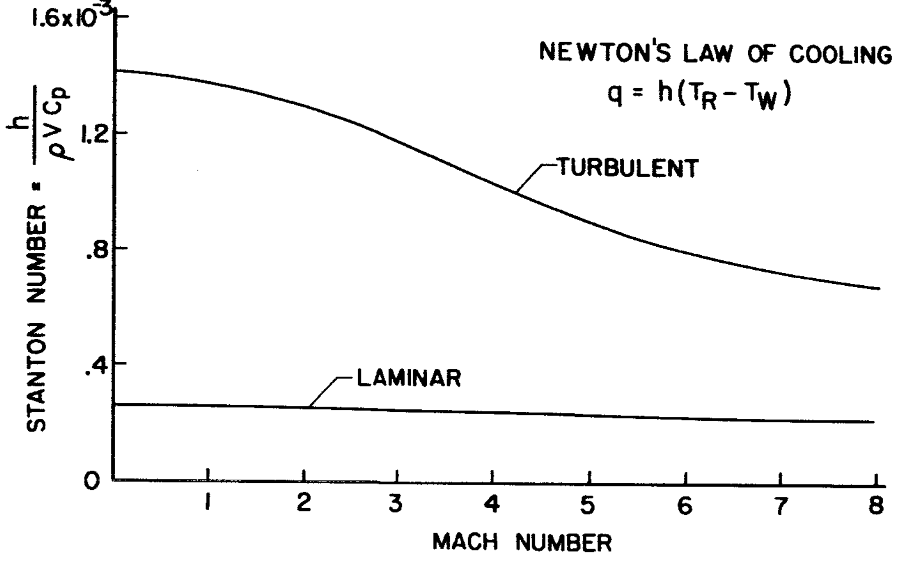

Figure 1

EFFECTS OF SURFACE TEMPERATURE AND PRESSURE GRADIENT ON TRANSITION

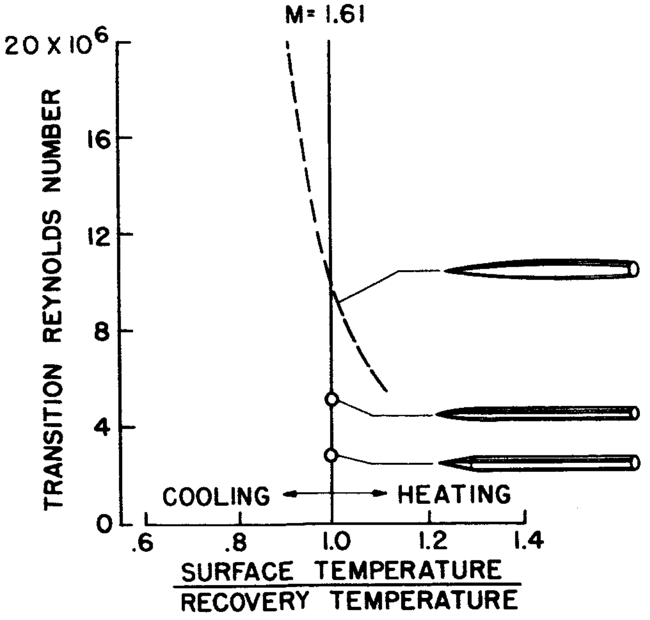

Figure 2

[redacted]

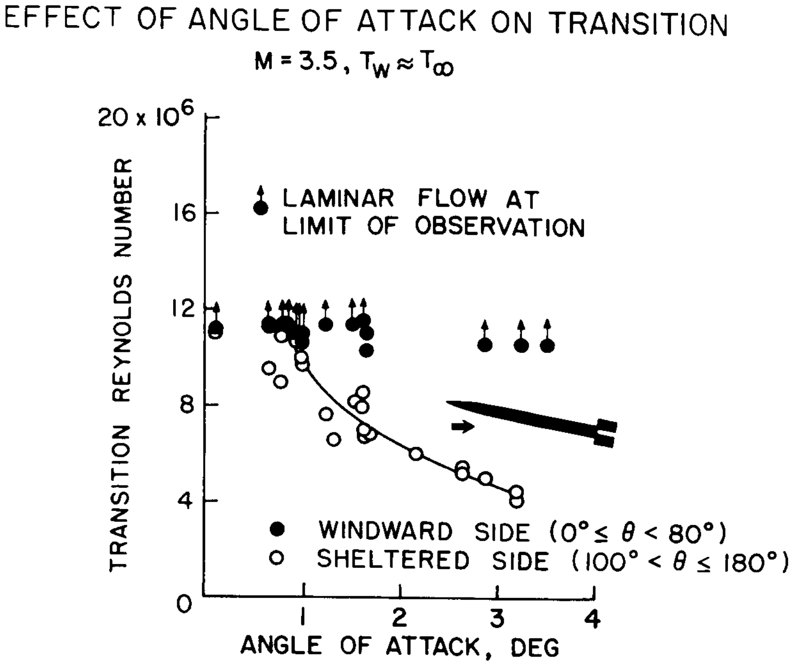

Figure 3

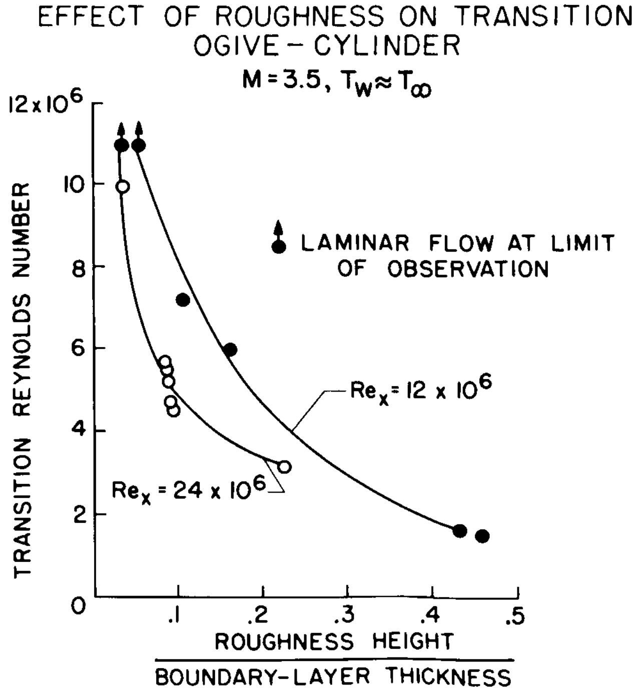

Figure 4

[redacted]

[redacted]

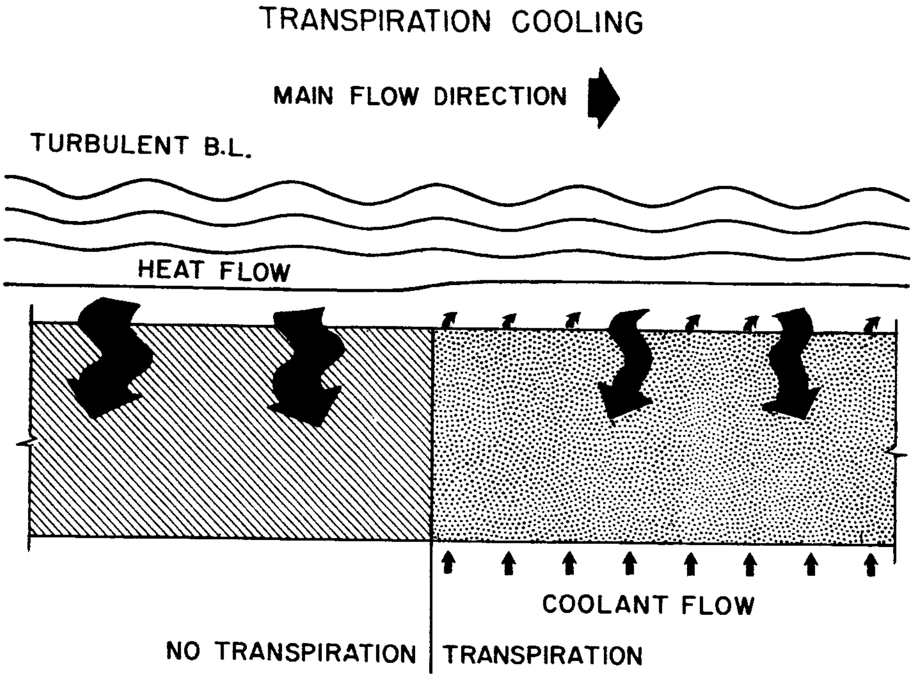

Figure 5

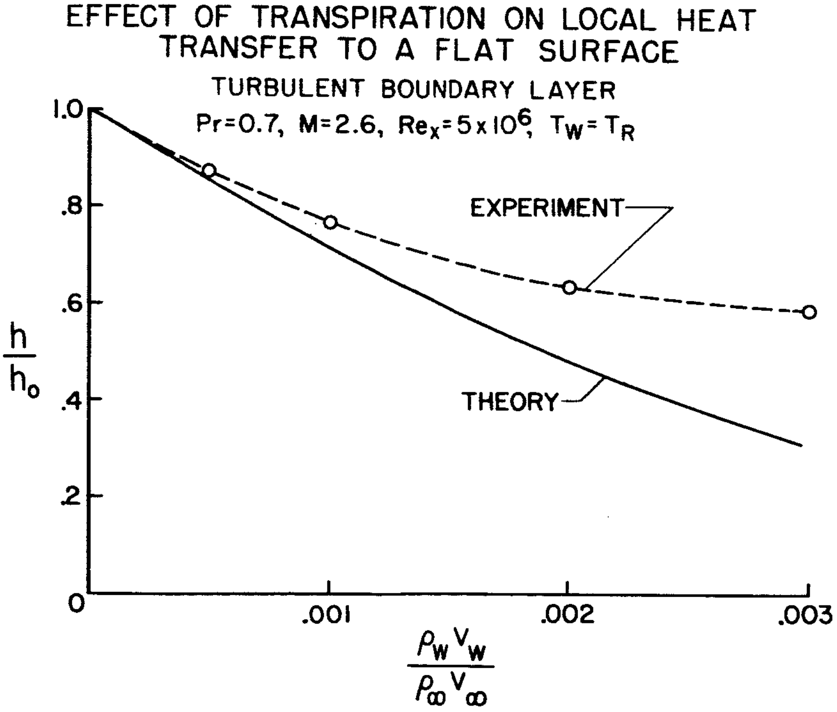

Figure 6

[redacted]

EFFECT OF BLUNTNESS ON HEAT TRANSFER TO CIRCULAR CYLINDERS

$M=9.8,\ T_t=2200°R,\ T_W=530°R$

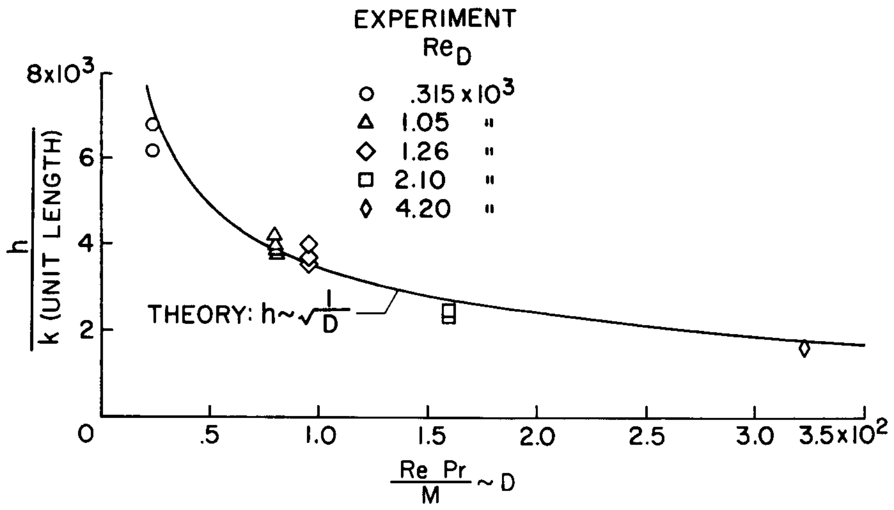

Figure 7

EFFECT OF SWEEP ON HEAT TRANSFER TO CIRCULAR CYLINDERS

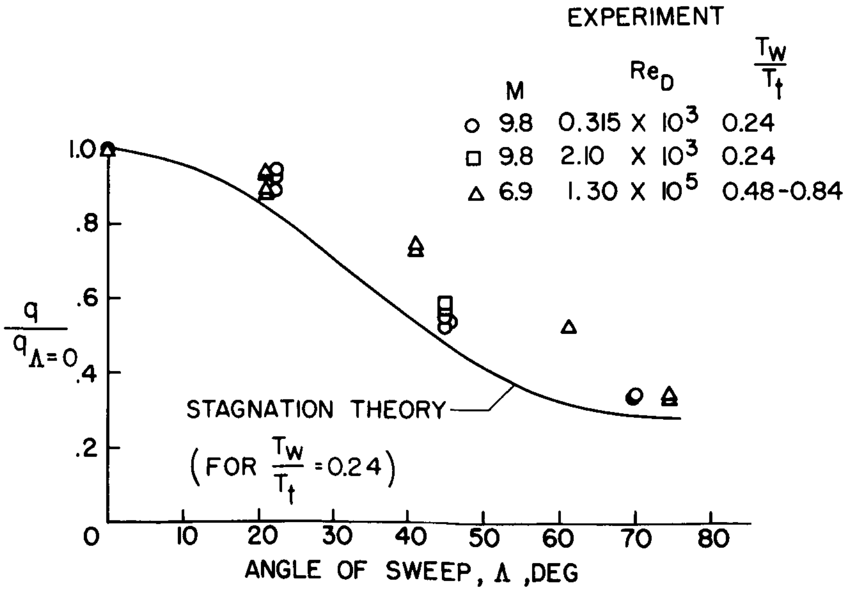

Figure 8

[redacted]

MODEL OF BOUNDARY-LAYER-VORTEX FLOW

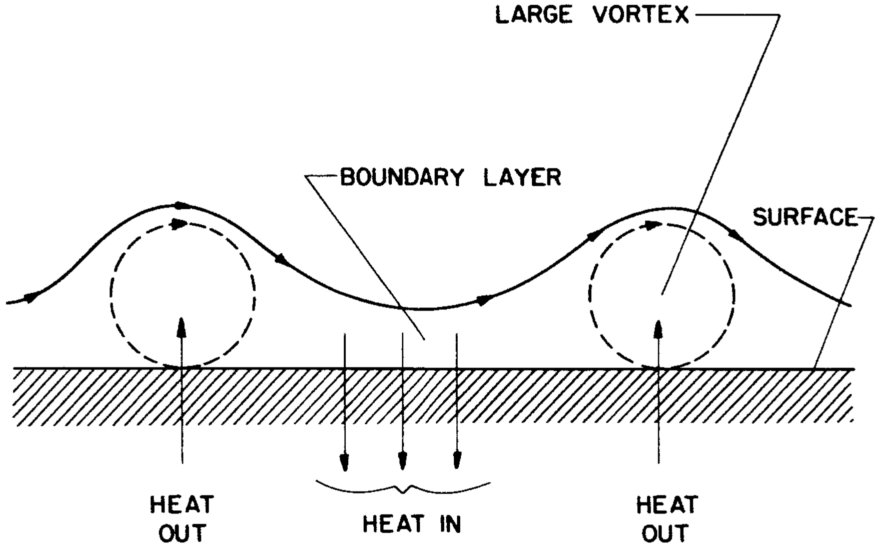

Figure 9

EFFECT OF SPIKE EXTENSION ON RECOVERY FACTOR

$Re_D = 1.9 \times 10^6, \alpha = 0°, M = 3.5$

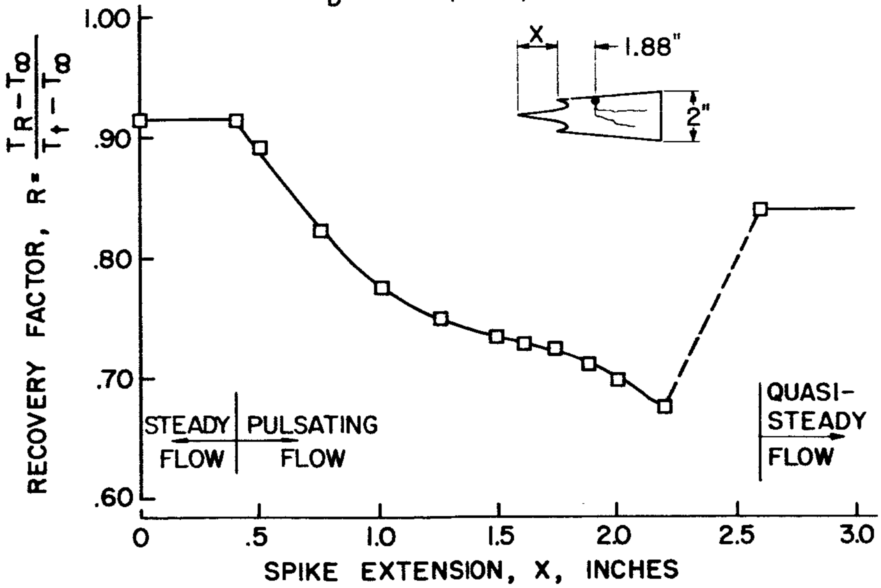

Figure 10

[redacted]

[redacted]

RECOVERY FACTORS ON SURFACE IN PULSATING FLOW

$\alpha = 0°$, M = 3.5

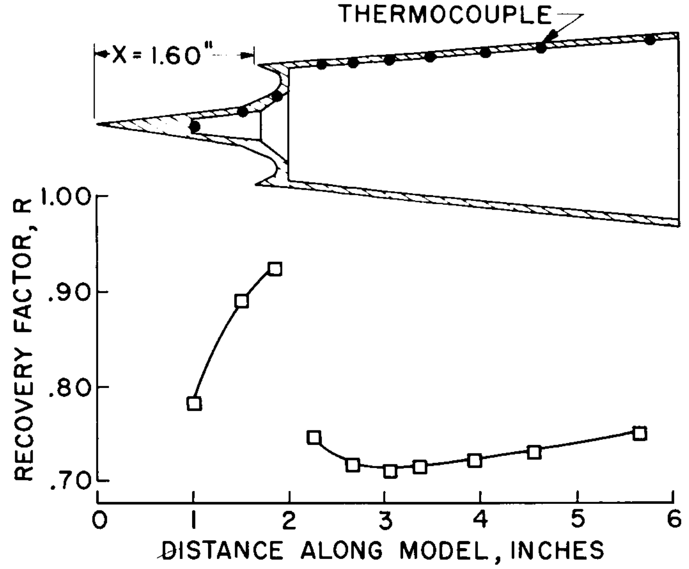

Figure 11

EFFECT OF PULSATING FLOW ON HEAT-TRANSFER COEFFICIENTS

$\alpha = 0°$, M = 3.5

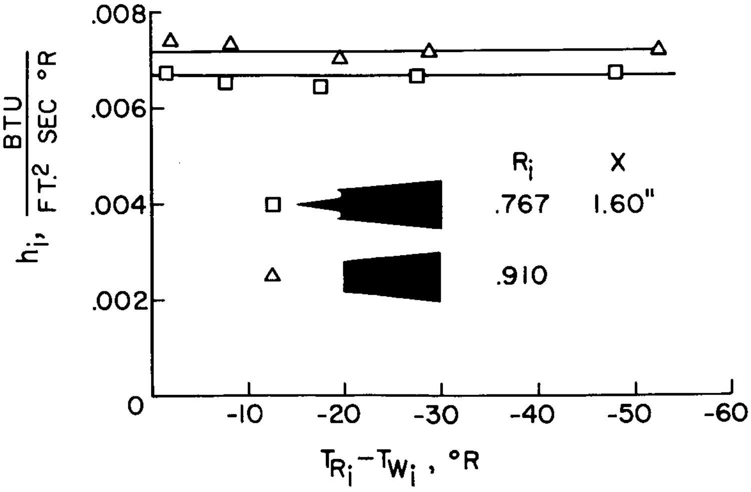

Figure 12

[redacted]

[redacted]

AERODYNAMIC HEATING OF ROCKET-POWERED RESEARCH VEHICLES AT HYPERSONIC SPEEDS

By Robert O. Piland

Langley Aeronautical Laboratory

SUMMARY

Skin temperature measurements have been obtained on two free-flight research vehicles; measurements were made up to Mach numbers of 5.4 in one case and up to 10.4 in the other. On the first model $(M = 5.4)$, temperature measurements were obtained at nine stations (between 6.5 and 29 inches) along the 15° conical nose. The temperature distribution along the nose, at a Mach number of 5.4, indicated transition to have occurred at a Reynolds number of about 9×10^6. The theories of Van Driest for laminar and turbulent flow proved adequate for predicting the skin temperature histories for laminar and turbulent stations, respectively.

A skin temperature history was obtained at a single station (26.6 inches from tip) on a fineness-ratio-5 Kármán nose shape to a Mach number of 10.4. The peak skin temperature of 1,200° F occurred shortly after the time of peak Mach number and calculations indicate that at this time the convective heat transfer to the model was being balanced by radiative heat transfer away from the model. The theory of Van Driest was used in calculating a skin temperature and appeared adequate up to a Mach number of about 6. Above this value, there is some divergence between calculated and measured data, possibly due to the existence of other than turbulent flow over the measuring station.

INTRODUCTION

It is well known that the problem of aerodynamic heating becomes more severe with increasing Mach number. In order to determine just what heating conditions will be encountered at higher Mach numbers, research vehicles are being flight tested, at present, to Mach numbers as high as 10.4.

The purpose of this paper is to present and discuss skin temperature measurements from two flight tests. Temperature measurements were obtained to a Mach number of 5.4 on the first flight and to a Mach number of 10.4 on the second flight.

[redacted]

SYMBOLS

M	Mach number
R	Reynolds number
T_o	static temperature, degrees Rankine
T	skin temperature, degrees Fahrenheit
l	length on which Reynolds number calculation is based

RESULTS AND DISCUSSION

Figure 1 presents the variation of static temperature, Mach number, altitude, and Reynolds number per foot with flight time for a three-stage vehicle which had a 15° total angle conical nose.

Figure 2 presents the variation of skin temperature with time measured at a distance of 29 inches from the nose tip. The nose cone was constructed of 0.027-inch-thick Inconel. The maximum measured temperature is seen to be 1,000° F, at which time (23.7 seconds) the vehicle is at a Mach number of 5.4.

A temperature history has been calculated using the turbulent theory of Van Driest (ref. 1) applying a conversion factor to make it applicable to the cone (ref. 2). Turbulent flow was assumed to exist from the nose tip, and the recovery factor used in calculating the adiabatic wall temperature was assumed equal to the cube root of the Prandtl number $Pr^{1/3}$ based on skin temperature (ref. 2). The ratio of specific heats γ was taken equal to 1.4. The calculated temperature history is indicated by the symbols in figure 2 and is seen to be in good agreement with the measured temperature history.

In addition to the temperatures measured at station 29, measurements were also made at eight other stations along the same 15° cone. Figure 3 presents the variation of skin temperature along the nose cone at a particular time during the flight. The flight time considered is 23.7 seconds at which time the Mach number is 5.4 and the Reynolds number per foot is 9.8×10^6. The measured temperature is indicated by the solid line and the ticks on this curve and along the center line of the cone indicate the stations at which the temperature measurements were made.

[redacted]

The shape of the measured curve indicates regions of laminar, transitional, and at least the early stages of turbulent flow. The abrupt change in slope of the temperature curve indicates that transition from laminar flow began at a Reynolds number of about 9×10^6. It is interesting to note that, in a flight time of only 23.7 seconds, a difference of 500° F exists between laminar-station and turbulent-station temperature measurements.

The lower broken line in figure 3 indicates temperatures calculated using the laminar theory of Van Driest (ref. 3), applying a conversion factor to make it applicable to the cone (ref. 2). The recovery factor was assumed equal to the square root of the Prandtl number (ref. 2). Fair agreement is seen to exist between the measured and calculated data at the stations where the laminar flow is believed to exist.

The upper broken line in figure 3 indicates temperatures calculated using the turbulent theory of Van Driest as described previously. Toward the aft end of the cone (station 29), where it is believed turbulent flow exists, the agreement between the measured and calculated data is quite good.

Let us now consider temperature measurements to a Mach number of 10.4 obtained during the flight test of a four-stage vehicle, which is described in reference 4.

Figure 4 presents the variation of static temperature, Mach number, altitude, and Reynolds number at the temperature measuring station, for the test vehicle. The nose shape on which the temperature measurements were made was a fineness-ratio-5 Kármán nose shape whose tip was modified to form a 15° total angle wedge. The nose skin was of 0.032-inch-thick Inconel. A sketch of the nose shape is presented in figure 5 and the temperature measuring station is shown to be 26.6 inches aft of the nose tip. The variation of skin temperature with time is also presented in figure 5 and is indicated by the solid line. A peak temperature of 1,200° F is seen to have been reached just after peak Mach number. At this time, the heating potential is still considerably higher than the skin temperature, and considering only convective heat transfer a peak temperature would not have been expected until a later flight time. The explanation for the peak at this time is that the convective heat transfer to the skin is being balanced by the radiative heat transfer away from the skin. Keeping this in mind, consider the temperature history calculated using the turbulent theory of Van Driest (ref. 1) for a cone and including radiative heat transfer. The calculated values (square symbols) agree quite well to about 28 seconds, a time which corresponds to a Mach number of about 6. At this point the measured and calculated values diverge and at the time of peak measured temperature the calculated curve is still rising rapidly. However, if transition to laminar flow is arbitrarily assumed to occur at a Reynolds number of 5×10^6 and laminar heat-transfer coefficients are used, the points indicated by the solid square symbols are obtained. The inference is that laminar flow must have actually existed on the model at this time of peak temperature. Calculations are also presented considering flat-plate theory; these are indicated by the circular symbols. At the higher temperatures, the agreement between the flat-plate calculations and the measured data is better than the calculations for the cone; this is probably fortuitous and may be due to the existence of transitional rather than turbulent flow over the measuring station for some time interval prior to time of peak temperature. The primary purpose of making the flat-plate calculations was to determine the difference in estimated maximum temperature occasioned by using the simpler flat-plate procedure. The difference is seen to be about 15 percent.

CONCLUDING REMARKS

The following observations are made from the data presented here:

1. Free-flight skin-temperature measurements have indicated transition to occur on a conical nose at a Reynolds number of about 9×10^6 at a Mach number of 5.4.

2. The theories of Van Driest for turbulent and laminar heat-transfer coefficients appear adequate for calculating skin temperature histories to Mach numbers on the order of 6.

3. Radiative heat transfer at Mach numbers of 10 can play an important role in the determination of peak skin temperature.

REFERENCES

1. Van Driest, E. R.: The Turbulent Boundary Layer for Compressible Fluids on a Flat Plate With Heat Transfer. Rep. No. AL-997, North American Aviation, Inc., Jan. 27, 1950.

2. Eckert, Ernst R. G.: Survey on Heat Transfer at High Speeds. WADC Tech. Rep. 54-70, Wright Air Dev. Center, U. S. Air Force, Apr. 1954.

3. Van Driest, E. R.: Investigation of Laminar Boundary Layer in Compressible Fluids Using the Crocco Method. NACA TN 2597, 1952.

4. Piland, Robert O.: Performance Measurements From a Rocket-Powered Exploratory Research Mi[redacted] a Mach Number of 10.4. NACA RM L54L29a, 1955.

[redacted]

FLIGHT CONDITIONS FOR MODEL TESTED
UP TO M=5.4

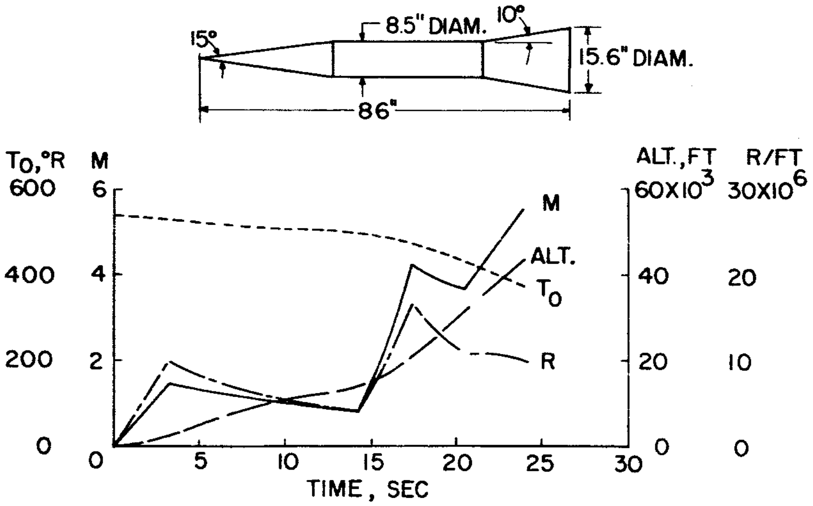

Figure 1

[redacted]

DECLASS [redacted]

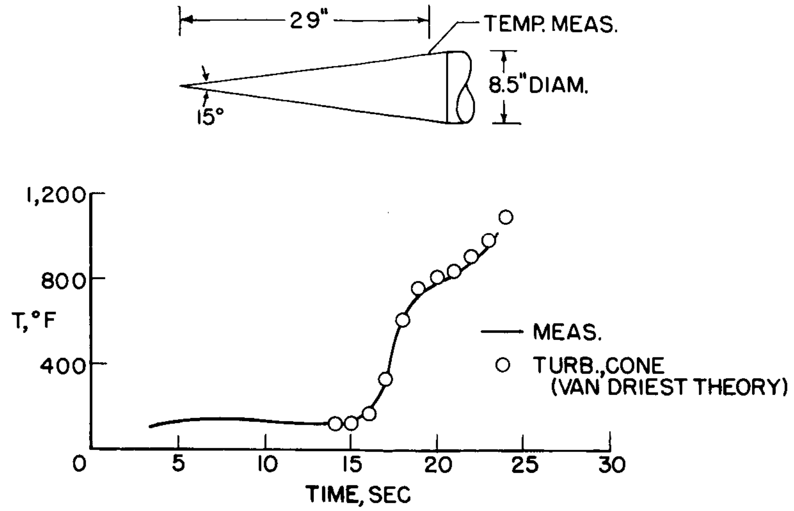
MEASURED AND CALCULATED TEMPERATURE HISTORY TO A MACH NUMBER OF 5.4

Figure 2

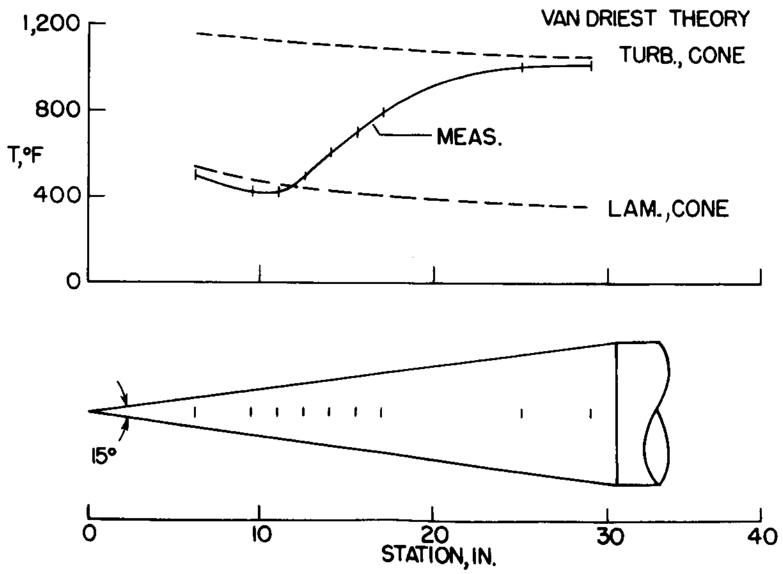
MEASURED AND CALCULATED TEMPERATURE DISTRIBUTION

FLIGHT TIME, 23.7 SEC; M = 5.4; R/FT = 9.8 x 10^6

Figure 3

[redacted]

FLIGHT CONDITIONS FOR MODEL TESTED UP TO M=10.4

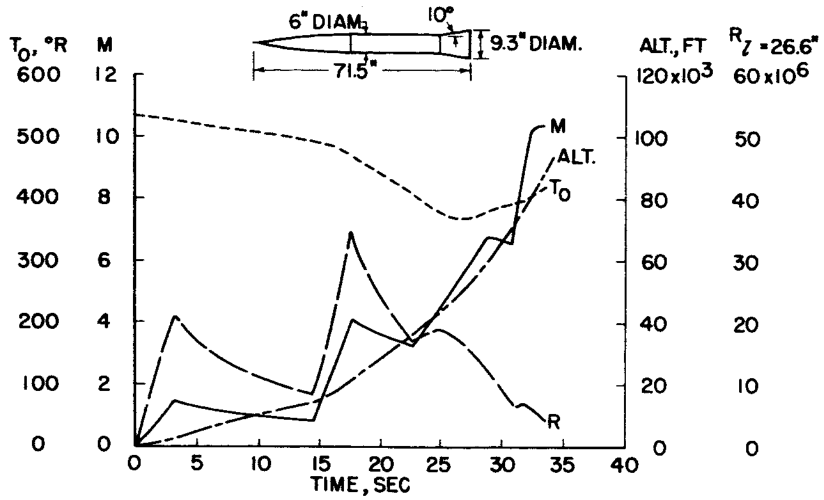

Figure 4

MEASURED AND CALCULATED TEMPERATURE HISTORY TO A MACH NUMBER OF 10.4

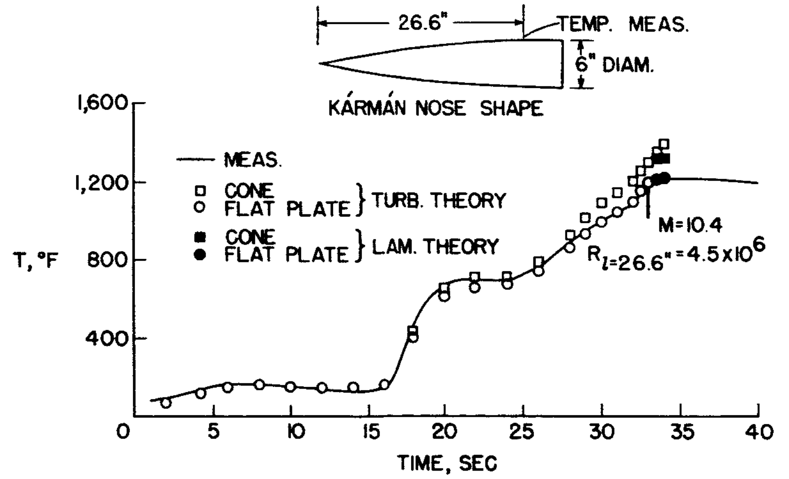

Figure 5

[redacted]

[redacted]

TENSILE PROPERTIES OF SOME SHEET MATERIALS UNDER RAPID-HEATING CONDITIONS

By George J. Heimerl and John E. Inge

Langley Aeronautical Laboratory

SUMMARY

Results are presented of some rapid-heating tests of some sheet materials - 7075-T6 and 2024-T3 (formerly 75S-T6 and 24S-T3, respectively) aluminum alloys, Inconel, and RS-120 titanium alloy - which are part of an investigation of a number of structural materials. The materials were tested at temperature rates from 0.2° F to 100° F per second under constant-load conditions. Yield and rupture temperatures, obtained under rapid-heating conditions, are compared with the tensile properties obtained under constant-temperature conditions for 1/2-hour exposure. Yield and rupture stresses are found to increase approximately in proportion to the log of the temperature rate except where effects such as aging altered the results. Master curves are presented for the determination of yield and rupture stresses and temperatures, which are based upon the use of a temperature-rate parameter derived from the data.

INTRODUCTION

Comparatively little is known about the properties of materials under rapid-heating conditions except for fairly recent tests of various materials by some investigators at temperature rates of hundreds of degrees or more per second (for example, refs. 1 to 5). This paper will cover some results of rapid-heating tests at relatively slow temperature rates up to 100° F per second for some sheet materials - 7075-T6 and 2024-T3 aluminum alloys, Inconel, and RS-120 titanium alloy - which are part of an investigation of a number of structural materials at the Langley Laboratory.

The rapid-heating test is a new kind of test and differs from the conventional stress-strain test. In the rapid-heating test, the load is held constant. The material is then heated at a constant temperature rate until failure occurs. In the stress-strain test, on the other hand, the temperature is held constant. After the material has been heated 1/2 hour or more at the test temperature, the load is then applied until failure takes place. Heating was accomplished in the rapid-heating tests

[redacted]

by passing an electric current through the specimen in such a manner as to obtain a constant temperature rate. Autographic strain and temperature-time records were obtained, and yield and rupture temperatures were determined for each test.

TEST RESULTS

The strain-temperature histories for the tests of 7075-T6 aluminum alloy under rapid-heating conditions are shown in figure 1. In this figure the strains, which include the elastic, thermal, and plastic strains, are plotted against the instantaneous temperatures for each test at the different stress levels and temperature rates. These rates varied from about 0.2° F to 100° F per second - a factor of about 500. The outstanding characteristic of these tests for this material is the regular family of curves obtained at each stress level for the different temperature rates when the material becomes plastic. As long as the material remains elastic, however, a single curve is obtained at each stress level regardless of temperature rate. This single curve coincides with the calculated thermal-expansion and change-in-elastic-modulus curve for the stress level. The extensions of these calculated elastic curves are shown by the dashed lines. A thermal-expansion curve is also shown in figure 1 which was obtained for the material after it had been repeatedly heated and cooled until the same curve was obtained on both heating and cooling. Yield temperatures at which 0.2-percent plastic flow occur are indicated by the tick marks; yield temperatures increase with the temperature rate in a very consistent manner.

Figure 2 shows the logarithmic nature of this increase in yield as well as in rupture temperatures for this material. The temperature rate is given by a logarithmic scale. The curves are faired through the test points and show that both yield and rupture temperatures increase approximately in proportion to the log of the temperature rate. This condition was also found to be the case for the other materials with certain specific exceptions, some of which will now be illustrated.

Figure 3 shows the effect of aging on the results for 2024-T3 aluminum alloy at 50 ksi. In this instance, all the test curves go more or less together up to yield, after which the individual curves fall into the normal pattern. Rupture temperatures follow a logarithmic relation but yield temperatures do not.

Another example of the effect of aging is shown in figure 4 for RS-120 titanium alloy at 75 ksi. In this case, the test results follow the usual pattern up to yield, but at higher temperatures the order of the curves is almost completely reversed. This behavior was not expected for this material in the stabilized annealed condition.

[redacted]

The last example (fig. 5) illustrates the unstable nature of the plastic flow obtained in the tests of Inconel at 28 ksi under rapid-heating conditions. Here, abrupt plastic flow occurs after intervals of more or less elastic action. In spite of this erratic behavior, yield temperatures appear to increase in regular fashion; this irregular behavior continued until near rupture. This type of action is associated with the development of Luder's lines.

COMPARISON OF RAPID-HEATING AND STRESS-STRAIN TESTS

Although rapid-heating and stress-strain tests are two distinctly different kinds of tests, comparisons can be made between results of such tests on the basis of yield and rupture or ultimate stresses at different temperatures. The comparative results for the yield stress for the aluminum alloys are shown in figure 6. The results of the rapid-heating tests are given by the solid lines for arbitrary temperature rates from 0.2° F to 100° F per second. The dashed lines give the tensile yield stress (0.2-percent offset) for 1/2-hour exposure obtained from the stress-strain test. The main result to be noted here is that the yield stress under rapid-heating conditions may be appreciably greater or about the same at a given temperature as that obtained from the stress-strain test for 1/2-hour exposure, depending on the temperature rate and the material. For the rapid-heating tests, the effect of increase in temperature rate levels off markedly for rates above about 60° F per second.

A comparison of the rapid-heating and stress-strain results for these same materials for rupture and ultimate stress is given in figure 7. The comparisons are very similar to those found for the yield shown in figure 6. Rupture temperatures, however, run from 20° F to 60° F higher than those for yield. As in the case of yield, the increase in rupture stress becomes very small for temperature rates above 60° F to 100° F per second. Similar comparisons between rapid-heating and tensile-test results for Inconel and RS-120 titanium alloy have not been completed.

MASTER YIELD AND RUPTURE CURVES

A temperature-rate parameter was derived from the data, which was based upon the logarithmic relationship between yield and rupture temperatures and the temperature rate previously shown. With this parameter, it was found possible to reduce the results of the rapid-heating tests to a single or master curve in plots of stress against the parameter.

The correlation of the data with the master curves for the two aluminum alloys is shown in figure 8. In this parameter, T applies either to the yield or rupture temperature in °F, and h is the temperature rate in °F per second; the additional numbers in the numerator and denominator are temperatures and temperature-rate constants, respectively. The validity of the parameter is shown by the correlation of the data with the master curves. Very good correlations were obtained in general for yield for both materials and fairly good correlation for rupture. Yield and rupture temperatures, calculated by means of the master curve and the parameter for the different stress levels, are in very close agreement with the test values, especially for the 7075-T6 aluminum alloy.

Figure 9 shows the correlation of the test points with the master curves for yield and rupture for Inconel and RS-120 titanium alloy. Good correlations were obtained for yield for Inconel and the titanium alloy except at 50 ksi for the latter where the parameter does not hold. Fairly good correlation was obtained for rupture for these materials except in the regions where aging affected the results.

CONCLUDING REMARKS

Although the rapid-heating tests for some of the materials have not been completed, the results obtained so far indicate, in general, that yield and rupture temperatures increase logarithmically with temperature rates below 100° F per second except for certain regions or stress levels for some of the materials. This increase levels off markedly for temperature rates from about 60° F to 100° F per second. Under rapid-heating conditions, materials may be stronger than indicated by conventional tensile data for 1/2-hour exposure, but the relative strength varies with the temperature rate and the material. At the present time, no theory is available for the complex transient behavior of materials under rapid-heating conditions. The use of master yield and rupture curves, however, employing a suitable temperature-rate parameter, affords a possible convenient method for determining yield and rupture stresses and temperatures for different temperature rates. In any case, adequate data are required for each material in order to establish such curves and the limitations of the parameter.

[redacted]

REFERENCES

1. Cross, H. C., McMaster, R. C., Simmons, W. F., and VanEcho, J. A.: Short-Time, High-Temperature Properties of Heat-Resisting Alloy Sheet. Project RAND (USAF Project MX-791) RA-15077, Douglas Aircraft Company, Inc., Feb. 27, 1948.

2. Smith, W. K., Wetmore, W. O., and Woolsey, C. C., Jr.: Tensile Properties of Metals While Being Heated at High Rates. NAVORD Rep. 1178, Pt. 1 (NOTS 234), U. S. Naval Ord. Test Station (Inyokern, Calif.), Sept. 7, 1949.

3. Smith, W. K., Woolsey, C. C., Jr., and Wetmore, W. O.: Tensile Properties of Metals While Being Heated at High Rates. Pt. 2 - Aluminum Alloys. NAVORD Rep. 1178 (NOTS 319), U. S. Naval Ord. Test Station, Inyokern (China Lake, Calif.), Sept. 1, 1950.

4. Smith, W. K., Woolsey, C. C., Jr., and Wetmore, W. O.: Tensile Properties of Metals While Being Heated at High Rates. Pt. 3 - Comparison of Results From High-Heating-Rate Tests With Results From Rocket Firing Tests. NAVORD Rep. 1178 (NOTS 336), U. S. Naval Ord. Test Station, Inyokern (China Lake, Calif.), Dec. 20, 1950.

5. Smith, W. K.: High-Heating-Rate Strength of Titanium and Two Titanium Alloys. NAVORD Rep. 1958 (NOTS 526), U. S. Naval Ord. Test Station, Inyokern (China Lake, Calif.), Apr. 10, 1952.

[redacted]

DECLASSI[redacted]

STRAIN-TEMPERATURE CURVES FOR 7075-T6 ALUMINUM ALLOY

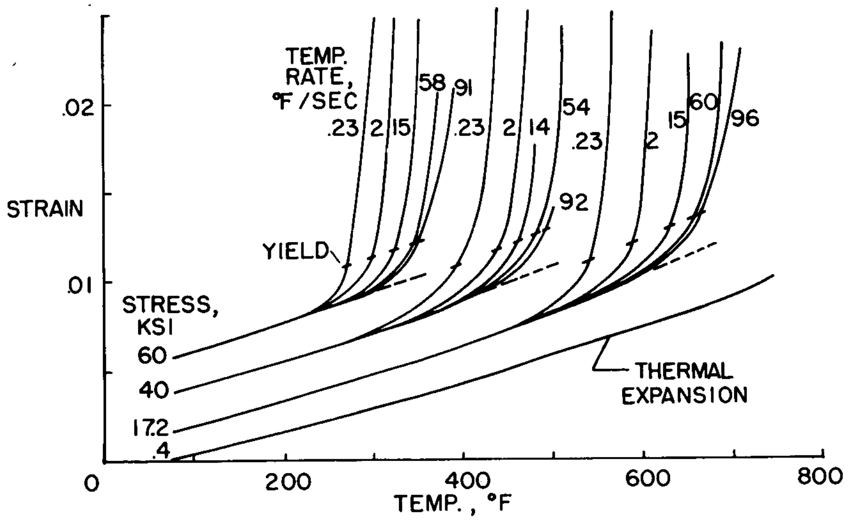

Figure 1

YIELD AND RUPTURE TEMP. FOR 7075-T6

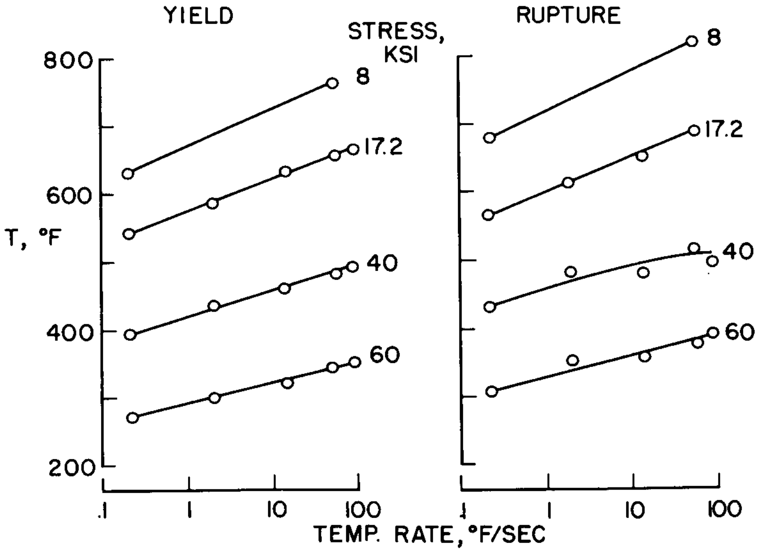

Figure 2

[redacted]

[redacted]

AGING OF 2024-T3 ALUMINUM ALLOY
AT 50 KSI

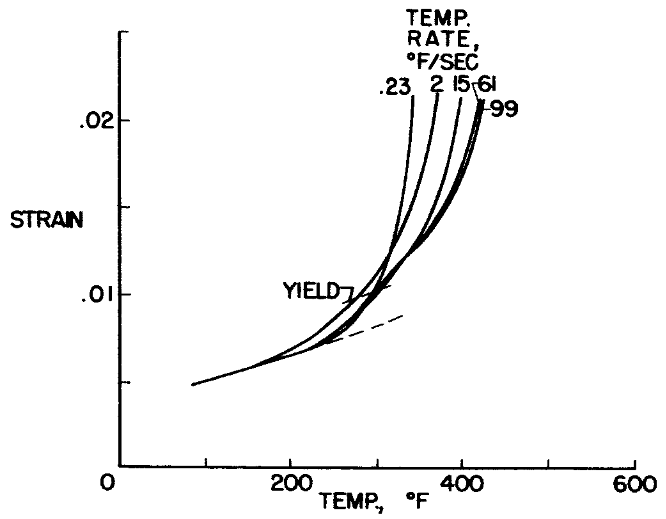

Figure 3

AGING OF RS-120 TITANIUM ALLOY AT 75 KSI

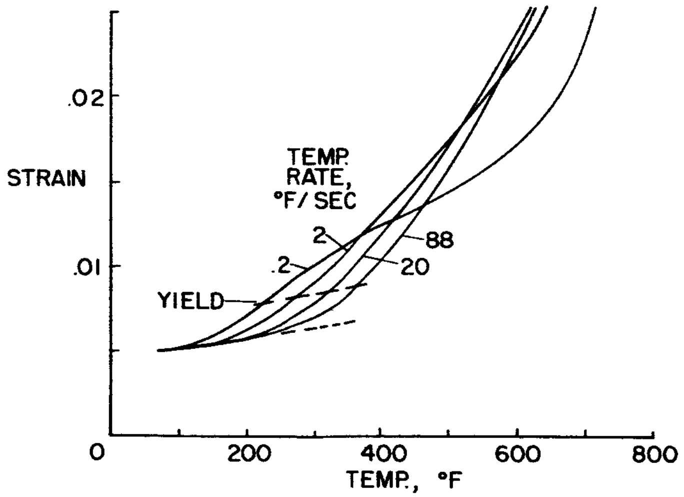

Figure 4

[redacted]

DECLASSI[redacted]

UNSTABLE PLASTIC FLOW OF INCONEL AT 28 KSI

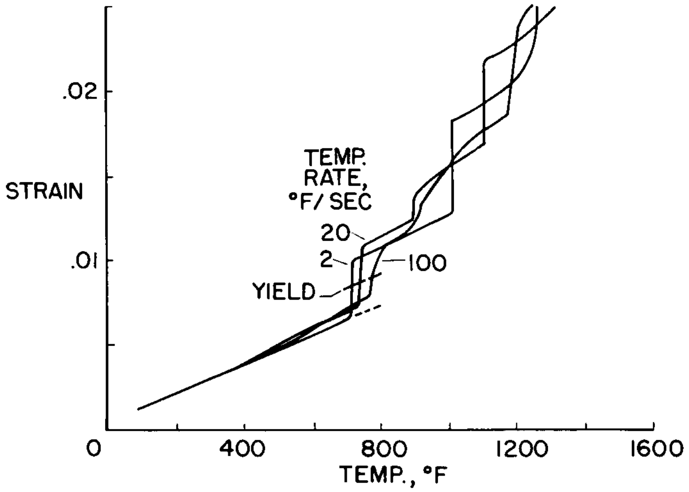

Figure 5

COMPARISON OF RAPID-HEATING AND STRESS-STRAIN RESULTS FOR YIELD

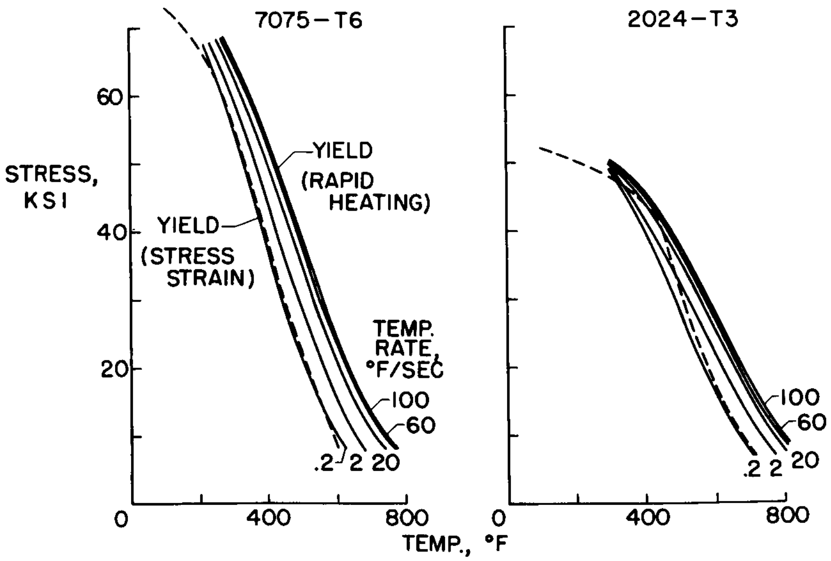

Figure 6

[redacted]

[redacted]

COMPARISON OF RAPID-HEATING AND STRESS-STRAIN RESULTS FOR RUPTURE AND ULTIMATE

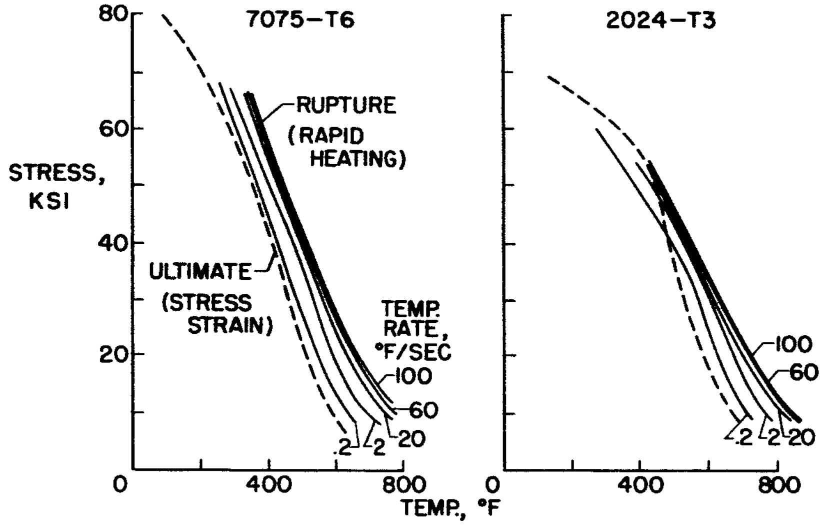

Figure 7

MASTER CURVES FOR YIELD AND RUPTURE

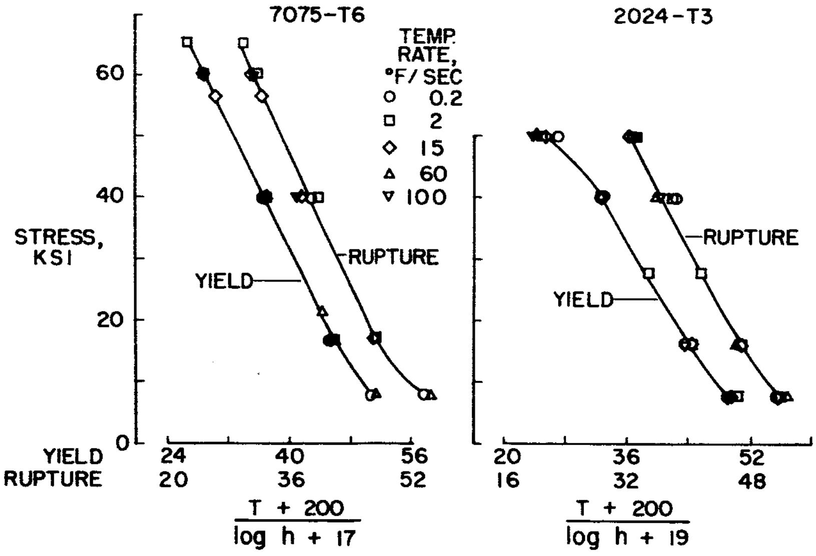

Figure 8

[redacted]

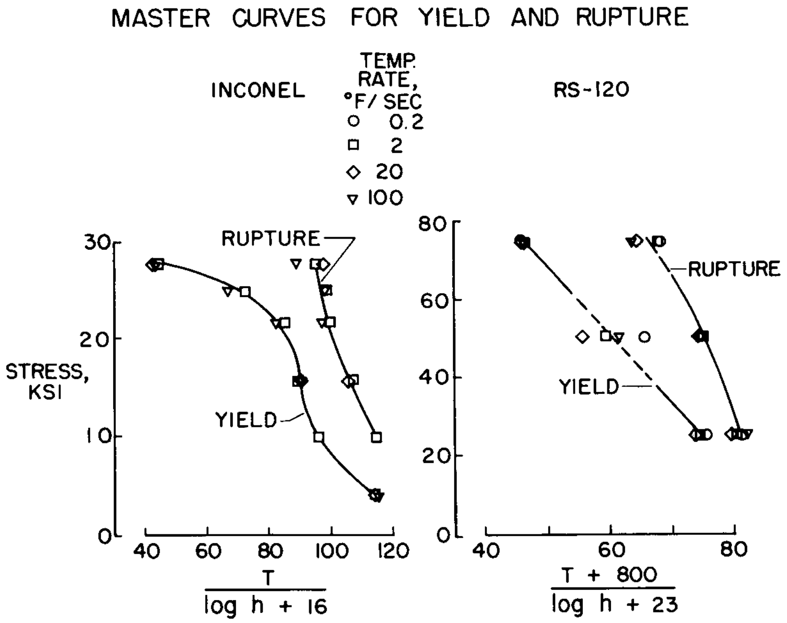

Figure 9

[redacted]

[redacted]

PRELIMINARY INVESTIGATION OF THE COMPRESSIVE STRENGTH AND CREEP LIFETIME OF 2024-T3 (FORMERLY 24S-T3) ALUMINUM-ALLOY PLATES AT ELEVATED TEMPERATURES

By Eldon E. Mathauser and William D. Deveikis

Langley Aeronautical Laboratory

SUMMARY

The results of elevated-temperature compressive strength and creep tests of 2024-T3 (formerly 24S-T3) aluminum-alloy plates supported in V-grooves are presented. For determining elevated-temperature strength, where creep effects are negligible, a relation previously developed for predicting plate compressive strength at room temperature was satisfactory. Creep-lifetime results are presented for the plates in the form of master creep-lifetime curves by using a time-temperature parameter that is convenient for summarizing tensile creep-rupture data. A comparison is made between tensile and compressive creep lifetime for the plates, and the magnitude by which the design stress is decreased because of material creep and loss of strength due to exposure at elevated temperatures is indicated.

INTRODUCTION

Since plates are one of the most important load-carrying components in the structure of an aircraft, knowledge of the elevated-temperature strength and creep behavior is becoming increasingly important. At the present time very little published information is available on the experimental maximum strength of plates at elevated temperatures (ref. 1), and no data have been found on experimental creep behavior of such members. In order to obtain such information, the National Advisory Committee for Aeronautics has recently made an experimental study of both compressive strength and creep lifetime of 2024-T3 aluminum-alloy plates at elevated temperatures.

In this investigation, the unloaded edges of the plates were supported in V-grooves. This type of support was used because room-temperature strength tests of plates supported in V-grooves showed good correlation with experimental plate strengths obtained from stiffened panel and box-beam tests. Width-thickness ratios ranging from 20 to 60 were investigated. A hydraulic testing machine was used to apply load in the compressive-strength te[redacted] creep tests a constant dead load was applied.

MATHAUSER &
DEVEIKIS

SYMBOLS

b	width, in.
C	constant
E_{SEC}	secant modulus, ksi
t	thickness, in.
t_{cr}	failure time, hr
T_R	temperature, $^{\circ}R$
σ_{cy}	0.2-percent-offset compressive yield stress, ksi
$\bar{\sigma}_f$	average stress at maximum load, ksi
μ	Poisson's ratio

RESULTS AND DISCUSSION

Compressive-Strength Tests

Test results.- An example of the results that were obtained which illustrates the behavior of the plates and the material when subjected to compressive loading is shown in figure 1. Average stress is plotted against unit shortening of the plates. Results are shown for plates tested at 400° F for width-thickness ratios of 20, 30, 45, and 60. The material compressive stress-strain curve is indicated by the dashed line.

For the plate of width-thickness ratio of 20, the maximum stress exceeded the 0.2-percent-offset compressive yield stress indicated by the tick mark before collapse occurred at about 0.8-percent shortening. Buckling and collapse of this plate as well as the plate of $b/t = 30$ occurred almost simultaneously. The plates of $b/t = 45$ and 60 buckled elastically, and considerable shortening occurred after buckling before maximum load was obtained. Maximum loads for plates of $b/t = 30, 45,$ and 60 were reached at approximately the same value of unit shortening, in this case about 0.4 percent.

The maximum stresses obtained in these tests at 400° F and in similar tests at other temperatures are shown in figure 2. Average stress at

[redacted]

[redacted]

maximum load is plotted against temperature in $^{\circ}$F. The curves represent the predicted maximum strength of the plates. Test results are indicated by the symbols. The method used for determining plate strength will be discussed later. Results are given for width-thickness ratios of 20, 30, 45, and 60 for temperatures ranging from room temperature to 600° F.

All plates were exposed to the test temperature for 1/2 hour before application of load. Several plates of each proportion were tested at room temperature and 400° F. The results at these two temperatures give an indication of the scatter that can be expected in the test data at the other temperatures. The increase in compressive strength produced by artificial aging of the aluminum alloy accounts for the increased strength of the plates in the vicinity of 400° F.

Prediction of plate compressive strength.- In determining the plate compressive strength at elevated temperatures, use was made of a relation that has been developed in a previous study for correlating plate compressive strength with material properties (ref. 2). This relation, shown in figure 3, defines the average stress at maximum load as follows:

$$\bar{\sigma}_f = C\sqrt{\frac{E_{SEC}\sigma_{cy}}{1 - \mu^2}}\,\frac{t}{b}$$

where C is a constant for all materials at any temperature, the quantities within the square-root sign are material properties, and the remaining term is plate geometry. The secant modulus E_{SEC} and Poisson's ratio μ are associated with the average stress at maximum load. The 0.2-percent-offset compressive yield stress σ_{cy} is indicated by the tick mark, and t/b is the plate thickness-width ratio.

This plate-compressive-strength relation indicates that, if the average stress at maximum load is divided by the term containing material properties and if this quantity is then plotted against the plate thickness-width ratio, a straight line will be obtained. The slope of this line determines the constant C. Figure 4 shows this type of plot in which the average stress at maximum load divided by the material parameter is plotted against the plate thickness-width ratio. Results obtained from a previous study of room-temperature compressive strength of plates of magnesium alloy, three aluminum alloys, and stainless steel are shown by the solid symbols. The value of C (fig. 3), determined from the slope of a straight line passing through the origin and the solid symbols, is equal to 1.51.

[redacted]

Since the elevated-temperature plate compressive strengths obtained in the present study and shown by the open symbols in figure 4 also lie essentially along the same line, the same value of C applies to these results. It thus appears that plate compressive strengths can be estimated satisfactorily from the previous strength relation for all materials at either room or elevated temperatures. Only the material compressive stress-strain curve at the corresponding temperature and exposure time is required in predicting the plate strength.

Creep Tests

Test results.- Creep test results were obtained for temperatures of 400°, 450°, and 500° F. The applied load in most cases produced creep failure of the plates within 6 hours after loading. Some typical plate creep curves are shown in figure 5 in which unit shortening is plotted against time in hours. These results were obtained for plates of width-thickness ratio of 20 exposed to test temperature for 1/2 hour before loading. The applied stress is shown for each plate, as well as the ratio of the applied stress to the stress that would produce immediate failure upon loading.

The applied stress for the plates that failed within 5 hours was a substantial percentage of stress that would produce immediate failure at 400° F. The plate with applied stress of 31.5 ksi failed in 33.8 hours. For the plates that failed within 5 hours, constant or secondary creep rate existed for only a small portion of the plate lifetime, whereas the plate with applied stress of 31.5 ksi exhibited constant creep rate for approximately 75 percent of the total lifetime.

These creep test results for $b/t = 20$ resemble the results obtained for other values of b/t at 400° F and for other test temperatures. Failure of the plates occurred in most cases at a value of shortening somewhat greater than the shortening obtained at maximum load in the compressive-strength tests. For example, for the results shown in figure 5, failure occurred soon after the shortening reached 0.8 percent, which corresponds to the shortening obtained at maximum load in the compressive-strength test for $b/t = 20$ given in figure 1.

The most significant information obtained from the creep tests is the lifetime. Lifetimes obtained from these tests and from similar tests at 400° F for other values of b/t are plotted in figure 6. In this figure, applied stress is plotted as open symbols for each value of b/t. The maximum strength of the plates determined from the compressive-strength tests is shown by the solid symbols on the vertical axis. Lines representing an average of the test results have been drawn through the data for each value of b/t. The relatively small amount of scatter in these data indicates that plate creep lifetime is not sensitive to initial imperfections since no attempt was made to control these imperfections in selecting the test specimens.

Comparison between tensile and compressive creep lifetime.- A comparison between the tensile-rupture lifetime of 2024-T3 aluminum alloy and the creep lifetime is made in figure 7. Applied stress is plotted against time. The symbols indicate creep-lifetime results for plates of $b/t = 20$ at 400°, 450°, and 500° F. The curves show tensile creep-rupture data for the material obtained from the literature (for example, see ref. 3). Since all test points appear on or above the corresponding tensile creep-rupture curves, it can be noted that a plate of width-thickness ratio of 20 will support a given load, either tensile or compressive, for approximately the same time. The implication of this result is that members such as box beams having equal-thickness cover plates with proportions of b/t of 20 will be of balanced design in the range from 400° F to 500° F; that is, the tension and compression covers will have approximately equal resistance to creep failure. This result has been verified experimentally from creep tests of three box beams tested at 375° F and 425° F (ref. 4). Two of the beams failed in tension and one failed in compression.

Master creep-lifetime curves.- Since the plate creep test results for $b/t = 20$ parallel tensile creep-rupture data, the use of a time-temperature parameter is suggested for presenting all the plate creep-lifetime results. One of the available time-temperature parameters (ref. 5) was used for plotting the test data as shown in figure 8.

Stress is plotted against the time-temperature parameter $T_R\left(17 + \log t_{cr}\right)$ where T_R is temperature in °R, 17 is a material constant, and t_{cr} is failure time in hours. The curve that predicts tensile creep rupture for the material is shown by the dashed line. Plate creep-lifetime results obtained for three test temperatures and four plate proportions are shown. The curves drawn through the plate creep data indicate an average value of the test results.

For $b/t = 20$ the results appear near the tensile-rupture curve and again indicate that a plate of this proportion will support a given load, either tensile or compressive, for approximately the same time. For the other values of b/t, the plates will fail sooner in compression than in tension. This type of plot is convenient for estimating failure time of the plates for stress and temperature combinations within the range of the tests. The results at one temperature overlap those obtained at the other temperatures and thus interpolation is justified.

Comparison of maximum compressive stresses and creep-failure stresses.- One additional result that will be discussed concerns the compressive strength of the plates after a given exposure time and the stresses that will produce creep failure of the plates in a corresponding time. Such a comparison is made in figure 9 in which stress is plotted against time in hours. The square symbols indicate the experimental compressive strength of the plates obtained by first exposing the specimens to the test temperature for the times shown in the abscissa and then loading to maximum strength. The predicted compressive strength for a similar range of exposure times is indicated by the dashed line. The solid line drawn through the circles indicates an average of the plate creep-lifetime results shown previously in figure 6. For this case, load was applied and maintained on the specimens until creep failure occurred.

This comparison of maximum compressive stresses and creep-failure stresses indicates the magnitude by which the design stress is reduced below the maximum strength because of material creep for times ranging up to 100 hours. Comparable results were obtained for other values of b/t and other test temperatures. Many materials do not exhibit marked changes in compressive strength with exposure time; consequently, results such as these may be obtained only with aluminum alloys for the temperature range investigated.

CONCLUDING REMARKS

In summary, experimental results from elevated-temperature strength and creep tests of aluminum-alloy plates supported in V-grooves have been presented. A relation previously developed for predicting plate compressive strength at room temperature was satisfactory for determining elevated-temperature strength. The creep test results indicate that plates of width-thickness ratio of 20 will support a tensile or compressive load for approximately the same time and that the plate creep-lifetime results for the temperature range investigated can be presented by using time-temperature parameters that are convenient for summarizing tensile creep-rupture data. In addition, a comparison was made to indicate the magnitude by which the design stress is decreased in plates because of material creep and loss of strength due to exposure at elevated temperature.

[redacted]

REFERENCES

1. Heimerl, George J., and Roberts, William M.: Determination of Plate Compressive Strengths at Elevated Temperatures. NACA Rep. 960, 1950. (Supersedes NACA TN 1806.)

2. Anderson, Roger A., and Anderson, Melvin S.: Correlation of Crippling Strength With Changes in Material Properties. (Prospective NACA paper.)

3. Dorn, J. E., and Tietz, T. E.: Creep and Stress-Rupture Investigation on Some Aluminum Alloy Sheet Metals. Preprint 26, A.S.T.M., 1949, pp. 1-17.

4. Mathauser, Eldon E.: Investigation of Static Strength and Creep Behavior of an Aluminum-Alloy Multiweb Box Beam at Elevated Temperatures. NACA TN 3310, 1954.

5. Larson, F. R., and Miller, James: A Time-Temperature Relationship for Rupture and Creep Stresses. Trans. A.S.M.E., vol. 74, no. 5, July 1952, pp. 765-771.

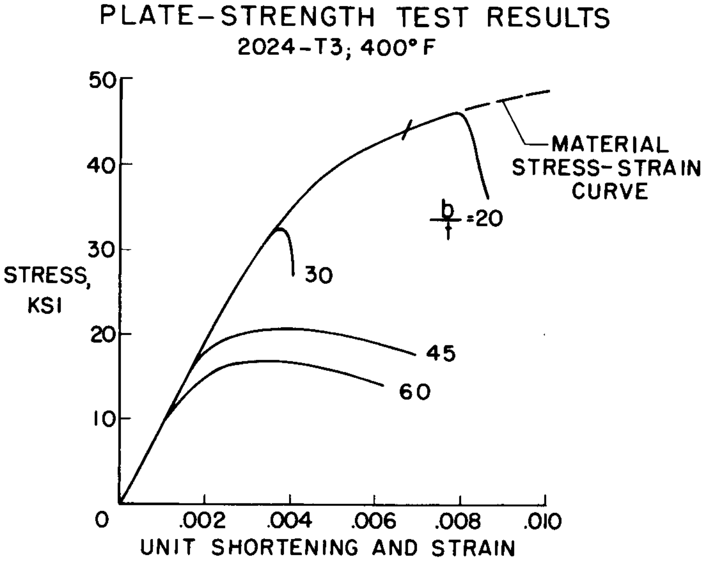
PLATE-STRENGTH TEST RESULTS
2024-T3; 400° F

Figure 1.

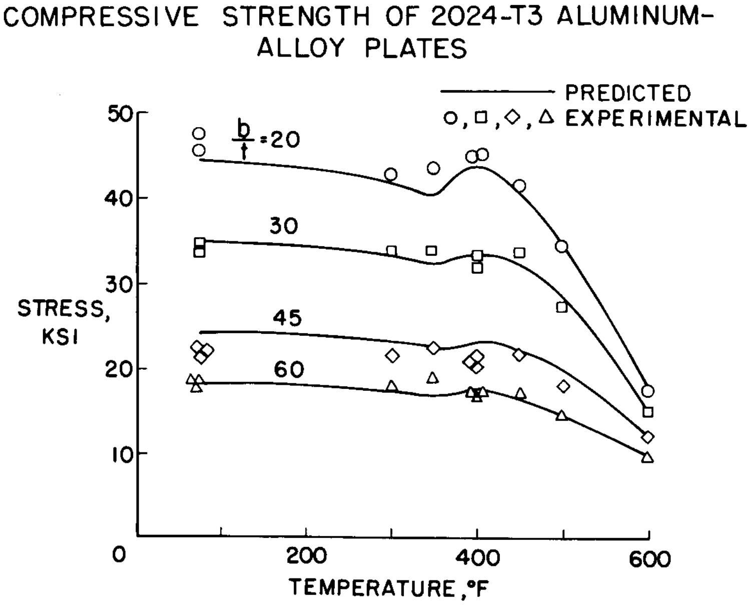
COMPRESSIVE STRENGTH OF 2024-T3 ALUMINUM-ALLOY PLATES

Figure 2.

[redacted]

[redacted]

[redacted]

RELATION FOR PREDICTING PLATE COMPRESSIVE STRENGTH

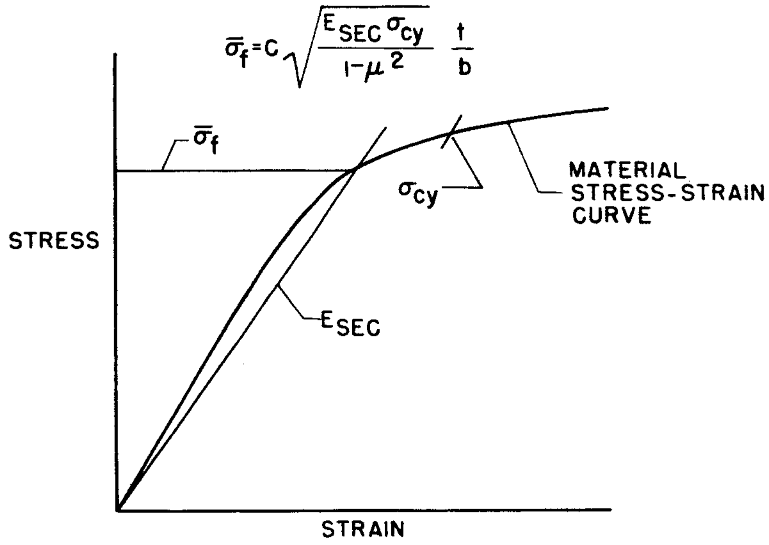
$\bar{\sigma}_f = C\sqrt{\frac{E_{SEC}\sigma_{cy}}{1-\mu^2}}\ \frac{t}{b}$
$\bar{\sigma}_f$
σ_{cy}
MATERIAL STRESS-STRAIN CURVE
STRESS
E_{SEC}
STRAIN

Figure 3.

CORRELATION OF STRENGTH WITH MATERIAL PROPERTIES

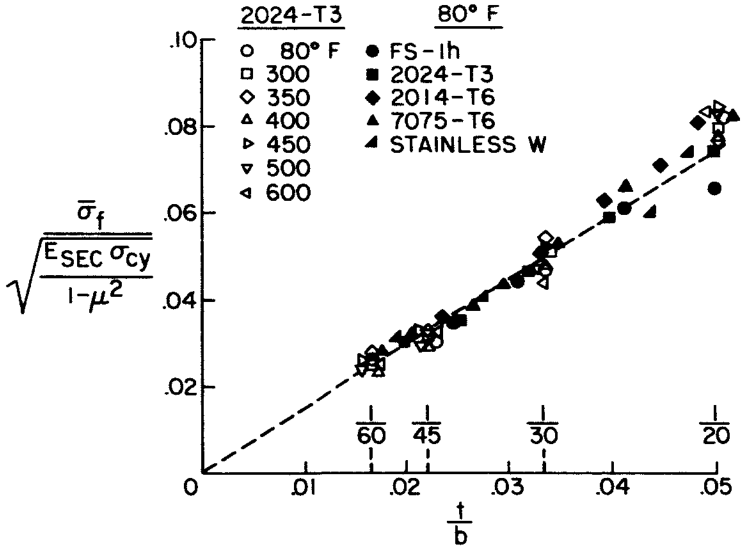

Figure 4.

[redacted]

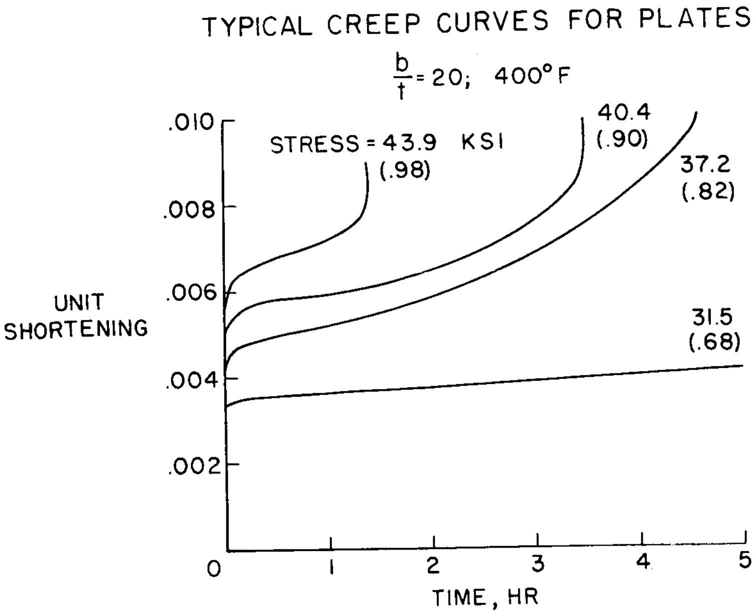

Figure 5.

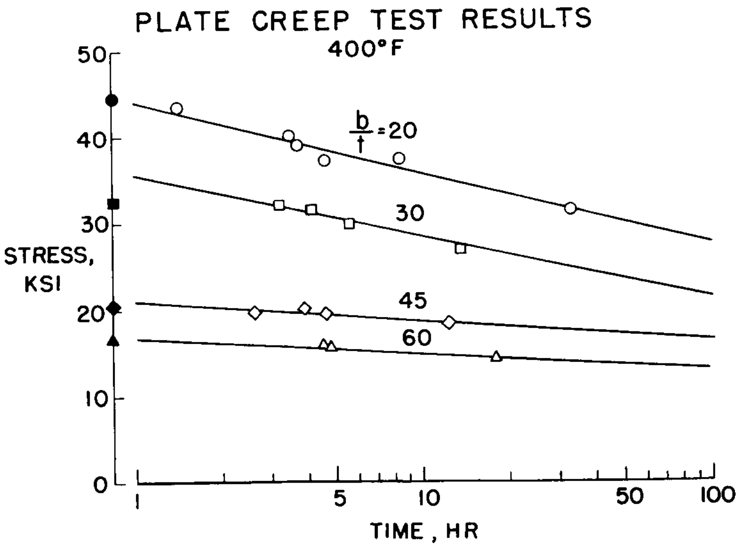

Figure 6.

[redacted]

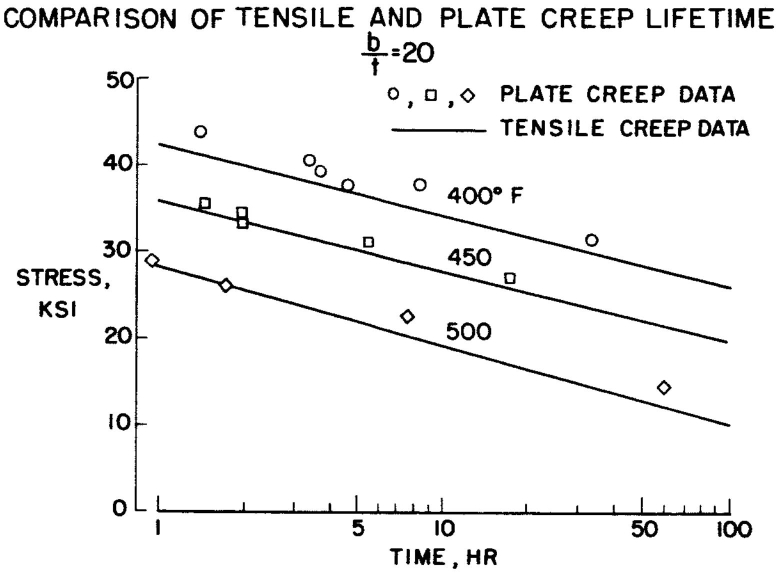

Figure 7.

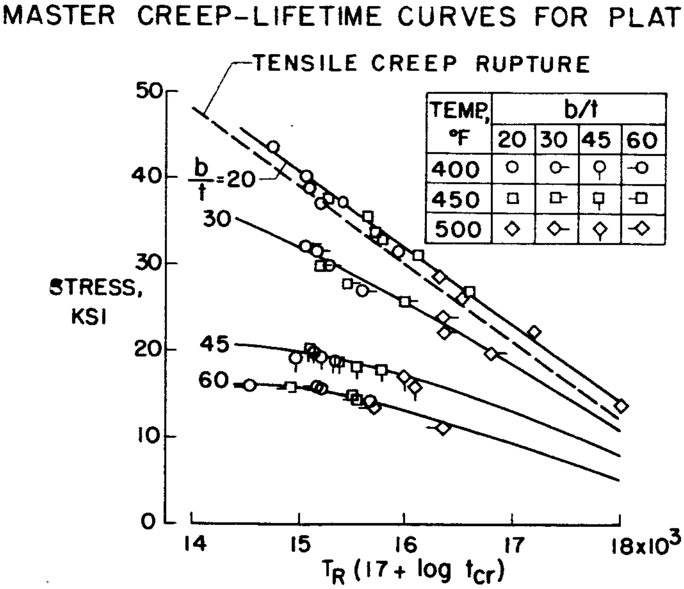

Figure 8.

[redacted]

[redacted]

COMPARISON OF COMPRESSIVE STRENGTH AND CREEP LIFETIME

$\frac{b}{t} = 20$; 400°F

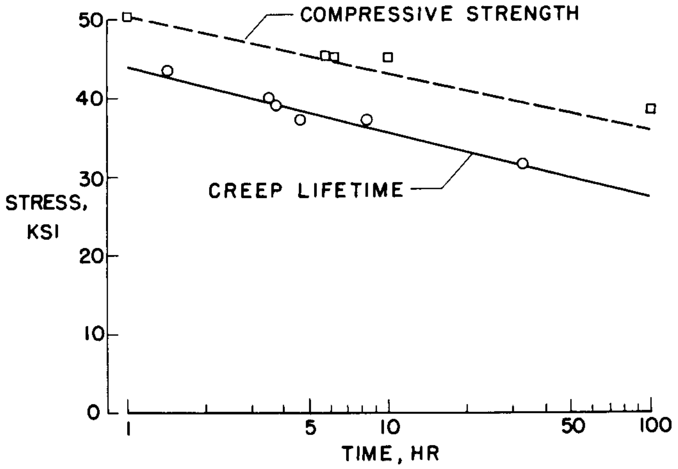

Figure 9

[redacted]

[redacted]

SOME EFFECTS OF RAPID HEATING ON BOX BEAMS

By Richard A. Pride and L. Ross Levin

Langley Aeronautical Laboratory

When a complex shell structure, such as an aircraft, is heated rapidly, a number of problems arise. The present paper describes the results of laboratory tests (see ref. 1) in which specimens simulating wing structures were subjected to heating rates of the order of magnitude encountered in extreme aerodynamic heating or in the vicinity of an atomic explosion. Heating rates up to about 100 Btu/sq ft/sec could be achieved in the laboratory with radiant-heating apparatus, but it was found that the effects on the specimens tested were essentially the same when considerably lower heating rates were employed.

A typical test consisted of applying a static bending load on an aluminum box beam to develop a predetermined load stress in the skin. Then, while this bending load was held constant, rapid heating was applied to the skins until failure occurred or until a maximum skin temperature of 600° F was reached. Figure 1 shows the large nonuniformity in temperatures that was created at representative points in a multiweb beam with a relatively thick skin. These temperatures were reached in 5 seconds with a skin heating rate of 29 Btu/sq ft/sec. As can be seen, the temperature of the internal structure lags far behind the skin temperature and, consequently, large thermal stresses result. When these stresses reach sufficient magnitude, thermal buckling of the skins occurs, as shown in figure 2 which is a photograph of one of the beams after it had been exposed to rapid skin heating. The buckles produced are permanent and are of large amplitude even when heating was terminated shortly after buckling occurred.

To study the effects of rapid heating on the load-carrying ability of these beams, tests were run at three values of bending load. Figure 3 presents the temperature-deflection history for two of these beams after the bending load stresses had been applied. As shown in the schematic diagram, the beam is loaded with a bending moment and then heated rapidly on both skins. Here the change in tip deflection is plotted against the average skin temperature. Note that, under constant load at the 9.8 ksi level, as the temperature increases, a slight change in deflection occurs due to the change in material stiffness. At a critical value of skin temperature, the difference between the skin temperature and the internal-structure temperature is large enough to produce sufficient thermal stress which, in combination with the 9.8 ksi load stress, buckles the skin. A marked increase in beam deflection is then evident with further heating. For the 22 ksi load stress, a much smaller temperature difference between skin and webs is required to produce the

[redacted]

thermal stress needed for buckling. The increase in deflection after buckling, in both cases, occurs because buckling of the compression skin reduces the effective stiffness of that side of the beam so that a structure of unsymmetrical stiffness is created. When such a structure is uniformly heated on both surfaces, it bends much like the familiar bimetallic strip. In the case of the beam, however, the bending is not due to different coefficients of expansion but is due to unequal resistance of the two skins to the thermal stresses being built up.

At the higher load-stress level, material plasticity in the buckled skin introduces further dissymmetry in stiffness, and deflections occur at an increasing rate as the temperature rises. At the peak temperature, heating was terminated; but because of the high stress level and temperature, 22 ksi and 511° F, respectively, failure occurred due to material creep before the beam cooled down. At the lower stress level, failure did not occur although enough plastic deformation of the buckled skin evidently took place to leave a permanent set in bending.

An important conclusion to be drawn from rapid-heating tests of this type is that the occurrence of thermal buckling in primary structures will lead to large distortions which will increase under constant external loads. It becomes important, therefore, to be able to predict the combinations of thermal stress and load stress which will cause buckling of a given structural component.

Figure 4 presents a buckling interaction relation for these beams. The average temperature difference between skin and webs required to cause buckling is plotted against applied load stresses, and a buckling interaction curve can be drawn. Combinations of temperature difference and load stress which lie below the curve will not produce buckling, and the combinations above the curve will result in a buckled structure. It can be seen that, for this particular structure, large nonuniformities in temperature cannot be tolerated at any load-stress level. The curve is calculated from the equation given in figure 4. This equation was derived from a simplified buckling analysis which assumes that average values of thermal stress in the skin can be superposed on the load stress. In the equation, σ_{cr} is the skin buckling stress, and σ_L is the compressive stress in the skin produced by the applied bending moment. The coefficient of thermal expansion is α and E_S is the material modulus of the skin which varies with temperature. The term $E_S A_S / E_W A_W$ is the ratio of the axial stiffness of the skin and webs. Similar curves can be calculated for any other beam proportion, and the shape of the curve will vary somewhat, depending upon the changes in beam material properties with stress and temperature.

The validity of this simplified analysis is borne out by the results of the rapid-heating tests of beams statically loaded in bending to different stress levels. The average temperatures in skins and webs which resulted in buckling were measured and these temperature differences are represented by the circles in figure 4. The agreement with the temperature predictions is as good as with the room-temperature prediction.

With regard to the ultimate strength of the beams under rapid-heating conditions, failures occurred by compressive crippling of the skin. Good agreement was found between experimental failing stresses and those calculated by taking into account the loss in material properties at the elevated temperatures. To obtain the best agreement it was necessary to take into account the rate at which properties are lost when the material is rapidly heated. Although thermal stresses had a profound influence on the buckling loads, no failures occurred until temperatures had been reached at which a strength calculation would predict failure with no consideration of thermal stress. Therefore, it was concluded that thermal stress produced no measurable effect on the ultimate strength of these beams.

Although high skin temperatures cannot be avoided during exposure to extreme heating conditions, some relief from the effect of temperature gradients can be obtained through redesign of the internal structure of the thick-skin type of construction. Such a structure would permit expansion of the heated skin without large build-ups in thermal stress. Figure 5 shows one type of structure which permits nearly free expansion of the cover skins. With the skin attached to corrugated webs at the crests of the corrugations, very little restraint is offered to in-plane movements of the skin. Only slightly greater restraint would exist if continuous connection angles of small cross-sectional area were used in place of clips, and structural efficiency comparable to the best conventional multiweb construction could be obtained.

In figure 6, the behavior of a corrugated-web beam under a rapid-heating test at constant load is compared with one of the channel-web beams previously discussed. Again, change in tip deflection is plotted against average skin temperature. These two tests were run with the same load-stress level and nearly identical heating rates. The corrugated-web beam was fabricated to be nominally the same as the channel-web beam, with the channel webs replaced by equal-weight corrugated webs at the same web spacing. No evidence of buckling was detected in the corrugated-web beam prior to failure. As a result, the change in deflection at a given skin temperature was much less than for the channel-web beam which had buckled at this point. The deflection which did occur could be accounted for by the changes in material stiffness with temperature. Failure again occurred by compressive crippling of the skin due to loss of material properties.

Thus, by redesigning internal structure to permit expansion of the hot skins, thermal stresses resulting from large temperature gradients in wings can be alleviated. With thermal stresses alleviated, the rate of heating to a temperature is no longer detrimental to the structure, and buckling and maximum strength become merely functions of the material properties at temperature.

Rapid-heating tests similar to those conducted on thick-skin construction also have been made on beams simulating thin-skin—stringer-rib construction. At heating rates comparable to those used for the thick-skin beams, skin temperatures approaching the melting temperature of the material were encountered. For such a construction, softening or melting of the thin skin overshadowed the other effects, such as thermal buckling and beam deflections. Although the skin shielded the primary internal structure from the heat, the major factor leading to failure for the thin-skin construction was found to be the extreme skin temperature encountered.

In summary, this paper has discussed some of the effects which occur when beams simulating thick-skin wing structures are subjected to rapid skin heating. Large deflections were noted with heating after buckling, due to the dissymmetry of the buckled beam. A simplified buckling analysis was presented which predicts the combinations of temperature difference and load stress required to cause buckling. Thermal stresses appeared to have no measurable effect on the ultimate strength of these beams. By redesign of the internal structure to permit expansion of the skins, thermal stresses were alleviated and the rate of heating was no longer detrimental to skin buckling. Similar tests on thin-skin construction indicated that, while thermal buckling did occur, the major factor leading to bending failures was the extreme skin temperature encountered.

REFERENCE

1. Pride, Richard A.: An Investigation of the Effects of Rapid Skin Heating on Box Beams Loaded in Bending. NACA RM L55B03, 1955.

[redacted]

[redacted]

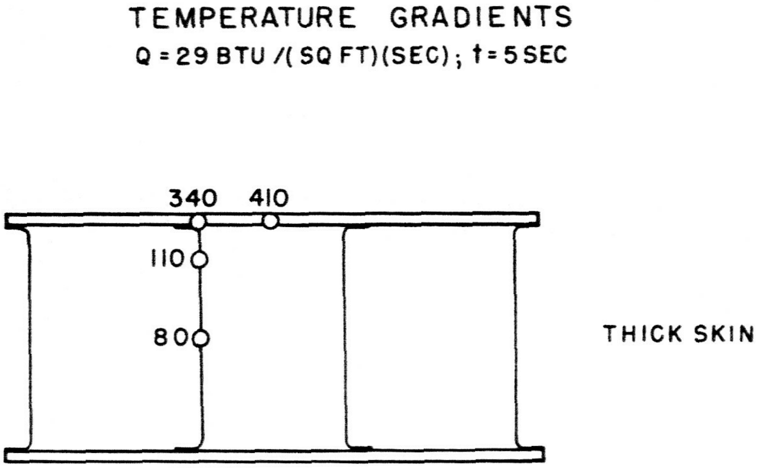

Figure 1

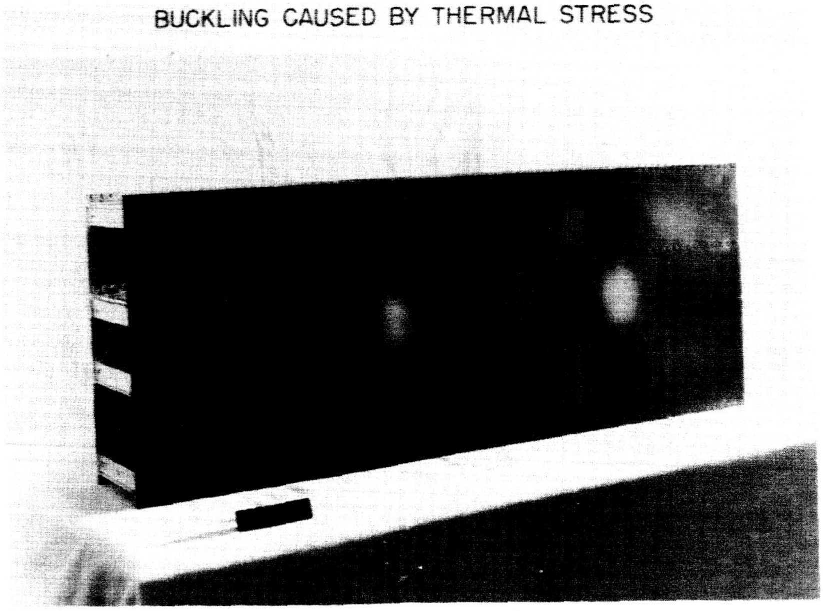

Figure 2

[redacted]

[redacted]

DECLASSIFIED

TEMPERATURE-DEFLECTION HISTORY
THICK-SKIN BEAMS WITH CHANNEL WEBS

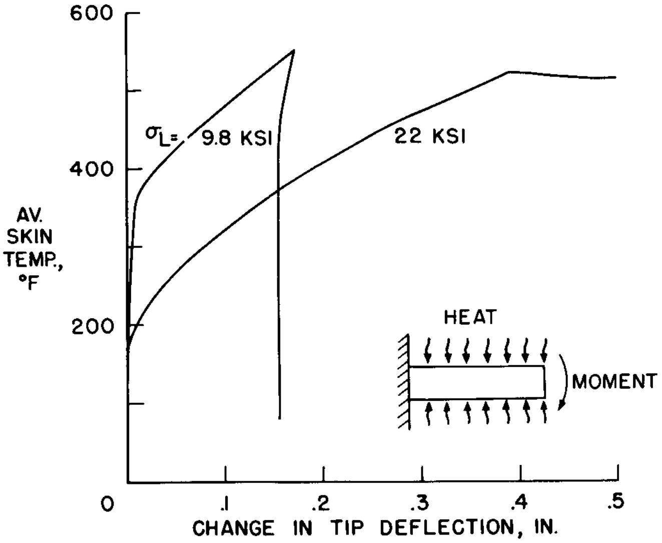

Figure 3

BUCKLING INTERACTION CURVE

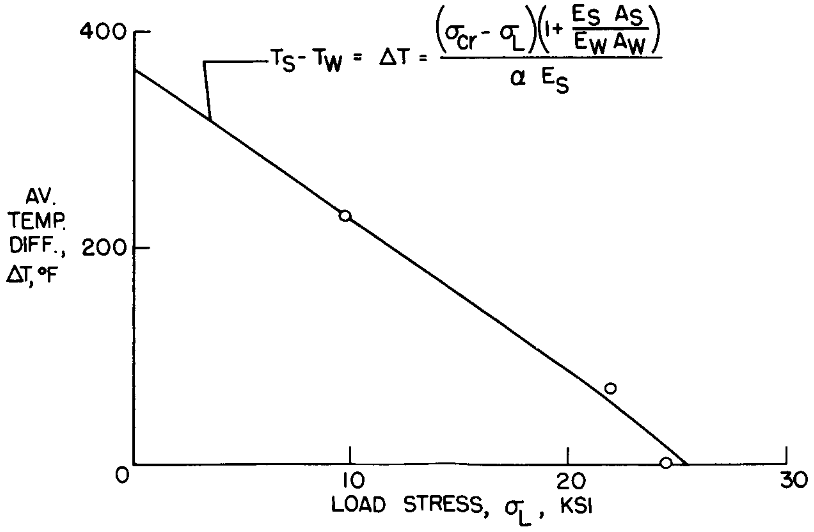

Figure 4

[redacted]

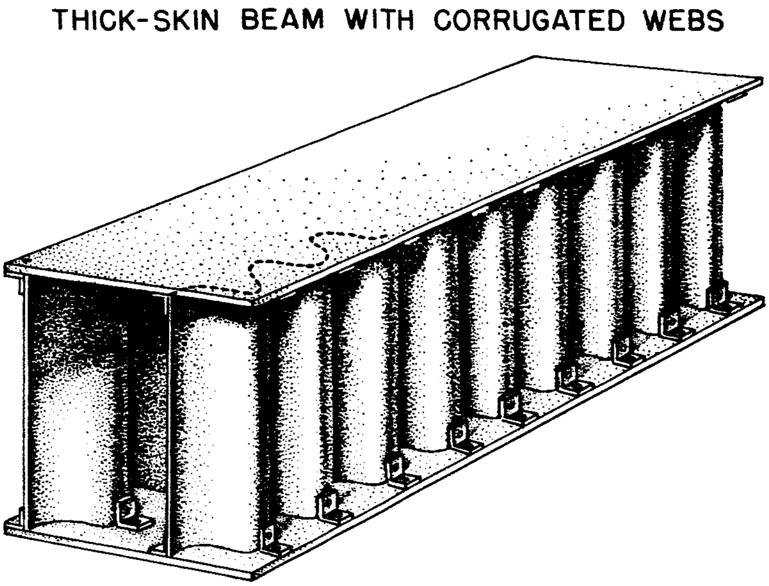

Figure 5

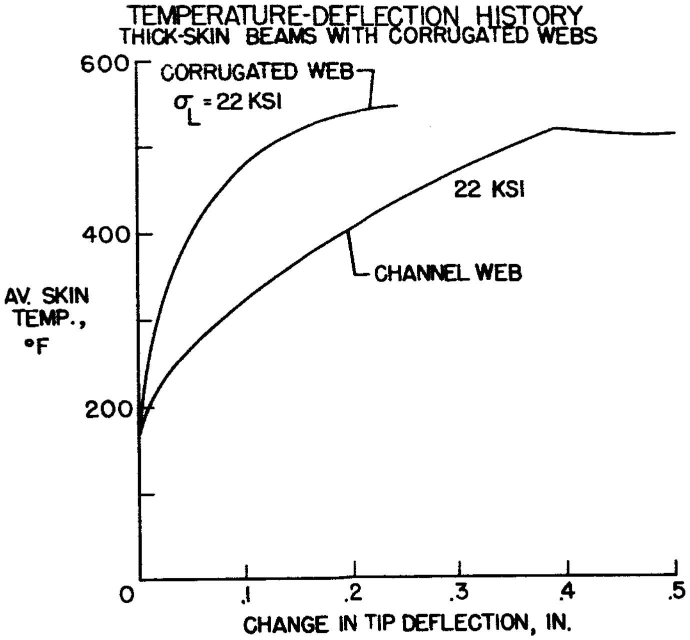

Figure 6

[redacted]

[redacted]

BEHAVIOR OF A CANTILEVER PLATE UNDER RAPID-HEATING CONDITIONS

By Louis F. Vosteen and Kenneth E. Fuller

Langley Aeronautical Laboratory

SUMMARY

Tests of a cantilever plate have shown that the midplane stresses imposed by a nonuniform temperature distribution can effectively reduce the stiffness of the plate. This reduction in stiffness is reflected in the increased deformation caused by the action of a constant applied torque and also in the reduction of the natural frequency of vibration of the first two modes of the plate. By using small-deflection theory and by employing energy methods, the effect of nonuniform heating on the plate stiffness was calculated. The theory predicts the general effects of the thermal stresses but is inadequate when the deformations become large. An extension of the analysis to account properly for large deflections is expected to give more satisfactory results near critical temperature.

INTRODUCTION

One of the structural problems produced by nonuniform heating is a change in the effective stiffness of the structure caused by thermal stresses. This change in stiffness is not associated with a change in the material properties but depends on the state of stress and may occur at stress levels well below those necessary to produce buckling. A reduction in stiffness produced by thermal stresses induced by aerodynamic heating has been cited as a key factor in the flutter of some wing structures described in references 1 and 2.

SYMBOLS

T	temperature, $^{\circ}$F
T_0	temperature of midchord, $^{\circ}$F

[redacted]

ΔT	difference in temperature between longitudinal edge and midchord, $^{\circ}F$
y	chordwise coordinate measured from midchord line
x	spanwise coordinate measured from root
a	plate span, in.
b	plate half chord, in.
w	deflection, in.
ω	natural frequency, cps
ω_0	room-temperature natural frequency, cps
γ	arbitrary exponent
E	Young's modulus, psi
K	arbitrary coefficient of stress function
ϕ	stress function
α	coefficient of thermal expansion, $\frac{\text{in.}}{\text{in.-}^{\circ}\text{F}}$
A_{mn}, A_{ij}	arbitrary coefficients of deflection function
θ	tip rotation, deg
U_S	strain energy, in-lb
U_H	strain energy due to thermal expansion, in-lb
U_B	potential energy of bending, in-lb
U_M	energy due to midplane stresses, in-lb
$\omega^2 U_V$	kinetic energy of vibration, in-lb
U_L	potential energy due to external load, in-lb

[redacted]

DISCUSSION

The type of temperature distribution produced by the aerodynamic heating of a thin missile wing is shown in figure 1. This figure (given in ref. 3) shows the variation in temperature across the chord for a solid double-wedge airfoil immediately following a 1 g acceleration to Mach number 4 at 50,000 feet. The temperatures on the surface and at the midplane are shown. Such a temperature distribution produces compressive stresses near the leading and trailing edges and tension in the central part of the wing. The effect of these stresses is a reduction in the stiffness of the structure that may be observed as an increased deformation under load, or as a reduction in natural frequency. Laboratory demonstrations have shown how the natural frequency of a simplified wing structure can be effectively reduced by the nonuniform temperature distribution associated with rapid heating. No quantitative data exist, however, which relate changes in frequency, and hence effective stiffness, to temperature distribution. The project to be discussed in this paper was devised to satisfy part of this need.

An arrangement was selected that required a simple test setup and which could be analyzed theoretically with relative ease. The test arrangement used and shown in figure 2 was a cantilever aluminum-alloy plate 1/4 inch thick and 20 inches square. A nonuniform temperature distribution, resembling that encountered in aerodynamic heating, was produced by rapidly heating the longitudinal edges with carbon-rod radiators. The temperature distribution along the span of the plate was constant except for a slight decrease toward the tip. Figure 3 shows the temperature histories.

In this figure, temperature in degrees Fahrenheit is plotted against time in seconds for the edge and midchord. Heat was applied to the plate for about 16 seconds. During this time, the edge temperature rises almost linearly to 315° F at the peak of the heating cycle. When the heating stops, the temperature drops quickly and slowly levels off as the plate cools. The variation in temperature across the chord has been shown in figure 2 for a time in the heating cycle (10 seconds), at the time of maximum edge temperature (16.5 seconds), and during cooling (30 seconds). These distributions show that the temperature remains relatively low over the center half of the plate but rises sharply near the heated edges.

The plate was tested under a variety of heating and loading conditions, and the data which will be presented represent the results of some of the more significant tests on this plate. Two investigations were made to determine the effect of the nonuniform temperature distribution on the stiffness. First, the deformations of the plate due to thermal stresses were obtained for various load conditions. Second, the changes in natural frequency of vibration during heating were investigated.

Deformations

Figure 4 shows the tip-rotation histories. The angle of rotation of the tip in degrees is plotted against time in seconds for heating with no external load and for heating with applied torques of 400 inch-pounds in each direction. In each case, the plate deformed by rotating torsionally about the midchord line. Note that the plate underwent an appreciable deformation without the application of an external load. This thermal buckling of the plate may be a significant factor in the control of missiles having solid fins.

The plate rotated in the same direction regardless of whether heat was applied symmetrically or on either edge because of an initial twist. The increased deformations, which occurred when a constant torque was applied in the same direction as the initial twist, indicate an approximate superposition of the deformation induced by the thermal stresses on the initial static deflection. When the torque was applied in the opposite direction, the plate twisted in the direction of the applied torque, but the maximum twist was slightly less.

Heating Effects on Natural Frequency

It is difficult to detect the frequency changes of the plate under transient heating conditions because of the time required to establish resonance. For this reason, the present investigation has so far been limited to the first bending and first torsion modes inasmuch as a frequency history could be obtained for these two modes by striking the plate at regular intervals during the test.

Figure 5 shows how the frequencies of the first two modes varied during the test. Here, frequency of vibration in cycles per second is plotted against time in seconds for the first bending and first torsion modes. The first bending frequency decreased from 19 cycles per second to 15 cycles per second at the point of maximum temperature gradient. This is a 21-percent reduction in frequency. The first torsion frequency begins at 48 cycles per second and drops to a minimum of 30 cycles per second - a reduction in natural frequency of about 35 percent. As the plate cools, both frequencies return to their original values. The small irregularity which occurs at the peak of the heating cycle has been observed in all the first-torsion-mode tests, but as yet its cause has not been determined.

[redacted]

Small-Deflection Theory

As a first approach to predicting the changes measured in these tests, small-deflection theory has been used. The analytical approach is a combination of the energy methods used to solve buckling and vibrational problems. The method used is outlined in figure 6. The temperature is assumed to be constant through the thickness of the plate and along the span; the distribution across the chord is approximated by a simple power law, which involves the edge-to-midchord temperature difference ΔT and the power γ required to describe the measured chordwise temperature distribution. The power γ, which varies during the test, determines how sharply the temperature rises near the edge of the plate. In order to find how γ varied, a curve of the form given was fitted to the experimental temperature distribution at various times. At the start of the test, γ was very large but decreased to $\gamma = 4$ at the peak temperature and continued to drop to about $\gamma = 2$ at the end of the test.

Thermal stresses were obtained from a simple stress function (see ref. 4), and deflections were represented by a power series. The complementary energy, used to evaluate the coefficient of the stress function, consists of the usual strain-energy expression plus terms which account for the strain energy due to the thermal expansion of the plate (ref. 5).

The change in energy during deflection consists of the potential energy due to bending, the energy imposed by midplane thermal stresses, the kinetic energy of vibration, and the potential energy resulting from any externally applied load - in this case a torque. (See refs. 6, 7, and 8.)

Comparison of Calculated and Measured Results

A comparison of the calculated and measured effect of the temperature gradient on the torsional stiffness for the case of no vibration is shown in figure 7. Here the tip rotation in degrees has been plotted against the edge-to-center temperature difference ΔT in degrees Fahrenheit for an applied torque of 400 inch-pounds. Curves are shown for the periods of heating (or increasing ΔT) and cooling (or decreasing ΔT). The small-deflection theory gives a reasonable approximation of the reduction in stiffness about halfway to the buckling temperature. Above this point, however, the theory indicates that the plate deflections would increase more rapidly than actually occurs.

Figure 8 compares the results of the calculations with test results when there are no external loads and the plate is vibrating in the first torsion mode. In this figure, the frequency in cycles per second is plotted against temperature difference between the edge and the midchord line for the periods of increasing and decreasing ΔT. The small-deflection theory again approximates the frequency change about halfway to the

[redacted]

critical buckling temperature. Above this value, the theory again overestimates the change. This disagreement occurs because the deflections have become large and the small-deflection theory is no longer valid. When the analysis is extended to include the effects of large deflections, more satisfactory agreement is expected at the critical ΔT.

Figure 9 shows a similar comparison of measured and calculated frequency as a function of time. The ratio of reduced frequency to room-temperature frequency is plotted against time in seconds. The calculated curve indicates that the theoretical critical-buckling temperature differential is reached in about 15 seconds. The small-deflection theory predicts that the plate would have lost all its stiffness at this point, but this is not the actual case. Since stiffness is proportional to the square of the frequency, the decrease obtained indicates that only about half of the stiffness was lost as a result of the induced thermal stresses. As the plate cools and the temperature difference becomes less than half that required for buckling, the theory is again in fair agreement with the test results.

CONCLUDING REMARKS

Tests of a cantilever plate have shown that the midplane stresses imposed by a nonuniform temperature distribution can effectively reduce the stiffness of the plate. This reduction in stiffness is reflected in the increased deformation caused by the action of a constant applied torque and also in the reduction of the natural frequency of vibration of the first two modes of the plate. By using small-deflection theory and by employing energy methods, the effect of nonuniform heating on the plate stiffness was calculated. The theory predicts the general effects of the thermal stresses but is inadequate when the deformations become large. An extension of the analysis to account properly for large deflections is expected to give more satisfactory results near the critical temperature.

[redacted]

REFERENCES

1. Heldenfels, Richard R., and Rosecrans, Richard: Preliminary Results of Supersonic-Jet Tests of Simplified Wing Structures. NACA RM L53E26a, 1953.

2. Heldenfels, Richard R.: Some Design Implications of the Effects of Aerodynamic Heating. (Prospective NACA paper.)

3. Kaye, Joseph: The Transient Temperature Distribution in a Wing Flying at Supersonic Speeds. Jour. Aero. Sci., vol. 17, no. 12, Dec. 1950, pp. 787-807, 816.

4. Timoshenko, S., and Goodier, J. N.: Theory of Elasticity. Second ed., McGraw-Hill Book Co., Inc., 1951, p. 169.

5. Heldenfels, Richard R., and Roberts, William M.: Experimental and Theoretical Determination of Thermal Stresses in a Flat Plate. NACA TN 2769, 1952.

6. Timoshenko, S.: Theory of Elastic Stability. McGraw-Hill Book Co., Inc., 1936, pp. 305-323.

7. Timoshenko, S.: Strength of Materials. Part I - Elementary Theory and Problems. Second ed., D. Van Nostrand Co., Inc., 1940, p. 281.

8. Timoshenko, S.: Vibration Problems in Engineering. Second ed., D. Van Nostrand Co., Inc., 1937, p. 423.

[redacted]

[redacted]

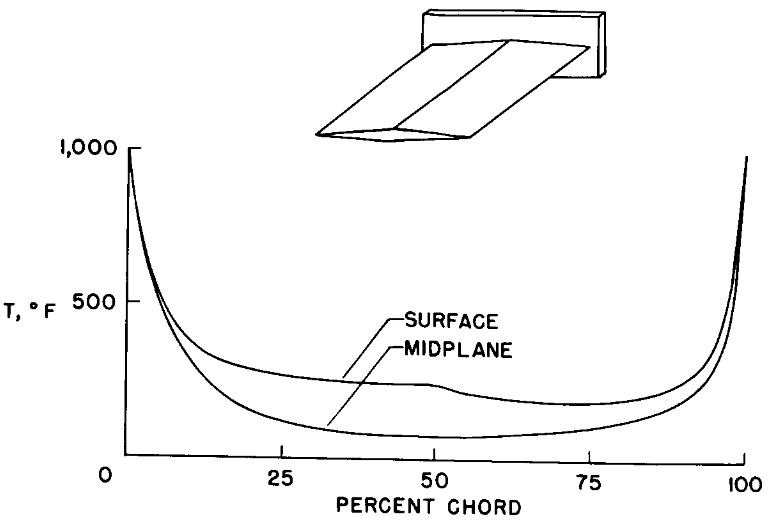

CHORDWISE TEMPERATURE DISTRIBUTION

AERODYNAMICALLY HEATED AIRFOIL

Figure 1

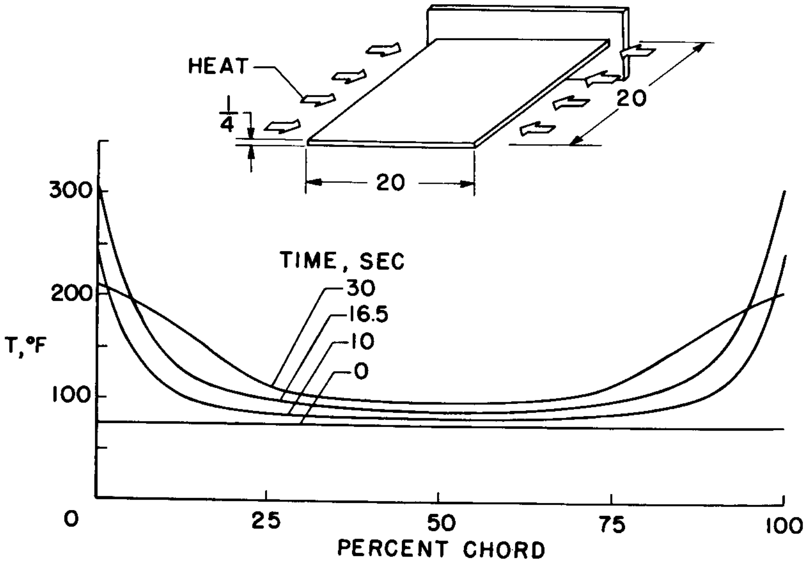

CHORDWISE TEMPERATURE DISTRIBUTION

RADIANTLY HEATED PLATE

Figure 2

[redacted]

[redacted]

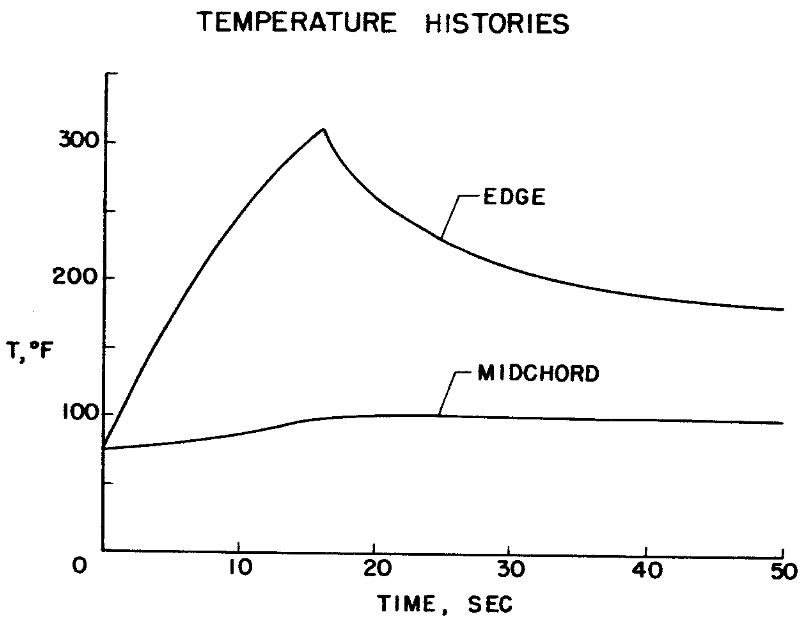

Figure 3

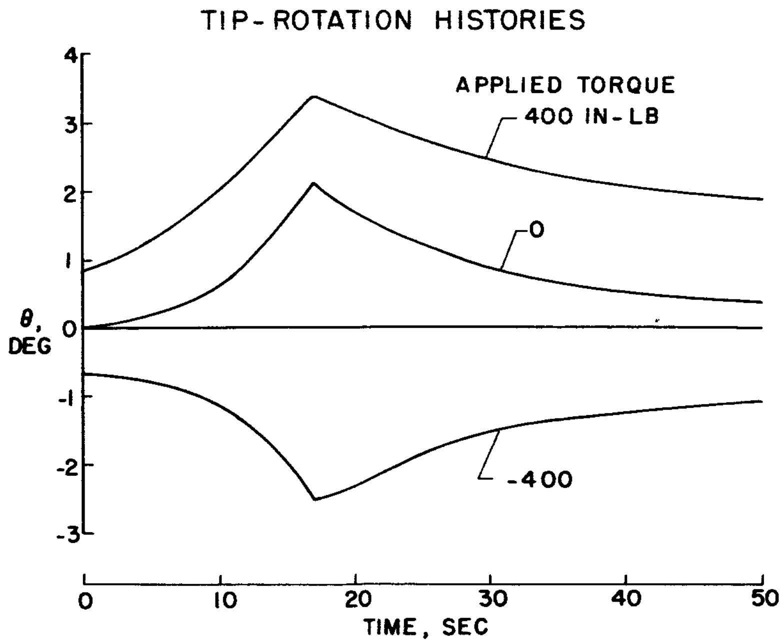

Figure 4

[redacted]

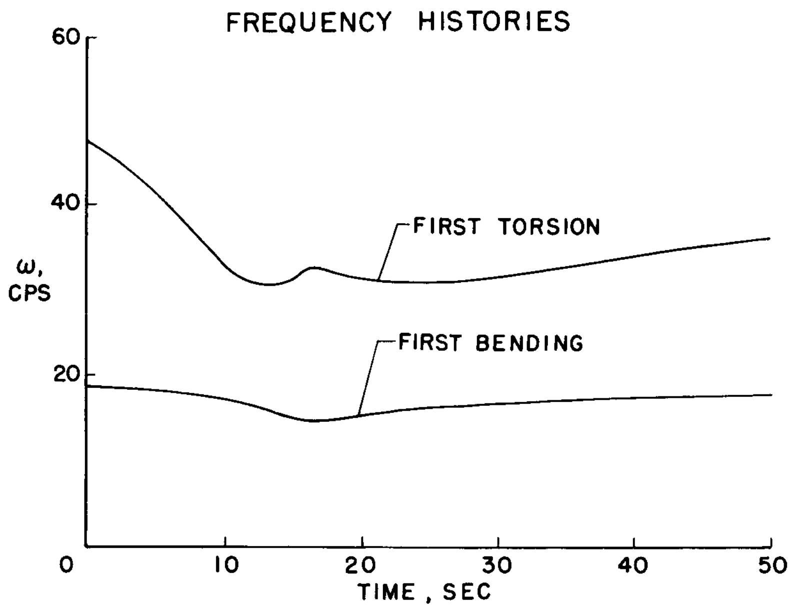

Figure 5

THEORETICAL APPROACH

TEMPERATURES

$$T = T_O + \Delta T \left(\frac{y}{b}\right)^{\gamma}$$

STRESSES

$$\phi = K E \alpha \Delta T \left(x^2 - a^2\right)^2 \left(y^2 - b^2\right)^2$$

$$\frac{\partial}{\partial K}\left(U_S + U_H\right) = 0$$

DEFLECTIONS

$$w = \sum_{m=1}^{3} \sum_{n=1}^{3} A_{mn}\, x^{m+1}\, y^{n-1}$$

$$\frac{\partial}{\partial A_{ij}}\left(U_B - U_M - \omega^2 U_V + U_L\right) = 0$$

Figure 6

[redacted]

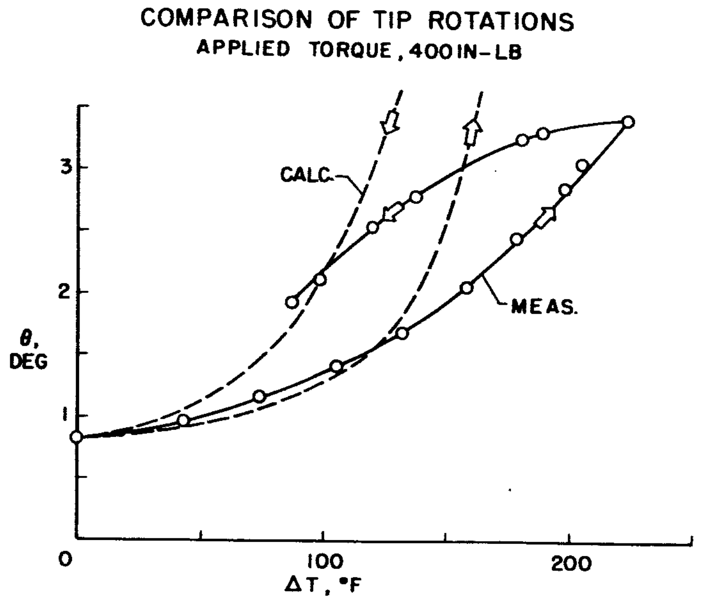
COMPARISON OF TIP ROTATIONS
APPLIED TORQUE, 400 IN-LB

Figure 7

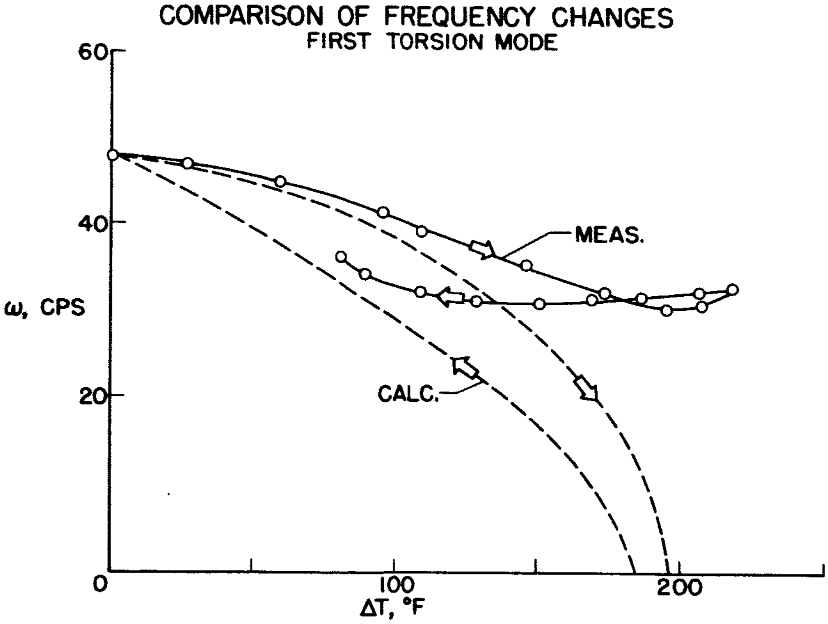
COMPARISON OF FREQUENCY CHANGES
FIRST TORSION MODE

Figure 8

[redacted]

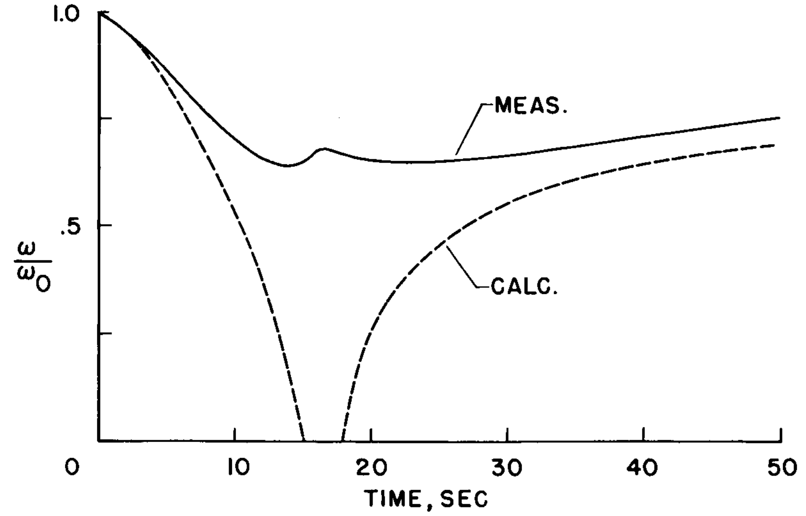

COMPARISON OF FREQUENCY HISTORIES

FIRST TORSION MODE

Figure 9

[redacted]

[redacted]

SOME DESIGN IMPLICATIONS OF THE EFFECTS OF AERODYNAMIC HEATING

By Richard R. Heldenfels

Langley Aeronautical Laboratory

INTRODUCTION

Previous papers at this conference and others in the recent literature (for example, ref. 1) have discussed the various structural effects of aerodynamic heating. These papers have made it clear that the resulting structural design problems are numerous, complex, and so severe that the performance capabilities of high-speed aircraft may be greatly restricted. A more optimistic view of the situation, however, indicates that the severity of most of these problems is often overemphasized. The purpose of this paper is to take a brief look at the effect of two problems, creep and thermal buckling, on the design of aircraft structures and to give some consideration to the use of insulation as a means of alleviating the effects of aerodynamic heating.

CREEP

The creep of aircraft structures at elevated temperature is often assumed to be a very important problem. Its importance, however, has not been established, and before accepting it as a major problem, its significance in aircraft design should be examined.

Creep is a primary design criterion in much high-temperature machinery, such as heat exchangers and gas turbines, but in this type of equipment the material must withstand the combined design temperatures and loads for long periods of time. The usual aircraft structure on the other hand is subjected to a variety of loads that occur under varying temperature conditions.

The relationship between load and time typical of present-day aircraft is shown in figure 1, where the load ratio n/n_L is plotted against the percentage of total flight time spent above that load ratio. The load ratio is the actual load n divided by the design limit load n_L. The solid line is for a fighter-type airplane and the dashed line for a bomber type. This figure was prepared from existing gust-loads data (ref. 2) and the generalized maneuver load curves presented

[redacted]

DECLAS[redacted]D

in reference 3. The time spent at the low load ratios for each type is primarily the result of gusts, and that at the higher loads is primarily due to maneuvers. Note that percent time is plotted on a logarithmic scale and that most of the total time is spent at low load ratios, about 90 percent of the time for the fighter and 99.9 percent for the bomber.

The foregoing results were from airplanes in flight at speeds below sonic. It is a matter of conjecture what similar relations will be for supersonic aircraft, but it seems reasonable to assume that the load-time relations will not be substantially different from those shown in figure 1. It is significant, then, that high-speed aircraft will spend a very small percentage of their lifetime at loads near the design limit load where creep is most likely to be important. In addition, these high loads will not necessarily occur in conjunction with high temperatures.

The uncertainties that exist in the expected loads and the limited data available on cyclic and intermittent creep make a detailed analysis of the effect of creep on structural weight impractical at present, but some approximate indications can be obtained as follows:

Let all the loads be represented by only two load levels, a low level representative of most of the flight time (for example, about 0.2 load ratio for 90 percent of the life of the fighter) and then assume, very conservatively, that the remainder of the life is spent at the design limit load. The lower load level then makes an insignificant contribution to the creep of the structure. The lower load level is more important for the bomber than for the fighter because it is a larger percentage of the design load and because the bomber would have a longer expected lifetime, but still the lower load ratio makes only a small contribution. For either case, the effect of creep on structural weight can be estimated very conservatively by fixing a lifetime of 100 hours at temperature and limit load combined. Results of such an analysis are shown in figure 2, where the weight required to support a given constant tensile load is plotted against temperature for three structural materials and for two design criteria. The solid curves indicate the weight required when the criterion is the ultimate tensile strength; the dashed lines give the weight required when creep rupture at limit load is used. The three materials selected for this analysis, 2024-T3 (formerly 24S-T3) aluminum alloy, RC-130A titanium alloy, and Inconel X cover the temperature range in which metals are useable. The stainless steels generally fall between RC-130A and Inconel X, but nearer RC-130A.

Consider first the aluminum alloy. The weight required to support the load on the basis of ultimate tensile strength $1\frac{1}{2}$ times the design limit load is given by the so[redacted] The weight required to meet the

[redacted]

creep criterion - failure after 100 hours at temperature and limit load - is given by the dashed line. Since the creep criterion requires less weight than the strength criterion throughout the temperature range of the aluminum alloy, creep is not a design problem for this material. A similar situation exists for Inconel X for most of the temperature range, but for temperatures above 1200° F creep requires more weight than ultimate strength. Creep thus becomes important for Inconel X structures only in the temperature range where strength is decreasing rapidly with increasing temperature. For the titanium alloy, creep becomes a design problem at temperatures above 500° F. Note that above the temperature where creep becomes important, the weight required by the creep criterion increases rapidly with temperature, and design efficiency would best be obtained by conversion to a material for which creep would not be a problem. This particular titanium alloy has poor creep characteristics; others are better in creep than RC-130A, but they have less tensile strength. Further development of titanium alloys will probably improve this situation.

Since the creep criterion used in this analysis usually required less weight than the ultimate strength criterion, it appears that creep may have little effect on aircraft structural design. In those cases where creep is a significant factor, conversion to another material will be desirable in the interest of structural efficiency and the task of designing for creep will be avoided. The results presented were obtained with a very conservative estimate of the load-temperature-time experience of the structure. If something less than 100 hours had been used for the lifetime, creep would appear to be even less important.

The importance of creep is also influenced by the type of creep criterion used, and other factors such as the permanent deformations due to creep and the effect of creep on ultimate strength should be considered, but indications are that these will be secondary design considerations. Creep failure was used as a design criterion in this analysis because of its obvious significance. A prescribed amount of permanent creep deformation could have been used, but the validity of such a criterion applied to an aircraft structure is extremely doubtful. This doubt arises from investigations of the creep behavior of aluminum-alloy structural elements and box beams coupled with the expected load-temperature-time experiences of aircraft structures. Creep may also affect the ultimate strength of the structure, but some exploratory tests on aluminum-alloy plates and box beams indicate that in many cases this effect will be negligible.

To summarize the remarks on creep, it appears that in general creep may not be a primary factor in the design of high-speed aircraft because of the character of the relationships between loads, temperatures, and time. Some materials are much more susceptible to creep than others; thus, in some cases a change in materials may be necessary in order to avoid creep problems.

[redacted]

THERMAL BUCKLING

Thermal buckling promises to be the most serious problem associated with the transient aspects of aerodynamic heating. Previous speakers have shown how thermal buckling had an adverse effect on the stiffness of beams and how thermal stresses less than those required for buckling reduced the stiffness of a cantilever plate. In reference 4, some flutter incited by aerodynamic heating and thermal stresses is discussed; this work is now reviewed in connection with more recent tests.

Motion pictures of a test of a multiweb wing structure (identical to model MW-1 of ref. 4) in a Mach number 2 blowdown jet at sea level showed that the model remained stationary for most of the test, but after the aerodynamic heating took effect, the model began to flutter without any evidence of buckling. The model fluttered for about 6 seconds before the rivets flew out and general destruction began. High-speed motion pictures showed that the flutter involved distortion of the airfoil section into an S-shape.

From the first tests of this type, it was concluded that flutter started after the model skin buckled. However, in other tests of similar models flutter was obtained without buckling, and the concept of reduced stiffness resulting from thermal stresses has been used to explain these results. It is thus possible for thermal stresses lower than those required for buckling to induce dangerous aeroelastic effects. This situation is not so serious as it seems, however, since test results show that small changes in the stiffness of a shell structure, such as the addition of a rib or two, prevented flutter without much increase in weight. Thus, careful design can prevent most such failures. The use of internal construction that minimizes thermal stresses may be required in some cases, but there are a wide variety of flight conditions in which more conventional designs can be used without danger of thermal buckling.

Figure 3 shows some combinations of dimensions of a simplified steel multiweb beam that make the structure subject to thermal buckling (thermal stress σ_T equal to buckling stress σ_{cr}) under symmetrical aerodynamic heating conditions. The distance between webs (on a logarithmic scale) is plotted against Mach number for three altitudes (sea level, 50,000 feet, and 100,000 feet). For web spacings above a solid line, thermal buckling of the skin will occur, while below the solid line, buckling will not occur.

A low level of thermal stress may be required to prevent critical changes in aeroelastic characteristics or to prevent buckling in the presence of wing bending loads. Present knowledge does not permit an

[redacted]

estimate of the aeroelastic effects of a given thermal stress distribution or of the level of thermal stress that may be tolerated, but an assumption that thermal stresses only 10 percent of those required for buckling may be permissible appears reasonable. The dash-line curves give the web spacings corresponding to this 10-percent condition.

The web spacings that would be used for an efficient load-carrying structure would be around 2 to 5 inches; thus such a structure would be in no danger of buckling due to heating alone, but a low level of thermal stress could not be attained in this structure at Mach numbers above 3 without very closely spaced webs.

This chart is based on several approximations and a simplified structure and thus indicates only the approximate combinations of dimensions and flight conditions that will produce buckling of one series of beams. Similar charts are easily prepared for other configurations, but an actual design should be checked by a more exact analysis.

In summarizing the remarks on thermal buckling, the present state of knowledge indicates that thermal buckling should be prevented. In many cases thermal stresses far below the buckling point may be required to avoid dangerous aeroelastic effects. The proper location of internal members may prevent failures without undue weight penalties under many flight conditions, but special types of internal structure that minimize thermal stresses will be necessary when severe aerodynamic heating is encountered.

INSULATION

Having discussed two of the problems resulting from aerodynamic heating, consideration is now given to one of the ways of alleviating heating effects, namely, insulating the structure. One of the many probable uses of insulation is to extend the aerodynamic heating conditions under which aluminum alloys are useful structural materials. Figure 4 presents results to show the effect of insulation on the temperature history of a 0.10-inch-thick skin of aluminum alloy.

Temperature T is plotted against time in minutes for an instantaneous acceleration to a Mach number of 4 at an altitude H of 50,000 feet. The temperature history of the uninsulated skin is shown by the upper solid line and the effect of 0.1 inch of insulation such as rock wool or asbestos (thermal conductivity 0.03 Btu per ft-hr-°F) is shown by the lower solid line. The temperature of the outer surface of the insulation is given by the dashed line. For this flight condition the aluminum alone would quickly reach a temperature at which its strength had vanished, while a relatively thin layer of insulation holds the temperature down for several minutes.

This is a very beneficial result insofar as the structure is concerned, but this benefit has been obtained by transferring difficult design problems to the insulation. The temperature of the heated surface of the insulation rises very quickly to a value near the equilibrium temperature T_{eq} (which is assumed equal to the adiabatic wall temperature T_{aw}) and thereafter changes very slowly. The insulation must thus withstand high temperatures and large temperature differences which will require special design techniques for the construction and attachment of such a protective coating.

The fact that the surface temperature of the insulation closely approximates the equilibrium temperature permits considerable simplification of the relation between the insulation required and the flight condition. By neglecting the specific heat of the insulation and assuming that the temperature of the outer surface of the insulation is the equilibrium temperature, a conservative estimate of the required thickness of insulation can be obtained as shown in figure 5. The required thickness is plotted against surface temperature for 0.10-inch-thick skin of aluminum that rises from zero to 200° F in the times indicated. Each of the curves is for a particular value of the time required for the structure to reach 200° F and the thermal conductivity of the insulation is assumed invariant with temperature. This figure shows that high equilibrium temperatures and long flight times require very thick layers of insulation, thicknesses that are impractical for many parts of the aircraft such as thin wings or control surfaces.

The situation improves somewhat for heavier structures since the same curves apply to other thicknesses of aluminum skin. For example, if the thickness of the skin is doubled, the time during which the insulation is effective will also be doubled or the required insulation thickness will be cut in half. The required thickness is substantially reduced if the skin is allowed to go to higher temperatures, but for this case the relationship is not so simple. Higher skin temperatures would necessitate another structural material and lead to considerations of structural efficiency.

The thicknesses indicated in figure 5 are rather large and somewhat discouraging; however, another approach to the insulation problem that can result in lower heat transfer, less thickness, and possibly lighter weight is the use of radiation shields.

Average heat transfer through two types of insulators is shown in figure 6 as a function of the surface equilibrium temperature. The solid lines are for two thicknesses l of the previously discussed bulk insulation such as rock wool or asbestos. The dashed lines are for a single radiation shield at two values of emissivity ϵ. The radiation shield would consist of a thin sheet of metal supported a short distance away from the outer surface of the structure. The aerodynamic surface of the shield would be a black-body radiator (high emissivity) to keep surface temperature low, but the inner surface of the shield and outer surface of the structure would be very bright (low emissivity) to minimize radiant-heat exchange. Some low-conductivity supporting structure, such as a honeycomb core, would be needed between them but in this analysis, the heat transferred by this supporting structure and the air between shield and structure has been neglected. The emissivity of 0.1 is about the upper limit for most shiny metals while the value of 0.02 can be attained only with special coatings such as gold or silver plate.

The average heat flow plotted is the average rate at which the insulators transfer heat to the structure while the structure rises from 0° to 200° F. The conditions considered are similar to those in figure 5, but by plotting average heat flow, all combinations of time and heat capacity of the structural material are included. Where two curves cross, the insulators are exactly equivalent for the conditions considered. At other points, the lowest curve indicates the best insulator. The curves show that the radiation shield provides excellent protection at the lower temperatures, but becomes increasingly inefficient as the temperature increases. The heat flow through the shield can be further reduced by using several of them, for example, five shields of 0.1 emissivity would transfer about the same amount of heat as the single 0.02 shield, but the added complication of multiple shield arrangements might prove to be impractical.

An effective radiation shield requires bright surfaces that are attainable only with metals at moderate temperatures; thus this approach would probably be limited to temperatures below about 1500° F. Above this temperature, a type of bulk insulation suitable for high temperature use would be required. For some applications, such as protection of occupants, a combination of insulation, radiation shields, and cooling may provide the most efficient combination.

The results presented indicate that insulation provides a suitable way to alleviate the effects of aerodynamic heating on the primary structure under certain flight conditions. These gains can be attained, however, only by creation of many difficult problems associated with the design, fabrication, and installation of the protective coatings.

CONCLUDING REMARKS

The problems of creep and thermal buckling have been discussed in an effort to indicate their [redacted] design of high-speed aircraft.

The results have shown that creep may not be a significant factor, but thermal buckling may have a substantial effect on the structural design. Consideration has also been given to the use of insulation for the alleviation of heating effects; such an approach has merit under certain conditions but poses many new design problems.

The results presented are based on the limited existing information on the structural problems of aerodynamic heating. The picture may change as more research results become available, but the design problems undoubtedly will be eased as knowledge increases. It was not intended to convey the impression that aerodynamic heating problems are easily overcome, but merely to indicate how careful design can solve some of them.

REFERENCES

1. Anon: Symposium on the Thermal Barrier. Presented by the Aviation Division of the ASME at the Annual Meeting Nov. 28 - Dec. 3, 1954.

2. Press, Harry, Meadows, May T., and Hadlock, Ivan: Estimates of Probability Distribution of Root-Mean-Square Gust Velocity of Atmospheric Turbulence From Operational Gust-Load Data by Random-Process Theory. NACA TN 3362, 1954.

3. Mayer, John P.: A Study of Means for Rationalizing Airplane Design Loads. (Prospective NACA paper.)

4. Heldenfels, Richard R., and Rosecrans, Richard: Preliminary Results of Supersonic-Jet Tests of Simplified Wing Structures. NACA RM L53E26a, 1953.

[redacted]

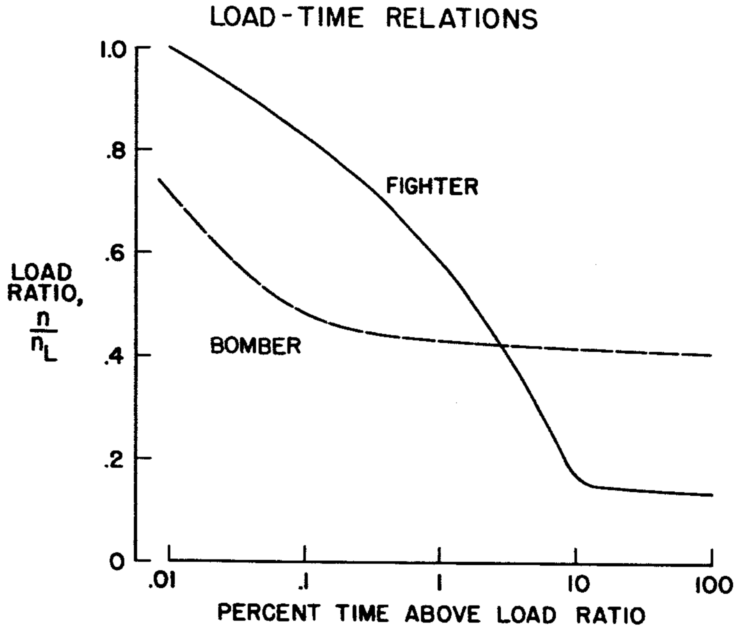

Figure 1

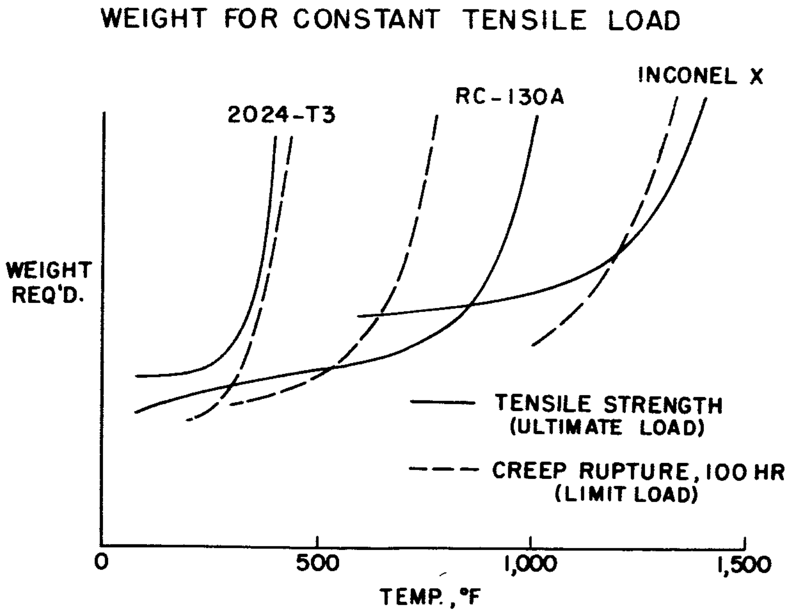

Figure 2

DECLAS [redacted]

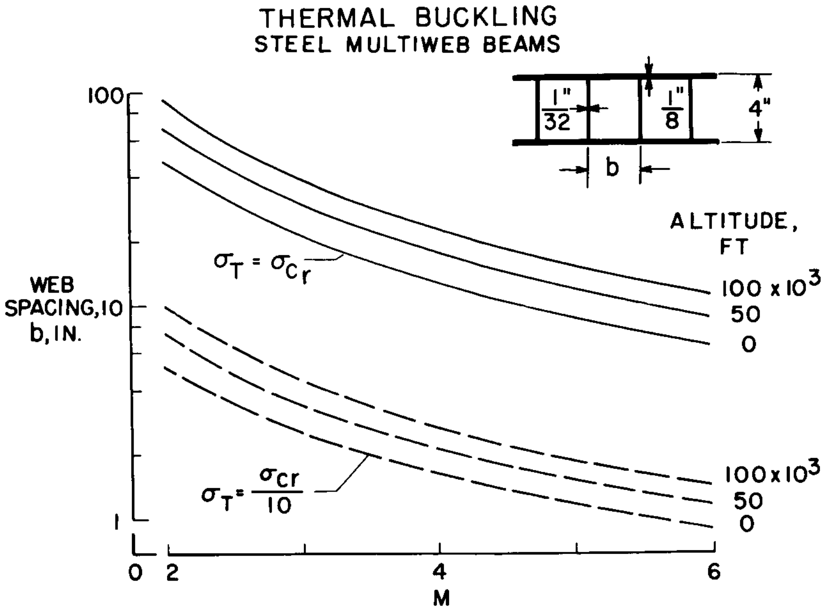

Figure 3

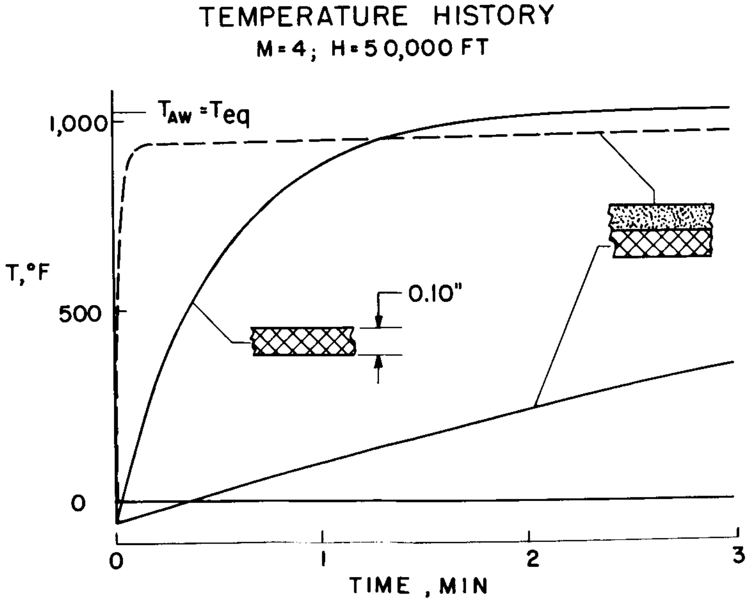

Figure 4

[redacted]

[redacted]

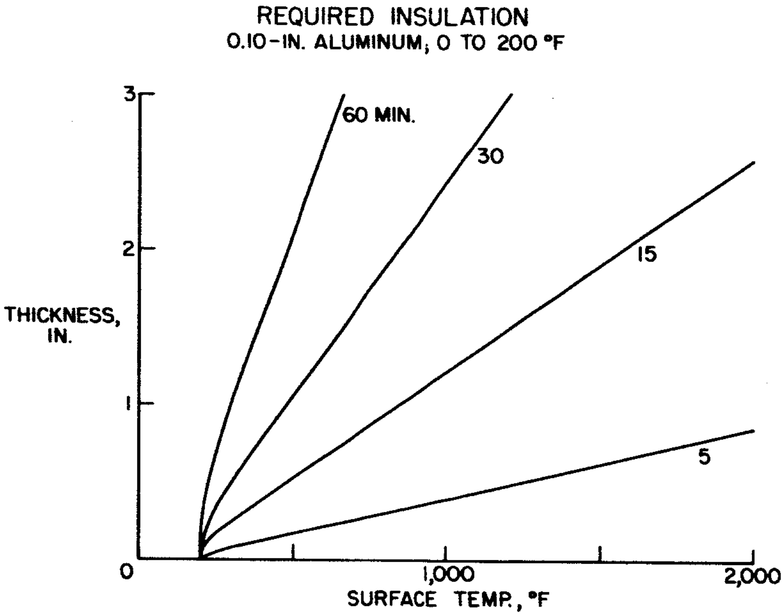

Figure 5

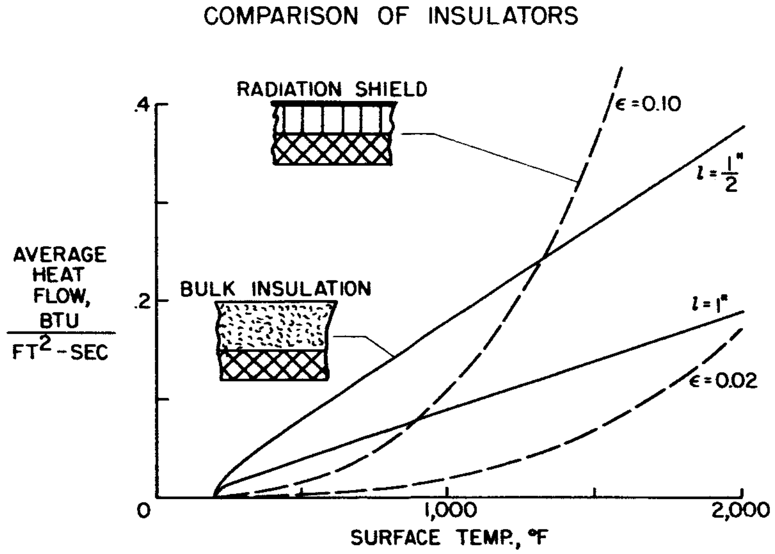

Figure 6

[redacted]

[redacted]

SUMMARY OF RECENT THEORETICAL AND EXPERIMENTAL WORK ON BOX-BEAM VIBRATIONS

By John M. Hedgepeth

Langley Aeronautical Laboratory

SUMMARY

A discussion of various secondary effects which have an important influence on the vibration characteristics of box beams is presented. Means of incorporating these effects in vibration analyses of actual built-up box beams are discussed. Comparisons with experiment are given; good agreement between theory and experiment is obtained when the secondary effects are included.

INTRODUCTION

The need of accurate vibration modes and frequencies of aircraft is well recognized. The reliability of a flutter-speed calculation, for example, is intimately related to the accuracy of the vibration modes and frequencies - especially the frequencies - used in the analysis. Furthermore, these modes and frequencies are often useful in the analysis of other dynamic problems, such as landing impact and gust loads.

The purpose of this paper is to summarize the results of research into the vibration characteristics of one of the main types of aircraft structures - the box beam. Most of the information to be discussed is recent; some of it is old and is included in order to present a complete story.

DISCUSSION

Shown in figure 1 is a drawing of a typical box beam which may be thought of as being the main load-carrying structure of a wing. It is composed of covers built up of sheet stiffened by stringers, and spars made up of flanges connected by webs. There are usually a number of ribs to provide cross-sectional stiffness.

[redacted]

The vibration analyses of beams like the one shown in figure 1 ordinarily have used elementary beam bending and torsion theory. The accuracy obtained from elementary theory was considered to be good enough for long beams. However, it is known that, in the deformation of box beams, certain secondary effects arise which are not taken into account in the elementary theory. These secondary effects can have an important influence on the vibration characteristics of box beams, particularly when the higher modes are desired.

In bending vibrations, the secondary effects that are generally recognized are transverse shear, shear lag, and longitudinal (rotary) inertia. Transverse shear arises from the fact that shear deflections of the box occur under load because of the finite shear stiffness of the webs. These shear deflections are in addition to the bending deflections considered in the elementary theory. Shear lag is caused by the finite shear stiffness of the covers which permits the direct-stress-carrying material in the middle of the cover to carry less than its full share of the load. Both of these effects tend to reduce the apparent stiffness of the box and, hence, to reduce the natural frequencies. Longitudinal inertia arises from the fact that, when the beam vibrates, inertia forces are developed because of accelerations in the longitudinal direction. This effect - which is often called rotary inertia in the bending problem - is of course not included in the elementary theory and tends to reduce the natural frequencies.

The quantitative influence of these effects on the bending frequencies of vibration of uniform, thin-walled box beams was investigated by Budiansky and Kruszewski (ref. 1). Reference 1 shows that the effects of transverse shear and shear lag are of comparable magnitude and can be quite important, particularly for short beams. On the other hand, the effect of longitudinal inertia is negligible for the shallow box beams that are typical of aircraft wing construction.

For torsional vibrations, the secondary effects that are generally recognized are restraint of warping and longitudinal inertia. When a beam is twisted, the cross sections tend to distort out of their own plane or to warp. In the elementary theory, this warping is allowed to occur without restraint. However, if the warping varies along the length, as it does in a vibration mode, direct stresses are created in the longitudinal direction which act to restrain the warping. The effect of this restraint of warping is to make the beam stiffer than it would be otherwise and, consequently, to raise the natural frequency. This warping motion also causes inertia forces in the longitudinal direction. This longitudinal inertia effect is not included in the elementary theory.

The quantitative influence of these secondary effects on the torsional frequencies of uniform, thin-walled box beams was investigated by Kruszewski and Kordes (ref. 2). Reference 2 shows that the effect of restraint of warping could be appreciable for short beams although the effects are not so pronounced as those incurred in the bending case. The effect of longitudinal inertia was unimportant for practical box beams.

Before considering the influence of these secondary effects on the bending and torsion frequencies of some actual test specimens, it is desirable to discuss how the effects of transverse shear, shear lag, and restraint of warping can be incorporated in vibration analyses of actual box beams. The results in references 1 and 2 were obtained for highly idealized beams for which exact solutions were possible. In an actual box beam, exact solutions are not feasible and some sort of simplified structure must be used.

The cross section of the box beam shown in figure 2 contains a large number of elements - stringers, flanges, and the sheet joining them. If all of these elements were treated separately in an analysis, the calculation job would be overwhelming. By lumping the properties of these elements, however, the effects of transverse shear and shear lag can be obtained without an inordinate amount of labor. The transverse-shear effect can be included simply by allowing the webs to have shear flexibility. The shear-lag effect can be duplicated by using the substitute-stringer idealization shown in figure 2. The direct-stress-carrying areas in the webs and flanges are concentrated at the corners; the direct-stress-carrying areas in the covers are concentrated as so-called substitute stringers. By properly locating the substitute stringers, it is possible to obtain frequencies within a couple of percent of those predicted by more refined theories. The use of the substitute-stringer idealization has been investigated in reference 3. For the torsion problem, the so-called four-flange box is useful in obtaining frequencies. In this idealization the direct-stress-carrying areas in both the covers and the webs are concentrated at the corners. The four-flange box does a good job of duplicating the effect of restrained warping on torsional vibrations. It might be mentioned that the substitute-stringer box can also be used for torsional vibrations with comparable success. This is fortunate since, in most actual box beams, bending and torsion will couple and the idealization used should be capable of taking all secondary effects into account.

Simplifying the cross section of the box beam is only part of what is necessary to achieve a practical vibration analysis. For a nonuniform box beam, further simplifications must be made as to the behavior in the spanwise direction. One approach is to break up the beam into a number of bays and to calculate influence coefficients. These influence coefficients then provide a basis for the vibration analysis. (See, for example, ref. 4.) Calculations have been made to determine the number of bays necessary to obtain accurate frequencies. The results indicate that, in order to obtain the first three symmetrical bending and torsion frequencies of a free-free box beam, it is necessary to use about eight bays on the half span.

An experimental vibration-test investigation has been conducted in order to check the accuracy of methods of computing natural modes and frequencies. Tests have been carried out on two structures - one a large-scale built-up box beam and the other a somewhat smaller, hollow rectangular tube.

Consider first the built-up box beam. In figure 3 is shown a photograph of the vibration-test setup used to determine its natural modes and frequencies experimentally. The beam was 20 feet long, 18 inches wide, and 5 inches deep. The aspect ratio was about 13. The beam was hung from the gallows and was vibrated horizontally. In this way an essentially free-free condition was attained. The beam was vibrated by means of four electromagnetic shakers attached at the corners. Power was supplied by the M-G set and controlled at the left-hand cabinet in figure 3. Pickups were mounted on the beam and were used to sense the motion; their output was recorded at the right-hand cabinet.

The vibration frequencies of this beam are given in table I. In the table, for simplicity, only symmetrical bending frequencies and antisymmetrical torsion frequencies have been shown; the antisymmetrical bending and symmetrical torsion frequencies follow the same trends. For both the bending and torsion, the frequencies in the first column were obtained experimentally; the frequencies in the second column were calculated by elementary theory. The frequencies including the secondary effects are given in the last column. The word "exact" has been used for these frequencies for want of a better term. By comparing experiment and elementary theory, it can be seen that the elementary theory is accurate enough for the torsion modes and for the first bending mode. For the higher bending modes, however, the situation is different. Errors varying from 20 percent in the second mode to 70 percent in the fourth mode are experienced. When the secondary effects are included, however, the agreement is considerably improved. By looking at the bending modes, it can be seen that the large reductions in frequency due to transverse shear and shear lag have brought the calculations into satisfactory agreement with the experiment. It might be mentioned that transverse shear and shear lag were about equally responsible for this reduction. For the torsion modes, inclusion of the smaller effect of restraint of warping has helped for the first two modes and hurt for the third. Even for this third antisymmetrical torsion mode - which is the twelfth mode of the beam - the error is only 6 percent.

The built-up box beam which has been discussed had a large amount of internal stiffening in the form of stringers and bulkheads. The other

[redacted]

specimen - a hollow rectangular tube - was considerably simpler and was tested for the purpose of checking theories before the vibration equipment necessary for testing large-scale built-up structures was obtained. The results for this hollow rectangular tube which is shown in figure 4 serve to illustrate an effect which may be important for box beams with little internal stiffening. This tube was approximately 8 feet long, 7 inches wide, and 2 inches deep. The aspect ratio was about 14. It was made by welding 1/4-inch plates together along the corners.

The results of vibration tests are given in table II. Again in this table only the symmetrical bending frequencies and antisymmetrical torsion frequencies are presented. Along with the experimental frequencies are given the "exact" calculated frequencies for which the secondary effects of transverse shear, shear lag, and restraint of warping have been included. For the first two symmetrical bending modes, the "exact" frequencies are fairly good; for the rest of the modes shown here, however, the errors are large - especially for the torsion modes. The reason for these large discrepancies is tied up with the occurrence of large cross-sectional distortions which were not taken into account in the calculations. The nature of these distortions is illustrated in figure 5.

When a box is undergoing a bending vibration, the inertia forces tend to bend the covers and webs in a manner like that shown at the top of figure 5. This distortion, in turn, causes additional inertia forces which tend to raise the effective mass of the beam and lower the frequency. For torsional vibrations there occurs a similar bending of the webs and covers. More importantly, however, the cross section undergoes an overall shear. Both of these effects tend to raise the effective mass moment of inertia and, hence, to lower the torsional frequencies. In an ordinary box, the presence of stiffening members, such as stringers and ribs or bulkheads, tends to prevent these cross-sectional distortions. In the tube, however, there were no such stiffeners, and the frequencies were therefore greatly reduced.

It should be mentioned that one of the present trends in structural design is in the direction of eliminating stringers and bulkheads and letting the skin carry most of the load. Therefore, this effect of cross-sectional flexibility may indeed become important for actual box beams, just as it is for the hollow tube.

Studies of the effects of cross-sectional distortions on the bending and torsional frequencies of box beams have been carried out. The effect of the local bending of the covers and webs has been presented in reference 5; an analysis of the effect of the overall shear of the cross-section has also been performed. Results of applying the corrections indicated by these studies to the frequencies of the hollow tube are shown by the frequencies in the last column of table II for both symmetrical bending and antisymmetrical torsion. The agreement with experiment is now satisfactory for all the bending modes. The agreement for the torsional modes is surprisingly good considering the large effects taken into account by the approximate correction.

CONCLUDING REMARKS

From the comparisons between theory and experiment that have been discussed for the box beams, it can be concluded that the secondary effects of transverse shear and shear lag can have an important influence on the bending vibrations of box beams. This is true even for long beams if the higher modes are desired. The effect of restraint of warping on the torsional modes is not nearly so important. The effects of cross-sectional distortion can be quite large unless stiffening members are used to minimize the distortion. In any event, the methods developed for taking all these effects into account are very successful.

REFERENCES

1. Budiansky, Bernard, and Kruszewski, Edwin T.: Transverse Vibration of Hollow Thin-Walled Cylindrical Beams. NACA Rep. 1129, 1953. (Supersedes NACA TN 2682.)

2. Kruszewski, Edwin T., and Kordes, Eldon E.: Torsional Vibrations of Hollow Thin-Walled Cylindrical Beams. NACA TN 3206, 1954.

3. Davenport, William W., and Kruszewski, Edwin T.: A Substitute-Stringer Approach for Including Shear-Lag Effects in Box-Beam Vibrations. NACA TN 3158, 1954.

4. Levy, Samuel: Computation of Influence Coefficients for Aircraft Structures With Discontinuities and Sweepback. Jour. Aero. Sci., vol. 14, no. 10, Oct. 1947, pp. 547-560.

5. Budiansky, Bernard, and Fralich, Robert W.: Effects of Panel Flexibility on Natural Vibration Frequencies of Box Beams. NACA TN 3070, 1954.

[redacted]

TABLE I

FREQUENCIES OF BUILT-UP BOX

SYMMETRICAL BENDING				ANTISYMMETRICAL TORSION			
MODE	EXP., CPS	ELEM., CPS	"EXACT", CPS	MODE	EXP., CPS	ELEM., CPS	"EXACT", CPS
1	18.1	18.4	18.0	1	64.7	63.0	63.3
2	84.7	101.0	86.4	2	194.0	189.0	194.0
3	176.0	247.0	181.0	3	313.0	315.0	332.0
4	271.0	458.0	285.0				

TABLE II

FREQUENCIES OF HOLLOW TUBE

SYMMETRICAL BENDING				ANTISYMMETRICAL TORSION			
MODE	EXP., CPS	"EXACT", CPS	CORR., CPS	MODE	EXP., CPS	"EXACT", CPS	CORR., CPS
1	68.7	70.2	70.2	1	301.0	377.0	316.0
2	342.0	348.0	328.0	2	455.0	1133.0	485.0
3	572.0	761.0	586.0	3	648.0	1911.0	705.0

DECLASS[redacted]ED

TYPICAL BOX BEAM

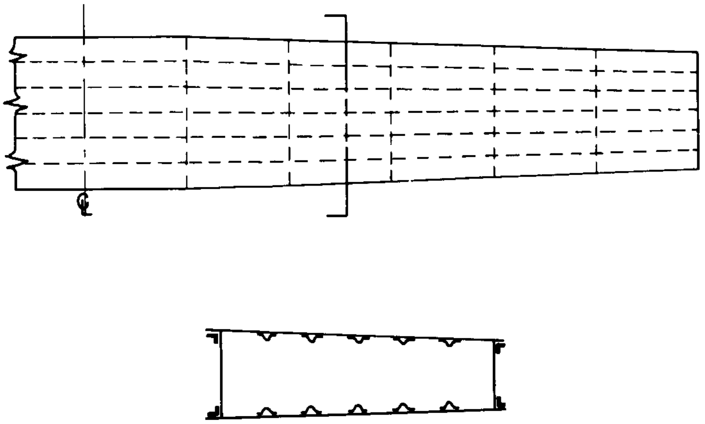

Figure 1

CROSS-SECTIONAL IDEALIZATIONS

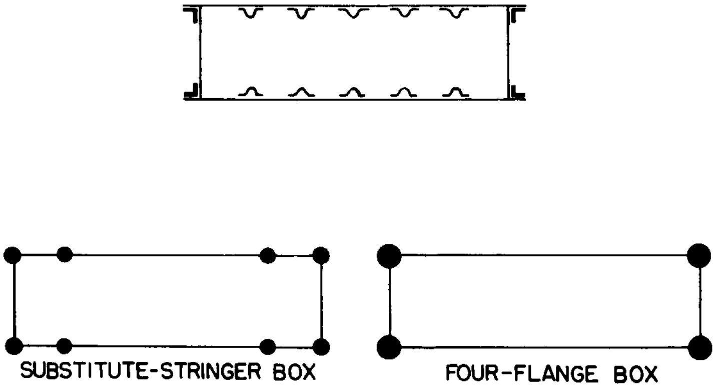
SUBSTITUTE-STRINGER BOX

FOUR-FLANGE BOX

Figure 2

[redacted]

[redacted]

VIBRATION TEST SET-UP OF BOX BEAM

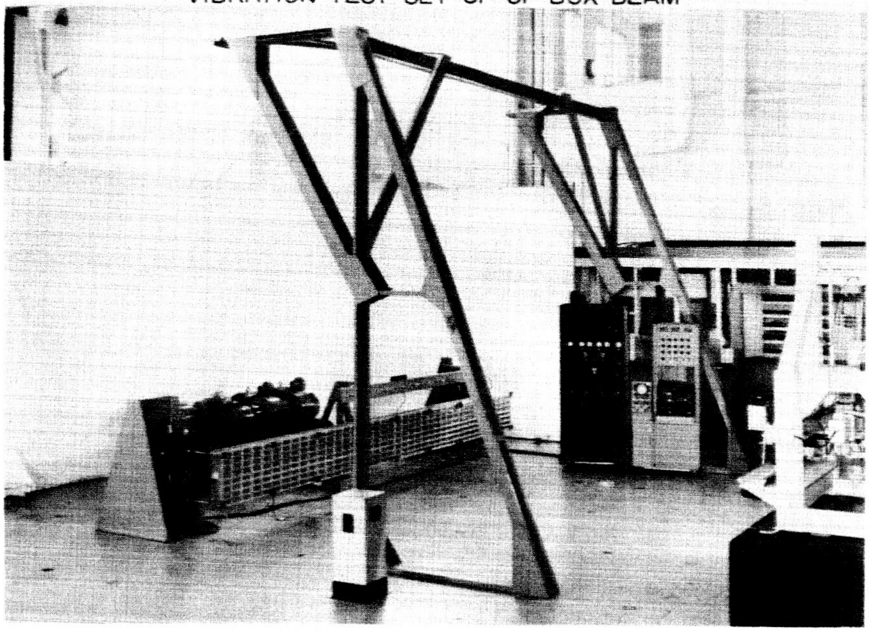

Figure 3

HOLLOW RECTANGULAR TUBE

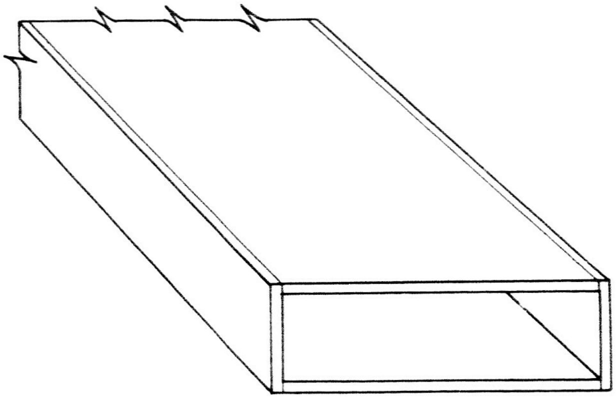

Figure 4

[redacted]

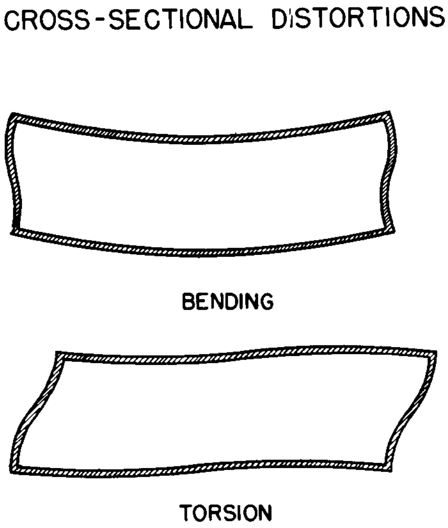

Figure 5

[redacted]

[redacted]

COMPARISON BETWEEN THEORETICAL AND EXPERIMENTAL STRESSES IN CIRCULAR SEMIMONOCOQUE CYLINDERS WITH RECTANGULAR CUTOUTS

By Harvey G. McComb, Jr., and Emmet F. Low, Jr.

Langley Aeronautical Laboratory

INTRODUCTION

In an effort to provide better procedures for estimating the stresses about doors, windows, and other openings in airplane fuselages, a method of stress analysis has been developed for handling cutouts in circular semimonocoque cylinders - a type of structure which approximates many large fuselages. This method of analysis was described in detail in reference 1. Calculations have now been carried out which enable direct comparisons to be made between this theory and test results. The theory is summarized and a few comparisons between theoretical stresses and the results of tests conducted at the Langley Aeronautical Laboratory are presented.

THEORY

A typical structure of the type for which this theory was developed is shown in figure 1. It consists of a thin-walled circular cylinder stiffened by rings circumferentially and by stringers in the axial direction. The rings and stringers divide the shell or skin into rectangular panels which are called shear panels. The cutout is rectangular; it removes a number of shear panels and interrupts the corresponding stringers. The theory can be used for any external loading where the stress distribution in the cylinder without a cutout is known. Some of these loadings are illustrated in figure 1; for instance, torque, bending, shear, and axial load are shown.

In the development of the theory it has been assumed that this stiffened shell is uniform and relatively long in comparison with the length of the cutout. It is also assumed that the skin takes all the shear stresses and the stringers carry all direct stresses - two assumptions which are usually made in the stress analysis of stiffened shell structures. A further assumption is that the shear stress is constant within a given shear panel and represents the average shear within that panel.

[redacted]

It is common practice in fuselage analysis to assume that the rings do not deform in their own planes. However, in the present theory the bending flexibility of the rings in their own planes has been taken into account; and, as will be seen, this factor is important in the calculation of stresses about cutouts.

The fundamental idea of the method of analysis is that the stress distribution in a stiffened cylinder with a cutout can be represented as a superposition of two stress fields - the stresses which would exist in the structure if it did not have a cutout and the stress perturbations which arise because of the cutout. Certain so-called perturbation stress distributions can be superposed on the stresses in the cylinder without a cutout in such a manner as to annihilate the effects of that portion of the cylinder which would lie within the cutout.

In general, three kinds of perturbation stress distributions are sufficient to handle rectangular cutouts in circular semimonocoque cylinders. These perturbation stress distributions are the stresses associated with the three loadings shown in figure 2. These loadings, called perturbation loads, are imposed on a uniform stiffened cylinder infinite in length. The concentrated perturbation load consists of a concentrated force applied to one stringer of the shell at its intersection with a ring. The shear perturbation load consists of uniformly distributed forces applied to the portions of stringers and rings which border one shear panel of the cylinder as shown in the upper right-hand sketch of figure 2. The distributed perturbation load consists of a single uniformly distributed force applied to a portion of one stringer extending between two adjacent rings.

The most difficult part of the analysis, that of finding the shear flows and stringer loads due to these perturbation loads, has been done mathematically, and the results can be presented in tabular form. With the help of such tables, the analysis of a cylinder with a cutout is not difficult. The calculation of the necessary tables for a wide range of structural properties has been carried out on an IBM Card-Programmed Electronic Calculator and the results are given in reference 2.

The theory is sufficiently versatile to account for the effects of shear and stringer reinforcement about the cutout without any essential increase in difficulty in the analysis. On the other hand, this theory does not appear to be entirely suitable for taking into consideration fuselage pressurization. The axial component of internal pressure can be handled satisfactorily. However, in the idealization on which the theory is based, circumferential loads in the skin are lumped into the rings; therefore, a detailed calculation of the redistribution about a cutout of hoop stresses arising from pressurization is beyond the scope of this theory.

TESTS

A test program was carried out at the Langley Aeronautical Laboratory to provide data for checking methods of stress analysis. Figure 3 illustrates the specimen which was tested. The test cylinder was cantilevered from the backstop and it could be loaded in various ways at the free end. Extensive testing was done on this specimen under several loading conditions and with successively larger cutout sizes. Strain measurements were made in the vicinity of the cutout with resistance wire strain gages.

COMPARISONS

Numerous comparisons have been made between theory and test, and a few of these are shown in figures 4, 5, and 6. In figure 4, there is shown a comparison between calculated and experimental shear stresses in the net section of a cylinder under torque loading. The sketch in the upper right-hand corner of the figure is a cross section through the cutout. The cutout extends around 90° of the circumference. The circles are test points measured by strain gages located at the center of successive shear panels in the circumferential direction. The dashed line represents the shear stress which would occur if the cutout did not exist - calculated from elementary torsion theory. The broken stepwise line is the theoretical result if the deformations of the rings are neglected, that is, if the rings are considered to be rigid - a common practice in fuselage analysis. The solid stepwise line represents the theoretical shear stresses when the bending flexibility of the rings in their own planes is taken into account. The theoretical curves are drawn in the step fashion because in the theory the shear is assumed to be constant between stringers. The abrupt jumps occur at the stringer locations where theoretically there exists a sudden change in shear stress. It is seen that there is good agreement between the flexible-ring theory and the test points. When the flexibility of the rings is neglected, the effect of the cutout is carried too far around the cylinder. The influence of ring flexibility on the shear stresses shown in this figure is rather typical of all the shear comparisons which have been made in that the sharp stress peaks and high gradients are more accurately defined and the disturbance due to the cutout decays more rapidly.

In figure 5 is shown stringer stresses at the ring bordering the cutout in the structure of figure 4. The loading condition again is torque. The circles are test points. The broken line is the theoretical result when ring deformations are neglected, and the solid line shows theoretical results when ring bending flexibility is accounted for. If there were no cutout in the structure, the stringer stresses would be zero under this loading condition. Again, there is good agreement between experiment and the flexible-ring theory.

[redacted]

Another loading condition is represented in figure 6 which also illustrates some effects of cutout size. In figure 6 are represented stresses in a cantilevered cylinder loaded at the tip by a shear load as indicated by the arrow in the sketch at the upper right. If the cutout is a fuselage side door located aft of the wing, this loading condition is caused by a down load on the tail. The stresses that are plotted are shears in the net section. The measured stresses indicated by squares and circles are obtained from strain gages located in the center of the shear panels, as before. The squares are for a cutout extending 50° around the circumference of the cylinder and the circles are for a 90° cutout. Both of the theoretical curves are the result of flexible-ring theory. It is seen that increasing the size of the cutout along the circumference increased the concentration of shear stress at the cutout, but had little influence on the shears on the other side of the cylinder - 180° from the cutout center line.

CONCLUDING REMARKS

Many other comparisons have been made between the theory and experiments carried out at the Langley Aeronautical Laboratory, and satisfactory agreement similar to that illustrated in the preceding figures is exhibited. It appears, therefore, that a relatively simple, rational method for estimating the stresses about cutouts in circular semimonocoque cylinders under many loading conditions is now available.

REFERENCES

1. McComb, Harvey G., Jr.: Stress Analysis of Circular Semimonocoque Cylinders With Cutouts by a Perturbation Load Technique. NACA TN 3200, 1954.

2. McComb, Harvey G., Jr., and Low, Emmet F., Jr.: Tables of Coefficients for the Analysis of Stresses About Cutouts in Circular Semimonocoque Cylinders With Flexible Rings. NACA TN 3460, 1955. (Prospective NACA paper.)

[redacted]

[redacted]

CYLINDRICAL SHELL WITH CUTOUT

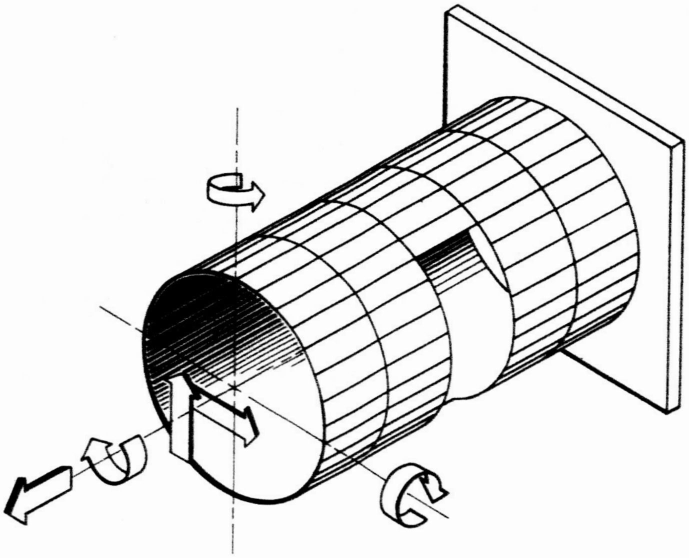

Figure 1

PERTURBATION LOADS

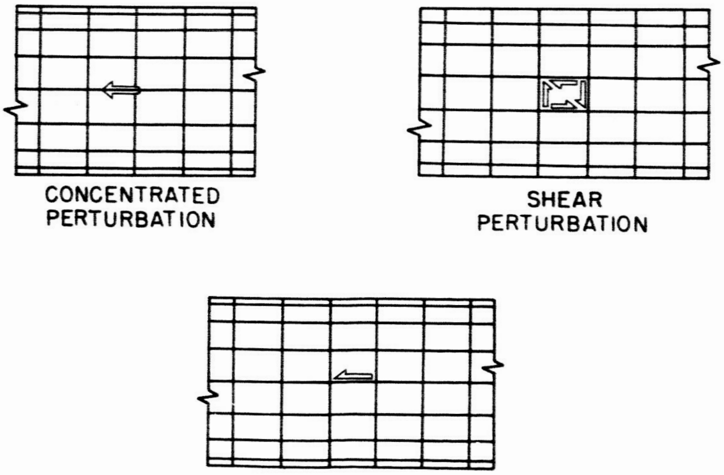

CONCENTRATED PERTURBATION

SHEAR PERTURBATION

DISTRIBUTED PERTURBATION

Figure 2

[redacted]

CYLINDER CUTOUT TEST

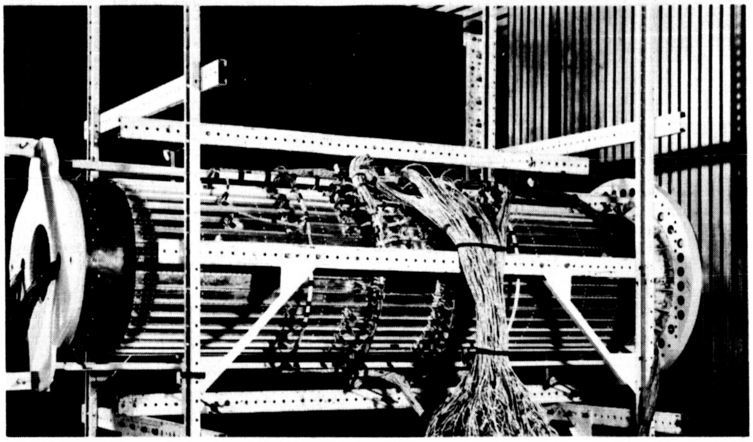

Figure 3

SHEAR STRESSES IN NET SECTION
PURE TORSION; 90° CUTOUT

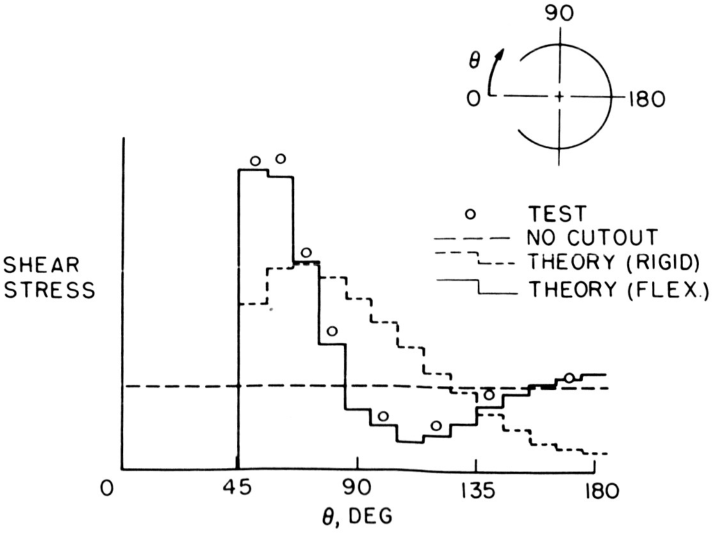

Figure 4

[redacted]

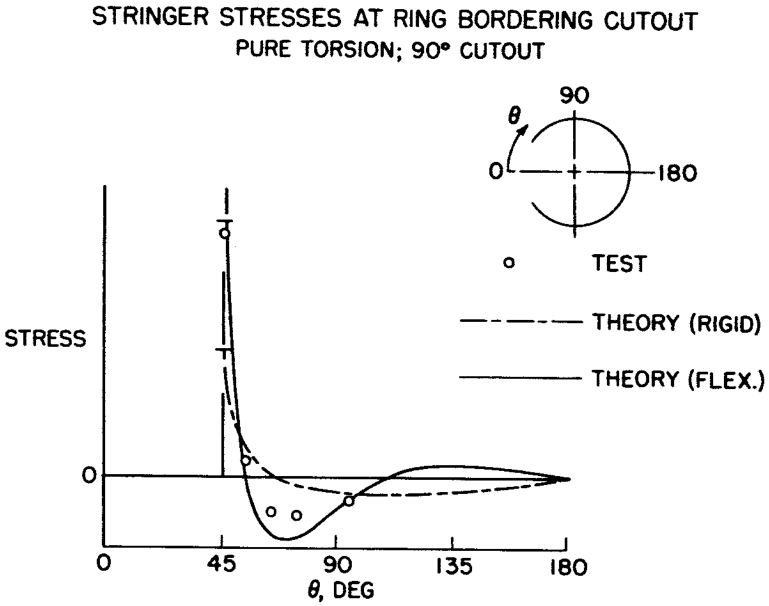

STRINGER STRESSES AT RING BORDERING CUTOUT
PURE TORSION; 90° CUTOUT

Figure 5

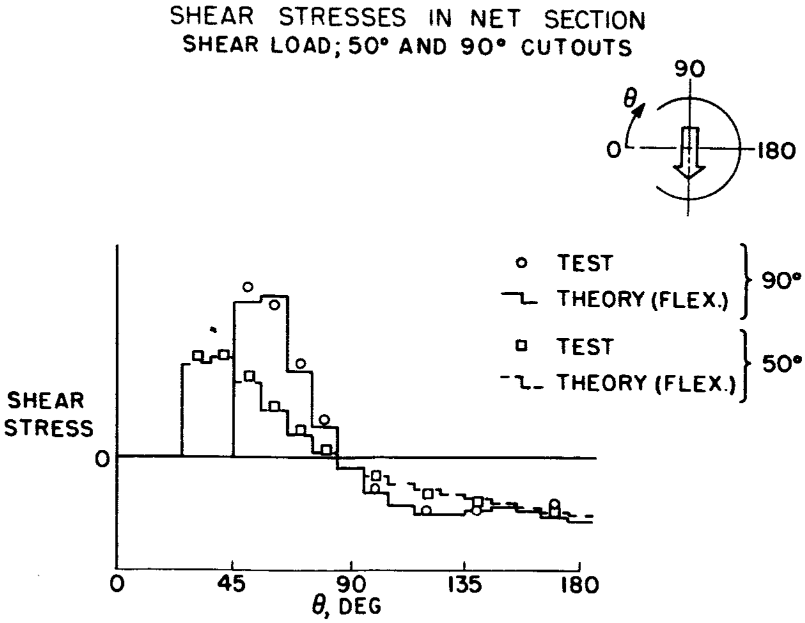

SHEAR STRESSES IN NET SECTION
SHEAR LOAD; 50° AND 90° CUTOUTS

Figure 6

[redacted]

[redacted]

DEFLECTION ANALYSIS OF LOW-ASPECT-RATIO WINGS

By J. Lyell Sanders, Jr., and Manuel Stein

Langley Aeronautical Laboratory

INTRODUCTION

One important structural problem brought on by the advent of the low-aspect-ratio wing is the development of an adequate load-deflection analysis for use in predicting the static and dynamic aeroelastic behavior of the airplane. It is generally recognized that simple-beam theory is inadequate for the analysis of delta wings. On the other hand, any brute-force methods for attacking such a complicated structure would involve so much computing that it would be impractical. Any practical analytical method must be a reasonable compromise between accuracy and amount of work. Since the amount of work involved is likely to be large in any case, the method should present a well-organized procedure starting from raw data readily available to the engineer and it should also be tailored to take advantage of high-speed automatic computers. Several analytical approaches to the solution of the problem have been set forth within the last three years in papers by Schuerch, Levy, and Williams, all of them based on the analysis of an idealized structure. (See refs. 1 to 3.) Other people have investigated the possibilities of analog methods, but these will not be discussed in this paper.

DISCUSSION

In the so-called "wide beam" theory proposed by Schuerch, the wing is idealized into a bundle of alternating beams and torsion tubes tied together with rigid ribs (fig. 1). In this theory a system of ordinary differential equations analogous to the simple-beam equations is written from the conditions of equilibrium at each chordwise section. The theory is a generalization of simple-beam theory that takes approximate account of the important effects of low aspect ratio.

Levy, and also later Schuerch, has presented a method in which the wing is broken down into a gridwork of interlocking beams representing the bending stiffness of the spars, ribs, and sheet plus a system of torsion boxes representing the shear resistance of the sheet (fig. 2). The deflections under load of the structure as a whole can be found from the load-deflection characteristics of the various components together with the requirement that the distortions of the components be compatible when fitted together.

[redacted]

[redacted]

In either of these two idealizations the shear-carrying capacity and direct-stress-carrying capacity of the sheet are separated as is often done in the analysis of semimonocoque structures. However, the approximation can only be expected to be accurate when the covers are thin. Williams has introduced a method appropriate for wings with thick skin and numerous light internal stiffeners. The theory is essentially a modified plate theory and Williams has outlined a systematic method for solving the appropriate equations by making use of automatic computers.

Roughly speaking, the relation of the methods introduced by Schuerch, Levy, and Williams to the method to be discussed in this paper is that whereas they simplified the problem by idealizing the structure, the method of this paper analyzes the real structure but assumes that it deforms in an idealized way. The success of the method depends on the possibility of choosing simple yet accurate expressions to approximate the displacements of the material points of the structure under the expected loads.

The choice made was motivated by the plate-like appearance of a delta wing. The displacements of all points are assumed to be given in terms of the deflection of a neutral surface (fig. 3). As a further approximation it is assumed that the chords deform into parabolas. This assumption was successfully used in a theory for the analysis of solid cantilevered delta wings developed by Reissner and Stein (see refs. 4 and 5) a few years ago and there is reason to believe it will be successful for built-up wings also, provided there is sufficient restraint to prevent large chordwise bending. Therefore, the deflection of the neutral surface is assumed to be given in terms of the equation

$$w = \phi_0(x) + y\phi_1(x) + y^2\phi_2(x)$$

where ϕ_0, ϕ_1, and ϕ_2 are arbitrary functions of x.

It is assumed that normals to the neutral surface remain normal during deformation; hence, the strains and also the strain energies of all the component parts of the wing are completely determined in terms of w.

Before the method is outlined in detail, the final results will be anticipated. In the first place, a particularly convenient way in which to present the load-deflection characteristics of a wing is in the form of a matrix of influence coefficients. A set of influence coefficients gives the deflection at a chosen number of reference points on the wing due to unit loads at these reference points. Of course, the influence coefficients depend on how the wing is assumed to be supported whether it is cantilevered, supported at a number of fixed points, or attached to a

[redacted]

[redacted]

flexible fuselage. Since there are so many possible kinds of support, it would be difficult to set up a standard procedure for finding influence coefficients unless it is possible to choose a standard kind of support. Fortunately, this turns out to be the case. Once influence coefficients are found with respect to the standard kind of support, they can be modified in a simple way to give the influence coefficients for any other kind of support. Usually two sets of influence coefficients are found, namely, those for symmetric deflections and those for antisymmetric deflections.

The kinds of supports chosen in these two cases are shown in figure 4. From a practical viewpoint these supports look rather artificial, but these choices were motivated by a desire for mathematical simplicity. In the symmetric case the wing is clamped at the middle of the trailing edge. In the antisymmetric case the wing is simply supported at two symmetrically placed points along the trailing edge and at one point along the center line.

In order to find an appropriate set of equilibrium equations in which the unknowns are ϕ_0, ϕ_1, and ϕ_2, the principle of minimum potential energy is used. The strain energy of the whole wing is found by adding up the strain energies of all the components. The energy of the covers is found as though they were the face plates of a sandwich plate and the energies of the ribs and spars are obtained from the standard formula for the energy of a bent beam. In these expressions all derivatives are approximated by standard difference forms and the integrations are replaced by finite sums according to the trapezoidal rule. Thus, the final expression for the total potential energy of the wing involves the unknown values of ϕ_0, ϕ_1, and ϕ_2 at a number of equally spaced stations along the span and also certain coefficients or section properties at discrete stations together with terms arising from the loads.

Minimizing the potential energy with respect to the unknown values of ϕ_0, ϕ_1, and ϕ_2 at the station points leads to a set of linear algebraic equations which can be written in the following matrix form:

$$\left[\begin{array}{c:c:c} A_{11} & A_{12} & A_{13} \\ \hdashline A_{21} & A_{22} & A_{23} \\ \hdashline A_{31} & A_{32} & A_{33} \end{array}\right] \left[\begin{array}{c} \phi_0 \\ \hdashline \phi_1 \\ \hdashline \phi_2 \end{array}\right] = \left[\begin{array}{c} p_1 \\ \hdashline p_2 \\ \hdashline p_3 \end{array}\right] \qquad (1a)$$

[redacted]

or

$$[A]\,[\phi] = [p] \qquad \text{(1b)}$$

The p's on the right of equations (1) are generalized loads derived from the potential energy of the loads. For purposes of application, the rather involved derivation that leads to this equation need not be repeated. The form of the matrix $[A]$ has been worked out in the symmetric and antisymmetric cases for arbitrary arrangement of the internal structure of the wing.

For example, the submatrix $[A_{11}]$ in the symmetric case is given by the following equation:

$$[A_{11}] = [D_1]\left([a_1] + \sum_s [\beta_s]\right)[D_1]' \qquad (2)$$

where $[D_1]$ is a purely numerical matrix and $[D_1]'$ is the transpose of $[D_1]$

$$[D_1] = \begin{bmatrix} 2 & -2 & 1 & & & \\ & 1 & -2 & 1 & & \\ & & & \ddots & & \\ & & & & 1 & -2 \\ & & & & & 1 \end{bmatrix} \qquad (3)$$

The matrices within parentheses (eq. (2)) depend on the properties of the wing. The matrix $[a_1]$ is a diagonal matrix where the elements are given by the integral from the trailing edge to leading edge, at a given station n along the span, of the stiffness D of the covers considered as an air-filled sandwich plate:

$$[a_1] = \begin{bmatrix} \frac{1}{2}a_{1,0} & & & & \\ & a_{1,1} & & & \\ & & \ddots & & \\ & & & a_{1,N-1} & \\ & & & & \frac{1}{2}a_{1,N} \end{bmatrix} \qquad (4)$$

[redacted]

$$a_{1,n} = \int_{c_0}^{c_1} D(x_n,y)dy \qquad (5)$$

The stiffness matrix $[\beta_s]$ of a typical span entering into the summation is shown below:

$$[\beta_s] = \begin{bmatrix} \frac{1}{2}\beta_{s,0} & & & & \\ & \beta_{s,1} & & & \\ & & \cdot & & \\ & & & \cdot & \\ & & & & \cdot \end{bmatrix} \qquad (6)$$

where

$$\beta_{s,n} = (EI_s)_n \cos^3\alpha_s \qquad (7)$$

The elements depend on the stiffness of the spars at the station points along the span. $(EI_s)_n$ is the stiffness of the sth spar at station n and α_s is the angle of sweep of that spar. The other submatrices in $[A]$ are formed in a similar way but are slightly more complicated.

The hardest part of the computation comes in inverting the matrix $[A]$. However, the operation can be done with the help of commonly available automatic computing machines. Once this is accomplished the generalized deflections ϕ are given in terms of the generalized loads p as shown

$$[\phi] = [A]^{-1}\,[p] \qquad (8)$$

The problem is essentially solved at this point. From here it is an easy step to get the final matrix of influence coefficients. The required set of influence coefficients are

$$[G] = [H]'\,[A]^{-1}\,[H] \qquad (9)$$

where $[H]$ is a matrix which converts generalized loads into concentrated loads and generalized displacements into displacements at particular points. The matrix $[H]$ depends on the coordinates of the chosen reference points on the plan form of the wing.

[redacted]

CONCLUDING REMARKS

A simple procedure has been worked out for finding symmetric or antisymmetric influence coefficients for the wing attached to a flexible fuselage by using the basic sets of influence coefficients resulting from the present method. The only additional information needed is a set of influence coefficients for the fuselage with the points of attachment as reference points.

The application of the method is more or less cut and dried and the results, being in the form of influence coefficients, are handy for subsequent calculations. The computations involved are arranged such as to make efficient use of automatic computing machines.

A rather thorough test program to obtain experimental influence coefficients, modes, and frequencies of a typical delta wing built up of ribs, spars, and covers is being undertaken and comparisons between the test results and the predictions of several theories including the present one will be made.

REFERENCES

1. Schuerch, Hans U.: Structural Analysis of Swept, Low-Aspect-Ratio, Multispar Aircraft Wings. Aero. Eng. Rev., vol. 11, no. 11, Nov. 1952, pp. 33 – 41.

2. Levy, Samuel: Structural Analysis and Influence Coefficients for Delta Wings. Jour. Aero. Sci., vol. 20, no. 7, July 1953, pp. 449 – 454.

3. Williams, D.: Recent Developments in the Structural Approach to Aeroelastic Problems. Jour. R.A.S., vol. 58, June 1954, pp. 403 – 428.

4. Reissner, Eric, and Stein, Manuel: Torsion and Transverse Bending of Cantilever Plates. NACA TN 2369, 1951.

5. Stein, Manuel, Anderson, J. Edward, and Hedgepeth, John M.: Deflection and Stress Analysis of Thin Solid Wings of Arbitrary Plan Form With Particular Reference to Delta Wings. NACA Rep. 1131, 1953. (Supersedes NACA TN 2621.)

[redacted]

SCHUERCH'S IDEALIZATION

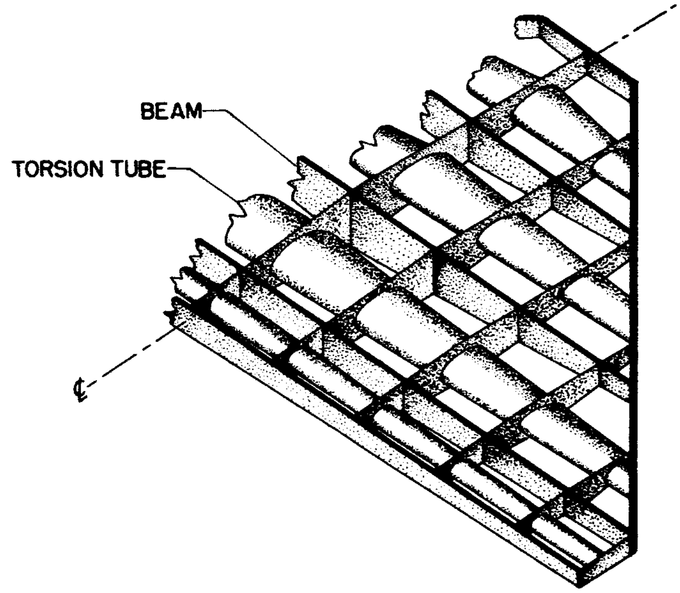

Figure 1

LEVY'S IDEALIZATION

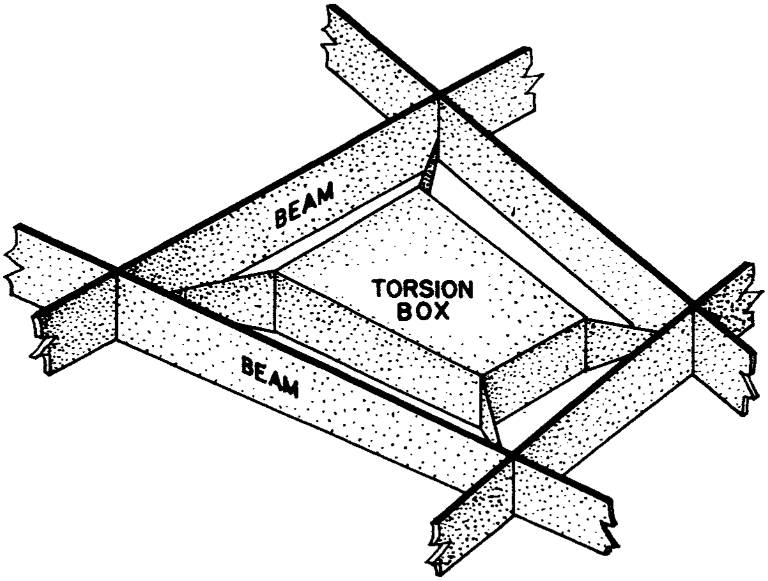

Figure 2

[redacted]

ASSUMED DEFLECTION OF NEUTRAL SURFACE

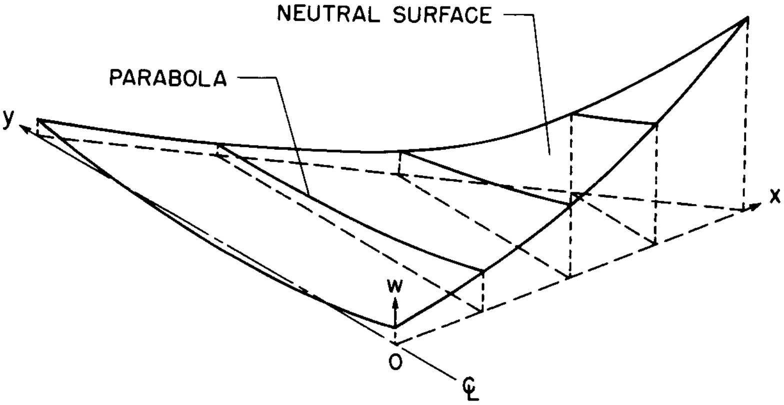

$$w = \phi_0(x) + y\phi_1(x) + y^2\phi_2(x)$$

Figure 3

SUPPORT CONDITIONS

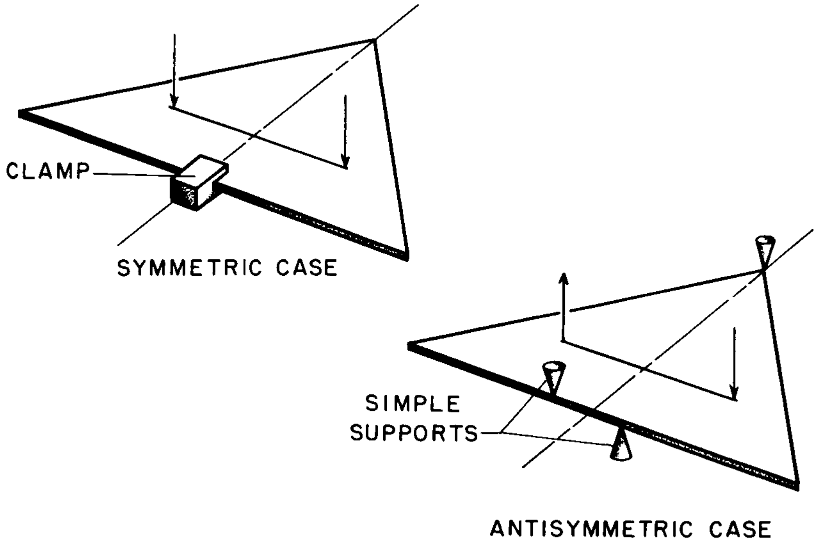

Figure 4

[redacted]

[redacted]

EXPERIMENTAL ANALYSIS OF MULTICELL WINGS

BY MEANS OF PLASTIC MODELS

By George W. Zender

Langley Aeronautical Laboratory

SUMMARY

The stresses and deflections of a plastic model of a delta multicell wing are presented and compared with theoretical results obtained by the use of the Cal-Tech analog computer. The comparison indicates that valuable information may be obtained for experimental structural analyses from tests of plastic models.

INTRODUCTION

The problems associated with low aspect ratio and high sweep have introduced difficulties which require extensive theoretical analyses and the use of intricate automatic computing machines in the structural analysis of aircraft wings. Such complications introduce considerable theoretical uncertainty and increase the demands for experimental evaluation of the structure. A method of experimental analysis which has been useful in the past involves the testing of scaled models made of plastic. Such a method has been used by Redshaw and Palmer (ref. 1) to obtain results directly applicable to a full-scale aircraft, whereas other investigators have obtained information useful in the analysis of various components of the structure. Nevertheless, the plastic-model approach is often rejected because of the peculiar properties of the plastic material. The National Advisory Committee for Aeronautics has made some tests using plastic models, and it is the purpose of this paper to show the methods which were employed to account for the peculiarities of the material and to present some of the results which have been obtained.

DISCUSSION OF TECHNIQUES

Considerable information on the properties of thermoplastic materials has been published by manufacturers. In general, such data indicate that for experimental purposes the temperature should be relatively low and closely controlled, and the humidity should be maintained reasonably

[redacted]

constant. In addition, the material experiences creep when subjected to stress and the severity of the creep is dependent upon the stress level.

An example of the type of results which are obtained from a structure made of one of the thermoplastic materials is shown in figure 1. The model in this case is a cantilever box beam constructed of $\frac{1}{10}$-inch Plexiglas I-A sheet, has a 2-inch width and depth, is 20 inches long, and has ribs located every 2 inches along the length. The beam was tested in bending in an air-conditioned room at a temperature of 68° F. The strain near the root was obtained on the tensile side of the beam, and a time history of the strain at three stress levels is shown. The circles show the strains for the lowest stress level when the stress at the gage location was 235 psi. After 13 minutes the load was removed, and the gradual tendency of the beam to relieve itself of strain is shown. The cycle was repeated for stress levels of 705 psi and 940 psi, and it is noted that more time is required for the beam to relieve itself of strain as the stress level is increased.

For experimental work it would be desirable to avoid stresses of the magnitudes shown by the upper curve in figure 1 since the strain does not reach a constant level. Tests are sometimes performed at such levels by waiting several minutes after loading before taking measurements in order to avoid the region of the primary effects of creep, and then unloading to permit the structure to relieve itself of strain before proceeding to the next loading. In most cases, however, it is possible to limit the maximum stresses to lower stress levels than those shown by the upper curves of figure 1 and to perform the test in the manner shown in figure 2. In this test the beam was loaded at small stress increments of 162 psi without unloading the beam between successive loadings. It is noted that essentially constant strains were obtained except for the 648 and 810 psi stress levels. Therefore, if it were possible to limit the maximum stresses to about 500 psi, it would appear permissible to perform the tests without unloading between successive loadings. The modulus of elasticity necessary for converting strains to stresses may be obtained from tests of an elementary beam, such as the beam shown in figures 1 and 2, constructed from samples of the same sheet material used in the plastic model.

COMPARISON OF EXPERIMENTAL AND ANALOG RESULTS

By using the experience gained from the tests of the simple box beam presented in the first two figures, a plastic delta-wing model was constructed and tested. The design selected was one analyzed theoretically by MacNeal and Benscoter (ref. 2) with the use of the Cal-Tech analog computer. The idealized structure analyzed by the analog computer

[redacted]

was believed closely representative of the actual structure; however, no experimental verification had been obtained and it was possible that such information might be provided by a plastic-model test. The plan form of the delta wing and the stresses obtained are shown in figure 3.

The wing as analyzed by the analog computer has a 90-inch semispan and an 80-inch-chord line at the root. The leading edge sweeps back at 45° and the wing has a biconvex cross section. The maximum thickness is a constant 5 inches in the carry-through section and tapers from 5 inches at the root-chord line to 2 inches at the tip. The cover thickness is 0.16 inch and the interior of the wing is broken up into cells by 0.14-inch-thick spars and ribs. The wing is supported along the root-chord line indicated by the solid line. The plastic model was constructed to three-eighths the scale of these dimensions and was made of Plexiglas I-A sheet material. The stresses obtained on the plastic model were made comparable with the analog-computer stresses by means of a similarity factor determined from the scale factor of the models. The results are shown for three loading cases: a tip load at the trailing edge, a tip load at the leading edge, and a torque loading at the tip. The plastic-model stresses along the root-chord line shown by the test points agree well with the analog-computer stresses shown by the curves for each of the loading cases.

Figure 4 shows the deflections of the wing for the same three loadings. The deflections are shown for three spanwise locations as identified by the three types of test points. Again, the agreement of the results is good, which indicates that most likely both the plastic-model results and the analog-computer results are correct for this particular design.

CONCLUDING REMARKS

One distinct advantage which favors the plastic-model approach is that models may be constructed very similar to the actual design, whereas, in most theoretical structural analyses, an idealized or substitute structure is assumed in order to simplify the mathematics. In the case of the relatively simple delta design presented here, the idealized or substitute structure analyzed by the analog computer was accurately representative of the actual structure. In practice, however, many cases exist where the proper idealization of the actual structure for theoretical purposes is uncertain. In such cases, the behavior of the structure might be obtained from tests of plastic models. It is believed that a more general use of plastic models for experimental structural analyses could contribute valuable information for some of the problems now associated with aircraft structures.

DECLAS[redacted]D

REFERENCES

1. Redshaw, S. C., and Palmer, P. J.: The Construction and Testing of a Xylonite Model of a Delta Aircraft. The Aeronautical Quarterly, vol. III, pt. II, Sept. 1951, pp. 83-127.

2. MacNeal, Richard H., and Benscoter, Stanley U.: Analysis of Multicell Delta Wings on Cal-Tech Analog Computer. NACA TN 3114, 1953.

[redacted]

[redacted]

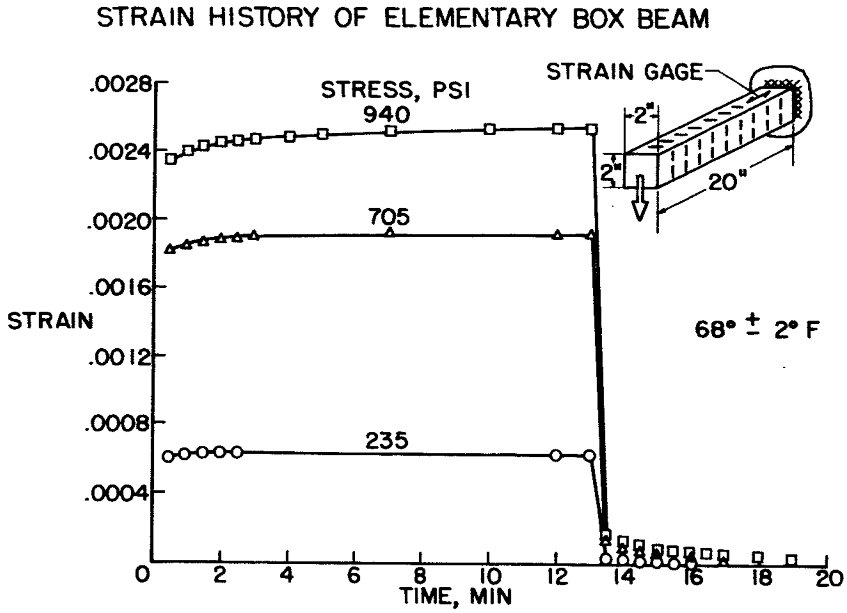

Figure 1

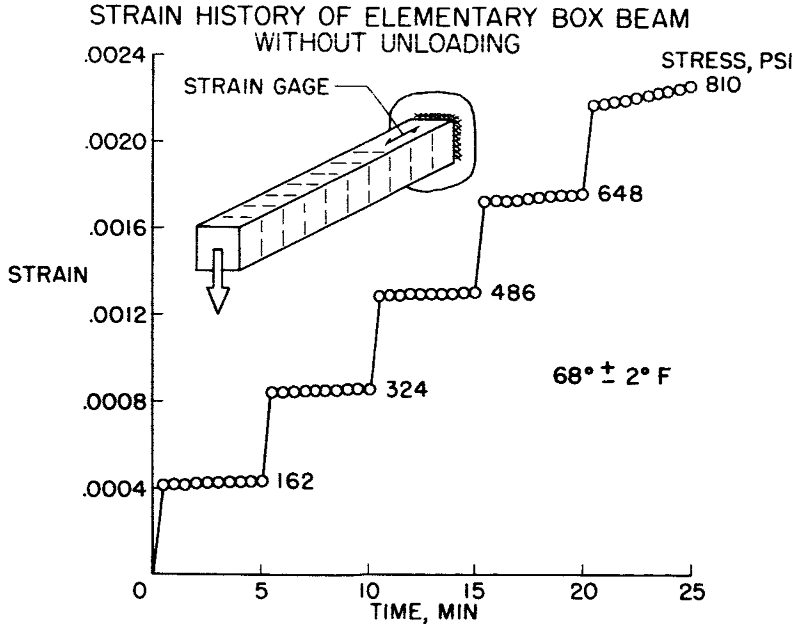

Figure 2

[redacted]

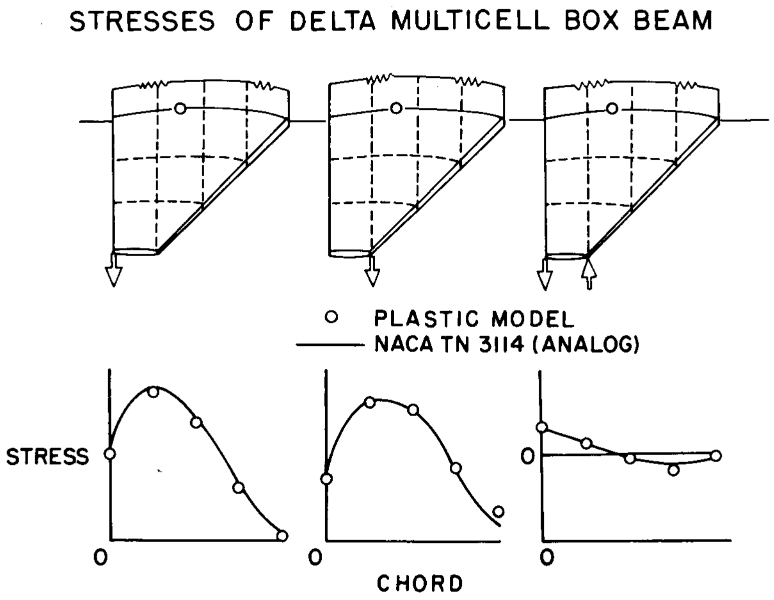

Figure 3

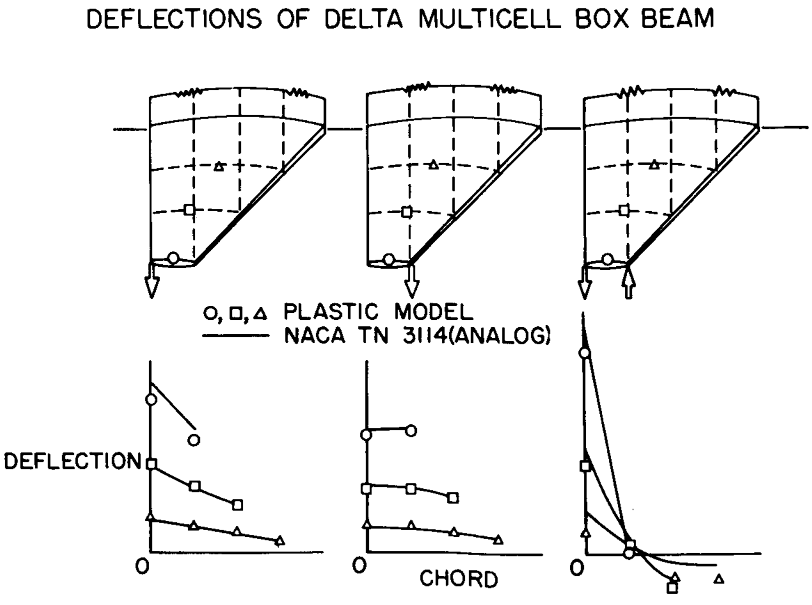

Figure 4

[redacted]

EFFECT OF RIVETED-JOINT GEOMETRY ON STRENGTH OF STIFFENED PLATES IN COMPRESSION

By James P. Peterson and Joseph W. Semonian

Langley Aeronautical Laboratory

Although rivets are used extensively to fasten the webs and stringers to the compression cover of aircraft wings, no generally accepted method exists for determining the pitch and diameter of these rivets. In order to provide a solution to this problem, the NACA has, in recent years, tested a large number of short compression panels to study the variation of panel strength with changes in riveting. At various times as data were accumulated, design criteria based on an evaluation of the data were published. (See, for example, ref. 1.) The use of these criteria generally produces conservative designs and in some cases overly conservative designs. More recently, these data have been reevaluated, and a method for designing the rivets in the compression cover of aircraft wings that is easy to apply and gives good correlation with experiment has been developed. This paper reviews some aspects of recent studies; the details of the studies are given in reference 2.

In order to understand the method, it is helpful to have a concept of the various local modes of failure of sheet-stringer panels in compression or multiweb beams in bending. These modes are illustrated in figure 1 where a curve of failing stress for a given panel is plotted against rivet pitch — the only structural dimension being varied. Below the curve are photographs of three panels that have been tested to failure in compression. Each photograph represents a distinct and different mode of failure; the names of the modes are labeled above the curve.

When the rivet pitch is small, the panel buckles in the local mode; this mode is characterized by consecutive in-then-out buckles as one progresses either across or up and down the panel. The panel fails as a result of the growth of the local buckles, and such failures are referred to as failure by local crippling or failure in the local mode. These failures occur at the highest stress level attainable in riveted structures that are short enough so that the column bending mode can be neglected, yet long enough so that the various local modes can form freely without end effects. The curve of stress against pitch is drawn horizontal for this mode, indicating that the failing stress is relatively independent of riveting as long as the riveting is adequate to force failure in the local mode. Consequently it is particularly informative to know the riveting required to force failure in the local mode; any additional riveting is useless unless it is needed to satisfy some other design criterion such as shear strength.

On the next section of the curve, wrinkling or forced-crippling-type instability occurs. This type of instability is characterized by troughs and crests extending across the cover, and failure results when the cover crushes or lifts away from the Z-stringers or channel webs that support it. The wrinkling mode has often been mistaken for the next mode shown in the figure – the interrivet mode. The interrivet mode becomes the predominant mode when the rivet pitch is approximately equal to the length of the buckles in the wrinkling mode so that the cover separates from the stringers or webs between rivets. In the wrinkling mode there is no separation between the cover and its supporting members; the flanges of the supporting members follow the cover contour as the buckles grow until just prior to failure. At failure, there may or may not be a separation, depending upon the riveting and the panel proportions as well as the amount of shortening to which the panel is subjected.

Methods of analysis of the wrinkling mode were first developed for multiweb beams in bending and are reported in reference 3. These methods have been extended to include sheet-stringer panels in compression and have developed to the extent that they can now be used to predict the strength of multiweb beams and sheet-stringer panels quite accurately. (See ref. 2.) The strength of these structures is highly dependent upon the flexibility of the riveted attachment between the cover and the webs of the Z-stringers or channel webs that support the cover. That is, if the attachment is flexible, it is easy for the troughs and crests to form and grow, and as a consequence they will form and grow at a low stress level. The analysis makes use of a new dimension, termed "the effective rivet offset," which is a measure of the flexibility of the riveted attachment. Figure 2 illustrates some of the more important structural dimensions that influence the flexibility of the riveted attachment; they are the geometric rivet offset b_0, the rivet pitch, and the rivet diameter. The effective rivet offset f can be considered to be a corrected or effective value of the geometric offset b_0. It has been evaluated empirically in terms of the dimensions shown in figure 2 from a large number of tests on sheet-stringer panels and multiweb beams. Figure 3 shows values of the effective rivet offset f divided by the web thickness plotted against the ratio of pitch to diameter of the attachment rivets for various values of the geometric rivet offset divided by the web thickness. It was found that changes in the attachment flexibility resulting from changes in the pitch and diameter of the rivets could be accounted for by changes in the single rivet parameter pitch/diameter, making the simple presentation shown in figure 3 possible. The only way that the rivet pitch, diameter, and location enter strength calculations is through the value of effective rivet offset f obtained from this figure. That value is valid only if the rivets satisfy an additional simple tensile strength criterion that has been developed and is given by formula (11) of reference 2. If the rivets do not satisfy the strength criterion, a rivet failure will occur in place of a panel failure. The strength criterion is relatively easy to satisfy and will not determine the size and

[redacted]

spacing of rivets for most designs, indicating that the stiffness of the attachment governs the design rather than the rivet strength. This may seem contrary to experience for many observers but actually it is not. The rivet failures observed in most cases actually occur after the structure has reached maximum load in the wrinkling mode.

Figure 3 does not illustrate very effectively the changes in structural strength associated with changes in the various riveting parameters. Two additional figures which better illustrate these changes have been prepared. They were prepared using figure 3 as a design chart. The first of these figures (fig. 4) presents curves of stress against riveting geometry somewhat similar to figure 1, except the interrivet-mode section of the curve is omitted. The curves are drawn for the 7075-T6 (formerly 75S-T6) aluminum-alloy panel whose dimensions are indicated in the figure. The top curve of figure 4 represents the panel with a rivet offset of 5 web thicknesses. This offset is representative of design practices where the designer is consciously attempting to keep the offset small. As the rivets are spaced closer together, the strength of the panel increases until the rivets are spaced at $6\frac{1}{2}$ diameters. This riveting is adequate to force failure in the local mode, and a further decrease in rivet spacing does not result in an increase in failing stress. The curve representing the panel with an offset of 7 web thicknesses indicates that increasing the offset by 2 web thicknesses makes an appreciable reduction in failing stress at any given rivet spacing and indicates that with the increase in offset it takes a rivet pitch of 4 diameters to obtain the local crippling strength of the panel. With an offset of 9 web thicknesses, it is impossible to obtain the local crippling strength of the panel. The curves are stopped at a pitch of 2 diameters because, at this pitch, rivet heads normally touch one another.

Consider the sketch of the panel in figure 4 and imagine a series of panels obtained by changing the distance between stringers b_S. As the stringer spacing is made smaller and smaller, the panel will fail at higher and higher stresses. The riveting required to force local crippling of the panel will also change with changes in stringer spacing, and figure 5 shows the riveting required to force local crippling of such a series of panels with a rivet offset of 5 web thicknesses. The riveting required to force a local-crippling failure for the panel represented by the top curve in figure 4 is indicated in figure 5 at a value of b_S/t_S of 40 and a pitch-diameter ratio of $6\frac{1}{2}$. It will be noted that as b_S/t_S is decreased and the panel becomes stronger, the rivet pitch required to force local crippling goes from about 7 diameters at $b_S/t_S = 50$ to 3 diameters at $b_S/t_S = 20$. Shown for comparison is the curve for similar 2024-T3 (formerly 24S-T3) aluminum-alloy panels. Here again, in going from the weaker 2024-T3 aluminum-alloy panels to the stronger 7075-T6 aluminum-alloy panels, closer riveting is required to force a local-crippling failure. The curves in this figure are drawn for a relatively small rivet offset. Had a larger offset been used, the values of the pitch-diameter ratio required would have been considerably less.

In summary, a method of strength analysis of structual components such as short sheet-stringer panels in compression and multiweb beams in bending has been developed. The method is simple to apply and takes into account the effect that the riveted attachments between the plate and its supporting members have on the strength of the structure. The use of the method permits the influence of rivet pitch, diameter, and location on structural strength to be calculated.

REFERENCES

1. Dow, Norris F., Hickman, William A., and Rosen, B. Walter: Effect of Variation in Rivet Strength on the Average Stress at Maximum Load for Aluminum-Alloy, Flat, Z-Stiffened Compression Panels That Fail by Local Buckling. NACA TN 2963, 1953.

2. Semonian, Joseph W., and Peterson, James P.: An Analysis of the Stability and Ultimate Compressive Strength of Short Sheet-Stringer Panels With Special Reference to the Influence of Riveted Connection Between Sheet and Stringer. NACA TN 3431, 1955.

3. Semonian, Joseph W., and Anderson, Roger A.: An Analysis of the Stability and Ultimate Bending Strength of Multiweb Beams With Formed-Channel Webs. NACA TN 3232, 1954.

[redacted]

MODES OF FAILURE IN MULTIWEB BEAMS AND SHEET-STRINGER PANELS

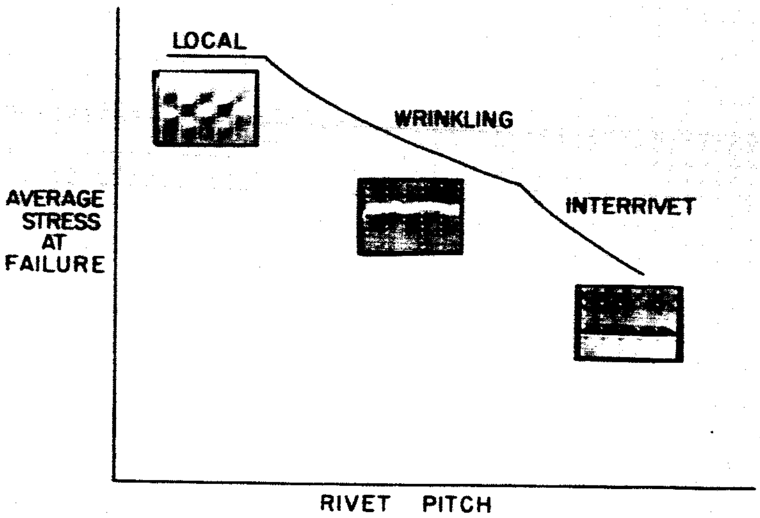

Figure 1

DIMENSIONS AFFECTING EFFECTIVE RIVET OFFSET

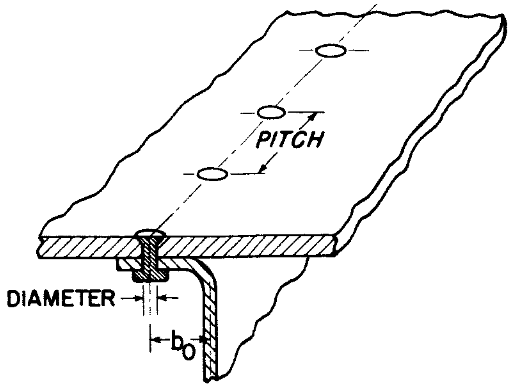

Figure 2

[redacted]

DECLA[redacted]ED

VARIATION OF EFFECTIVE RIVET OFFSET WITH RIVET PITCH, DIAMETER, AND OFFSET

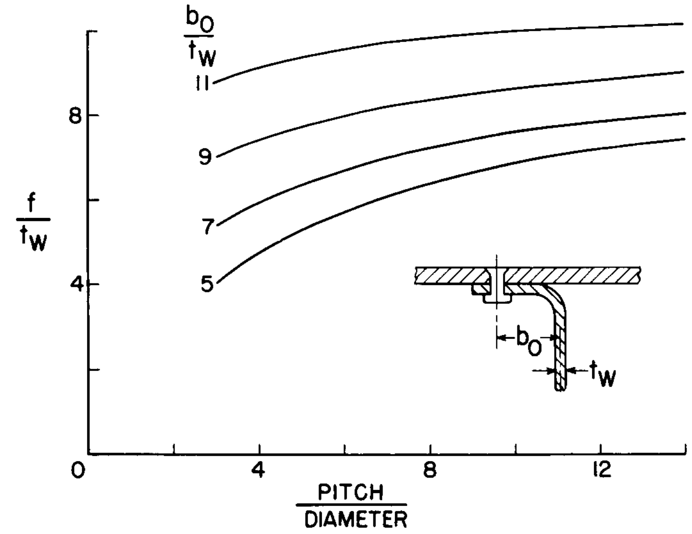

Figure 3

EFFECT OF RIVET PITCH, DIAMETER, AND LOCATION ON STRENGTH OF 7075-T6 SHEET-STRINGER PANEL

$\frac{b_w}{t_w} = 20.0;\ \frac{b_s}{t_s} = 40.0;\ \frac{t_w}{t_s} = 0.63$

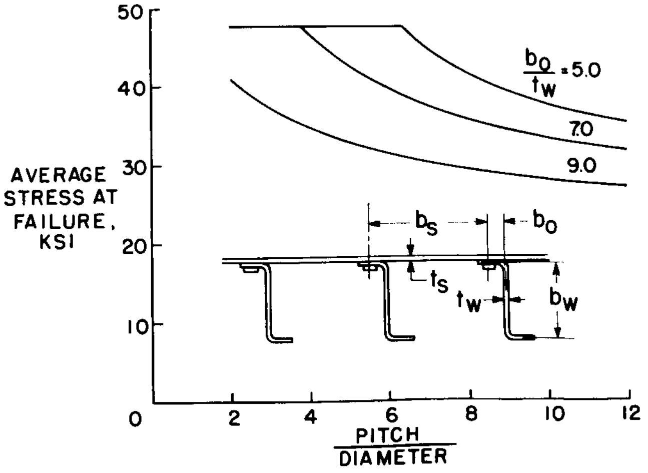

Figure 4

[redacted]

EFFECT OF CHANGING PANEL CONFIGURATION ON RIVETING REQUIRED TO FORCE LOCAL CRIPPLING

$\frac{b_w}{t_w} = 20; \frac{b_o}{t_w} = 5.0; \frac{t_w}{t_s} = 0.63$

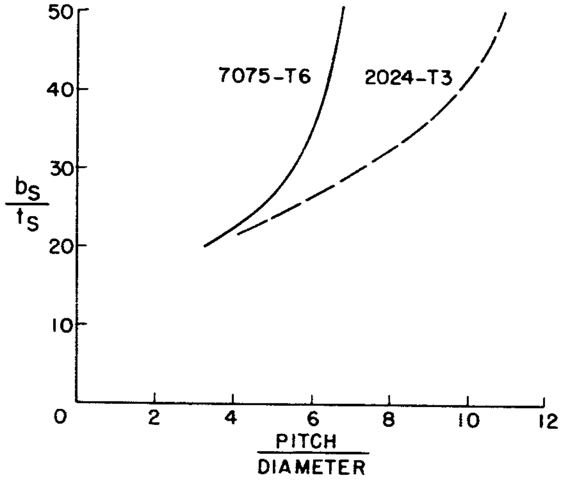

Figure 5

[redacted]

[redacted]

MINIMUM-WEIGHT STRUCTURES FOR WINGS OF GIVEN STRENGTH AND STIFFNESS

By B. Walter Rosen and Roger A. Anderson

Langley Aeronautical Laboratory

Efficiency diagrams derived on a strength-weight basis for certain components of a wing structure are in common use, although they are in many cases not directly applicable in the determination of minimum-weight wing design. The purpose of this report is to define a type of structural efficiency diagram which considers the entire compression structure of a wing and permits the determination of the minimum-weight design that satisfies both strength and stiffness requirements. The use of the diagram is demonstrated by several weight comparisons.

A common type of strength efficiency diagram is illustrated in figure 1. A plot of this type is used to show the efficiency with which plates supported at width b can transmit a compressive load per inch P_i. As in all efficiency charts, a measure of weight is plotted against a parameter which incorporates the design conditions for the structure. Here, failing stress is plotted logarithmically against the plate structural index P_i/b. For a plate, stress is inversely proportional to weight.

The curve for flat plates of 7075-T6 (formerly 75S-T6) aluminum alloy which will be used as the reference material in the comparisons to follow is presented. If plates of this material are integrally stiffened to improve their resistance to buckling, this efficiency can be improved as is shown by this curve for integrally stiffened waffle plates. The curve of equivalent stress, or maximum load divided by the average cross-sectional area, against the structural index indicates the resulting weight saving. The distance between the arrows represents a 10-percent weight change at any point on the logarithmic plot. Both of these curves are for plates made of an efficient material for low-temperature application.

For elevated-temperature applications, other materials must be used and the diagram of figure 1 can be used to indicate the plate efficiency of these materials. Thus, the lowest curve is for a heat treated SAE 4340 steel plate at 600° F. Maximum average stress has been multiplied by the ratio of densities of aluminum and steel to yield an equivalent stress for a direct weight comparison with these aluminum-alloy plates. The increased stiffness of steel is offset by the increased density, resulting in the large weight increases indicated by this diagram for plates at elevated temperatures.

[redacted]

When the efficiency of plate elements of a structure is viewed in this manner, indicated changes in structural weight tend to be exaggerated because resistance to buckling is the only consideration. The usefulness of this plot lies in the fact that qualitative effects of basic changes are immediately apparent. However, the weight change of a wing structure which results from these differences in plate efficiency will be influenced by the type of structure in which the plate is used. This will be shown by comparison with the structural efficiency analysis of multiweb wing construction.

A maximum strength analysis of multiweb design under a bending moment has been made and has been substantiated by numerous tests of fabricated multiweb beams.

The webs are of the minimum thickness required to prevent failure under the crushing loads resulting from beam bending and to prevent destabilization of the cover due to web buckling. The results of the analysis are shown in figure 2. Again a measure of weight has been plotted against a measure of loading intensity. These efficiency curves show the solidity A_i/H as a function of the structural index M_i/H^2. The design bending moment per chordwise inch is M_i, and H is the wing depth. The index, then, incorporates the design conditions for strength under a bending moment. The symbol A_i is the average cross-sectional area per chordwise inch of the compression skin and supporting members. The solidity is the ratio of area of compression and support material to total cross-sectional area of the structural box; the lower the value, the less the weight. Stress is not an adequate measure of efficiency for this structure.

In order to lend perspective to this diagram (fig. 2) the weight of a fictitious structure consisting of two unsupported cover skins acting at the compressive yield stress has been calculated and is given by the line labeled "MAX. EFF.". Actual structures will be of greater weight than such a structure because:

(1) Cover skins for most proportions have maximum stresses below the yield stress because of local instability.

(2) Web material is needed to support the covers.

Wing stiffness requirements are usually met by specifying a minimum skin gauge; therefore, skin thickness is treated as a primary variable. Each of the curves in figure 2 is for a different ratio of wing depth to skin thickness. Low values of H/t_s correspond to shallow thick-skin wings; high values, to deep or thin-skin wings. For given design conditions, each curve represents a different skin thickness t_s. Along one curve of constant t_S, the deviation from a horizontal line represents the weight increase resulting from increasing web weight required to stabilize the covers to higher stresses.

For each loading intensity, there is one skin thickness that yields minimum weight. The curve of optimum skin thicknesses is the lower envelope to these curves and it represents minimum structural weight from a strength viewpoint alone. This envelope curve is essentially what has been calculated by previous investigators of the strength-weight problem (for example, ref. 1). Figure 2 shows, in addition, weight changes resulting from changes in skin thickness dictated by wing stiffness requirements.

In most regions of the chart, increasing skin thickness $\left(\text{that is, decreasing } H/t_S\right)$ results in increased weight. For such proportions the minimum skin thickness that meets stiffness requirements will be the most efficient one that can be used. It is of interest to note however that, in certain regions, increasing skin thickness results in decreased weight. In such ranges, the envelope value of skin thickness will be most efficient for stiffness as well as strength.

The structural proportions corresponding to each point on these curves can be determined readily with the aid of a simple auxiliary diagram. The curves as presented are utilized in much the same manner as the commonly used plate efficiency plot (fig. 1); that is, for:

(1) Determining minimum weight for given design conditions

(2) Determining weight penalties associated with the use of non-optimum proportions

(3) Comparing the weight of this type of wing construction to any other.

The latter application is illustrated in figure 3 using the same materials for comparison that were used on the plate efficiency chart (fig. 1). The solid-line curves in figure 3 are taken from figure 2 and are presented for several H/t_S values. The arrows again indicate a 10-percent weight change.

One type of construction considered for comparison utilizes the aforementioned waffle plates of 7075-T6 aluminum as cover skins of a multiweb wing. This results in decreased weight in certain design ranges as shown by the long-dashed-line curves. The torsional stiffness of the waffle cover beams is the same as that of the solid cover beams of the H/t_S values shown. Waffle covers permit increased web spacing for a given cover load. This permits the web material to satisfy more efficiently the buckling and crushing requirements. As wing depth increases, webs become a greater portion of the total structure and the savings in web weight result in an increasingly larger saving in overall wing weight as shown by the larger gap between the curves for H/t_S of 50 as compared to those for H/t_S of 30. It is seen that the weight savings indicated by the plate efficiency chart (fig. 1) are difficult to achieve.

Next consider a structure made of the previously discussed steel for use at 600° F. The short-dashed-line curves represent optimum steel multiweb beams having the same torsional stiffness as room-temperature 7075-T6 beams with the H/t_S values indicated. Thus, there is roughly a factor of 3 between the skin thicknesses associated with corresponding curves. The solidity values for the steel wings take into account the density difference so that this is a direct weight comparison. For the deep steel wings, buckling is more of a problem than for the corresponding aluminum-alloy wings. Hence, more webs are required at a given loading intensity and they cause the rapid increase in weight shown. These weight differences are of the same order of magnitude as those shown on the plate efficiency chart. For the shallow thick-skin beams, however, buckling is not as serious a problem and web weight is a small portion of total weight. Thus, for high-speed aircraft with severe stiffness requirements, the indicated weight differences between steel wings at 600° F and aluminum-alloy wings of the same stiffness at room temperature are rather small for a large range of index values.

So far, the efficiency of several types of multiweb wing construction has been considered. It is also of interest to determine the ranges for efficient use of multiweb construction as compared with skin-stringer-rib construction. For this purpose, the extensive test data available for stiffened panels have been used to determine optimum proportions of skin-stringer wings. The effects of varying each of the panel dimensions have been considered. The skin-stringer-rib efficiency chart resulting from these computations is shown in figure 4. The parameters are the same as those used in the multiweb efficiency study. Skin thickness is a primary variable as before and, in addition, rib weight must be explicitly considered. Hence, rib spacing as well as stiffener size and spacing have been optimized. The results indicate that, from a maximum-strength viewpoint, there is no envelope to the curves and thin-skin construction is always most efficient, neglecting shear-lag effects. Hence, torsional stiffness requirements will govern the cover-skin thickness.

The band associated with the H/t_S value of 30 represents typical variations resulting from assumed rib weight. These particular computations assumed rib weight to be a simple function of the amount of material in the compression panel. The value of $t_R/\bar{t}$ was varied from 0.2 to 0.4 where t_R is the rib thickness of an equivalent flat-sheet rib

[redacted]

and $\bar{t}$ is the average or smeared out thickness of the compression panel. Thus doubling the rib thickness causes approximately a 10-percent change in overall weight.

Figure 5 shows the weight comparison between high-strength aluminum-alloy multiweb and panel-type constructions. Solid-line curves are for multiwebs and dashed-line curves for skin-stringer wings. For deep wings, as would be expected, panels show higher efficiency than multiweb wings. For about an H/t_S value of 30, it is seen that the two types could be used with essentially the same structural efficiency. In this region, the choice of construction will be influenced by various production considerations. For shallow thick-skin wings, multiweb construction is most efficient.

The comparisons presented demonstrate that an efficiency analysis must consider the entire compression structure of a wing including both strength and stiffness requirements. The establishment of optimum proportion curves such as those of figure 2 over the complete range of the design parameters permits a rather simple evaluation of minimum-weight design and of the effects on structural weight of any deviations therefrom, whether such deviations be in the form of changed dimensions, different materials, or other types of construction.

REFERENCE

1. Conway, William J.: Factors Affecting the Design of Thin Wings. Preprint No. 357, SAE Los Angeles Aero. Meeting, Oct. 5-9, 1954.

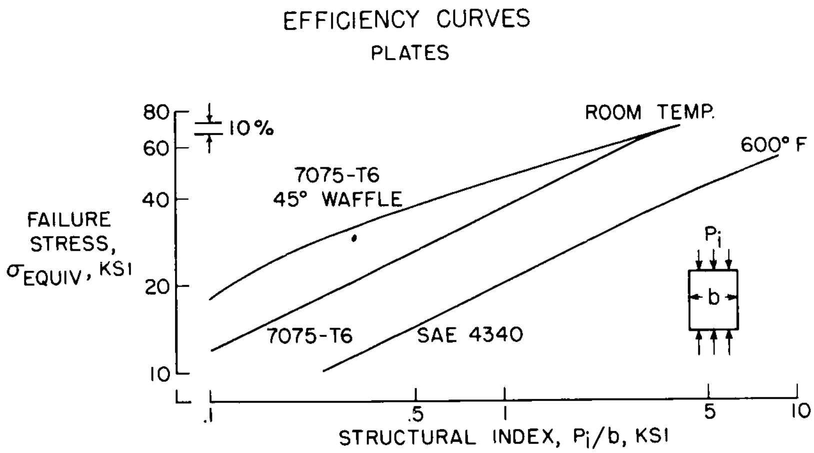

Figure 1

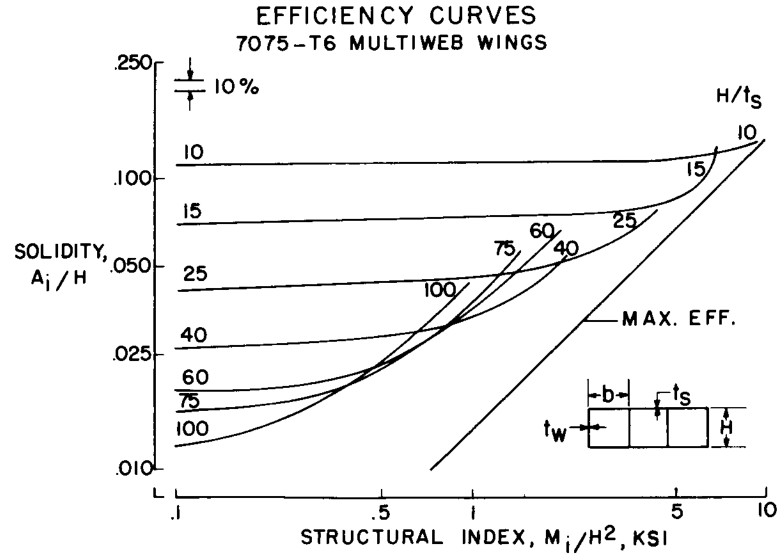

Figure 2

[redacted]

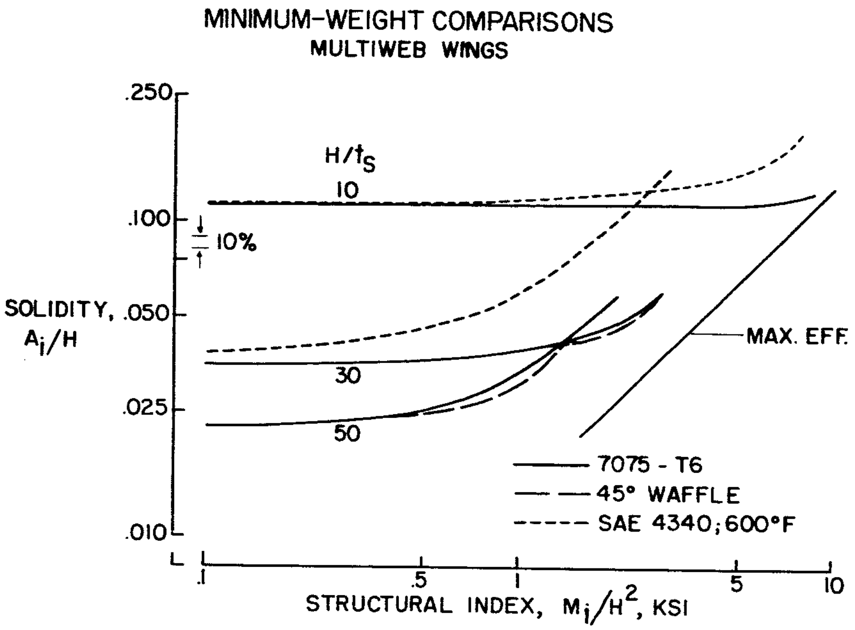

Figure 3

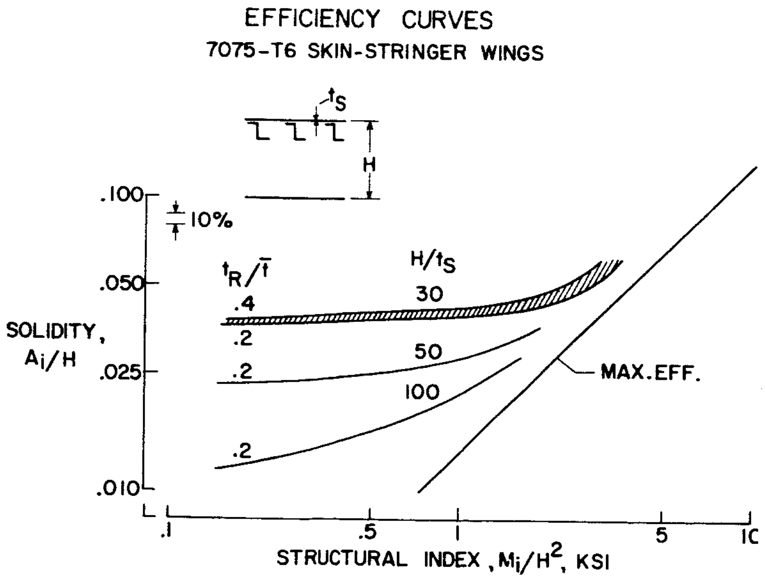

Figure 4

[redacted]

COMPARISON OF MULTIWEB AND
SKIN-STRINGER WING EFFICIENCY

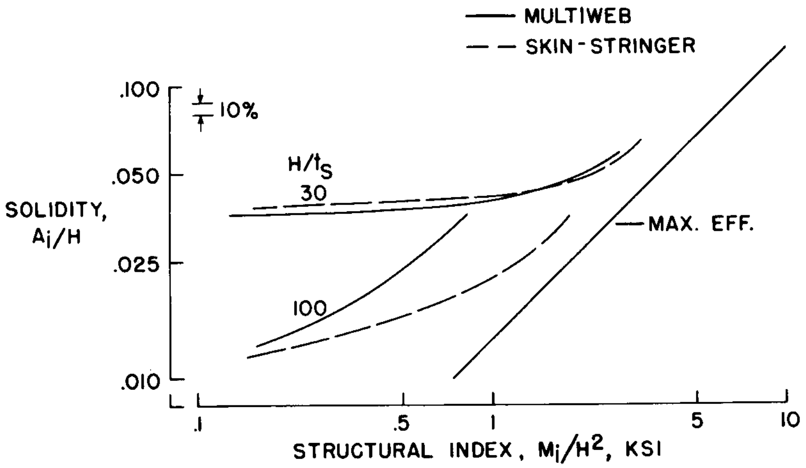

Figure 5

[redacted]

[redacted]

SOME OBSERVATIONS ON LOSS OF STATIC STRENGTH DUE TO FATIGUE CRACKS

By Walter Illg and Herbert F. Hardrath

Langley Aeronautical Laboratory

SUMMARY

Static tensile tests were performed on simple notched specimens containing fatigue cracks. Four types of aluminum alloys were investigated: 2024-T3 (formerly 24S-T3) and 7075-T6 (formerly 75S-T6) in sheet form, and 2024-T4 (formerly 24S-T4) and 7075-T6 (formerly 75S-T6) in extruded form. The cracked specimens were tested statically under four conditions: unmodified and with reduced eccentricity of loading by three methods. Results of static tests on C-46 wings containing fatigue cracks are also reported.

It was found that the static strength of 7075 aluminum alloy was somewhat more sensitive to fatigue cracks than was that of 2024 aluminum alloy. There was little difference between the behavior of extruded and sheet material in the same alloy. In cases where the eccentricity of loading was minimized, the effective stress-concentration factor for a fatigue crack at static failure was approximately 1.33. The built-up wing structure was found to have somewhat better strength properties than single-element parts for two reasons: (1) the adjoining structural elements provided restraints which minimized the eccentricity of loading on the failing section, and (2) the load was probably redistributed among the various elements during progressive failure in the wing.

INTRODUCTION

One problem of extreme practical interest which arises as the result of the formation of a fatigue crack of finite size is the prediction of the static strength of a member containing such a crack. Certain failures of aircraft in service and a very limited laboratory investigation indicated very serious loss of static strength due to small fatigue cracks. Other than this, information pertinent to this problem in aircraft structural materials is very sketchy.

In order to provide such information, the Structures Research Division of the Langley Aeronautical Laboratory has begun a systematic study of loss of static strength due to fatigue cracks in simple specimens. Figure 1 shows the configuration of the specimens used in this investigation.

[redacted]

[redacted]

TESTS AND SPECIMENS

The specimens were $2\frac{1}{4}$ inches wide and they had a free length of 12 inches between grips. Two semicircular notches with a $\frac{3}{8}$-inch radius were used to aid crack initiation. The net width in the test section was 1.5 inches. Four materials were tested: 2024 and 7075 aluminum alloys in both sheet and extruded forms.

The sheet material was 0.075 inch thick and the extruded material was 0.125 inch thick. The specimens were subjected to repeated axial tensile loads producing average net section stresses not greater than 35,000 pounds per square inch. At least 100,000 cycles were required to produce cracks of the desired length. The cracks were measured prior to static test with the aid of a toolmaker's microscope. Inspection of the surface after failure revealed a sharp contrast between fatigue-cracked and statically failed sections and indicated that the cracks had been measured with less than 1-percent error. More elaborate methods of checking crack depths were, therefore, not used. The specimens were then subjected to static test to determine the remaining static tensile strength. The maximum tensile load was reached after necking occurred at the ends of the cracks but before the crack lengths increased to a noticeable extent. Since the crack proceeded from only one side of a specimen in nearly all cases, the static load was eccentric with respect to the remaining material. The effect of this eccentricity on the results will be discussed subsequently.

RESULTS AND DISCUSSION

Figure 2 presents some of the results obtained in tests of 7075-T6 sheet specimens. The ordinate is the static strength of a cracked specimen expressed as a percentage of the static strength of an uncracked specimen. The abscissa is the percent of the original area remaining. The dashed line represents the strength of a cracked specimen based on the assumption that the loss of strength is equal to the loss of area. The symbols represent test points. The loss of static strength was found to be much greater than the loss of area over the complete range of the tests. The effect is most marked in the early stages of crack growth. For instance, when the net section was reduced to 90 percent, the strength was reduced to 50 percent.

A similar plot (fig. 3) presents a comparison between results of tests on 2024-T4 and 7075-T6 extrusions. The curve for 7075-T6 is essentially the same as that shown previously for 7075-T6 sheet; similarly, the curve for the 2024-T3 sheet is essentially the same as that

[redacted]

for extrusion shown in figure 3. The strength of the 2024 materials appears to have been reduced somewhat less than the strength of the 7075.

In contrast to these tests on simple specimens, the Loads Calibration Section of the Langley Aeronautical Laboratory has performed static tests of C-46 wings which were subjected to fatigue loading until varying amounts of tension material had been tested to failure. The results of these tests are presented in figure 4. In this case the static strength of the wing containing no fatigue cracks is the strength of the wing as estimated for a tensile failure. One specimen, containing a crack which removed 3 percent of the tension material in the critical cross section, failed by buckling of the compression cover at a load 8 percent lower than that predicted for tensile failure in a new wing. The remaining specimens failed in tension, and for cracks penetrating less than 30 percent of the material, the reduction in strength is approximately equal to that which would be predicted by loss of area alone. These results contrast sharply with the results of tests on simple specimens previously described.

In figure 4, the points with tails represent cases where the crack penetrated one or more spar caps or their connections during the fatigue loading. This large loss of primary structural material causes a large increase in the eccentricity of loading and a large decrease in the wing-section properties. When such radical structural changes are considered, the large deviations of the C-46 wings containing cracks which penetrated less than 30 percent, from predictions based on a simple analysis such as represented by the dashed line, are probably expected.

Two important differences in test conditions appear to be among the factors responsible for the greater strength of the C-46 wings containing cracks less than 30 percent. First, in the simple specimens the fatigue crack was almost always initiated on only one side of the specimen and this crack generally grew during the static test. The resulting eccentricity of loading undoubtedly contributed to the reduction in the static strength. For small cracks in the C-46 wing, the eccentricity of loading on the failing section is minimized by a very large effective moment of inertia to resist bending in the plane of the cover; therefore somewhat better strength might be expected. Second, in the case of the C-46 wing with small cracks, whenever a given element fails, the load it carried may be shared by other elements which do not contain fatigue cracks. Depending upon the relative stiffnesses of the various elements, the remaining parts may carry more load than they were carrying previously. In the simple specimens, the stress is shifted to the neighboring material, but a very high stress concentration as a result of the crack is still present.

The effect of eccentricity of loading in simple specimens was studied by modifying specimens [redacted] fatigue cracks in such a way

[redacted]

DECL[redacted]ED

that the bending stress on the failing section was at least partially eliminated. This was accomplished in three ways as shown in figure 5.

The first sketch of the figure shows an unmodified specimen containing a fatigue crack. In the specimens illustrated by the second sketch, material was removed from the cracked side of the specimens so that the depth of the crack was equal to the depth of the notch on the other side. The third sketch illustrates those specimens in which a cut was made with a fine jeweler's saw to simulate a crack on the side opposite the fatigue crack, and finally the fourth sketch shows the specimens shortened to 4 inches between the grips instead of 12 inches as in the other specimens.

The results for 2024-T3 sheet are shown in figure 6. The circles in this figure represent tests on unmodified specimens, and the triangles, squares, and diamonds represent tests in which the specimens were modified in the aforesaid three ways to reduce the eccentricity of loading and thereby the bending stress on the failing section. The results of these three series of tests are essentially the same and show a significant improvement in strength over most of the range of the tests. The dashed line was computed on the assumption that the stress on the failing section was 75 percent of the original ultimate tensile strength. In other words, it appears that the effective stress-concentration factor of a fatigue crack at static failure was about 1.33. The greater reduction of strength for the unmodified specimens was evidently due to the bending stresses set up by unsymmetrical loading. This eccentricity was less important for small cracks than for large ones, and the tests indicated equivalent strengths for the small cracks.

SUMMARY OF RESULTS

Although the tests performed to date are not sufficient to arrive at definite relationships for loss of static strength, the following qualitative conclusions seem justified. The static strength of 7075 aluminum alloy was somewhat more sensitive to fatigue cracks than was that of 2024 aluminum alloy. There was little difference between the behavior of extruded and sheet material in the same alloy. In cases where the eccentricity of loading was minimized, the effective stress concentration for a fatigue crack under static load was approximately 1.33. A complex structure is likely to have somewhat better strength properties than single-element parts for two reasons: (1) the adjoining structural elements usually provide restraints which minimize eccentricity of loading on the failing section, and (2) the load is probably redistributed among the various elements during progressive failures.

[redacted]

[redacted]

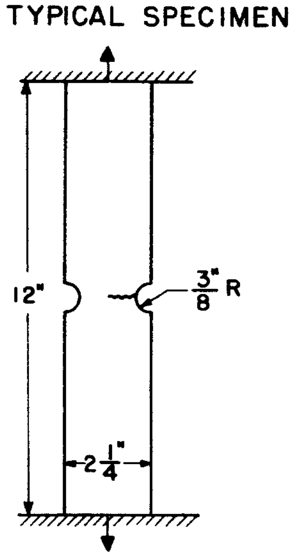

Figure 1

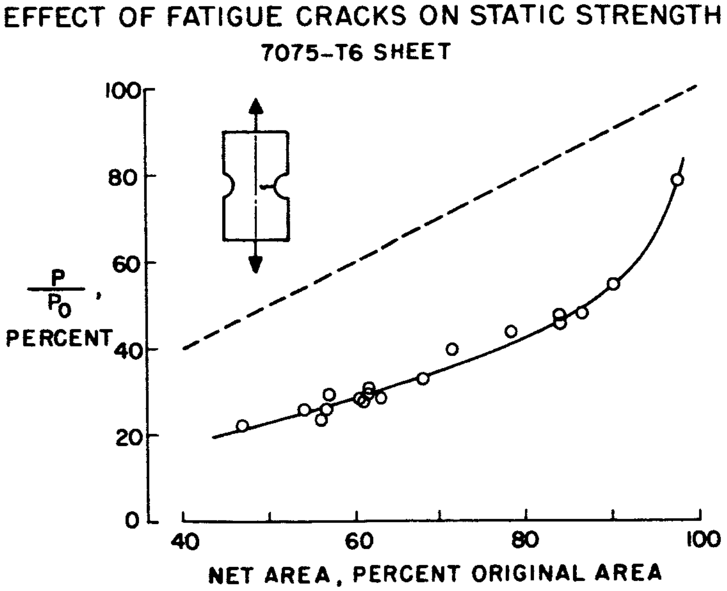

Figure 2

[redacted]

[redacted]

EFFECT OF FATIGUE CRACKS ON STATIC STRENGTH
2024-T4 AND 7075-T6 EXTRUSIONS

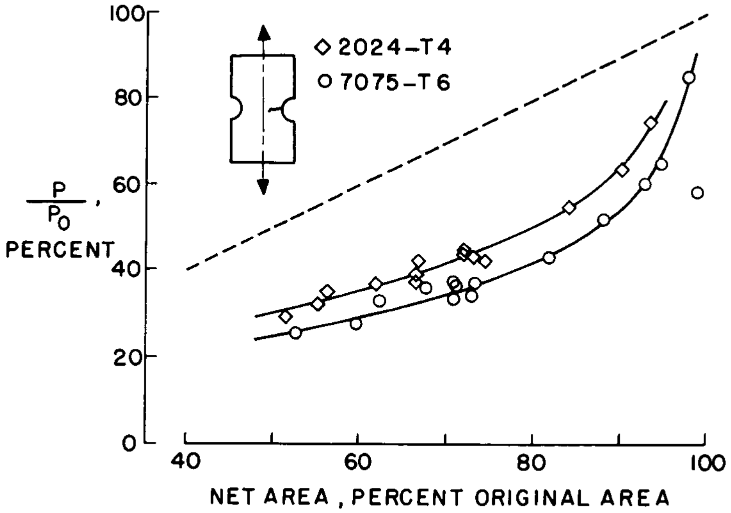

Figure 3

EFFECT OF FATIGUE CRACKS ON STATIC STRENGTH
C-46 WINGS

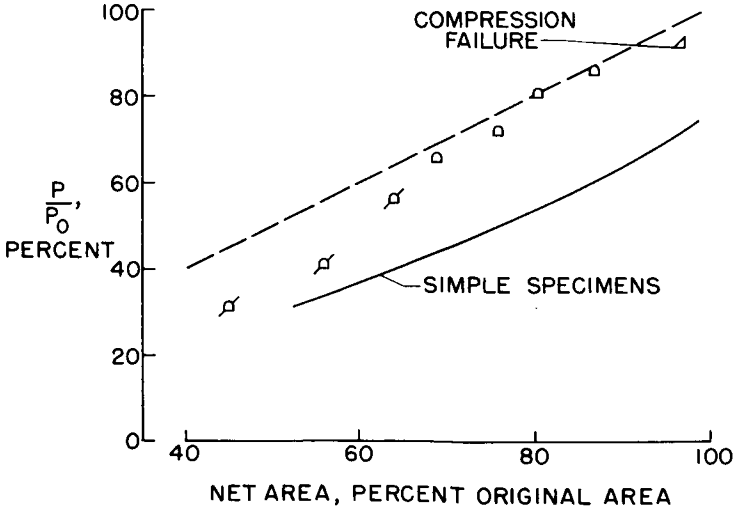

Figure 4

[redacted]

[redacted]

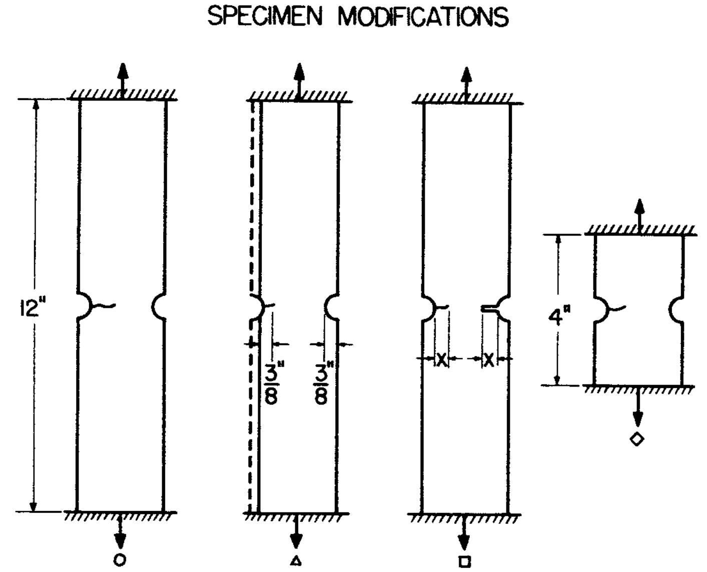

Figure 5

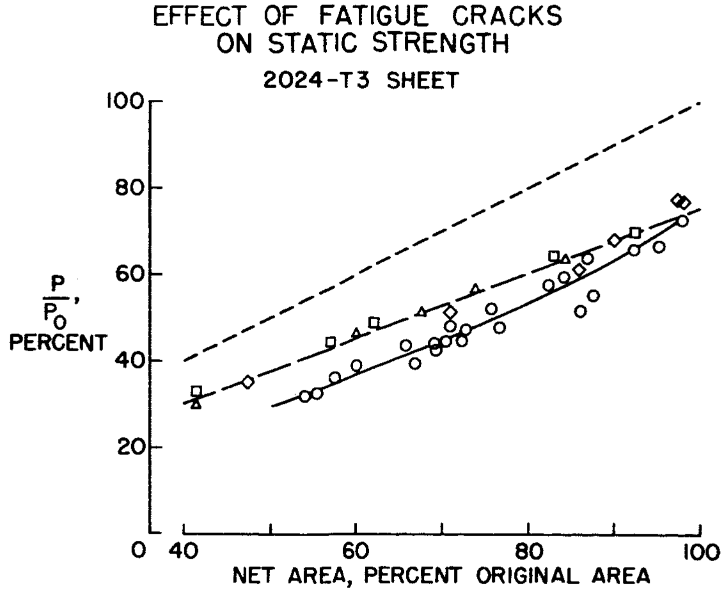

Figure 6

[redacted]

[redacted]

PRELIMINARY INVESTIGATION OF THE FAILURE OF PRESSURIZED STIFFENED CYLINDERS

By Norris F. Dow and Roger W. Peters

Langley Aeronautical Laboratory

INTRODUCTION

The failures of pressurized fuselages that have occurred have varied in character from rather minor rupture to catastrophic explosion (ref. 1). The factors which influence the seriousness of the failure are being investigated in the Langley structures research laboratory. Various structural configurations and loading conditions are being tested in an effort to determine which are conducive to mild failure on the one hand and explosive failure on the other.

SYMBOLS

A_R	minimum cross-sectional area of ring, in.^{2}
L	ring spacing, in.
p	internal pressure, ksi
R	radius of cylinder, in.
t_S	skin thickness, in.
δ_{cr}	maximum length of crack that can be tolerated before explosive failure of cylinder occurs, in.
σ_{Hoop}	simple hoop tension stress in skin, pR/t_S, ksi

TEST SPECIMENS

Two cylinder configurations (fig. 1) approximately representative of 1/4-scale models of fuselage construction have been studied so far. The cylinders are identical except for skin gages and ring spacings - 0.012-inch skin thickness and 7.5-inch ring spacing on the first cylinder and 0.040-inch skin thickness and 15-inch ring spacing on the second

[redacted]

[redacted]

cylinder. The rings are 0.051-inch spun Z-sections, $1\frac{1}{4}$ inches deep, notched for the 20 longitudinal Z-section stringers to have a ring cross-sectional area A_R above the notch of 0.063 square inch. The longitudinals are 0.040-inch-thick extrusions having a web-width—thickness ratio of $12\frac{1}{2}$ and an outstanding ratio of flange width to web height of 0.4. The cross-sectional area of the longitudinals is 0.045 square inch. All material is 2024-T3 or 2024-T4 (formerly 24S-T3 and 24S-T4, respectively) aluminum alloy.

The proportions described were chosen for investigation on the basis of the elementary consideration illustrated in figures 2 and 3.

DESIGN CONSIDERATIONS FOR TEST SPECIMENS

Analysis of the failure of pressurized cylinders on the most elementary possible basis suggested that, if a crack opens up in the skin of a cylinder, it must grow to some critical proportion of the distance between rings δ_{cr}/L before explosive propagation of the crack occurs. According to this highly simplified analysis, the critical crack length varies from zero, when the hoop tension in the skin is equal to the ultimate strength of the material, to a length equal to the ring spacing at the stress at which the rings alone have sufficient area to carry the hoop-tension load. Thus, at $\delta_{cr}/L = 1$, for an ultimate tensile strength of 70 ksi,

$$\frac{pRL}{A_R} = 70 \tag{1}$$

or

$$\frac{pR}{t_S} = 70\,\frac{A_R}{Lt_S} = \sigma_{Hoop} \tag{2}$$

If a linear variation with stress from $\delta_{cr}/L = 0$ to $\delta_{cr}/L = 1$ is assumed, the critical crack length depends directly upon the reinforcement ratio, that is, the ratio of cross-sectional area in the rings A_R to the associated skin area Lt_S. Thus, the critical crack length at a given hoop stress is longer for a large value of A_R/Lt_S than for a small value of the reinforcement ratio; hence, the cylinder with the large value of A_R/Lt_S is less prone to explosive failure.

[redacted]

Because this analysis is oversimplified, the plotted straight-line relationship (fig. 2) for critical crack length should perhaps be regarded as an upper limit or maximum value which can never actually be achieved. Such factors as bulging of skin between rings and local stress concentrations probably tend to reduce the length of crack that can be tolerated appreciably below that given by the straight-line relationship. A rigorous analysis of the stress distribution along the cracked skin is required to establish a true critical-crack-length criterion.

However, because the end points - that is, when the critical crack length to ring spacing ratio is equal to one - represent rings of heavy enough cross section to carry the entire hoop-tension load by themselves with the skin cracked over the full bay length; in that case, this simplified analysis may come into better agreement with more rigorous analysis.

With these end points (see fig. 2) as a criterion, for example, for a hoop tensile stress much above 7 ksi, the cylinder with the 0.040-inch skin thickness is in danger of having a short critical crack length and hence is in danger of explosive failure, whereas for a hoop tensile stress appreciably less than 40 ksi, the cylinder with the 0.012-inch skin thickness should be unlikely to explode even if the crack grows over the full distance between the rings.

With hoop tension plotted against the reinforcement ratio (fig. 3) as given by the end points of the curves of figure 2, this criterion thus roughly suggests that there may be a boundary between regions of slow and explosive crack propagation. The boundary, drawn in figure 3, being just a crossplot of the end points of figure 2 represents the ring area required at any hoop tension to carry the entire hoop-tension load with the skin cracked along the entire bay length, as calculated from equation (2).

In order to investigate whether the regions of slow and explosive crack growth shown in figure 3 exist, cylinders of the proportions previously described were built and tested at identical values of hoop tension as indicated by the x point representative of the thick-skinned cylinder and the circle point representative of the thin-skinned cylinder.

DESCRIPTION OF TESTS

The tests were run in the combined load testing machine of the Langley structures research laboratory as shown in figure 4.

Internal pressure was supplied from a hydraulic pumping unit and held constant throughout the test. A cycling device was fitted to the torsion loading component to apply cyclic shear at the 2-inch square

[redacted]

cutout in the center of the cylinder and thus induce a fatigue crack in the skin.

In the test of the 0.012-inch cylinder, the internal pressure was held constant at the value required to give a hoop tensile stress of 20 ksi. A cyclic torsion loading of ±210 inch-kips was applied, and the first crack was induced at the upper left-hand corner of the cutout after 281 load cycles. (See fig. 5.) As the crack gradually grew, more and more oil was pumped into the cylinder to maintain the internal pressure constant. Eventually cracks opened up at all four corners of the cutout and grew to such a size that, at maximum pumping capacity, pressure could not be maintained; and the test was terminated after 528 load cycles.

In the test on the cylinder with the 0.040-inch skin at the same hoop stress of 20 ksi, the applied torsion was ±820 inch-kips in order to produce stress conditions similar to those existing in the thinner skin cylinder under a torque of 210 inch-kips. Again the crack started at the upper left-hand corner of the cutout. (See fig. 6.) The number of cycles before cracking in this case was 136. The crack grew rapidly with succeeding load cycles, but before it had progressed very far the cylinder exploded. Explosion occurred at zero applied torsion load after $147\frac{1}{2}$ load cycles.

RESULTS AND CONCLUDING DISCUSSION

Tests of two cylinders subjected to nearly identical stress conditions and constructed with identical internal reinforcing structure except for ring spacing revealed very different characteristics as regards crack growth for the two specimens. As predicted by the simple criterion used for the design of the test specimens, the thick-skinned cylinder exploded and the crack in thin-skin cylinders grew in a less destructive manner. Thus, it has been established that regions of slow as well as explosive crack growth exist for pressurized stiffened cylinders.

Further testing will be required to clarify the factors which determine the boundary between safe and unsafe conditions for pressurized cylinders to determine accurately where the boundary lies and to determine the range of usefulness of such a simplified criterion as that used herein. That the range of application of this criterion must be limited to some extent is clear since it obviously does not apply, for example, to completely unstiffened cylinders. The primary objectives of the present study are to establish the relative importance of

[redacted]

[redacted]

the various factors involved in the failure of pressurized cylinders and to determine ways - possibly similar to the method of this paper - of evaluating whether a given design is in a safe or unsafe region.

REFERENCE

1. Anderton, David A.: RAE Engineers Solve Comet Mystery. Aviation Week, vol. 62, no. 6, Feb. 7, 1955, pp. 28-30, 34, 37, 39, 40, 42.

[redacted]

[redacted]

DECLASSIFIED

[redacted]

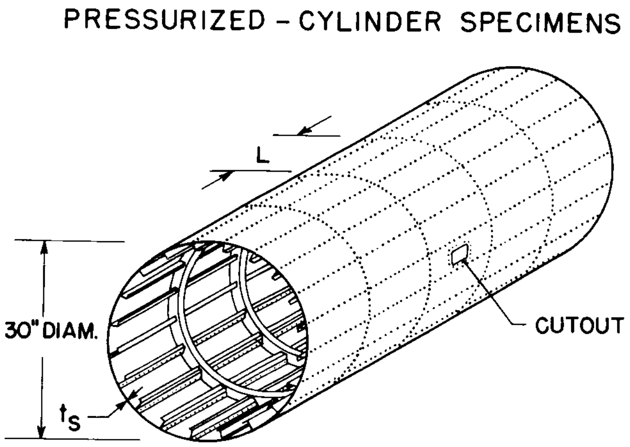

CYLINDER	t_S	L
1	0.012	7.5
2	.040	15

Figure 1

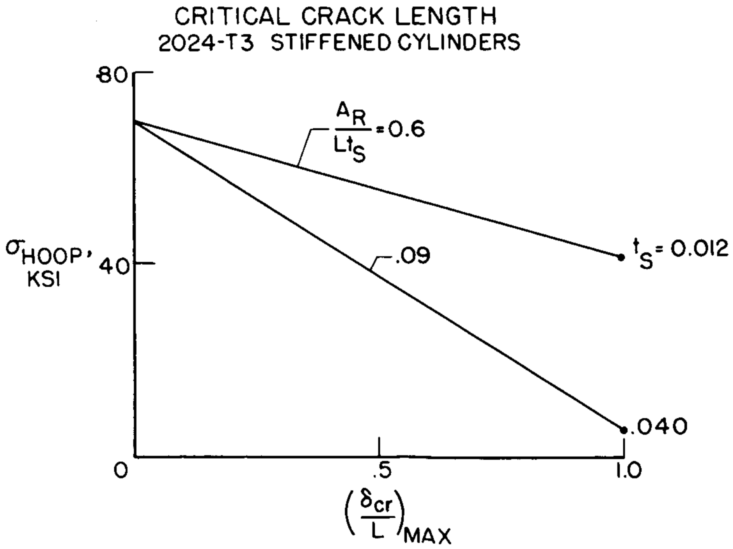

Figure 2

[redacted]

[redacted]

[redacted]

REGIONS OF SLOW AND EXPLOSIVE CRACK GROWTH
2024-T3 STIFFENED CYLINDERS

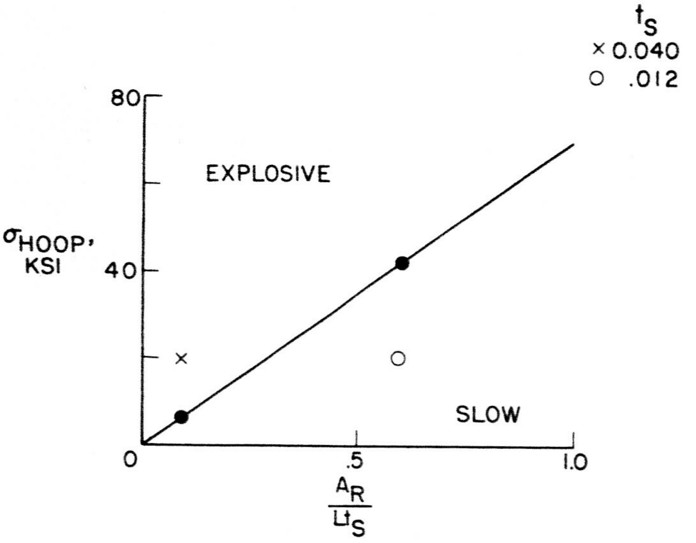

Figure 3

TEST ARRANGEMENT FOR PRESSURIZED CYLINDERS

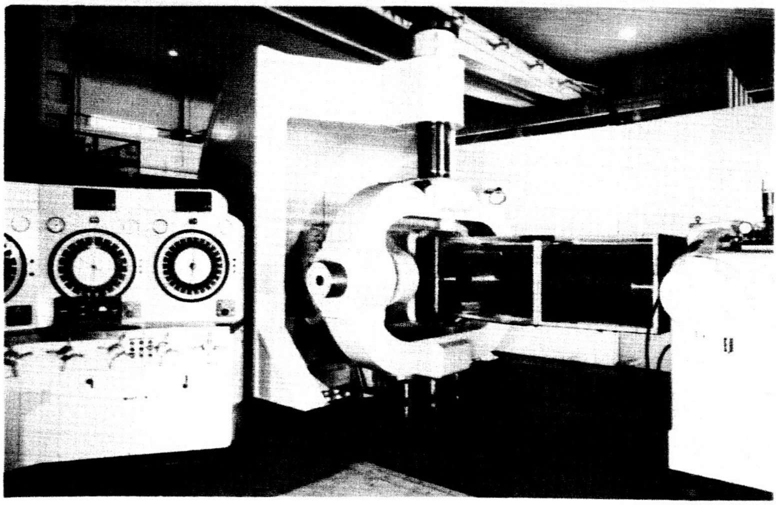

Figure 4

[redacted]

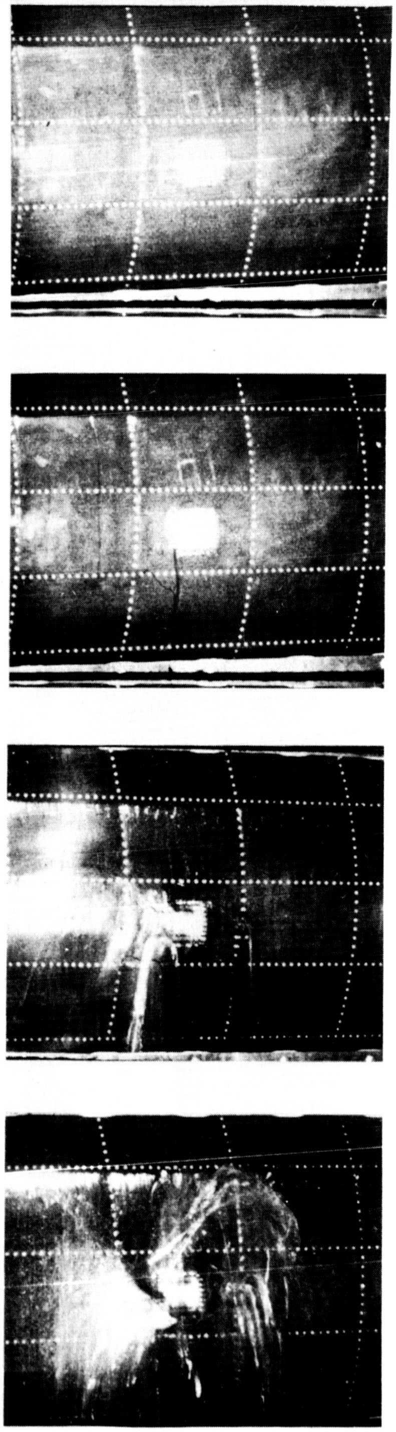

GROWTH OF CRACK IN CYLINDER
WITH 0.012-INCH SKIN THICKNESS

Figure 5

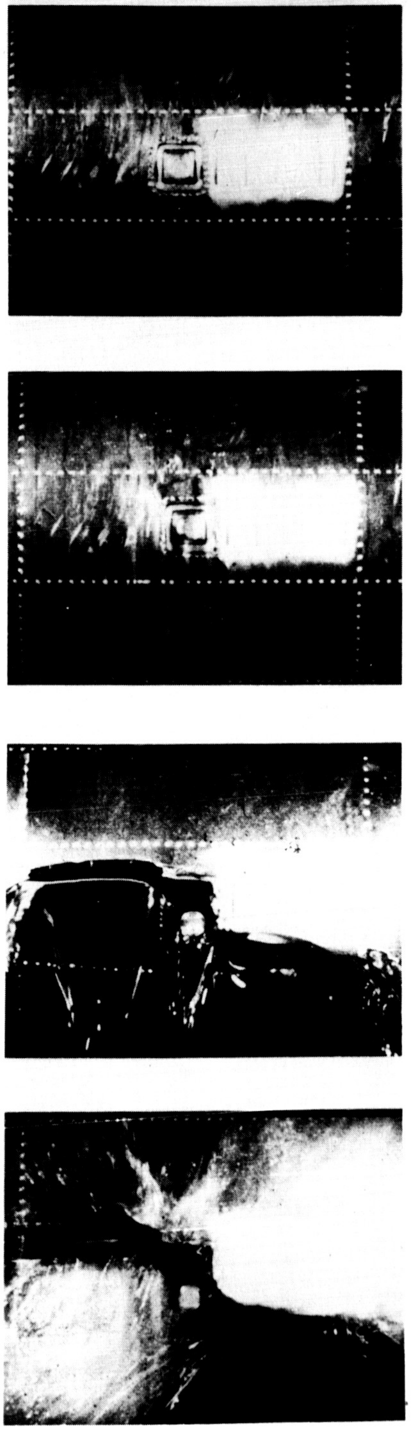

GROWTH OF CRACK IN CYLINDER
WITH 0.040-INCH SKIN THICKNESS

Figure 6

[redacted]

NACA-Langley - 3-18-55 - 625